Do cancers really have identifiable microbiomes? p. 590

Conductive bioadhesives for wet tissues pp. 608 & 686

African hydropower is getting less competitive p. 645

Science

$15
11 AUGUST 2023
SPECIAL ISSUE
science.org
AAAS

AUSTRALIA

ENVIRONMENTAL CHALLENGES

NEW ENGLAND BioLabs® Inc.

be INSPIRED
drive DISCOVERY
stay GENUINE

Clone with Confidence.

Whether you are performing your first cloning experiment or constructing multi-fragment DNA assemblies, NEB® has the solution for you. Our high quality reagents are available for every workflow, including popular DNA assembly methods such as NEBuilder® HiFi DNA Assembly and NEBridge® Golden Gate Assembly. We also offer solutions for automation, site-directed mutagenesis, as well as your favorite restriction enzyme, ligase or competent cell products. When you are looking to clone with confidence, think of NEB.

Explore the wise choice at
CloneWithNEB.com.

Products and content are covered by one or more patents, trademarks and/or copyrights owned or controlled by New England Biolabs, Inc (NEB). The use of trademark symbols does not necessarily indicate that the name is trademarked in the country where it is being read; it indicates where the content was originally developed. The use of these products may require you to obtain additional third-party intellectual property rights for certain applications. For more information, please email busdev@neb.com.

© Copyright 2023, New England Biolabs, Inc.; all rights reserved.

CONTENTS

11 AUGUST 2023 • VOLUME 381 • ISSUE 6658

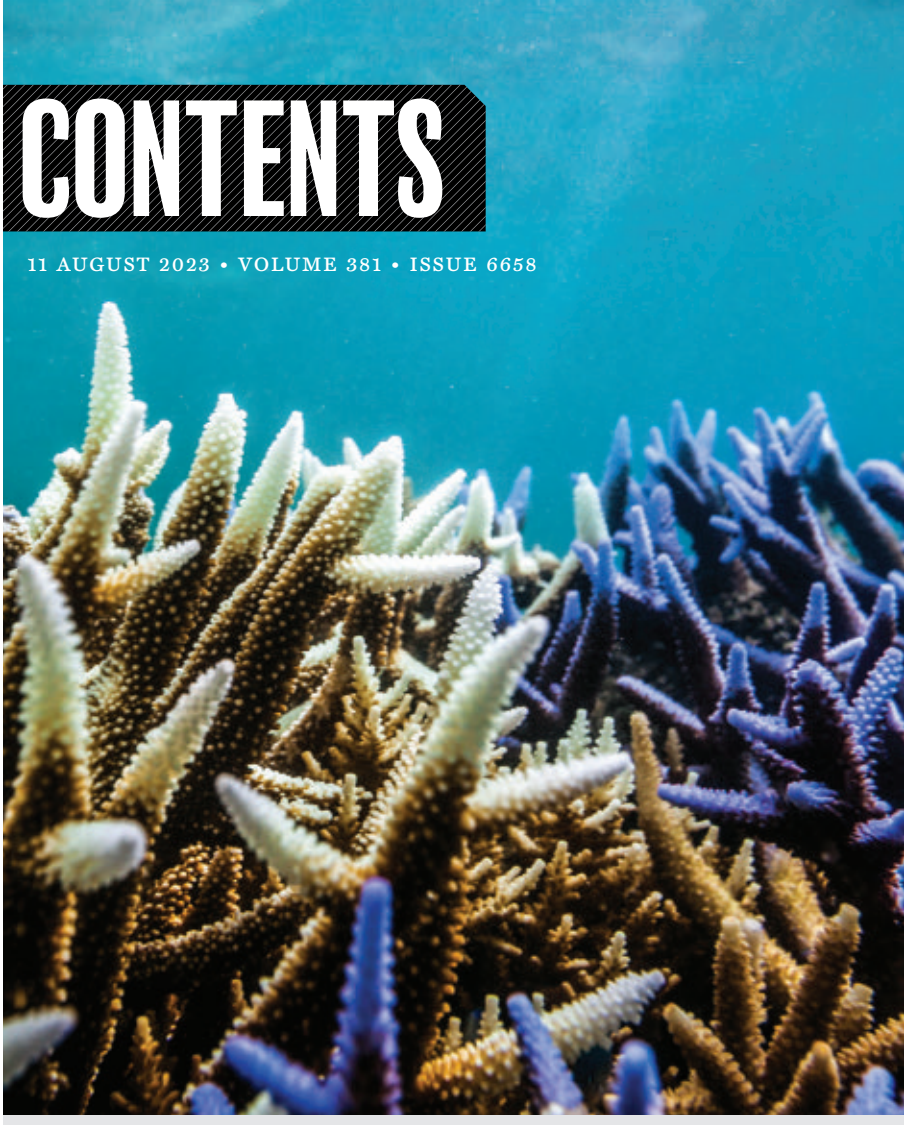

PHOTO: ABRAM POWELL/GREENPEACE

SPECIAL SECTION

Australia's environmental challenges

INTRODUCTION

614 Lessons from ecosystems in crisis

PERSPECTIVE

616 Taming the flame, from local to global extreme wildfires
D. M. J. S. Bowman and J. J. Sharples

POLICY FORUM

619 Cultural water and Indigenous water science *E. O'Donnell* et al.

REVIEWS

622 Loss of terrestrial biodiversity in Australia: Magnitude, causation, and response *S. Legge* et al.

631 Management approaches to conserve Australia's marine ecosystem under climate change *L. K. Bay* et al.

636 Justice, culture, and relationships: Australian Indigenous prescription for planetary health *V. Matthews* et al.

ON THE COVER

Australia has been subject to a wide variety of large-scale, environmentally damaging events, from decimation of its distinctive biodiversity to extreme wildfires. Harvesting Indigenous knowledge for landscape management, such as controlled burns practiced by the Nawarddeken people of West Arnhem Land, can offer alternative ways of reducing risks. This image shows controlled burning, using aerial drops of incendiary devices, guided by Indigenous advice. See the special section beginning on page 614. *Photo: Matthew Abbott*

SEE ALSO NEWS STORY p. 598

NEWS

IN BRIEF

588 News at a glance

IN DEPTH

590 Key study of cancer microbiomes challenged
"Major" errors may undermine research that identified cancers based on their microbes
By C. Offord

591 Observatory to probe origins of ferocious gamma rays
With approval imminent, construction will soon begin on Cherenkov Telescope Array
By D. Clery

593 Superconductivity claim electrifies social media
Report of room-temperature material goes viral, but many physicists are skeptical
By A. Cho

594 NASA scales back its next flagship climate mission
As two landmark satellites go dark, cuts loom for new bid to probe clouds, aerosols, and warming *By P. Voosen*

595 On the Afghanistan-Iran border, a fight over water
Researchers fear a warming climate is intensifying a sometimes violent conflict
By R. Kumar

596 Disease alert system in trouble
Money woes and staff strike threaten ProMED dispatches *By S. Reardon*

FEATURES

598 Wandering seeds
Millennia before Europeans arrived in Australia, humans helped shape the distribution of the continent's plants *By E. Pennisi*
AUSTRALIA'S ENVIRONMENTAL CHALLENGES SECTION p. 614

INSIGHTS

PERSPECTIVES

602 A mammalian DNA methylation landscape
A study of 348 species offers clues into the diversity of mammalian life spans
By A. de Mendoza
RESEARCH ARTICLE p. 647

604 Fine tuning an atomic mesh
Controlling the angle in atomic meshes could result in quantum properties on demand
By J. Park
RESEARCH ARTICLE p. 677

WE DON'T JUST APPLAUD YOUNG RESEARCHERS. WE REWARD THEM.

Submit your innovative research and you can not only win $30,000 but get your work published in the print and online editions of *Science*. The Michelson Philanthropies & *Science* Prize for Immunology was created to support and reward young investigators across a wide range of disciplines who make a long-lasting impact on vaccine development and immunotherapy research. This prestigious award is given annually to honor bold, trailblazing, and transformative research completed in the past three years. The winner will receive a grand prize of $30,000, and two finalists will be awarded $10,000 each.

"Through this partnership with Science, we offer the next generation of innovators financial support, a network of experts, and a renowned platform for their bold ideas."
Dr. Gary K. Michelson
Founder & Co-Chair of
Michelson Philanthropies
MICHELSON
PHILANTHROPIES
& Science
PRIZE FOR
IMMUNOLOGY

Apply by October 1, 2023, to enter to win $30K and get published in *Science*

michelsonmedical.org/prize

DNA methylation patterns relate to species characteristics such as life span.

605 Using climate to model ancient human migration
Modeling fills gaps in the fossil record of early hominin movement from Africa *By E. J. Beverly*
RESEARCH ARTICLES pp. 693 & 699

607 Plastic waste recycling is gaining momentum
Production of detergents and aldehydes could help tackle plastic pollution
By K. M. Van Geem
RESEARCH ARTICLES pp. 660 & 666

608 Tissue adhesive semiconductors
Bioelectronic implants could use semiconductors that adhere to wet, dynamic tissues *By S. J. Wu and X. Zhao*
RESEARCH ARTICLE p. 686

BOOKS *ET AL.*

610 The forgotten future of the phage
As antibiotic resistance soars, a journalist revisits an often overlooked antimicrobial strategy *By A. Woolfson*

611 Linnaeus and his life's work
A historian's unvarnished biography reveals the complicated man who invented modern taxonomy *By D. Incorvaia*

LETTERS

612 China's canal project threatens biodiversity *By Q. Yang and S. Yang*

612 Begin ocean garbage cleanup immediately *By Z. Long*

613 Rapid reversal of ecological extinction *By D. McAfee and S. D. Connell*

RESEARCH

IN BRIEF

642 From *Science* and other journals

RESEARCH ARTICLES

645 Renewable energy
Declining cost of renewables and climate change curb the need for African hydropower expansion *A. Carlino* et al.
RESEARCH ARTICLE SUMMARY; FOR FULL TEXT: DOI.ORG/10.1126/SCIENCE.ADF5848

646 Melanogenesis
A genome-wide genetic screen uncovers determinants of human pigmentation
V. K. Bajpai et al.
RESEARCH ARTICLE SUMMARY; FOR FULL TEXT: DOI.ORG/10.1126/SCIENCE.ADE6289

647 Evolutionary biology
DNA methylation networks underlying mammalian traits *A. Haghani* et al.
RESEARCH ARTICLE SUMMARY; FOR FULL TEXT: DOI.ORG/10.1126/SCIENCE.ABQ5693
PERSPECTIVE p. 602

648 Nanophotonics
Wafer-scale δ waveguides for integrated two-dimensional photonics *M. Lee* et al.

653 Molecular biology
RHINO directs MMEJ to repair DNA breaks in mitosis *A. Brambati* et al.

Plastic upcycling
660 Hydroformylation of pyrolysis oils to aldehydes and alcohols from polyolefin waste *H. Li* et al.
666 Chemical upcycling of polyethylene, polypropylene, and mixtures to high-value surfactants *Z. Xu* et al.
PERSPECTIVE p. 607

672 Plant water use
Global water use efficiency saturation due to increased vapor pressure deficit
F. Li et al.

677 2D materials
Programming twist angle and strain profiles in 2D materials *M. Kapfer* et al.
PERSPECTIVE p. 604

682 Cancer detection
Engineered bacteria detect tumor DNA
R. M. Cooper et al.

686 Biomaterials
Bioadhesive polymer semiconductors and transistors for intimate biointerfaces
N. Li et al.
PERSPECTIVE p. 608

Human evolution
693 Extreme glacial cooling likely led to hominin depopulation of Europe in the Early Pleistocene *V. Margari* et al.
699 Climate shifts orchestrated hominin interbreeding events across Eurasia
J. Ruan et al.
PERSPECTIVE p. 605

DEPARTMENTS

587 Editorial
Generative approach to research integrity
By H. H. Thorp

706 Working Life
Sustained by science
By M. J. Dean

Science Staff 586
Science Careers 705

SCIENCE (ISSN 0036-8075) is published weekly on Friday, except last week in December, by the American Association for the Advancement of Science, 1200 New York Avenue, NW, Washington, DC 20005. Periodicals mail postage (publication No. 484460) paid at Washington, DC, and additional mailing offices. Copyright © 2023 by the American Association for the Advancement of Science. The title SCIENCE is a registered trademark of the AAAS. Domestic individual membership, including subscription (12 months): $165 ($74 allocated to subscription). Domestic institutional subscription (51 issues): $2411; Foreign postage extra: Air assist delivery: $107. First class, airmail, student, and emeritus rates on request. Canadian rates with GST available upon request, GST #125488122. Publications Mail Agreement Number 1069624. **Printed in the U.S.A.**
Change of address: Allow 4 weeks, giving old and new addresses and 8-digit account number. **Postmaster:** Send change of address to AAAS, P.O. Box 96178, Washington, DC 20090–6178. **Single-copy sales:** $15 each plus shipping and handling available from backissues.science.org; bulk rate on request. **Authorization to reproduce** material for internal or personal use under circumstances not falling within the fair use provisions of the Copyright Act can be obtained through the Copyright Clearance Center (CCC), www.copyright.com. The identification code for *Science* is 0036-8075. *Science* is indexed in the *Reader's Guide to Periodical Literature* and in several specialized indexes.

PHOTO: ANUP SHAH/MINDEN PICTURES

Science AAAS

Editor-in-Chief Holden Thorp, hthorp@aaas.org

Executive Editor Valda Vinson

Editor, Research Jake S. Yeston **Editor, Insights** Lisa D. Chong **Managing Editor** Lauren Kmec

DEPUTY EDITORS Gemma Alderton (UK),Stella M. Hurtley (UK), Phillip D. Szuromi, Sacha Vignieri **SR. EDITORS** Caroline Ash (UK), Elisa Collado Fregoso (UK), Michael A. Funk, Brent Grocholski, Di Jiang, Priscilla N. Kelly, Marc S. Lavine (Canada), Sarah Lempriere (UK), Mattia Maroso, Yevgeniya Nusinovich, Ian S. Osborne (UK), L. Bryan Ray, Seth Thomas Scanlon (UK), H. Jesse Smith, Keith T. Smith (UK), Jelena Stajic, Peter Stern (UK), Valerie B. Thompson, Brad Wible **ASSOCIATE EDITORS** Bianca Lopez, Madeleine Seale (UK), Corinne Simonti, Yury V. Suleymanov, Ekeoma Uzogara **LETTERS EDITOR** Jennifer Sills **NEWSLETTER EDITOR** Christie Wilcox **RESEARCH & DATA ANALYST** Jessica L. Slater **LEAD CONTENT PRODUCTION EDITORS** Chris Filiatreau, Harry Jach **SR. CONTENT PRODUCTION EDITOR** Amelia Beyna **CONTENT PRODUCTION EDITORS** Anne Abraham, Robert French, Julia Haber-Katris, Nida Masiulis, Abigail Shashikanth, Suzanne M. White **SR. EDITORIAL MANAGERS** Carolyn Kyle, Beverly Shields **SR. PROGRAM ASSOCIATE** Maryrose Madrid **EDITORIAL ASSOCIATE** Joi S. Granger **SR. EDITORIAL COORDINATORS** Aneera Dobbins, Jeffrey Hearn, Lisa Johnson, Ronmel Navas, Jerry Richardson, Alice Whaley (UK), Anita Wynn **EDITORIAL COORDINATORS** Maura Byrne, Clair Goodhead (UK), Alexander Kief, Isabel Schnaidt, Qiyam Stewart, Brian White **ADMINISTRATIVE COORDINATOR** Karalee P. Rogers **ASI DIRECTOR, OPERATIONS** Janet Clements (UK) **ASI OFFICE MANAGER** Victoria Smith **ASI SR. OFFICE ADMINISTRATORS** Dawn Titheridge (UK), Jessica Waldock (UK) **SCIENCE PRESS PACKAGE EXECUTIVE DIRECTOR** Meagan Phelan **DEPUTY DIRECTOR** Matthew Wright **SENIOR WRITER** Walter Beckwith **WRITERS** Joseph Cariz, Abigail Eisenstadt, Nyla Hussain **SENIOR COMMUNICATIONS ASSOCIATE** Zachary Graber **COMMUNICATIONS ASSOCIATES** Kiara Brooks, Haley Riley, Mackenzie Williams, Sarah Woods

News Editor Tim Appenzeller

NEWS MANAGING EDITOR John Travis **INTERNATIONAL EDITOR** David Malakoff **DEPUTY NEWS EDITORS** Rachel Bernstein, Shraddha Chakradhar, Elizabeth Culotta, Martin Enserink, David Grimm, Eric Hand (Europe) Kelly Servick **SR. CORRESPONDENTS** Daniel Clery (UK), Jon Cohen, Jeffrey Mervis, Elizabeth Pennisi **ASSOCIATE EDITORS** Jeffrey Brainard, Michael Price **NEWS REPORTERS** Adrian Cho, Jennifer Couzin-Frankel, Jocelyn Kaiser, Rodrigo Pérez Ortega (Mexico City), Robert F. Service, Erik Stokstad, Paul Voosen, Meredith Wadman **CONTRIBUTING CORRESPONDENTS** Warren Cornwall, Andrew Curry (Berlin), Ann Gibbons, Sam Kean, Kai Kupferschmidt (Berlin), Andrew Lawler, Mitch Leslie, Virginia Morell, Dennis Normile (Tokyo), Elisabeth Pain (Careers), Charles Piller, Gabriel Popkin, Joshua Sokol, Richard Stone, Emily Underwood, Gretchen Vogel (Berlin), Lizzie Wade (Mexico City) **CAREERS** Katie Langin (Associate Editor) **INTERNS** Tanvi Dutta Gupta, Celina Zhao **COPY EDITORS** Julia Cole (Senior Copy Editor), Cyra Master (Copy Chief) **ADMINISTRATIVE SUPPORT** Meagan Weiland

Creative Director Beth Rakouskas

DESIGN MANAGING EDITOR Chrystal Smith **GRAPHICS MANAGING EDITOR** Chris Bickel **PHOTOGRAPHY MANAGING EDITOR** Emily Petersen **MULTIMEDIA MANAGING PRODUCER** Kevin McLean **WEB CONTENT STRATEGY MANAGER** Kara Estelle-Powers **DESIGN EDITOR** Marcy Atarod **DESIGNER** Noelle Jessup **SENIOR SCIENTIFIC ILLUSTRATOR** Noelle Burgess **SCIENTIFIC ILLUSTRATORS** Austin Fisher, Kellie Holoski, Ashley Mastin **SENIOR GRAPHICS SPECIALISTS** Holly Bishop, Nathalie Cary **GRAPHICS EDITOR** Drew An-Pham **SENIOR PHOTO EDITOR** Charles Borst **PHOTO EDITOR** Elizabeth Billman **SENIOR PODCAST PRODUCER** Sarah Crespi **SENIOR VIDEO PRODUCER** Meagan Cantwell **SOCIAL MEDIA STRATEGIST** Jessica Hubbard **SOCIAL MEDIA PRODUCER** Sabrina Jenkins **WEB DESIGNER** Jennie Pajerowski **INTERN** Julia Greenwood

Chief Executive Officer and Executive Publisher Sudip Parikh

Publisher, Science Family of Journals Bill Moran

DIRECTOR, BUSINESS SYSTEMS AND FINANCIAL ANALYSIS Randy Yi **DIRECTOR, BUSINESS OPERATIONS & ANALYSIS** Eric Knott **MANAGER, BUSINESS OPERATIONS** Jessica Tierney **MANAGER, BUSINESS ANALYSIS** Cory Lipman **MANAGER, WEB ANALYTICS** Samantha Cressman **BUSINESS ANALYSTS** Kurt Ennis, Maggie Clark **FINANCIAL ANALYST** Isacco Fusi **BUSINESS OPERATIONS ADMINISTRATOR** Taylor Fisher **SENIOR PRODUCTION MANAGER** Jason Hillman **SENIOR MANAGER, PUBLISHING AND CONTENT SYSTEMS** Marcus Spiegler **CONTENT OPERATIONS MANAGER** Rebecca Doshi **SENIOR CONTENT & PUBLISHING SYSTEMS SPECIALIST** Jacob Hedrick **SENIOR PRODUCTION SPECIALIST** Kristin Wowk **PRODUCTION SPECIALISTS** Kelsey Cartelli, Audrey Diggs **DIGITAL PRODUCTION MANAGER** Lisa Stanford **SENIOR DIGITAL ADVERTISING SPECIALIST** Kimberley Oster **ADVERTISING PRODUCTION OPERATIONS MANAGER** Deborah Tompkins **DESIGNER, CUSTOM PUBLISHING** Jeremy Huntsinger **SR. TRAFFIC ASSOCIATE** Christine Hall **SPECIAL PROJECTS ASSOCIATE** Shantel Agnew

ASSOCIATE DIRECTOR, BUSINESS DEVELOPMENT Justin Sawyers **GLOBAL MARKETING MANAGER** Allison Pritchard **DIGITAL MARKETING MANAGER** Aimee Aponte **JOURNALS MARKETING MANAGER** Shawana Arnold **MARKETING ASSOCIATES** Ashley Hylton, Mike Romano, Lorena Chirinos Rodriguez, Jenna Voris **SENIOR DESIGNER** Kim Huynh

DIRECTOR AND SENIOR EDITOR, CUSTOM PUBLISHING Erika Gebel Berg **ASSISTANT EDITOR, CUSTOM PUBLISHING** Jackie Oberst **PROJECT MANAGER** Melissa Collins

DIRECTOR, PRODUCT & PUBLISHING DEVELOPMENT Chris Reid **DIRECTOR, BUSINESS STRATEGY AND PORTFOLIO MANAGEMENT** Sarah Whalen **DIRECTOR, PRODUCT MANAGEMENT** Kris Bishop **PRODUCT DEVELOPMENT MANAGER** Scott Chernoff **PUBLISHING PLATFORM MANAGER** Jessica Loayza **SR. PRODUCT ASSOCIATE** Robert Koepke **PRODUCT ASSOCIATES** Caroline Breul, Anne Mason

ASSOCIATE DIRECTOR, INSTITUTIONAL LICENSING MARKETING Kess Knight **BUSINESS DEVELOPMENT MANAGER** Rasmus Andersen **ASSOCIATE DIRECTOR, INSTITUTIONAL LICENSING SALES** Ryan Rexroth **INSTITUTIONAL LICENSING MANAGER** Marco Castellan, Claudia Paulsen-Young **SENIOR MANAGER, INSTITUTIONAL LICENSING OPERATIONS** Judy Lillibridge **SENIOR OPERATIONS ANALYST** Lana Guz **SYSTEMS & OPERATIONS ANALYST** Ben Teincuff **FULFILLMENT ANALYST** Aminta Reyes

ASSOCIATE DIRECTOR, US ADVERTISING Stephanie O'Connor **US MID WEST, MID ATLANTIC AND SOUTH EAST SALES** Chris Hoag **US WEST COAST SALES** Lynne Stickrod **ASSOCIATE DIRECTOR, ROW** Roger Goncalves **SALES REP, ROW** Sarah Lelarge **SALES ADMIN ASSISTANT, ROW** Victoria Glasbey **DIRECTOR OF GLOBAL COLLABORATION AND ACADEMIC PUBLISHING RELATIONS, ASIA** Xiaoying Chu **ASSOCIATE DIRECTOR, INTERNATIONAL COLLABORATION** Grace Yao **SALES MANAGER** Danny Zhao **MARKETING MANAGER** Kilo Lan **ASCA CORPORATION, JAPAN** Rie Rambelli (Tokyo), Miyuki Tani (Osaka)

DIRECTOR, COPYRIGHT, LICENSING AND SPECIAL PROJECTS Emilie David **RIGHTS AND PERMISSIONS ASSOCIATE** Elizabeth Sandler **LICENSING ASSOCIATE** Virginia Warren **RIGHTS AND LICENSING COORDINATOR** Dana James **CONTRACT SUPPORT SPECIALIST** Michael Wheeler

EDITORIAL
science_editors@aaas.org

NEWS
science_news@aaas.org

INFORMATION FOR AUTHORS
science.org/authors/science-information-authors

REPRINTS AND PERMISSIONS
science.org/help/reprints-and-permissions

MULTIMEDIA CONTACTS
SciencePodcast@aaas.org
ScienceVideo@aaas.org

MEDIA CONTACTS
scipak@aaas.org

PRODUCT ADVERTISING & CUSTOM PUBLISHING
advertising.science.org/products-services
science_advertising@aaas.org

CLASSIFIED ADVERTISING
advertising.science.org/science-careers
advertise@sciencecareers.org

JOB POSTING CUSTOMER SERVICE
employers.sciencecareers.org
support@sciencecareers.org

MEMBERSHIP AND INDIVIDUAL SUBSCRIPTIONS
science.org/subscriptions

MEMBER BENEFITS
aaas.org/membership/benefits

INSTITUTIONAL SALES AND SITE LICENSES
science.org/librarian

AAAS BOARD OF DIRECTORS

CHAIR Gilda A. Barabino

PRESIDENT Keith R. Yamamoto

PRESIDENT-ELECT Willie E. May

TREASURER Carolyn N. Ainslie

CHIEF EXECUTIVE OFFICER Sudip Parikh

BOARD Cynthia M. Beall, Janine Austin Clayton, Kaye Husbands Fealing, Kathleen Hall Jamieson, Jane Maienschein, Robert B. Millard, Babak Parviz, William D. Provine, Juan S. Ramírez Lugo, Susan M. Rosenberg, Vassiliki Betty Smocovitis

BOARD OF REVIEWING EDITORS (Statistics board members indicated with **(S)**)

Erin Adams, *U. of Chicago*
Takuzo Aida, *U. of Tokyo*
Leslie Aiello, *Wenner-Gren Fdn.*
Deji Akinwande, *UT Austin*
Judith Allen, *U. of Manchester*
Marcella Alsan, *Harvard U.*
James Analytis, *UC Berkeley*
Paola Arlotta, *Harvard U.*
Delia Baldassarri, *NYU*
Nenad Ban, *ETH Zürich*
Christopher Barratt, *U. of Dundee*
Franz Bauer, *Pontificia U. Católica de Chile*
Ray H. Baughman, *UT Dallas*
Carlo Beenakker, *Leiden U.*
Yasmine Belkaid, *NIAID, NIH*
Philip Benfey, *Duke U.*
Kiros T. Berhane, *Columbia U.*
Joseph J. Berry, *NREL*
Alessandra Biffi, *Harvard Med.*
Chris Bowler, *École Normale Supérieure*
Ian Boyd, *U. of St. Andrews*
Malcolm Brenner, *Baylor Coll. of Med.*
Emily Brodsky, *UC Santa Cruz*
Ron Brookmeyer, *UCLA* **(S)**
Christian Büchel, *UKE Hamburg*
Johannes Buchner, *TUM*
Dennis Burton, *Scripps Res.*
Carter Tribley Butts, *UC Irvine*
György Buzsáki, *NYU School of Med.*
Mariana Byndloss, *Vanderbilt U. Med. Ctr.*
Annmarie Carlton, *UC Irvine*
Simon Cauchemez, *Inst. Pasteur*
Ling-Ling Chen, *SIBCB, CAS*
Wendy Cho, *UIUC*
Ib Chorkendorff, *Denmark TU*
Chunaram Choudhary, *Københavns U.*
Karlene Cimprich, *Stanford U.*
Laura Colgin, *UT Austin*
James J. Collins, *MIT*
Robert Cook-Deegan, *Arizona State U.*
Virginia Cornish, *Columbia U.*
Carolyn Coyne, *Duke U.*
Roberta Croce, *VU Amsterdam*
Molly Crocket, *Princeton U.*
Christina Curtis, *Stanford U.*
Ismaila Dabo, *Penn State U.*
Jeff L. Dangl, *UNC*
Nicolas Dauphas, *U. of Chicago*
Frans de Waal, *Emory U.*
Claude Desplan, *NYU*
Sandra Díaz, *U. Nacional de Córdoba*
Samuel Díaz-Muñoz, *UC Davis*
Ulrike Diebold, *TU Wien*
Stefanie Dimmeler, *Goethe-U. Frankfurt*
Hong Ding, *Inst. of Physics, CAS*
Dennis Discher, *UPenn*
Jennifer A. Doudna, *UC Berkeley*
Ruth Drdla-Schutting, *Med. U. Vienna*
Raissa M. D'Souza, *UC Davis*
Bruce Dunn, *UCLA*
William Dunphy, *Caltech*
Scott Edwards, *Harvard U.*
Todd Ehlers, *U. of Tübingen*
Nader Engheta, *UPenn*
Tobias Erb, *MPI Terrestrial Microbiology*
Karen Ersche, *U. of Cambridge*
Beate Escher, *UFZ & U. of Tübingen*
Barry Everitt, *U. of Cambridge*
Vanessa Ezenwa, *U. of Georgia*
Toren Finkel, *U. of Pitt. Med. Ctr.*
Natascha Förster Schreiber, *MPI Extraterrestrial Phys.*
Peter Fratzl, *MPI Potsdam*
Elaine Fuchs, *Rockefeller U.*
Caixia Gao, *Inst. of Genetics and Developmental Bio., CAS*
Daniel Geschwind, *UCLA*
Lindsey Gillson, *U. of Cape Town*
Gillian Griffiths, *U. of Cambridge*
Nicolas Gruber, *ETH Zürich*
Hua Guo, *U. of New Mexico*
Taekjip Ha, *Johns Hopkins U.*
Daniel Haber, *Mass. General Hos.*
Sharon Hammes-Schiffer, *Yale U.*
Wolf-Dietrich Hardt, *ETH Zürich*
Louise Harra, *UCL*
Kelley Harris, *U. of Wash*
Carl-Philipp Heisenberg, *IST Austria*
Janet G. Hering, *Eawag*
Christoph Hess, *U. of Basel & U. of Cambridge*
Heather Hickman, *NIAID, NIH*
Hans Hilgenkamp, *U. of Twente*
Janneke Hille Ris Lambers, *ETH Zürich*
Kai-Uwe Hinrichs, *U. of Bremen*
Deirdre Hollingsworth, *U. of Oxford*
Christina Hulbe, *U. of Otago, New Zealand*
Randall Hulet, *Rice U.*
Auke Ijspeert, *EPFL*
Gwyneth Ingram, *ENS Lyon*
Darrell Irvine, *MIT*
Akiko Iwasaki, *Yale U.*
Erich Jarvis, *Rockefeller U.*
Peter Jonas, *IST Austria*
Johanna Joyce, *U. de Lausanne*
Matt Kaeberlein, *U. of Wash.*
Daniel Kammen, *UC Berkeley*
Kisuk Kang, *Seoul Nat. U.*
V. Narry Kim, *Seoul Nat. U.*
Nancy Knowlton, *Smithsonian*
Etienne Koechlin, *École Normale Supérieure*
Alex L. Kolodkin, *Johns Hopkins U.*
LaShanda Korley, *U. of Delaware*
Paul Kubes, *U. of Calgary*
Chris Kuzawa, *Northwestern U.*
Laura Lackner, *Northwestern U.*
Gabriel Lander, *Scripps Res.* **(S)**
Mitchell A. Lazar, *UPenn*
Hedwig Lee, *Duke U.*
Fei Li, *Xi'an Jiaotong U.*
Ryan Lively, *Georgia Tech*
Luis Liz-Marzán, *CIC biomaGUNE*
Omar Lizardo, *UCLA*
Jonathan Losos, *WUSTL*
Ke Lu, *Inst. of Metal Res., CAS*
Christian Lüscher, *U. of Geneva*
Jean Lynch-Stieglitz, *Georgia Tech*
David Lyons, *U. of Edinburgh*
Fabienne Mackay, *QIMR Berghofer*
Zeynep Madak-Erdogan, *UIUC*
Vidya Madhavan, *UIUC*
Anne Magurran, *U. of St. Andrews*
Ari Pekka Mähönen, *U. of Helsinki*
Asifa Majid, *U. of Oxford*
Oscar Marín, *King's Coll. London*
Charles Marshall, *UC Berkeley*
Christopher Marx, *U. of Idaho*
David Masopust, *U. of Minnesota*
Geraldine Masson, *CNRS*
Jennifer McElwain, *Trinity College Dublin*
Rodrigo Medellín, *U. Nacional Autónoma de México*
C. Jessica Metcalf, *Princeton U.*
Tom Misteli, *NCI, NIH*
Jeffery Molkentin, *Cincinnati Children's Hospital Medical Center*
Alison Motsinger-Reif, *NIEHS, NIH* **(S)**
Danielle Navarro, *U. of New South Wales*
Daniel Neumark, *UC Berkeley*
Thi Hoang Duong Nguyen, *MRC LMB*
Beatriz Noheda, *U. of Groningen*
Helga Nowotny, *Vienna Sci. & Tech. Fund*
Pilar Ossorio, *U. of Wisconsin*
Andrew Oswald, *U. of Warwick*
Isabella Pagano, *Istituto Nazionale di Astrofisica*
Giovanni Parmigiani, *Dana-Farber* **(S)**
Sergiu Pasca, *Standford U.*
Daniel Pauly, *U. of British Columbia*
Ana Pêgo, *U. do Porto*
Julie Pfeiffer, *UT Southwestern Med. Ctr.*
Philip Phillips, *UIUC*
Matthieu Piel, *Inst. Curie*
Kathrin Plath, *UCLA*
Martin Plenio, *Ulm U.*
Katherine Pollard, *UCSF*
Elvira Poloczanska, *Alfred-Wegener-Inst.*
Julia Pongratz, *Ludwig Maximilians U.*
Philippe Poulin, *CNRS*
Lei Stanley Qi, *Stanford U.*
Simona Radutoiu, *Aarhus U.*
Trevor Robbins, *U. of Cambridge*
Joeri Rogelj, *Imperial Coll. London*
John Rubenstein, *SickKids*
Mike Ryan, *UT Austin*
Miquel Salmeron, *Lawrence Berkeley Nat. Lab*
Nitin Samarth, *Penn State U.*
Erica Ollmann Saphire, *La Jolla Inst.*
Joachim Saur, *U. zu Köln*
Alexander Schier, *Harvard U.*
Wolfram Schlenker, *Columbia U.*
Susannah Scott, *UC Santa Barbara*
Anuj Shah, *U. of Chicago*
Vladimir Shalaev, *Purdue U.*
Jie Shan, *Cornell U.*
Beth Shapiro, *UC Santa Cruz*
Jay Shendure, *U. of Wash.*
Steve Sherwood, *U. of New South Wales*
Brian Shoichet, *UCSF*
Robert Siliciano, *JHU School of Med.*
Lucia Sivilotti, *UCL*
Emma Slack, *ETH Zürich & U. of Oxford*
Richard Smith, *UNC* **(S)**
John Speakman, *U. of Aberdeen*
Allan C. Spradling, *Carnegie Institution for Sci.*
V. S. Subrahmanian, *Northwestern U.*
Naomi Tague, *UC Santa Barbara*
Eriko Takano, *U. of Manchester*
A. Alec Talin, *Sandia Natl. Labs*
Patrick Tan, *Duke-NUS Med. School*
Sarah Teichmann, *Wellcome Sanger Inst.*
Rocio Titiunik, *Princeton U.*
Shubha Tole, *Tata Inst. of Fundamental Res.*
Maria-Elena Torres Padilla, *Helmholtz Zentrum München*
Kimani Toussaint, *Brown U.*
Barbara Treutlein, *ETH Zürich*
Li-Huei Tsai, *MIT*
Jason Tylianakis, *U. of Canterbury*
Matthew Vander Heiden, *MIT*
Wim van der Putten, *Netherlands Inst. of Ecology*
Ivo Vankelecom, *KU Leuven*
Judith Varner, *UC San Diego*
Henrique Veiga-Fernandes, *Champalimaud Fdn.*
Reinhilde Veugelers, *KU Leuven*
Bert Vogelstein, *Johns Hopkins U.*
Julia Von Blume, *Yale School of Med.*
David Wallach, *Weizmann Inst.*
Jane-Ling Wang, *UC Davis* **(S)**
Jessica Ware, *Amer. Mus. of Natural Hist.*
David Waxman, *Fudan U.*
Alex Webb, *U. of Cambridge*
Chris Wikle, *U. of Missouri* **(S)**
Terrie Williams, *UC Santa Cruz*
Ian A. Wilson, *Scripps Res.* **(S)**
Hao Wu, *Harvard U.*
Li Wu, *Tsinghua U.*
Amir Yacoby, *Harvard U.*
Benjamin Youngblood, *St. Jude*
Yu Xie, *Princeton U.*
Jan Zaanen, *Leiden U.*
Kenneth Zaret, *UPenn School of Med.*
Lidong Zhao, *Beihang U.*
Bing Zhu, *Inst. of Biophysics, CAS*
Xiaowei Zhuang, *Harvard U.*
Maria Zuber, *MIT*

Science serves as a forum for discussion of important issues related to the advancement of science by publishing material on which a consensus has been reached as well as including the presentation of minority or conflicting points of view. Accordingly, all articles published in *Science*—including editorials, news and comment, and book reviews—are signed and reflect the individual views of the authors and not official points of view adopted by AAAS or the institutions with which the authors are affiliated.

EDITORIAL

Generative approach to research integrity

H. Holden Thorp
is Editor-in-Chief, *Science* Journals.
hthorp@aaas.org;
@hholdenthorp

It's been a bad few weeks for public perceptions of research integrity, as multiple cases at elite universities have received wide news coverage. Francesca Gino, a scientist at Harvard University, is in a legal dispute over whether data in newly retracted papers about dishonesty were manipulated; she is now suing Harvard and the researchers who surfaced the alleged problems. Likewise, Duke University is investigating published work by scientist Daniel Ariely. Johns Hopkins University may initiate an investigation of research misconduct by Nobel laureate Gregg Semenza. And most prominently, the president of Stanford University, Marc Tessier-Lavigne, recently resigned after the institution's report determined that the "culture" in his laboratory contributed to manipulation of results.

The conclusion about culture in the Tessier-Lavigne lab stood out to me. More than 10 years ago, I chaired a National Academies study on laboratory safety after a tragic death in a chemistry laboratory at the University of California, Los Angeles. The study connected chemists with safety culture experts from other industries. These experts taught researchers about three different kinds of culture: pathological, bureaucratic, and generative. In a pathological culture, crucial information about potentially damning errors or hazards is hoarded by those in power and often used as a weapon to silence critics. In a bureaucratic culture, emphasis is on policies, rules, and compliance where similar information is either unwelcome or ignored. And a generative culture is one oriented on performance, where potentially damaging information is welcomed and distributed to the right people to act on.

This general split in culture exists across the scientific enterprise. There are, arguably, a few laboratories with pathological cultures. However, it's not just the culture of the labs per se that is at issue with respect to research integrity, but rather the culture of the larger system through which research is conducted and communicated. Institutions and the maintenance of the scientific record generally fall squarely in the bureaucratic realm. Publishers have policies aimed at research integrity and are part of entities that have legal and public relations functions. Universities have even more policies, lawyers, reputational managers, and highly professional administrative staff who handle research integrity. And governments add a research funding layer to the already complex bureaucracy. The result is a system that produces sluggish responses to research integrity issues that neither engender trust among the public nor among those skeptical of the ability of these entities to promote research integrity.

Although science's bureaucratic culture doesn't cause misconduct, it appears to define how misconduct is handled—by litigating and clamming up about allegations rather than collaborating to find out what happened. Instead of suing each other, parties should be talking about how to get to a better place. It's the generative culture that needs fostering. When honest mistakes are made—such as when *Science* failed to post two corrections in 2015 that were approved by its editors in the Tessier-Lavigne case—it is difficult to dispel suspicions that journals or authors are trying to hide something. Honest mistakes happen, and journals need to be accessible and on the record about their behaviors. Issuing carefully worded statements and "no comment" has no place in a generative culture. Meanwhile, although there have been good recent discussions about universities and journals working together to accelerate corrections and retractions, the universities need to realize that threats of litigation may not be the major consideration when so many within and outside the scientific community are losing trust in science. Rather, a healthy generative culture would direct universities to be forthcoming with information and encourage journals to correct the record.

> **"Instead of suing each other, parties should be talking about how to get to a better place."**

Science will continue to work to increase trust in its role in maintaining the scientific record. *Science Advances* now has a scientific integrity officer who handles questions that arise about papers, and we regularly monitor PubPeer and related websites for concerns about all the *Science* journals. There will always be humans involved at institutions, laboratories, and journals, so there will always be errors. The scientific community will decide when its constituents, including journals, have reached a point when errors can accurately be ascribed to either honest mistakes or misconduct. Ultimately, corrections to the scientific record must materialize faster and more frequently. This will help forge a path to a more generative culture in which information about all potential problems—especially errors and misconduct related to research—is welcomed.

– H. Holden Thorp

10.1126/science.adk1852

PHOTO: CAMERON DAVIDSON

NEWS

IN BRIEF

Edited by **Kelly Servick**

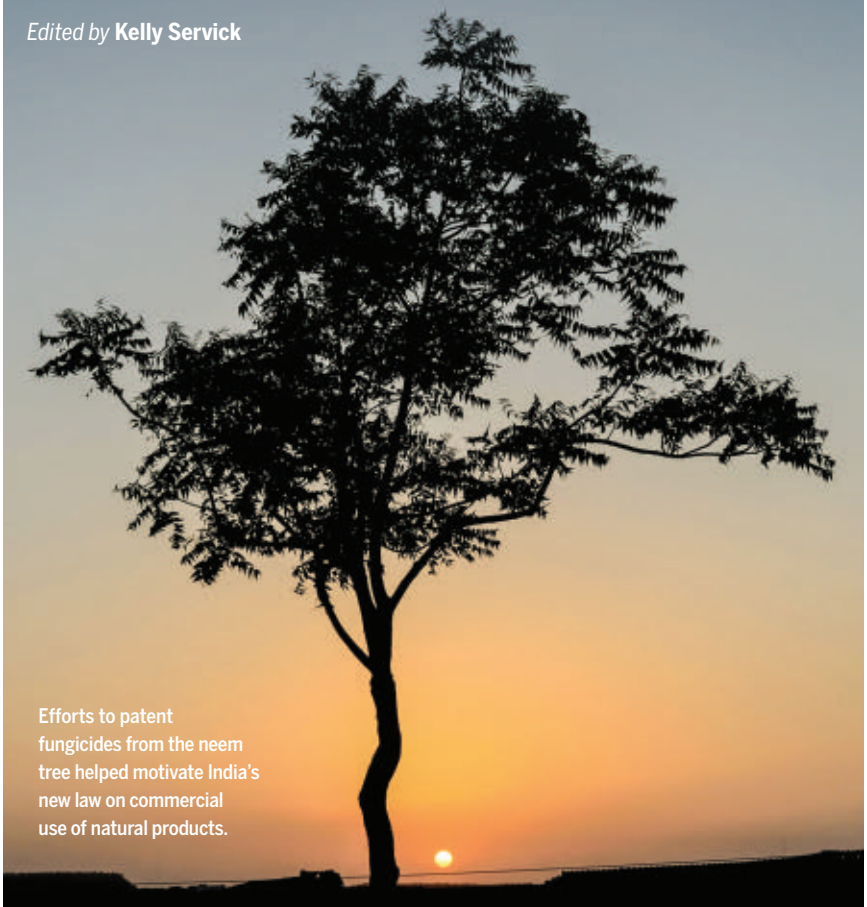

Efforts to patent fungicides from the neem tree helped motivate India's new law on commercial use of natural products.

POLICY

Indian biodiversity law softened

India's parliament last week approved a controversial set of amendments to the 2002 Biological Diversity Act that will make it easier for companies to use the country's biological resources and traditional knowledge for commercial R&D. The legislation streamlines approval processes for such uses and decriminalizes violations of the act. It also waives approvals for practitioners of traditional Indian medicine, cultivated plants, and use of traditional knowledge derived from a designated set of texts. Proponents say the new bill will help promote research and entrepreneurship based on India's biological diversity. But environmental advocates fear the amendments could weaken adherence to an already poorly enforced law, and enable companies to exploit Indian ecosystems without sharing benefits with local communities.

Obesity drug reduces heart risks

BIOMEDICINE | The weight-loss drug semaglutide, marketed as Wegovy, decreased risk of cardiovascular problems by 20% in a highly anticipated clinical trial, its maker, Novo Nordisk, announced in a press release this week. The 5-year, randomized study included more than 17,500 people ages 45 and older who were overweight or obese and had cardiovascular disease. Participants were given weekly injections of either a placebo or semaglutide, which activates the receptor for the hormone GLP-1 to slow stomach emptying and reduce appetite. The reported reduction in heart attack, stroke, or death because of heart problems is likely to boost interest in semaglutide and other GLP-1 receptor agonists, first approved to treat diabetes but increasingly prescribed for obesity. Novo Nordisk says it will release detailed trial results later this year.

Fauci's successor named

LEADERSHIP | Physician and epidemiologist Jeanne Marrazzo will become director of the $6.3 billion National Institute of Allergy and Infectious Diseases (NIAID) in the fall. She will succeed Anthony Fauci, who became the public face of the federal response to the COVID-19 pandemic. Fauci stepped down in December 2022 after 38 years at NIAID's helm. Marrazzo, 61, currently directs the Division of Infectious Diseases at the University of Alabama at Birmingham. She has expertise in HIV prevention, vaginal infections, hormonal contraception, and antibiotic resistance, and has led international clinical trials. Marrazzo will be the first openly gay director of a National Institutes of Health institute. NIAID funds research on a wide range of topics including basic microbiology, allergies, and biodefense. Like Fauci, Marrazzo will likely face grilling by conservatives in Congress about NIAID's role in funding bat coronavirus research in China that some claim sparked the pandemic.

Honesty researcher sues Harvard

SCIENTIFIC INTEGRITY | Francesca Gino, who is on administrative leave from Harvard Business School following an investigation into apparent data fabrication in her research on dishonesty, is suing Harvard University, the dean of HBS, and the three researchers who first raised concerns about her work. According to a 100-page lawsuit filed in a federal district court in Massachusetts last week, Gino is seeking $25 million for damage to her reputation, as well as lost

PHOTO: DINODIA PHOTOS/ALAMY

CONSERVATION

Researchers raise alarm over threat to Mexican fireflies

Scientists from the International Union for Conservation of Nature (IUCN) last week delivered a letter to the Mexican government requesting it regulate tourism centered on the threatened firefly species *Photinus palaciosi*. Endemic to Mexico's Tlaxcala forests, *P. palaciosi* is one of the few species that glow in synchrony, offering an annual spectacle that attracts thousands of visitors during summer mating season. The letter describes how littering, artificial light, and noise interfere with the insects' courtship and egg-laying behaviors. In an accompanying public statement, IUCN's Firefly Specialist Group asks visitors and the tourism industry to avoid putting accommodations near breeding sites and to minimize artificial lighting, and calls for further research into the insects' needs and distribution.

PHOTO: REBECCA BLACKWELL/AP IMAGES

income and career opportunities, among other claims. The filing alleges that statements made by HBS and the three behavioral scientists—who outlined the evidence they had gathered on their blog, Data Colada—were "false and defamatory," and didn't show that Gino herself intentionally fabricated or falsified data. It also alleges sex-based discrimination, claiming that HBS treated Gino more harshly than men colleagues accused of misconduct.

Measles behind mystery illness

INFECTIOUS DISEASE | The World Health Organization (WHO) is responding to more than 200 cases of what initially seemed like viral hemorrhagic fever in a remote area of South Sudan. The illnesses, first reported in June and linked to 29 deaths so far, include symptoms such as fever, red eyes, and bloody vomiting and stool. Many patient samples tested positive for measles, malaria, or both. But tests for Ebola and other hemorrhagic fever–associated viruses came back negative, as did broader molecular tests for other pathogens, says Patrick Otim, a health emergency officer with WHO. Cases appear to be due to measles infections in a largely unvaccinated population, exacerbated by malnutrition, poor access to basic health care, and in some cases malaria coinfection. WHO is now focused on improving health care access in the region.

NIH opposes unionization effort

LABOR RELATIONS | Early-career researchers who work in labs operated by the U.S. National Institutes of Health (NIH) have hit a roadblock in their attempt to unionize. Last week, they learned that NIH submitted paperwork to the Federal Labor Relations Authority (FLRA), which oversees the certification of unions by federal employees, seeking to block the unionization effort. The NIH filing claims most of the proposed union's 4800 members—a group that includes postdocs and graduate students—aren't "employees" and therefore don't have a right to unionize. The union organizers expect FLRA to hold a hearing where both sides can voice their arguments, although a date hasn't been set.

Peru defamation suit tossed

#METOO | A court in Peru this week dismissed a defamation lawsuit against archaeologist Marcela Poirier brought by Luis Jaime Castillo Butters, a prominent archaeologist she accused of sexual harassment. Castillo Butters's institution, the Pontifical Catholic University of Peru, found evidence of harassment in a 2020 investigation, but did not sanction him. He then sued Poirier for her Facebook posts describing the findings. A judge ruled against Poirier in May 2021, but an appeals court found irregularities in the trial and ordered a retrial. On Monday, a court closed the case because Castillo Butters and his defense failed to appear. The outcome "leads me to believe that we will be able to eradicate, little by little, gender violence in educational spaces," Poirier says. "The criminalization of victims must stop." Castillo Butters did not respond to requests for comment.

THEY SAID IT

> "The racial inequity which was so eloquently argued in the complaint ... really I think carried the day."

Lawyer Lori Andrews of the Chicago-Kent College of Law, theorizing on why Thermo Fisher Scientific last week settled a lawsuit with the family of Henrietta Lacks over the commercial use of her cancer cells. (See full Q&A where Andrews discusses the implications for other cases at https://scim.ag/HeLaQA.)

If cancers harbor distinctive communities of microbes, or microbiomes, a blood test for microbial sequences might reveal the presence of specific kinds of tumors.

BIOMEDICINE

Key study of cancer microbiomes challenged

"Major" errors may undermine research that identified cancers based on their microbes

By **Catherine Offord**

Several years ago, when scientists reported in *Nature* that various types of cancer were consistently associated with distinct communities of microbes, the clinical possibilities were tantalizing. The 2020 paper used a form of artificial intelligence to tease out microbial DNA indicative of particular cancers and proposed a "new class of microbiome-based cancer diagnostic tools." The research has since garnered hundreds of citations, provided data for more than 10 other studies, and helped justify at least one commercial venture aiming to use microbial sequences in a person's blood to reveal a cancer's presence.

But that promise is under scrutiny now that a group of researchers claims to have found "major data analysis errors" that undermine the paper's conclusions. According to a manuscript the critics posted last week on the preprint server bioRxiv, the *Nature* authors failed to properly filter out human DNA from a database of sequenced cancer tissues. This led to millions of human sequences being wrongly classified as microbial—perhaps explaining why the study found improbable microbes linked to human tumors such as a seaweed bacterium associated with bladder cancer, for example.

A separate, computational error made during the team's analysis inadvertently generated cancer-specific patterns where there weren't any, the preprint also contends. The paper's "major conclusions are completely wrong," says one of the preprint's authors, Johns Hopkins University computational biologist Steven Salzberg.

Rob Knight, a microbiologist at the University of California, San Diego, and senior author on the *Nature* paper, rejects the criticisms, noting his lab already rebutted them in a response to an earlier preprint from some of the same scientists. "There's really nothing this new preprint has that hasn't already been addressed openly," says Knight, who co-founded the company Micronoma in 2019 to develop microbiome-based cancer diagnostics. He also highlights his team's 2022 paper in *Cell*, which used updated methods to analyze fungi and bacteria in tumors and drew similar conclusions to the *Nature* paper.

But researchers watching from the sidelines say the new preprint goes beyond earlier charges and that its arguments are compelling. "It's a forensic deconstruction of the places where errors have crept into the original manuscript," says Julian Parkhill, a bacterial geneticist at the University of Cambridge.

Microbiome science undoubtedly holds biomedical promise, and other groups have associated microbes with particular cancers, multiple researchers tell *Science*. But the debate offers a cautionary tale for microbiome studies relying heavily on computational approaches, says Lesley Hoyles, a microbiologist and bioinformatician at Nottingham Trent University. "There's a lack of critique of what's coming out," she says. "We need people doing these kinds of analyses."

The *Nature* paper used a repository known as the Cancer Genome Atlas (TCGA), which stores reams of DNA sequences from human cancer samples. Sequences are classified by the database as human or nonhuman based on whether they match a so-called human reference genome—although that classification is known to be imperfect.

The *Nature* study authors compared TCGA's "nonhuman" sequences, as well as sequences from several dozen cancer-free people and 100 with cancer, with a database of DNA from bacteria, viruses, and other microbes. Doing so showed that different cancer types had specific communities of resident microbes. From the data, machine learning algorithms could reliably predict—sometimes with accuracies approaching 100%—whether a person had cancer and, if they did, the tumor type.

These correlations, the researchers suggested, could be used to devise tests to detect cancers from a person's blood sample. Knight's team shared detailed results on a public website.

But some readers noticed puzzling findings. Although the work identified many human bacteria in cancerous tissues, there was, in addition to the mysterious seaweed

PHOTO: ROGER HARRIS/SCIENCE SOURCE

bacterium, a marine hydrothermal vent bacterium linked to prostate cancer, and a coral bacterium associated with melanoma. In a January preprint, researchers at the University of East Anglia suggested this might signal problems in the study's methodology. In particular, they noted, the presence of unexpected microbes in cancer tissue could be a result of database mistakes where sequences of one species are mislabeled as another's.

Parkhill explains it's common for human DNA to accidentally end up in microbial databases, where it's wrongly listed under microbial species names. Unless researchers properly filter out human DNA from their human tissue sequencing data before comparing them with a microbial database, they risk detecting organisms that aren't really in the tissue. This, the first preprint proposed, is what happened in the *Nature* study.

> **"It's a forensic deconstruction of the places where errors have crept into the original manuscript."**
>
> **Julian Parkhill**, University of Cambridge

In a 27-page response, Knight and colleagues disputed the importance of the East Anglia team's observations, adding that their *Cell* paper, which used updated methods, had replicated the *Nature* paper's conclusions. But the response wasn't convincing to Salzberg, who developed some of the computational tools used in the *Nature* paper.

Teaming up with the East Anglia researchers (who themselves have a patent application for using bacteria as biomarkers for prostate cancer), Salzberg downloaded and reanalyzed a subset of the *Nature* study's data. When they included extra filters for human DNA—one alone is rarely sufficient, Salzberg says—their analysis found that millions of sequences the *Nature* authors had assumed were microbial were, in fact, human. Many of the microbes the study identified, the new preprint argues, were never in the TCGA cancer samples at all.

Knight says the exact identity of sequences found in specific cancers doesn't change his group's conclusions. For diagnostic purposes, "If what you're trying to do is distinguish … cancer cases from controls or one cancer from another, it matters much more that those distinguishing sequences exist rather than what you call them." Analyses "can be refined with successive techniques and data sources," he adds, noting that other research—and a minianalysis he and his colleagues ran last week—shows the microbial differences remain even when human sequences are more stringently ruled out.

The new preprint from Salzberg and colleagues also addresses the impressive ability of the *Nature* paper's computer models to predict cancer type based on a sample's microbiome. Because the tissue samples came from multiple different medical centers and times, Knight and colleagues used a technique called normalization to try to remove some of the variability. But this process was problematic, the new preprint alleges: It introduced a distinct electronic tag to the data from each cancer type. This meant that when the team fed normalized data into their algorithms, the computer could surreptitiously just use the tag, rather than the microbial data, to determine which cancer type a sample came from.

Knight says his group disagrees with the preprint's analysis, and reemphasizes that the *Cell* paper, which didn't process data in the same way, reached the same conclusions. He adds his team isn't "especially motivated" to comb through the preprint's lengthy analysis or address it on social media, where it is already generating a buzz. "If they were to publish this in a peer-reviewed journal, we would address [it], … which I think is the appropriate way to do science, as over the past few centuries."

In a statement, Micronoma CEO Sandrine Miller-Montgomery notes the company's products in development don't rely on the *Nature* paper. "We developed additional human filtering and quality control methods that minimized human genomic DNA contamination, finding that doing so did not hinder the ability to diagnose cancer presence or types," she says.

Repercussions for research by other academic teams that relied on the conclusions of the *Nature* paper aren't clear. "These are very early days and this is a quite complex issue," says the National Cancer Institute's Eytan Ruppin, who used the normalized data set for a 2022 paper. "It is now pertinent to hear from the original authors of the *Nature* paper, should they choose to respond, to get a possibly more balanced and even-handed perspective on this important topic."

Ivan Vujkovic-Cvijin, a microbiome scientist at Cedars-Sinai Medical Center, notes a lack of standards in how to use machine learning in microbiome science. "I think this scientific disagreement underscores the need to develop them."

Others hope the ensuing discussion will help fix any problems in the original paper. "As scientists, we should be open to challenge," Parkhill says. "We should be capable of dealing with it objectively and correcting things when necessary. Hopefully that's what will happen." ■

ASTRONOMY

Observatory to probe origins of ferocious gamma rays

With approval imminent, construction will soon begin on Cherenkov Telescope Array

By **Daniel Clery**

Along with the gentle light of stars and galaxies, Earth receives much rarer and more aggressive signals from the cosmos: photons that slam into the atmosphere with 10 trillion times the energy of visible light. Just how they reach such enormous energies is a puzzle, but a group of mostly European countries will soon start to build an observatory that will trace them to their sources by watching for the flash of their atmospheric impacts. By 2026, if all goes well, the €330 million Cherenkov Telescope Array Observatory (CTAO) should be pinpointing the cosmic powerhouses that spawn the photons and probing their inner workings.

Other observatories have already glimpsed more than 250 gamma ray sources in the Milky Way and beyond. With dozens of telescopes split between sites on Spain's Canary Islands and Chile's Atacama Desert, CTAO should have the sensitivity and sharp vision to find five times as many sources and figure out how they tick. "CTAO is a tremendous step forward," says Werner Hofmann of the Max Planck Institute for Nuclear Physics, spokesperson for the CTA consortium, a group of 1500 scientists that will analyze the data. "We'll be able to pin down accelerator mechanisms and sources."

With most of its funders in Europe, the CTAO team applied in 2018 for official status as a European research infrastructure consortium—a step needed for funding to flow. Approval is expected from the European Union soon, possibly next month. At that point construction can begin at the two sites.

Because the atmosphere blocks gamma rays, high-altitude balloons and spacecraft were the first to glimpse these cosmic photons. But higher energy gamma rays are too rare for small space telescopes—they might

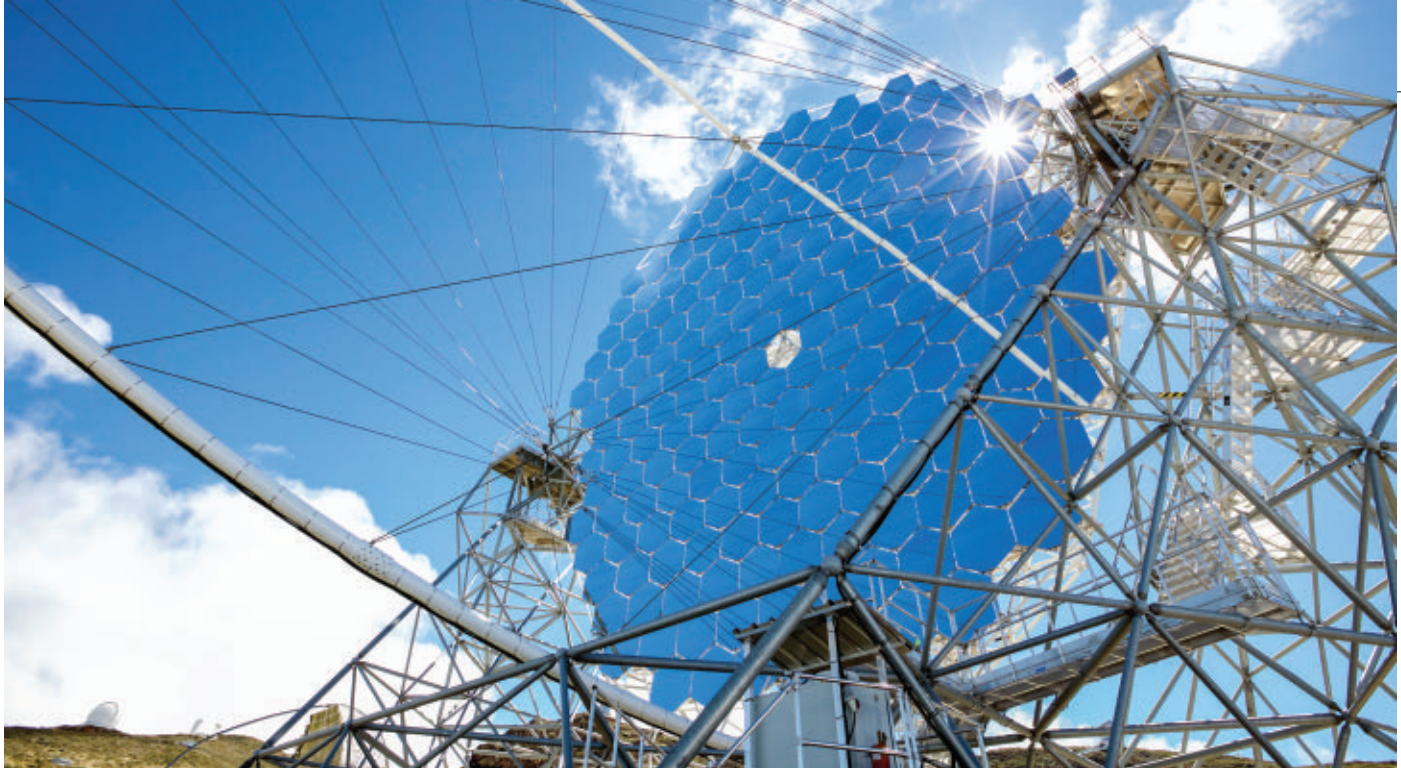

In 2018, astronomers completed a prototype 23-meter gamma ray telescope in the Canary Islands. Three similar instruments will soon join it.

have to wait a year to catch a single photon from a bright source. The solution is to use Earth's atmosphere as a giant detector. When a gamma ray strikes an atom in the air, it creates a shower of particles cascading toward the ground. Some gamma ray detectors rely on huge tanks of water to capture those particles. CTAO will instead look for the faint flash of blue "Cherenkov" light they trigger, which forms a cone that reaches the ground with a footprint 250 meters across. From the shape and brightness of that glowing footprint, astronomers can work out the direction and energy of the original gamma ray.

Cherenkov telescopes don't require expensive, exquisitely polished mirrors to see the close-up air showers. The technical challenge is in the camera, which must capture the extremely faint and brief flashes, lasting just a few billionths of a second. Instead of the usual charge-coupled device, or CCD, sensors, Cherenkov telescope cameras rely on a technology usually seen in particle physics: photomultipliers, which can amplify the signal of single photons.

In 1989, the Fred Lawrence Whipple 10-meter telescope in Arizona was the first to detect gamma rays this way, tracing them to the Crab nebula, the remnant of a supernova. A generation of larger telescope arrays followed. "They proved the [Cherenkov] technique to be really powerful," says Roberta Zanin, CTAO project scientist.

CTAO will take the next step, deploying more than 70 telescopes with segmented mirrors in three different sizes—from 4 meters to 23 meters across—optimized for different energies and spread across wider areas to catch showers more reliably. The observatory should be able to detect gamma rays with energies as high as 300 teraelectronvolts—44 times as energetic as the particles revved up by CERN's Large Hadron Collider—and pin down their sources with twice the resolution of existing arrays. "CTAO will be fundamentally different in the level of science it produces," says Stuart McMuldroch, the project's director general designate.

Supernovae are thought to be the main sources of high-energy gamma rays. As the blast of gas and dust from the stellar explosion hits the thin vapors that fill interstellar space, it creates a shock wave. The shock's roiling gases create magnetic fields that slingshot particles to near light speeds. "Supernova remnants are the most efficient particle accelerators in our galaxy," says Anabella Araudo, an astrophysicist at the Czech Republic's Extreme Light Infrastructure Beamlines Facility. The speeding particles may in turn generate gamma rays, for example by colliding with photons and boosting their energy.

The particles themselves arrive at Earth as cosmic rays, which Cherenkov telescopes can also detect. But because the particles are charged, magnetic fields in space cause their paths to bend, making them hard to trace to their sources. In contrast, gamma rays follow straight paths. With its improved resolution and ability to produce detailed spectra of gamma ray energies, CTAO's data should help refine theoretical models of the supernova particle accelerators, Araudo says.

Other candidate gamma ray generators include pulsars, the highly magnetized spinning cinders of dead stars, and newborn stars, which blast out strong particle winds. Baby stars may also emit powerful jets of particles from their poles, which could generate gamma rays when the jets hit surrounding gas. Existing telescopes don't have to resolution to tell. "We can't identify the emitters," says Giovanni Pareschi of Italy's National Institute of Astrophysics. If there is a supernova hidden in a stellar nursery, "which is the source?" he asks.

Jets from quasars, the supermassive black holes gobbling gases and stars at the center of distant galaxies, may also be generating gamma rays. "Imaging was not possible before; we were lacking angular resolution. CTAO will achieve this," Zanin says.

The supermassive black hole at the heart of the Milky Way is much sleepier than a quasar, but in 2010 NASA's Fermi Gamma-Ray Space Telescope discovered gamma rays coming from two enormous "bubbles" stretching 25,000 light-years above and below the galactic center, perhaps vestiges of past jets shot from the black hole. "We don't exactly know what it's doing," Hofmann says, but CTAO will be on the lookout for any residual jets or other gamma ray signals from the black hole.

CTAO may even be able to detect dark matter, the mysterious stuff that makes up most of the mass of the universe. Some proposed dark matter particles are thought to emit a burst of gamma rays when pairs of particles meet and annihilate. CTAO will survey the background of lower energy gamma rays. If the background is elevated in areas where dark matter is thought to congregate, such as in the galactic center, that would be evidence for its presence, Hofmann says. "If it's there, we should see it." ■

PHOTO: AKIRA OKUMURA/CC BY-NC-ND

MATERIALS SCIENCE

Superconductivity claim electrifies social media

Report of room-temperature material goes viral, but many physicists are skeptical

By **Adrian Cho**

For the past 2 weeks, the social media platform X (formerly Twitter) has been aflutter over a paper titled "The First Room-Temperature Ambient-Pressure Superconductor." The title of the paper, which was posted with a companion on the arXiv preprint server on 22 July, says it all: When seasoned with copper, a humble lead-based mineral becomes a superconductor that works far above room temperature and at atmospheric pressure. To date, all superconductors—materials that can convey electricity without resistance or loss of energy to heat—have required temperatures far colder than room temperature or crushing pressures.

If the claim by Sukbae Lee and Ji-Hoon Kim of South Korea's Quantum Energy Research Centre and their colleagues holds up, the material could usher in all sorts of technological marvels, such as levitating vehicles and perfectly efficient electrical grids. "Today might have seen the biggest physics discovery of my lifetime," enthused Alex Kaplan, an executive at a small coffee company who obtained a bachelor's degree in physics from Princeton University in 2021. "I don't think people fully grasp the implications of an ambient temperature/pressure superconductor," he wrote in a 25 July X thread that has 30 million views.

But some physicists are deeply skeptical. The authors "come off as real amateurs," says Michael Norman, a theorist at Argonne National Laboratory. "They don't know much about superconductivity and the way they've presented some of the data is fishy." On the other hand, he says, "People here are taking it seriously and trying to grow this stuff." Already, some experimental groups have reported that they could not reproduce the work, whereas others have provided modest support. The South Korean team did not respond to a request for comment.

Superconductivity is inherently a low-temperature phenomenon. Ordinarily, electrons cannot pass easily through a crystalline solid because they bounce off vibrating atoms in the crystal lattice. However, in some materials, at low enough temperatures, the electrons form loosely bound, overlapping pairs that can't be deflected without breaking the pairs. And at low temperatures, the vibrations aren't strong enough to break the bonds, so those electron pairs glide through the material unimpeded.

The catch is, there's no rule for predicting how cold a material must be to superconduct. Some so-called high-temperature superconductors convey current without resistance at up to 133 K (more than 100° below freezing). After 30 years theorists still can't explain exactly how the materials do that, so they can't predict a limiting temperature. And controversial claims abound, for example around new "hydride" superconductors, said to work at room temperature though generally at ultrahigh pressures (*Science*, 30 September 2022, p. 1474).

> **"You have a rock, and [after doping] you should still end up with a rock."**
>
> **Michael Norman**,
> Argonne National Laboratory

But even in a field filled with bold assertions, the South Korean researchers' claim is extraordinary. In the papers, which have not been peer reviewed, they argue that when doped with copper, the mineral lead apatite—which contains lead, oxygen, and phosphorus—superconducts at ambient pressure and temperatures of at least 400 K, higher than the boiling point of water. If that is true, then just sitting on your desk, the stuff should convey electricity without resistance. The papers present data that purport to show the material not only has zero resistance, but can also expel a magnetic field. That's a key sign of superconductivity—although not a unique signature—and the reason a superconductor levitates when placed on a magnet.

"I appreciate that the authors took appropriate data and were clear about their fabrication techniques," says Nadya Mason, a condensed matter physicist at the University of Illinois Urbana-Champaign. Still, she cautions, "The data seems a bit sloppy." For example, when viewed in detail, key voltage-versus-current graphs do not show the telltale plunge straight to zero, which would indicate vanishing resistance. The papers also show identical magnetic data in plots with incommensurate axes. And, according to press reports, the papers were posted without the permission of all authors. South Korea has started an investigation into the matter.

There are also questions of basic physics, Norman says. Conventional superconductors, such as niobium, tin, and mercury, are all metals. High-temperature superconductors, such as yttrium barium copper oxide, have to be doped to make them metallic before they'll superconduct. In contrast, undoped lead apatite is an insulator, Norman says. What's more, copper and lead atoms are similar enough that substituting copper atoms for some of the lead atoms in lead apatite shouldn't affect the material's electrical properties. "You have a rock, and [after doping] you should still end up with a rock," Norman says.

Still, with no theory of high-temperature superconductivity, there's no way to say for sure the material can't be a superconductor. In an ordinary superconductor, vibrations of the crystal lattice provide the glue that binds the electron pairs. In high-temperature superconductors, physicists think, the glue somehow emerges from—paradoxically—the strong repulsion among the electrons themselves. "Maybe this material really just hits the sweet spot of a strongly interacting unconventional superconductor," Mason says.

The South Korean researchers speculate that within their material, the doping slightly distorts long, naturally occurring chains of lead atoms. They say these 1D channels might carry current without resistance. Lee and Kim also suggest that a kind of undulation of charge might exist in the chains. Mason notes that similar charge patterns have been seen in high-temperature superconductors.

As *Science* went to press, more than a dozen follow-up studies, most theoretical, had hit arXiv. One group in China claims to see zero resistance in the material, but only at temperatures below 100 K—cooler than some known superconductors. Three others report no sign of superconductivity. Several theoretical papers suggest the material may have an electrical structure promising for, but far from guaranteeing, superconductivity.

No one can say for sure where this is all going. But Kaplan, condensed matter physics' first internet influencer, has changed his mind, posting on 7 August that the evidence rules out superconductivity. ■

ATMOSPHERIC SCIENCE

NASA scales back its next flagship climate mission

As two landmark satellites go dark, cuts loom for new bid to probe clouds, aerosols, and warming

By **Paul Voosen**

Speaking during a historic heat wave last month, NASA Administrator Bill Nelson vowed to protect climate research from upcoming congressional budget battles. "We're going to have the least possible effect on any climate science," he said. "This is a huge priority for us."

Yet *Science* has learned that months ago, NASA downgraded plans for its next-generation climate mission, a suite of satellites dubbed the Atmosphere Observing System (AOS). It is set to launch later this decade with a cost up to $2 billion. To rein in cost overruns of hundreds of millions of dollars, the mission will lose an advanced laser sensor that probes pollution particles and perhaps also a special cloud-sensing radar band. Their absence will limit AOS's ability to answer critical questions, including how pollution influences clouds, and how cloud changes might speed up global warming. "People are just sad," says Courtney Schumacher, a meteorologist at Texas A&M University. "Some people are pissed."

Dozens of researchers have signed three different letters protesting the decision. They argue that a downgraded AOS will not break enough scientific ground and that its cost caps were set before the rampant inflation of recent years. They also complain that NASA has accommodated higher cost growth for other flagship projects, such as a mission to return rocks from Mars.

Even with the cuts, AOS will "do a tremendous amount of science," says Karen St. Germain, director of NASA's Earth Science Division. "We've got to do the best science we can within what's appropriated."

AOS was designed to build on insights from two pioneering satellites: Calipso, which revolutionized studies of atmospheric particles, or aerosols; and CloudSat, which did the same for clouds. When they turned on, "we had a whole other view of the Earth system that we didn't have before," says Jeffrey Reid, an aerosol scientist at the U.S. Naval Research Laboratory. The duo, launched in 2006, ran far past their designed life. Calipso finally went offline last month, its fuel reserves depleted. CloudSat will follow suit in September. "It is an end of an era," says Graeme Stephens, CloudSat's principal investigator at NASA's Jet Propulsion Lab.

Following the advice of the 2018 decadal survey of earth science priorities, overseen by the National Academies of Sciences, Engineering, and Medicine (NASEM), NASA's centers put together a proposal for a pair of large successor satellites. Each one would offer simultaneous views of aerosols, clouds, and precipitation while also tracking the rising airflows that help fuel storms—feats never done from space.

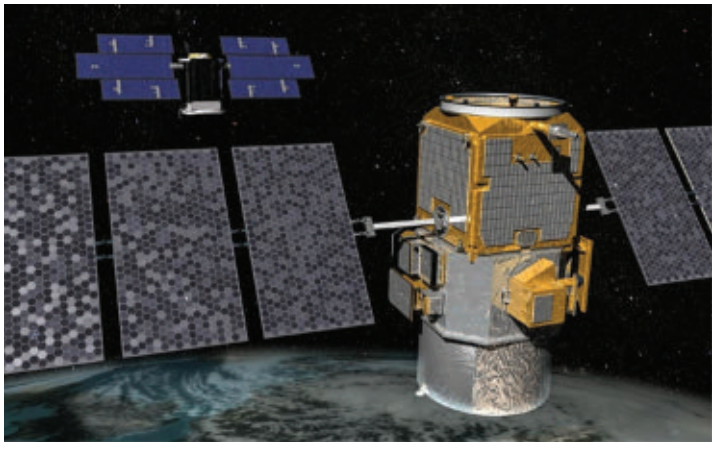

The pioneering satellites Calipso and CloudSat (artist's conception) are getting a replacement.

PHOTO: NASA

One of them, called AOS-Sky, was to carry the advanced lidar, which would fire a laser through the atmosphere and capture reflected light. The lidar, unlike Calipso's, would resolve layered features, like wildfire smoke over pollution, offering much better insight into low-lying clouds, pollution, and the interactions between them. "This is a crucial component of the climate puzzle," says Jens Redemann, a meteorologist at the University of Oklahoma. AOS-Sky would also carry a Doppler radar intended to pulse in two bands, tuned to bounce off rainfall and cloud droplets, respectively. That would enable it to outdo CloudSat by tracking clouds as they burgeon into rainstorms.

As costs began to mount, a NASA review board estimated last year that AOS would cost at least 25% more than the decadal survey recommended. It suggested replacing the advanced lidar with a simpler one and removing the cloud-sensing radar band. "The choice was to reduce science or increase the budget," says Geoffrey Yoder, the former NASA official who co-led the report. Yoder says the review board recommended the agency first consult with NASEM or outside experts on what science would be lost with those cuts—but no such consultation ever happened.

Although the advanced lidar is out of the picture, the fate of AOS-Sky's Doppler radar is less clear. Even if NASA eliminates the high frequency, cloud-sensitive band, Pavlos Kollias, an atmospheric scientist at Stony Brook University, is hopeful that design tweaks can minimize the science loss. The team is pondering using a much larger deployable radar antenna, increasing its resolution, and new techniques will allow it to measure the total amount of water in the air below it much better than CloudSat, while also penetrating closer to the surface, Kollias says. Schumacher, however, is less hopeful. No matter how far you stretch a radar's capabilities within one band, she says, it can't do it all. "You won't see the full evolution of the storm—only when it's gotten big enough to rain."

In NASA jargon, AOS is in "phase A," a time when the final budget is not set and options can be explored. One is a collaboration with the Italian Space Agency, which would provide a lidar that would be more capable than the Calipso-style one that NASA now favors, although no match for the originally planned one. "It's a very real possibility, and we're excited about exploring it," St. Germain says.

Nonetheless, some researchers worry NASA is losing its long-standing edge in Earth observation. The European and Japanese space agencies, among others, are now proposing missions with more advanced technology. With these cuts in its flagship climate mission, Redemann says, "There's a real concern that NASA will be seen as falling behind the earth system science race." ■

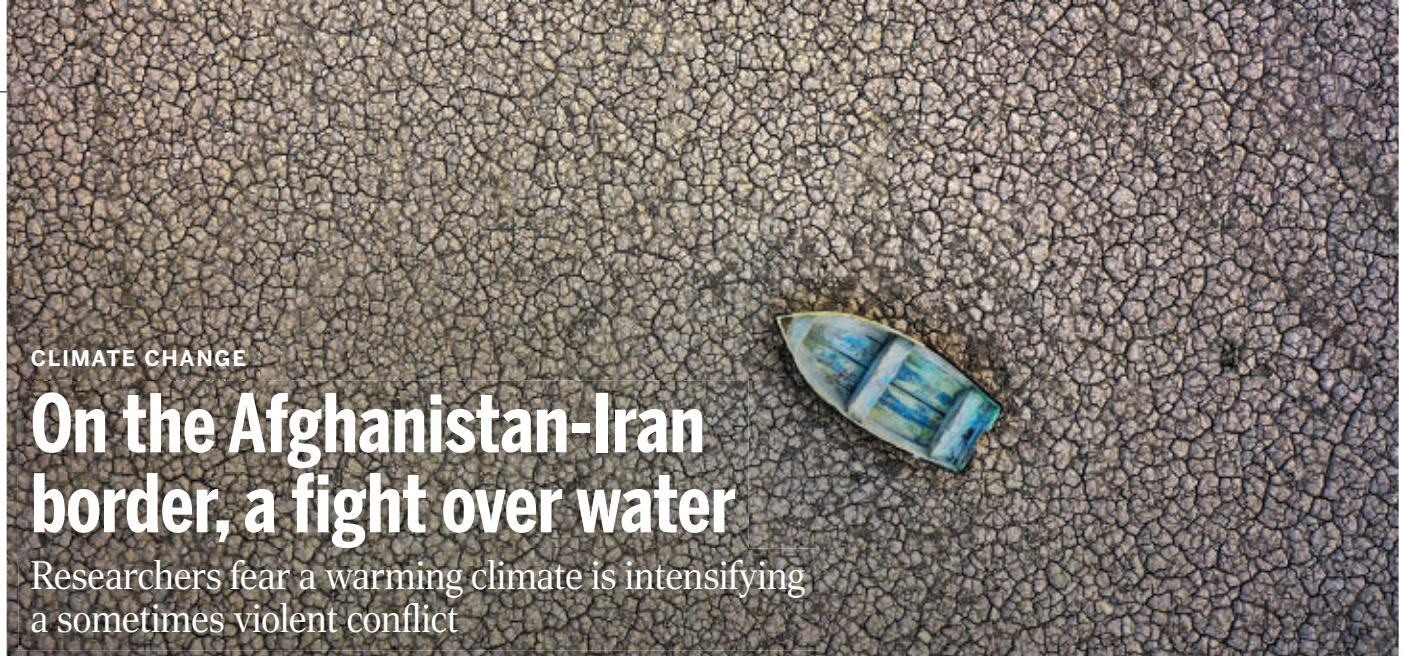

CLIMATE CHANGE

On the Afghanistan-Iran border, a fight over water

Researchers fear a warming climate is intensifying a sometimes violent conflict

By **Ruchi Kumar**

Earlier this year, Mohammed Noman could hear the faint but persistent sound of gunshots from his farm in western Afghanistan near the border with Iran. The gunfire was a reminder that, since the Taliban won control of the nation in 2021, conflict has continued. This time, however, "The fight is over the precious water," Noman says.

Fueled in part by a prolonged drought, tensions over water between Iran and Afghanistan have escalated this year, with Iran accusing Taliban leaders of violating a long-standing agreement to share water from the Helmand River, which flows from Afghanistan into Iran. In late May, clashes near the river reportedly killed at least two Iranian border guards and one Taliban fighter. "We are close to the border, so we witnessed these battles with our own eyes," Noman told *Science* in June. "We live in constant fear."

It's a familiar spat, says Najibullah Sadid, an Afghan water specialist at the University of Stuttgart. "If you look at the history of dispute between Iran and Afghanistan—starting from 1872, 1898, 1902, and 1935—they all coincide with the years of droughts," he says.

But this time climate change may be contributing. Although detailed data are scarce, a recent study concluded that average temperatures in Afghanistan have risen by 0.6°C to 1.8°C since 1950. "If you look at the map [of Afghanistan], the area that has the highest change in temperatures [is] … where the conflict has occurred," says water specialist Assem Mayar, a former lecturer at Kabul Polytechnic University.

The warming comes on top of precipitation shifts, population growth, and expanding agriculture. All have put increasing pressure on water supplies in the Helmand River Basin, which covers some 40% of Afghanistan. Satellite data show that groundwater levels dropped by an average of 2.6 meters from 2003 to 2021, researchers reported this year in *Earth Science Informatics*. The Hāmūn Lakes along the border have shrunk by more than 90% since 1999, noted a study published last year in *Science of the Total Environment*. Researchers estimate the amount of Helmand River water reaching Iran has dropped by more than half over the past 2 decades, in part because of the construction of new dams and the expansion of irrigation in Afghanistan.

In recent years, the annual snow depth in Afghanistan has been markedly below average, reducing runoff, notes the Famine Early Warning Systems Network. In 2021, the greatest snow deficit was in the central Hindu Kush mountains, where all of Afghanistan's major rivers, including the Helmand, originate.

Those trends have exacerbated long-standing tensions over a 1973 treaty between Afghanistan and Iran that guarantees Iran a share of the Helmand's water. In 2021, Afghanistan gained greater control over the river's flow with the completion of the Kamal Khan Dam, which created a reservoir not far from the Iranian border that can store 52 million cubic meters of water. Iran has accused the Taliban of operating the reservoir in ways that violate the 1973 treaty, claiming this year that it has been receiving less than 4% of the promised amount. The Taliban, in turn, has blamed drought for the restricted flow.

One factor fueling distrust between the two nations is a lack of robust monitoring data. A key water gauge along the Helmand in Afghanistan, for example, "was destroyed in the conflict years ago … making it difficult to estimate flows," Sadid says. In June, Iranian officials said the Taliban had agreed to a request for an Iranian "technical team" to visit the dam to measure water levels. Late last month, the Iranian Ministry of Foreign Affairs said it had reached a "preliminary agreement" with the Taliban on water sharing but released no details.

A stranded row boat on the Hāmūn Lakes, which are fed by Afghanistan's Helmand River.

Over the long term, researchers say extensive changes in water management will be needed to ease the crisis. Iran, for example, has built four reservoirs near the border that lose enormous amounts of water to evaporation, Sadid says. And both nations have highly inefficient irrigation systems. Overall, researchers estimate up to 70% of the available water is wasted. "If systems are updated … it will help save and allocate water downstream," Mayar says.

A shift in crops could also help. In Afghanistan, many farmers grow wheat varieties that are poorly adapted to heat and drought, Mayar notes. Other options, including saffron and some vegetables, need less water, but "Afghan farmers don't opt for them since there aren't sufficient facilities such as transport," Mayar says. Water shortages have prompted some Afghan farmers to switch to growing opium poppies, which are more drought-tolerant—despite a government ban on the crop because it is used to make heroin and other narcotics.

Noman says some farmers in his area have switched to growing opium, but he will not. "My father and grandfather considered it a dirty crop," he says. But he worries what the future will bring if Afghanistan and Iran do not find a way to share water. "The world should not ignore us and the situation we are in," Noman says. "This conflict could spill over into the entire region." ■

Ruchi Kumar is a journalist covering South Asia.

PHOTO: MOHAMMAD DEHDAST/PICTURE-ALLIANCE/DPA/AP IMAGES

GLOBAL HEALTH

Disease alert system in trouble

Money woes and staff strike threaten ProMED dispatches

By **Sara Reardon**

The first news outside China about the COVID-19 pandemic came from a disease-alert system called ProMED. This fateful post in December 2019 about mysterious pneumonia cases in Wuhan is just one example of how physicians and public health experts around the world have used the nearly 30-year-old, free service to share real-time information about local disease outbreaks.

But ProMED is now on life support. Since last week, 25 of its 38 paid editors and moderators have gone on strike. Most signed a letter suggesting the service find a new home because of a lack of input into decisions made by ProMED's parent organization and sponsor, the International Society for Infectious Disease (ISID). The society had weeks earlier announced ProMED faced a financial crisis and had begun to take actions to keep the service alive, such as charging its 20,000 subscribers for its emails and website.

Some scientists see the subscription plan as a blow to researchers and health workers, especially in developing countries, who rely on its announcements. "The fiber of ProMED has always been open source and it serves a very broad international community," says Harvard University epidemiologist John Brownstein. "It provides a real global public health service."

Others worry outbreaks could be missed if ProMED were to shutter. That would be "a tragic and preventable loss," University of Saskatchewan virologist Angela Rasmussen posted online.

In a statement, ISID CEO Linda MacKinnon said ProMED would continue to operate "in a limited capacity" while ISID worked with the letter's signatories. "We also know that we could have communicated changes more clearly to the community and apologize for any confusion and distress caused," she added.

Three volunteers founded ProMED in 1994, the early days of the internet, as a simple listserv whose emails collected disease news from around the world. ISID took it over in 1999. In addition to alerting the world to COVID-19, it relayed news of the first cases of other coronavirus diseases: severe acute respiratory syndrome in China in 2003 and Middle East respiratory syndrome in Saudi Arabia in 2012. The site now averages eight to 10 alerts per day.

Nevertheless, ProMED has struggled to maintain a funding stream. Its longtime editor-in-chief, Lawrence Madoff, who says he was forced out by ISID leadership in 2021, says for a time foundation grants for projects helped keep the alert system afloat. But donors tend to balk at supporting staff salaries and infrastructure, he says.

In October 2022, ISID turned to soliciting donations from ProMED's members to raise the $1 million needed annually to run the service. But it collected only $20,000, according to a 14 July email to ProMED members from ISID.

"ProMED is in dire financial straits," the letter said. Despite increased attention to public health during COVID-19, the service "has been unable to capitalize on the unprecedented amounts of money that were infused into [the pandemic] space." So ISID said it was instituting a model that would charge users as-yet-unspecified fees to receive different levels of information and to search ProMED's post archive. Blocking free archive access was necessary to prevent data scraping by governments and corporations that have been "unwilling or unable to help ensure our financial viability."

The July letter was signed "ProMED Team." But the 3 August letter from ProMED staff said ISID had failed to consult with or even inform them about the subscription plan or that the archive was being closed to the public.

The ProMED staff also said ISID hadn't discussed other recent decisions, such as ousting Madoff, and its new fundraising strategies. "It is therefore with great sadness and regret that we, the undersigned, are hereby suspending our work for ProMED," they wrote. Editors also lament an ISID announcement on 14 July that ProMED staff's stipends would be delayed. Although payments are modest, some moderators depend on that income, says Martin Hugh-Jones, a veterinary ProMED moderator who covers anthrax.

Leo Liu, an infectious disease physician and one of ProMED's "top mods" who signed the letter, says he is not against a subscription model with tiered pricing for lower income countries. But ISID "didn't do even the most basic market research" on this plan, he says. The ideal outcome, he says, would be for ISID to partner with a university or foundation to support the listserv, with ISID potentially retaining the ProMED archive.

Establishing such a partnership is among three demands made in the letter, in addition to ProMED representation on ISID's executive committee and editorial independence. "It's really about having a voice and really pleading for overseers to take an active role," Liu says.

MacKinnon's statement said the organization is "working tirelessly on all fronts for unrestricted grants, and [is] exploring and open to strategic partnerships." But in the meantime, "The only viable path forward is to move to a subscription-based model." ■

The ProMED system has given early warnings of outbreaks such as severe acute respiratory syndrome in 2003.

PHOTO: J.P. MOCZULSKI/AFP VIA GETTY IMAGES

Sara Reardon is a biomedical journalist based in Bozeman, Montana.

NEWS FROM Science | AAAS

Subscribe to **News from Science** for unlimited access to authoritative, up-to-the-minute news on research and science policy.

bit.ly/NewsFromScience

FEATURES

WANDERING SEEDS

Millennia before Europeans arrived in Australia, humans helped shape the distribution of the continent's plants

By **Elizabeth Pennisi**

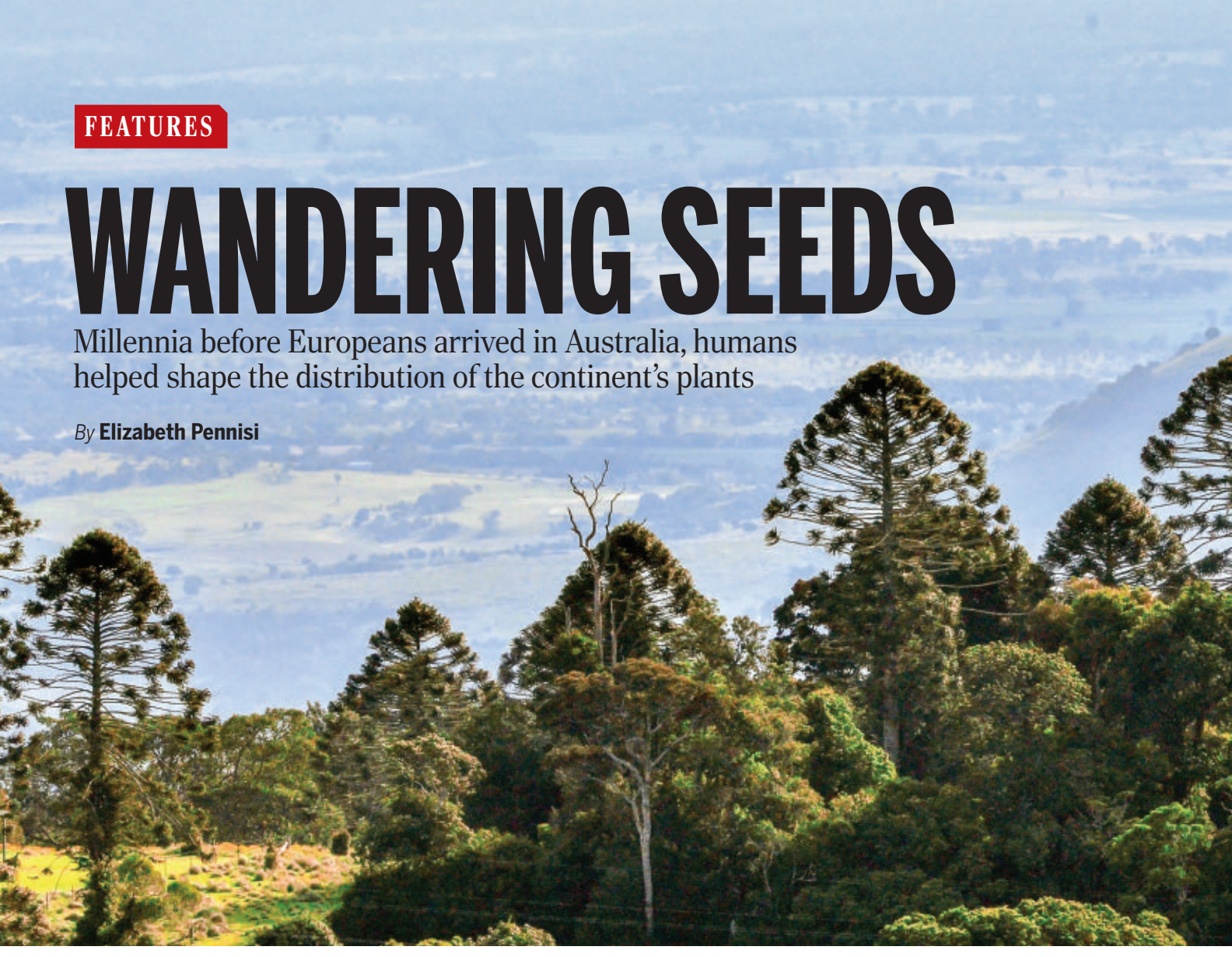

PHOTO: ZAQQYJAM/WIKIMEDIA COMMONS CC BY-SA

On shady, densely wooded riverbanks in eastern Australia, the black bean tree is easily missed. It can reach 12 stories tall, but *Castanospermum australe* mostly blends in with its rainforest peers. Each November, however, it catches the eye as sprays of large red and orange blossoms adorn its dark, glossy leaves. Six months later, cylindrical pods longer than a banana encase three to five large seeds.

The seed pods are buoyant, so those that end up in the water can drift away, allowing the seeds to germinate far from the parent tree. But each seed weighs about as much as a mouse—too heavy to be carried off by the wind or easily dispersed by birds and most rodents.

Therein lies a mystery: Black bean trees sprout not just along waterways and coastal areas, but also along ridges high above rivers, far from the water. A few years ago, Maurizio Rossetto, an evolutionary ecologist at the Royal Botanic Garden Sydney, began to wonder how they got there.

One potential answer was that these unusual patches were the remnants of forests created long ago by large, now extinct animals that once helped spread black bean seeds across eastern Australia. Rossetto knew that most large-seeded plants thought to have lost their ancient distributors had retreated to small areas, yet the black bean trees are widespread. So, he wondered about another possible disperser: prehistoric Australians, who arrived on the continent at least 50,000 years ago.

Rossetto was experienced in using genetic data to reconstruct the historic distributions and movements of other Australian plants. But to link the distribution of the black bean tree to people, he would need help from today's Indigenous Australians, who use the tree for food and ritual purposes. He turned to ecologist Emilie Ens of Macquarie University, who is a pioneer in the emerging field of cross-cultural ecology, in which stories told by Indigenous grandmothers and their ancestors can carry as much scientific weight as studies of DNA. By developing collaborations with Indigenous people, Ens and Rossetto have been able to combine oral histories, Indigenous knowledge, and scientific data to unravel how the histories of Australia's plants and people are often closely intertwined.

"Increasingly, there is an acceptance that it would make a lot of sense to consult the people who have lived here for tens of thousands of years" when trying to reconstruct Australia's ecological evolution, says Tony Hughes-d'Aeth, a cultural historian at the University of Western Australia (UWA).

Ens's and Rossetto's cross-cultural study of the black bean tree isn't unique. A second Australian team is working closely with Indigenous partners to understand how other culturally important plants arrived

Towering bunya trees were a source of nutritious nuts and the focus of Aboriginal festivals.

PHOTO: KONRAD WOTHE/MINDEN PICTURES

at their current distributions. Together the two groups are finding that the seemingly natural distributions of key food plants likely reflect the habits and travels of the first Australians. "We are increasingly aware that what we thought of as 'wild' ranges of species did not take into account traditional activities," Rossetto says.

The findings could aid efforts to conserve plants and help them adapt to climate change. They also echo similar revelations about Brazil nut trees and other plants in South America. And the research speaks to the underrecognized sophistication of the people who occupied landscapes long before the arrival of Europeans. In Australia, the work has helped further undermine colonial-era assumptions that native people were aimless wanderers, as well as claims of *terra nullius*—that the land belonged to no one when the first British settlers arrived.

"Humans have [long] been part of Australia's ecosystems," says ecologist Alison Lullfitz of UWA. "But it's only in the last decade that ecologists have started to meaningfully try to consider that."

TO TRACE THE JOURNEY of the black bean tree, Ens and her colleagues first scoured the literature for accounts by early European settlers that mentioned how Aboriginal people used the species or recorded their stories about the plant. She contacted Oliver Costello, a Bundjalung man who runs the Jagun Alliance, a nonprofit organization advocating for culturally informed resource management. He said he was glad to be involved. His parents planted his placenta under a black bean tree, and he gave his daughter seeds from that tree so she could plant her own tree. "I had a personal connection to it," Costello says.

Costello helped interview five Indigenous "knowledge custodians." Among other things, the researchers learned of a ritual that involved mashing the seeds, or nuts, and then soaking the mash for several days in a river to detoxify it so it can be eaten. In some cultures, "the processing of the nuts was part of the initiation of becoming a woman," says Monica Fahey, a molecular ecologist at the Sydney botanic garden and a Macquarie Ph.D. student who works with Rossetto and Ens.

The custodians also recounted "songlines," narratives memorized by Aboriginal travelers to help them navigate from place to place. One songline, recorded in the 1950s, described how an ancestral spirit carried a bag of black beans as it traveled from Australia's east coast to mountains in the west. Using their intimate knowledge of the region, Costello and a "traditional pathway" expert, Ian Fox, predicted that this route included ridges near the Nightcap and McPherson mountain ranges. Some ridges mark the boundary between the states of Queensland and New South Wales, where black bean trees now grow. In other conversations, the researchers learned that Aboriginal people often buried black bean seeds as they moved from camp to camp.

Rossetto and his colleagues soon found that their genetic data aligned remarkably well with these oral histories. Black bean tree leaves collected at a number of sites, including traditional camping spots just below the mountain ridges, yielded chloroplast and ribosomal DNA sequences that were notably similar, the team reported in 2017 in *PLOS ONE*. That supported the idea that even trees found in widely separated watersheds shared a common ancestor, and that the species had spread across the region in just a few millennia. The pattern "makes sense," Costello says.

In contrast, DNA sequences taken from black bean trees growing in wetter, more tropical areas farther north—where Indigenous people appear to have weaker cultural connections to the tree—showed less similarity and ancient divergences, suggesting prehistoric people played a lesser role in moving seeds across the landscape.

"It was exciting to see new genomic techniques being combined with traditional knowledge, songlines, and biogeography," recalls Jennifer Silcock, an ecologist at the University of Queensland who was not involved in the work.

Costello himself was surprised by the results. He grew up in Bundjalung country, along Australia's east coast, thinking black bean was native there. Now, knowing how these and perhaps other plants were introduced "helps us think through how we might do that in the future," perhaps to aid conservation efforts.

Black bean seeds, too heavy to be dispersed by modern animals, were spread by Indigenous people.

LULLFITZ EMBARKED on her own cross-cultural journey at about the same time. She grew up on a farm next to a large national park in southwestern Australia, but she had thought little about that area's human history until she met Shandell Cummings and her mother Lynette Knapp, members of the Noongar Aboriginal group native to that area. The women "took me under their wing," Lullfitz says. At times, they would meet to gather food plants in the bush, including the tuber *Platysace deflexa*, which has various names, including yoowak, youlk, and youaq. Lullfitz was impressed by the mother's and daughter's knowledge and passion about what they called their "country," by which they meant not just the land and its plants and animals, but also their links to it through traditions and stories.

When Lullfitz started her Ph.D. in 2014, she embraced these connections, both personally and professionally. She decided to

PHOTO: STEVE HOPPER

study the distribution of yoowak and two related species—and to recruit Cummings and Knapp as close collaborators.

That was a wise approach, says Alan Williams, an archaeologist at EMM Consulting Pty Unlimited. "Researchers are generally only briefly in country and therefore may miss the nuances and longer changes in the environment that Indigenous people will be aware of," he says.

Lullfitz's work focused on Australia's southwest floristic region, a biodiversity hot spot that includes a United Nations Biosphere Reserve because it's so rich in unique species. The landscape is dotted with heathlands, eucalyptus woodlands, and granite outcrops that include water sources Indigenous people visit for ceremonies and use as way stations during long-distance travel.

For her study, Lullfitz collected three *Platysace* species. Historically, Indigenous people harvested two of them: yoowak, which grows on sandy plains; and *P. trachymenioides*, which Lullfitz dubbed rock youlk because it grows on outcrops. The third, *P. effusa*, is not eaten because it lacks tubers.

Lullfitz and her colleagues analyzed DNA isolated from the three species at dozens of locations. The yoowak sequences were remarkably similar, even though the highly variable soils might be expected to isolate populations and lead to genetic divergence. The same pattern held for rock youlk—but only in the southeastern part of its range. In contrast, there were large genetic differences among the *P. effusa* samples, Lullfitz and her colleagues reported in 2020.

The yoowak pattern suggests humans were moving that plant—but not the inedible *P. effusa*—from place to place, Lullfitz says. And it fits with the traditional knowledge related by Cummings and Knapp, who said their ancestors often carried yoowak on trips because it holds a lot of water and remains edible for a long time, particularly if stored underground.

The women also believe they can explain why rock youlk is genetically homogenous in only a small region. That plant was considered less desirable than yoowak, so they and Lullfitz think it was not used very much—except in the southeastern part of its range, where other, tastier edible tubers are much rarer. Such findings add to the "increasing evidence that some occurrences or populations of species may be cultural," Silcock says.

INCORPORATING INDIGENOUS knowledge into research projects can produce valuable insights, but it can require ecologists to adopt new ways of working. Ens, for example, notes that it can be "very hard to access" Indigenous sources of information—particularly for academic scientists juggling grant deadlines, teaching obligations, and other commitments. So, when her group wanted to trace the history of another culturally important tree in 2018, she recruited Patrick Cooke to help build ties. Cooke, a member of the Gungalida Aboriginal group, had experience working with native communities on health and social issues.

Cooke says he was eager to use his connections—and develop new ones—to help reconstruct the distribution of *Araucaria bidwillii*, a massive conifer whose common and Aboriginal names include bunya-bunya, the monkey puzzle tree, Bonyee, and Bonyi-Bonyi. Striking for its dome-shaped symmetry and now often planted by landscape designers, it comes from a lineage that dates back to the dinosaurs and has relatives across the Southern Hemisphere. In its homeland, the tree grows wild only in a few places in southeast and north Queensland.

Bunya cones, which can weigh more than a small dog, are a rich source of nutritious seeds. The tree was so important to Aboriginal people that they would travel hundreds of kilometers to stands in the Bunya and Blackall ranges for periodic festivals. Some older trees bear foot- and handholds created by climbers who harvested cones. These ceremonies ended at the turn of the 20th century, when loggers started to cut bunya.

At first, finding people willing to share their knowledge of bunya trees "was very hard," Cooke recalls. "No one knows who you are." Always, the initial outreach simply involved "yarning"—making small talk about friends and family that barely touched on the project at hand. Often, however, people became interested in sharing their bunya stories after Cooke described the earlier black bean project. The process of properly developing collaborations, he says, "is like peeling back the layers" of an onion. (In 2022, Cooke and colleagues described in *Ecological Management & Restoration* eight "layers" of protocols and guidelines

Noongar member Shandell Cummings (left) works with researcher Alison Lullfitz to unravel the history of rock youlk (left photo), a tuber traditionally important in Cummings's culture.

PHOTO: STEVE HOPPER

that scientists should consider when forging Indigenous collaborations, ranging from expectations set by international treaties to rules for one-to-one conversations.)

As with the black bean tree, it turned out "there is strong agreement between Indigenous knowledge and genetic and distributional data" for the bunya, says Rossetto, who was involved in the work. In an upcoming doctoral thesis, Fahey notes that the evidence suggests that before Europeans arrived in Australia, bunya stands were scattered across southeastern Queensland, but only two small populations grew in northern Queensland. Those southern stands are genetically similar, Fahey says, suggesting humans had a hand in their appearance. But the two northern pockets are genetically distinct, suggesting little human influence.

Indigenous knowledge shared with the team supports this picture. In the north, for example, there were no stories about people using or celebrating with bunya. And archaeological evidence suggests prehistoric people in the north consumed other nut species. As a result, bunya "didn't take hold [in the north] as it did in the south," Ens says.

Even in the south, bunya tree stands are scattered, which Fahey says is consistent with reports that families controlled bunya trees and who got seeds—and therefore how far they were distributed. Only after European colonization, when Aboriginal families were forcibly scattered to missions far from their homes, did bunyas became more widespread, as displaced families often planted trees on mission lands.

When Fahey publishes her work, Indigenous collaborators will be among the authors. And that, Ens says, represents a significant step toward acknowledging the value of cross-cultural research collaborations. "Having people involved and being able to talk about their scientific knowledge in a scientific space is very important," she says. In addition, demonstrating that genetic data back up stories told by Elders gives others "the confidence to talk." Hughes-d'Aerth agrees: "For an Indigenous child to hear and know that their culture is a source of valuable knowledge literally means the world."

THE RESEARCHERS involved in reconstructing Australia's past interplay of plants and people say there is plenty of work left to do. Fahey and colleagues, for example, are continuing to gather knowledge about the black bean tree and collect samples from more sites. Fahey has sequenced the bean's whole genome and hopes these data will enable researchers to refine the tree's history and perhaps even pinpoint the origins of the existing populations.

They have also launched a systematic effort to identify more examples of human-dispersed wild species. In a paper published in *Genes* in 2022, the researchers identified 15 species with nutritious, edible seeds too large to be easily dispersed by other means. Five of those species have known cultural significance, and Fahey is now working with Indigenous collaborators to decide which ones to study further.

The findings from these kinds of studies could be of more than just academic interest. They could also offer practical insights into how to make conservation projects more effective. Research in South America and elsewhere has shown that Aboriginal populations have helped maintain biodiversity over long periods, says Maria Beatriz N. Ribeiro, a plant ecologist who works with the Socio-Environmental Institute, a Brazilian Indigenous organization. "In past decades, it was believed that the protection of ecosystems without human presence would be essential to save biodiversity," she says. "But today, in many places, this paradigm is being overthrown."

In Australia, understanding the bunya tree's human-influenced past could help ensure its future. The species is threatened by a soil pathogen, and translocating it could provide refuge. "Understanding how plants reacted to past redistribution can help with restoration efforts today," Fahey says.

For the moment, however, "For most species, inferences or suspicions of [Aboriginal] dispersal remain untested," Silcock says. But Scott Mooney, a paleoecologist at the University of South Wales, expects that to change. The recent cross-cultural studies, he says, are "part of a trend. There will be more. … These are at the front of that wave." ■

EPIGENETICS

A mammalian DNA methylation landscape

A study of 348 species offers clues into the diversity of mammalian life spans

By **Alex de Mendoza**

Mammals vary greatly in life span; for example, the bowhead whale (*Balaena mysticetus*) can live up to 200 years, whereas giant Sunda rats (*Sundamys muelleri*) only live for about 6 months in the wild. This disparity is encoded in the genomes of each species; however, which genes are linked to these traits is still poorly understood. Because mammals have approximately the same genes, variation in how these genes are regulated should be important in determining the timing of aging. On page 647 of this issue, Haghani *et al.* (*1*) describe a large-scale study of DNA methylation (which has a role in gene regulation) in a diverse range of mammalian species. They identified genomic regions that might govern life-span variation among lineages, which could help uncover the molecular drivers of life span and other traits in mammals.

PHOTO: ANUP SHAH/MINDEN PICTURES

DNA methylation is a small chemical modification that occurs in most cytosines that are followed by a guanine (CpGs) in mammalian genomes. DNA methylation information is inherited after mitosis; however, it is not static during development or among tissues. DNA methylation differences occur mostly at "enhancers," stretches of DNA that dictate the expression of nearby genes. Thus, each cell type and tissue in the body has a precise DNA methylation signature, like a barcode. Although DNA methylation is frequently not the main factor that dictates gene regulation, it is a robust biomarker for gene activity and cell identity (*2*, *3*).

DNA methylation is easier to measure than other classic gene regulatory mechanisms, such as histone modifications or transcription factors. However, reliable quantification of DNA methylation across the genome is not trivial because current gold-standard methods such as whole-genome bisulfite sequencing require a reference genome and large amounts of data. This makes studying DNA methylation across a large number of samples difficult, but large sample sizes are required to find significant associations between DNA methylation and complex traits such as life span or weight (*4*). This limitation can be overcome by using microarrays to probe for specific subsets of CpGs. Such microarrays have previously been used for studies in humans and mice. Haghani *et al.* used a recently designed pan-mammalian DNA methylation microarray that captures a subset of the CpGs that are conserved across all mammals, including marsupials and egg-laying mammals (although with lower resolution for these two lineages), at high confidence and for a fraction of the cost of other methods (*5*). The microarray does not need a reference genome, and the CpGs are directly comparable across samples and species.

Haghani *et al.* profiled the DNA methylation of 15,456 samples from 348 species, including up to 70 tissues per species. They used the data from blood (a tissue comparable across species) to obtain species relationships solely on the basis of DNA methylation. This clustering largely recapitulated the mammalian tree of life, which indicates that phylogeny and species relatedness is a major factor that underlies variation in DNA methylation. Still, this "phylogenetic" signal did not explain all the variation.

To disentangle the variation in DNA methylation explained by phylogeny from that explained by other traits such as age or tissue of origin, the authors performed unsupervised clustering of all the CpGs (in all species and all tissues) according to their covariation. CpGs that gained or lost methylation in a coordinated manner across many samples were grouped together into modules. The authors then looked for associations between these modules and a range of features, including species traits such as taxonomy or life span and individual traits such as age, sex, or weight. As expected, many CpG modules had methylation patterns that were specific to a taxonomic group. However, other modules included groups of CpGs whose methylation status was enough to discriminate the organ or sex of the sample regardless of species.

DNA methylation was profiled in species including the African elephant (*Loxodonta africana*, left), which lives for 70 years on average, and the lab mouse (*Mus musculus*, above), which lives for an average of 2 years.

PHOTO: HEIDI AND HANS-JUERGEN KOCH/MINDEN PICTURES

Several CpG modules were associated with life span. Variation in DNA methylation in these genomic regions explained, to some extent, the differences in life span across species. This finding is linked to the discovery that as humans and mice age, DNA methylation changes in many genomic regions (*6*). This has allowed the construction of so-called "epigenetic clocks," which are mathematical models that enable the prediction of biological age on the basis of methylation status of specific CpGs (*7*). Because the relative onset of aging could be a major factor in determining species maximum life span (*8*), identifying CpG modules that are linked to cross-species variation in life span might identify gene regulatory events that are responsible for differential aging processes in mammals.

Among the genomic regions that were associated with life-span variation, some were predicted to be regulated by transcription factors important for pluripotency. These pluripotency factors encode proteins, such as octamer-binding protein 4 (OCT4) or SRY-box transcription factor 2 (SOX2), whose expression can revert an adult differentiated cell to an embryonic-like cell. OCT4 and SOX2 belong to a group of transcription factors known as the Yamanaka factors, the experimental reactivation of which decreases markers of aging in mice (*9*, *10*). Haghani *et al.* found that experimental reexpression of the Yamanaka factors in adult mice affected the methylation status of some CpG modules associated with life-span variation. Therefore, regulation of these factors across the life of mammals might drive different life spans, with some species expressing them for longer.

The study of Haghani *et al.* shows that DNA methylation can be a powerful biomarker across mammals. The ability to rapidly measure methylation in any DNA sample and discriminate characteristics such as age, tissue, or sex may have multiple applications. For example, in conservation biology, it could help predict the age of individual animals that would be otherwise hard to assess in the field. Similarly, the epigenetic signature of exposure to pollutants and its effect on biological aging could now be assessed in wild animals (*11*).

The association between DNA methylation and life span is fascinating, although the molecular determinants of aging onset and how life span is encoded in the genome are still far from clear. Because the DNA methylation microarrays represent just a subset of the genome, further technological developments that provide full-resolution methylation maps across the genome might be able to identify species-specific adaptations in nonconserved genomic regions. Furthermore, because CpG methylation status is usually the consequence of complex upstream processes rather than the cause, precisely how these DNA methylation changes explain aging or life span is not yet clear. But now there is a robust high-throughput DNA-based marker to molecularly assess traits across mammals. Therefore, experimental treatments aimed at modifying aging, such as calorie-restricted diets or high-fat diets, can now be tested in nontraditional model species with distinct metabolic adaptations, and epigenetic aging can be measured. ■

School of Biological and Behavioural Sciences, Queen Mary University of London, London, UK.
Email: a.demendozasoler@qmul.ac.uk

REFERENCES AND NOTES

1. A. Haghani *et al.*, *Science* **381**, eabq5693 (2023).
2. E. Kreibich, A. R. Krebs, *FEBS Lett.* **597**, 1805 (2023).
3. D. Schübeler, *Nature* **517**, 321 (2015).
4. P. D. Yousefi *et al.*, *Nat. Rev. Genet.* **23**, 369 (2022).
5. A. Arneson *et al.*, *Nat. Commun.* **13**, 783 (2022).
6. K. Seale *et al.*, *Nat. Rev. Genet.* **23**, 585 (2022).
7. C. G. Bell *et al.*, *Genome Biol.* **20**, 249 (2019).
8. S. C. Stearns, *The Evolution of Life Histories* (Oxford Univ. Press, 1992).
9. K. C. Browder *et al.*, *Nat. Aging* **2**, 243 (2022).
10. A. Ocampo *et al.*, *Cell* **167**, 1719 (2016).
11. H. Wu, C. M. Eckhardt, A. A. Baccarelli, *Nat. Rev. Genet.* **24**, 332 (2023).

10.1126/science.adj4904

MATERIALS SCIENCE

Fine tuning an atomic mesh

Controlling the angle in atomic meshes could result in quantum properties on demand

By **Jiwoong Park**

Holding up two meshes that are slightly misaligned reveals periodic wavy stripes called moiré patterns. Something similar happens when meshes are several million times smaller. Stack and misalign layers of two-dimensional (2D) crystals such as graphene, which are essentially meshes made of carbon atoms, and a moiré lattice forms. In these lattices, electrons are under a periodic potential because carbon atoms from the two layers alternate between being perfectly overlapped and being shifted. Controlling this periodicity could enable the engineering of superconductors and quantum materials that are currently unavailable (*1*). But further optimization of quantum materials' properties requires a new approach to fine tune the moiré lattice periodicity. On page 677 of this issue, Kapfer *et al.* (*2*) report a solution: pushing and bending a long ribbon-shaped 2D crystal lying flat on the surface of another crystal. They successfully create moiré lattices that are continuously varying, programmable, and high quality.

Accurate tuning of moiré lattices requires complete control of the mechanical state of the 2D crystals (*3*). To generate a desired moiré lattice, 2D crystals should be rotated, stretched, compressed, and sheared by measurable and controlled amounts because the periodicity is sensitive to misalignments. Of these strategies, rotational control, which alters the interlayer twist angle, has been the most explored and the easiest to manipulate. Producing a sample with a target twist angle involves thinning down a thick crystal to a monolayer of 2D crystals (exfoliation), splitting a 2D crystal into two (cutting), detaching one-half from the substrate (delaminating), and then putting it on top of the other half (restacking).

> **"... tuning of moiré lattices requires complete control of the mechanical state of the two-dimensional crystals."**

Although this method appears straightforward to implement, in practice it is difficult to generate samples with the necessary quality, reproducibility, and yield. This is because 2D crystals are prone to deformations that vary across the crystal and can be introduced at every step during the sample-making. As a result, the moiré lattice may not have a single repeating motif in the structure. Even if a few high-quality moiré lattices are fabricated, they only provide access to discrete twist angles instead of a continuously varying one. This is a problem because properties of interest are often highly sensitive to the moiré structure, and their optimization would require fine tuning. For example, superconductivity in twisted bilayer graphene is seen with a twist angle of around 1.1°, which is often called the magic angle, and has a tolerance of only 0.1° (*4*).

The method that Kapfer *et al.* developed is based on pushing and bending atomic mesh ribbons, which could address the problems with quality and reproducibility. They placed a graphene ribbon and other 2D materials such as tungsten diselenide (WSe_2), tens of micrometers long and 1 to 5 μm wide, on a thick crystal of hexagonal boron nitride (hBN), which adheres well to graphene and keeps it flat. Then they placed and pushed a specially made handle over the ribbon using the tip of an atomic force microscope (AFM), a tool that can move microscopic objects with atomic-scale precision (*5*). This process successfully bent the graphene ribbon on the hBN without inducing out-of-plane buckling, which could occur if the ribbon were unsupported or subjected to excessive stress (*6*).

This method allowed for the continuous tuning of the two key parameters (the twist angle and the strain) of the 2D ribbon. The resulting ribbon had a small lattice period in the inner part of the bend and a larger one outside (see the figure). When a layer of WSe_2 was bent, a slight blueshift in the photoluminescence spectra was measured from the inner part of the bent ribbon compared with the outer part, which confirmed the sensitivity of the material's electronic properties to the

Bending graphene for fine tuning a moiré lattice

A two-dimensional (2D) monolayer graphene (MLG) ribbon is placed on a thick crystal of hexagonal boron nitride (hBN) and bent by pushing a special handle [made with few graphene layers (FLGs)] using an atomic force microscope (AFM) tip (top left). The result is a bent graphene ribbon, where the lattice is shrunk inside and stretched outside. The strain exerted on the MLG results in a continuously twisted MLG (bottom left). After bending, an unbent MLG flake (blue) is placed over the twisted MLG (purple) to create continuously tuned moiré lattices (right).

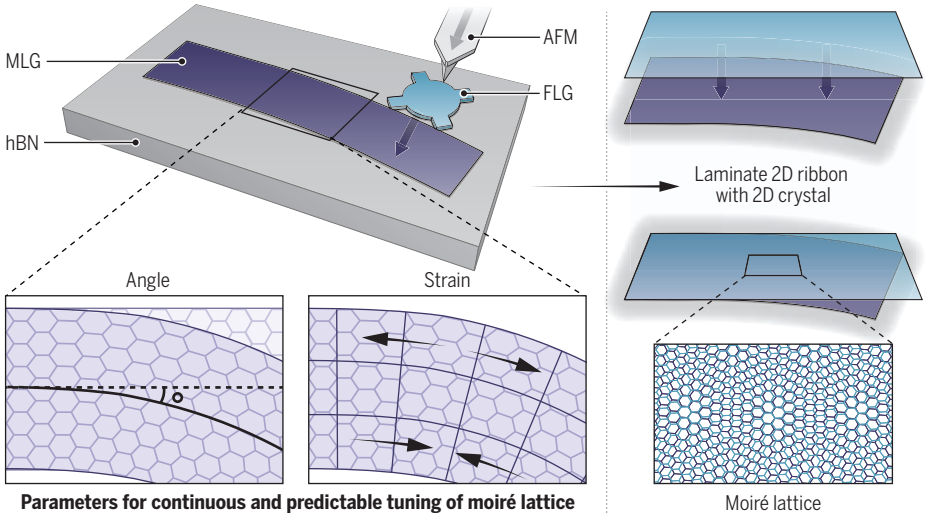

Parameters for continuous and predictable tuning of moiré lattice

GRAPHIC: N. BURGESS/*SCIENCE*

Department of Chemistry, Pritzker School of Molecular Engineering, and James Franck Institute, University of Chicago, Chicago, IL, USA. Email: jwpark@uchicago.edu

bending process. Laminating the bent 2D ribbon with an unbent 2D crystal creates a moiré lattice with both the local twist angle and relative strain changing continuously and predictably along and across the ribbon. For example, in one graphene bilayer sample reported by Kapfer *et al*., the twist angle monotonically increased from below 1.0° to >1.1° across its 1-μm width. Furthermore, the data showed exceptional twist angle uniformity; they observed an extremely small residual angle disorder below 0.01°. Although the precise origin of this improved quality is unknown, a possible explanation is that stretching a mesh makes it flat and uniform, removing most disorder during the process. Therefore, pushing a graphene ribbon with an AFM tip likely stretches and compresses the mesh, removing disorder at the same time.

The abilities introduced by the study of Kapfer *et al*. to fine tune the twist angle and strain in 2D crystals, and to minimize uncontrolled disorder, could lead to the design and fabrication of simulators of quantum materials. This would generate a single object with a continuously tuned specification that could be used to design superconductors and topological insulators. The continuous tuning approach would avoid fabricating many individual samples, each with different properties. This work also highlights the growing importance and potential of strain engineering and solid mechanics of 2D crystals (*7*). An exciting next challenge will be to produce and bend 2D crystal ribbons in large numbers and sizes, which will require multiple innovations that can replace individual exfoliated 2D crystal ribbons with large-scale patterned arrays and the single AFM tip with a mechanical force that bends the entire array in unison. Another challenge is to minimize the twist angle and strain disorder, which could make studying the desired electronic states difficult at every step, including 2D crystal synthesis, delamination, and restacking. Meet these challenges, and more discoveries and applications from perfectly tuned moiré lattices will be within reach. ■

REFERENCES AND NOTES

1. L. Balents, C. R. Dean, D. K. Efetov, A. F. Young, *Nat. Phys.* **16**, 725 (2020).
2. M. Kapfer *et al*., *Science* **381**, 677 (2023).
3. C. N. Lau, M. W. Bockrath, K. F. Mak, F. Zhang, *Nature* **602**, 41 (2022).
4. Y. Cao *et al*., *Science* **372**, 264 (2021).
5. R. Ribeiro-Palau *et al*., *Science* **361**, 690 (2018).
6. S. Xie *et al*., *Science* **359**, 1131 (2018).
7. J. Yu *et al*., *Nano Lett.* **22**, 7180 (2022).

ACKNOWLEDGMENTS

J.P. thanks J. Yu for help with writing and the Air Force Office of Scientific Research for research support.

10.1126/science.adj1420

PHOTO: RDIMAGES/EPICS/GETTY IMAGES

This is the fossilized skull of a Neanderthal man found in Gibraltar. Because there are gaps in the fossil record, climate modeling has been used to predict where Neanderthals and other hominins might have lived.

ANTHROPOLOGY

Using climate to model ancient human migration

Modeling fills gaps in the fossil record of early hominin movement from Africa

By **Emily J. Beverly**

Over the past 30 years, studying the evolution of hominins (humans and their close ancestors) has shifted from locating fossils and artifacts to understanding the ecological drivers behind where these items are found. Since these materials were first discovered, many drivers of hominin evolution have been hypothesized (*1*), but testing these ideas is difficult because of limited data on environmental and climate factors that could have influenced migration and because of the challenges of establishing the age of the sediments in which the materials are found. On pages 693 and 699 of this issue, Margari *et al*. (*2*) and Ruan *et al*. (*3*), respectively, address these difficulties by modeling how both climate and ecosystems changed during various periods of time over the past 3 million years A similar approach was also described by Zeller *et al*. (*4*). These models use current understanding of the environment and climate to extrapolate from incomplete records and provide ecological context for evolutionary changes.

The number of records, such as samples of pollen or lake sediments, that can provide information on environmental change has substantially increased through interdisciplinary projects with earth scientists on terrestrial outcrops (*5*, *6*), targeted continental scientific drilling projects near archaeological sites (*7*, *8*), and analysis of marine cores (sediments retrieved from nearby oceans) (*9*). Analytical tools have also greatly improved, and primary environmental and climate parameters such as temperature and vegetation can now be estimated using proxies—that is, characteristics preserved in rocks or sediments that are used to reconstruct past environments when direct measurements are impossible (*5*, *10*–*12*).

Nevertheless, fossil records are incomplete because they are limited to the rare environments that are conducive to preserving fossils. Furthermore, the sedimentary record where these proxies are preserved is discontinuous across Africa and Asia and through time. Therefore, in areas where such records are lacking, researchers must depend on matching patterns in behavioral changes or speciation and extinction events to those in environmental and climate data obtained from other sites, which can be a great distance away from the fossils or artifacts. As a result, some basic questions about human history remain unanswered. For example, whether past climate change prompted hominin evolution is not known. It is also not clear where and why hominins migrated over the past 3 million years or why *Homo sapiens* (modern humans) is the only hominin to have survived to the present.

Although there is now consensus that all modern humans originated from a popu-

Department of Earth and Atmospheric Sciences, University of Houston, Houston, TX, USA. Email: ejbeverly@uh.edu

Climate-based modeling of hominin habitats

Humans are descended from a population of hominins that left Africa and migrated into Europe, Asia, and eventually Australia and the Americas over the past 75,000 years. Other hominin species, Neanderthals and Denisovans, lived contemporaneously with humans. Climate modeling was used to discover where hominins migrated and when interbreeding could have occurred. For example, climate modeling of preferred habitats of Denisovans and Neanderthals in Africa and Eurasia shows possible windows for breeding between the two species.

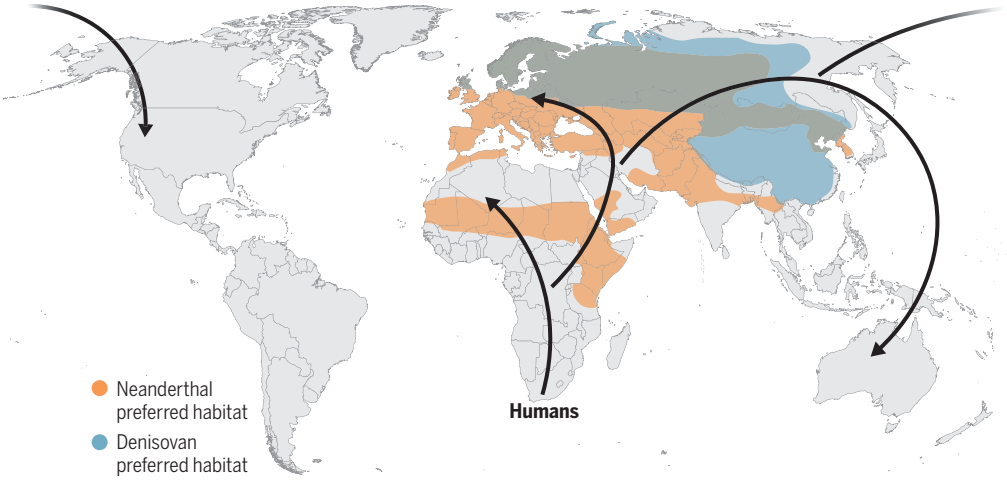

lation in Africa, there is considerable disagreement as to how, when, and why they migrated to Europe and what happened once they arrived. Therefore, the focus of research has shifted to the identification of when humans could feasibly have migrated out of Africa. For example, a climate model was used to identify windows of time over the past 300,000 years in which humans could have migrated across difficult terrain in northern Africa and the Arabian Peninsula (*13*). Other researchers took a different approach, determining whether freshwater springs would persist through major climate swings in Africa related to long-term changes in Earth's orbit around the Sun. This was combined with mapping the maximum distance that a human could travel from these perennial sources of water (~3 days, 150 km) to determine potential migration pathways during different wet and dry scenarios from the Pleistocene (~2.58 million to 11,700 years ago) (*14*).

There is also considerable controversy about whether, once these hominins had migrated out of Africa, they could have survived glacial periods in Europe or instead repeatedly repopulated from Asia. This question is difficult to answer because there are gaps in the fossil record for the oldest known hominins in Europe. Therefore, Margari *et al.* used a marine core with a more complete record from 0.8 to 1.4 million years ago that was collected from off the southwestern coast of Portugal. Proxies for temperature (identified from foraminifera, single-celled organisms living in the ocean) and vegetation (pollen blow from land) were used to reconstruct a continuous picture of the environment. From these data, they created a climate envelope model—a technique to constrain the geographic range of any species using climate variables, such as temperature and precipitation.

The model showed that around 1.1 million years ago, habitats in Europe would likely have been unsuitable for permanent hominin occupation. This is because glacial conditions were so strong that it would have been too cold for hominins to survive without adaptations such as fire or clothing, for which there is currently no evidence. This suggests that hominins might not have permanently settled in Europe at this time and may have instead repeatedly repopulated from Asia, but additional hominin sites with better age control are needed to further test this hypothesis.

Modeling has also been used to combine climate and fossil datasets from throughout Africa and Eurasia. Rather than focusing on a specific location or hominin species, these projects aim to model the preferred habitats of all species, how and when these species might have interacted, and why they migrated (*15*). Climate models have estimated how temperature and precipitation might have varied throughout the past 3 million years. From this information, Zeller *et al.* were able to model changes in habitat suitability for five different hominin species. Their results suggest that hominins were responding to changes in temperature, precipitation, and net primary productivity (a measure of the amount of carbon in an ecosystem) caused by long-term changes in Earth's orbit. The data also suggest that early hominins in Africa preferred open environments, such as grasslands; after their migration to Europe, they began to adapt to a broader range of environments. The modeling of *H. sapiens* showed that they likely adapted to or chose to live in areas with a higher diversity of habitats over the past ~300,000 years to make use of the more varied resources.

Throughout hominin evolutionary history, more than one hominin species lived simultaneously and interbred. Studies of ancestral and modern DNA show that *H. sapiens* have DNA from both *Homo neanderthalensis* (Neanderthals) and Denisovans and that Neanderthals and Denisovans were also interbreeding. However, there are only ~20 archaeological sites attributable to Denisovans compared with more than 700 sites attributed to Neanderthals, which makes it difficult to draw conclusions from location alone. Instead, Ruan *et al.* ran models to simulate climate and habitat change for the past 400,000 years and then determined the habitat preference for both Neanderthals and Denisovans based on the locations of the fossils. Both species likely lived in a variety of environments, but Neanderthals seem to have preferred temperate forests, whereas Denisovans lived in a much wider range of habitats. During this simulation, orbitally driven climate shifts in habitat caused the preferred habitats of Denisovans and Neanderthals to overlap (see the figure). This occurred primarily during interglacial periods when an east-west zone of mutually preferred habitats formed, but interbreeding would have also been possible in Europe during glacial periods.

An added benefit of these types of studies is that the models can be rerun as more fossil and climate records are added. Furthermore, the rapid improvements in neural networks and machine learning over the past 5 years will likely provide new methods to answer outstanding questions about hominin evolution and migration. For example, despite more than a century of research, why hominins developed stone tool technologies is still not clear. ■

REFERENCES AND NOTES

1. J. T. Faith *et al.*, *Trends Ecol. Evol.* **36**, 797 (2021).
2. V. Margari *et al.*, *Science* **381**, 693 (2023).
3. J. Ruan *et al.*, *Science* **381**, 699 (2023).
4. E. Zeller *et al.*, *Science* **380**, 604 (2023).
5. T. E. Cerling *et al.*, *Nature* **476**, 51 (2011).
6. R. Potts *et al.*, *Science* **360**, 86 (2018).
7. A. S. Cohen *et al.*, *Annu. Rev. Earth Planet. Sci.* **50**, 451 (2022).
8. R. Potts *et al.*, *Sci. Adv.* **6**, eabc8975 (2020).
9. J. E. Tierney, P. B. deMenocal, P. D. Zander, *Geology* **45**, 1023 (2017).
10. B. H. Passey, N. E. Levin, T. E. Cerling, F. H. Brown, J. M. Eiler, *Proc. Natl. Acad. Sci. U.S.A.* **107**, 11245 (2010).
11. T. C. Johnson *et al.*, *Nature* **537**, 220 (2016).
12. R. L. Lupien *et al.*, *Sci. Rep.* **12**, 3170 (2022).
13. R. M. Beyer, M. Krapp, A. Eriksson, A. Manica, *Nat. Commun.* **12**, 4889 (2021).
14. M. O. Cuthbert *et al.*, *Nat. Commun.* **8**, 15696 (2017).
15. A. Timmermann *et al.*, *Nature* **604**, 495 (2022).

10.1126/science.adj4631

GRAPHIC: D. AN-PHAM/*SCIENCE*

CHEMICAL ENGINEERING

Plastic waste recycling is gaining momentum

Production of detergents and aldehydes could help tackle plastic pollution

By **Kevin M. Van Geem**

Not a week passes without a chemical company announcing that it will be investing in a new recycling facility. Four major reasons explain the increasing interest in this field: pressure from citizens, stricter legal requirements, new and better technologies, and improved business cases. Rightfully, the public is dissatisfied with recycling rates, notably below 9% in the United States (*1*). This makes governments respond by enforcing a minimum recycled plastic content, such as the 30% target in the European Union. Therefore, a plastics circular economy, in which new, high-quality plastics can be remanufactured from plastic waste, is becoming increasingly popular. Plastics should no longer be considered waste but rather valuable resources. On pages 660 and 666 of this issue, Li *et al.* (*2*) and Xu *et al.* (*3*), respectively, report strategies to recycle plastic waste into potentially valuable products, such as alcohols, aldehydes, surfactants, and detergents.

A recent study showed that it is possible, by 2050, to produce all plastics in a circular way, without requiring fossil resources (*4*). At present, primarily virgin fossil resources are used to make the chemical building blocks to manufacture polymers (see the figure). Plastics can then be fabricated by combining different polymer grades and introducing additives or fillers (*5*). After their use, they should be collected, sorted, and recycled. If possible, mechanical recycling, comprising sorting, washing, drying, regranulating, and compounding, is preferred because it is the shortest recycling loop and is more energy efficient. But this requires homogeneous, relatively clean waste streams to transform the sorted and washed flakes into granulates of recycled plastics. Mechanical recycling of plastic packaging has been extensively implemented (*6*). Advances have also emerged in physical recycling, wherein the use of solvents and low temperatures preserves the polymer's chemical structure. In 2023, a patent presented a seven-stage physical recycling process on an industrial scale, which integrates extraction and filtration methods (*7*). Yet, more than 65% of the plastics will likely have to be chemically recycled—that is, broken down to their building blocks and transformed into secondary raw materials. Today, chemical recycling amounts to almost zero percent of total plastic recycling (*8*), which means that the main technological developments and market growth in the coming decade will likely be in this area.

Other issues in waste management include size and scalability. Several hundred million metric tons per year of plastic waste must be dealt with worldwide (*8*). As prices fluctuate between USD 400 per metric ton to negative values, a key challenge for any large-scale recycling company is to operate economically without relying on subsidies (*9*). Technologies such as gasification—which transforms carbon-containing products into syngas—and, to a lesser extent, pyrolysis—which transforms carbonaceous compounds primarily into oil—are known to have processing difficulties with cheap, typically highly contaminated waste streams. Yet, such robustness is a prerequisite for large-scale chemical recycling plants, and thus new chemical recycling methods should overcome these challenges.

Laboratory for Chemical Technology, Center for Sustainable Chemistry, Ghent University, Technologiepark 125, 9052 Ghent, Belgium. Email: kevin.vangeem@ugent.be

The circular plastics economy

The circularity concept aims to create a closed-loop system in which plastic waste is minimized and materials are continuously produced (orange); used, collected, and sorted (blue); and recycled and regenerated (green). To close the loop, mechanical, physical, and chemical recycling can be used, depending on waste quality. Waste can also be considered as a resource for the production of high-value chemicals such as surfactants and aldehydes.

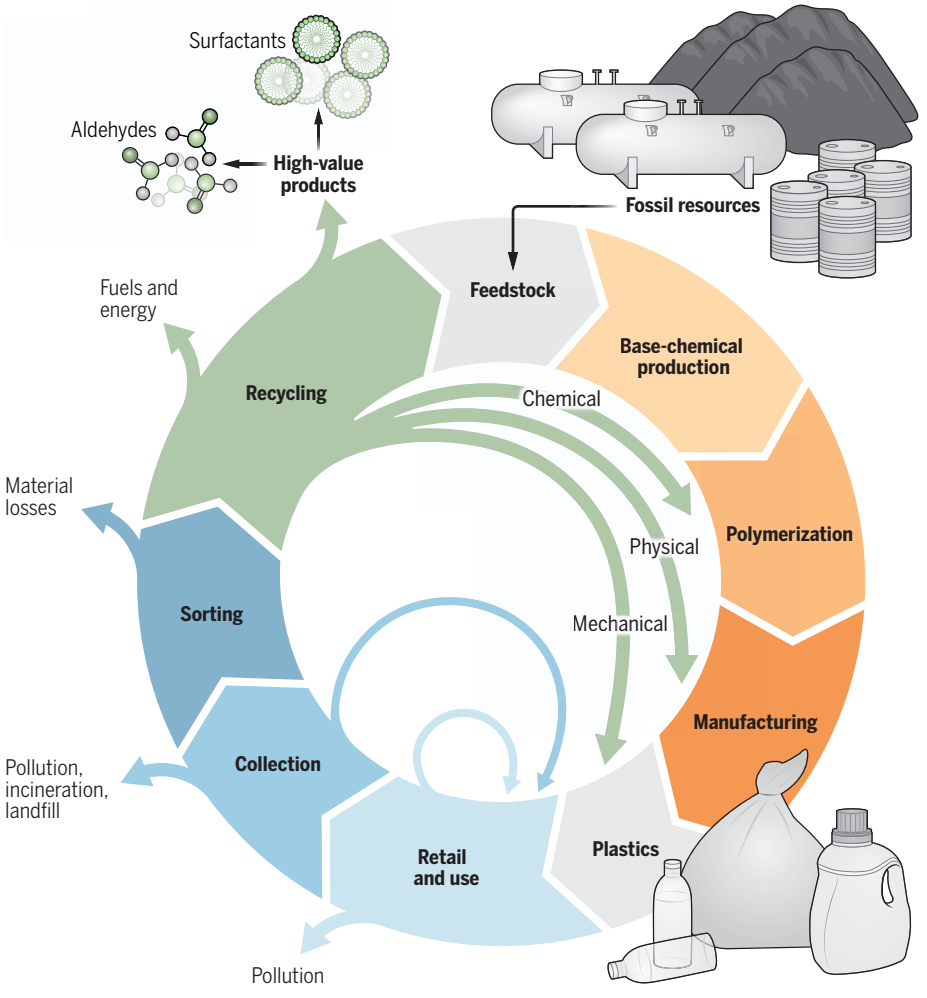

GRAPHIC: N. BURGESS/*SCIENCE*

Li *et al.* obtained olefin-rich pyrolysis oils from plastic waste. Olefins can be converted into aldehydes, which can be reduced to alcohols, oxidized to carboxylic acids, or aminated to amines by using catalysts. This innovative route produces valuable chemicals, the building blocks for polyesters and polyurethanes, from postconsumer recycled polyethylene (PE). This could reduce greenhouse gas emissions by around 60% compared with petrochemical production of the equivalent base chemicals. Li *et al.* also show that their technology works for highly contaminated waste plastics, which are difficult to recycle (*8*). Indeed, the oils that Li *et al.* produced contain almost the whole periodic table, including chlorine, iron, and silicon.

There are other solutions to large-scale plastic waste recycling. Xu *et al.* showed how PE and polypropylene (PP) waste can be converted in a potentially profitable process to high-value surfactants and detergents with a market size of USD 45 billion. By using temperature-gradient thermolysis—that is, decomposing the polymer by providing heat—PE and PP are converted into waxes. The key is that the temperature gradient prevents violent pyrolysis reactions, quenches vaporized waxes, and inhibits complete degradation to small molecules through difficult-to-control free-radical chemistry. The waxes are then transformed into fatty acids through oxidation and saponification, with double the value per kiloton compared with virgin plastics.

One disadvantage of the approaches of Li *et al.* and Xu *et al.* is that they only fit partially in the circular economy concept, because they do not recycle plastic waste back into plastics but instead produce chemicals. For example, for polyolefins, the main difficulty is making sure that no carbon is lost in the form of CO_2 emissions or as fuel. With current chemical processes—for example, pyrolysis followed by steam cracking—only 50% of the carbon in the waste can be transformed to new plastics (*8*). By using a ZSM-5 zeolite catalyst during pyrolysis, so-called catalytic pyrolysis, the carbon loss can be reduced to 15% or less from mixed plastic waste (*10*).

It is also essential that recycling technologies are less selective on the specifications of plastic waste. Economically, it is crucial that there is sufficient waste in a circular region with a diameter of 50 to 100 km to ensure that a recycling plant can run 8000 hours per year with a full capacity of about 100 kilotons per year. In this context, a revolutionary low-temperature pyrolysis technology was developed to upcycle mixed end-of-life plastics, multilayered plastics, discarded mechanically recyclable plastics, and even ocean plastics by adding a small amount of a mixture of copper, rare-earth materials, and carbon-based nanomaterials (*11*). Notably, ocean plastics contain many textiles such as nylon-6 and nylon-66 from fishing nets (*12*), which can be even more challenging to recycle than polyolefins. In a recent breakthrough, commercial and postconsumer nylon-6 was selectively recycled to the ϵ-caprolactam monomer in high yields by readily accessible lanthanide tris(amide) catalysts in a solvent-free process (*13*).

Reducing CO_2 emissions for plastic recycling technologies is also crucial. By electrifying the chemical process and using electricity from nonfossil sources, millions of tons of greenhouse gas emissions can be avoided (*14*). Because large volumes of plastic waste need to be treated, high-temperature processes are still favored because they scale better. However, hybrid processes, such as the combination of chemical oxidation and biological conversion using microorganisms, offer potential because they operate at much lower temperatures (*15*).

When will the technology of Li *et al.* and Xu *et al.* be implemented? Obtaining investment and establishing long-term waste supply contracts is a time-consuming process (*14*). Safety must be addressed to protect workers, communities, and the environment from hazards and risks. It typically takes more than 5 years from the initial assessment of a potential investment to the start of production. Nevertheless, innovative technologies targeting plastic waste recycling should greatly improve the circularity in the chemical industry in the coming years. ■

REFERENCES AND NOTES

1. E. Barone, "U.S. plastic recycling rates are even worse than we thought," *Time*, 19 May 2022.
2. H. Li *et al.*, *Science* **381**, 660 (2023).
3. Z. Xu *et al.*, *Science* **381**, 666 (2023).
4. M. R. Stuchtey, T. Dillon, "Breaking the plastic wave: A comprehensive assessment of pathways towards stopping ocean plastic pollution," The Pew Charitable Trusts and SYSTEMIQ (2022).
5. P. Garcia-Gutierrez *et al.*, "Environmental and economic assessment of plastic waste recycling" (JRC Technical Report, Publications Office of the European Union, 2023).
6. Z. O. G. Schyns, M. P. Shaver, *Macromol. Rapid Commun.* **42**, 2000415 (2021).
7. J. M. Layman *et al.*, Patent US 20180171094 (2018).
8. M. Kusenberg *et al.*, *Waste Manag.* **138**, 83 (2022).
9. B. M. Weckhuysen, *Science* **370**, 400 (2020).
10. A. Eschenbacher *et al.*, *Chem. Eng. J.* **428**, 132087 (2022).
11. M. Reyes *et al.*, paper presented at the Chemical Upcycling of Waste Plastics annual meeting, Univ. of Wisconsin–Madison, 29 March 2022.
12. G. C. Faussone, T. Cecchi, *Sustainability* **14**, 1235 (2022).
13. L. Wursthorn *et al.*, *Angew. Chem. Int. Ed.* **62**, e202212543 (2023).
14. K. M. Van Geem, B. M. Weckhuysen, *MRS Bull.* **46**, 1187 (2022).
15. K. P. Sullivan *et al.*, *Science* **378**, 207 (2022).

ACKNOWLEDGMENTS

The author received funding from the European Research Council under the European Union's Horizon 2020 research and innovation program and European Research Council grant agreement no. 818607.

10.1126/science.adj2807

MATERIALS SCIENCE

Tissue adhesive semiconductors

Bioelectronic implants could use semiconductors that adhere to wet, dynamic tissues

By **Sarah J. Wu**[1] *and* **Xuanhe Zhao**[1,2]

More than 1 million bioelectronic devices are implanted into human bodies each year worldwide for monitoring and modulating physiological processes, such as cardiac pacemakers for regulating heartbeat (*1*). The potential applications of bioelectronics have expanded across numerous organ systems and pathologies, promising to deliver precise diagnostics and drug-free therapeutics. However, establishing robust and high-efficacy interfaces between bioelectronic devices and biological tissues is a critical challenge. On page 686 of this issue, Li *et al.* (*2*) report a new strategy for achieving device-tissue integration using a bioadhesive polymer semiconductor (BASC). By combining a semiconducting polymer and a bioadhesive brush polymer in a double-network architecture, the BASC provides a promising tool for fabricating soft, tissue-bonded transistors that are capable of stable and sensitive bioelectrical recording, even on wet and constantly moving tissues.

Traditional bioelectronic device fixation methods, such as sutures and staples, often inflict tissue damage and can cause various complications, including bleeding, infection, and the foreign body response (FBR) (which involves inflammation and fibrosis). Although sutureless attachment of thin-film bioelectronics to tissues has been demonstrated, weak physical adhesion and constraints associated with their ultrathin geometry impose limitations on their performance (*3*). Thus, bioadhesive materials hold considerable appeal owing to their ability to establish atraumatic, conformal, and stable interfaces, thereby facilitating safe, long-term sensing and stimulation (*4*–*8*). Notably, to ensure effective signal transmission across the interface, achieving favorable electrical properties alongside

[1]Department of Mechanical Engineering, Massachusetts Institute of Technology, Cambridge, MA, USA. [2]Department of Civil and Environmental Engineering, Massachusetts Institute of Technology, Cambridge, MA, USA.
Email: sarahw@mit.edu; zhaox@mit.edu

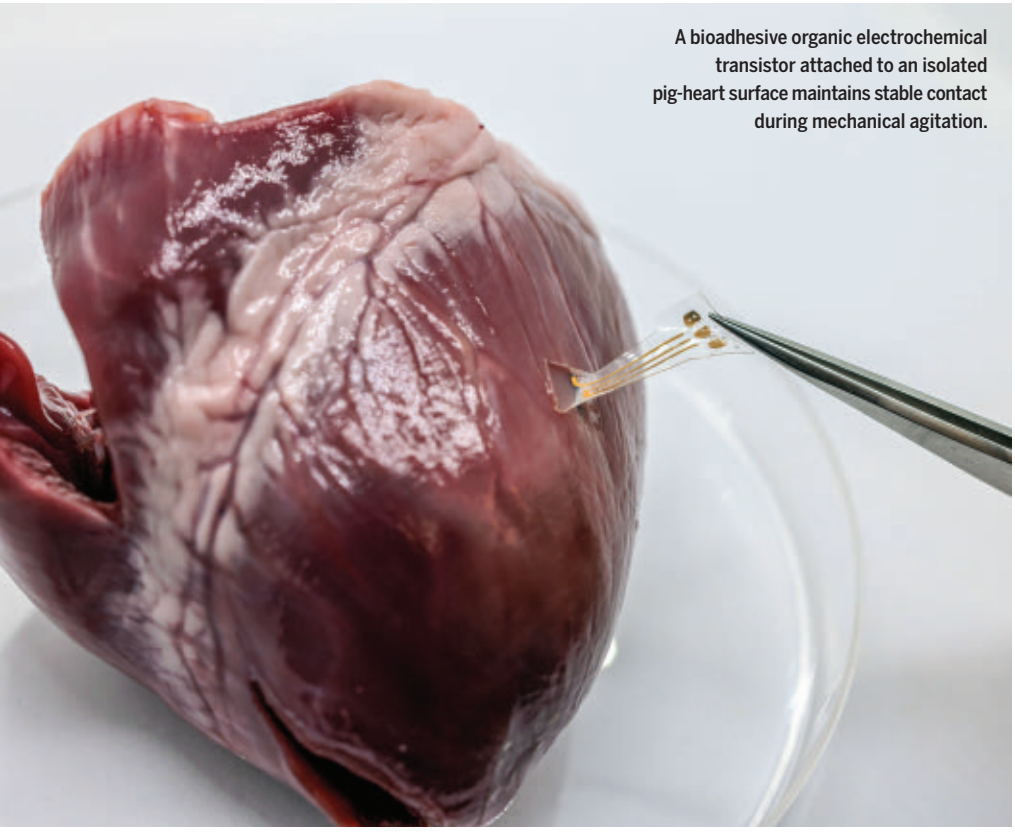

A bioadhesive organic electrochemical transistor attached to an isolated pig-heart surface maintains stable contact during mechanical agitation.

PHOTO: JOHN ZICH/PRITZKER MOLECULAR ENGINEERING

robust adhesion performance emerges as a central challenge. Previous endeavors to develop bioadhesives for bioelectronic devices have mainly focused on incorporating conducting polymers or fillers into bioadhesive polymer networks, which have been used as passive electrodes (*5*, *9*, *10*). However, the integration of semiconductors, which underpin the active components in circuits (e.g., transistors), has remained relatively unexplored in bioadhesives (*11*).

To achieve the desired multifunctional properties, Li *et al*. harnessed the strengths of a semiconducting polymer and a bioadhesive brush polymer by blending them together into a double-network film. Specifically, a redox-active semiconducting polymer is spin-coated with a bioadhesive brush polymer comprising a polyethylene backbone adorned with long side chains functionalized with carboxylic acid (COOH) and *N*-hydroxysuccinimide (NHS) ester groups. These functional groups confer fast and strong adhesion to wet tissues by promoting rapid water removal at the interface and enabling electrostatic and covalent interactions between the polymer and the tissue (*3*). The strategic incorporation of these functional groups at the ends of the long side chains is key to ensuring sufficient exposure to tissue surfaces, thereby overcoming potential hindrance caused by the long chains of the semiconducting polymer.

The resulting BASC films demonstrate fast adhesion (less than 1 min) with wet porcine tissues (interfacial toughness >20 J m^{-2}, shear strength >7 kPa, and tensile strength >4 kPa), as well as high charge-carrier mobility (~1 cm^2 V^{-1} s^{-1}). The BASC films also exhibit high stretchability (up to 100% strain with no cracking), which allows them to conform to nonplanar tissue surfaces and adapt to deformations. One of the main challenges to achieving long-term functionality of implanted devices is the FBR, which can give rise to fibrous tissues that interfere with signal transmission. Owing in part to their soft, tissue-like mechanical properties, the BASC films elicit low levels of fibrosis and FBR-associated biomarkers when implanted subcutaneously in rats, demonstrating a promising alternative to traumatic sutures and staples.

The benefits of the BASC material become especially evident when considering the integration of bioelectronic devices with wet, dynamic tissues. Suturing is particularly challenging in the presence of tissue movement, and adhesives that require prolonged contact for adhesion formation are impractical. The BASC can be directly attached by applying gentle pressure for less than a minute. This efficient attachment process circumvents the difficulties associated with tissue dynamics and improves the signal readout stability. To demonstrate this point, Li *et al*. fabricated BASC-based organic electrochemical transistor (OECT) devices to record an ex vivo epicardial electrocardiogram (ECG) from an isolated rat heart, as well as an in vivo electromyogram (EMG) from the leg muscle of a rat. Compared with OECT devices attached using sutures or a separate (nonconductive) adhesive layer, the BASC-based OECTs exhibited higher recorded signal amplitude and stability. Moreover, the built-in biosignal amplification provided by the OECT equips it with a higher recorded signal amplitude compared with passive recording devices composed of conducting polymers.

Several aspects warrant further investigation to fully realize the potential of the BASC material. In comparison to state-of-the-art bioadhesive materials, the adhesion performance of the BASC is relatively weak, which may pose challenges for its stability in more demanding, long-term in vivo applications, such as in vivo ECG (*12*). The BASC could also benefit from incorporating a means to trigger atraumatic detachment from the tissue surface in the event of device repositioning or removal. Moreover, comprehensive studies that examine the chronic durability, electrical performance, and biocompatibility of the BASC will be imperative to fully assess the performance of implanted devices over time and thus its clinical utility. Nonetheless, bioadhesive semiconductors represent a promising avenue for improving the signal sensitivity, spatial resolution, and surgical workflow of bioelectronic devices. Beyond semiconductors, the development of next-generation bioadhesives with tailored chemical, mechanical, optical, acoustic, or thermal properties could unlock substantial advances across a wide spectrum of biointegrated devices, transforming the way human health is monitored and managed. ■

REFERENCES AND NOTES

1. H. G. Mond, A. Proclemer, *Pacing Clin. Electrophysiol.* **34**, 1013 (2011).
2. N. Li *et al.*, *Science* **381**, 686 (2023).
3. H. Yuk *et al.*, *Nature* **575**, 169 (2019).
4. J. Deng *et al.*, *Nat. Mater.* **20**, 229 (2021).
5. T. Zhou *et al.*, *Nat. Mater.* **22**, 895 (2023).
6. C. M. Tringides *et al.*, *Nat. Nanotechnol.* **16**, 1019 (2021).
7. Q. Yang *et al.*, *Nat. Mater.* **20**, 1559 (2021).
8. D.-H. Kim *et al.*, *Science* **333**, 838 (2011).
9. F. Fu, J. Wang, J. Yu, *J. Mater. Chem. C Mater. Opt. Electron. Devices* **9**, 11794 (2021).
10. X. Wang *et al.*, *Matter* **5**, 1204 (2022).
11. Y. Dai *et al.*, *Adv. Mater.* **34**, 2201178 (2022).
12. S. Nam, D. Mooney, *Chem. Rev.* **121**, 11336 (2021).

ACKNOWLEDGMENTS

S.J.W. acknowledges the US National Science Foundation (NSF) Graduate Research Fellowship Program. X.Z. has a financial interest in SanaHeal, Inc., a biotechnology company focused on the development of medical devices for surgical sealing and repair.

10.1126/science.adj3284

A pharmacist prepares a solution of phages, which are viruses that can destroy bacteria.

PHOTO: ROMAIN LAFABREGUE/AFP VIA GETTY IMAGES

BOOKS *et al.*

MICROBIOLOGY

The forgotten future of the phage

As antibiotic resistance soars, a journalist revisits an often overlooked antimicrobial strategy

By **Adrian Woolfson**

In his Nobel Lecture delivered on 11 December 1945, Alexander Fleming recounted how his pursuit of a "chance observation" of a mold contaminating a culture plate led eventually to the industrial production of penicillin, the first-ever antibiotic (*1*). While anticipating the remarkable impact the drug would have on global health, Fleming also made a prescient warning: If used negligently, resistance to penicillin would inevitably change "the nature of the microbe," resulting in treatment failure.

More than 70 years later, in 2019, a report released by the United Nations predicted that antimicrobial resistance could force up to 24 million people into extreme poverty by 2030 and cause up to 10 million annual deaths by 2050 (*2*). Journalist Tom Ireland's *The Good Virus*, which recounts the intriguing history of a different type of antibiotic principle, a process by which viruses known as bacteriophages or phages destroy bacteria, is thus incredibly timely for its potential to renew interest in an orthogonal antimicrobial modality.

The Good Virus
Tom Ireland
Norton, 2023. 400 pp.

First indirectly observed in 1915 by the English physician Frederick Twort, bacteriophages are composed of a piece of DNA wrapped in a protein capsule. Their genetic instructions are entirely reliant on the hardware of their bacterial hosts, which perform all the phage's metabolic and replicative functions. Ireland recounts how these ruthless predators penetrate bacteria "like pins in a voodoo doll," forming conduits through which they inject their genes at high pressure. When they trigger their own replication and self-assembly, bacteriophages obliterate their hapless hosts.

The antimicrobial properties of bacteriophages were first documented in 1896 by the Cambridge naturalist Ernest Hanbury Hankin, who traveled to India to investigate reports that outbreaks of cholera upstream of the river Ganges often did not spread downstream. There, he noted that "the unboiled water of the Ganges kills the cholera germ in less than three hours" (*3*). It was subsequently shown that the bacterial profusion swirling around the Ganges is accompanied by an abundance of bacteriophages. When phage numbers decline, *Vibrio cholerae* proliferates, resulting in disease outbreaks.

The pugnacious and "roguishly handsome" French-Canadian autodidact Félix d'Hérelle would be the first to realize that these "invisible microbe[s]" might form the basis of an antimicrobial therapy. He called them bacteriophages, translated from the Greek "bacteria eaters," and set about testing preparations of them on himself, family members, and attending physicians at the Hôpital des Enfants-Malades in Paris. In August 1919, d'Hérelle successfully treated a boy with *Shigella* dysentery using phage therapy.

After controversially suggesting that phages form part of the human immune system and being accused of plagiarizing Twort, d'Hérelle turned his back on the West. Dedicating his third book on phages to the Soviet dictator Joseph Stalin, he accepted an invitation to relocate to the USSR from the aristocrat and bon viveur George Eliava, who in 1936 set up a phage institute in Tbilisi, Georgia. The use of phage therapy was widespread in the Soviet Union until its collapse in 1991, with penicillin and its derivatives being largely unavailable and the use of antibiotics decried as evidence of *nizkopoklonstvo*, or "adulation of the West."

Although, to date, there are still no definitive randomized clinical study data demonstrating the efficacy of bacteriophage therapy, there is sufficient reason to believe that bespoke bacteriophage treatments targeting individual strains could be successfully developed and deployed on a global scale. A "universal" antimicrobial system of this sort might comprise large, automated libraries of therapeutic phages or the point-of-care de novo synthesis of natural and artificial bacteriophages (*4*) using sequence databases, synthetic genomics, and generative artificial intelligence. The astonishing prevalence of bacteriophages, which outnumber bacteria by at least 10 to 1, provides an almost limitless supply of genetic information for this purpose. ■

The reviewer is executive chairman, president, and cofounder of Replay Holdings Inc., San Diego, CA, USA, and the author of *Life Without Genes* (HarperCollins, 2000).
Email: adrianwoolfson@yahoo.com

REFERENCES AND NOTES

1. A. Fleming, "Penicillin," Nobel Lecture, 11 December 1945.
2. "New report calls for urgent action to avert antimicrobial resistance crisis," World Health Organization, 29 April 2019; https://www.who.int/news/item/29-04-2019-new-report-calls-for-urgent-action-to-avert-antimicrobial-resistance-crisis.
3. E. Hankin, *Ann. Inst. Pasteur Microbiol.* **10**, 511 (1896).
4. J.-P. Pirnay, *Front. Microbiol.* **11**, 1171 (2020).

10.1126/science.adi5079

SCIENCE LIVES

Linnaeus and his life's work

A historian's unvarnished biography reveals the complicated man who invented modern taxonomy

The Man Who Organized Nature: The Life of Linnaeus
Gunnar Broberg, Translated by Anna Paterson
Princeton University Press, 2023. 512 pp.

By **Darren Incorvaia**

In 1741, the famed "father of taxonomy" Carl Linnaeus experienced a setback that will be familiar to many modern scientists: He had a paper rejected. His account of his travels to the Swedish island of Gotland was denied publication due to its being "most carelessly written" and covered in corrective ink marks, with no mention of the quality of the narrative itself. This anecdote, recounted in chapter 12 of historian Gunnar Broberg's biography of the Swedish botanist, *The Man Who Organized Nature*, is an apt metaphor for the book itself, which is rife with convoluted writing that at times masks the text's otherwise rich illumination of the life of one of history's most influential scientists.

Broberg charts a cradle-to-grave biography of Linnaeus, from his bucolic boyhood in Småland, to his prized professorship at Uppsala University, to his death at the rural manor house he occupied after his ennoblement as Carl von Linné. The text is largely organized chronologically, with several interludes explaining Linnaeus's family life as well as the taxonomic classification system that became his legacy.

Broberg succeeds in providing a rich portrait of Linnaeus's life, including the less savory aspects of his personality. References to the polymath's naked ambition and careerism are peppered throughout the text. Readers learn, for example, that after Linnaeus's friend Petrus Artedi, a well-known ichthyologist, drowned in an Amsterdam canal, Linnaeus took credit for posthumously publishing his masterwork, *Ichthyologia*. "We do not know if we should more regard as its author our Artedi or our Linnaeus," wrote Linnaeus in his autobiography, even though it was actually a student who rewrote the text into a clean copy for printing. (Linnaeus's tendency to write about himself in the third person also did not help mitigate accusations of self-importance.)

More whimsical anecdotes abound. We learn, for example, that while on a research trip, Linnaeus and his students extensively documented the feeding habits of a hedgehog. Later in life, he allowed crickets to infest his bedroom because he enjoyed having them sing him to sleep, and "only when they became too numerous could he be persuaded to with poison eliminate some of them."

A portrait depicts Carl Linnaeus, known as the "father of taxonomy."

PHOTO: PICTURES FROM HISTORY/UNIVERSAL IMAGES GROUP VIA GETTY IMAGES

Although best known as a botanist, Linnaeus had various other interests, including economics and ethnology. Ever the patriot, he was adamant about finding ways to exploit Sweden's natural resources for the country's economic benefit while at the same time extolling the virtues of the natural living of the indigenous Sami people. The man contained multitudes, and Broberg gives readers a peek into his many facets.

The book quotes extensively from primary sources, especially Linnaeus himself, who used a mixture of unstandardized 18th-century Swedish and Latin that is challenging to parse, all the more so because Broberg leaves many Latin and other foreign words untranslated. In chapter 15, for example, Broberg extensively quotes a local gossip who wrote about a scandal in Linnaeus's home life: "Then L attempted to win her favor with caresses although it would appear that by his *exès* in such a moment he made himself as *dégoutant* to her. *Enfin*, he in every way showed as little *conduit* as in all other things." Here, readers could have benefited from the author's extensive knowledge of Linnaeus and the time period in which he lived had he summarized the quoted passage in simple language. Instead, Broberg follows the lengthy anecdote with "pretty minor stuff, it would seem."

Broberg's commitment to primarily letting Linnaeus and his contemporaries speak for themselves does succeed in making the reader feel as though they are there with Linnaeus on his many travels or during his lectures. But this strategy is also problematic at times. In some places, for example, the author inexplicably reproduces offensive ethnic terms outside of quoted text, offering no context for how such phrases are viewed today. And while Linnaeus's classification of humanity is a known origin point for modern scientific racism, Broberg rather flippantly dismisses this concern, writing that "labels such as 'racism' and 'racist' are frequently misleading when applied to circumstances and people in the past."

Gunnar Broberg, who died in 2022, spent his career trying to shed light on Carl Linnaeus as a man, a scientist, and a Swede. His final work offers readers an immersive glimpse into the life of a scientist who was instrumental to the formation of botany, zoology, and taxonomy. Despite its shortcomings, *The Man Who Organized Nature* is sure to become the definitive biography of Linnaeus. ■

The reviewer is a freelance science writer based in Berkeley, CA, USA. Email: darrenincorvaia@gmail.com

10.1126/science.adj0804

Construction on China's Pinglu Canal has begun, putting the country's wetlands at risk.

PHOTO: CAO YIMING/XINHUA VIA GETTY IMAGES

Edited by **Jennifer Sills**

China's canal project threatens biodiversity

The Wuhan Declaration and the United Nations Biodiversity Agreement were adopted in November and December 2022, respectively (*1*, *2*). These plans aim to support the UN Sustainable Development Goals for 2030 by conserving wetland ecosystems, reversing biodiversity loss, and promoting climate security (*1*, *2*). As the host of the 14th and 15th Conference of the Parties to the United Nations Convention on Biological Diversity, China was expected to play an important role in global conservation. However, the country commenced the rapid construction of the Pinglu Canal in June (*3*), undermining the objectives of the 2022 agreements to which it has committed.

China approved the canal in a bid to boost burgeoning trade with the 10 members of the Association of Southeast Asian Nations (*3*). The project is a 134.2-km inland river I-class waterway between Xijin reservoir on the Yu River in Hengzhou and the lower part of the Qin River, providing access to the Beibu Gulf (*4*). The canal will occupy 13.9 ha of mangrove forests, an integral part of the coastal mangrove wetlands.

The construction of the canal will have negative and potentially irreversible impacts on biodiversity and wetland ecosystems. The plans will disrupt the breeding, wintering, and migration of international migratory birds (*5*). Among them, 33 species of birds are protected under the agreements between China and Australia and China and Japan to protect migratory birds and their habitats (*5*). The project will also cause a loss of millions of fish and hundreds or thousands of tons of biomass, including oyster resources, benthic organisms, and swimming animals (*6*). The ship locks of the canal will cause fragmentation in the river, hindering the distribution of migratory fish species such as the Japanese eel (*Anguilla japonica*) and the Chinese tapertail anchovy (*Coilia nasus*), both of which are listed on the International Union for Conservation of Nature's Red List of Threatened Species (*7*, *8*). The water transfer from the canal will result in insufficient water supply for the ecological environment of the Xijin National Wetland Park, reducing the water body's self-purification capacity, causing wetland destruction, and posing a threat to 442 plant species and 353 vertebrate species, including rare and endangered species such as the black stork (*Ciconia nigra*) and the Burmese python (*Python bivittatus*) (*6*, *9*–*11*).

The protection of wetlands and biodiversity is a crucial pathway toward achieving sustainable development. The Chinese government should uphold its commitments to the Wuhan Declaration and the UN Biodiversity Agreement (*1*, *2*, *12*). China should suspend canal construction until a sustainable development path is devised to protect biological resources.

Qiying Yang[1] and Shanshan Yang[1,2]*
[1]Institute for Advanced Marine Research, China University of Geosciences, Guangzhou 511462, China. [2]College of Marine Science and Technology, China University of Geosciences, Wuhan 430074, China.
*Corresponding author.
Email: yangshanshan@cug.edu.cn

REFERENCES AND NOTES

1. "Ministers and Ambassadors adopt the Wuhan Declaration," *Ramsar* (2022).
2. Convention on Biological Diversity, "COP15: Nations adopt four goals, 23 targets for 2030 in landmark UN Biodiversity Agreement" (2022).
3. C. K. Tan, "China's massive new canal aims for closer ASEAN connectivity," *NIKKEI Asia* (2023); https://archive.ph/FhOMj.
4. K. Guo *et al.*, "Construction of Pinglu Canal begins in S China" *China Daily* (2023).
5. Y. C. Tian *et al.*, *Remote Sens.* **15**, 2622 (2023).
6. China Biodiversity Conservation and Green Development Foundation, "Letter to the Department of Ecology and Environment of Guangxi: We suggest careful consideration before making a decision on the construction of the Pinglu Canal project" (2022); https://www.sohu.com/a/560249937_100001695 [in Chinese].
7. A. Kasai *et al.*, *Front. Ecol. Evol.* **9**, 621661 (2021).
8. F. Ma *et al.*, *Sci. Data* **10**, 360 (2023).
9. "The Hengxian Xijin National Wetland Park has officially been approved as a national brand," *People.cn* (2017); https://kknews.cc/zh-my/society/ypmxzag.html [in Chinese].
10. W. L. Liang *et al.*, *Mitochondrial DNA B Resour.* **4**, 2519 (2019).
11. S. N. Smith *et al.*, *Sci. Rep.* **11**, 7014 (2021).
12. Ministry of Foreign Affairs of the People's Republic of China, "Building a shared future for all life on Earth: China in action" (2020).

10.1126/science.adj1395

Begin ocean garbage cleanup immediately

In the *Science* News story "Cleaning up ocean 'garbage patches' could destroy delicate ecosystems" (17 May, https://scim.ag/3vU), A. B. Vigil describes research showing that cleaning up garbage patches in the ocean could harm some marine

species (*1*), but she neglects to weigh these risks against the harm caused by failing to clean up the garbage. Although cleaning up ocean dumps could have local effects on some species, cleanup efforts should proceed without delay.

The three species found in the research Vigil cites—blue button jellies, by-the-wind sailors, and violet snails—play distinct roles in maintaining the balance and stability of the marine ecosystem, as the News story explains. However, potential harm to these species should not serve as a justification to postpone cleanup. These jellies, sailors, and snails have wide geographical distributions, and none of their populations is endangered or at risk of substantial decline (*2*–*4*). Removing the garbage would likely not reduce their populations to the point that ecosystem balance would be at risk (*5*). Furthermore, the openness and complexity of marine ecosystems grant them resilience (*6*), enabling gradual recovery to a healthier state even if some species are removed.

The News story reflects the concern of some people that any action that affects specific organisms or their habitats (including removing garbage) is potentially undesirable and should be carefully considered. One source notes, with apparent approval, that temporarily preserving garbage patches within protected areas could delay cleanup, providing time to gather more data. This reluctance would make sense if the entire ecosystem were at risk. However, given that the harm would likely be temporary (*5*), a delay would prioritize individual organisms over broader ecosystem health, flouting the original intention of marine protected areas: to achieve the long-term conservation of nature with associated ecosystem services and cultural values (*7*).

The News story does not sufficiently emphasize that cleaning up ocean garbage patches would have substantial benefits that outweigh any direct impact on individual organisms. Reducing plastic pollution in these areas would improve water quality and reduce harm to marine life from ingesting plastic or becoming entangled in ghost fishing gear (*8*). Removing floating macroplastics would prevent them from sinking, degrading into microplastics (*9*), and releasing additional harmful chemicals.

Delaying cleanup efforts will only result in the accumulation of more plastic waste in the ocean (*9*). With the current most efficient cleanup technology and capacity (*10*), it would take about 100 years to fully clean up the Great Pacific Garbage Patch, without accounting for the continuous accumulation of new plastic debris (*11*). The investigations and assessments advocated in the News story should be conducted during the cleanup process. If evidence shows that certain cleanup methods can minimize additional environmental or ecological damage, adjustments should be made accordingly.

Zouxia Long
Third Institute of Oceanography, Ministry of Natural Resources, Xiamen 361005, China.
Email: zouxialong@tio.org.cn

REFERENCES AND NOTES

1. F. Chong *et al.*, *PLOS Biol.* **21**, e3001646 (2023).
2. S. K. Pattnayak *et al.*, *Mar. Fish. Sci.* **36**, 197 (2023).
3. E. F. Ricketts *et al.*, *Between Pacific Tides* (Stanford University Press, 1985).
4. C. K. C. Churchill *et al.*, *Invertebr. Syst.* **28**, 174 (2014).
5. M. Spencer *et al.*, *Peer J.* **11**, e15021 (2023).
6. P. J. Mumby *et al.*, *Curr. Opin. Environ. Sustain.* **7**, 22 (2014).
7. J. Day *et al.*, "Guidelines for applying the IUCN protected area management categories to marine protected areas" (IUCN, 2012).
8. K. Richardson, B. D. Hardesty, J. Vince, C. Wilcox, *Sci. Adv.* **8**, eabq0135 (2022).
9. L. Lebreton, *Nat. Rev. Earth Environ.* **3**, 730 (2022).
10. B. Slat, "First 100,000 kg removed from the Great Pacific Garbage Patch," The Ocean Cleanup (2022); https://theoceancleanup.com/updates/first-100000-kg-removed-from-the-great-pacific-garbage-patch/.
11. L. Lebreton *et al.*, *Sci. Rep.* **8**, 4666 (2018).

10.1126/science.adj0102

The benefits of cleaning up ocean garbage patches outweigh the risks to the species that live in them.

PHOTO: GARY BELL/OCEANWIDE/MINDEN PICTURES

Rapid reversal of ecological extinction

Humanity has inflicted widespread ecocide on global marine ecosystems since the industrial revolution (*1*). Indiscriminate dredging of the seabed has decimated thriving ecosystems and vast biogenic empires, leaving only barren sedimentary plains [e.g., (*2*)]. However, despite the extent of habitat loss and humanity's increasing impact on the ocean, many marine habitats still demonstrate astonishing capacity for rapid recovery (*3*, *4*). In southern Australia, for example, a rapid reversal of ecological extinction is underway.

Two centuries ago, flat oyster reefs carpeted the seafloors of more than 5000 km of Australian coastline. Within about a century of European colonization, the reefs had been eradicated (*5*). Yet, this lost ecosystem still has a heartbeat. Just 2.5 years after the construction of a 5-ha boulder reef restoration along South Australia's most populated coast, densities of mature flat oysters in the area exceed the densities observed on Australia's only surviving natural flat oyster reef in Tasmania (*6*). With the provision of suitable substrate, seldom seen and sparsely spread oysters have seeded this astounding recovery. A seafloor of shifting sediment has become a highly biodiverse reef formed by more than 2 million reproductive oysters (*7*) and hundreds of millions of juveniles (*8*).

Many marine populations possess traits that enable rapid ecological change. Short life histories and highly fecund spawning adults mean that coastal seas can be a soup of dispersing larvae ready to saturate available substrate. Without major roads or fences restricting larval movement, even decimated habitats can receive intense propagule pressure from neighboring remnant populations.

Of course, such rapid ecological recovery is not always possible. For example, at a nearby reef restoration, competition for space from other rapid colonizers (turf-forming algae) has restricted oyster recruitment, slowing the restoration process (*9*). Furthermore, restoration sites seeded by a limited number of adults may restrict genetic diversity, potentially compromising long-term restoration success (*10*).

Nevertheless, coastal restorations that generate rapid ecological recoveries should be publicized and celebrated. Such successes can help to inspire hope and widespread public engagement, both of which are needed to achieve a unified approach (*11*) to repairing the biosphere.

Dominic McAfee* and Sean D. Connell
School of Biological Sciences, The University of Adelaide, Adelaide, SA, Australia, and Environment Institute, The University of Adelaide, Adelaide, SA, Australia.
*Corresponding author.
Email: dominic.mcafee@adelaide.edu.au

REFERENCES AND NOTES

1. J. B. C. Jackson *et al.*, *Science* **293**, 629 (2001).
2. M. W. Beck *et al.*, *BioScience* **61**, 107 (2011).
3. C. M. Duarte *et al.*, *Nature* **580**, 39 (2020).
4. M. I. Saunders *et al.*, *Curr. Biol.* **30**, R1500 (2020).
5. C. L. Gillies *et al.*, *PLOS One* **13**, e0190914 (2018).
6. C. Crawford *et al.*, *Mar. Freshw. Res.* **71**, 972 (2019).
7. R. Carlucci *et al.*, *Aquaculture* **306**, 167 (2010).
8. D. McAfee *et al.*, *J. Appl. Ecol.* **60**, 111 (2023).
9. D. McAfee *et al.*, *J. Appl. Ecol.* **58**, 286 (2021).
10. L. K. Reynolds *et al. PLOS One* **7**, e38397 (2012).
11. UN Convention on Biological Diversity, "Kunming-Montreal Global Biodiversity Framework" (UN Environment Program, Montreal, Canada, 2022).

10.1126/science.adi7443

AUSTRALIA

LESSONS FROM ECOSYSTEMS IN CRISIS

PERSPECTIVE

Taming the flame, from local to global extreme wildfires p. 616

POLICY FORUM

Cultural water and Indigenous water science p. 619

REVIEWS

Loss of terrestrial biodiversity in Australia: Magnitude, causation, and response p. 622

Management approaches to conserve Australia's marine ecosystem under climate change p. 631

Justice, culture, and relationships: Australian Indigenous prescription for planetary health p. 636

RELATED ITEM

NEWS STORY p. 598

Corals on Australia's iconic Great Barrier Reef have suffered repeated years of bleaching (left) as a result of climate change, which has caused the ocean to warm beyond the thermal tolerance of the coral organisms.

By **Caroline Ash**, **Bianca Lopez**, **Ekeoma E. Uzogara**, *and* **Sacha Vignieri**

Australia is at a unique nexus of endemic biodiversity and 60,000-year-old human cultures that are adapted to the planet's most ancient and driest ecosystems. Over the past 200 years, the continent's special ecosystems and human societies have proved vulnerable to waves of immigration by Europeans, who brought with them their companion species and unsustainable activities. During this time, Australia has lost more species of mammal than any other continent. Although Australia is more sensitive to the dangers of invasive species than countries of many larger continents, these species have still wreaked appalling harm on its ecosystems and human economies. The historical record of dispossession and disenfranchisement of Aboriginal and Torres Strait Islands Peoples has denied them their role as environmental guardians and caretakers. Acute climate change, and the exclusion of Indigenous Peoples and their specific knowledge of land management, has led to extreme wildfire and flooding events, coral reef degradation, biodiversity loss, and the disproportionate suffering of Indigenous Peoples themselves from these hazards. All of this has occurred in a country with a total population roughly the size of that of Shanghai, China.

In this special issue, we recognize Australia's exceptional exposure to the risks of climate change and ecosystem degradation. Meeting these challenges means redoubling efforts to find solutions, but Australia can offer valuable messages to the rest of the world, which is increasingly facing similar challenges. 10.1126/science.adj9747

PHOTO: ABRAM POWELL/GREENPEACE

PERSPECTIVE

Taming the flame, from local to global extreme wildfires

Australia rethinks strategies after 2019 to 2020 bushfires

By **David M. J. S. Bowman**[1] *and* **Jason J. Sharples**[2]

The surge of extreme wildfires around the world, most recently in Canada, provides a frightening glimpse of the potential for intense fires driven by climate change to cause remarkable damage to human and environmental life. From 2019 to 2020, Australia experienced unprecedented wildfires (commonly referred to as bushfires), which increased the burned area by 800% relative to the 1988 to 2001 average (*1*). As well as causing dangerous "fire weather," extreme heat combined with record low rainfall caused widespread dieback of vegetation, guaranteeing that wildland fuels burnt at maximal intensity (*2*). The societal and environmental impacts have spurred Australia to rethink wildfire management and work toward innovative solutions. This includes driving research into the effects of climate change on fire, optimizing approaches to prescribed burns, and leveraging Indigenous knowledge and expertise of Aboriginal communities. These approaches could prove vital not only for Australia but for managing extreme fires elsewhere in the world.

From September 2019 to March 2020, Australia experienced frequent and dangerous fire weather, which led to large uncontrolled fires that were started by both lightning and anthropogenic ignitions (*1*, *3*). The geographic scale of these fires was nationally and globally anomalous, burning 20% of the temperate eucalypt forests

PHOTO: MATTHEW ABBOTT

The 2019 to 2020 Australian wildfires were driven by extreme weather conditions and destroyed large areas of bushland.

that fringe the populated regions of southeastern Australia (*4*). The wildfires were the culmination of multidecadal drying and warming trends linked to anthropogenic climate change that lengthened the fire season and contributed to a prolonged and unusually intense drought that desiccated landscapes (*1*, *3*).

The 2019 to 2020 fires had unparalleled effects. Direct national financial costs exceeded 10 billion AUD, 33 people were killed, and more than 3000 homes were destroyed in addition to numerous other adverse effects on human physical and mental health (*5*). The fires burned biodiversity hotspots, harming the habitat of floral and faunal species that are vulnerable to extinction, and made large areas of postfire regenerating vegetation susceptible to ecological collapse if reburned (*6*). Estimates of greenhouse gas emissions suggest that these fires released around 715 Tg of carbon dioxide (CO_2), an amount equivalent to 80% of Australia's combined annual fire and fossil fuel emissions, signaling the potential for dangerous climate-carbon feedbacks (*7*). Fire could switch forests from important carbon sinks to sources of CO_2, thereby amplifying climate change and increasing the risk of more frequent, ecologically destructive wildfires. Smoke from the fires caused widespread and protracted pollution, which affected most of the Australian population and caused an estimated 429 premature deaths and at least 3230 hospital admissions (*8*). Annual health costs associated with deaths and hospitalization from smoke increased by 900% in the financial year encompassing the fires compared with the prior 19-year median. The smoke was transported across the Southern Hemisphere, triggering anomalous algal blooms in the Southern Ocean, with unknown effects on marine ecosystems, including whether the captured carbon was sequestered in the deep ocean (*9*) (see the figure).

"The Australian fires show that extreme wildfire events can harm societies and amplify climate change..."

The 2019 to 2020 fires also produced high levels of pyroconvective activity with 44 fire thunderstorms. Fires were large enough to spur the formation of pyrocumulonimbus clouds that stoked lightning and wind, further exacerbating the fires. These fire thunderstorms represent 35% of such events detectable in the satellite record since it began in 1978 and included several rare nighttime pyrocumulonimbus (*3*). One outbreak of extreme pyroconvection, involving a total of 38 pyrocumulonimbus "pulses," injected about 1 Tg of smoke particles into the lower stratosphere (*10*). With parallels to volcanic eruptions and nuclear winter scenarios in terms of energy released, aerosol emissions, and plume height, this pollution encircled the Southern Hemisphere and persisted for more than 15 months (*10*). The smoke also affected stratospheric circulation patterns (*10*), causing a cooling of Earth's surface (*11*). This possibly contributed to a 3-year La Niña climate mode that triggered widespread flooding across eastern Australia (*12*). A completely unexpected effect of the stratospheric aerosol pollution was a new atmospheric organic chemistry that caused a 3 to 5% loss of ozone in Southern Hemisphere mid-latitudes. This could slow recovery of the ozone layer, especially if pyrocumulonimbus outbreaks become more frequent (*13*).

The Australian fires show that extreme wildfire events can harm societies and amplify climate change, highlighting the urgency to find means to mitigate them. Policy discussion after the 2019 to 2020 fires mostly centered on disaster management responses and firefighting capability and capacity. This included the use of sophisticated technologies to detect fires when they start but much less consideration of climate change and the consequences for fire management (*1*–*3*, *5*). Furthermore, because this fire activity outstripped firefighting capacity, consistent with global trends, scientific and public debates focused on appropriate reduction of vegetative fuel to help control future climate-driven fires (*2*).

Australia has a long-established fire management practice of reducing fuel loads in flammable vegetation types, particularly dry eucalypt forests and woodlands (bushland), by setting fires under moderate fire weather conditions. Current amounts of this prescribed burning treat around 3071 ± 732 km^2 of forest and woodland per year, but the area burned in wildfire events continues to increase (*1*). The protective effect of prescribed burning diminishes under extremely hot, dry, and windy weather conditions because fires can burn across areas with low surface fuel loads (*2*). Nonetheless, such fuel management can reduce the intensity of wildfires, making them easier to control and reducing their severity. For example, geospatial analyses showed that house losses in the 2019 to 2020 fires were reduced proximate to areas that had recent prescribed burning (*2*). Theoretically, prescribed burning could help decrease the risk of extreme pyroconvection by reducing fire intensity, although this is yet to be demonstrated. Prescribed burning necessarily involves complex and unresolved trade-offs associated with the risk of fires escaping control relative to reducing the risk of fire disasters. There is also the harmful versus protective effect on public health, biodiversity, and cultural values. Achieving environmentally sustainable prescribed burning will require the spatial pattern, extent, and frequency of burned area to

[1]Fire Centre, School of Natural Science, University of Tasmania, Hobart, Tasmania, Australia. [2]UNSW Bushfire Research Group, School of Science, University of New South Wales, Canberra, ACT, Australia.
Email: david.bowman@utas.edu.au; j.sharples@unsw.edu.au

Global fire effects

The 2019 to 2020 Australian fires killed and injured humans, destroyed property, and severely polluted all urban areas in southeastern Australia. Substantial ecological harms included damage to vegetation cover and reduced wildlife populations. Earth system processes were adversely affected through prodigious smoke and greenhouse gas emissions, which caused stratospheric pollution that damaged the ozone layer and caused regional cooling, with fallout causing anomalous Southern Ocean algal blooms.

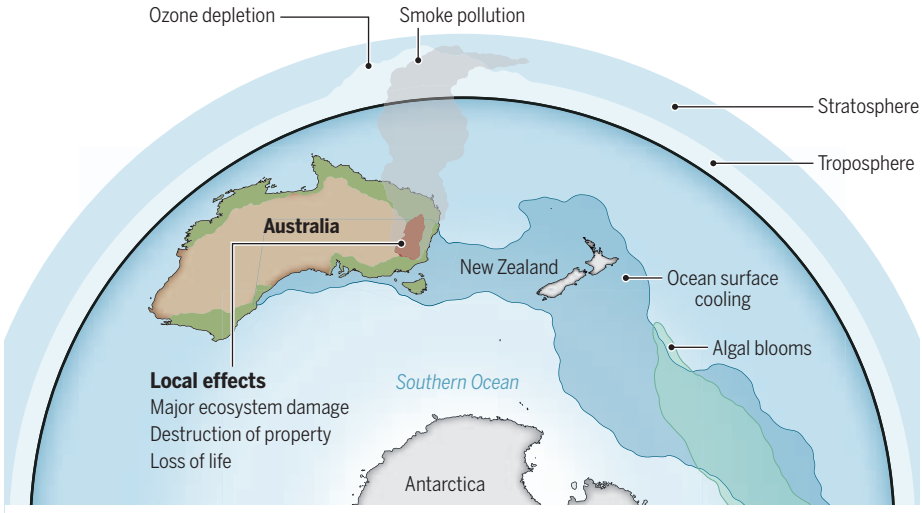

Fire management strategies

Local management actions to reduce wildland fuels include cultural and prescribed burning, herbivory, and forest thinning. Green fire breaks could also be created by the cultivation of plants with low flammability to provide a barrier between fire-prone areas and human settlements.

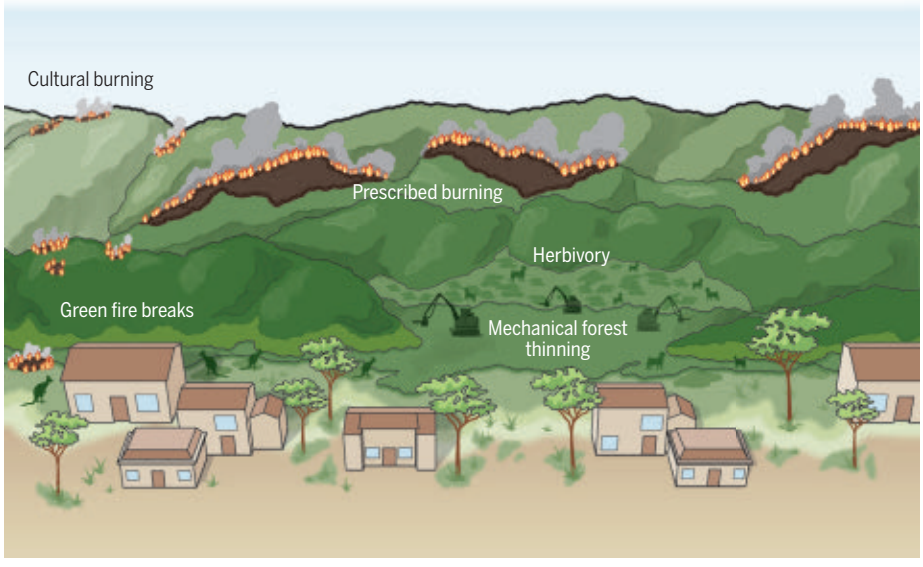

be optimized to maximize benefits for fuel reduction while minimizing adverse effects on ecosystem services (e.g., carbon storage and soil health) and biodiversity.

Before European settlement, Aboriginal people across Australia managed clan estates by setting small and frequent fires that created biodiverse habitat mosaics. However, this system was drastically disrupted by colonial processes. A deeper understanding of how Aboriginal people managed landscapes is a critical research topic that will require a variety of techniques to reconstruct precolonial fire regimes and landscape ecologies using a range of environmental archives (such as lake sediments, tree rings, and historical records). It will also depend on working with Aboriginal fire managers to codesign research programs. The findings of such collaborative research could provide an evidence-based framework for creating prescribed burning programs as well as restoring "cultural burning" to manage wildfire—an approach now firmly on the fire management agenda (*2*, *5*, *14*).

It is important to acknowledge that although both cultural burning and prescribed burning use fire to reduce fuel loads, they are not the same. Prescribed burning typically involves burning large areas in the most economically efficient way possible to meet institutional targets, whereas Aboriginal fire management emphasises social processes associated with cultural connection to landscapes (called "Country" in Aboriginal English) (*2*, *5*, *14*). Notably, such cultural connections have been shown to have measurable physical and psychosocial health benefits for Aboriginal people (*2*). Cultural burning is typically low intensity and is applied regularly to small areas to create a patchwork of habitats with different postfire ages. It also involves social justice issues given that Aboriginal people suffer social disadvantages, including disposition from their ancestral lands. Consequently, effective cultural burning programs demand ongoing government and nongovernment support to train and employ Aboriginal fire managers. Whether cultural burning can be implemented at sufficient scale to mitigate the risk of extreme wildfire events and sustain ecosystems is uncertain and requires landscape-scale evaluation.

An important constraint on both prescribed and cultural burning is the increased density of woody plants that followed the substitution of Aboriginal fire management with colonial approaches (*14*). To restore Australian landscapes to the lower–fire risk state that likely existed before colonization requires evaluating the effectiveness of mechanical removal of understoreys and thinning overstocked forests. Such ecological restoration projects need to also investigate the effectiveness of marsupial and non-native herbivores in reducing understorey biomass and controlling tree and shrub recruitment (*2*, *14*).

Another constraint of prescribed burning, and possibly also of cultural burning if conducted at large scales, is the potential for pollution to cause public health harm. This is especially true given that climate change is shifting the window suitable for prescribed burning toward winter months when temperature inversions (i.e., when the atmospheric base is cooler than the air layer above it) and light breezes favor pooling of smoke close to the ground surface. In principle, prescribed burning can also diminish greenhouse gas emissions from fires by reducing the intensity and scale of wildfires. However, demonstrating this has not been achieved, except possibly for tropical savannas (*15*)—a finding that requires further

GRAPHIC: A. FISHER/*SCIENCE*

scientific validation. The imperative to reduce air pollution from prescribed burning provides an incentive for exploring alternatives. In addition to mechanical removal of vegetation or the action of herbivores, other options might include constructing "green fire breaks" by planting, and possibly irrigating with wastewater, native and non-native plants with low flammability to provide barriers between fire-prone wildlands and urban areas.

Meeting the escalating challenges of sustainable economic and environmental coexistence with landscapes prone to extreme fire events requires Australia—and indeed any country threatened by extreme wildfires—to rethink the basis of fire management and embrace a diversity of approaches (*2*). This involves sustained and serious investment in landscape-scale interventions that use innovative combinations of prescribed and cultural burning, mechanical thinning, and herbivory close to urban areas as well as in wildland areas prone to enhanced pyroconvection. It also must draw on the wisdom and skills of Indigenous fire management practices. Such ambitious applied research demands better coordination among scientists, managers, and other stakeholders, including Indigenous communities, underpinned by the acquisition, curation, and analysis of high-quality biophysical, social, and economic data. Moreover, international comparative studies of wildfire management are of prime importance to drive innovation to control and adapt to climate-driven extreme wildfires. ■

REFERENCES AND NOTES

1. J. G. Canadell *et al.*, *Nat. Commun.* **12**, 6921 (2021).
2. R. H. Nolan *et al.*, *Fire* **4**, 97 (2021).
3. N. J. Abram *et al.*, *Commun. Earth Environ.* **2**, 8 (2021).
4. M. M. Boer, V. Resco de Dios, R. A. Bradstock, *Nat. Clim. Change* **10**, 171 (2020).
5. M. Binskin *et al.*, "Royal Commission into National Natural Disaster Arrangements Report" (Commonwealth of Australia, 2020).
6. M. Ward *et al.*, *Nat. Ecol. Evol.* **4**, 1321 (2020).
7. I. R. van der Velde *et al.*, *Nature* **597**, 366 (2021).
8. F. H. Johnston *et al.*, *Nat. Sustain.* **4**, 42 (2021).
9. W. Tang *et al.*, *Nature* **597**, 370 (2021).
10. D. A. Peterson *et al.*, *NPJ Clim. Atmos. Sci.* **4**, 38 (2021).
11. E. Hirsch, I. Koren, *Science* **371**, 1269 (2021).
12. J. T. Fasullo, N. Rosenbloom, R. Buchholz, *Sci. Adv.* **9**, eadg1213 (2023).
13. S. Solomon *et al.*, *Nature* **615**, 259 (2023).
14. M.-S. Fletcher, A. Romano, S. Connor, M. Mariani, S. Y. Maezumi, *Fire* **4**, 61 (2021).
15. A. Edwards *et al.*, *J. Environ. Manage.* **290**, 112568 (2021).

ACKNOWLEDGMENTS

D.M.J.S.B. is supported by an Australian Research Council Laureate Fellowship (FL220100099). D.M.J.S.B. and J.J.S. are supported by the New South Wales Bushfire and Natural Hazards Research Centre.

10.1126/science.adi8066

POLICY FORUM

Cultural water and Indigenous water science

Australia shows the need for more sustainable and just water management

By **Erin O'Donnell[1], Melissa Kennedy[2], Dustin Garrick[3], Avril Horne[4], Rene Woods[5]**

Rivers and freshwater ecosystems are in trouble, which deeply affects communities who depend on them (*1*) and undermines international commitments to the United Nations (UN) Sustainable Development Goals. Australia's Murray-Darling Basin (MDB) is a prime example. Water governance in this transboundary river system in southeastern Australia, seen by some as a gold standard for managing water scarcity, has nonetheless failed to meet environmental water recovery targets, despite the investment of AUD$13 billion. Water management failings in the MDB, which is home to more than 40 First Nations who have lived sustainably with water for tens of thousands of years through the creation and application of Indigenous water science (*2*) (see the first box), have drawn attention to the living legacies of colonial exploitation and the associated social and ecological impacts. We need to learn from Australia's failures and change the way we know, value, and manage water, including learning from Indigenous scientists and Elders.

The MDB, which supports a center of irrigated agriculture across more than 1 million km^2, is known for its multiyear "boom-bust" riverine cycles, but climate change is intensifying these extremes (*3*). Over the past three decades, major efforts to improve MDB governance have included intergovernmental agreements in 1994 and 2004 (the National Water Initiative), new federal legislation in 2007, and the MDB Plan in 2012, overseen by the MDB Authority. More than AUD$13 billion has been invested in water recovery for the environment by using water markets and increasing water delivery efficiency. Despite this long-standing attention and investment, the MDB suffers from poor water quality, overextraction of water for irrigation, flow modification, increasingly disconnected and degraded floodplains, and declining biodiversity (*4*). We trace these contemporary problems to a root cause—aqua nullius—that, in Australia and elsewhere, excludes Indigenous Peoples' from ownership of and control over water (*5*, *6*). First Nations in the MDB now own less than 0.2% of all water rights and have little power in the management of waterscapes (*7*). In a reflection of the need for urgent action, in 2023, the UN hosted its first water conference since 1977, which argued for full participation of Indigenous Peoples in water management.

Terminology

When describing Indigenous Peoples in the Murray-Darling Basin (MDB), we use specific terminology.

Aboriginal and Torres Strait Islander Peoples refers to the Indigenous Peoples of Australia.

First Nations and Traditional Owners refer to Indigenous polities and governance structures in the MDB. Some groups have been formally recognized by the settler state (e.g., native title), but some have not.

Country is an Aboriginal English word that refers to the world around us, a living entity including people, land, water, air, sky, and all plants and animals.

AQUA NULLIUS: FUNDAMENTAL FLAW

When the British invaded Australia, the legitimacy of their occupation was founded on the assumption of terra nullius, or land belonging to no one, despite the clear presence of First Nations with laws governing access to and use of land. This flawed beginning enabled the equally erroneous assumption of aqua nullius, or water belonging to no one, with no acknowledgment that First Nations had and continue to have laws governing the care and management of water (*5*). These flawed assumptions became the foundation for more than two centuries of extractive, unsustainable water management.

Water colonialism is intertwined with globalization, neoliberalism, and extractive capitalism (*8*). The commoditization of water and the separation of water from land are foundational concepts in Western water management but are fundamentally at odds with Indigenous Peoples' relationship with

Country. Although other English-speaking settler colonial states, unlike Australia, have treaties or agreements with Indigenous Peoples, the impacts of aqua nullius (and the associated erasure of Indigenous water science and law) are global (*6*).

The flawed assumption of aqua nullius is comprehensively embedded within the settler-state legal, regulatory, and institutional arrangements for water management in the MDB. Failure to acknowledge the pluralist nature of water law and governance sets up a collision between Indigenous Peoples and the state in terms of the way the world is seen and how knowledge and evidence are constructed. Rather than understanding rivers and water ecosystems as living entities with whom we are in a reciprocal relationship, settler-state laws establish water systems as resources for human consumption and exploitation, fostering competition for water and undermining collective-action policy responses (*9*).

Aqua nullius also means that Western science remains the dominant source of knowledge. In the MDB, non-Indigenous water scientists and water managers continue to largely neglect the knowledge built over tens of thousands of years of sustainable water management by Indigenous Peoples (*10*). For example, neither of the two separate reports that were commissioned to determine the causes of and define water management responses to the catastrophic fish kills in the Barka-Darling River in 2018–2019 included an Indigenous water scientist as an author. This is both a justice issue, because Indigenous representation matters, and a knowledge issue, because both reports suffered from a lack of Indigenous knowledge of the river, which would have identified other potential solutions, including holistic land and water management.

Just and effective water resource management in settler colonial contexts requires the acknowledgment of and engagement with the water rights and water laws of Indigenous Peoples. In undermining both the legitimacy and sustainability of Australia's water management, aqua nullius affects the well-being of both Indigenous (*5*) and non-Indigenous people (*11*).

THE CULTURAL WATER PARADIGM

Solutions to the global crisis of unsustainable water management caused by the false assumption and flawed science of aqua nullius are already being advanced by leading Indigenous water scientists and scholars (*6*). In the MDB, Indigenous leadership has informed the development of the Cultural Water Paradigm, which connects environmental health, economic development, self-determination, connection to place, upholding responsibility to Country, strengthening culture through praxis, and emotional and spiritual well-being (see the figure). Under a cultural water paradigm, First Nations are water decision-makers.

Just as ecological values of rivers depend on "environmental water," maintaining the cultural traditions and community development needs of First Nations requires "cultural water." Cultural water intersects with outcomes achieved through environmental watering, but it is guided by Indigenous knowledge (not just Western ecology). In the MDB, Indigenous partnerships in environmental watering show how to provide water to keep scar trees alive and produce blooms of aquatic plants, such as Old Man Weed (*Centipeda cunninghamii*), that have cultural, spiritual, and medicinal, as well as biodiversity, values.

Cultural water also addresses the ongoing exclusion of First Nations in the MDB from the use of water to support economic development by including water for economic development, which overlaps with, but is not the same as, capitalist commercial water uses (see the figure). The cultural water paradigm thus contributes to the wider policy shift toward regenerative, circular economies.

Although Western science has recognized the importance of integrated water management, it gives far less weight to the cultural and spiritual well-being that is essential for First Nations. Water managers still categorize water into different uses that can be traded-off against each other, whereas Indigenous knowledge shows that cultural water economies are built on healthy Country and support healthy people.

In addition to creating a pathway to restore First Nations' water rights, the cultural water paradigm shows how the separate silos of settler water management (environmental, commercial, and household uses) can be integrated (or reintegrated) into a holistic approach based on the deep knowledge and science of Indigenous Peoples. Although yet to be applied in full, elements of the cultural water paradigm in action are already demonstrating the power of Indigenous-led, holistic water management in the MDB (see the second box).

The cultural water paradigm directly addresses the problem of aqua nullius, because First Nations are empowered to assert their rights to care for and make decisions about water, establishing a foundation for transformational change that is already driving settler water law and policy reform in the MDB (*12*). Further reform opportunities to address the path-dependence created by aqua nullius will occur as Australia reviews both the Water Act 2007 (in 2024) and the MDB Plan (in 2026). Inclusion of First Nations' water rights and interests is already emerging as a key priority.

PATHWAYS TO CULTURAL WATER

The legitimacy and sustainability of water management are inextricably interconnected. A starting point for change must be a willingness to recognize multiple worldviews on water (*13*). Indigenous water science in the MDB shows the importance of diverse

The cultural water paradigm

Within the paradigm, First Nations are empowered to assert their rights to care for and make decisions about water, establishing a foundation for transformational change in water-management policy in a contemporary context. Although yet to be applied in full, elements of the paradigm are already demonstrating the power of Indigenous-led, holistic water management.

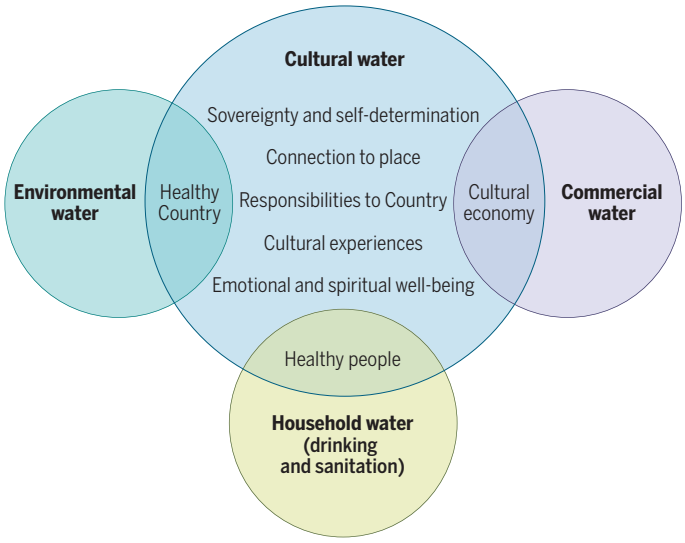

GRAPHIC: A. MASTIN/*SCIENCE*

[1]University of Melbourne, Law School, Melbourne, VIC, Australia. [2]Faculty of Architecture, Building and Planning, University of Melbourne, Melbourne, VIC, Australia. [3]School of Environment, Resources, and Sustainability, University of Waterloo, Waterloo, ON, Canada. [4]School of Engineering, University of Melbourne, Melbourne, VIC, Australia. [5]The Nature Conservancy, Melbourne, VIC, Australia.
Email: erin.odonnell@unimelb.edu.au

Examples of the cultural water paradigm in action

Nari Nari Tribal Council land and water management

Gayini Nimmie-Caira is an 88,000-ha property on the Lowbidgee floodplain that is rich in cultural heritage, with 50,000 years of Indigenous occupation. Located on Nari Nari Country in the southern Murray-Darling Basin, the property is owned by the Nari Nari Tribal Council (NNTC), who manage the wetland with an integrated economic, social, cultural, and ecological vision for Country. The NNTC, the Nature Conservancy, the University of New South Wales, and the Murray Darling Wetlands Working Group brought together cultural objectives, Indigenous science, Western environmental science, community partnerships, conservation skills, and sustainable agriculture to deliver a new, holistic "Healthy Country Planning" approach to land and water management. By recreating floodplain functions, the NNTC aims to increase cultural-environmental health outcomes that reverse the harm done by colonial land management, as well as create economic value. A partnership between the NNTC and the Commonwealth Environmental Water Holder provided environmental watering to Gayini Nimmie-Caira, which achieved multiple ecological and cultural benefits.

Tati Tati Cultural Water Management Plan

Margooya Lagoon is a permanent wetland on Tati Tati Country on the Murray floodplain near Robinvale in Victoria, Australia. The natural function of the lagoon has been disrupted by river regulation, and a water regulator was installed at the easier-to-access downstream end of the lagoon to facilitate a wetting and drying cycle. This was done without adequate consultation with Tati Tati Traditional Owners, who seek the removal of the regulator and reinstatement of water flowing through the wetland via natural inlets. Doing so requires a holistic land management system that connects cultural watering to cultural burning, which ensures that dry creeks remain clear and prevents blackwater events by reducing the amount of organic material entering the waterways.

and pluralistic ways of knowing and types of knowledge. Indigenous knowledge opens up a much longer history of water management in the MDB than Western hydrological datasets and shows how people have lived sustainably in this unpredictable waterscape (*10*).

For those deeply embedded within a Western-science framework, this can be extremely challenging. Western science is not neutral, and our understanding of the world around us is informed by our position in that world: our culture, our experiences, and our relative privileges. Indigenous Peoples remain chronically underrepresented within Western science disciplines and face considerable barriers to participating in and accessing Western science (*14*). Diverse forms of knowledge can be complementary and move beyond a simplistic dichotomy of Western and Indigenous knowledge (*13*).

We offer the following guiding questions for water scientists, policy-makers, and water managers to help create a pathway to a cultural water paradigm.

How do Western water scientists and water managers get started?

In the MDB, pathways toward the cultural water paradigm include increasing Indigenous representation in water governance (such as the recent appointment of an Aboriginal member to the board of the MDB Authority), joint management agreements, collaboration on environmental flows, and holistic land and water management (see the second box). Every pathway to a cultural water paradigm will be different, depending on the relationships, rights, and interests of Indigenous Peoples and settler water managers. But everyone can make a start.

How can we lower the barriers to Indigenous participation in water management?

Braiding Indigenous and non-Indigenous knowledge requires engagement with the political questions of water justice (*6*, *13*, *14*). Lowering barriers requires tackling water injustice in research programs and priorities, building long-term research partnerships with Indigenous communities, and broadening the criteria for who counts as a water scientist to address the roadblocks faced by Indigenous scientists and practitioners in water management. One of the MDB's success stories, led by the Nari Nari Tribal Council, shows the absolute necessity of partnerships to support holistic water management (see the second box).

How do we perform effective water science, together?

Science must be coupled with policy reform so that Indigenous Peoples are empowered to lead both water science and water management (*6*). In the MDB, as in many other parts of the world, there is a well-earned distrust of researchers and policy-makers by Indigenous Peoples. Indigenous knowledge is ontologically and epistemologically different to Western science, but they can be complementary. A best-practice approach focuses on establishing a collaborative process from the beginning, thereby embedding collaborative knowledge-braiding processes at multiple points during a research project (*13*). Western water scientists need to be prepared to be humble, embrace discomfort, engage in radical listening, and follow rather than lead. Collaborative knowledge sharing requires the sharing of power between Western scientists and Indigenous communities, thereby ensuring that the identification of problems and potential solutions is undertaken together. In the MDB, good science forms part of Indigenous nation-building (*15*).

Water science and management must be pluralist and centered on a cultural water paradigm that tackles the legacies of aqua nullius and fosters legitimacy. By accelerating the transition to a cultural water paradigm, we can create new pathways for broadening knowledge, partnerships, and possibilities for a just water future. ■

REFERENCES AND NOTES

1. E. P. Anderson *et al*., *WIREs. Water* **6**, e1381 (2019).
2. B. J. Moggridge, *J. R. Soc. Qld*. **126**, 11 (2020).
3. B. Asadieh, N. Y. Krakauer, *Hydrol. Earth Syst. Sci*. **21**, 5863 (2017).
4. J. L. Swirepik *et al*., *River Res. Appl*. **32**, 1153 (2016).
5. V. Marshall, *Overturning Aqua Nullius: Securing Aboriginal Water Rights* (Aboriginal Studies Press, 2017).
6. K. Leonard *et al*., *Water Altern*. **16**, 374 (2023).
7. L. D. Hartwig, S. Jackson, N. Osborne, *Land Use Policy* **99**, 104869 (2020).
8. M. Z. Zwarteveen, R. Boelens, *Water Int*. **39**, 143 (2014).
9. R. Q. Grafton, J. Williams, *Int. J. Water Resour. Dev*. **36**, 484 (2020).
10. B. J. Moggridge, R. M. Thompson, *Australas. J. Water Resour*. **25**, 4 (2021).
11. S. Daghagh Yazd, S. A. Wheeler, A. Zuo, *Ecol. Econ*. **169**, 106564 (2020).
12. Victoria State Government, Environment, Land, Water and Planning, "Water is life: Traditional owner access to water roadmap" (State of Victoria Department of Environment, Land, Water and Planning, 2022); https://www.water.vic.gov.au/aboriginal-values/the-aboriginal-water-program.
13. S. Mehltretter, S. Longboat, B. Luby, A. Bradford, "Indigenous and Western knowledge: Bringing diverse understandings of water together in practice" (Technical Report, Global Commission on the Economics of Water, 2023); https://watercommission.org/wp-content/uploads/2023/03/Mehltretter.pdf.
14. L. Ignace *et al*., *Science* **381**, 129 (2023).
15. S. Hemming, D. Rigney, S. Bignall, S. Berg, G. Rigney, *Australas. J. Environ. Manage*. **26**, 216 (2019).

ACKNOWLEDGMENTS

This work was funded by Australian Research Council Discovery Early Career Research Fellowship DE230100622 and the Australian Research Council Centre of Excellence Life Course Centre. The authors declare the following competing interests: E.O. is a member of the Birrarung Council; R.W. is a board member of the MDB Authority, a member of the National Committee on Aboriginal Water Interests, and an employee of The Nature Conservancy in Australia; and M.K. is the chief executive officer of Tati Tati Kaiejin, a not-for-profit, Indigenous-led environmental organization. E.O., D.G., and A.H. are people of settler heritage living in settler colonial states. M.K. is a Tati Tati Traditional Owner (Indigenous person). R.W. is a Nari Nari Traditional Owner (Indigenous person).

10.1126/science.adi0658

REVIEW

Loss of terrestrial biodiversity in Australia: Magnitude, causation, and response

Sarah Legge[1,2]*†, Libby Rumpff[3]†, Stephen T. Garnett[1]†, John C. Z. Woinarski[1]†

Australia's biota is species rich, with high rates of endemism. This natural legacy has rapidly diminished since European colonization. The impacts of invasive species, habitat loss, altered fire regimes, and changed water flows are now compounded by climate change, particularly through extreme drought, heat, wildfire, and flooding. Extinction rates, already far exceeding the global average for mammals, are predicted to escalate across all taxa, and ecosystems are collapsing. These losses are symptomatic of shortcomings in resourcing, law, policy, and management. Informed by examples of advances in conservation practice from invasive species control, Indigenous land management, and citizen science, we describe interventions needed to enhance future resilience. Many characteristics of Australian biodiversity loss are globally relevant, with recovery requiring society to reframe its relationship with the environment.

Australia makes a distinctive contribution to global biodiversity, supporting >8% of all the world's species (*1*). An exceptional proportion of Australian species are endemic: >90% of its frogs and reptiles and >80% of its mammals and plants occur nowhere else (*1*). Australia's rich biological diversity is a legacy of a long period of geographic isolation after its separation from the Gondwanan supercontinent 30 million years ago (*2*), combined with an unusual combination of low-nutrient soils, a highly variable climate, and a long history of widespread fire. As a result, many Australian lineages offer glimpses into deep evolutionary time, and some important species groups, such as songbirds (*3*), emerged in Australia before radiating to other parts of the world.

Severe degradation of Australia's natural world began ~250 years ago, when European colonization began removing Indigenous peoples from the land they had managed for >60,000 years. Some conservation challenges in Australia are characteristic of global patterns of loss, and the mechanisms for attempting recovery are relatively generic. Others are idiosyncratic, and conservation efforts are thus necessarily more tailored to local circumstance.

The situation is dire, yet there is cause for hope. Australia has distinct advantages that could help stem losses and enable recovery: (i) The continent is a single nation, making legislative, policy, and management responses theoretically simple; (ii) it is politically stable and wealthy, which should allow consistent, strategic, and long-term responses to conservation problems; (iii) it has a low population density, which should cap pressure on the environment; and (iv) the country's Indigenous peoples retain a culture of caring for Country (a term for the interlinked spiritual, cosmological, cultural, ecological, and physical environmental attributes) and continue to manage large areas of the continent. In addition, many Australians celebrate their natural world, and a large majority want no further extinctions (*4*).

Here, we review recent advances in knowledge of biodiversity loss in Australia since colonization and the drivers underpinning these losses. We describe some Australian examples of advances in conservation practice and derive more generic lessons about key responses to rapid, deteriorating environmental change. Our focus is on terrestrial biota and complements a companion review on the marine environment (*5*). Although Australia experienced a pulse of species extinctions in the late Pleistocene (*6*), we focus here on biodiversity loss since European colonization, particularly the contemporary processes shaping the status of biodiversity and the conservation response.

Biodiversity loss in Australia: Extent and characteristics

Recent studies have done much to clarify the status and trends of, and prospects for, Australian biodiversity. The conclusions from these studies are generally dispiriting: Many species have been lost, are precariously imperiled, or are declining; ecosystems are collapsing; and the outlook is worsening (*7*), just as it is elsewhere (*8*) (Fig. 1).

A recent review found that 97 Australian species (a protist, 38 plants, 10 invertebrates, four frogs, one reptile, nine birds, and 34 mammals) have become extinct since 1788, with three additional species (one fish and two reptiles) extinct in the wild (*9*). However, this tally vastly underrepresents the number of extinct invertebrate species, as is the case globally (*10*), and probably of other little-known groups such as fungi. Reported Australian extinctions also fail to consider likely extinctions of codependent species such as parasites and pollinators (*11*). The rate of known Australian extinctions (about four species per decade) has been more or less constant over this period, and at least four extinctions have occurred over the past 15 years (*8*). However, the rate of extinctions is predicted to increase over the next few decades, based on assessments of vertebrates, plants, and some invertebrate groups (*12*–*17*), and step-changes of loss caused by environmental disasters (*18*).

The 34 extinctions of mammal species comprise ~10% of the Australian terrestrial mammal fauna at the time of colonization and vastly outnumber extinctions of mammals in any other country over this period. For example, in continental North America, only one native land mammal has become extinct since European settlement (*19*). An unusual feature of the Australian mammal extinctions is that many of these species were formerly extremely abundant and widespread. Losses have occurred across a broad spectrum of environments, from intensively developed regions to remote areas with sparse human populations. As with global trends (*20*), endemic species on Australia's islands have suffered disproportionately high rates of loss.

Under Australian national environmental legislation (https://www.dcceew.gov.au/environment/biodiversity/threatened/species), 1908 species and 103 ecological communities are currently (as of April 2023) listed as threatened, with this tally rapidly increasing and with many highly imperiled species not yet listed (*14*). Far more species have been up-listed (i.e., to a more imperiled status) than down-listed (120 and 38, respectively) over the past 20 years (*21*). Although there are major inadequacies in monitoring of Australian biodiversity (*22*, *23*), recent aggregation and analysis of monitoring data have documented an ongoing rapid and severe decline for populations of Australian threatened species, with threatened birds declining by an average of 44% over the period 2000–2016, threatened mammals by 35% during 2000–2017, and threatened plants by 72% during 1995–2017 (*24*–*26*). The severe ongoing decline of Australia's threatened birds contrasts sharply with marked trends for recovery for threatened birds in the United States (average 624% increase) from 1967 to 2014 (*27*).

Increases in extinction risks to threatened biodiversity constitute the final stages in only part of Australia's biodiversity decline. Many other species and ecosystems are experiencing marked ongoing losses (*12*, *28*–*33*), with many more likely to go undetected (*34*, *35*). Mass mortality events are increasing in frequency and eroding resilience across ecosystems. Examples include a series of fish kill events between 2018 and 2020 in the Murray Darling Basin, when drought and poor water management

[1]Research Institute for the Environment and Livelihoods, Charles Darwin University, Casuarina, Northern Territory, Australia. [2]Fenner School of Society and the Environment, The Australian National University, Acton, Canberra, Australian Capital Territory, Australia. [3]School of Agriculture, Food and Ecosystem Sciences, The University of Melbourne, Parkville, Victoria, Australia.
*Corresponding author. Email: sarah.legge@cdu.edu.au
†These authors contributed equally to this work.

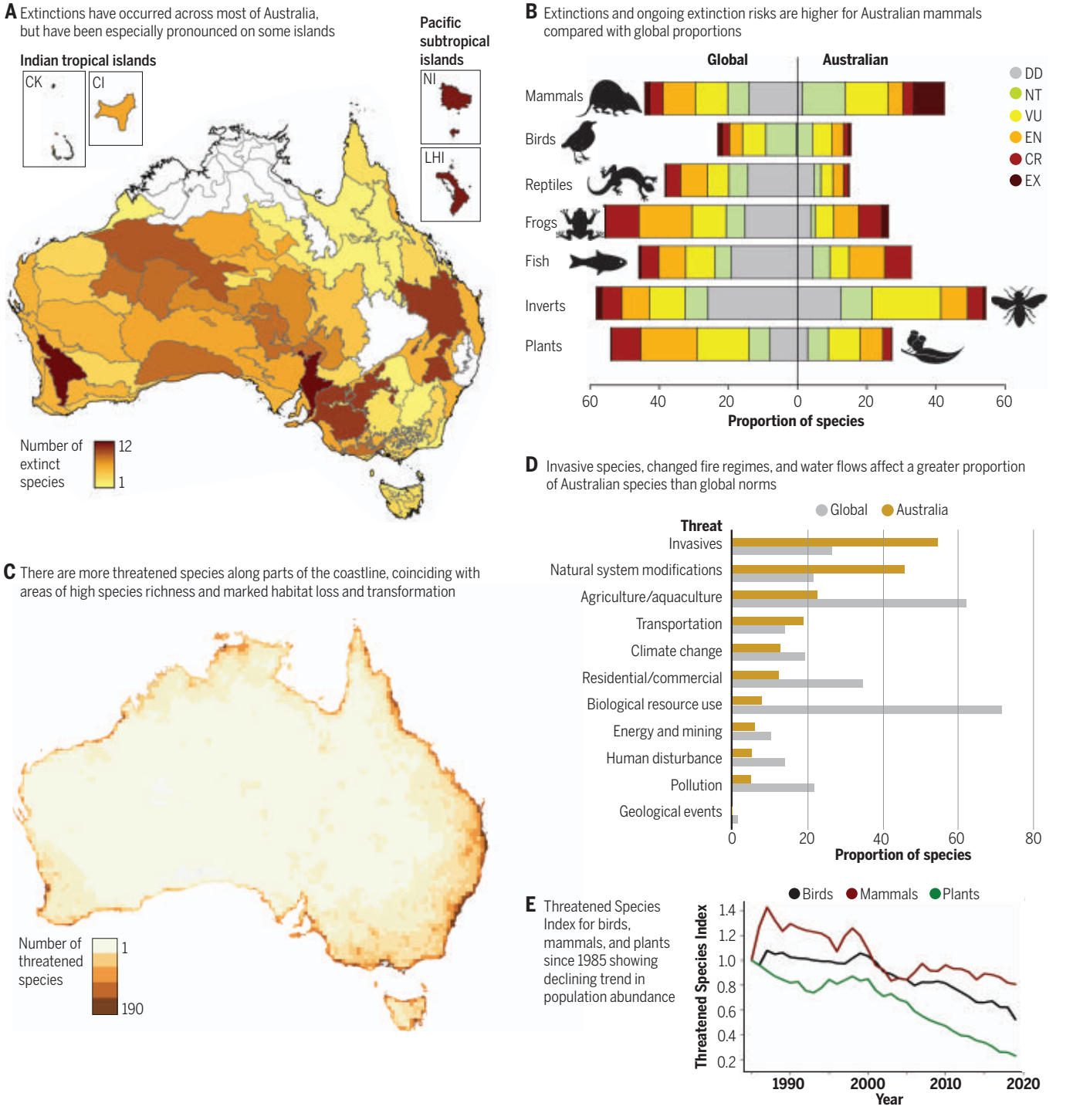

Fig. 1. Biodiversity declines in Australia since colonization. (**A**) Patterns showing the former ranges of Australian species rendered extinct, with darker shading indicating larger numbers of extinct species in the bioregion. Note the high extinction rates on islands. CK, Cocos (Keeling) islands; CI, Christmas Island; LHI, Lord Howe Island; NI, Norfolk Island (*9*). (**B**) Comparison of global with Australian extinction risks across terrestrial species groups, according to the IUCN Red List (downloaded 17 March 2023). Non-native and marine species are excluded from Australian IUCN Red List figures, and the search included the land regions of Australia, Christmas Island, Cocos (Keeling) Islands and Norfolk Island. The legend refers to EX: extinct, CR: critically endangered, EN: endangered, VU: vulnerable, NT: near threatened, NT: data deficient. (Extinct in the wild category not visible at graph scale). Proportions are based on the number of assessed species, which are low for some groups, especially invertebrates. The numbers of extinct Australian species in the IUCN database differs slightly from the numbers in the main text, which are based on (*9*). (**C**) Spatial variation in the number of threatened species in subregions across Australia. High concentrations of threatened species on some islands are not detectable at this displayed scale. Map created using data from Australian government database (https://www.dcceew.gov.au/environment/environmental-information-data/databases-applications/snes). (**D**) Comparison of the threats affecting Australian threatened species versus global patterns using International Union for Conservation of Nature (IUCN) Red List data for global figures (data extracted 16 March 2023) and (*119*) for threats facing Australian species (noting that a broad IUCN Category threat is only counted once per relevant species even if multiple related subcategory threats affect that species). (**E**) Threatened Species Index (*25*) for Australian birds, mammals, and plants from 1985 to 2020 (downloaded 17 March 2023).

FIG. 1C: P. CARLILLE

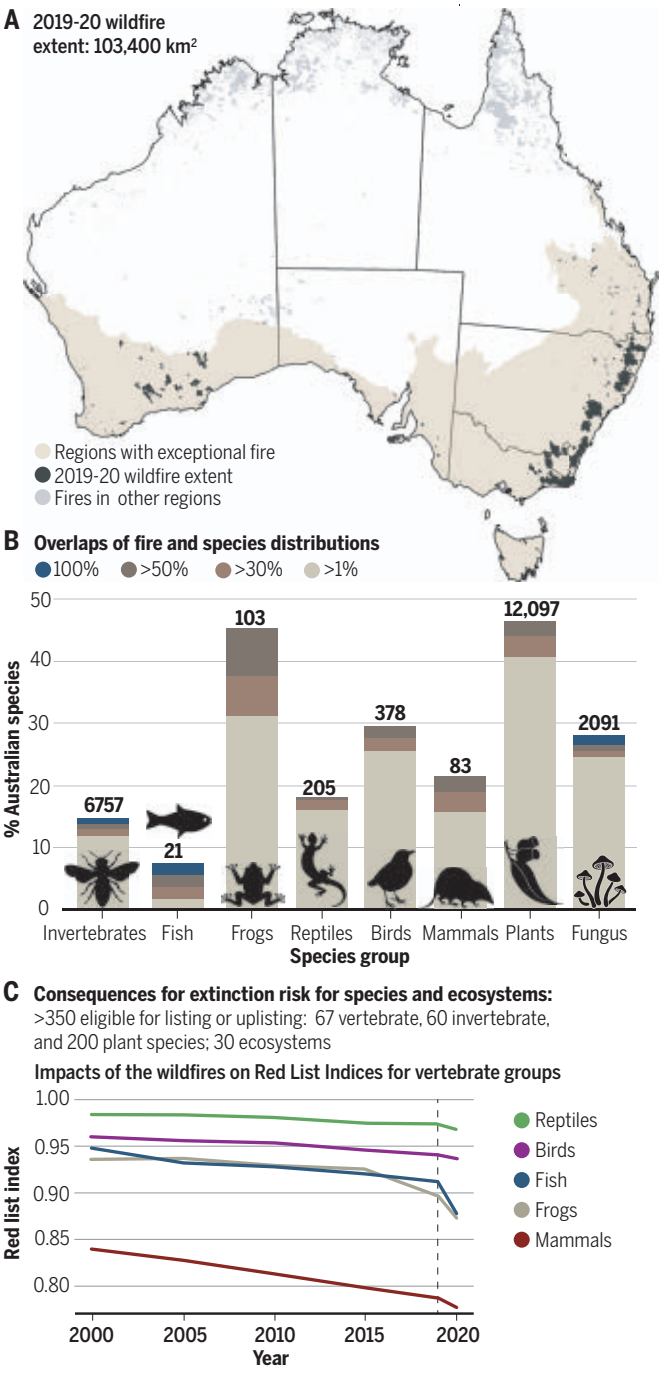

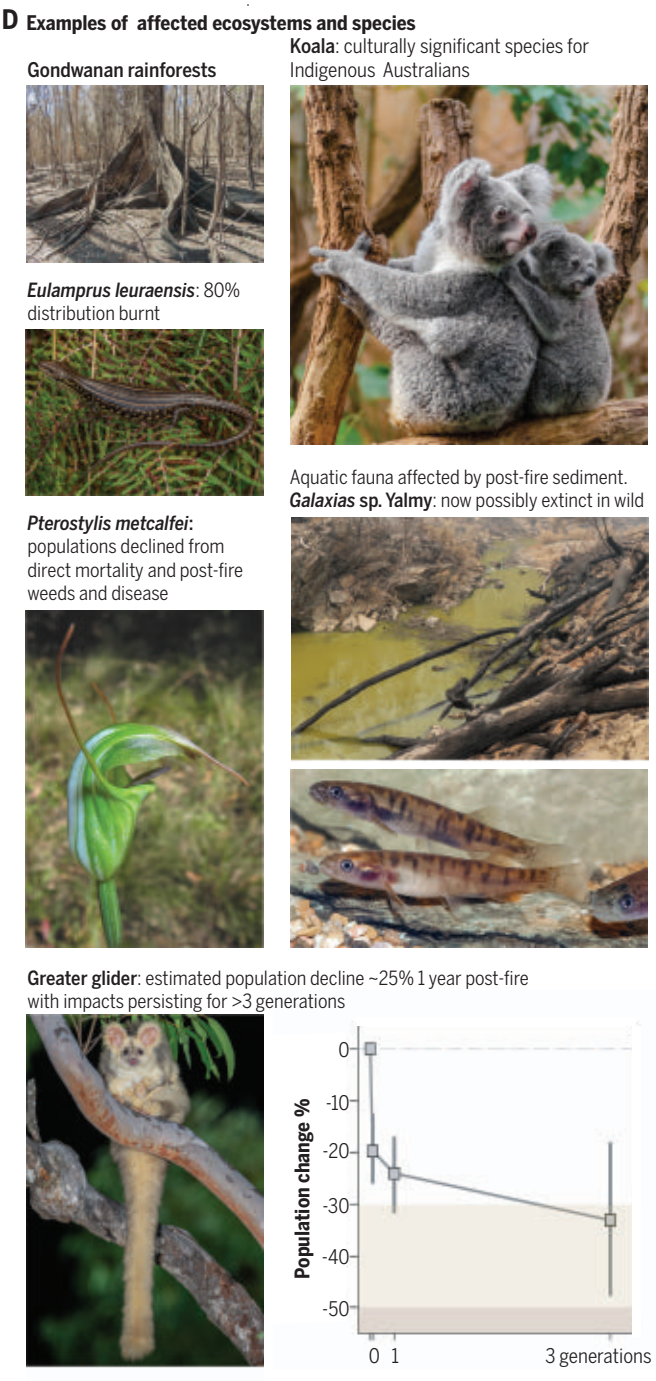
D
Examples of affected ecosystems and species
Gondwanan rainforests
Eulamprus leuraensis: 80% distribution burnt
Pterostylis metcalfei: populations declined from direct mortality and post-fire weeds and disease
Koala: culturally significant species for Indigenous Australians
Aquatic fauna affected by post-fire sediment.
Galaxias sp. Yalmy: now possibly extinct in wild
Greater glider: estimated population decline ~25% 1 year post-fire with impacts persisting for >3 generations
Population change %
0
-10
-20
-30
-40
-50
0 1
3 generations

Fig. 2. Impacts of climate change–induced events. (**A**) In 2019–2020, wildfires burned >103,400 km^2 in southern and eastern Australia. More than 20% of the forest biome burned, more than any other forest biome globally since 2000 (*37*). (**B**) Many species were affected. The graph shows the proportion of species in each group with distributions that overlapped with fire by 100%, >50 to 99%, >30 to 49%, and >1 to 29%. The numbers of fire-affected species (>1% overlap) in each group are indicated above the bars (noting that numbers of fire-affected invertebrates and fungi are underestimated because most species in these groups are undescribed or their distributions are unknown) (*37*). (**C**) Some species and ecosystems experienced sudden declines or amplification of pre-existing declines sufficient to warrant assessment for listing or uplisting as threatened under national environmental legislation. Estimated changes in extinction risk caused visible inflections in Red List Index trends for vertebrates (*18*). (**D**) Examples of fire-affected species and ecosystems. Ecosystems included some that rarely (if ever) burn such as Gondwanan rainforests (*120*). Fire overlapped large proportions of some species' distributions, e.g., *Eulamprus leuraensis* (80% overlap) (*37*). The fires affected species of cultural significance to Indigenous people, e.g., koalas, and highlighted that Indigenous values and fire practice are poorly incorporated into contemporary fire management (*121*). Many plant species are resilient to fire, but interactions between fire and other threats such as drought and postfire weed invasion caused declines in species such as *Pterostylis metalfei* (*122*). Severe fire changed soil properties, causing massive post-rain sediment pulses in waterways that depleted dissolved oxygen, filled pools, and smothered streambed substrates. Sediment was transported many kilometers downstream, affecting littoral and marine areas. The entire distribution of *Galaxias* sp. Yalmy experienced sedimentation, and this species may now be extinct in the wild (*123*). More than 40% of the distribution of the greater glider (*Petauroides volans*) burned, and impacts are predicted to persist for more than three generations (*18*).

PHOTO CREDITS: CLOCKWISE FROM TOP RIGHT: D. PUGH, S. MAHONY, M. APPEL, L. COPELAND, J.L. PEARCE, T. A. RAADIK, S. HORTON

led to low dissolved oxygen, killing millions of fish from >25 species (*36*). This drought led directly to the 2019–2020 wildfires, which killed or displaced an estimated 3 billion mammals, birds, frogs, and reptiles. The fires were quickly followed by widespread flooding and blackwater events that caused substantial pulses of mortality in freshwater fauna (*37*). Even iconic species such as the koala (*Phascolarctos cinereus*), platypus (*Ornithorhynchus anatinus*), and Tasmanian devil (*Sarcophilus harrisii*), which were previously common and are deeply embedded in Indigenous culture, are declining despite substantial conservation investment and public advocacy.

The losses and declines of Australian biodiversity have had broader ecological ramifications. Many now extinct or declining mammal species provided critical roles in ecosystem function, such as turnover of soil, seed dispersal, and germination and as keystone predators (*38*). Relatedly, measures of ecosystem integrity are also plummeting. An analysis of the state of 12 terrestrial ecosystems covering >70% of the Australian continent showed that all are collapsing or have already collapsed in some part of their former extent, as demonstrated by marked decline or loss of their pivotal or characteristic species, reduced resilience to disturbance, or transitions to less diverse and productive states (*39*). A national-scale assessment found that Australia has crossed, or is approaching, thresholds for several key systems functions, or "planetary boundaries," including the genetic and functional integrity of its biodiversity due to extremely high rates of extinction and decline (*40*).

Causes of biodiversity loss

Many changes since European colonization have buffeted Australia's biodiversity and transformed its environments. Habitat conversion to agriculture and urban areas has reduced Australia's forest extent by 40% (*41*), and habitat loss continues to be pervasive across Australia. More than 7.7 million hectares of the habitat of threatened species was cleared between 2000 and 2017 (*42*). Across most of Australia, long-established skillful and purposeful custodianship of Country by Indigenous peoples, including management of fire, has been disrupted, destabilizing former ecological equilibria. Most aquatic systems have been extensively modified and water resources overexploited (*43*). Livestock and feral herbivores have degraded ecosystems, many of which are ill-adapted to high grazing pressure from hard-hooved animals (*44*), and invasive predators are ubiquitous and devastating (*45*).

The main factors that have caused Australian extinctions over the past two centuries have varied among taxonomic groups. For plants, the main driver of loss has been habitat clearance and degradation. For frogs, it has been chytrid fungus (*Batrachochytrium dendrobatidis*), first evident in the 1970s. Many native freshwater fish are highly imperiled because of predation by introduced fish, especially trout (*Oncorhynchus mykiss* and *Salmo trutta*) (*14*). For mammals, introduced predators [feral cats (*Felis catus*) and European red foxes (*Vulpes vulpes*)] are the main threat. Feral cats kill 1.5 billion native vertebrates annually (*45*), and their devastating impact has been demonstrated through successful translocations of predator-susceptible native mammals to islands and to mainland areas from which cats and foxes have been excluded by fencing (*46*). However, the threat posed by introduced predators beyond these havens remains mostly uncontrolled. For birds, hunting (formerly), habitat degradation, and predation are the main threats (*9*). Today, most of Australia's threatened species are affected by multiple threats, with invasive species (affecting 82% of threatened species) and modification of ecosystem processes (e.g., changed fire regimes; 74%) being particularly pervasive (*47*). Australian threat rankings differ from the global norm, for which exploitation and urban development rate more highly (*48*) (Fig. 1).

Although Australia is a continent, the profound impact of alien invasive species on Australian biodiversity resembles (albeit it in a magnified way) the pattern of disproportionately high rates of biodiversity loss, and its causes, on islands (*49*). The susceptibility of Australian biodiversity to introduced species is largely a consequence of the continent's long isolation, during which its distinctive biota has evolved with little history of dealing with new competitors, predators, or disease. Some invasive species are widespread and having a profound impact: the European rabbit (*Oryctolagus cuniculus*) and the soil-borne cinnamon fungus (*Phytophthora cinnamomi*) affect hundreds to thousands of native plant species and the fauna and ecosystems that rely on them. New species continue to be introduced. For example, myrtle rust (*Austropuccinia psidii*), which was accidently introduced in 2010, has subsequently spread extensively, causing high rates of mortality for many of Australia's 2250 myrtaceous plant species. Losses are likely to include widespread and common keystone components of ecosystems, and many extinctions are expected (*50*). Conversely, Australia's isolation has also provided at least temporary protection from some factors that have caused severe biodiversity loss elsewhere in the world, such as white nose syndrome in bats (*51*). This illustrates that a continuing major challenge for Australia's biodiversity conservation is the effectiveness of its biosecurity systems.

Climate change is both compounding the impacts of existing threats and imposing new stresses, including gradational range contractions and population declines for many species (*31*, *52*), ecosystem shifts (*53*), and episodes of acute loss, such as in the wildfires of 2019–2020 (*37*). The loss of the Bramble Cay melomys (*Melomys rubicola*) around 2010 after episodes of inundation of its 4-hectare island home may be the first vertebrate extinction directly caused by global climate change (*54*). In Australia, the many manifestations of climate change include increased severity and extent of drought, with catastrophic impacts on terrestrial and aquatic biota (*36*); increased frequency of days of extreme heat leading to major mortality events such as the death of >45,000 flying foxes on a single day (*55*); phenological mismatches for some pollinator systems (*56*); and ongoing range contractions, such as for endemic birds of high-elevation rainforests (*57*).

As is the case globally, climate change is also driving increases in the incidence and severity of wildfires in Australia (*58*). For example, the 2019–2020 wildfires, precipitated by extensive and severe drought, burned an unprecedented >10 million hectares of forest. These wildfires contributed to at least one extinction (*11*), marked population declines for hundreds of species, and severe damage to many ecosystems (*37*), including vegetation types that rarely burn and are poorly adapted to fire (*59*) (Fig. 2). Given that the incidence of extensive and severe fires will increase with ongoing climate change, some ecosystems and species are unlikely to recover before the next comparable event, leading to major shifts in vegetation composition and losses of many species, especially among animal and plant groups of ancient lineages that are have evolved under conditions of much less disturbance.

Options for management are complicated because threats are both interactive and cumulative. For example, wildfire and timber harvesting have individual detrimental impacts on the fauna of the tall eucalypt forests of southeastern Australia, but timber harvesting may increase the likelihood of severe wildfire (*60*). Similarly, lethal control of dingoes (*Canis familiaris dingo*) across much of rangeland Australia has allowed populations of kangaroos (*Macropus* and *Osphranter* spp.) to increase, exerting higher total grazing pressure on habitats and threatened plant species (*61*). Management is particularly challenging for threats that operate pervasively across land tenures (*62*). A weakness of Australia's conservation reserve system, contrary to global patterns, is that although it protects species threatened by land clearing, it has provided little succor for species affected by invasive species or climate change.

The accumulating and deepening array of threats to Australian biodiversity reflect the low value placed on conservation of the environment, with this perspective deeply ingrained in inadequate legislation, policy, and management (*63*). Australia's environmental legislation has failed to conserve biodiversity, with weaknesses in relation to taxonomic biases, biosecurity,

Fig. 3. Conservation impact and management response to invasive predators in Australia. (**A**) Cats and foxes have had substantial impacts on Australian native species, especially mammals. Australia has had the most mammal extinctions of any country in the world in the past 250 years, largely the result of cat and fox predation (e.g., pig-footed bandicoots, *Chaeropus* spp.). Map shows proportional loss, where 0% represents an intact mammal fauna and 100% that all previously occurring species are now extinct (*9*). (**B**) These predators continue to cause population declines and extirpations in mammals and other groups such as breeding seabirds. Recent research has quantified the predation toll [in this map, numbers of animals killed per square kilometer per year (*45*)] and identified the species most at risk from predation. (**C**) A key component of the conservation response has been the creation of a network of cat- and fox-free islands (now >2845, each from 0.01 to 628 km^2, total area of 6530 km^2, including 30 from which predators were eradicated) and mainland fenced areas (now 32, each up to 90 km^2, total area of 715 km^2). Many of these sites are managed by conservation NGOs. The map extent excludes islands in the Norfolk, Lord Howe, Macquarie, and Cocos-Keeling island groups. The large, temporary spike in the cumulative fenced area shown in the graph relates to the creation of a fenced peninsula that was cat and fox free for a short period before being breached. Despite such occasional failures, the occurrence of predator-susceptible mammals on islands and in fenced areas, whether naturally or by translocation, has prevented the extinction of 13 mammal taxa and led to increases for many more (*46*). (**D**) However, in most cases, these species persist now in <1% of their former distributions (*46*).

A 34 Australian mammal species have become extinct since European colonization, mostly due to introduced predators, e.g., pig-footed bandicoots. Almost all bioregions have lost some mammal fauna.

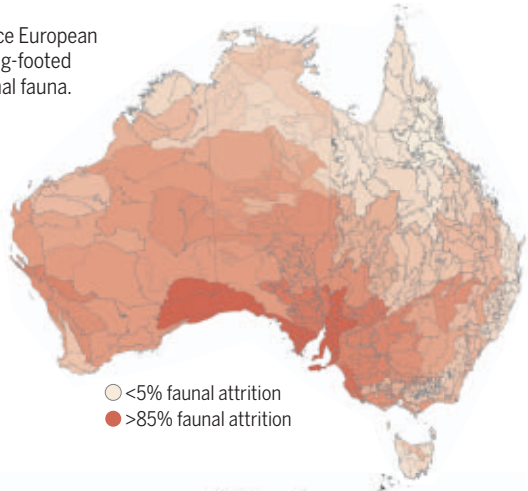

B The toll of Australian animals killed by foxes and cats occurs continent-wide; much of this impact falls on threatened mammals and nesting seabirds.

Cat about to take a red-tailed tropicbird chick (*Phaethon rubricauda*)

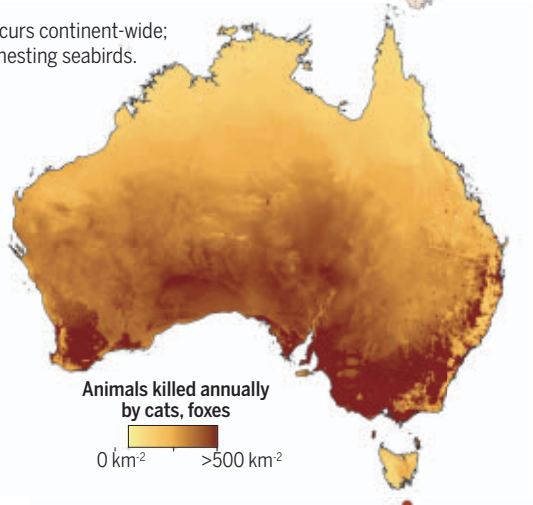

C Cat- and fox-free islands and mainland fenced areas have reduced extinction risk for many mammal taxa

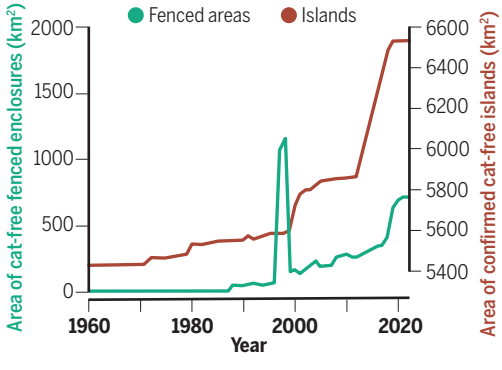

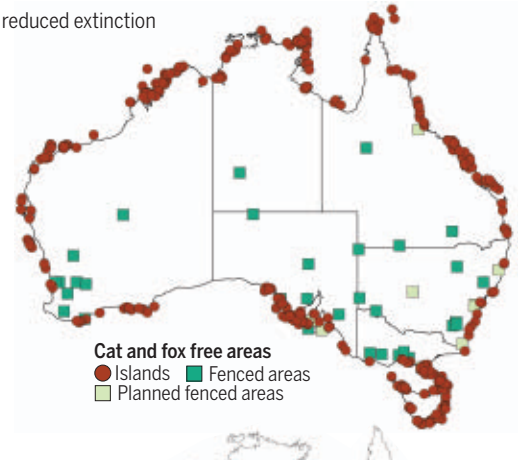

D Many predator-susceptible mammal species had very large distributions; their loss from vast areas is contributing to ecosystem degradation

Boodie at Arid Recovery

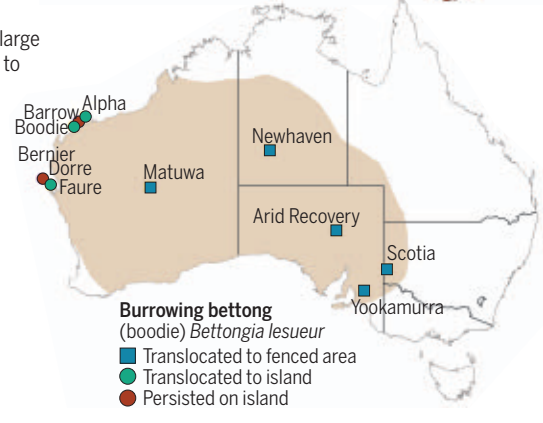

PHOTO CREDITS: FROM TOP TO BOTTOM: MUSEUMS VICTORIA (ARTIST: J. GOULD, LITHOGRAPHER: H. C. RICHTER), J. HENNICKE, H. MCGREGOR/ARID RECOVERY

timber harvesting, cumulative impacts, climate change, water use, and control of land clearing. Many threats remain unabated because no effective control methods have yet been discovered or because costs of control are prohibitive in the context of a history of inadequate funding allocated for conservation of Australian biodiversity (*64*). Thus, despite Australia's economic wealth and political stability, its societal and thus political priorities have focused on other values at the expense of the environment. The result is that most threats affecting Australia's biodiversity are inadequately controlled, and at least some of these threats are becoming worse.

Australian advances in conservation practice

Despite the prevailing backdrop of biodiversity decline and loss, there have been some recent conservation successes, with otherwise likely extinctions averted and recoveries of some species (*21*, *65*). These successes have occurred mostly where the pivotal factor causing decline has been effectively controlled or localized populations have been intensively managed (*66*) and flag the potential for greater achievement. In addition, conservation practice is being transformed by enhanced community participation in conservation objective setting and implementation. In this section, we note three areas where conservation practice is achieving more promising outcomes than the background norm: (i) the response to invasive species, especially introduced predators; (ii) the growing collaboration between Indigenous caring for Country and science; and (iii) the increasing engagement of the broader community with the environment through biodiversity monitoring. These examples provide exemplars for, and have parallels across, global conservation responses, illustrating the opportunities for tackling biodiversity loss at the vast scales required.

Managing impacts from invasive species

The profound impacts of invasive species on Australian biodiversity have driven world-leading conservation research and management. Research over the past decade has substantially enhanced knowledge of how invasive species impacts are moderated by environmental factors, how individual invasive species interact with each other, and how invasive species respond to and interact with other threats such as severe fire (*67*). These insights have highlighted the ways in which broader habitat management can be used to reduce the impacts of invasive species and the importance of integrated management. For example, translocations of native frogs that are susceptible to chytrid fungus are more successful, even into marginal habitat, if host sites are suboptimal for the fungus (i.e., warmer, drier, or more saline) (*68*). In another example, integrating management of livestock grazing and fire to maintain thick ground cover can, in some circumstances, impede the hunting success of cats and foxes and thus reduce their impacts on native vertebrates (*69*).

There have been notable successes in the eradication of invasive species from islands. More than 220 examples of such eradications from >170 Australian islands, including many with outstanding biodiversity significance, such as Dirk Hartog Island (628 km^2, largest island in the world from which cats and goats were eradicated; by 2018); Macquarie Island [128 km^2, largest island in the world where rabbits, black rats (*Rattus rattus*), and house mice (*Mus musculus*) were eradicated; by 2014]; and Lord Howe Island (15 km^2, largest inhabited island from which black rats and house mice were eradicated; by 2022) (*70*). These efforts have reduced the extinction risk for many endemic taxa, led to reversals of historic declines in breeding seabird colonies, and created opportunities to translocate threatened taxa from the mainland onto these "arks" (*71*).

Building on the success of invasive eradications from islands, a network of large mainland fenced areas constructed over the past 30 years specifically to exclude cats, foxes, and other introduced species has played a key role in Australian mammal conservation, with 13 native mammal species or subspecies now persisting only within fox- and cat-free mainland fenced areas or on offshore islands (Fig. 3). Many of the sites in this network have been created, and are managed, by nongovernmental organizations (NGOs) (*46*). Systematic planning has helped to identify the most efficient mixture of additional islands and potential fenced areas for predator removal to reduce extinction risks across all predator-susceptible mammal taxa (*72*).

Mammals have been the subject of most of the >400 animal translocations (*73*). However, translocations of other vertebrates facing other threats, including habitat shifts caused by climate change, are increasing (*74*). More than 1000 plant translocations have occurred, mostly as a response to ongoing habitat loss in areas subject to development pressures (*75*).

The reliance on translocations as a conservation tool is an Australian variation on the global rewilding movement (*76*). It has stimulated leading research and management of associated issues, such as the risks and benefits of assisted colonization (*74*) and the population genetic risks of small founding population size, repeated population bottlenecks, and heavily fragmented populations (*77*). Genetic management is increasingly being incorporated into initial translocation and ongoing metapopulation management (*78*). Trials of genetic rescue for small, inbred populations such as mountain pygmy possums (*Burramys parvus*) (*79*) have shown promising results, and genetic augmentation trials to prepare species for climate shifts are being considered (*80*). For plants, seed-banking and germplasm storage efforts are also increasing, with more than two-thirds of threatened plants now represented across the network of seed banks in Australia (*81*).

These translocation successes are welcome but there are caveats. Mammal translocations have staved off extinctions but have not returned these species to anything other than fragments of their previous distributions because broader landscape threats (including predation) are not effectively managed. Also, even on relatively small islands, some invasive species remain beyond current technological capacity to control, such as wolf snakes (*Lycodon capucinus*) on Christmas Island (*82*). In some cases, invasive species management has been thwarted by animal welfare concerns and unsupportive legislation; an example is the policy constraints on culling feral horses in Kosciuszko National Park, notwithstanding the severe damage that they cause (*83*). These examples highlight the complex mixture of social, technological, and economic factors that need to be overcome to achieve recovery of species affected by threats driving biodiversity decline.

Indigenous caring for Country

The rights and responsibilities of Indigenous Australians to care for Country and their critical role in biodiversity conservation are increasingly recognized in policy and management implementation. Indigenous Protected Areas (https://www.niaa.gov.au/indigenous-affairs/environment/indigenous-protected-areas-ipas) now comprise almost half of the national reserve system, and a growing workforce of Indigenous ranger teams deliver culturally informed conservation management over these and other tenures. Indigenous tenures cover more than half of Australia's land area and overlap with the distributions of many threatened species and ecosystems (*84*), and Indigenous management is now contributing to enhanced conservation success (*85*, *86*).

Australian Indigenous land custodianship is a manifestation of connection to Country through many generations, codified in cultural practice and responsibility. Integrating this Indigenous perspective with science has substantially enriched conservation practice, for example by emphasizing more holistic and participatory approaches to managing ecosystems, offering an alternative relationship between people and Country (*87*, *88*), and providing substantial cultural and social co-benefits to Indigenous communities (*89*, *90*). Many Indigenous groups now develop planning documents that outline and organize management activities through the lens of cultural priorities and traditional ecological knowledge (or biocultural knowledge) and incorporate economic opportunities where appropriate. Policy support for the integration of science with Indigenous

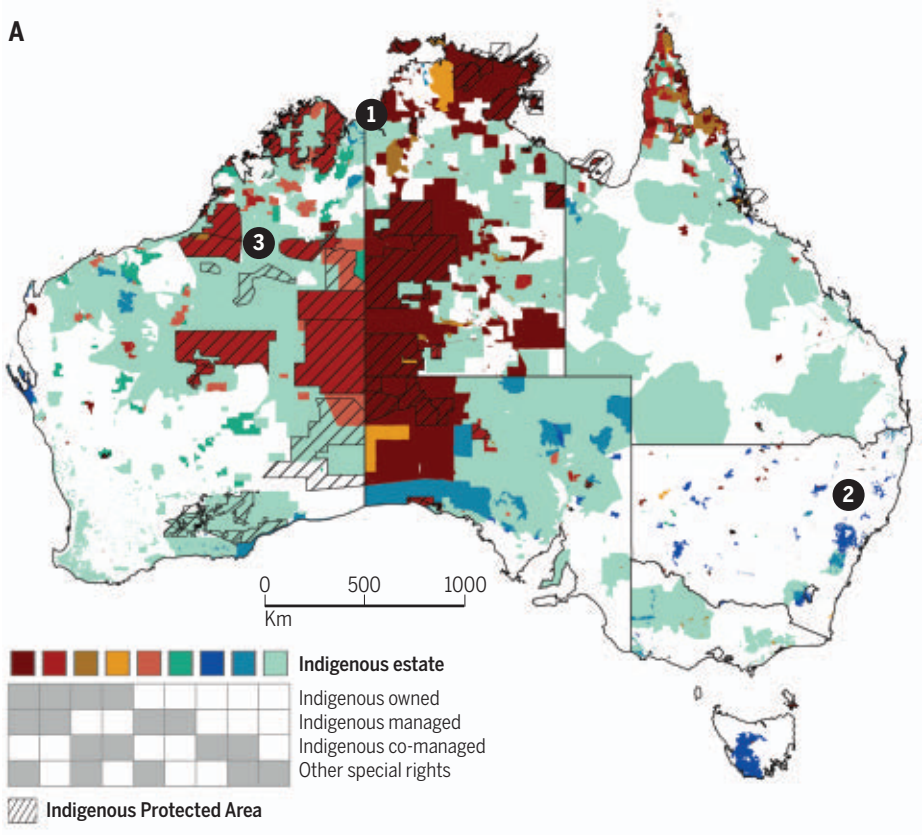

B Examples of contemporary Indigenous fire management (**1**) for carbon, biodiversity, and cultural benefits, in northern Australia; (**2**) for cultural reinvoration in the forests of eastern Australia; and (**3a**) to emulate fire regimes that were produced by traditional practice in the deserts, as seen in archived aerial photographs (**3b**) .

PHOTO CREDITS: BOTTOM, LEFT TO RIGHT: T. NEALE, KARAJARRI RANGERS

Fig. 4. Indigenous ownership and management of land. (**A**) Map showing the Indigenous Estate, color coded to indicate different ownership and management attributes. Indigenous Protected Areas, part of the National Reserve System, are shown in the hatched overlay. Shown are spatial data on tenures from Australian Bureau of Agricultural and Resource Economics and Sciences (https://doi.org/10.25814/cfm3-db86) and on the Indigenous Protected Areas from Commonwealth of Australia (https://www.environment.gov.au/fed/catalog/search/resource/details.page?uuid=%7BC64658F0-95AD-4209-8D1E-F94BD0A4E827%7D) (downloaded 12 March 2023). (**B**) Examples of contemporary Indigenous fire management. Numbers show the locations of these examples on the map in (A). 1: Aerial incendiary operations in northern Australia, where the carbon economy (https://www.cleanenergyregulator.gov.au/maps/Pages/erf-projects/index.html) has incentivized the landscape application of Indigenous-informed burning to reduce emissions. Emissions abatement projects cover >1.2 million km^2; three-quarters of them are Indigenous owned or led. 2: Bundjalung man and fire practitioner Oliver Costello in a smoking ceremony before applying cultural fire. Traditionally, cultural fire was used in forests to protect resources and values and to ensure safe landscapes. Now, it is being used to reconnect people to country and to restore ecosystems degraded by neglected fire management (*121*). Costello says, "For Bundjalung people, plants teach fire lore in their flowers, seeds, leaves, bark and roots. The animals that belong there know lots of fire stories, taught over time in the same way the plants learnt. People learnt this lore through kinship." 3a: Karajarri Rangers burning in the Great Sandy Desert to emulate fire patterns created when traditional custodians lived on-country, as seen 3b: in the 1948 aerial photograph (*94*). "Yulpurujangka photo ngangara kankarajangka jungkujangka Karajarrikura ngurrangka, kulurrangujangka pirrangka nangujungku janjaja rangersju kampanya. Kulurrangungku kampayana wupatu jungku. Janja nangujungku kampanya wupatu janja, wurtujangka jungu kamanya ngurra wakaj. Nangujangka wupatajangka jungku kuwi nyangara malurrangu, nganinaku warrkamjangka." Translation from the Karajarri language by Jess Bangu, cultural leader: "We looked at old aerial photographs from the 1940s to understand the fire regimes on Karajarri Country in the 1940s, when our forebears were still using traditional burning practices. Compared to today, these old people made fires that were smaller, and the amount of fire in any one spot was lower. This helps us with our fire management goals, because we know we need to aim for many small fires spread right across the country."

caring for Country and for Indigenous participation in on-ground conservation may be more advanced in Australia than in other countries, although control of such policy remains largely in the hands of non-Indigenous governments (as it does elsewhere in the world), which can fail to appreciate alternative world views (*90*, *91*).

The growing leadership of Indigenous Australians in a range of fire management initiatives provides an example of rich cross-cultural solutions to challenging contemporary conservation problems (Fig. 4). Indigenous Australians have used fire for millennia on this fire-prone continent, with cultural practices symbiotically shaping local ecology. Colonization disrupted this relationship in many regions, but Indigenous people are rekindling fire practices, with environmental, cultural, social, and economic benefits. For example, in the tropical savannas, a regulated carbon emissions reduction scheme combines greenhouse gas accounting methods with Indigenous burning practices, which are applied at large scales using modern technology (*92*). Eighty registered projects covering ~300,000 km^2 have led to avoidance of over 11.3 million tons of CO_2 equivalents emissions since 2012 (*93*). In the Great Sandy Desert, Karajarri people are using historical aerial photographs from the 1940s to reconstruct fire patterns produced by their forebears, then applying this information to contemporary fire management objectives (*94*). Desert fire outcomes are monitored using satellite imagery and biodiversity surveys, with the aim of using these data in environmental accounts and in emerging biodiversity credit markets (*95*).

There are increasing examples of Indigenous-led research, and "two-way" collaborative research between scientists and Indigenous land custodians (*88*). This work explicitly recognizes that threatened biodiversity may not match what Indigenous communities consider to be culturally significant (i.e., species that are totems, food, medicine, or ceremonial and thus central to stories, lore, place, and survival), and that conservation policy, management, and research should encompass this worldview if it is to be effective and sustained (*96*). There are similar efforts to include Indigenous people in the management of resource extraction, especially around water (*97*).

Community engagement in biodiversity monitoring

Inadequate biodiversity monitoring, constraining trend assessment, and evaluation of management effectiveness has hampered conservation in Australia and thereby contributed to ongoing biodiversity loss (*98*). This has led to persistent underestimation of the scale of the extinction crisis and prevented estimation of the return on investment of existing actions (*99*). However, the trifecta of inadequate funding, the predominance of short-term government programs, and a vast country with low population density is being circumvented, in a few cases, by programs that leverage new technologies, an organized citizen science workforce, or both. Drones, thermal cameras, motion-sensing cameras, acoustic monitors, artificial intelligence, and environmental DNA capability are improving the ability to detect and monitor rare species, even in remote areas. Many of these tools can be used by citizen scientists, and user-friendly apps are making data collection and collation simpler, more consistent, and engaging. The increasing involvement of the community in biodiversity monitoring and management is providing substantial biodiversity benefits, but is also resulting in greater public awareness, care for nature, and appreciation of its value, with increasing co-benefits to human health and well-being (*100*).

There are increasing efforts to organize citizen scientist data collection into robust sampling designs. Established continent or region-wide examples include programs on frogs, butterflies, birds, and charismatic mammals (*101*). For example, bird presence and count data collected by citizen scientists contribute regularly to national assessments of species trends (*31*, *98*). A citizen science program to record frog calls contributed data on the impacts of, and recovery after, the catastrophic 2019–2020 wildfires (*102*). In Victoria, citizen scientists recently carried out a state-wide sampling program of water from streams using environmental DNA to detect platypus presence in waterways (*103*).

Citizen science programs have tended to be geographically biased toward more densely populated areas, but increasingly coordinated activities across Indigenous ranger groups are now allowing the collection of data across the least-populated inland areas. For example, the tracking skills of Indigenous rangers have contributed to improved knowledge of species distribution and trends for >70 species across 3 million km^2 of sandy deserts over the past 20 years (*91*, *104*). Large-scale data collection programs for threatened species such as bilbies (*Macrotis lagotis*), malleefowl (*Leipoa ocellata*), marsupial moles (*Notoryctes* spp.), and great desert skinks (*Liopholis kintorei*) are now organized, including by Indigenous-led umbrella organizations such as the Indigenous Desert Alliance (https://www.indigenousdesertalliance.com/).

Conclusions: Scaffolds for enhanced responsibility and resilience

Without radical changes, species loss and widespread ecosystem degradation will continue, both in Australia and globally, with consequences to our economies, life, culture, and future (*7*, *8*). The changes needed begin with resetting the paradigm of how we interact with and value our environment, developing stronger environmental legislation, far more ambitious policy, hugely expanding institutional and human capabilities, and matching this with substantially greater levels of investment by both government and nongovernment sectors.

Although our examples of improved conservation practice highlight the critical contributions of many groups and organizations, government processes and systems remain foundational. In a nature-positive world, legislation needs to embed conservation as core to decision-making (*105*). If properly delivered, current reform of Australia's environmental legislation could mark transformational change, including much greater accountability for environmental loss and degradation, market-driven opportunities to contribute to conservation, more effective control of land clearing and degradation, improved approaches to threat abatement, better ways of addressing cumulative impacts across development proposals that are currently assessed independently of each other, mandating conservation actions for threatened biodiversity, and regular assessments and reporting of status and trends. These features, critical for instigating management and driving its improvement, are absent from the existing legislation (*106*).

Such transformational legislative reforms will need to be matched with policy that drives major upscaling of conservation ambition and practice. In addition to focusing on preventing extinction, recovering threatened biodiversity, and reacting to rapid environmental change, there must be a focus on building resilience across ecosystems to better withstand future stresses such as those expected to result from climate change. Threats need to be managed in an integrated manner. The Australian experience suggests that traditional management approaches such as invasive species control and fire management can achieve success, but such management must be strategically expanded in spatial scale and intensity, and emerging tools such as assisted colonization and translocation for genetic augmentation will need to move from small-scale trials to wider implementation. Increased conservation ambition will require substantial improvements in data infrastructure and targeted data acquisition to resolve critical knowledge gaps and inform decision-making (*107*). Given the accumulating direct and interactive effects of climate change, enhanced forecasting will be critical for predicting the biodiversity outcomes of alternative management scenarios; the occurrence of extreme events with sudden, large-scale impacts; new biosecurity threats; and the associated priority management actions.

Achieving upscaled conservation ambition and practice will require substantial resourcing. Overall government spending on the environment is currently dwarfed by need (*64*). Although mechanisms such as biodiversity markets (*108*) could play an important role, the potential is currently uncertain, but there

is good evidence that increased and consistent government investment can deliver results. The new Australian policy commitment to prevent further extinctions, as articulated in the national Threatened Species Action Plan (*109*), has been built on a track record of improved population trajectories for target species (*66*), albeit often after decades of research and investment. There are also accumulating examples from case studies (*65*) and time-series data (*24*, *26*) that sustained investment and management does improve conservation outcomes. If broader-based environmental resilience is to be achieved, then such evidence must be deeply leveraged so that funding for the environment becomes as core to national budgets as health or education.

The nongovernment sector has already proven critical to conservation efforts in Australia (Figs. 3 and 4), and policy changes could further expand the roles of NGOs, Indigenous rangers, and the broader community to complement the critical role of government in environmental regulation and management. To date, the nongovernment sector has been supported with short-term government funding, philanthropy, and public donations, but long-term funding security needs to be enhanced (*108*). Advocacy NGOs have also been influential, in some cases (e.g., for native forest logging in some states) forcing governments to deliver better conservation outcomes (*110*). In addition to the examples from invasive species management and the growing support for Indigenous-managed lands noted above, the Landcare movement (including private lands committed to conservation) has made major contributions to the extent of the conservation reserve estate and the protection and recovery of threatened species. Provided that government policy (*111*) in Australia and globally (*112*) is supportive, such contributions will be essential for delivering the major biodiversity commitment of protecting 30% of lands for conservation by 2030 (*113*).

As elsewhere in the world (*114*), Australians have much to learn from an increased respect for, and application of, Indigenous ways of knowing. Embedding human social, spiritual, and general well-being objectives as an emergent property of healthy ecosystems is a core principle of the Kunming Montreal Global Biodiversity Framework (*112*) and is reflected in the paradigm of nature-based solutions (*115*). The public response to recent ecological catastrophes in Australia, such as the 2019–2020 wildfires and the drought-related fish kills in the Murray-Darling Basin (*36*, *37*), showed clearly that nature-led recovery programs are important for healing people as well as nature, and that the Australian public cares deeply about both their environment and the principles of intergenerational equity. It has taken two and a half centuries since colonization, but the maturing relationships of the Australian nation with its First Peoples and with its unique biota are intensifying community expectations to prevent extinctions and recover nature for interlinked social, economic, and biodiversity outcomes.

Effective conservation policy and management can achieve not only success for biodiversity but also collateral and intimately connected benefits to regional and national economies (*116*), climate change mitigation and adaptations (*92*, *117*, *118*), human health and well-being, and cultural values (*89*, *100*). Enhanced biodiversity conservation makes our lives better, and human lives and livelihoods in the future will depend increasingly upon maintaining or enhancing the resilience of biodiversity and the ecological health of the planet (*8*).

REFERENCES AND NOTES

1. G. Cassis, S. W. Laffan, M. C. Ebach, in *Handbook of Australasian Biogeography*, M. C. Ebach, Ed. (CRC Press, 2017), pp. 11–26.
2. L. Joseph *et al.*, in *Biodiversity: Science and Solutions for Australia*, S. Morton, A. Sheppard, M. Lonsdale, Eds. (CSIRO Publishing, 2014), pp. 13–36.
3. S. V. Edwards, W. E. Boles, *Trends Ecol. Evol.* **17**, 347–349 (2002).
4. K. K. Zander, M. Burton, R. Pandit, S. T. Garnett, *Environ. Conserv.* **50**, 116–124 (2023).
5. L. K. Bay, J. Gilmour, B. Muir, P. E. Hardisty, *Science* **381**, 631–636 (2023).
6. F. Saltré *et al.*, *Nat. Commun.* **10**, 5311 (2019).
7. H. T. Murphy, S. Van Leeuwen, "Australia State of the Environment 2021: Biodiversity" (Commonwealth of Australia, 2021); https://soe.dcceew.gov.au/biodiversity/introduction.
8. E. S. Brondizio, J. Settele, S. Díaz, H. T. Ngo, "Global assessment Report of the Intergovernmental Science-Policy Platform on Biodiversity and Ecosystem Services," (IPBES, 2019); https://doi.org/10.5281/zenodo.6417333.
9. J. C. Z. Woinarski *et al.*, *Biol. Conserv.* **239**, 108261 (2019).
10. C. Régnier, B. Fontaine, P. Bouchet, *Conserv. Biol.* **23**, 1214–1221 (2009).
11. M. L. Moir, *Austral Entomol.* **60**, 89–97 (2021).
12. J. Silcock, R. Fensham, *Aust. J. Bot.* **66**, 541–555 (2018).
13. H. M. Geyle *et al.*, *Austral Entomol.* **60**, 98–110 (2021).
14. M. Lintermans *et al.*, *Pac. Conserv. Biol.* **26**, 365–377 (2020).
15. S. Garnett *et al.*, *Biol. Conserv.* **270**, 109561 (2022).
16. H. M. Geyle *et al.*, *Pac. Conserv. Biol.* **24**, 157–167 (2018).
17. H. M. Geyle *et al.*, *Pac. Conserv. Biol.* **27**, 3–12 (2020).
18. S. Legge *et al.*, *Glob. Ecol. Biogeogr.* **31**, 2085–2104 (2022).
19. J. C. Z. Woinarski, A. A. Burbidge, P. L. Harrison, *Proc. Natl. Acad. Sci. U. S. A.* **112**, 4531–4540 (2015).
20. C. Bellard, P. Cassey, T. M. Blackburn, *Biol. Lett.* **12**, 20150623 (2016).
21. J. C. Z. Woinarski *et al.*, *Biol. Conserv.* **279**, 109946 (2023).
22. T. Lavery *et al.*, *Biol. Conserv.* **260**, 109193 (2021).
23. B. C. Scheele *et al.*, *Biol. Conserv.* **235**, 273–278 (2019).
24. E. Bayraktarov *et al.*, *Conserv. Sci. Pract.* **3**, e322 (2021).
25. Threatened Species Index, "The first threatened plant index (2020)" (Univ. of Queensland, 2020); https://tsx.org.au/visualising-the-index/2020-threatened-plant-index/.
26. A. I. T. Tulloch *et al.*, *Conserv. Biol.* **37**, e14032 (2023).
27. K. Suckling, L. Mehrhoff, R. Beam, B. Hartl, "A wild success: A systematic review of bird recovery under the Endangered Species Act" (Center for Biological Diversity, 2016); https://www.esasuccess.org/pdfs/WildSuccess.pdf.
28. G. R. Gillespie *et al.*, *Biol. Conserv.* **247**, 108543 (2020).
29. D. Chapple *et al.*, *The Action Plan for Australian Lizards and Snakes 2017* (CSIRO Publishing, 2019).
30. J. C. Z. Woinarski, A. A. Burbidge, P. L. Harrison, *The Action Plan for Australian Mammals 2012* (CSIRO Publishing, 2014).
31. S. T. Garnett, G. B. Baker, *The Action Plan for Australian Birds 2020* (CSIRO Publishing, 2021).
32. G. Bino, R. Kingsford, K. Brandis, *Pac. Conserv. Biol.* **22**, 116–129 (2016).
33. R. Fensham *et al.*, *Biol. Conserv.* **243**, 108455 (2020).
34. G. S. Taylor *et al.*, *Austral Entomol.* **57**, 124–149 (2018).
35. R. V. Gallagher *et al.*, *Plants People Planet* 10.1002/ppp3.10369 (2023).
36. J. D. Koehn, *Mar. Freshw. Res.* **73**, 269–281 (2022).
37. L. Rumpff, S. Legge, S. van Leeuwen, B. Wintle, J. C. Z. Woinarski, *Australia's 2019-20 Megafires: Biodiversity Impacts and Lessons for the Future*, (CSIRO Publishing, 2023).
38. P. A. Fleming *et al.*, *Mammal Rev.* **44**, 94–108 (2014).
39. D. M. Bergstrom *et al.*, *Glob. Chang. Biol.* **27**, 1692–1703 (2021).
40. Climateworks Centre, "Living within limits: Adapting the planetary boundaries to understand Australia's contribution to planetary health. Summary report" (Climateworks Centre, 2022); https://www.climateworkscentre.org/wp-content/uploads/2022/04/Living-within-limts-report-Climateworks-Centre-04-2022.pdf.
41. C. J. A. Bradshaw, *J. Plant Ecol.* **5**, 109–120 (2012).
42. M. S. Ward *et al.*, *Conserv. Sci. Pract.* **1.11**, e117 (2019).
43. R. T. Kingsford, G. Bino, J. L. Porter, *Glob. Chang. Biol.* **23**, 4958–4969 (2017).
44. J. W. Morgan, *Ecol. Manage. Restor.* **22**, 9–15 (2021).
45. A. Stobo-Wilson *et al.*, *Divers. Distrib.* **28**, 976–991 (2022).
46. S. Legge *et al.*, *Wildl. Res.* **45**, 627–644 (2018).
47. S. G. Kearney *et al.*, *Pac. Conserv. Biol.* **25**, 231–244 (2019).
48. S. L. Maxwell, R. A. Fuller, T. M. Brooks, J. E. M. Watson, *Nature* **536**, 143–145 (2016).
49. T. S. Doherty, A. S. Glen, D. G. Nimmo, E. G. Ritchie, C. R. Dickman, *Proc. Natl. Acad. Sci. U. S. A.* **113**, 11261–11265 (2016).
50. R. J. Fensham, J. Radford-Smith, *Biol. Conserv.* **261**, 109276 (2021).
51. C. Turbill, J. A. Welbergen, *Austral Ecol.* **45**, 89–96 (2020).
52. B. Wagner *et al.*, *Ecosphere* **11**, e03262 (2020).
53. E. J. Bowd, L. McBurney, D. B. Lindenmayer, *For. Ecol. Manage.* **529**, 120673 (2023).
54. N. L. Waller, I. C. Gynther, A. B. Freeman, T. H. Lavery, L. K.-P. Leung, *Wildl. Res.* **44**, 9–21 (2017).
55. H. U. Ratnayake, M. R. Kearney, P. Govekar, D. Karoly, J. A. Welbergen, *Anim. Conserv.* **22**, 386–395 (2019).
56. A. A. Hoffmann *et al.*, *Austral Ecol.* **44**, 3–27 (2019).
57. S. E. Williams, A. de la Fuente, *PLOS ONE* **16**, e0254307 (2021).
58. J. T. Abatzoglou, A. P. Williams, R. Barbero, *Geophys. Res. Lett.* **46**, 326–336 (2019).
59. R. C. Godfree *et al.*, *Nat. Commun.* **12**, 1023 (2021).
60. D. B. Lindenmayer, R. M. Kooyman, C. Taylor, M. Ward, J. E. M. Watson, *Nat. Ecol. Evol.* **4**, 898–900 (2020).
61. T. Morris, M. Letnic, *Proc. Biol. Sci.* **284**, 20170111 (2017).
62. S. Legge *et al.*, *Biol. Conserv.* **206**, 293–303 (2017).
63. J. C. Z. Woinarski, S. T. Garnett, S. M. Legge, D. B. Lindenmayer, *Conserv. Biol.* **31**, 13–23 (2017).
64. B. A. Wintle *et al.*, *Conserv. Lett.* **12**, e12682 (2019).
65. S. T. Garnett, P. Latch, D. B. Lindenmayer, J. C. Z. Woinarski, *Recovering Australian Threatened Species: A Book of Hope* (CSIRO Publishing, 2018).
66. H. Fraser *et al.*, *Biol. Conserv.* **274**, 109731 (2022).
67. T. S. Doherty *et al.*, *Biol. Rev. Camb. Philos. Soc.* **97**, 1539–1558 (2022).
68. B. C. Scheele *et al.*, *Conserv. Sci. Pract.* **3**, e524 (2021).
69. S. Legge *et al.*, *Conserv. Sci. Pract.* **1.7**, e52 (2019).
70. J. Shaw, R. Willacy, "Informing island eradications: Lessons learned" (NESP Threatened Species Recovery Hub, 2021), project 7.10; https://www.nespthreatenedspecies.edu.au/media/qx3gzvli/7-10-informing-island-eradications-lessons-learned-report_v6.pdf.
71. A. A. Burbidge, S. Legge, J. C. Z. Woinarski, in *Australian Island Arks: Conservation, Management and Opportunities*, D. Moro, D. Ball, S. Bryant, Eds. (CSIRO Publishing, 2018), pp. 99–113.
72. J. Ringma *et al.*, *Conserv. Lett.* **12**, e12611 (2019).
73. J. Short, "The characteristics and success of vertebrate translocations within Australia" (Wildlife Research and Management Pty Ltd and Australian Government Department of Agriculture, Fisheries and Forestry, 2009); http://www.wildliferesearchmanagement.com.au/Final%20Report_0609.pdf.
74. I. D. Lunt *et al.*, *Biol. Conserv.* **157**, 172–177 (2013).
75. J. Silcock *et al.*, *Biol. Conserv.* **236**, 211–222 (2019).
76. O. F. Sweeney *et al.*, *Conserv. Biol.* **33**, 812–820 (2019).
77. Y. Willi *et al.*, *Proc. Natl. Acad. Sci. U. S. A.* **119**, e2105076119 (2022).
78. D. J. White *et al.*, *Diversity* **12**, 448 (2020).
79. A. R. Weeks *et al.*, *Nat. Commun.* **8**, 1071 (2017).
80. T. S. Rudin-Bitterli, J. P. Evans, N. J. Mitchell, *Commun. Biol.* **4**, 1195 (2021).
81. E. Breman *et al.*, *Plants* **10**, 2371 (2021).
82. J. P. Emery *et al.*, *Conserv. Sci. Pract.* **3**, e358 (2021).
83. D. A. Driscoll *et al.*, *Ecol. Manage. Restor.* **20**, 63–72 (2019).
84. A. R. Renwick *et al.*, *PLOS ONE* **12**, e0173876 (2017).
85. M. L. Wysong *et al.*, *Ecol. Manage. Restor.* **23**, 139–149 (2022).
86. I. Leiper *et al.*, *Conserv. Biol.* **32**, 1038–1047 (2018).
87. L. Robin, K. Robin, E. Camerlenghi, L. Ireland, E. Ryan-Colton, *Ecol. Manage. Restor.* **23**, 43–52 (2022).

88. E. J. Ens, G. Turpin, *Ecol. Manage. Restor.* **23**, 3–16 (2022).
89. Social Ventures Australia, "Consolidated report on Indigenous Protected Areas following Social Return on Investment analyses" (Department of the Prime Minister & Cabinet, 2016); https://www.niaa.gov.au/sites/default/files/publications/SROI-Consolidated-Report-IPA_1.pdf.
90. G. Reed, N. D. Brunet, S. Longboat, D. C. Natcher, *Conserv. Biol.* **35**, 179–189 (2021).
91. Arid Zone Monitoring Project Partners, S. Legge, "Arid zone monitoring: surveys for vertebrates across arid and semi arid zones" (NESP Threatened Species Recovery Hub, 2021), project 3.2.5; https://www.nespthreatenedspecies.edu.au/projects/arid-zone-monitoring-surveys-for-vertebrates-across-arid-and-semi-arid-zones.
92. A. Edwards *et al.*, *J. Environ. Manage.* **290**, 112568 (2021).
93. Australian Government Clean Energy Regulator, "Emissions Reduction Fund project map" (Australian Government, 2023); https://www.nespthreatenedspecies.edu.au/projects/arid-zone-monitoring-surveys-for-vertebrates-across-arid-and-semi-arid-zones.
94. E. M. J. Blackwood *et al.*, *Ecol. Manage. Restor.* **23** (S1), 83–92 (2021).
95. J. Ruscalleda-Alvarez *et al.*, *J. Environ. Manage.* **331**, 117234 (2023).
96. C. Gore-Birch, O. Costello, T. Goolmeer, B. Moggridge, S. van Leeuwen, *Ecol. Manage. Restor.* **23** (S1), 26–26 (2022).
97. B. J. Moggridge, R. M. Thompson, *Australasian Journal of Water Resources* **25**, 4–14 (2021).
98. S. Legge *et al.*, *Monitoring Threatened Species and Ecological Communities* (CSIRO Publishing, 2018).
99. Australian National Audit Office, "Funding models for threatened species management" (ANAO, 2018), Report No. 32 of 2017–18; https://www.anao.gov.au/work/performance-audit/funding-models-threatened-species-management.
100. S. Bekessy *et al.*, *Planning News* **48**, 5–6 (2022).
101. T. J. Lloyd *et al.*, *Glob. Ecol. Conserv.* **23**, e01048 (2020).
102. J. J. Rowley, C. T. Callaghan, W. K. Cornwell, *Conserv. Sci. Pract.* **2**, e287 (2020).
103. J. Griffiths, R. Impey, S. Marwood, H. van Leeuwen, A. Weeks, "The Great Australian Platypus Search - Victoria 2021" (EnviroDNA, Odonata, 2022); https://www.thegreataustralianplatypussearch.org/results-2021.
104. D. Southwell *et al.*, *Ecol. Appl.* **33**, e2762 (2023).
105. J. Fischer *et al.*, *Trends Ecol. Evol.* **22**, 621–624 (2007).
106. G. Samuel, "Independent review of the EPBC Act: Final report" (Department of Agriculture, Water and the Environment, 2021); https://epbcactreview.environment.gov.au/.
107. Australian Academy of Science, "Environment reform must include a 'Biodiversity BoM'" (AAS, 2020); https://www.science.org.au/files/userfiles/support/position-statements/environment-reform-must-include-biodiversity-bom.pdf.
108. D. Lindenmayer, B. C. Scheele, M. Young, M. Vardon, *Ecol. Manage. Restor.* **24**, 3–6 (2023).
109. Commonwealth of Australia, "Threatened species action plan 2022–2032" (Commonwealth of Australia, 2022); https://www.dcceew.gov.au/sites/default/files/documents/threatened-species-action-plan-2022-2032.pdf.
110. D. Lindenmayer, P. Burnett, *Pac. Conserv. Biol.* **28**, 393–397 (2021).
111. Australian Government Department of Climate Change, Energy, the Environment and Water, "Nature positive plan: Better for the environment, better for business" (DCCEEW, 2022); https://www.dcceew.gov.au/sites/default/files/documents/nature-positive-plan.pdf.
112. Convention on Biological Diversity, "COP15: Final text of the historic Kunming-Montreal Global Biodiversity Framework CBD/COP/15/L25" (UN Environment Programme, 2022); https://www.cbd.int/article/cop15-final-text-kunming-montreal-gbf-221222.
113. E. Dinerstein *et al.*, *Sci. Adv.* **5**, eaaw2869 (2019).
114. Á. Fernández-Llamazares *et al.*, *J. Ethnobiol.* **41**, 144–169 (2021).
115. E. Cohen-Shacham, G. Walters, C. Janzen, S. Maginnis, "Nature-based solutions to address global societal challenges" (IUCN, 2016); https://portals.iucn.org/library/sites/library/files/documents/2016-036.pdf.
116. M. Vardon, H. Keith, D. Lindenmayer, *Ecosyst. Serv.* **39**, 101004 (2019).
117. H. F. Davies, B. P. Murphy, C. Duvert, G. Neave, *Wildl. Res.* 10.1071/WR22134 (2023).
118. H. Keith, M. Vardon, J. Stein, D. Lindenmayer, *Environ. Sci. Policy* **93**, 189–199 (2019).
119. M. Ward *et al.*, *Ecol. Evol.* **11**, 11749–11761 (2021).
120. D. A. Keith *et al.*, *Glob. Ecol. Biogeogr.* **31**, 2070–2084 (2022).
121. C. Robinson, O. Costello, M. Lockwood, P. L. Pert, S. T. Garnett, in *Australia's 2019-20 Megafires: Biodiversity Impacts And Lessons For The Future*, L. Rumpff, S. Legge, S. van Leeuwen, B. Wintle, J. C. Z. Woinarski, Eds. (CSIRO Publishing, 2023), pp. 430–441.
122. R. V. Gallagher *et al.*, *Glob. Ecol. Biogeogr.* **31**, 2056–2069 (2022).
123. M. Ward *et al.*, *Divers. Distrib.* **28**, 2429–2442 (2022).

ACKNOWLEDGMENTS

As this article went to press, Jess Bangu, Karajarri cultural leader, passed away. Sincere condolences to her family and to the Karajarri people. We pay our respects to all past and current Karajarri leaders. We sincerely thank J. Bangu, the Karrajarri Rangers, and O. Costello for permission to describe their work and quote their perspectives on Indigenous fire management in this article and P. Carlile for producing Fig. 1C. We are also grateful to the following people for photos used in figures: D. Pugh, S. Mahony, M. Appel, L. Copeland, L. Pearce, T. A. Raadik, S. Horton, Museums Victoria (artist: J. Gould, lithographer: H. C. Richter), J. Hennicke, H. McGregor/Arid Recovery, T. Neale, and the Karajarri Rangers. **Funding:** This work received no funding. **Competing interests:** The authors declare no competing interests. **License information:** Copyright © 2023 the authors, some rights reserved; exclusive licensee American Association for the Advancement of Science. No claim to original US government works. https://www.science.org/about/science-licenses-journal-article-reuse

Submitted 17 March 2023; accepted 8 June 2023
10.1126/science.adg7870

REVIEW

Management approaches to conserve Australia's marine ecosystem under climate change

Line K. Bay*, James Gilmour, Bob Muir, Paul E. Hardisty

Australia's coastal marine ecosystems have a deep cultural significance to Indigenous Australians, include multiple World Heritage sites, and support the nation's rapidly growing blue economy. Yet, increasing local pressures and global climate change are expected to undermine the biological, social, cultural, and economic value of these ecosystems within a human generation. Mitigating the causes of climate change is the most urgent action to secure their future; however, conventional and new management actions will play roles in preserving ecosystem function and value until that is achieved. This includes strategies codeveloped with Indigenous Australians that are guided by traditional ecological knowledge and a modeling and decision support framework. We provide examples of developments at one of Australia's most iconic ecosystems, the Great Barrier Reef, where recent, large block funding supports research, governance, and engagement to accelerate the development of tools for management under climate change.

Australia's 15-million-km^2 marine estate (Fig. 1) is the world's third-largest exclusive economic zone and delivers enormous economic prosperity from fisheries, tourism, and natural resources. In 2021, Australia's blue economy had grown to $118 billion per year, employing more than half a million people in full-time jobs (*1*). So far, Australia's marine estate has escaped the worst of the chronic pressures that affect other benthic ecosystems around the world (*2*). However, key habitat-forming species, such as reef-building coral, seagrass, and kelp, are increasingly affected by cumulative pressures, particularly climate change (*3*). Ocean temperatures are projected to warm 1° to 2°C by 2030 and as much as 3°C in the coming decades (*4*), threatening the socio-ecological value and diversity of these as well as other Australian ecosystems (*5*, *6*).

Threats to marine ecosystems

Although large parts of Australia's coastline remain undeveloped, this is changing rapidly. Steady population growth of 1 to 2% over the past century has concentrated on the coastline (*7*), with increasing impacts on coastal marine ecosystems from pollution and urban development (*3*). Substantial industrial and agricultural development has degraded water quality in many coastal ecosystems, including parts of the Great Barrier Reef (*8*), and especially in regions where dredging and port maintenance support resource industries (*9*). Impacts on benthic ecosystems from recreational and commercial fishing are generally low by global standards but vary according to regulation and compliance, whereas pollution from plastic and marine debris is a growing threat (*3*). By far the most important threat is global climate change, which has already caused widespread periodic losses of coral reefs (*10*, *11*), seagrass (*12*), and kelp (*6*) around Australia. Global climate change can dramatically manifest as acute heat stress, flooding, and cyclones, but there are many chronic effects that influence ecosystems through changes in nutrient supply, ocean chemistry, and circulation (*4*).

Status and trend

The consequences of variable and increasing anthropogenic pressures have been summarized in Australia's current State of the Environment report, in which the conditions of several foundational species groups, including coral, seagrass, and kelp, were classified as good to poor (*3*). The range in classification is partly a result of gaps in knowledge (*3*, *6*), particularly for some of Australia's most remote regions. Most ecosystems have an inherent resilience to extreme conditions and rising pressures, demonstrated by the recovery

Australian Institute of Marine Science, Townsville, QLD, Australia. ***Corresponding author. Email: l.bay@aims.gov.au**

of Australian coral reefs during two decades of recurrent disturbances, such as tropical cyclones, mass coral bleaching, and outbreaks of crown-of-thorns starfish (*11*, *13*). However, increasing frequency and severity of pressures has eroded this resilience, and the outlook for most coastal marine ecosystems is generally poor (*3*), with models projecting the near collapse of some under all but the most-optimistic emission scenarios (*4*). We are now faced with a situation where intervention in some form will be required to maintain the socio-ecological value of these ecosystems in coming decades (*14*–*16*). Choosing if, when, and how to intervene remain our biggest challenges (*17*, *18*). Indeed, management strategies in coming decades may consider active interventions to slow the degradation of existing ecosystems and to speed the transition to novel ecosystems.

Supporting ecosystem services into the future

As climate change and other human impacts escalate, Australia's environmental managers will increasingly be forced to simultaneously conserve (protect what we have) and restore (regenerate what we had) or intervene (help what we have to adapt, resist, or transition) (*19*, *20*) in ways that optimize socio-ecological value (*14*, *16*, *18*) (Fig. 2). New interventions—such as seeding selected corals into natural ecosystems for restoration and adaptation—require research to test feasibility, cost, risk, and benefit (*5*). Progress will build on a strong understanding of the fundamental processes of impact, recovery, and adaptation in marine ecosystems and a decision framework built on collaboration and joint management with Indigenous Australians. This Review describes the projected impacts of environmental change on some of Australia's key benthic marine ecosystems (coral, seagrass, and kelp) and explores advances in research for interventions, focusing on tropical coral reefs. We highlight how recent research investment and focus (*19*) have progressed assisted evolution and aquaculture toward a goal of delivering genetically diverse corals with enhanced ability to cope with ocean warming at scale. We explore how these results are applied in modeling and decision-support tools that can assess strategies for assisting adaptation to climate change and predicting ecosystem condition under different management scenarios. Finally, we discuss progress toward joint management of coastal marine ecosystems with Indigenous Australians in ways that apply contemporary and traditional ecological knowledge to better conserve the socio-ecological values that benefit all Australians.

New approaches to manage the Great Barrier Reef under climate change

New advances in research and management are needed to conserve Australia's coastal marine ecosystems, with recent focus and funding on the Great Barrier Reef providing an example of how effort may be prioritized in other ecosystems. Australia's Great Barrier Reef is one of the natural wonders of the world and contributes significantly to the nation's economy (*21*). However, the corals that sustain the reef are particularly susceptible to increasing ocean temperatures and other climate pressures. Corals live in symbiosis with a range of microbes, and the effect of Symbiodiniaceae dinoflagellate partners on coral physiology and fitness, including heat tolerance, have been well described (*22*). The disruption of the symbiotic relationship between the coral host and its photosynthetic dinoflagellate, known as coral bleaching, occurs in response to a range of stressors but most significantly in response to rising ocean temperatures and heat stress (*23*). Bleaching has primarily been attributed to photo-oxidative stress within corals; however, external nutrient availability and their metabolism can play a role in destabilizing the symbiosis during early stages of heat stress (*24*). Understanding if and how corals' stress thresholds vary in space and time are critically important, yet empirical estimates of natural adaptive rates remain elusive.

Natural variation in corals' heat tolerance

Corals are characterized by substantial variation in heat and bleaching tolerance across species, reefs, and habitats (*25*). At the reef level, bleaching thresholds have increased by 0.5° in a decade (*23*), partly as a result of shifts in community assemblage (*26*). Within species, populations in warmer or extreme environments, or those exposed to recurrent but moderate heat stress, are more tolerant compared with those living in more benign conditions (*27*–*29*). The literature on bleaching and heat tolerance is rapidly growing; however, few studies provide a common measure of coral heat tolerance, which makes generalizations difficult. Most studies also focus on symbiont-related traits, such as declines in photophysiology (*30*), rather than on fitness consequences for the coral host that ultimately drive genetic adaptation [but see (*31*)]. The genetic architecture of heat tolerance and other coral traits is complex (*32*). Single genes of large effect have been identified for some coral traits

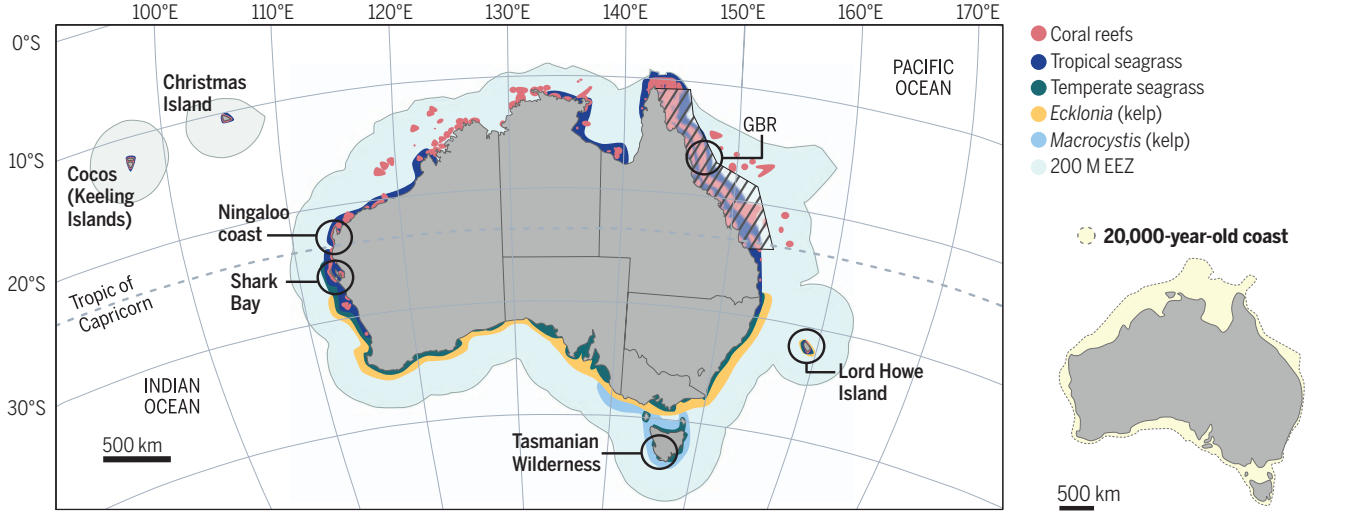

Fig. 1. Australia's marine estate is huge, traversing tropical to temperate climates. The benthic ecosystems alone have multiple World Heritage sites, including the Great Barrier Reef and the world's southernmost coral reefs at Lord Howe Island, the world's longest fringing reef at Ningaloo and vast seagrass meadows and ancient stromatolites at Shark Bay, and the Tasmanian Wilderness surrounded by kelp forests (*Ecklonia* and *Macrocystis*) that reach the west coast as the Great Southern Reef. Australia's northern coastline and adjacent island chains include a diversity of habitats that are largely unknown to modern science. (Insert) Indigenous Australians have managed these ecosystems since long before the last glacial maximum, when far less of the continent was submerged, as indicated by the shaded line (*55*). The colored depiction of key taxa is representative of the linear extent of their coastal distribution but not the area. GBR, Great Barrier Reef; EEZ, exclusive economic zone.

CREDIT: OOID SCIENTIFIC

(*33*, *34*), but heat tolerance is likely polygenic and influenced by many genes, the environment, and their microbial partners (*32*). This complicates but does not preclude the use of genetic and genomic information to support existing management actions, such as the establishment of marine reserves at high-value sites, or new approaches to boost the abundance of heat-tolerant corals on the reef (*35*). Understanding the biological and environmental drivers of heat tolerance in corals, how they are transmitted across generations and populations, and any associated trade-offs in fitness are all research priorities required to understand the potential for natural adaptation and the future role of assisted evolution.

Selecting coral stock to increase heat tolerance and adaptation

Several assisted evolution approaches focused on the host together with its microbial symbionts have been proposed to increase the heat tolerance and adaptation potential of corals (*36*). For the coral host, quantitative genetics provides a theoretical platform to understand the potential for enhancement of heat tolerance by reproductively crossing individuals or species and then examining the tolerance of their offspring (*37*). To date, interbreeding wild corals of the same species shows that selecting colonies from warmer habitats or reefs can influence heat tolerance of the next generation (*29*). These studies still find considerable variation in the tolerance among reproductive crosses (*29*), and more consistent benefits may be achieved by also selecting the most tolerant individuals within habitats or reefs (*37*). Tools are currently being developed to identify these individuals during natural bleaching events (*37*), from rapid heat stress experiments (*28*) or with physiological or genomic biomarkers (*38*). Heritability of heat tolerance in these breeding experiments is generally high (*25*) but is rarely measured beyond the juvenile stages and can decline later in life (*39*). Multigenerational studies, spanning several years to decades, are needed to determine how heat tolerance and other coral fitness–related traits are maintained under field conditions.

The symbiotic dinoflagellate algae that live within corals vary in their physiology, and some genera (e.g., *Durusdinium*) can confer on their host sufficient tolerance to withstand increased temperatures (*40*). However, on the Great Barrier Reef, many corals associate with another genus (*Cladocopium*), whose species convey less tolerance but support faster coral growth (*41*). Experimental manipulations of these common symbionts have significantly increased heat tolerance in both the symbiont and coral host under laboratory settings (*42*), with little evidence of slower growth and

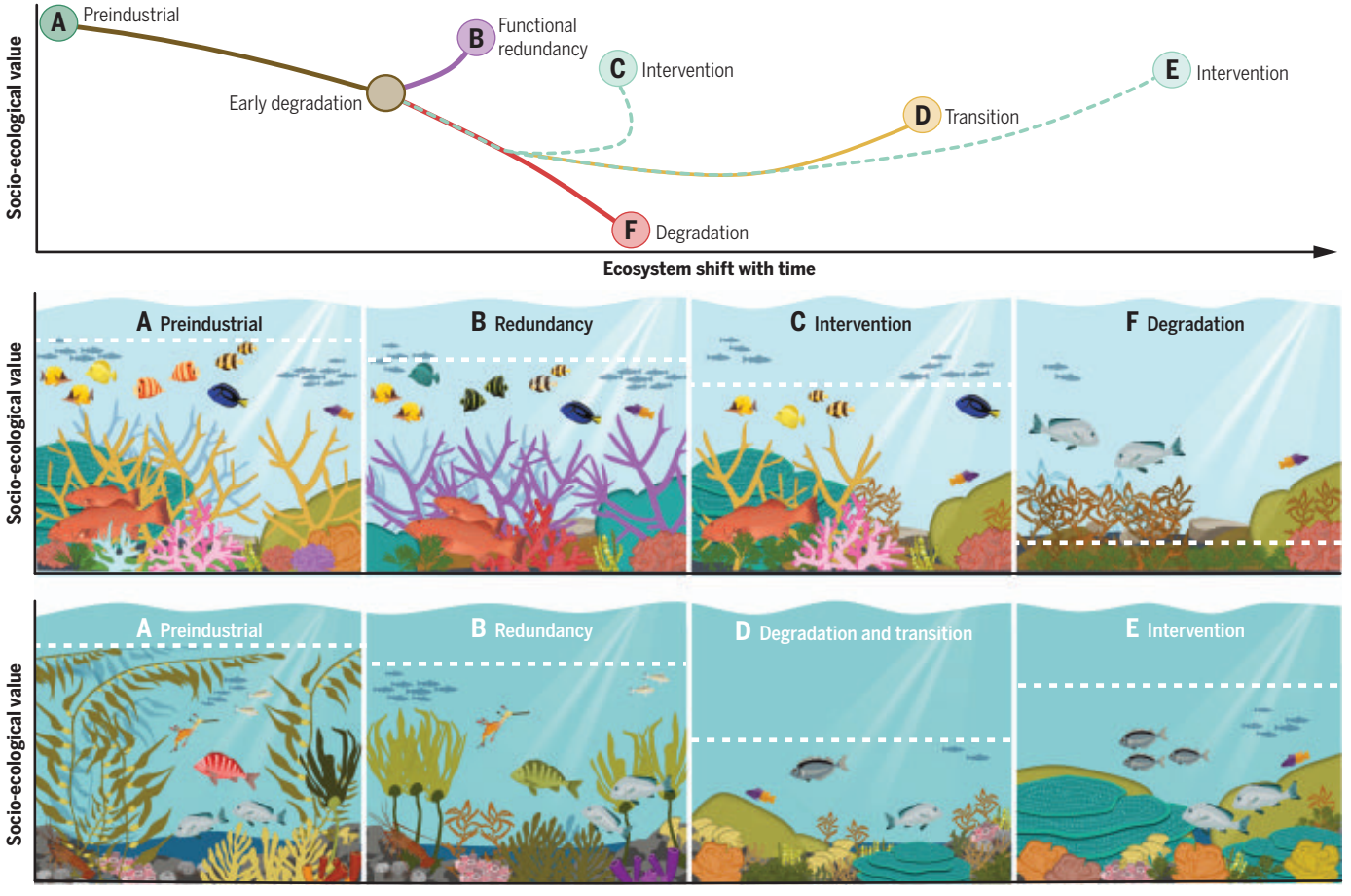

Fig. 2. Considering long-term trajectories of ecosystem change, future management will focus on maximizing socio-ecological value. (**A**) Compared with their preindustrial state, benthic ecosystems such as coral reefs (middle) and kelp forests (bottom) have already degraded. (**B**) Degradation can be slowed by functional redundancy, whereby less-susceptible genotypes or taxa replace others and provide similar ecological roles (*64*), but this cannot compensate for the projected rate of environmental change. (**D** and **F**) Ecosystems will transition toward a state of chronic degradation (F) or degrade and transition to a novel state (D). (**C** and **E**) The projected shifts in environmental conditions, natural rates of adaptation, and the success of proposed interventions will dictate whether management aims to maintain the current ecosystem, such as for some coral reefs (C), or to guide transition to a novel ecosystem, such as for some kelp forests being invaded by more tropical species (E). We can no longer focus on restoring marine ecosystems to their previous composition; we must maximize their function and value by adopting new approaches to management and governance.

CREDIT: OOID SCIENTIFIC

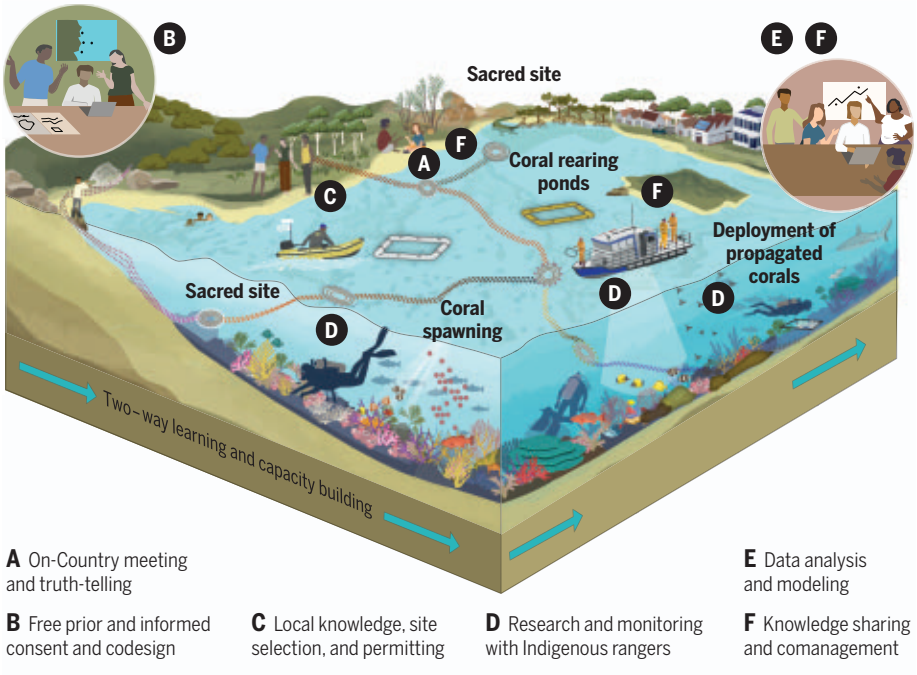

Fig. 3. A process for engagement and collaboration between Traditional Owners, scientists, and environmental managers to conserve Australia's natural assets under climate change. This process is exemplified by the Woppaburra Coral Project depicted in this reef scene, which is a codesigned and cofunded collaboration between Traditional Owners, science, and an industry partner. A mobile vessel coral aquaculture setup was used at the local reef environment, and Traditional Owners participated in the design and execution of the research to uncover foundational knowledge to understand the costs, benefits, and risks of reef restoration and adaptation (*65*).

other trade-offs in fitness-related traits. If applicable to other coral species, this approach of optimizing coral symbionts (*43*) to then inoculate the offspring of selectively bred corals could achieve even greater heat tolerance, with methods that can be scaled for mass production. We still have much to learn about adaptation of symbionts across species, populations, and environments, but harnessing this capacity may significantly increase survival of their coral hosts under environmental change (*44*).

Production of corals for deployment

To date, restoration and adaptation have been undertaken at relatively small scales and at a high cost (*45*). However, propagation methods that seed young or small corals derived from sexual and asexual sources within aquaculture facilities onto reefs have the potential to substantially upscale what was achieved in the past (*46*). Aquaculture facilities can be stationary, mobile, and customized for local conditions (Fig. 3). Based on fundamental knowledge of coral reproduction, a new aquaculture propagation model consisting of a two-part settlement and deployment system has been designed to drive up production and minimize costs (*46*). Coral settlement density is optimized on small tabs (~1 cm^2) within modular sheets, whose husbandry and assembly can be automated. Several tabs, with small sexually produced colonies or asexual fragments, are attached to larger (~5 to 10 cm) structures (devices) immediately before deployment on the reef. Deployment structures are designed to reduce postrecruitment mortality on the reef, which can be a major bottleneck in corals' life cycles (*13*). Early versions of this system have supported 50% survivorship after 6 to 9 months, with additional features to reduce competition and predation likely to increase survival further (*47*).

Corals seeded onto reefs need to be healthy and fit for purpose, thus explicit quality parameters must be imposed during the aquaculture process. This includes a consideration of genetic diversity at the species, population, and individual levels for brood stock selection and throughout the production process to reduce unintended batch effects and genetic bottlenecks (*48*). Short residence time in the aquaculture facility and the inclusion of multiple individuals and/or species per seeding device aim to mitigate the effects of domestication selection. Currently, the reproductive knowledge to underpin aquaculture is available for ~50 coral species on the Great Barrier Reef—a subset of biodiversity that is sufficient to represent morphological and life history variation in corals (*49*). Species selection models can be further refined with ecological attributes, including distribution, abundance, growth, reproduction, and stress tolerance (*49*), to support population and ecological adaptation or to maintain critical taxa, depending on the socio-ecological context.

Progressing this research to the point where successful interventions are possible at scale presents several challenges. The needed studies typically require many years, involving long-term commitments from research partners and funders. Findings then need to be translated into useable and affordable technologies that can be tested on the reef and have their performance evaluated on a lifetime colony fitness basis.

Where to next?

Advances in population and adaptation genetics, aquaculture, automation, and deployment logistics mean that it will soon be feasible to undertake larger field trials, in which assisted evolution methods, such as seeding genetically diverse corals with enhanced tolerance, could be tested in realistic ecological settings. These interventions come with potential risks to socio-ecological values, but so does the status quo (*17*). Frameworks need to be developed on the basis of technical and social understanding of risk and to evaluate the range of potential consequences—intended and unintended, positive and negative. Ecological risks are context dependent and may be acceptable when selective breeding, mass seeding, or other manipulations are restricted to stocks sourced locally but can be different using other methods. If risks are deemed significant, they can be reduced by trialing deployments on isolated reefs with negligible connectivity to others. Large field trials are essential to collect empirical data at an appropriate scale to understand the benefits of selecting coral and symbiont species, populations, and individuals to deliver more-heat-tolerant corals (*39*). Monitoring these coral populations across generations then provides the data required to estimate efficacy, parameterize models, refine deployment designs, and adjust management strategies (*16*).

Modeling to support management decisions

Managing Australia's marine ecosystems under climate change is a substantial challenge because cycles of impacts, damage, and recovery typically occur over many years, so long-term degradation can take decades to confirm (*50*). Yet, the further ecosystems move along a trajectory of degradation, the fewer options remain for improving their condition (*6*, *18*). Strategic decisions at the national level weigh up management options, including whether intervention is a priority over other national goals and should be added to existing management strategies (*17*). Existing (modern and Indigenous) management strategies remain critically important to control chronic pressures, such as pollution and overfishing (*8*), whereas networks of marine protected areas facilitate the exchange of offspring aid recovery after severe,

CREDIT: OOID SCIENTIFIC

periodic disturbances (*51*). However, model projections of these efforts alone show long-term decline and loss of socio-ecological value, which suggests the urgent need to undertake research to explore the benefits of adding different combinations of active interventions.

Modeling and decision support tools provide an important framework for assessing if, how, and when to intervene through space and time (*19*). Poor decisions early on have significant long-term consequences for ecosystem health, given the cost of development and the time to demonstrate successes and failures. Observational (correlative) and mechanistic models of key taxa (*50*, *52*, *53*) allow interventions to be tailored to habitat conditions at local scales, with regional connectivity among communities explored through biophysical models (*51*, *54*). Optimizing the design of connectivity networks will improve the regional success of local efforts by increasing the spread of seeded offspring and the exchange with other communities in marine protected areas, including refuges and sources of natural adaptation. Collectively, the ecological benefits of management scenarios can be considered by comparing model projections in which future climate and other pressures are included but the proposed interventions are not. Beyond these ecological benefits, decision support tools assess the costs of proposed management strategies and provide the information needed for approval from Traditional Owners and environmental managers and for wider endorsement from community stakeholders. The model projections demonstrate the need to rapidly mitigate the causes of degradation and to ground community expectation of what is feasible in the future compared with current ecosystem diversity and abundance.

Working in partnerships with First Nations' people

The Indigenous people of Australia have maintained a deep spiritual connection to and knowledge of the land and sea for more than 70,000 years through vastly different climates and coastal geomorphology (Fig. 1, insert) (*55*). Yet, in only a few hundred years, colonization and climate change have degraded most coastal marine ecosystems (*4*). Combining conventional science and traditional ecological knowledge can bring profound insights into ecosystem dynamics across space and time (*56*, *57*). For example, marine management at Groote Eylandt in Australia's far north is based on benthic habitat maps produced by researchers working with Anindilyakwa people, combining scientific data and traditional knowledge documented through participatory mapping (*58*). Traditional Owners also lead ranger programs to manage natural resources on Country (*59*). Indigenous marine rangers increasingly participate in research and monitoring, including early detection of climate impacts (*10*), and are well placed to aid the delivery of active management activities, particularly in remote areas (Fig. 3).

The research underpinning newer and more-active management solutions can provide education, training, and employment opportunities on and off Country for Indigenous people (Fig. 3). However, the first steps of engagement require acknowledgement of proper processes and institutions, including how and who to consult to obtain free prior informed consent to conduct research (*60*) and a genuine spirit of collaboration with Indigenous people. Truth-telling is an essential component, to acknowledge prior activities that occurred without consent and to allow Traditional Owners to provide feedback, exchange knowledge, and amend or reject proposed activities (Fig. 3). As governance and management of Australia's natural resources evolves to include and empower Indigenous people, formal joint management models are emerging. For example, the Great Barrier Reef Marine Park Authority shares reef management with eleven Traditional Owner groups through traditional use of marine resources agreements; joint management has also been implemented across Western Australia (*61*, *62*). However, comanagement and Indigenous ranger programs currently exist in a fraction of Australia's tropical marine estate, and genuine support for greater participation by Indigenous Australians in all aspects of environmental research and management is required if we hope to combine contemporary scientific and traditional ecological knowledge to better conserve socio-ecological values.

Conclusions

Until recently, environmental conservation was based on prevention: Protect the ecosystem from impacts, limit access, and restrict exploitation, and the resilience of the system will maintain function and productivity. In the Anthropocene, this conservation paradigm alone is not sufficient because local protection cannot compensate for global pressures, such as gradual and acute heating. Human impacts on Earth's processes are already substantive and are projected to worsen still. It is incumbent on scientists to uncover the knowledge needed to effectively manage natural ecosystems and to support their resilience while also communicating the need to mitigate the root cause of their decline. Many questions are outstanding regarding natural adaptation, and this knowledge forms the foundation for restoration and adaptation science, including an analysis of the benefits and risks of coral breeding and other manipulations at scale. There will be no easy answers, and success requires a new way of collaboration among scientists and the community.

Discussions around the merits and ethics of action—and importantly also inaction—must be open and inclusive, informed by scientific research but led by Traditional Owners, local managers, and community stakeholders that depend most on coastal marine ecosystems (*14*). Large, integrated, and long-term research programs that bring science, policy, Traditional Owners, marine industries, and the public together will also require appropriate governance arrangements and will need to reduce systemic biases that remain prevalent in coral reef science (*63*). Funding for such mission-driven research on the Great Barrier Reef has led to unprecedented coordination and collaboration among groups and disciplines, with rapid developments in knowledge and innovation occurring in a short period, with only a few areas explored in this Review. Similar approaches are emerging in Australia's other iconic marine ecosystems, such as those dominated by seagrass and kelp, which collectively provide a road map for managing their socio-ecological values in the Anthropocene.

REFERENCES AND NOTES

1. Australian Institute of Marine Science, "AIMS Index of Marine Industry 2020" (2021); https://www.aims.gov.au/information-centre/aims-index-marine-industry.
2. B. S. Halpern *et al*., *PLOS ONE* **10**, e0117863 (2015).
3. R. Trebilco *et al*., "Australia State of the Environment 2021: Marine, Independent Report to the Australian Government Minister for the Environment" (2021); https://soe.dcceew.gov.au/.
4. S. Cooley *et al*., in *Climate Change 2022: Impacts, Adaptation and Vulnerability. Contribution of Working Group II to the Sixth Assessment Report of the Intergovernmental Panel on Climate Change*, H.-O. Pörtner *et al*., Eds. (Cambridge Univ. Press, 2022), pp. 379–550.
5. A. Abelson *et al*., *Front. Mar. Sci.* **7**, 544105 (2020).
6. G. J. Edgar *et al*., *Nature* **615**, 858–865 (2023).
7. Australian Bureau of Statistics, "Population" (2023); https://www.abs.gov.au/statistics/people/population.
8. M. A. MacNeil *et al*., *Nat. Ecol. Evol.* **3**, 620–627 (2019).
9. R. Jones, R. Fisher, P. Bessell-Browne, *PLOS ONE* **14**, e0216248 (2019).
10. J. P. Gilmour *et al*., *Coral Reefs* **38**, 651–667 (2019).
11. Australian Institute of Marine Science, "Long-Term Monitoring Program Annual Summary Report of Coral Reef Condition 2021/22" (2022); https://www.aims.gov.au/monitoring-great-barrier-reef/gbr-condition-summary-2021-22.
12. J. A. Thomson *et al*., *Glob. Change Biol.* **21**, 1463–1474 (2015).
13. J. P. Gilmour, L. D. Smith, A. J. Heyward, A. H. Baird, M. S. Pratchett, *Science* **340**, 69–71 (2013).
14. E. S. Darling *et al*., *Nat. Ecol. Evol.* **3**, 1341–1350 (2019).
15. N. Knowlton *et al*., "Rebuilding Coral Reefs: A Decadal Grand Challenge" (International Coral Reef Society and Future Earth Coasts, 2021); https://doi.org/10.53642/NRKY9386.
16. A. J. Woodhead, C. C. Hicks, A. V. Norström, G. J. Williams, N. A. J. Graham, *Funct. Ecol.* **33**, 1023–1034 (2019).
17. K. R. N. Anthony *et al*., *PLOS ONE* **15**, e0236399 (2020).
18. M. A. Coleman *et al*., *Front. Mar. Sci.* **7**, 237 (2020).
19. I. M. McLeod *et al*., *PLOS ONE* **17**, e0273325 (2022).
20. A. Vergés *et al*., *Funct. Ecol.* **33**, 1000–1013 (2019).
21. J. O'Mahoney *et al*., "At what price? The economic, social and icon value of the Great Barrier Reef" (Deloitte Access Economics, 2017); https://hdl.handle.net/11017/3205.
22. M. R. Nitschke *et al*., *Adv. Mar. Biol.* **92**, 55–127 (2022).
23. S. Sully, D. E. Burkepile, M. K. Donovan, G. Hodgson, R. van Woesik, *Nat. Commun.* **10**, 1264 (2019).
24. L. A. Morris, C. R. Voolstra, K. M. Quigley, D. G. Bourne, L. K. Bay, *Trends Microbiol.* **27**, 678–689 (2019).
25. E. J. Howells, L. K. Bay, R. A. Bay, in *Coral Reef Conservation and Restoration in the Omics Age*, M. J. H. van Oppen, M. Aranda Lastra, Eds. (Springer, 2022), pp. 55–70.
26. T. P. Hughes *et al*., *Nature* **556**, 492–496 (2018).
27. M. R. Marzonie *et al*., *Glob. Change Biol.* **29**, 404–416 (2023).
28. J. J. V. Nielsen *et al*., *Sci. Rep.* **12**, 16831 (2022).

29. K. M. Quigley, M. J. H. van Oppen, *Nat. Commun.* **13**, 1543 (2022).
30. R. H. McLachlan, J. T. Price, S. L. Solomon, A. G. Grottoli, *Coral Reefs* **39**, 885–902 (2020).
31. L. Lachs *et al.*, *Commun. Biol.* **6**, 400 (2023).
32. Z. L. Fuller *et al.*, *Science* **369**, eaba4674 (2020).
33. P. A. Cleves *et al.*, *Proc. Natl. Acad. Sci. U.S.A.* **117**, 28899–28905 (2020).
34. A. I. Tinoco *et al.*, *Proc. Natl. Acad. Sci. U.S.A.* **120**, e2216144120 (2023).
35. M. J. H. van Oppen, M. A. Coleman, *PLOS Biol.* **20**, e3001801 (2022).
36. M. J. H. van Oppen, J. K. Oliver, H. M. Putnam, R. D. Gates, *Proc. Natl. Acad. Sci. U.S.A.* **112**, 2307–2313 (2015).
37. C. Drury, C. Caruso, K. Quigley, in *Coral Reef Conservation and Restoration in the Omics Age*, M. J. H. van Oppen, M. Aranda Lastra, Eds. (Springer, 2022), pp. 71–84.
38. J. E. Parkinson *et al.*, *Conserv. Lett.* **13**, e12687 (2020).
39. A. Humanes *et al.*, *Proc. Biol. Sci.* **289**, 20220872 (2022).
40. A. M. Palacio-Castro *et al.*, *Proc. Natl. Acad. Sci. U.S.A.* **120**, e2202388120 (2023).
41. K. M. Quigley *et al.*, *Sci. Adv.* **8**, eabq8349 (2022).
42. P. Buerger *et al.*, *Sci. Adv.* **6**, eaba2498 (2020).
43. H. J. Scharfenstein, W. Y. Chan, P. Buerger, C. Humphrey, M. J. H. van Oppen, *ISME J.* **16**, 1676–1679 (2022).
44. M. J. H. van Oppen, M. R. Nitschke, in *Coral Reef Conservation and Restoration in the Omics Age*, M. J. H. van Oppen, M. Aranda Lastra, Eds. (Springer, 2022), pp. 117–133.
45. L. Boström-Einarsson *et al.*, *PLOS ONE* **15**, e0226631 (2020).
46. C. J. Randall *et al.*, *Mar. Ecol. Prog. Ser.* **635**, 203–232 (2020).
47. C. J. Randall, C. Giuliano, A. J. Heyward, A. P. Negri, *Front. Mar. Sci.* **8**, 662263 (2021).
48. I. B. Baums *et al.*, *Ecol. Appl.* **29**, e01978 (2019).
49. J. S. Madin *et al.*, *J. Appl. Ecol.* 10.1111/1365-2664.14447 (2023).
50. J.-C. Ortiz *et al.*, *Sci. Adv.* **4**, eaar6127 (2018).
51. M. Beger *et al.*, *Trends Ecol. Evol.* **37**, 1079–1091 (2022).
52. S. Bennett, C. M. Duarte, N. Marbà, T. Wernberg, *Phil. Trans. R. Soc. B* **374**, 20180550 (2019).
53. Y. M. Bozec *et al.*, *Ecol. Monogr.* **92**, e01494 (2022).
54. C. Riginos, M. Beger, in *Coral Reef Conservation and Restoration in the Omics Age*, M. J. H. van Oppen, M. Aranda Lastra, Eds. (Springer, 2022), pp. 7–33.
55. P. D. Nunn *et al.*, *Quat. Int.* **638–639**, 212–224 (2022).
56. R. Carmona *et al.*, *Research Square* [Preprint] (2023). https://doi.org/10.21203/rs.3.rs-2471382/v1.
57. R. Hill *et al.*, *Glob. Environ. Change* **65**, 102161 (2020).
58. H. N. Davies, J. Gould, R. K. Hovey, B. Radford, G. A. Kendrick, *Front. Mar. Sci.* **7**, 716 (2020).
59. GHD, "Indigenous Ranger Sector Strategy. Consultation Summary Report to the NIAA from GHD" (Indigenous Ranger Sector Strategy, National Indigenous Australians Agency, 2023).
60. United Nations General Assembly, "United Nations Declaration on the Rights of Indigenous Peoples (UNDRIP)" (United Nations Resolution 61/295, 2007); https://social.desa.un.org/issues/indigenous-peoples/united-nations-declaration-on-the-rights-of-indigenous-peoples.
61. Great Barrier Reef Marine Park Authority, "Traditional Use of Marine Resources Agreements" (2023); https://www2.gbrmpa.gov.au/learn/traditional-owners/traditional-use-marine-resources-agreements.
62. Department of Biodiversity, Conservation and Attractions, "Joint Management" (2021); https://www.dbca.wa.gov.au/management/aboriginal-engagement/joint-management.
63. G. N. Ahmadia *et al.*, *Front. Mar. Sci.* **8**, 731037 (2021).
64. M. McWilliam *et al.*, *Ecology* **104**, e3863 (2023).
65. Australian Institute of Marine Science, "Coral spawning on Woppaburra sea-Country" (2023); https://www.aims.gov.au/research-topics/environmental-issues/climate-change/australian-coral-reef-resilience-initiative/coral-spawning-woppaburra-sea-country.

ACKNOWLEDGMENTS

We acknowledge the Traditional Owners of Australia's coastal marine ecosystems. We pay our respects to their Elders past, present, and emerging and recognize their continuing spiritual connection to Country. We thank L. Evans-Illidge, C. Riginos, J.-C. Ortiz, R. Pears, C. Robillot, and H. Scharfenstein for their insightful comments and suggestions on an earlier version that much improved this manuscript. We acknowledge B. Martin and N. Joyce from Ooid Scientific who drew the original figures. We acknowledge our colleagues within the Reef Restoration and Adaptation Program, the Woppaburra Coral Project, and the Coral Research and Development Accelerator Platform specialist working group on natural adaptation and assisted evolution for sharing their thoughts and knowledge that formed part of the arguments presented here. The Reef Restoration and Adaptation Program is funded by the partnership between the Australian Government's Reef Trust and the Great Barrier Reef Foundation. The Woppaburra Coral Project is funded by the Australian Institute of Marine Science and BHP. The Coral Research and Development Accelerator Platform is funded by G20 nations. **Funding:** All authors were employed by the Australian Institute of Marine Science at the time of writing and did not receive additional funding to write this manuscript. **Author contributions:** L.K.B., J.G., B.M., and P.E.H. contributed to the development of the concepts and ideas presented here and the writing of the manuscript. They were accountable for their areas of expertise, and all authors read and approved the final version of the manuscript. **Competing interests:** The authors declare no competing interests. **License information:** Copyright © 2023 the authors, some rights reserved; exclusive licensee American Association for the Advancement of Science. No claim to original US government works. https://www.science.org/about/science-licenses-journal-article-reuse

Submitted 25 April 2023; accepted 23 June 2023
10.1126/science.adi3023

REVIEW

Justice, culture, and relationships: Australian Indigenous prescription for planetary health

Veronica Matthews[1,2]*†, Kristina Vine[1,2], Amba-Rose Atkinson[3]‡, Jo Longman[1,2], Grace W. Lee[4], Sotiris Vardoulakis[2,5], Janine Mohamed[2,6]§

Indigenous communities shoulder a disproportionate burden of ill health compounded by climate change. In Australia, the oldest surviving cultures have adapted their ecological knowledge over millennia and across climatic ages. However, European colonization has severely curtailed Indigenous peoples' ability to adjust to climate change. An effective response to the climate crisis requires decolonizing processes to reform our relationship with the planet. From an Australian Indigenous perspective, precursors for a self-determined and healthier future are justice, culture, and relationships. We review existing studies on Indigenous-led contemporary climate and health initiatives to assess these precursors. There are examples that highlight the need to attend to issues of restorative justice as the basis for respectful valuing of culture and genuine collaboration to address the climate crisis.

Indigenous scholars globally view anthropogenic climate change as an extension of colonialism, further eroding the rights of Indigenous peoples to practice their culture and live on traditional lands (*1*, *2*). Colonization, capitalism, and climate change all reflect the continued dominance of Western individualistic ("egocentric") philosophies that place humans above and separate from their environment, commodifying and exploiting the environment for power and profits (*2*). By contrast, the collectivistic ("ecocentric") Indigenous cultures focus on deep, holistic connections to the environment in which valuable knowledge systems have developed from careful custodianship through which ecosystems flourished over millennia (*1*–*4*).

Australia is home to the oldest continuing cultures on Earth (*5*), where Aboriginal knowledge systems have survived for more than 60,000 years. Because Aboriginal knowledge is holistic and relational, the environment (land, sea, and sky) and peoples' place within it are intertwined. The knowledge has been shared within and across generations through storytelling, songs, dance, and ceremonies, presenting sophisticated understandings of geological history (*6*), astronomy (*7*), agriculture (*8*), and other domains. Specific responsibilities were allocated through customary law and totemic systems—sacred associations that meant individuals must protect their designated plant and/or animal totems (*9*). Culture and survival relied on a deep understanding of complex ecological interconnections between night skies, seasonal cues, animal behavior, and plant physiology that provided knowledge on where and when to plant, sow, harvest, and source bush food and medicinal resources (*8*). For example, the Kamilaroi and Euahlayi peoples were guided by the position of the celestial "dark emu" about appropriate times to sustainably hunt emus and collect eggs (*7*, *10*). Ancient caring for Country management practices, such as cultural burns, illustrate the integral role of Aboriginal people in maintaining rich biodiversity and sustainability of bush resources (Box 1) (*3*). Aboriginal and Torres Strait Islander communities continue to apply knowledge of caring for Country because it is an important healing practice and the foundation to Aboriginal and Torres Strait Islander health and well-being (*9*).

European dispossession severely disrupted Aboriginal and Torres Strait Islander connections to Country and undermined their mental health. European colonization also hindered

[1]University Centre for Rural Health, University of Sydney, Sydney, NSW, Australia. [2]Healthy Environments and Lives (HEAL) National Research Network, Acton, ACT, Australia. [3]School of Public Health, University of Queensland, Brisbane, QLD, Australia. [4]School of Public Health, University of Sydney, Sydney, NSW, Australia. [5]College of Health and Medicine, Australian National University, Canberra, ACT, Australia. [6]Lowitja Institute, Carlton South, VIC, Australia.
***Corresponding author. Email: veronica.matthews@sydney.edu.au**
†Quandamooka.
‡Gumbaynggirr.
§Narrunga Kaurna.

intergenerational transference of languages and knowledge integral to their traditional caring obligations, cultural identity, and well-being. The policies of Australian governments were designed to socially isolate Aboriginal and Torres Strait Islander communities on missions and reserves where every aspect of their lives was controlled (for example, movement on and off the reserves and regulated marriages) and cultural practices were forbidden (*11*). Children of mixed European-Indigenous heritage were forcibly removed from their Indigenous parents, fracturing kinship systems. Collectively, these policies violated human rights and amounted to systemic genocide of Aboriginal and Torres Strait Islander communities and cultures (*12*). The historical trauma continues today in many Aboriginal and Torres Strait Islander families and has manifested as posttraumatic stress, depression, anger, suicidal ideation, substance misuse, antisocial behavior, and dysfunction (*13*). Loss of connection to traditional lands has contributed to intergenerational trauma from an inability to care for Country and the healing that comes from undertaking cultural responsibilities (*9*).

There are stark health and socioeconomic disparities between Indigenous and non-Indigenous Australians published in annual Australian government "Closing the Gap" reports (*14*). Instituted in 2008, these reports monitor efforts to improve social determinants of health such as early childhood development, education, housing, criminal justice, and economic participation. Years later, there has been minimal progress in closing the gap. For example, Aboriginal and Torres Strait Islander life expectancy is estimated to be around eight years less than that of the non-Indigenous Australian population, and burden of disease rates are 2.3 times that of the non-Indigenous population (*15*). Although links between colonial legacies and present-day inequities are complex, colonization is recognized as a primary driver of Indigenous health (*16*, *17*). Colonization has historically impeded access to social and economic resources for Aboriginal and Torres Strait Islander people, and its vestiges persist in present-day Australian governance institutions (*18*). Recently, a coronial inquiry into a "cluster" of rheumatic heart disease (RHD) deaths of three young Aboriginal women in the remote community of Doomadgee concluded that privilege, institutional racism, lack of cultural competency, and poor communication contributed to substandard health care and these avoidable deaths (*19*). Understanding links between colonialism and health inequities will enable design of effective solutions (*17*). Both the 2022 Closing the Gap and RHD cluster coronial report emphasize the importance of listening to and working with Aboriginal and Torres Strait Islander communities for place-based solutions that target structural health reforms (*14*, *19*).

However, Indigenous voices are largely absent from Australian political and policy-making structures. Unlike other colonized, high-income countries, Australia's constitution does not recognize Aboriginal and Torres Strait Islanders as its Indigenous Peoples (*20*). By the end of 2023, a national referendum will be held offering Australians an opportunity to vote for constitutional recognition and to establish a body called the Aboriginal and Torres Strait Islander Voice ("the Voice") that can provide advice to the Australian Parliament and government. The Voice extends constitutional recognition beyond symbolism to permanently guarantee Indigenous participation in policy dialogues on matters relating to Aboriginal and Torres Strait Islander peoples (*20*). Although there are differing views about its likely effectiveness, it provides a permanent vehicle for local Aboriginal and Torres Strait Islander voices at the policy-making table on issues such as health, housing, Country, and climate change.

Climate change and Aboriginal and Torres Strait Islander health

Like many countries, Australia is also experiencing the tragic effects of climate change: an intense and widespread "Black Summer"

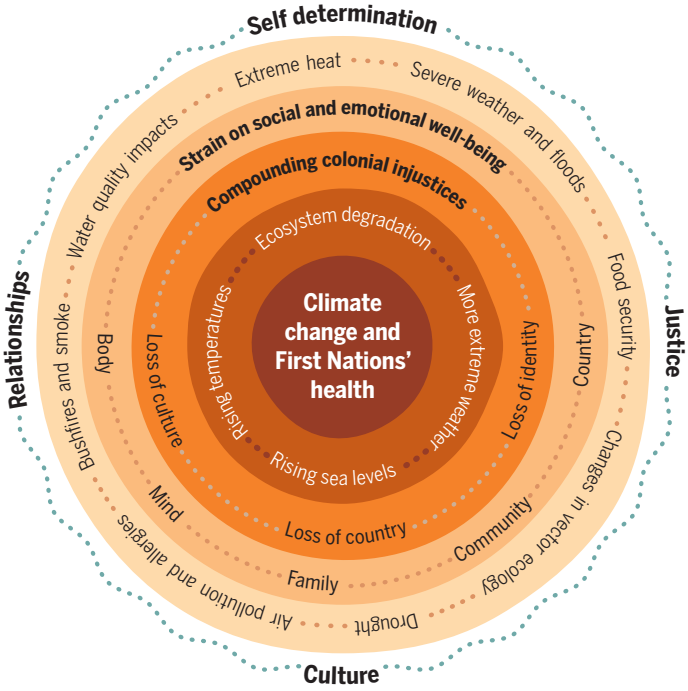

Water quality impacts
Harmful algae blooms
Saltwater intrusion
Waterborne diseases

Bushfires and smoke
Injury and fatalities
Loss of homes
Cardiovascular and respiratory disease

Food security
Malnutrition
Food insecurity
Higher food prices
Foodborne illnesses

Extreme heat
Heat-related illness and death
Cardiovascular failure

Drought
Water supply impacts
Dust storms
Bushfire risk

Sever weather and floods
Injuries and fatalities
Loss of homes
Indoor mold

Air pollution and allergies
Asthma and allergies
Cardiovascular and respiratory issues

Changes in vector ecology
Ross River virus
Japanese Encephalitis virus
Dengue fever

Fig. 1. Climate change and Aboriginal and Torres Strait Islander health. Summarized here are the connections between climate change and Aboriginal and Torres Strait Islander health and well-being. Existing health disparities and the close spiritual bond that Indigenous people hold with Country exacerbate adversity from climate change for Aboriginal and Torres Strait Islander people. Along with direct impacts—deaths, injuries, and worsening health from excessive heat, bushfires, floods, and sea level rise—there are indirect "cascading consequences" for communities resulting from altered natural systems (air quality, water and food security, and vector-borne and infectious diseases) and from altered social systems (employment and workforce productivity, housing comfort, and health service delivery) (*26*). Adverse health effects from climate change include poor social and emotional well-being, heat-related disorders, vector-borne diseases, food and waterborne diseases, respiratory disorders, and exacerbation of chronic diseases, including heart and kidney disease (*26*).

2019–2020 bushfire season, followed by catastrophic flooding across many parts of the country in 2022 and 2023. Low socioeconomic households (often Aboriginal and Torres Strait Islander families) tend to live in flood zones and bushfire hazard areas (*21*–*24*). For example, during the Black Summer season, although Aboriginal people comprised 2.3% of the population in Victoria and New South Wales, 5.4% lived in the fire-affected areas in these two states (*22*). Similarly, although Aboriginal people comprised 4.5% of the population in Northern New South Wales in 2022, they accounted for 40% of residents who were still homeless 6 months after unprecedented floods (*25*). Climate scientists are predicting more frequent and intense extreme weather unless we radically reduce carbon emissions. Aboriginal and Torres Strait Islanders are already disproportionately affected because of increased exposure to extreme weather, existing health disparities, and the close spiritual bond they hold with Country (Fig. 1). Community stories related to excessive heat and sea level rise are presented in Box 2.

In 2021, the Lowitja Institute led a national roundtable discussion on climate change and Aboriginal and Torres Strait Islander health centered on the voices of Indigenous community leaders and advocates (*26*). Community members shared their stories about being on the front lines of climate change (Box 2). These stories are examples of inequitable power structures, lack of decision-making authority, and lack of access to resources that are hindering Aboriginal and Torres Strait Islander peoples' ability to build adaptive capacity and effectively apply their knowledge to respond to climate challenges (*27*). They demonstrate a continuation of injustice metered out to Australian Indigenous communities since colonization. Roundtable participants signaled an urgent need for inclusive climate action planning that addresses and does not perpetuate existing inequities, strengthens and values Indigenous culture and knowledges, and works in respectful partnership with Aboriginal and Torres Strait Islander communities. As one participant stated, "There is no climate justice without First Nations justice" (*26*).

Several themes surfaced during the roundtable to restore planetary health: justice, strengthened cultural knowledge, and respectful relationships, underpinning a self-determined and healthier future. These prescriptions align with a global Indigenous consensus of the determinants of planetary health: (i) respecting Country and Indigenous governance that draws on knowledge from, and gives voice to, Country; (ii) rights of Indigenous people to land, language, health, and intergenerational connections; and (iii) healthy connections and relationships between Country and people (*4*). Planetary ill health has largely come about as humans have forgotten their relationship and responsibility to Country (*4*). The restoration of this relationship is crucial for planetary well-being.

This Review was prompted by the roundtable to assess the current state of justice, culture, and relationships in climate mitigation or adaptation projects led by Aboriginal and Torres Strait Islander communities. We aim to identify good practice and enabling factors as well as gaps for future focus.

A comprehensive search strategy was designed with five broad concepts for inclusion of Australian peer-reviewed literature, including "Aboriginal and Torres Strait Islander people," "climate change," "health," "mitigation or adaptation," and "strategy or intervention." The search was applied to five online databases. Publications were dated from January 2007 to January 2023. Only a handful of published studies were found that describe application of Aboriginal- and/or Torres Strait Islander–led climate mitigation and adaptation strategies that included human health outcomes.

Box 1. Key terminology.

Aboriginal and Torres Strait Islander Peoples: Indigenous peoples of Australia, of which there were more than 500 different language groups before British colonization.

Country: Traditional lands and waters of Aboriginal and Torres Strait Islander peoples and their interconnecting system of reciprocal caregiving (known as "caring for Country"). Country is used as a reference point for introductions when meeting other Aboriginal and Torres Strait Islander people (*47*).

Cultural burns: Traditional "patch" burning of the landscape during dry months while weather is cool. Removes dry fuel load to prevent uncontrolled wildfires, which release substantial amounts of carbon emissions into the atmosphere. These also stimulate under-canopy regrowth and forage for animals (*31*), which stimulates ecosystem biodiversity.

Elders: Senior Aboriginal and Torres Strait Islander people recognized by their community as leaders and cultural knowledge holders.

Indigenous: The earliest known inhabitants of lands and seas across the globe, also referred to as "First Nations people."

Indigenous cultural and intellectual property rights: The rights that Indigenous peoples have to protect their cultural heritage, including knowledge systems, arts, languages, resources, and related documentation about their heritage and histories (*48*).

Indigenous data sovereignty: The rights of Indigenous peoples to access data about themselves and to govern the collection, ownership, and application of data about their communities, lands, and resources, regardless of where the data are held (*49*).

Social and emotional well-being: Indigenous holistic concept of mental health that encompasses domains such as connection to Country, culture, family, and community.

Summary of peer-reviewed studies

Our review of the peer-reviewed literature identified nine studies that describe Aboriginal- and/or Torres Strait Islander–led climate mitigation or adaptation strategies that directly or indirectly referred to health outcomes. Many studies (n = 4) focused on different aspects of Aboriginal ranger programs that use traditional knowledge and practices such as cultural burns to manage land and sea Country (*28*–*30*) and, in some cases, to participate in formal carbon emission abatement schemes (*31*). Ranger group programs address more than environmental conservation: It is core to individual and community well-being, supporting Aboriginal and Torres Strait Islander identity and belief systems. There is a positive link between ranger and "caring for Country" activities and health and well-being, with improved indicators for diabetes, hypertension, renal disease, and psychological distress (*32*) and very high life satisfaction and family well-being (*33*). Such positive health and economic correlates have led to development of frameworks to integrate activities related to "caring for Country" into primary health care (*30*). Other topic areas included documentation of traditional knowledge into seasonal calendars (*34*, *35*) and development of cogovernance and participatory processes to manage Country for climate adaptation (*36*–*38*).

The studies are presented in table S1, structured around the key principles of self-determined climate action: justice, culture, and relationships. In table S1, green cells indicate that there is clear evidence within the paper that the principles were applied; amber cells indicate some uncertainty that the principles were applied; and red cells indicate that there is no evidence of the principles' application.

Our traffic-light assessment of published Aboriginal- and Torres Strait Islander–led climate and health strategies shows mixed results. However, Aboriginal ranger programs demonstrated all key principles. Combined with land rights tenure and long-term security working on Country, this intervention used traditional knowledge systems (sometimes in conjunction

with other knowledge) and passed the knowledge and practices on to future generations.

Justice

Colonization and enduring institutional racism in public and political institutions have stripped Aboriginal and Torres Strait Islander people of their governance over traditional land and waters and have resulted in vastly inequitable distribution of power and resources to support local community decision-making. There is yet to be a nationwide reckoning that acknowledges and accepts the true history of Australia. From an Aboriginal and Torres Strait Islander perspective, there is a need for restorative justice—a reflective process of understanding and acceptance by the Australian population of the harm created by colonization, and commitment to address that harm and its intergenerational consequences. Appropriate reparations to enable climate adaptation and improvements in health would be access to Country; equitable power sharing and cogovernance arrangements over land and waters; and enabling supports to strengthen adaptive capacity, including appropriate housing and access to quality education and employment opportunities.

Perhaps Aboriginal ranger programs are successful because an innate feature is that they are carried out on traditional lands and seas where local communities have already secured a form of land rights. Aboriginal and Torres Strait Islander ranger programs are funded through the Australian government to provide employment opportunities for local communities to use traditional knowledge to conserve and manage their land and sea Countries. Traditional activities that historically protected the land and sea include cultural fire practices for wildfire mitigation, native ecosystem restoration and protection of threatened species, research and education partnerships, and generation of additional income through carbon abatement (*31*). There are more than 100 Indigenous ranger groups funded, located on land with varying tenure.

Land rights and cultural heritage legislation is complex, with different systems operating at national and state levels (*39*). Native Title and Land Rights and Indigenous Protected Areas uphold and protect the rights of Aboriginal and Torres Strait Islander peoples on the basis of their ancestral relationships with the land and seas as well as traditional customs. They provide traditional custodian group access and decision-making authority over activities, increasing their ability to lead planning and implementation of climate mitigation and adaptation programs. However, these laws do not always provide full autonomy over use of Country, as recently demonstrated by the extinguishment of Native Title by the Queensland government for a coal mine and the willful destruction by a mining company of a 46,000-year-old sacred rock shelter at Juukan Gorge in the Kimberley region of Western Australia (*26*). Power imbalances remain in land rights legislation, which limits development of trust and collaboration.

Similarly, land rights do not extend to waterways (such as lakes, rivers, and underground aquifers) that are just as culturally important as the land on which they are located. Legislation separates rights to water and land, even where Native Title and Land Rights have been granted (*40*). Water policy in Australia has enhanced its commodification of water through trading schemes, and although it explicitly recognizes Aboriginal rights and interests, these are relegated to one of many minority "other public benefits" among recreation, tourism, and fisheries (*40*, *41*). Cultural governance systems that existed before colonization unified neighboring clans through key values, ethics, and codes of conduct to promote equitable sharing and to protect their collective well-being. Similar Indigenous systems of cogovernance proposed for water management of the Martuwarra are seen as important power-sharing arrangements, as opposed to participatory models in which colonial structures of power are maintained (*38*). It remains to be seen whether these equitable systems of governance will be adopted by the Australian government.

Strengthened cultural knowledge

Restorative justice acknowledges the strength of Aboriginal and Torres Strait Islander culture and valuable knowledge systems that have accumulated over 60,000 years. As the oldest continuous living culture, Aboriginal knowledge holders intimately understand their Country and have adapted to various climactic shifts. This knowledge must be celebrated, preserved, and protected by strengthening intergenerational transmission, Indigenous cultural and intellectual property rights, and Indigenous data sovereignty (*42*). Sharing and bringing together Indigenous and Western knowledge systems will enhance understanding of ecological processes and improve effectiveness of climate adaptation and mitigation strategies (*43*). A collaboration between Yugul Mangi rangers and university-based ecologists in northern Australia demonstrates the benefit of two-way sharing of information that has increased understanding of species presence to inform land-management practices and protection of biodiversity in changing climate conditions (*28*).

Two studies reported the development of seasonal calendars as education and communication tools for Aboriginal and Torres Strait Islander communities. They demonstrate Aboriginal and Torres Strait Islander peoples' holistic systems

Box 2. Stories from the Climate Change and Aboriginal and Torres Strait Islander Health Roundtable.

Increasing heat, poor housing, and energy insecurity for Warumungu community (Central Australia)

Prolonged excessive heat raises body temperatures, inducing heat stroke, body fluid imbalances, and increased cardiac stress from internal thermoregulatory responses that may exacerbate heart and kidney disease (*50*). Norman Frank Jupurrurla, a Warumungu Elder from Tennant Creek, discussed the poorly insulated and low-quality housing in his community that is not suited to the increasing number of very hot days in Central Australia (*51*). These same households also experience energy insecurity owing to mandatory prepaid power card systems. With limited financial resources and high levels of chronic disease, householders are often deciding whether to air condition homes or keep the refrigerator running for food and critical medicines (*51*). Remote community housing tenants are not afforded access to rooftop solar technology that is available to most other Australian households in urban and regional areas, which are often subsidized. Frank Jupurrurla led a long-term campaign to install solar panels on his roof, overcoming many bureaucratic hurdles to benefit from a cheaper and more secure renewable energy supply. It remains the only remote Aboriginal public community house in the Northern Territory connected to solar power (*52*).

Rising sea levels in Zenadth Kes (Torres Strait Islands)

Sea level rises and coastal surges lead to salt inundation of freshwater sources and may result in forced relocation and loss of economic livelihood (*53*). At the very northern tip of Australia, communities of the Torres Strait Islands are losing their land, food sources, and livelihoods as well as important cultural and burial sites to rising sea levels. A group of eight Torres Strait Islanders led by Daniel Billy lodged a complaint to the United Nations (UN) claiming that the Australian government neglected its duty to protect their rights to life and culture by failing to take appropriate climate mitigation and adaptation measures (*54*). In 2022, the UN Human Rights Committee found in the Torres Strait Eight's favor, taking into account their close, spiritual connection to their traditional lands and compelling Australia to increase adaptation and mitigation strategies for the Torres Strait and compensate the Islanders for the harm they have suffered (*55*).

approach to understanding Country. Rather than measuring the passing of time, they record seasonal activities according to the presence of biological indicators. As such, seasonal calendars can be used to monitor climate and environmental change over time (*44*). The seasons documented in Australia are more varied than the Western-oriented four seasons; for example, the Ngan'gi People of Naiuyu record 13 overarching seasons (*34*). Climate change is modifying seasonal calendars to an extent that communities are being required to adjust this knowledge (*45*). In this way, seasonal calendars can be an important advocacy and communication tool as Aboriginal and Torres Strait Islander people witness changes to Country.

Ensuring appropriate protection of Indigenous cultural and intellectual property and Indigenous data sovereignty will be key to providing security and certainty to communities against exploitation of their knowledge, as demonstrated by genuine worry of Elders deciding not to include in the Ngan'gi seasonal calendar information about medicinal use of plants or any knowledge deemed to have potential economic interest (*34*).

Relationships

Restorative justice also requires respectful engagement with Aboriginal and Torres Strait Islander people that in turn creates trust required for enduring partnerships. Equitable power and cogovernance arrangements are a crucial ingredient, along with firm commitments to appropriately resource adaptation initiatives. Having initiatives led by Aboriginal and Torres Strait Islanders enhances the cultural integrity of processes and ensures that projects feature relationality (centering community and their relationship to Country) and reciprocity (cobenefits for community and Country) (*4*, *42*).

Climate change provides an immediate opportunity for "two-way seeing" (*42*)—the weaving together of Aboriginal, Torres Strait Islander, and Western science to inform mitigation and adaptation approaches. The transformational change required in the way we treat Country will require an embrace of diverse knowledge systems and being open to different perspectives (*42*). From our review, it is evident that close collaboration with Indigenous communities takes time and commitment of resources. Community-led adaptation planning is vulnerable to the stop-start nature of research initiatives (*36*) and the current way that service provision and planning related to caring for Country and health promotion activities are conducted in siloes; this is not conducive to Indigenous ways of holistic thinking (*30*).

Gaps in literature

At present, there are very few examples in peer-reviewed literature of Aboriginal- and Torres Strait Islander–led climate action that report health outcomes. There were gaps geographically with no Torres Strait Islander community–led adaptation that met our search criteria or projects relating to emerging opportunities such as renewable energy transitions. However, we acknowledge that our search strategy focused on climate change and health initiatives and may have missed other papers that describe implementation of Indigenous-led climate adaptation and mitigation strategies. Additionally, our assessments were limited to the information provided in each article. However, rigorous documentation of the implementation and evaluation of Aboriginal- and Torres Strait Islander–led climate change strategies is essential for the spread of best practices according to the principles of restorative justice, strengthening culture and knowledge, and respectful enduring partnerships. Given the importance of Country for health and well-being, studies should factor in processes and indicators to assess these connections (*46*).

Conclusions

Despite historic and contemporary systemic racism, Aboriginal and Torres Strait Islander communities are strong and resilient, maintaining the oldest continuing culture on the planet. There is a climate emergency, and scientists are realizing the central importance of Indigenous knowledge in informing climate change mitigation and adaptation strategies.

We used an Australian Indigenous prescription for planetary health—justice, culture, and relationships—to assess Indigenous-led climate adaptation and mitigation strategies in terms of issues related to the colonial context of Australia and the role that colonization has played in limiting community adaptive capacity. Examples of published research in academic literature are few and far between, perhaps representing that as a society, we have a long way to go in redressing past wrongs and embracing the strengths of Aboriginal and Torres Strait Islander culture.

To build a shared evidence base relating to Aboriginal- and Torres Strait Islander–led climate and environmental solutions, we need to address power structures and provide Aboriginal and Torres Strait Islander communities equitable governance over their traditional lands. After this is achieved, communities can revitalize and strengthen cultural practices that protect Country and simultaneously build respectful collaborations for two-way sharing of different knowledge systems necessary for the benefit of all. In the Australian context, an important first step in shifting policy processes to embed genuine and open engagement with Aboriginal and Torres Strait Islander communities will be a successful referendum on the Voice. Without a Voice to the Australian Parliament, the Aboriginal and Torres Strait Islander prescription for planetary health will be much harder to achieve in the limited time we have left to address the climate crisis.

REFERENCES AND NOTES

1. K. Whyte, *Engl. Lang. Notes* **55**, 153–162 (2017).
2. R. Jones, P. Reid, A. Macmillan, *Lancet Planet. Health* **6**, e834–e841 (2022).
3. M. S. Fletcher, A. Romano, S. Connor, M. Mariani, S. Y. Maezumi, *Fire (Basel)* **4**, 61 (2021).
4. N. Redvers *et al*., *Lancet Planet. Health* **6**, e156–e163 (2022).
5. M. Rasmussen *et al*., *Science* **334**, 94–98 (2011).
6. F. Robertson, G. Stasiuk, N. Nannup, S. D. Hopper, "Ngalak koora koora djinang (Looking back together): A Nyoongar and scientific collaborative history of ancient Nyoongar boodja," Australian Aboriginal Studies (Canberra, 2016), pp. 40–54.
7. K. Noon, K. De Napoli, *First Knowledges Astronomy: Sky Country*, M. Neale, Ed. (Thames & Hudson Australia Pty, 2022).
8. B. Pascoe, Dark Emu: Aboriginal Australia and the birth of agriculture (Magabala Books, 2018).
9. W. Casey, in *Working Together: Aboriginal and Torres Strait Islander Mental Health and Wellbeing Principles and Practice*, P. Dudgeon, H. Milroy, R. Walker, Eds. (Commonwealth of Australia, Canberra, ed. 2, 2014).
10. M. Raven, D. Robinson, J. Hunter, *Antipode* **53**, 1526–1545 (2021).
11. A. D. Moses, in *Genocide and Settler Society: Frontier Violence and Stolen Indigenous Children in Australian History*, A. D. Moses, Ed. (Berghahn Books, 2004).
12. Human Rights and Equal Opportunity Commission, "Bringing them Home: National inquiry into the separation of Aboriginal and Torres Strait Islander children from their families" (Canberra, 1997).
13. J. Atkinson, *Trauma Trails: Recreating Song Lines* (Spinifex Press, 2003).
14. Commonwealth of Australia, "Commonwealth Closing the Gap Annual Report 2022" (2022).
15. Australian Institute of Health and Welfare, "Aboriginal and Torres Strait Islander Health Performance Framework: summary report July 2023" (Canberra, 2023).
16. K. Griffiths, C. Coleman, V. Lee, R. Madden, *J. Popul. Res. (Canberra)* **33**, 9–30 (2016).
17. E. Curtis *et al*., *Discov. Soc. Sci. Health* **3**, 10 (2023).
18. Y. Paradies, *J. Popul. Res. (Canberra)* **33**, 83–96 (2016).
19. Coroners Court of Queensland, "Coroners Court of Queensland Findings of Inquest: Inquest into the Deaths of: Yvette Michelle Wilma Booth, Adele Estelle Sandy, Shakaya George ("RHD Doomadgee Cluster") (Cairns, 2023).
20. F. Kunc, *Aust. Law J.* **97**, 301–301 (2023).
21. M. I. Rolfe *et al*., *Nat. Hazards* **101**, 631–650 (2020).
22. B. Williamson, F. Markham, J. Weir, "Aboriginal peoples and the response to the 2019–2020 bushfires," working paper no. 134/2020 (Australian National University, 2020).
23. S. Akter, R. Q. Grafton, *Clim. Change* **165**, 53 (2021).
24. V. Matthews *et al*., *Front. Public Health* **7**, 367 (2019).
25. C. Williams, "Indigenous families still homeless months after the floods, as leaders say First Nations people are being overlooked for rentals," *ABC News* (2022); https://www.abc.net.au/news/2022-08-12/indigenous-homelessness-in-northern-rivers-communities/101323636.
26. HEAL Network, CRE-STRIDE, "Climate Change and Aboriginal and Torres Strait Islander Health Discussion Paper" (Lowitja Institute, 2021).
27. I. Lyons, R. Hill, S. Deshong, G. Mooney, G. Turpin, *Reg. Environ. Change* **19**, 1597–1610 (2019).
28. E. Ens, M. L. Scott, Y. M. Rangers, C. Moritz, R. Pirzl, *Biodivers. Conserv.* **25**, 2889–2906 (2016).
29. C. J. Robinson *et al*., *Environ. Sci. Policy* **56**, 129–134 (2016).
30. R. Schultz, T. Abbott, J. Yamaguchi, S. Cairney, *BMC Health Serv. Res.* **18**, 960 (2018).
31. J. Altman, J. Ansell, D. Yibarbuk, *Postcolonial Stud.* **23**, 552–574 (2020).
32. C. P. Burgess *et al*., *Med. J. Aust.* **190**, 567–572 (2009).
33. A. Wright *et al*., *Int. J. Environ. Res. Public Health* **18**, 3053 (2021).
34. E. Woodward, P. Marrfurra McTaggart, *Glob. Health Promot.* **26** (suppl. 3), 26–34 (2019).
35. M. B. McKemey *et al*., *Austral Ecol.* **46**, 1011–1029 (2021).
36. M. Nursey-Bray, R. Palmer, *Heliyon* **4**, e00565 (2018).
37. R. Hill *et al*., *Glob. Environ. Change* **65**, 102161 (2020).
38. M. RiverOfLife, K. S. Taylor, A. Poelina, *Austral. J. Water Resources* **25**, 40–56 (2021).

39. National Indigenous Australians Agency (NIAA), National Indigenous Australians Agency, (1 June 2023); https://www.niaa.gov.au.
40. V. Marshall, in *New Directions for Law in Australia*, R. O. N. Levy, M. O'Brien, S. Rice, P. Ridge, M. Thornton, Eds. (ANU Press, 2017), pp. 221–230.
41. B. J. Moggridge, R. M. Thompson, *Australasian J. Water Resources* **25**, 4–14 (2021).
42. B. Orlove *et al*., *Ambio* (2023).
43. Intergovernmental Panel on Climate Change (IPCC), "Climate Change 2022: Impacts, Adaptation and Vulnerability. Contribution of Working Group II to the Sixth Assessment Report of the Intergovernmental Panel on Climate Change" (IPCC, 2022).
44. L. E. Chambers *et al*., *Weather Clim. Soc.* **13**, 159–172 (2021).
45. M. Nursey-Bray, R. Palmer, T. F. Smith, P. Rist, *Local Environ.* **24**, 473–486 (2019).
46. M. Barber, S. Jackson, *Ecol. Soc.* **22**, art11 (2017).
47. A. Thorpe, A. Yashadhana, B. Biles, E. Munro-Harrison, J. Kingsley, Indigenous Health and Connection to Country, in *Oxford Research Encyclopedia of Global Public Health* (Oxford Univ. Press, 2023).
48. Terri Janke and Company, Indigenous Cultural and Intellectual Property (ICIP) (13 July 2023); https://www.terrijanke.com.au/icip.
49. Maiam nayri Wingara, "Indigenous Data Sovereignty Communique Indigenous Data Sovereignty Summit 20th June 2018" (Canberra, ACT, 2018).
50. K. L. Ebi *et al*., *Lancet* **398**, 698–708 (2021).
51. S. Quilty, N. Frank Jupurrurla, R. S. Bailie, R. L. Gruen, *Med. J. Aust.* **217**, 9–12 (2022).
52. S. Quilty, B. Riley, L. White, N. F. Jupurrurla, Many First Nations communities swelter without power. Why isn't there solar on every rooftop? The Conversation. (2023); https://theconversation.com/many-first-nations-communities-swelter-without-power-why-isnt-there-solar-on-every-rooftop-204032.
53. A. L. Dannenberg, H. Frumkin, J. J. Hess, K. L. Ebi, *Clim. Change* **153**, 1–14 (2019).
54. Y. Mosby, C. Keller, *Native Title Newsletter*, issue 1, 14–16 (2020).
55. The Office of the High Commissioner for Human Rights, "Australia violated Torres Strait Islanders' rights to enjoy culture and family life, UN Committee finds," press release (2022); https://www.ohchr.org/en/press-releases/2022/09/australia-violated-torres-strait-islanders-rights-enjoy-culture-and-family.

ACKNOWLEDGMENTS

We pay respect to Aboriginal and Torres Strait Islander custodians of the lands and seas across this continent now called Australia. This paper was made possible by three Australian Aboriginal and Torres Strait Islander health research collaborations: the Lowitja Institute, which is the preeminent Indigenous community–controlled health research organization in Australia; the Centre for Research Excellence in Strengthening Systems for Indigenous Health Care Equity (CRE-STRIDE); and the Indigenous knowledge hub of the Healthy Environments and Lives (HEAL) National Research Network. As a collaboration of Aboriginal and non-Indigenous researchers, our approach is guided by principles of Indigenist research that foregrounds Aboriginal and Torres Strait Islander experiences and perspectives. We acknowledge the wisdom of Aboriginal and Torres Strait Islander ancestors and their ways of knowing, being, and doing. This wisdom was built from their relationship with Country, and we acknowledge Country too as our intergenerational teacher. **Competing interests:** The authors declare no competing interests.

License information: Copyright © 2023 the authors, some rights reserved; exclusive licensee American Association for the Advancement of Science. No claim to original US government works. https://www.science.org/about/science-licenses-journal-article-reuse

SUPPLEMENTARY MATERIALS

science.org/doi/10.1126/science.adh9949
Table S1

Submitted 27 March 2023; accepted 14 July 2023
10.1126/science.adh9949

RESEARCH

IN *SCIENCE* JOURNALS

Edited by **Michael Funk**

PLANT WATER USE

Balancing act

How have plants managed the trade-off between carbon gain and water loss in a world of increasing atmospheric carbon dioxide concentrations and rising temperatures? Li et al. showed that plant water use efficiency, the ratio between the net assimilation of carbon through photosynthesis and the stomatal conductance of transpiration, increased from 1982 to 2000, but then remained constant from 2001 to 2016. The authors interpret this as being the result of increases in the vapor pressure and intensifying evapotranspiration. Their results illustrate one more way in which the adverse effects of climate warming make it more difficult to achieve carbon neutrality. —HJS *Science*, adf5041, this issue p. 672

Satellite observations of vegetation indicate changing water use efficiency in many biomes, including croplands such as those pictured in here Brazil.

CANCER DETECTION

Bacteria sniff out specific mutations

Bacteria have been previously engineered to detect diseases by responding to specific metabolites or pathogens. Cooper *et al.* have now engineered a species of bacteria to detect specific mutations in human DNA. These bacteria, *Acinetobacter baylyi*, are normally nonpathogenic and naturally competent to take up DNA by horizontal gene transfer. The authors took advantage of this property, engineering these bacteria to become resistant to a specific drug only when they took up DNA containing a cancer-associated mutation in a specific oncogene, but not its wild-type counterpart. The bacteria detected their target both in culture and in mice bearing tumors with the relevant mutation after the bacteria were delivered by rectal enema, suggesting a potential clinical application. —YN *Science*, adf3974, this issue p. 682

NANOPHOTONICS

Guiding light in atomic monolayers

Chip-scale optical circuits require the ability to confine, control, and propagate light over ever-decreasing length scales and across different components. Addressing the optical mismatch between components typically results in compromises in size and performance for practical devices. Lee *et al.* showed that they could confine and guide light in an ultrathin two-dimensional (2D) material (<1 nanometer thick). Using molybdenium disulfide monolayers, they trapped a laser beam and generated a 2D photonic wave propagating along the film over centimeter distances. By integrating microfabricated thin-film optical components, the authors demonstrated various optical functionalities, thereby providing a general platform for 2D nanophotonics. —ISO *Science*, adi2322, this issue p. 648

HUMAN EVOLUTION

Reconstructing the past

Most of what we know about hominin evolution comes from fossil evidence, and these fossils come from a world shaped by climate and ecological dynamics, as ours is today. The ability to estimate these past

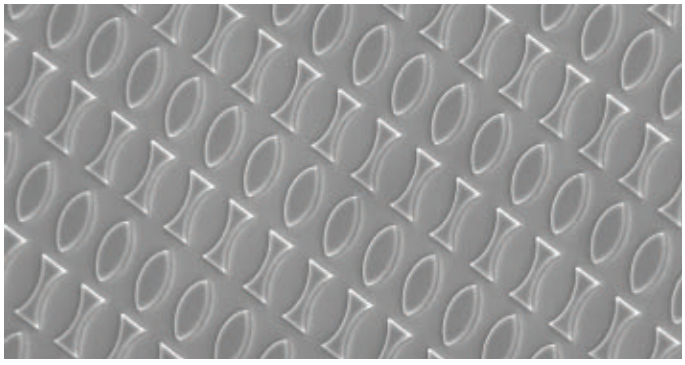

An array of convex- and concave-shaped optical elements for use in two-dimensional photonics

PHOTOS: (FROM TOP) WILLIAM L. STEFANOV, NASA-JSC; LEE *ET AL.*

environments permits us to better understand the forces that shaped our evolution. Using climate models to estimate past environments and spatial distribution models to predict species occurrence, two studies now reveal details about hominin evolution that fossils alone cannot (see the Perspective by Beverly). Looking at habitat overlap for Neanderthals and Denisovans, Ruan *et al.* found patterns of interbreeding between the two that correlate with climate and environmental change in Eurasia. Margari *et al.* have identified a previously unknown climate-driven depopulation of hominins in southern Europe during the early Pleistocene. —SNV

Science, add4459, adf4445, this issue p. 699, 693
see also adj4631, p. 605

MOLECULAR BIOLOGY

MMEJ prevails in mitosis

DNA double-strand breaks pose a threat to genome integrity, and during interphase, they are repaired by nonhomologous end joining and homologous recombination. Brambati *et al.* showed that during mitosis, when these pathways are suppressed, mutagenic repair by microhomology-mediated end joining (MMEJ) prevails. The authors uncovered a critical role for a partner protein named RHINO in restricting MMEJ to mitosis. RHINO accumulates exclusively in the M phase, and its phosphorylation by PLK1 facilitates the recruitment of polymerase θ to condensed chromosomes to promote end joining. Ultimately, mitotic MMEJ ensures that cellular division does not proceed with unrepaired DNA lesions, thus preserving the stability of our genome. —DJ

Science, adh3694, this issue p. 653

MOLECULAR GENETICS

Structural basis for epigenetics silencing

The catalytic activities of polycomb repressive complex groups (PcG) 1 and 2 in histone monoubiquitination and methylation are central for epigenetic silencing of gene expression. The BAP1/ASXL complexes, which are highly mutated in a large number of cancers and other human diseases, function as deubiquitinase machinery regulating PcG activities in the epigenetic regulation of gene expression. Armache *et al.* used cryo–electron microscopy to determine the structure of human BAP1 with ASXL1, providing insight into specificity for monoubiquitinated nucleosomes by this complex. They also studied how mutations in the *BAP1* and *ASXL1* genes result in deregulation of its deubiquitinase activity, a process relevant to cancer pathogenesis and treatment. —AS

Sci. Adv. (2023) 10.1126/sciadv.adg9832

MUCOSAL IMMUNOLOGY

A place for gut macrophages to grow up

Intestinal macrophages are a heterogenous population of cells that contribute to gut homeostasis and host defense, but the signals regulating their development within the gut are not fully understood. Chiaranunt *et al.* describe a microanatomic niche in solitary isolated lymphoid tissue (SILT) that guides the differentiation of a specialized monocyte-derived macrophage population. Colonic macrophage development in SILT required colony-stimulating factor 2–producing group 3 innate lymphoid cells and exposure to microbiota-derived extracellular ATP. This macrophage subset of highly expressed genes were involved in energy metabolism and reactive oxygen species production and were required for protection against *Citrobacter rodentium* infection. These findings identify SILTs as being a specialized niche for integrating microbial and host-derived signals to support immune defenses at the intestinal mucosa. —CO

Sci. Immunol. (2023) 10.1126/sciimmunol.abq4573

METABOLISM

Keeping fetuses fed and happy

Pregnancy involves immunological, cardiovascular, and metabolic adaptations to support fetal growth and survival. Lopez-Tello *et al.* examined metabolic adaptations to pregnancy in mice. They found that the gene for insulin-like growth factor 2 (*Igf2*) plays a key role in maternal resource allocation during pregnancy. Production of IGF2 causes transient insulin resistance during pregnancy, which ensures glucose availability to the fetus. If IGF2 is lacking, reduced glucose availability results in fetal growth impairment. The impact of metabolic abnormalities on the fetus during pregnancy persists into the offspring's adulthood, underscoring potential clinical implications. —YN

Cell Metab. (2023) 10.1016/j.cmet.2023.06.007

Metabolic abnormalities in mice during pregnancy can have lifelong effects on their offspring.

CIVIC HONESTY

Collective passive protection

A benchmark for civic honesty was established by an experiment conducted across 40 countries, and published in *Science**, in which wallets containing various amounts of money, together with the owners' Email details, were "lost." Honesty was assumed solely in terms of the numbers of finders who made contact through Email. The experiment ranked China the lowest among the countries tested in civic honesty, sparking controversy and concerns that relying solely on Email response rates neglects important cultural differences. Yang *et al.* replicated the study in China and applied cultural measures to the data. It appears that the Chinese attribute of collectivism, which would incline finders into passive safekeeping of the

PHOTO: STEVE GSCHMEISSNER/SCIENCE SOURCE

BIOMATERIALS

Simplifying vascular graft construction

Tissue-engineered vascular grafts are an alternative to autografts for replacing small-diameter blood vessels. A key challenge to manufacturing engineered grafts is to ensure the proper alignment of the various cell layers, including the innermost axially aligned endothelial cells and the multiple layers of circumferentially aligned smooth muscle cells. Alkazemi *et al.* used freezing to axially align the electrospun polycaprolactone fibers used to seed the endothelial cells and controlled the stiffness of a surrounding layer of hydrogel to encourage proper smooth muscle cell growth. All of this was achieved in a few hours rather than over several weeks, and the vascular grafts showed mechanical properties similar to native ones. —MSL

ACS Appl. Mater. Interfaces (2023) 10.1021/acsami.3c08511

Small-diameter blood vessels can be replaced with tissue-engineered vascular grafts during human heart bypass surgery.

abandoned wallets rather than the more individualistic behavior required for contacting owners, accounted for the unexpected conclusion. Therefore, sole reliance on Email response rates may give biased estimates of civic honesty in different cultural contexts. —EEU

Proc. Natl. Acad. Sci. U. S. A. (2023) 10.1073/pnas.2213824120

*See also *Science* (2019) 10.1126/science.aau8712

EXOPLANETS

Direct images of a gas giant exoplanet

Direct images of exoplanets are rare because of the overwhelming brightness of the host star, which requires special instrumentation and analysis processes to remove. This method is only sensitive to high-mass young planets on wide orbits but provides direct measurements of their atmospheres. Carter *et al.* used the James Webb Space Telescope (JWST) to obtain direct images of HIP 65426b, a previously known gas giant. They detected the exoplanet at wavelengths of 2 to 5 micrometers and 11 to 16 micrometers, thereby extending the direct imaging technique into the mid-infrared range. Modeling of the spectral energy distribution showed that HIP 65426b is seven times more massive than Jupiter. —KTS

Astrophys. J. Lett. (2023) 10.3847/2041-8213/acd93e

STEM WORKFORCE

Missing the point

As the body of research centered on historically marginalized populations in STEM continues to grow, research focused on privileged identities remains sparse. Cis white men dominate most STEM fields, where they are overrepresented in positions of status and influence. Dancy and Hodari interviewed 27 self-identified progressive white male physics faculty and graduate students to better understand their perceptions of race and gender in physics. The authors found that despite their interest in addressing inequity, this population engaged in patterns of belief, speech, and actions that ultimately support the status quo. Specifically, this population tended to deny inequity around them, place the cause of inequity on societal structures over which they have no impact, and justify their inaction. Recommendations for helping cis men engage their status and power to disrupt inequity are provided. —MMc

Int. J. STEM Educ. (2023) 10.1186/s40594-023-00433-8

EVOLUTION

Still the same after all these years

Tunicates, or sea squirts, are marine invertebrate chordates that have become valuable models for understanding the origin of vertebrates. One enduring question in chordate evolution is whether the last common ancestor of tunicates was a free-swimming tadpole-like larva or if it resembled the stationary adult animal. Nanglu *et al.* describe a rare, 500-million-year-old tunicate fossil from western Utah that features a barrel-shaped body with two prominent siphons on the top and longitudinal muscles along the body, just like present-day sea squirts. Thus, it appears that the fundamental attributes of sea squirts were already present in the Cambrian and we will have to dig deeper to find ancestral fossils. —DJ

Nat. Commun. (2023) 10.1038/s41467-023-39012-4

EATING DISORDERS

Understanding her binge eating

Women have been shown to be more susceptible than men to eating disorders. Anversa *et al.* investigated the mechanistic basis of stress-induced binge eating using a mouse model, which showed that only female mice ate abnormally after an acute emotional stressor. The authors found that binge eating was associated with activation of interneurons in the paraventricular thalamus projecting to the insular cortex. Inhibiting this projection abolished binge eating in the stressed female mice. This pathway might offer a therapeutic target for alleviating abnormal eating behavior. —MMa

Neuropsychopharmacology (2023) 10.1038/s41386-023-01665-6

PHOTO: ARNO MASSEE/SCIENCE SOURCE

Edited by **Michael Funk**

MELANOGENESIS

Genes that influence pigmentation

Skin pigmentation provides crucial protection from the DNA damage caused by sun exposure, but the production of melanin in the skin and hair is known to vary across populations. In this study, Bajpai *et al.* used flow cytometry and the light-scattering properties of melanin to identify genes important to melanogenesis in human skin cells. The authors performed a genome-wide CRISPR screen and identified 169 genes whose loss was associated with reduced light scattering, and thus melanin. Many of these genes are associated with skin pigmentation in humans, and the authors performed functional work on several of their candidates. This study reveals many new candidate genes with roles in melanogenesis. —CNS

Science, ade6289, this issue p. 646

RENEWABLE ENERGY

Watered-down demand

A growing population and increasing energy demand have spurred investments in hydropower generation in Africa. At the same time, the cost of power from other types of renewable sources has continued to drop. Carlino *et al.* explored the ramifications of this trend on the economics of hydropower. They analyzed the African energy landscape from 2020 to 2050, and predicted that the declining cost of wind and solar power will make a large fraction of the current hydropower candidate installations economically uncompetitive over that period. Cooperation between countries could help to overcome the regionally unequal distribution of investment costs and potential energy deficits. —HJS

Science, adf5848, this issue p. 645;

EVOLUTIONARY BIOLOGY

Phyloepigenetic trees take shape

DNA methylation installs a methyl group to cytosine, placing an epigenetic mark that regulates gene expression. Comparative epigenomics combines epigenetic signatures with phylogenetic relationships to understand species characteristics. Haghani *et al.* evaluated methylation levels in highly conserved DNA sequences, profiling ~15,000 samples across 348 mammalian species (see the Perspective by de Mendoza). Phylogenetic trees suggest that the divergence of DNA methylation profiles closely mirrors genetic evolution. Species with longer maximum life spans have developed tidier methylation patterns within the genome, characterized by unique peaks and troughs of methylation. Methylation patterns associated with maximum life spans generally differ from those connected to age or interventions that affect mortality risk in mice. These data provide a rich resource of information for fields including evolutionary biology and longevity research. —DJ

Science, abq5693, this issue p. 647; see also adj4904, p. 602

BIOMATERIALS

Conducting bioadhesives for wet tissue

Bioelectronic devices can be used to monitor or repair vital tissues in the body, but this often requires direct interfacing and adhesion, which is a particular challenge when the surface is wet. Li *et al.* designed a double-network copolymer that combines a bioadhesive with a semiconductor (see the Perspective by Wu and Zhao). In particular, the brush component included a side group that could absorb water so that on initial contact with the tissue surface, it helps to dry it to enhance adhesion. The authors demonstrate the capabilities of their material by building a sensor for electrophysiological recording on an isolated rat heart and on in vivo rat muscles. —MSL

Science, adg8758, this issue p. 686; see also adj3284, p. 608

PLASTIC UPCYCLING

Using polyolefins as feedstock

As plastic waste continues to accumulate, chemists are focused on finding ways to use it as feedstock for valuable compounds. Polyolefins are especially hard to break back down into their original monomers, but two reports in this issue show that they can be useful starting materials for other products (see the Perspective by Van Geem). Li *et al.* report that pyrolysis of polyethylene and polypropylene produces olefin mixtures that can be directly subjected to hydroformylation. The well-known cobalt-catalyzed reaction produces aldehydes that the authors then hydrogenated to produce alcohols and diols. Xu *et al.* show that precise temperature control during heating can break down the same plastics into waxes that can then be readily oxidized over manganese catalysts to produce valuable surfactants. —JSY

Science, adh0993, adh1853, this issue p. 666, 686; See also adj2807, p. 607

2D MATERIALS

Making more ordered moirés

Moiré superlattices formed by stacking single-layer materials in a twisted configuration can host many exotic states. However, such structures have been found to be disordered, with the twist angle and strain varying unpredictably within a single sample. Kapfer *et al.* found an elegant method for controlling the twist angle and decreasing the disorder (see the Perspective by Park). The researchers placed a ribbon-shaped graphene layer on top of hexagonal boron nitride and bent one end of the ribbon using the tip of an atomic force microscope. The resulting structure had a twist angle that increased continuously from the point at which the ribbon started bending to its end. Such control is expected to improve reproducibility and understanding of this class of materials. —JS

Science, ade9995, this issue p. 677; see also adj1420, p. 604

IMMUNOLOGY

The TGF-β twist on macrophage metabolism

Macrophages can initiate or resolve inflammatory responses. Usually, glycolytic metabolism results in an inflammatory phenotype in immune cells, but Gauthier *et al.* found that macrophages activated by the cytokine transforming growth factor–β (TGF-β) had a glycolytic metabolism but were less inflammatory. TGF-β decreased the survival of mice with sepsis, which was associated with increased coagulation, a complication of sepsis that can lead to organ dysfunction. In septic patients, COVID-19 disease correlated with enhanced expression of genes encoding a TGF-β receptor, a glycolytic enzyme, and a coagulation factor. —WW

Sci. Signal. (2023) 10.1126/scisignal.ade0385

KIDNEY DISEASE

Protecting podocytes

Mutations in the podocin-encoding *NPHS2* gene can cause steroid-resistant nephrotic syndrome in children, with no effective targeted treatments available. Ding *et al.* demonstrated the effectiveness of adeno-associated virus (AAV)–LK03 at transducing human podocytes in vitro. The authors

then developed an AAV-based gene therapy to treat *NPHS2* mutations using a minimal human nephrin promoter and tested it using AAV serotype 2/9, which can transduce murine podocytes, in two different mouse models of disease. Treatment before induction of disease and after disease onset reduced albuminuria and improved serum albumin in nephrotic mice, providing proof-of-concept that gene therapy might be a viable treatment strategy for patients with monogenic causes of nephrotic syndrome. —MN

Sci. Transl. Med. (2023)
10.1126/scitranslmed.abc8226

RESEARCH ARTICLE SUMMARY

RENEWABLE ENERGY

Declining cost of renewables and climate change curb the need for African hydropower expansion

Angelo Carlino, Matthias Wildemeersch, Celray James Chawanda, Matteo Giuliani, Sebastian Sterl, Wim Thiery, Ann van Griensven, Andrea Castelletti*

INTRODUCTION: Driven by population growth and the goal of improving living standards, especially in the least-developed regions, many African countries plan to expand their power generation capacities to meet future energy demand. Indeed, total electricity demand is expected to grow by 5 to 6% per year until 2050, mainly in sub-Saharan Africa. Yet the future of African energy systems will not only be driven by the additional energy demand but also by the need to mitigate and adapt to anthropogenic climate change. Hydropower is an important component of African power systems, especially in sub-Saharan countries. It provides around 20% of total electricity generation, but its full potential has not been exploited yet. Traditionally considered a cheap source of low-carbon electricity, more than 300 hydropower plants, corresponding to an additional 100-GW power capacity, are under consideration across the continent.

RATIONALE: Although an apparently effective strategy, the long-term planning of hydropower systems is complex. First, as the cost of renewables continues to decline, solar and wind power are becoming more competitive and potentially cheaper alternatives. Second, in recent years, hydroclimatic variability has negatively affected hydropower generation in major river basins. Climate change will alter the spatiotemporal distribution of water availability, exacerbating the impacts of extreme events and reducing the predictability of future power generation. Finally, future energy demands and climate policies depend on evolving socioeconomic conditions that are fundamentally uncertain. In this work, we investigated the power capacity expansion across the African continent over the next 30 years and elucidated the cost-optimal sequencing of hydropower projects. We built an integrated modeling framework that captures individual power project characteristics within an energy system model that simulates three socioeconomic scenarios that harmonize land-use change, climate impacts on water availability, final energy demands, and climate policy options. Our model relies on a combination of the Shared Socioeconomic Pathways (SSPs) and Representative Concentration Pathways, namely SSP1-2.6, SSP4-6.0, and SSP5-8.5. SSP1-2.6 describes a sustainable development scenario that aims to maintain the global mean temperature below 2°C, whereas the other two scenarios result in higher levels of warming and are characterized by rising inequalities and fossil-fueled development, respectively. We considered median (MED) and very dry (DRY) water availability scenarios to capture hydroclimatic variability reflecting a risk-neutral and risk-averse planning perspective.

RESULTS: Our results show that between 32 and 60% of the proposed hydropower capacity is not cost-optimal. Moreover, our analysis suggests that hardly any new hydropower will be built after 2030, meaning that its role in terms of installed capacity and generation will gradually decrease in favor of solar and wind power. Across the scenarios, hydropower expansion is robust in the Nile, Congo, and Niger river basins, whereas it remains uncertain in the Zambezi and smaller river basins. These findings emphasize the importance of connecting hydropower planning with capacity expansion models, because cost-optimality cannot be determined solely based on each project's technical characteristics. Finally, we discover that an increase in annual capital investment between 1 and 4% at the continental level can ensure the reliability of the power system against hydroclimatic variability. Yet the required increase in capital investments and the observed reductions in vulnerability do not necessarily overlap at the country level. As local interests conflict and diverge from system-wide ones, we underline the importance of electricity exchanges between countries and cooperation for power system reliability.

CONCLUSION: Traditional planning of hydropower facilities is challenged by the dynamics of technological innovation, climate impacts on water availability, and uncertainty in long-term socioeconomic projections that affect energy demands and climate policies. Using a multisectoral modeling framework, we designed capacity expansion plans that avoid commitments to cost-inefficient hydropower infrastructures that are often associated with substantial impacts on the local communities and environment. Yet, in the short term, especially in the transition to a net-zero emissions energy system, hydropower represents a cheap alternative to displace fossil fuels, especially coal. ■

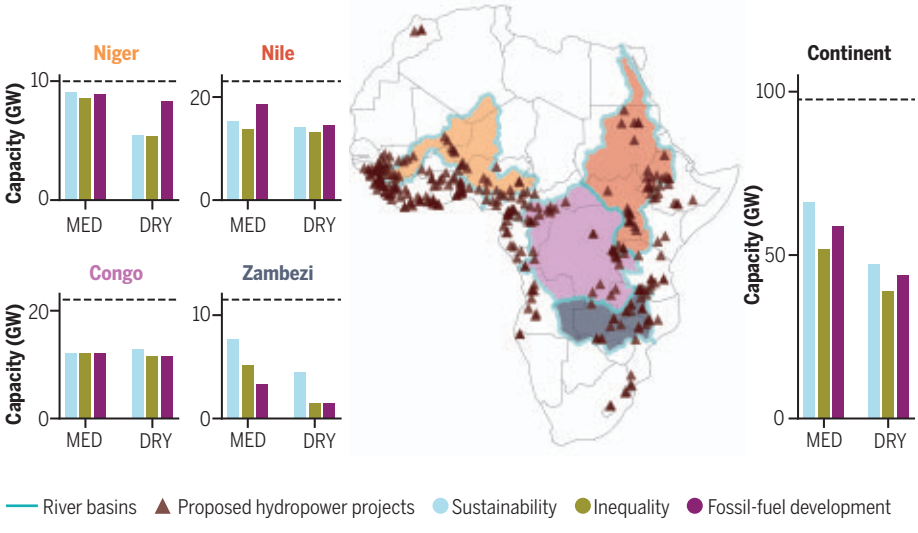

Cost-optimal hydropower expansion. Proposed (dashed line) and cost-optimal (bars) capacity expansion for continental Africa and its major river basins under the scenarios considered. In total, 32 to 60% of the proposed capacity is not cost-optimal. More than half of the capacity proposed for the Nile, Congo, and Niger basins is always cost-optimal, whereas the expansion in the Zambezi River basin depends on the considered scenario. The colors of the shaded areas in the map correspond to the river basins represented by each graph.

The list of author affiliations is available in the full article online.
*Corresponding author. Email: andrea.castelletti@polimi.it
Cite this article as A. Carlino *et al.*, *Science* 381, eadf5848 (2023). DOI: 10.1126/science.adf5848

READ THE FULL ARTICLE AT
https://doi.org/10.1126/science.adf5848

RESEARCH ARTICLE

RENEWABLE ENERGY

Declining cost of renewables and climate change curb the need for African hydropower expansion

Angelo Carlino[1,2]†, Matthias Wildemeersch[2]‡, Celray James Chawanda[3], Matteo Giuliani[1], Sebastian Sterl[3,4], Wim Thiery[3], Ann van Griensven[3], Andrea Castelletti[1]*

Across continental Africa, more than 300 new hydropower projects are under consideration to meet the future energy demand that is expected based on the growing population and increasing energy access. Yet large uncertainties associated with hydroclimatic and socioeconomic changes challenge hydropower planning. In this work, we show that only 40 to 68% of the candidate hydropower capacity in Africa is economically attractive. By analyzing the African energy systems' development from 2020 to 2050 for different scenarios of energy demand, land-use change, and climate impacts on water availability, we find that wind and solar outcompete hydropower by 2030. An additional 1.8 to 4% increase in annual continental investment ensures reliability against future hydroclimatic variability. However, cooperation between countries is needed to overcome the divergent spatial distribution of investment costs and potential energy deficits.

Over the next few decades, African energy systems are expected to undergo profound changes. The total electricity demand is predicted to increase by 5 to 6% per year over the next 10 years until 2050 (*1*–*3*), an increase that is driven by sustained population growth, mainly in sub-Saharan Africa (*4*), and the continuous infrastructural investments aimed at improving energy access and living standards, especially in the least-developed areas (*5*, *6*). This increasing demand, together with the need to mitigate and adapt to anthropogenic climate change (*7*), will shape the future development of African energy systems. The use of low-carbon energy sources (*3*, *8*, *9*) will gradually lessen the historical dependency on fossil fuels, which are abundant across the continent (*10*). In the short term, annual investments of US$190 billion are required to ensure such a successful energy transition, with more than two-thirds of this financial investment allocated to clean-energy sources (*3*). Among these, hydropower has historically been favored as a low-cost source of baseload power (*11*), and policies that are in place now imply a substantial infrastructural expansion (*12*). Moreover, hydropower is an attractive component of the future African power system owing to its ability to balance grid load in support of intermittent renewable electricity sources (*13*–*15*) and because the remaining untapped potential across the continent is relatively large (*11*). According to plans of national and regional agencies, more than 300 new hydropower projects are, at present, committed, planned, or under consideration across the African continent (*16*). These projects amount to a total of around 100 GW of additional hydropower capacity, with 168 large (≥100-MW) projects accounting for almost 90 GW (*16*).

Nevertheless, climate change makes future hydropower generation uncertain (*17*) and increases the risk of cascading power system failures across countries and power pools (*18*), likely jeopardizing its potential to foster resilience (*19*). Moreover, capacity expansion projections are linked to future energy demand, technology costs, and climate policy, which are fundamentally uncertain factors (*20*, *21*). The excessive reliance on hydropower in many sub-Saharan countries is presently a source of concern and a reason for caution in additional hydropower investment (*22*). Further doubts are cast on hydropower capacity expansion (*23*) when socioeconomic and environmental impacts of hydropower are analyzed, such as population displacement (*24*), reduced sediment connectivity (*25*), loss of biodiversity (*26*), and competition with other water uses, most importantly with agriculture (*21*).

Given the scale of future infrastructure development, the socioeconomic and environmental impacts of hydropower expansion, and the need to bridge continental as well as regional power system development, it is crucial to identify the hydropower projects that should be prioritized and the ones that should be discarded based on the cost-optimal power system capacity expansion. Indeed, the selection and sequencing of the required hydropower infrastructure, given energy, socioeconomic, and technological development, is a critical first step. Further research should evaluate the ensuing social, climatic, and environmental impacts on the alternatives of interest to support final planning decisions. To what extent do the planned hydropower expansion and its spatial distribution over the main river basins change depending on socioeconomic, land-use, and climatic uncertainties? What are the costs of climate-proofing the energy system, and how are these costs spatially distributed compared with power deficits driven by hydroclimatic variability?

In this work, we build an integrated modeling framework to examine the role of hydropower in a sustainable energy transition that is cognizant of hydroclimatic and land-use change, socioeconomic projections, and climate policy options. Although previous studies on strategic dam planning (*27*–*30*) rarely included the power system and rarely went beyond the basin scale (*31*, *32*), our analysis examines the full energy portfolio at the continental scale. Specifically, we consider cross-basin interactions across the power grid (*33*), hydropower projects proposed at the river basin and national scales, and socioeconomic and land-use projections. By doing so, we limit undesirable outcomes that result from the integration of national, regional, and continental policies across multiple sectors and scales (*34*).

Our results show that hydropower will have lost its dominant role in Africa's renewable electricity mix by 2050, with solar and wind power representing at least 29 to 38% and 8 to 12% of generation, respectively, and hydropower's share shrinking to 7 to 14% under all considered scenarios. Between 40 and 68% of the proposed new hydropower capacity or, in other words, between 120 and 251 of the 367 proposed projects could potentially be cost-optimal, and nearly no new hydropower plants are recommended to be built after 2030. Although the viability of hydropower expansion in the Zambezi River basin is dependent on the scenario that is considered, many of the proposed projects for the Nile, Congo, and Niger remain economically viable under all considered scenarios. Finally, guaranteeing the reliability of the energy system against hydroclimatic risks only requires reallocating some of the investments in hydropower toward other sources, especially solar power and firming technologies, with a small increase in annual capital investments. Yet the need for additional investment and the risk of shortages are often located in different regions. As a consequence, we highlight the importance of transnational governance measures to guarantee climate-resilient energy systems.

[1]Department of Electronics, Information, and Bioengineering, Politecnico di Milano, Milano, Italy. [2]International Institute for Applied Systems Analysis, Laxenburg, Vienna, Austria. [3]Department of Hydrology and Hydraulic Engineering, Vrije Universiteit Brussel, Brussels, Belgium. [4]World Resources Institute, Regional Hub for Africa, Addis Ababa, Ethiopia.
*Corresponding author. Email: andrea.castelletti@polimi.it
†Present address: Department of Global Ecology, Carnegie Institution for Science, Stanford, CA, USA.
‡Present address: Environmental Change Institute, Oxford University, Oxford, UK.

Sequencing hydropower projects within power capacity expansion

To obtain plans for hydropower project sequencing and associated power capacity expansion, we set up a multiscale, multisector modeling approach (fig. S1). We combined input data from three main datasets. First, we used the Shared Socioeconomic Pathways (SSPs) database (*35*) to obtain projected energy demands. Second, we relied on the African Hydropower Atlas (*16*) to characterize each hydropower project in the OSeMOSYS-TEMBA model (*36*). Third, to coherently account for the coevolution of the climatic and the socioeconomic system, we used the Inter-Sectoral Impact Model Intercomparison Project (ISIMIP2b) scenarios (*37*) to represent the future hydrological regime that will result from changes in the climate system and the land-use sector. Natural climate variability was considered using a median and a very dry hydrological scenario. These correspond to the 50th and 5th percentiles of the distribution of simulated annual average generation, which is obtained by simulating a distributed hydrological model under an ensemble of climate projections from 2020 to 2050 (see materials and methods).

We used this model to study the expansion trajectory of the African energy systems over the period from 2020 to 2050 at the continental scale assuming centralized decision-making. We considered three socioeconomic scenarios that aggregate socioeconomic, land-use, and climatic assumptions: (i) a sustainable development scenario, using a carbon emission constraint compatible with a 2°C long-term warming, according to SSP1-2.6; (ii) a scenario designed to focus on heterogeneous economic development among regions not associated with climate policy efforts, according to SSP4-6.0; and (iii) a fossil-fueled economic growth scenario associated with high greenhouse gas emissions, according to SSP5-8.5. For each socioeconomic scenario, we consider the median (MED) and very dry (DRY) hydrological scenarios. We use the first to represent traditional hydropower planning and the second to stress-test the power system under worst-case hydroclimatic conditions. Indeed, these two scenarios can be seen as describing different risk-preparedness targets (risk–neutral and risk-averse, respectively) with respect to the uncertainty associated with hydroclimatic variability. For each considered scenario, we optimized the power capacity expansion for each energy source and the sequencing of the proposed (i.e., planned, committed, and candidate) hydropower projects collected in the African Hydropower Atlas. Moreover, we examined the cost-reliability trade-off at different spatial scales, which would otherwise remain hidden behind the large-scale formulation of the least-cost capacity expansion problem.

Cost-effectiveness of solar energy avoids the need for long-term hydropower expansion

Our model results show that at least one-third of the new hydropower capacity proposed at the regional and country levels is not cost-optimal across continental Africa, and this result holds under all considered scenarios (Fig. 1). Under ensemble median hydrologic change (i.e., under the MED scenarios), new hydropower installed capacity ranges from 52 GW under SSP4-6.0 to 66 GW under SSP1-2.6, whereas these values drop to between 39 GW (SSP4-6.0) 47 GW (SSP1-2.6) when considering dry hydrology conditions under the risk-averse approach (i.e., under the DRY scenarios), meaning that more than half of the proposed capacity is not economically viable at the continental scale. In all these plans, two large projects are responsible for more than 17 GW of viable capacity: the soon to be completed 6.4-GW Grand Ethiopian Renaissance Dam and the 11.0-GW Inga 3 candidate project in the Democratic Republic of the Congo. In general, the SSP1-2.6 scenario consistent with a warming of 2°C at the global level requires more hydropower than other scenarios owing to the reduced reliance on fossil fuels. To isolate the impact of climate change on hydropower expansion, we examined capacity expansion strategies by considering hydropower generation based on observations from 1986 to 2005. We see that climate change is particularly affecting the scenarios with the largest hydropower expansion and is responsible for a reduction of 9 GW (SSP1-2.6) and 8 GW (SSP5-8.5) (fig. S2). As we consider the salvage value of infrastructure at the end of the planning horizon that corresponds with the remaining operational life, our results remain consistent when we extend the horizon until 2070 (fig. S3).

Under all socioeconomic and hydrological scenarios, at least half of the additional hydropower capacity is installed in the period from 2020 to 2030 (Fig. 1, A to C), with the window in which hydropower can still compete economically with solar photovoltaics (PV) rapidly closing. Beyond 2030, the share of new investments in solar power increases substantially, and further development of hydropower in Africa is unlikely to be cost-effective (Fig. 2). Although hydropower could still be competitive with solar PV until the end of this decade, the often-witnessed build time and cost overruns for hydropower projects (*38*) may even preclude large-scale hydropower expansion before that time, paving the way for further solar PV deployment. In addition, all capacity investments are expected to grow rapidly in the decades after 2030, thus further diminishing the role of hydropower in the future energy portfolio (*39*). Similarly, given the large expansion of the power system in the next few decades, the decline of hydropower is also substantial in the total capacity share (fig. S4). The gap is even more pronounced for the DRY scenarios in which more than half of the

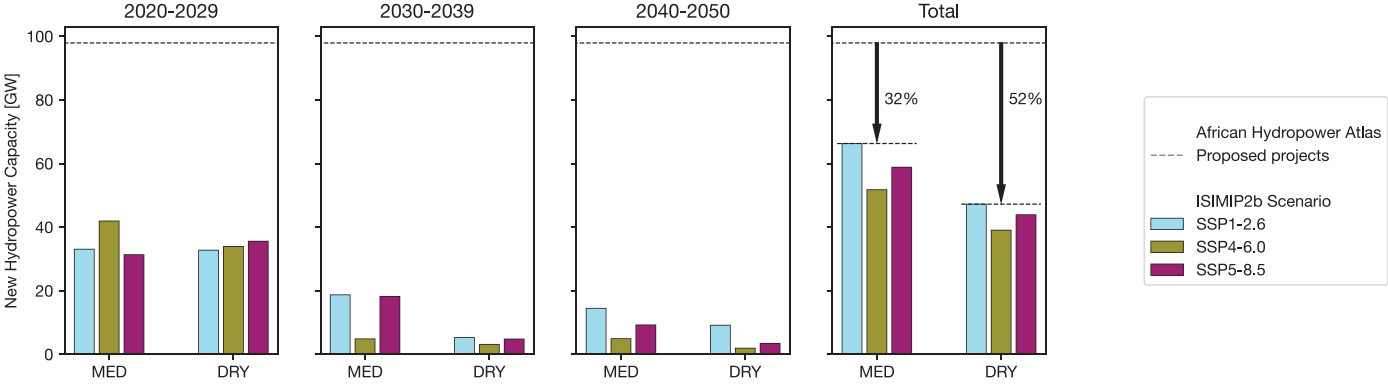

Fig. 1. Decadal and total hydropower capacity expansion under the considered scenarios. The dashed line indicates the capacity of proposed projects reported in the African Hydropower Atlas. The colors of the bars are associated with the considered SSP scenarios, which coherently capture socioeconomic, land-use, and hydroclimatic change. For each decade and for the total, the bars on the left report the capacity expansion plan designed under ensemble median hydrology (MED), and the bars on the right correspond to the capacity expansion plan designed under dry hydrology (DRY). The arrows indicate the fraction of proposed capacity, which is not cost-optimal under the two different risk-preparedness targets.

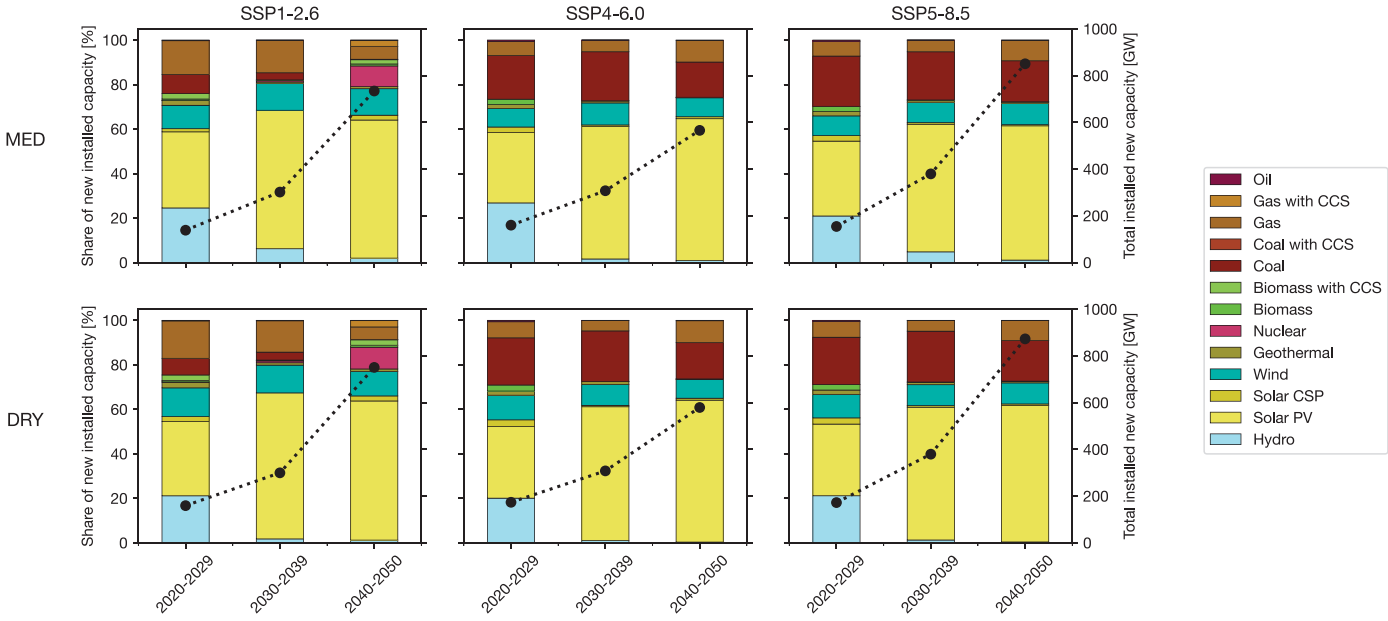

Fig. 2. Power capacity expansion at the continental level. The share of new installed capacity for each power source (left *y* axis) and the new installed capacity (right *y* axis) are reported against the three decades examined. The top row reports the share of each power source in new capacity under median hydrology (MED scenarios), and the bottom row reports the capacity expansion plans designed under dry hydrology (DRY scenarios). Each column represents the different SSP scenarios. Each power source is described in the legend, the order of which, from top to bottom, follows the order of the stacked bars from top to bottom. CCS, carbon capture and storage; CSP, concentrating solar power.

proposed capacity is not economically optimal, resulting in higher investments in solar power (bottom row in Fig. 2). Solar power becomes a option, displacing hydropower projects whose generation changes the most from median to very dry hydrology. In SSP1-2.6, an important role is played by nuclear power by mid-century, which is used to further reduce investment in fossil fuel power sources and represents an important share of energy generation in 2050 (fig. S5). Contrary to SSP1-2.6, where coal becomes almost absent, under SSP4-6.0 and SSP5-8.5, it still contributes around 40% of the energy generation mix by mid-century, with more than 2000 terawatt-hours under SSP5-8.5 (fig. S5). With respect to the flexibility required in the power system to balance the reduced output of solar plants at night, hydropower comes after biomass and fossil fuels, and wind has a complementary diurnal profile to solar as well (fig. S6). Consequently, our results do not suggest that hydropower will still be a major provider of firm generation and flexibility by mid-century.

Location and drivers of hydropower expansion

Most of the planned African hydropower projects concentrate in four major river basins—Nile, Congo, Zambezi, and Niger—which account for around 66% of the total proposed additional hydropower capacity (*16*). Across the socioeconomic and risk-preparedness scenarios, the cost-optimal dam portfolio varies substantially, even though some projects are consistently selected (fig. S7). A robust finding over the considered scenarios and river basins is that less hydropower is installed in the DRY capacity expansion scenarios and under SSP4-6.0 and SSP5-8.5 (Fig. 3). The Congo River basin is consistently cost-optimal for around half of its potential through the Inga 3 Dam, accounting for 11 GW in the Democratic Republic of the Congo and built in all the scenarios. Half of the proposed potential for the Nile River basin is always cost-optimal, mainly in Ethiopia and Uganda, up to 80% in SSP5-8.5 with MED capacity expansion. The hydropower expansion in the Zambezi River basin is instead very uncertain and strongly dependent upon the considered scenario, ranging from 30% (SSP5-8.5) to 70% (SSP1-2.6) of the proposed capacity in the MED scenarios and between 13% (SSP4-6.0 and SSP5-8.5) and 39% (SSP1-2.6) in the DRY scenarios. Finally, the cost-optimal hydropower potential in the Niger River basin is between 86% (SSP4-6.0) and 91% (SSP1-2.6) of the proposed capacity for the MED scenarios, and it is reduced to between 53% (SSP4-6.0) and 83% (SSP5-8.5) in the DRY scenarios. These projects are located mainly in Nigeria, a potential hotspot of hydropower development. For what concerns the remaining smaller basins, the development of projects varies considerably from 38% (SSP4-6.0) to 71% (SSP1-2.6) of their total capacity in the MED capacity expansion scenarios and between 24% (SSP4-6.0) and 32% (SSP1-2.6) for the DRY capacity expansion scenarios.

Given these results, we can partially trace the cost-optimal power expansion decisions back to the characteristics of the proposed hydropower projects. High average capacity factors and high capacity are usually good indicators of cost-optimality (Fig. 4). Indeed, the higher the capacity, the lower the capital cost of new hydropower (*40*), even though the probabilities of delays and cost overruns increase as well (*41*). Furthermore, the higher the average capacity factor, the higher the annual generation of a power plant. The construction of new hydropower projects is not sensitive to the interannual variability in the capacity factor. Then again, spatial and temporal energy system constraints, such as transmission line capacity and proximity to more economically favorable hydropower projects, enable a full understanding of the cost-optimal power system development. This is, for example, the case for projects in the Zambezi basin in Zambia, a region well connected to the Democratic Republic of the Congo. The development of the Inga 3 Dam in the latter allows for substantial cheap electricity exports to neighboring countries, reducing the viability of domestic hydropower expansion in Zambia.

The regional distribution of costs and deficits requires cooperation

It is presently unclear how the magnitude of drought-induced power deficits compares with the size of additional investment costs that are required to climate-proof the energy system

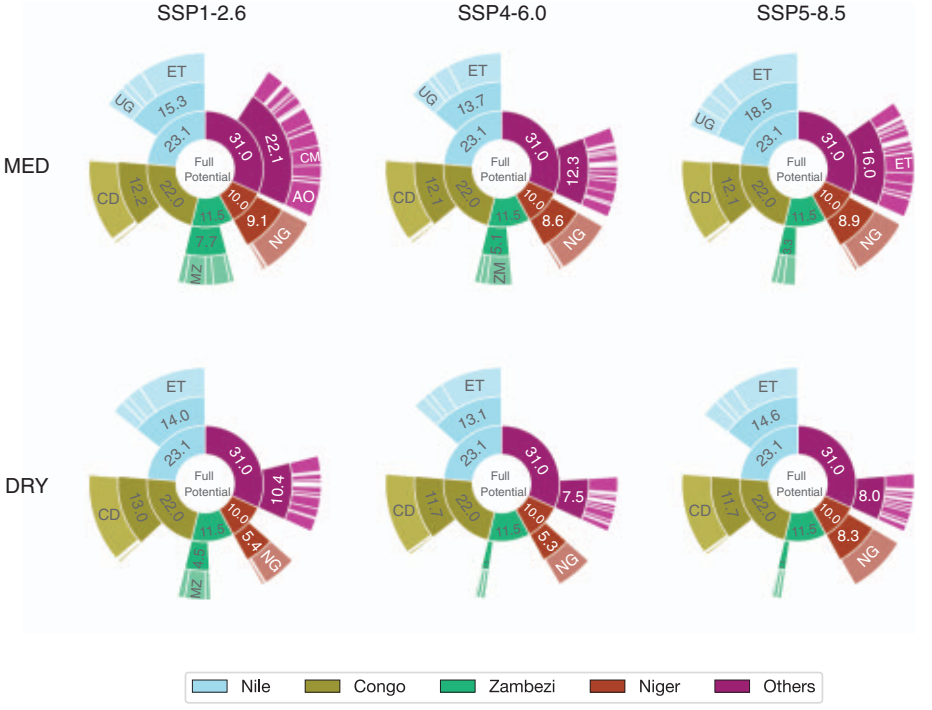

Fig. 3. Basin- and country-level hydropower capacity expansion. The full capacity of proposed projects is reported by river basin in the inner ring. The cost-optimal capacity in each river basin is reported in the middle ring and is assigned to the corresponding countries in the outer ring. All values are reported in GW units. The columns correspond to the SSP scenarios examined. The top and bottom rows report results from the MED and DRY capacity expansion scenarios, respectively. For each scenario, only countries that are building more than 2.5 GW of new hydropower are labeled, namely Angola (AO), Democratic Republic of the Congo (CD), Cameroon (CM), Ethiopia (ET), Mozambique (MZ), Nigeria (NG), Uganda (UG), and Zambia (ZM).

(i.e., to guarantee demand satisfaction under dry hydrological conditions). For this reason, we stress-test the MED capacity expansion plans, obtained under median hydrology, by simulating it under dry hydrology to estimate the potential deficit that can occur. The observed generation deficits should be understood as the result of planning the power capacity expansions for each source, not only for hydropower, without explicitly accounting for hydroclimatic variability. The reported deficits present a worst-case scenario because safety mechanisms such as reserve margins are supposed to be in place to reduce the probability of occurrence and the magnitude of these events. The DRY capacity expansion plans can remove this risk with a capital cost increase between 1.8% (SSP5-8.5) and 4% (SSP1-2.6) in annual capital investments at the continental level under all the socioeconomic scenarios. Yet at the country level, the cost increase and potential deficit are unevenly distributed and vary widely across the scenarios (Fig. 5).

Generally, reduced hydropower generation requires backing up with existing, mainly fossil fuel–based technologies or with additional capacity. This additional capacity is typically solar PV under cost-optimal expansion scenarios, especially under SSP1-2.6, in which the reliance on fossil fuels for power generation is constrained. Consequently, spatial planning of the deployment of renewable power plants will be affected as well.

For many regions that are not dependent on hydropower, there is no difference between the two plans because they are not affected by power deficits or additional costs induced by hydrological variability (Northern Africa and South Africa). Nonetheless, power pools strongly dependent on hydropower, such as the Southern African, Eastern Africa, and West African Power Pools, are more subject to cost increase and power deficit. Under SSP1-2.6, West Africa is affected by generation deficit events that require substantial capital investments to ensure reliability (e.g., Senegal, Guinea-Bissau, Ghana, and Togo). Conversely, the power deficits in Nigeria and Burkina Faso require a modest increase in annual capital cost. In the other scenarios, the power deficit affects mostly Mali, Niger, and Benin, but the costs to achieve reliability remain low in all the power pool.

With respect to the Eastern Africa Power Pool, Ethiopia, Tanzania, Uganda, Rwanda, and South Sudan are most at risk of power outages induced by hydroclimatic variability. All of these countries require substantial investments to reduce this risk, and additional economic efforts will be required from Egypt, Sudan, and Kenya, especially in the case of SSP1-2.6. With respect to the Southern African Power Pool and scenario SSP1-2.6, Zambia, Namibia, and Mozambique remain most vulnerable to droughts. Zambia is particularly at risk because the power deficit would be around 13%, which could be mitigated with an 11% increase in annual capital investment. In addition to the above-mentioned countries, in the Central African Power Pool, Angola, Zimbabwe, and the neighboring Democratic Republic of the Congo are also required to increase their investments to climate-proof their energy systems to a substantial extent. Under the other scenarios, Zambia always remains exposed to drought-related power outage risk, together with Namibia, whose cost to ensure reliability remains lower. In all scenarios, a generation deficit is observed if power trade is not allowed between countries, underscoring the importance of cooperation and political stability in the region (fig. S8).

Discussion

As African power demand grows, especially in sub-Saharan Africa, the remaining untapped hydropower potential represents a cheap, clean energy source, which explains the large number of infrastructural projects that are presently under consideration. However, as costs associated with solar and wind power generation continue to decline, the historical reliance on hydropower of many sub-Saharan African countries might come to an end. Solar and wind power are expected to become the primary power sources in 2050, representing 50% of the electricity mix of the continent in the sustainable development scenario compatible with a 2°C long-term warming (SSP1-2.6) and always representing at least 50% of new installed capacity in the next three decades under all scenarios considered. Even under the SSP1-2.6 scenario, which pushes for extensive renewable capacity expansion, no more than 67% of proposed hydropower capacity is cost-optimal, and this percentage shrinks to 48% under the assumption of aversion to hydroclimatic risk. Project delays and cost overruns might further favor solar and wind projects, making hydropower development even less competitive from an economic perspective (*42*). Yet in the short term, especially in the transition to a final net-zero configuration, hydropower represents a cheap alternative to avoid the high costs of installing solar and wind at the present level of technological maturity and to displace fossil fuels, mainly coal. The Nile, Congo, and Niger River basins provide reliable hydropower generation. Yet the development of projects in these regions needs to be accompanied by investment in grid capacity in order to reap all the benefits of large hydropower. Climate-proofing the energy system against hydroclimatic variability requires reducing investment in hydropower

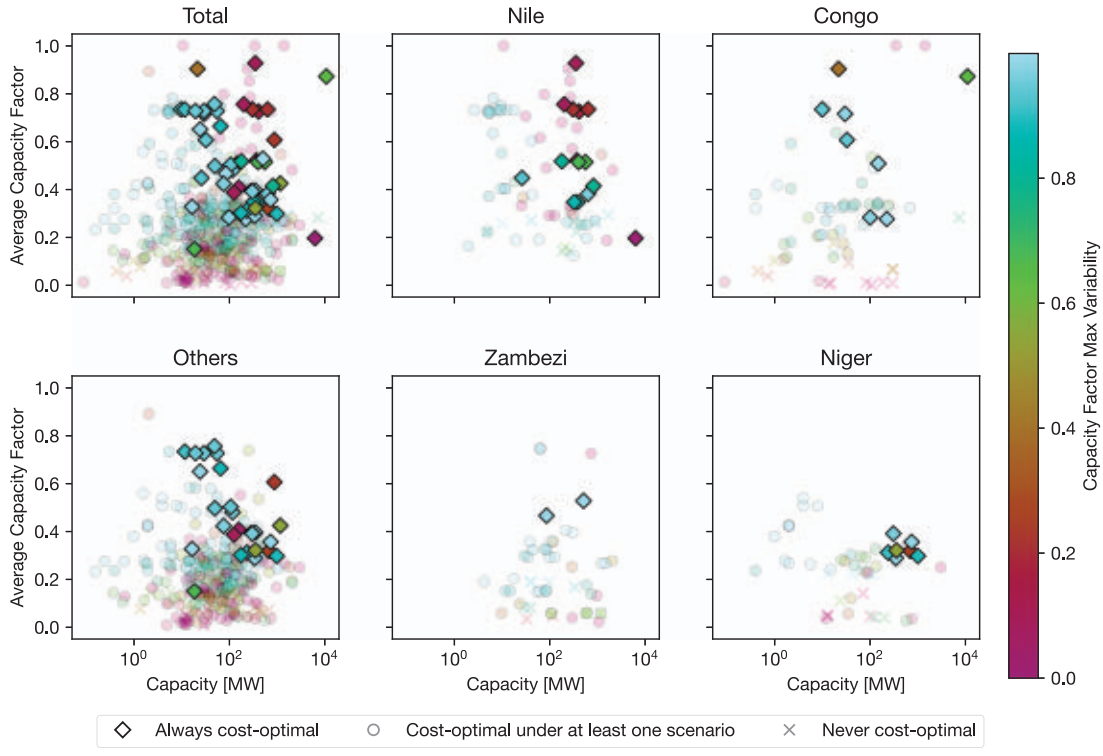

Fig. 4. Main characteristics of projects and their role in least-cost capacity expansion. Capacity, average capacity factor under very dry hydrology, and maximum interannual capacity factor variability under very dry hydrology of the examined hydropower projects are reported on the *x* axis, the *y* axis, and with different colors, respectively. The diamond marker indicates a project that is always cost-optimal. The circles correspond to projects that are cost-optimal at least once, whereas the crosses correspond to the projects that are never built. The always–cost-optimal projects correlate with the average capacity factor (point biserial correlation coefficient = 0.37; $p = 2 \times 10^{-19}$) and capacity (point biserial correlation coefficient = 0.18; $p = 3 \times 10^{-5}$). Their correlation with capacity factor's variability is weaker (point biserial correlation coefficient = 0.09; $p = 0.03$).

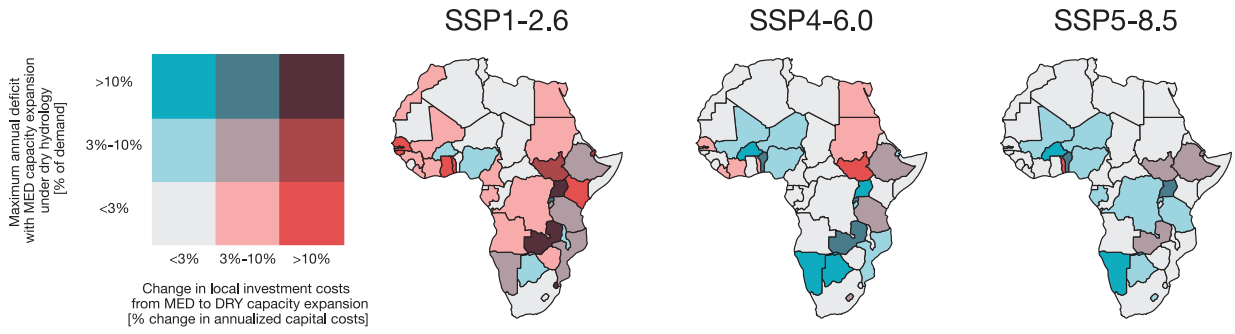
SSP1-2.6
SSP4-6.0
SSP5-8.5
Maximum annual deficit with MED capacity expansion under dry hydrology [% of demand]
>10%
3%-10%
<3%
Change in local investment costs from MED to DRY capacity expansion [% change in annualized capital costs]

Fig. 5. Country-level cost-deficit trade-offs. Maximum annual power deficit as a percentage of demand over the period from 2020 to 2050 obtained from simulation of the MED capacity expansion plan under dry hydrology. The additional cost of eliminating the power deficits is derived as the percentage increase obtained from the annualized capital costs of the MED and the DRY capacity expansion plans. Their joint value is reported for each country in the maps by the bidimensional color scale that is visible in the legend, and each map corresponds to a different SSP scenario.

and investing in additional solar, wind, and firming capacity, particularly in the scenarios where emissions are constrained. These additional costs are not necessarily distributed uniformly or fairly across the countries, highlighting the need for coordination and incentive mechanisms to support capacity expansion plans, which are robust to climate change impacts.

Through the reduction in economically viable hydropower capacity associated with the declining cost of wind and solar, technological innovation helps reduce pressure on riverine ecosystems and small communities in the proximity of proposed impoundments and further downstream as far as the impacts of these changes propagate (*43*). Indeed, previous research on hydropower's social and environmental trade-offs (*25*, *27*, *30*) and the effects of environmental risks on the financial performance of this infrastructure (*44*) has suggested caution in construction of new projects. Introducing these factors into our modeling framework is likely to further reduce the space for hydropower in future energy systems. Analyses at the river-basin level remain complementary to our study and might be better tailored to address such concerns. However, additional research and development of new methods are needed to connect local, regional, and continental scales for a robust planning of water and energy systems (*34*). Similarly, greenhouse gas emissions from reservoirs (*30*, *45*–*47*) are a deterrent for hydropower capacity expansion, particularly in tropical areas where life-cycle emissions associated with new dams might be comparable to those of fossil fuel power sources (*48*, *49*). Accounting for this factor will likely further promote the expansion of wind, solar, and other carbon-neutral technologies.

Additionally, we are not able to fully capture the contribution of hydropower projects to ancillary services such as frequency regulation and improved renewable integration associated with the rapid ramp-up of power output. Although these services are rarely considered

in hydropower planning, their importance will rise as more wind power and solar power are added to the grid, potentially affecting our results. Moreover, electricity generation is not always the main purpose for which water reservoirs are built. If some of the reservoir hydropower projects were to be associated with other needs (e.g., agriculture, flood control, drinking water supply), cross-sectoral interactions could improve their economic performance and make them attractive investments. In this case, reservoir greenhouse gas emissions should not be attributed to electricity generation only, but the exact attribution of greenhouse gas emissions to the different sectors remains a complex issue.

Governance and political stability are key to ensuring sustainable exploitation of the economically viable hydropower potential, particularly in transboundary river basins (*50*). The Nile and the Niger River basins, identified as hotspots of hydropower development, are high-risk areas because of their transboundary nature in regions of political instability and presence of armed conflict (*51*). Implementation of cooperation schemes is crucial to reduce tensions and provide water and energy security in these areas (*13*, *15*, *52*–*54*).

In a broader sense, cooperation and governance are fundamental to allow all African countries to switch their focus from energy independence to energy security (*55*). In this regard, establishing power pools and the Africa Clean Energy Corridor has been crucial for energy governance. These mechanisms and investments paved the way for increased energy security across the continent (*56*). To prepare for the impacts of dry years, investment in alternative power sources is required, even in locations that might not be directly affected by generation deficits. Understanding the consequences of interconnected power systems can therefore promote the design of agreements and policy interventions that foster energy security and resilience in the face of hydroclimatic change. Growing evidence motivates concerns about the increased risk of conflict and instability associated with the growing impacts of climate change (*57*). Governments and power pools must prepare for stressful contexts where local strategies do not match large-scale cost-optimal development. To confront the friction between coordinated and decentralized decision-making levels, mechanisms building on incentive schemes and side payments need to be designed. In this conundrum, our results can inform future research to ensure multiscale coordination for energy security and sustainable hydropower development within the African continent.

REFERENCES AND NOTES

1. N. S. Ouedraogo, Africa energy future: Alternative scenarios and their implications for sustainable development strategies. *Energy Policy* **106**, 457–471 (2017). doi: 10.1016/j.enpol.2017.03.021
2. I. Pappis, M. Howells, V. Sridharan, W. Usher, A. Shivakumar, F. Gardumi, E. Ramos, "Energy projections for African countries," G. Hidalgo, H. Medarac, R. González-Sánchez, I. Kougias, Eds. (JRC Technical Report JRC118432, Publications Office of the European Union, 2019). doi: 10.2760/678700
3. International Energy Agency (IEA), "Africa energy outlook 2022" (IEA, 2022); https://iea.blob.core.windows.net/assets/220b2862-33a6-47bd-81e9-00e586f4d384/AfricaEnergyOutlook2022.pdf.
4. United Nations Department of Economic and Social Affairs, "World population prospects 2022: Summary of results" (United Nations, 2022); https://www.un.org/development/desa/pd/sites/www.un.org.development.desa.pd/files/wpp2022_summary_of_results.pdf.
5. N. D. Rao, J. Min, A. Mastrucci, Energy requirements for decent living in India, Brazil and South Africa. *Nat. Energy* **4**, 1025–1032 (2019). doi: 10.1038/s41560-019-0497-9
6. F. Dalla Longa, B. van der Zwaan, Heart of light: An assessment of enhanced electricity access in Africa. *Renew. Sustain. Energy Rev.* **136**, 110399 (2021). doi: 10.1016/j.rser.2020.110399
7. C. Trisos, I. O. Adelekan, E. Totin, A. Ayanlade, J. Efitre, A. Gemeda, K. Kalaba, C. Lennard, C. Masao, Y. Mgaya, G. Ngaruiya, D. Olago, N. P. Simpson, S. Zakieldeen, "Africa" in *Climate Change 2022: Impacts, Adaptation and Vulnerability*, H.-O. Pörtner, D. C. Roberts, M. M. B. Tignor, E. Poloczanska, K. Mintenbeck, A. Alegria, M. Craig, S. Langsdorf, S. Löschke, V. Möller, A. Okem, B. Rama, Eds. (Cambridge Univ. Press, 2022), pp. 1285–1455.
8. B. van der Zwaan, T. Kober, F. Dalla Longa, A. van der Laan, G. J. Kramer, An integrated assessment of pathways for low-carbon development in Africa. *Energy Policy* **117**, 387–395 (2018). doi: 10.1016/j.enpol.2018.03.017
9. D. Puig *et al*., An action agenda for Africa's electricity sector. *Science* **373**, 616–619 (2021). doi: 10.1126/science.abh1975; pmid: 34353936
10. J. C. Steckel, J. Hilaire, M. Jakob, O. Edenhofer, Coal and carbonization in sub-Saharan Africa. *Nat. Clim. Change* **10**, 83–88 (2020). doi: 10.1038/s41558-019-0649-8
11. D. E. Gernaat, P. Bogaart, D. P. V. Vuuren, H. Biemans, R. Niessink, High-resolution assessment of global technical and economic hydropower potential. *Nat. Energy* **2**, 821–828 (2017). doi: 10.1038/s41560-017-0006-y
12. C. Zarfl, A. Lumsdon, J. Berlekamp, L. Tydecks, K. Tockner, A global boom in hydropower dam construction. *Aquat. Sci.* **77**, 161–170 (2015). doi: 10.1007/s00027-014-0377-0
13. S. Sterl *et al*., Smart renewable electricity portfolios in West Africa. *Nat. Sustain.* **3**, 710–719 (2020). doi: 10.1038/s41893-020-0539-0
14. E. G. Dimanchev, J. L. Hodge, J. E. Parsons, The role of hydropower reservoirs in deep decarbonization policy. *Energy Policy* **155**, 112369 (2021). doi: 10.1016/j.enpol.2021.112369
15. S. Sterl, D. Fadly, S. Liersch, H. Koch, W. Thiery, Linking solar and wind power in eastern Africa with operation of the Grand Ethiopian Renaissance Dam. *Nat. Energy* **6**, 407–418 (2021). doi: 10.1038/s41560-021-00799-5
16. S. Sterl *et al*., A spatiotemporal atlas of hydropower in Africa for energy modelling purposes. *Open Res. Eur.* **1**, 29 (2022). doi: 10.12688/openreseurope.13392.3
17. S. G. Yalew *et al*., Impacts of climate change on energy systems in global and regional scenarios. *Nat. Energy* **5**, 794–802 (2020). doi: 10.1038/s41560-020-0664-z
18. D. Conway, C. Dalin, W. A. Landman, T. Osborn, Hydropower plans in eastern and southern Africa increase risk of concurrent climate-related electricity supply disruption. *Nat. Energy* **2**, 946–953 (2017). doi: 10.1038/s41560-017-0037-4
19. V. Sridharan *et al*., Resilience of the Eastern African electricity sector to climate driven changes in hydropower generation. *Nat. Commun.* **10**, 302 (2019). doi: 10.1038/s41467-018-08275-7; pmid: 30655521
20. P. A. Ray *et al*., Multidimensional stress test for hydropower investments facing climate, geophysical and financial uncertainty. *Glob. Environ. Change* **48**, 168–181 (2018). doi: 10.1016/j.gloenvcha.2017.11.013
21. X. Zhang *et al*., Impacts of climate change, policy and water-energy-food nexus on hydropower development. *Renew. Energy* **116**, 827–834 (2018). doi: 10.1016/j.renene.2017.10.030
22. G. Falchetta, D. E. Gernaat, J. Hunt, S. Sterl, Hydropower dependency and climate change in sub-Saharan Africa: A nexus framework and evidence-based review. *J. Clean. Prod.* **231**, 1399–1417 (2019). doi: 10.1016/j.jclepro.2019.05.263
23. E. F. Moran, M. C. Lopez, N. Moore, N. Müller, D. W. Hyndman, Sustainable hydropower in the 21st century. *Proc. Natl. Acad. Sci. U.S.A.* **115**, 11891–11898 (2018). doi: 10.1073/pnas.1809426115; pmid: 30397145
24. A. Mayer, L. Castro-Diaz, M. C. Lopez, G. Leturcq, E. F. Moran, Is hydropower worth it? Exploring amazonian resettlement, human development and environmental costs with the Belo Monte project in Brazil. *Energy Res. Soc. Sci.* **78**, 102129 (2021). doi: 10.1016/j.erss.2021.102129
25. R. J. P. Schmitt, S. Bizzi, A. Castelletti, J. J. Opperman, G. M. Kondolf, Planning dam portfolios for low sediment trapping shows limits for sustainable hydropower in the Mekong. *Sci. Adv.* **5**, eaaw2175 (2019). doi: 10.1126/sciadv.aaw2175; pmid: 32047852
26. V. Barbarossa *et al*., Impacts of current and future large dams on the geographic range connectivity of freshwater fish worldwide. *Proc. Natl. Acad. Sci. U.S.A.* **117**, 3648–3655 (2020). doi: 10.1073/pnas.1912776117; pmid: 32015125
27. R. J. Schmitt, S. Bizzi, A. Castelletti, G. M. Kondolf, Improved trade-offs of hydropower and sand connectivity by strategic dam planning in the Mekong. *Nat. Sustain.* **1**, 96–104 (2018). doi: 10.1038/s41893-018-0022-3
28. A. Vinca, K. Riahi, A. Rowe, N. Djilali, Climate-land-energy-water nexus models across scales: Progress, gaps and best accessibility practices. *Front. Environ. Sci.* **9**, 691523 (2021). doi: 10.3389/fenvs.2021.691523
29. R. M. Almeida *et al*., Strategic planning of hydropower development: Balancing benefits and socioenvironmental costs. *Curr. Opin. Environ. Sustain.* **56**, 101175 (2022). doi: 10.1016/j.cosust.2022.101175
30. A. S. Flecker *et al*., Reducing adverse impacts of Amazon hydropower expansion. *Science* **375**, 753–760 (2022). doi: 10.1126/science.abj4017; pmid: 35175810
31. R. J. Schmitt, N. Kittner, G. M. Kondolf, D. M. Kammen, Joint strategic energy and river basin planning to reduce dam impacts on rivers in Myanmar. *Environ. Res. Lett.* **16**, 054054 (2021). doi: 10.1088/1748-9326/abe329
32. K. Siala, A. K. Chowdhury, T. D. Dang, S. Galelli, Solar energy and regional coordination as a feasible alternative to large hydropower in Southeast Asia. *Nat. Commun.* **12**, 4159 (2021). doi: 10.1038/s41467-021-24437-6; pmid: 34230491
33. A. L. Cáceres, P. Jaramillo, H. S. Matthews, C. Samaras, B. Nijssen, B., Potential hydropower contribution to mitigate climate risk and build resilience in Africa. *Nat. Clim. Change* **12**, 719–727 (2022). doi: 10.1038/s41558-022-01413-6
34. M. Giuliani, J. R. Lamontagne, M. I. Hejazi, P. M. Reed, A. Castelletti, Unintended consequences of climate change mitigation for African river basins. *Nat. Clim. Change* **12**, 187–192 (2022). doi: 10.1038/s41558-021-01262-9
35. K. Riahi *et al*., The Shared Socioeconomic Pathways and their energy, land use, and greenhouse gas emissions implications: An overview. *Glob. Environ. Change* **42**, 153–168 (2017). doi: 10.1016/j.gloenvcha.2016.05.009
36. I. Pappis *et al*., The effects of climate change mitigation strategies on the energy system of Africa and its associated water footprint. *Environ. Res. Lett.* **17**, 044048 (2022). doi: 10.1088/1748-9326/ac5ede
37. K. Frieler *et al*., Assessing the impacts of 1.5 °C global warming–simulation protocol of the Inter-Sectoral Impact Model Intercomparison Project (ISIMIP2b). *Geosci. Model Dev.* **10**, 4321–4345 (2017). doi: 10.5194/gmd-10-4321-2017
38. B. K. Sovacool, A. Gilbert, D. Nugent, An international comparative assessment of construction cost overruns for electricity infrastructure. *Energy Res. Soc. Sci.* **3**, 152–160 (2014). doi: 10.1016/j.erss.2014.07.016
39. A. K. Chowdhury *et al*., Enabling a low-carbon electricity system for Southern Africa. *Joule* **6**, 1826–1844 (2022). doi: 10.1016/j.joule.2022.06.030
40. International Renewable Energy Agency (IRENA), "Renewable power generation costs in 2020" (IRENA, 2021); https://www.irena.org/publications/2021/Jun/Renewable-Power-Costs-in-2020.
41. C. Callegari, A. Szklo, R. Schaeffer, Cost overruns and delays in energy megaprojects: How big is big enough? *Energy Policy* **114**, 211–220 (2018). doi: 10.1016/j.enpol.2017.11.059
42. A. Ansar, B. Flyvbjerg, A. Budzier, D. Lunn, Should we build more large dams? The actual costs of hydropower megaproject development. *Energy Policy* **69**, 43–56 (2014). doi: 10.1016/j.enpol.2013.10.069
43. G. M. Kondolf *et al*., Save the Mekong Delta from drowning. *Science* **376**, 583–585 (2022). doi: 10.1126/science.abm5176; pmid: 35536906
44. J. J. Opperman *et al*., Balancing renewable energy and river resources by moving from individual assessments of

hydropower projects to energy system planning. *Front. Environ. Sci.* **10**, 1036653 (2023). doi: 10.3389/fenvs.2022.1036653
45. J. A. Harrison, Y. T. Prairie, S. Mercier-Blais, C. Soued, Year-2020 global distribution and pathways of reservoir methane and carbon dioxide emissions according to the greenhouse gas from reservoirs (G-res) model. *Glob. Biogeochem. Cycles* **35**, e2020GB006888 (2021). doi: 10.1029/2020GB006888
46. G. Wohlfahrt, E. Tomelleri, A. Hammerle, The albedo-climate penalty of hydropower reservoirs. *Nat. Energy* **6**, 372–377 (2021). doi: 10.1038/s41560-021-00784-y; pmid: 33898056
47. C. Soued, J. A. Harrison, S. Mercier-Blais, Y. T. Prairie, Reservoir CO_2 and CH_4 emissions and their climate impact over the period 1900–2060. *Nat. Geosci.* **15**, 700–705 (2022). doi: 10.1038/s41561-022-01004-2
48. R. M. Almeida *et al*., Reducing greenhouse gas emissions of Amazon hydropower with strategic dam planning. *Nat. Commun.* **10**, 4281 (2019). doi: 10.1038/s41467-019-12179-5; pmid: 31537792
49. M. Li, N. He, Carbon intensity of global existing and future hydropower reservoirs. *Renew. Sustain. Energy Rev.* **162**, 112433 (2022). doi: 10.1016/j.rser.2022.112433
50. C. Llamosas, B. K. Sovacool, The future of hydropower? A systematic review of the drivers, benefits and governance dynamics of transboundary dams. *Renew. Sustain. Energy Rev.* **137**, 110495 (2021). doi: 10.1016/j.rser.2020.110495
51. P. M. Link, J. Scheffran, T. Ide, Conflict and cooperation in the water-security nexus: A global comparative analysis of river basins under climate change. *WIREs Water* **3**, 495–515 (2016). doi: 10.1002/wat2.1151
52. J. Yang *et al*., Quantifying the sustainability of water availability for the water-food-energy-ecosystem nexus in the Niger River basin. *Earths Futur.* **6**, 1292–1310 (2018). doi: 10.1029/2018EF000923; pmid: 31032375
53. K. G. Wheeler *et al*., Exploring cooperative transboundary river management strategies for the Eastern Nile Basin. *Water Resour. Res.* **54**, 9224–9254 (2018). doi: 10.1029/2017WR022149; pmid: 30774162
54. M. Zaniolo, M. Giuliani, S. Sinclair, P. Burlando, A. Castelletti, When timing matters-misdesigned dam filling impacts hydropower sustainability. *Nat. Commun.* **12**, 3056 (2021). doi: 10.1038/s41467-021-23323-5; pmid: 34031413
55. A. Azzuni, C. Breyer, Definitions and dimensions of energy security: A literature review. *WIREs Energy Environ.* **7**, e268 (2018). doi: 10.1002/wene.268
56. N. Saadi, A. Miketa, M. Howells, African Clean Energy Corridor: Regional integration to promote renewable energy fueled growth. *Energy Res. Soc. Sci.* **5**, 130–132 (2015). doi: 10.1016/j.erss.2014.12.020
57. K. J. Mach *et al*., Climate as a risk factor for armed conflict. *Nature* **571**, 193–197 (2019). doi: 10.1038/s41586-019-1300-6; pmid: 31189956
58. A. Carlino, Data in support of "Declining cost of renewables and climate change curb the need for African hydropower expansion". *Zenodo* (2023). doi: 10.5281/zenodo.7931050

ACKNOWLEDGMENTS

Part of the research was developed while A.Car. was participating in the Young Scientists Summer Program at the International Institute for Applied Systems Analysis, Laxenburg. **Funding:** European Union's Horizon 2020 grant 101003722 (GoNEXUS) (M.G., A.Cas.) **Author contributions:** Conceptualization: All authors contributed to the conceptualization; Methodology: A.Car., M.W., and M.G. A.Cas. designed the integrated modeling framework and the computational experiments. A.Car. performed data processing and ran the energy system model optimizations. C.J.C., S.S., W.T., and A.v.G. designed and performed computational experiments needed for this specific version of the African Hydropower Atlas; Visualization: A.Car.; Writing – original draft: A.Car., M.W., M.G., and A.Cas.; Writing – review and editing: All the authors reviewed and edited the manuscript. **Competing interests:** The authors declare that they have no competing interests. **Data and materials availability:** The code and the instructions for replication of the computational experiments and to produce the figures supporting the results discussed in this paper are available at Zenodo (*58*). In particular, the repository contains the final energy demands, the updated version of the African Hydropower Atlas, the scripts for data processing and input preparation for the energy system model, the energy system model with instructions to run the optimizations, and the scripts to produce the figures. **License information:** Copyright © 2023 the authors, some rights reserved; exclusive licensee American Association for the Advancement of Science. No claim to original US government works. https://www.science.org/about/science-licenses-journal-article-reuse

SUPPLEMENTARY MATERIALS

science.org/doi/10.1126/science.adf5848
Materials and Methods
Supplementary Text
Figs. S1 to S8
Table S1
References (*59*–*82*)

Submitted 2 November 2022; accepted 1 July 2023
10.1126/science.adf5848

Science
JOURNALS AAAS

Publish your research in the *Science* family of journals

The *Science* family of journals (*Science, Science Advances, Science Immunology, Science Robotics, Science Signaling*, and *Science Translational Medicine)* are among the most highly-regarded journals in the world for quality and selectivity. Our peer-reviewed journals are committed to publishing cutting-edge research, incisive scientific commentary, and insights on what's important to the scientific world at the highest standards.

Submit your research today!

Learn more at **Science.org/journals**

RESEARCH ARTICLE SUMMARY

MELANOGENESIS

A genome-wide genetic screen uncovers determinants of human pigmentation

Vivek K. Bajpai, Tomek Swigut, Jaaved Mohammed†, Sahin Naqvi†, Martin Arreola, Josh Tycko, Tayne C. Kim, Jonathan K. Pritchard, Michael C. Bassik, Joanna Wysocka*

INTRODUCTION: Melanin is a heterogenous polymer found across life forms and has roles in pigmentation, environmental adaptation, and species survival. In humans, melanin synthesis is compartmentalized within a subcellular organelle called the melanosome, which is present in specialized pigment cells called melanocytes. Variable melanin synthesis within melanosomes results in variation in skin, hair, and eye color in human populations, whereas perturbations in melanogenesis are associated with diseases.

RATIONALE: Melanin's particular physicochemical properties such as high refractive index determine its optical properties. We reasoned that an accumulation of melanin within melanosomes would change melanocytes' light-scattering properties. Thus, measuring light-scatter index with flow cytometry could serve as a proxy for cellular melanin content of live pigment cells and could be used as an assay for a CRISPR-Cas9–based genetic screen to identify factors that govern melanin synthesis within melanosomes.

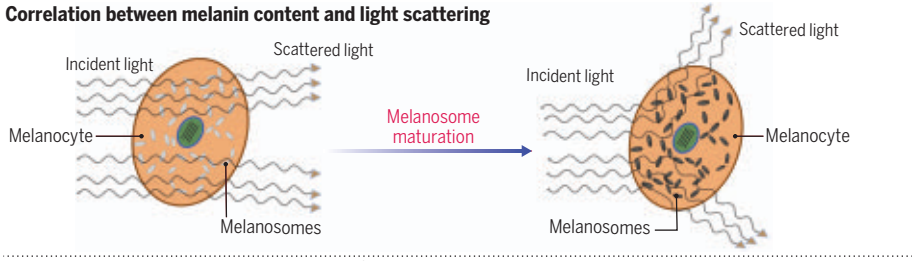

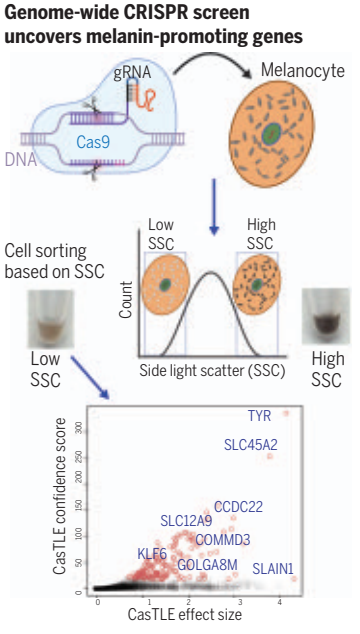

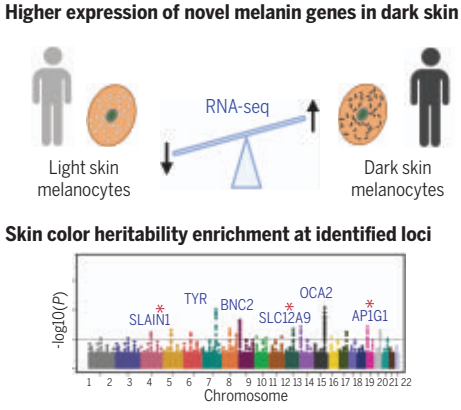

Genetic screen finds previously unidentified loci for human melanogenesis. By exploiting melanin's light-scattering properties, we conducted a genome-wide screen and uncovered genes regulating melanin content and hence, melanogenesis, in human cells. These melanin-promoting genes are expressed at higher levels in darkly pigmented melanocytes and show association with pigmentation in human populations. *KLF6* deletion reduces melanogenesis and pigmentation in vivo, whereas *COMMD3* exerts melanogenic effect by modulating melanosomal pH and tyrosinase (TYR) activity.

RESULTS: Using pigmented cell lines and human melanocytes at different stages of melanosomal maturation, we established a quantitative linear relationship between melanin levels and light scattering measured as side scatter (SSC) through flow cytometry. We further demonstrated that SSC changes capture dynamic shifts in melanin levels within melanosomes. Using SSC as a proxy for melanin content, we then conducted a genome-wide CRISPR-Cas9 genetic screen to systematically uncover regulators of melanogenesis. Our screen identified both previously known pigmentation genes and 135 previously unidentified hits that we refer to as melanin-promoting genes, and whose deletion resulted in decreased melanin production. The melanin-promoting genes are involved in diverse biological pathways such as transcription regulation, RNA processing, and endosomal transport, among others. Consistent with their melanin-promoting role, the expression of the majority of our screen hits is elevated in darkly pigmented, compared with lightly pigmented, human melanocytes. Our analyses revealed that select melanin-promoting genes are associated with skin color variation and show evidence of local adaptation in human populations. We further characterized the products of two genes, *KLF6* and *COMMD3*, for their role in melanogenesis. We showed that deletion of the transcription factor KLF6 inhibits melanosome maturation and reduces pigmentation in vitro and in vivo, whereas COMMD3, a protein involved in endosomal transport, regulates melanosomal pH. Loss of COMMD3 leads to a decreased melanosomal pH, which in turn perturbs melanosome maturation; this effect can be reversed by chemicals that raise the melanosomal pH.

CONCLUSION: Our work demonstrates that changes in melanin content can be robustly quantified by measuring the side scattering property of live pigment cells. By exploiting this relationship in the context of a genetic screen, we identified melanin-promoting genes with diverse biological functions. By focusing on specific previously unidentified candidates, we implicated a new cargo recycling pathway in melanosome function and identified a transcription factor involved in melanosome maturation. Our work provides a rich resource for further studies of melanogenesis and its relationship with skin color variation and human diseases. ■

The list of author affiliations is available in the full article online.
*Corresponding author. Email: wysocka@stanford.edu
Cite this article as V. K. Bajpai *et al.*, *Science* **381**, eade6289 (2023). DOI: 10.1126/science.ade6289.
†These authors contributed equally to this work.

READ THE FULL ARTICLE AT
https://doi.org/10.1126/science.ade6289

RESEARCH ARTICLE

MELANOGENESIS

A genome-wide genetic screen uncovers determinants of human pigmentation

Vivek K. Bajpai[1,2,3], Tomek Swigut[1], Jaaved Mohammed[1,2]†, Sahin Naqvi[1,2,4]†, Martin Arreola[2], Josh Tycko[4], Tayne C. Kim[1,2], Jonathan K. Pritchard[4,5], Michael C. Bassik[4,6,7], Joanna Wysocka[1,2,8,9]*

Skin color, one of the most diverse human traits, is determined by the quantity, type, and distribution of melanin. In this study, we leveraged the light-scattering properties of melanin to conduct a genome-wide screen for regulators of melanogenesis. We identified 169 functionally diverse genes that converge on melanosome biogenesis, endosomal transport, and gene regulation, of which 135 represented previously unknown associations with pigmentation. In agreement with their melanin-promoting function, the majority of screen hits were up-regulated in melanocytes from darkly pigmented individuals. We further unraveled functions of KLF6 as a transcription factor that regulates melanosome maturation and pigmentation in vivo, and of the endosomal trafficking protein COMMD3 in modulating melanosomal pH. Our study reveals a plethora of melanin-promoting genes, with broad implications for human variation, cell biology, and medicine.

Skin and hair color are genetically derived traits that are highly variable between and within human populations and determined by the quantity, type, and distribution of melanin (*1*–*3*). Melanocytes developmentally originate from the embryonic neural crest cells, reside in the epidermis, and synthesize melanin within subcellular lysosome-related organelles called melanosomes (*4*, *5*). Melanosomes undergo characteristic stages of maturation during melanin synthesis in which stage I melanosomes contain intraluminal vesicles, stage II melanosomes deposit PMEL fibrils on which melanogenesis takes place, and stage III and IV melanosomes represent partially and fully melanized melanosomes, respectively (fig. S1A) (*4*, *5*). Maturing melanosomes are transported extracellularly to the surrounding epidermal keratinocytes, which results in skin and hair pigmentation (fig. S1A) (*1*–*5*).

Key insights into human pigmentation have come from the mapping of genes involved in hypo- and hyperpigmentation diseases, and from candidate gene and genome-wide association studies (GWASs) of normal-range skin and hair color variation in human populations (*1*–*3*). Furthermore, studies in model organisms—in particular, those of mouse coat color—have revealed genes and pathways involved in pigmentation, many of which converge on the melanin synthesis pathway (*1*–*3*, *6*). Nonetheless, GWASs that have estimated the cumulative contribution of major skin color genetic variants identified in a given human population could only explain a relatively small (23 to 35%) fraction of skin color variation in the analyzed population (*2*, *7*–*10*). Similarly, using a GWAS summary statistic-based method (*11*), we estimated that only 15.2% of skin color variation in white British individuals from the UK Biobank (UKBB) could be explained by the set of genomic regions corresponding to the genome-wide significant skin color GWAS hits from this population. Taken together, these observations suggest that although key loci that control pigmentation in our species have been found, other contributing loci remain to be discovered.

Melanin is a heterogeneous and structurally ill-defined biopolymer (*12*) that encompasses two forms, namely black or brown eumelanin and red or yellow pheomelanin. The quantity and type of produced melanin determines its physicochemical properties such as high refractive index, which forms the basis of melanin's characteristic light-absorbance and scattering properties (*12*). These are thought to be critical for protecting the skin from sun exposure-related damage. Light scattering measured as a side-scatter (SSC, 90° scatter) parameter in flow cytometry reflects the internal complexity of the cells (*13*). We investigated the extent to which changes in cellular melanin content influence light scattering measured as SSC and whether SSC can be used to capture dynamic changes in the melanin levels upon inducing genetic perturbations. In this study, we demonstrate that cellular melanin concentration indeed determines light-scattering properties of pigment cells. Taking advantage of this feature and using SSC as a proxy for melanin levels, we performed a CRISPR-Cas9–based genetic screen to identify regulators of human pigmentation, which led to the discovery of 169 candidate genes with promelanogenic function. We validated a subset of the screen hits, confirming their transcriptional up-regulation in primary melanocytes from the dark-skin individuals and their involvement in different stages of melanosome biogenesis. Furthermore, through follow-up functional studies, we uncovered previously uncharacterized roles for transcription factor KLF6 in melanosome maturation and pigmentation in vivo, and a function for the endosomal trafficking protein COMMD3 in modulating melanosomal pH.

Melanin content of the pigment cells can be reliably monitored by measuring their side-scattering properties

To establish a link between melanin content and SSC, we used two different cellular models of human melanogenesis. First, we investigated the relationship between SSC and pigmentation in a developmental context by modeling melanogenesis by using pluripotent stem cells (fig. S1B) (*14*). To this end, we differentiated *SOX10*::*GFP*-reporter H9 human embryonic stem cells to SOX10$^+$ neural crest cells, then toward unpigmented melanocyte precursors called melanoblasts, and last into mature pigmented melanocytes (fig. S1, C and D). During the maturation of melanoblasts to melanocytes, the expression of melanogenic genes (e.g., *OCA2*, *TYR*, *SLC45A2*, *OA1*, and *PMEL*) was strongly up-regulated (fig. S1G), melanin content increased (fig. S1, E, F, and H), and pigmented melanosomes gradually accumulated (Fig. 1A and fig. S1H). We observed that an increase in melanin content was accompanied by an increase in SSC (Fig. 1, B and C) and that there was a strong linear correlation between SSC and melanin content (coefficient of determination, $R^2 = 0.82$; $P = 1.88 \times 10^{-6}$) (Fig. 1C).

In an orthogonal approach to establishing the relationship between SSC and pigmentation, we used the MNT-1 melanoma cell line, which is transcriptionally similar to normal primary human melanocytes (*15*) and has been previously used as a model to study melanogenesis (*16*–*19*). Using several independent RNA guides, we deleted the key melanogenic gene tyrosinase (*TYR*) in MNT-1 cells, which resulted in loss of pigmentation and decreased melanin absorbance measurements (Fig. 1, D and G, and fig. S1I). Loss of melanin was accompanied by a significant decrease in SSC (Fig. 1, E and F). Transmission electron microscopy (TEM) images of *TYR* mutant cells

[1]Department of Chemical and Systems Biology, Stanford University School of Medicine, Stanford, CA 94305, USA. [2]Institute for Stem Cell Biology and Regenerative Medicine, Stanford University School of Medicine, Stanford, CA 94305, USA. [3]School of Chemical, Biological, and Materials Engineering, The University of Oklahoma, Norman, OK 73019, USA. [4]Department of Genetics, Stanford University, Stanford, CA 94305, USA. [5]Department of Biology, Stanford University, Stanford, CA 94305, USA. [6]Chemistry, Engineering, and Medicine for Human Health (ChEM-H), Stanford University, Stanford, CA 94305, USA. [7]Program in Cancer Biology, Stanford University School of Medicine, Stanford, CA 94305, USA. [8]Department of Developmental Biology, Stanford University School of Medicine, Stanford, CA 94305, USA. [9]Howard Hughes Medical Institute, Stanford University School of Medicine, Stanford, CA 94305, USA.
*Corresponding author. Email: wysocka@stanford.edu
†These authors contributed equally to this work.

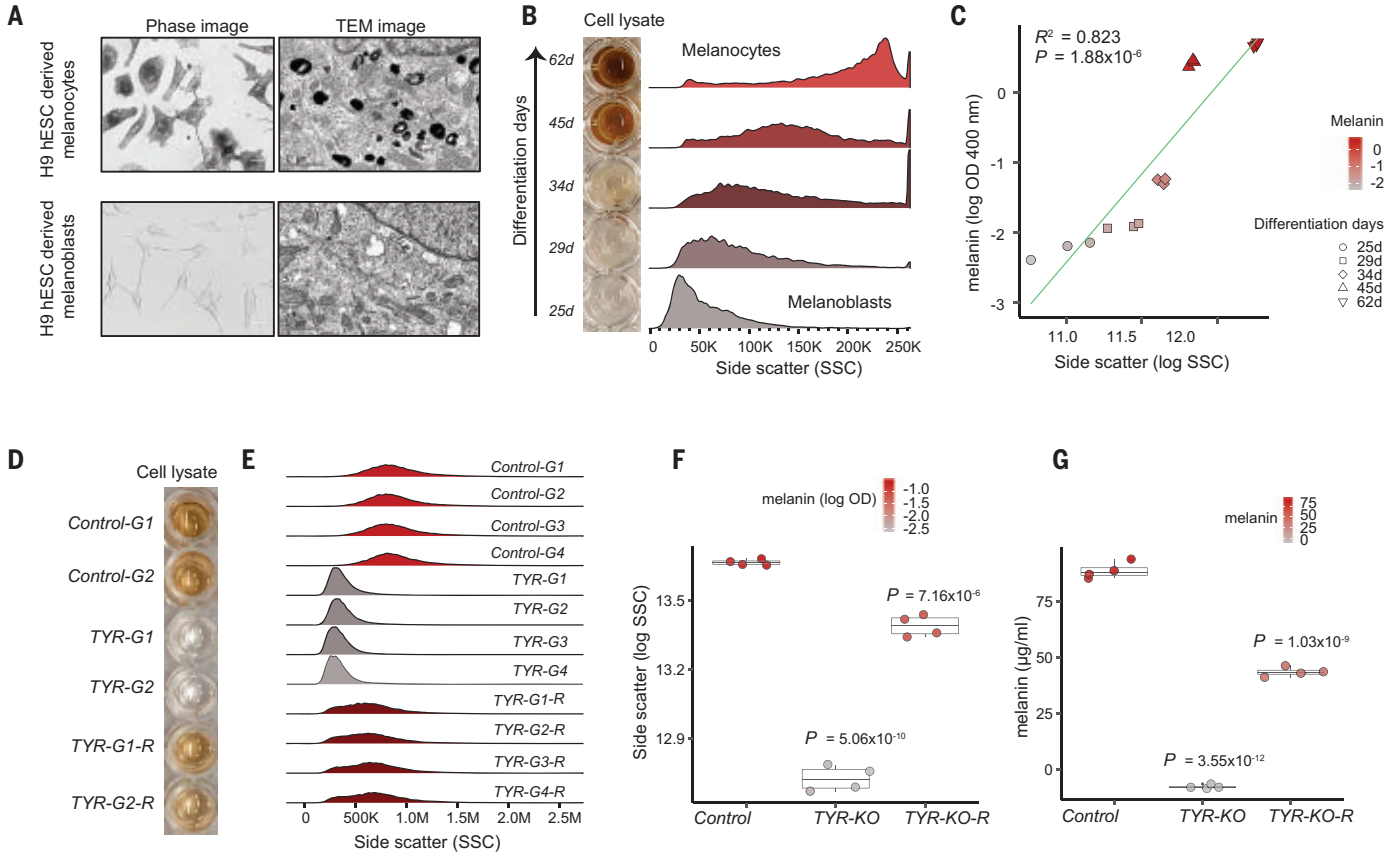

Fig. 1. Melanin concentration determines light-scattering property of pigment cells. (**A**) Differentiation of H9 human embryonic stem cell (hESC)–derived melanoblasts (bottom) into melanocytes (top) results in increased melanized stage III to IV melanosomes as shown by phase and transmission electron microscopy (n = 3 independent differentiations). Scale bars; phase images, 25 μm; TEM images, 1 μm. (**B**) Increased melanin concentration during melanocyte differentiation from hESC (days of differentiation are indicated on the left) is accompanied by an increase in light scattering as measured by the SSC parameter of flow cytometer. (**C**) Relationship between melanin (log OD 400 nm) and SSC as modeled by linear regression. R^2 = 0.823, P = 1.88 × 10^{-6}. (**D**) CRISPR-Cas9–mediated loss of *TYR* gene makes pigmented MNT-1 melanoma cells amelanotic and reexpression of *TYR* transgene recovers the pigmentation (n = 4 sgRNAs treatments). Cell lysates from two representative delete-and-rescue experiments are shown. (**E**) *TYR* loss significantly reduces the SSC, and *TYR* re-expression restores it. Four different sgRNAs against *TYR* and control sgRNAs are labeled as G1, G2, G3 and G4. (**F**) Boxplot showing SSC (log SSC) changes in response to *TYR* loss and rescue in comparison with control-edited cells. The color within the dots corresponds to total melanin (log OD at 400 nm). Box plots show median and IQR; whiskers are 1.5x interquartile range (IQR). Significance was tested for control, TYR-KO, and TYR-KO-R groups with analysis of variance (ANOVA), followed by a two-sided Welch t test with Benjamini and Hochberg (BH) correction. P values shown are relative to control. (**G**) Total melanin concentration calculated for loss and rescue of *TYR* (tyrosinase) experiment (n = 4 sgRNAs treatment). Box plots show median melanin concentration (micrograms per milliliter) and IQR; whiskers are 1.5x IQR. Significance was tested for four sgRNA and the TYR rescue treatment with ANOVA, followed by a two-sided Welch t-test with BH correction. P values shown are relative to control.

showed a preponderance of stage II unpigmented melanosomes and a lack of stage III or IV melanized melanosomes, which thus provided evidence that the melanosome maturation state is directly linked to changes in SSC (fig. S1I). Furthermore, overexpression of wild-type *TYR* restored both pigmentation and SSC (Fig. 1, D to G). Together, these experiments establish that perturbations in the melanosome biogenesis of pigment cells can be monitored by measuring SSC.

A genome-wide CRISPR screen to identify melanin-promoting genes

We reasoned that the close correlation between melanin content and SSC could be used as a paradigm for a CRISPR-Cas9 genetic screen, in which the loss of genes important for melanosome biogenesis and maturation would result in diminished SSC (Fig. 2A). We generated a clonal MNT-1 cell line that, when induced, expresses SpCas9 nuclease upon doxycycline treatment and infected it with a genome-wide lentiviral single guide RNA (sgRNA) library (*20*) (Cas9-MNT-1 cell line; fig. S2A). After puromycin selection to kill non-infected cells, expression of Cas9 was induced to carry out gene-editing, and after 2 weeks, cells from the top and bottom 10% of the SSC distribution were sorted with fluorescence-activated cell sorting (FACS) (Fig. 2, A and B). As we expected, the low SSC fraction was enriched for hypopigmented cells relative to the high SSC fraction (Fig. 2B). Genomic DNA was subsequently isolated, and the frequencies of sgRNAs in both populations (low and high SSC) were measured with deep sequencing and analyzed by using the Cas9 high-throughput maximum likelihood estimator (CasTLE) algorithm, which provides a confidence score for the effect of each gene (*21*). Analysis of CasTLE scores in two independent biological replicates (i.e., independent sgRNA infections and FACS sorting after Cas9 induction) revealed good concordance (R^2 = 0.59, P < 2.2 × 10^{-16}) between the replicates (fig. S2B). We focused our subsequent analysis on genes with a positive CasTLE effect (those whose loss corresponded

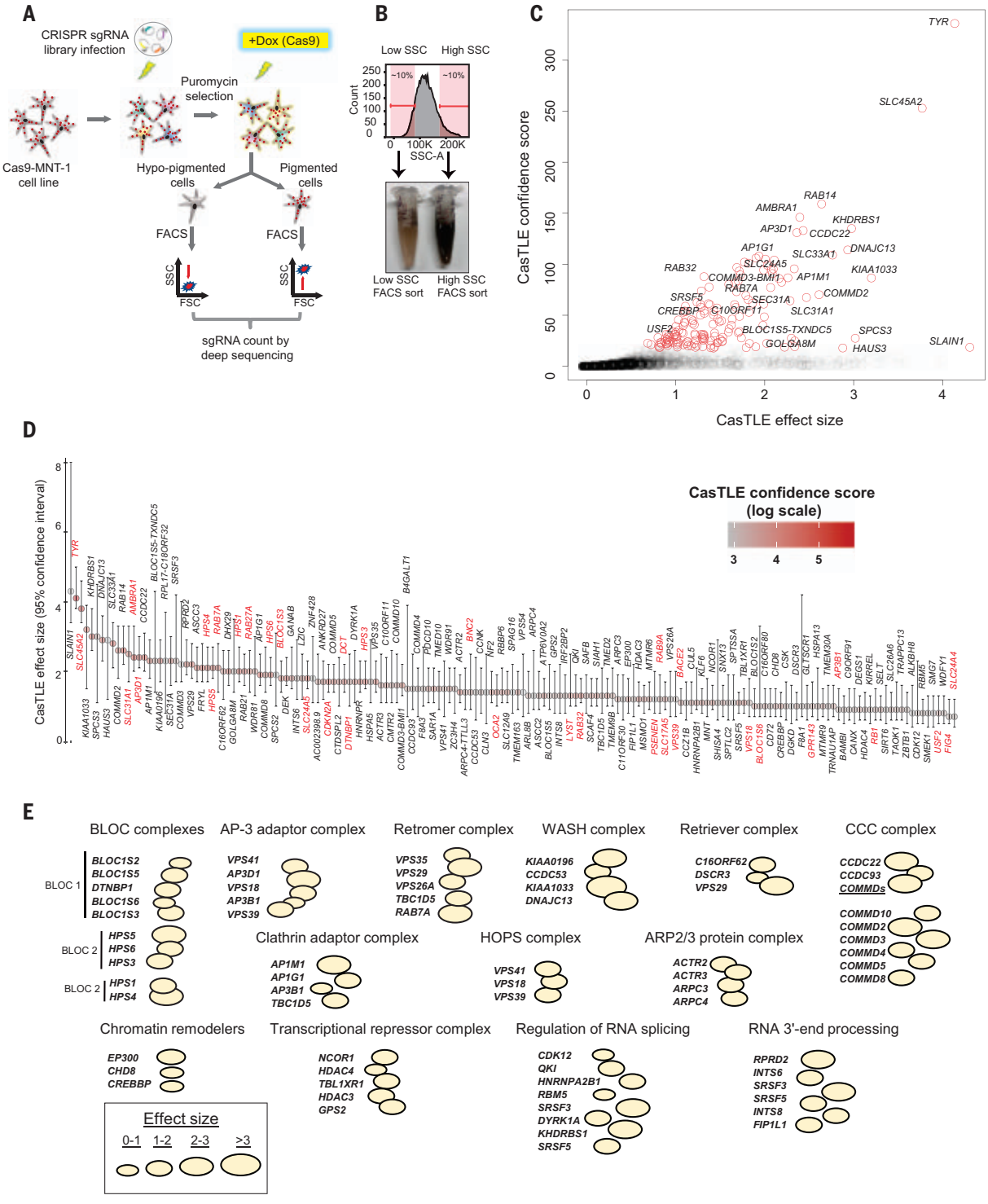

Fig. 2. Genome-wide CRISPR-Cas9 screen for regulators of human melanogenesis. (**A**) Schematic of the screen design. (**B**) FACS cell sorting on low and high SSC enriches hypopigmented and hyperpigmented cells, respectively. (**C**) CasTLE likelihood ratio test analysis of two independent genome-wide pigmentation screens. Genes at <10% FDR cutoff are indicated with brown circles. (**D**) The maximum effect size (center value) estimated with CasTLE from two independent genome-wide pigmentation screens with 10 independent sgRNAs per gene. Bars, 95% confidence interval. Melanogenesis regulators as sorted by CasTLE effect size. The colors indicate CasTLE confidence score (log scale). Previously known pigmentation genes are highlighted in red. (**E**) Classification of screen hits on the basis of biological functions and presence in common macromolecular complexes. Bubble size indicates CasTLE effect size for the respective gene in the screen. Bubbles touching each other indicates that the proteins have been reported to make a physical protein complex, with the name of the complex and/or associated molecular function indicated on top.

to a reduction in SSC) and which are therefore predicted to have a melanin-promoting function. Although our screen also identified genes with a negative CasTLE effect (e.g., those enriched in the high-SSC sorted fraction), we reasoned that gain of SSC may be more challenging to interpret because it can be affected by other factors that increase cellular granularity (*22*).

Our screen identified 169 putative melanin-promoting genes (i.e., genes whose deletion was associated with diminished SSC) in common between the two biological replicates at <10% false discovery rate (FDR) (Fig. 2, C and D, and table S1). We cross-referenced our 169 screen hits with a curated list of 650 pigmentation-associated genes (*6*). Notably, 34 of the 169 screen hits corresponded to known melanogenic genes (e.g., *TYR*, *OCA2*, *SLC45A2*, *DCT*, *SLC24A5*, *HPS1*, *HPS3-6*, *LYST*, *AP3D1*, and others, highlighted in red in Fig. 2D), whereas 135 (79.9%) screen hits represented previously unidentified candidates for regulation of melanogenesis.

At lower statistical confidence, between 10 to 20% FDR, the screen discovered an additional 75 hits (table S1), which included several known pigmentation genes (e.g., *MYO5A*, *ATP7A*, and *RAB1A*). This suggested that the 10% FDR cutoff we selected for our analysis is conservative and may miss additional genuine hits. Our screening paradigm had several limitations that precluded us from recovering all previously known pigmentation genes. First, it focused on measurement of melanin content of differentiated pigmented cells; therefore, genes that affect pigmentation by contributing to the developmental process of melanocyte lineage formation, but not to melanin content in mature melanocytes, would have been missed in our screen. Second, genes that are essential in a particular cell type are frequent dropouts in genetic screens (*23*–*25*). Given that key pigmentation-associated genes such as *MITF*, *SOX10*, and *PAX3* are essential for melanocyte survival (*26*–*29*), this may potentially explain why these genes were not identified in our screen; future screens for genes essential in MNT-1 cells may help to clarify this. And third, our screen focused on genes with melanin-promoting function and therefore missed suppressors of melanogenesis, such as *TPCN2* (*30*, *31*) or *MFSD12* (*8*, *32*).

Despite these noted limitations, our screen uncovered many genes that are known to regulate steps of melanosome maturation and whose functional loss leads to oculocutaneous albinisms (OCAs) and ocular albinism (OA) syndromes in humans, such as *TYR* (*OCA1*), *OCA2*, *SLC45A2* (*OCA4*), *SLC24A5* (*OCA6*), *LRMDA* (*OCA7*), *DCT* (*OCA8*), and *GPR143* (*OA*). These results further highlight that our screening approach captures genes involved in melanosome biogenesis.

Pigmentation screen hits regulate melanosome biogenesis and maturation through diverse biological mechanisms

Gene ontology analysis of screen hits revealed enrichment for melanosome organization, pigment granule organization, vesicle organization, and intracellular transport (fig. S3A and table S2). The screen hits were not only enriched for previously known melanosome biogenesis– or maturation-related factors such as BLOC (biogenesis of lysosomal organelles complex) and AP-3 adaptor complexes (*4*, *5*) but also encompassed genes whose products form molecular complexes implicated in endosomal recycling [such as retromer, retriever, WASH, ARP2/3, and CCC (COMMD-CCDC22-CCDC93) complexes] (*33*–*35*) (Fig. 2E, fig. S3B, and table S2). These results emphasize the role of endosome recycling pathways in melanosome biogenesis and human pigmentation. Screen hits also included genes regulating chromatin modification and remodeling, as well as RNA splicing and processing, which suggests that both transcriptional and posttranscriptional modes of gene regulation contribute toward melanogenesis (Fig. 2E).

67.7% of screen hits are more highly expressed in primary melanocytes from darkly pigmented individuals

We reasoned that because our screen has uncovered candidate melanin-promoting genes, at least some of these genes should be differentially expressed in melanocytes isolated from individuals with dark versus light skin color. These differences do not necessarily imply genetically encoded differences in expression, but rather that they may arise as a consequence of different rates of melanogenesis, in turn leading to a differential expression of melanogenesis-associated genes. To survey transcriptomes of diversely pigmented human melanocytes, we obtained foreskin tissues from 33 newborn males of diverse skin color and isolated primary melanocytes from them (Fig. 3A and table S3). Foreskin tissues were histologically analyzed for melanin presence in situ with Fontana-Masson staining, which confirmed the presence of differential melanin content in the epidermis of diversely pigmented individuals (Fig. 3A). Isolated melanocytes all expressed key lineage transcription factor MITF and melanosome specific marker PMEL but had distinct pigmentation levels (Fig. 3B). We spectrophotometrically quantified total melanin content of isolated melanocytes (Fig. 3C and fig. S1F). As we expected, melanin content correlated with the parent-reported donor ancestry, with melanocytes derived from African-American donors showing higher melanin content, followed by Asian and European donors, respectively (Fig. 3C and table S3).

Next, we performed RNA sequencing (RNA-seq) on isolated diversely pigmented melanocyte samples (n = 30) (table S4). Principal components analysis (PCA) of RNA-seq results demonstrated that gene-expression divergence correlated well with measured melanin content of the cells, even more so than reported ethnicity (Fig. 3D). We then calculated Spearman's rank correlation coefficients (ρ) between expression (TPM, transcripts per kilobase million) of genes corresponding to our screen hits and melanin content [optical density (OD), 400 nm]. Out of the total 169 screen hits, 158 genes had measurable expression in all melanocytes and were therefore used for these calculations. We found that the expression of 107 hits (out of 158; 67.7%) was significantly positively correlated (q value < 0.1) with melanin, 12 genes were negatively correlated (q value < 0.1), and 39 were not significant (q value > 0.1) (Fig. 3, E and F, fig. S4, and table S5), demonstrating that the majority of screen hits are more highly expressed in darkly pigmented melanocytes. The key known skin variation genes picked up by our screen, such as *OCA2* and *SLC24A5*, as well as genes encoding BLOC and AP complexes involved in melanogenesis, showed significant up-regulation in dark melanocytes (with a notable exception of BLOC-2 subunit HPS6, which showed negative correlation) (Fig. 3E, fig. S4, and table S5). Notably, endosomal recycling complexes identified in this study—including components of retromer, retriever, WASH, ARP2/3, and CCC complexes—were also differentially expressed between lightly and darkly pigmented melanocytes (figs. S4 and S5). At the gene regulatory level, genes that encode chromatin remodelers and modifiers (*EP300*, *CHD8*, and *CREBBP*), transcriptional repressor complex (*NCOR1*, *HDAC4*, and *TBL1XR1*), alternative mRNA splicing regulators (*QKI*, *HNRNPA2B1*, and *DYRK1A*) and RNA 3′-end–processing factors (*INTS6*, *INTS8*, and *FIP1L1*) were all significantly up-regulated in dark melanocytes (Fig. 3, E and F, and figs. S4 and S5). Altogether, these results further support the connection between identified screen hits and pigment levels in primary melanocytes isolated from human skin.

Differences in expression of select screen hits may contribute to skin color variation in humans

As discussed previously, the differential expression of the majority of screen hits between darkly and lightly pigmented individuals is likely a secondary consequence of their involvement in sustaining a high rate of melanin synthesis, rather than being indicative of the role in driving skin color variation in humans. Nonetheless, given that one of the key mechanisms by which phenotypic variation arises is through gene regulatory divergence (*36*, *37*), it is likely that for select loci identified in our screen, divergence in gene expression is indeed genetically encoded and may contribute to skin color variation. To provide a proof of

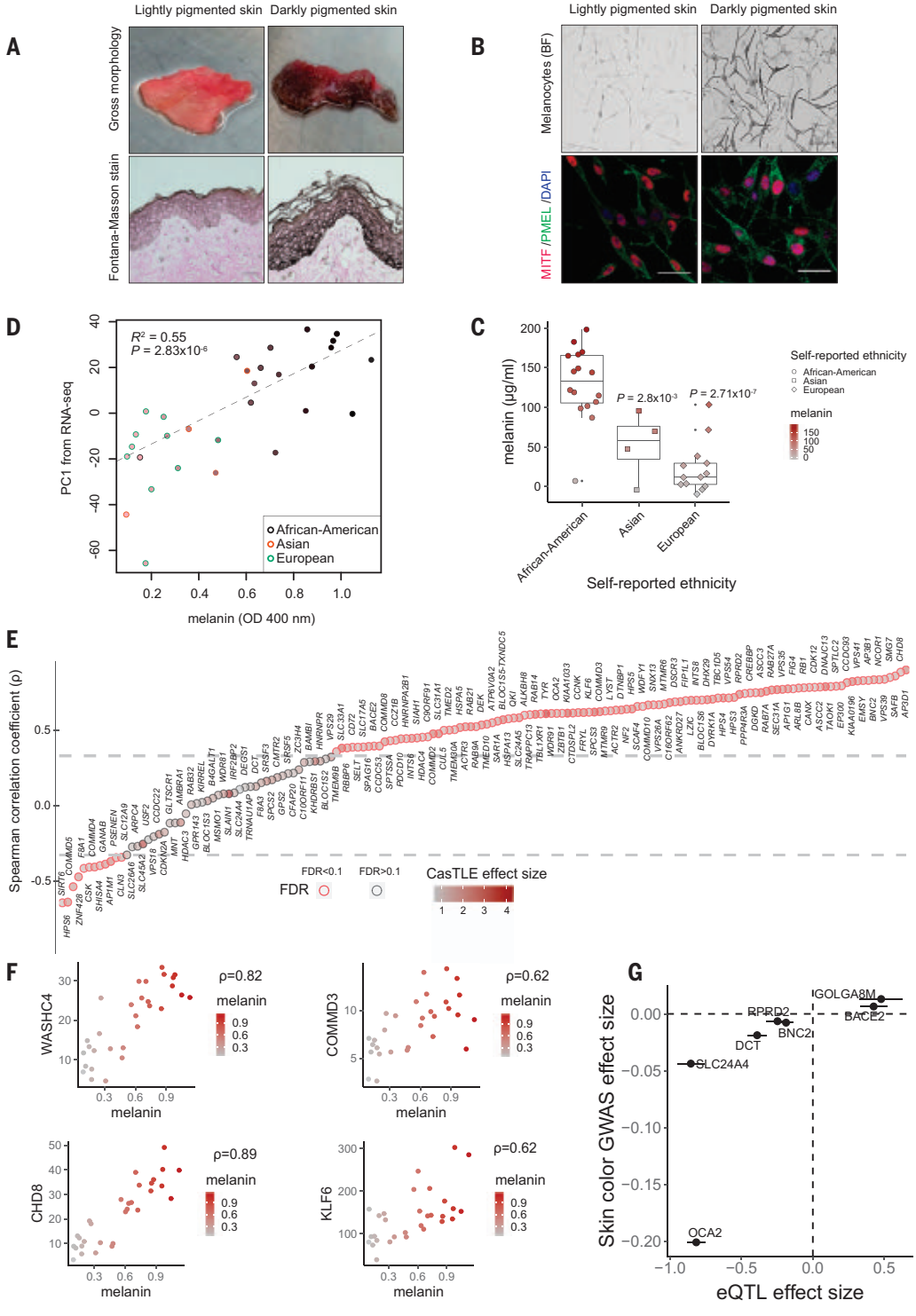

Fig. 3. Pigmentation screen hits are differentially expressed in melanocytes of distinctly pigmented individuals. (**A**) Gross morphology of foreskin tissue obtained from diversely pigmented human donors. Fontana-Masson (FM) staining shows melanin pigment (black) in epidermis. (**B**) Brightfield (BF) and immunofluorescence (IF) images of melanocytes confirm differential pigment levels and presence of melanocyte markers MITF (red) and PMEL (green). DNA, blue. (**C**) Melanin quantification of melanocytes derived from diversely pigmented individuals. Box plots show median; whiskers are 1.5x IQR. Significance tested with ANOVA followed by two-sided Welch *t*-test with BH correction. (**D**) Correlation between RNA-seq gene expression profiles and melanin content of melanocytes. Plotted is melanin concentration (OD 400 nm) versus first principal component of the RNA-seq analysis from the same melanocytes. Ethnicity is indicated by the color of the outline of the plotting symbol. Fill color within each point represents measured melanin content. (**E**) Spearman's ρ comparing relationship between TPM of candidate screen hits with melanin measurements in 30 melanocyte samples of diverse skin color. The intensity of brown color within each point indicates CasTLE effect size. Horizontal lines indicate (−0.33, 0.33) correlation coefficient cutoffs at <10% FDR. (**F**) Spearman's ρ for selected CRISPR screen hits, with each point representing measurements from one human donor. Plotted is melanin OD at 400 nm (ordinate) versus RNA-seq expression level (TPM, abscissa). (**G**) Concordant effects of melanocyte eQTL and skin color GWAS for select melanin-promoting gene hits. For each of the indicated genes, the effect of a SNP's alternate allele on that gene's expression (defined as the slope of the eQTL; *x* axis) is plotted against the same allele's effect on skin color from GWAS in white British individuals (β value from GWAS, where positive is associated with darker skin). Points and bars represent mean estimate ± standard error. Scale bars, (A) and (B), 25 µm.

principle for this hypothesis, we first asked whether the pigmentation screen hits are enriched for skin color heritability. We applied stratified linkage disequilibrium score regression (S-LDSC) (*38*) to assess skin color heritability enrichment in the vicinity (within 100 kb) of our screen hits by using publicly available summary statistics from a GWAS of individuals of white British ancestry in the UKBB. Skin color in this GWAS was represented as a self-reported, categorical trait (details of categories can be found in the supplementary materials, materials and methods), with negative GWAS effect sizes indicating a greater fraction of individuals self-reporting with lighter skin color categories. The 169 screen hits (at FDR < 10%) were significantly enriched for skin color heritability (fold-enrichment 9.61; standard error 3.80; $P = 3.11 \times 10^{-2}$) in comparison with all nonhits (FDR > 10%) (fold-enrichment 1.15; standard error

0.073; $P = 3.37 \times 10^{-2}$) (fig. S6A). Next, we collected lists of genes implicated by various GWASs, including (i) all genes annotated to pigmentation or skin color–associated single-nucleotide polymorphisms (SNPs) in the National Center for Biotechnology Information (NCBI)–European Bioinformatics Institute (EBI) GWAS catalog, representing a mix of ancestries (*39*); (ii) genes nearby lead SNPs associated with skin color variation in white individuals from the UKBB; and (iii) genes nearby lead SNPs associated with pigmentation variation in African individuals (*8*). Relative to all other genes assayed, screen hits were strongly enriched for pigmentation genes across the three datasets (table S6). For example, 8 of 169 hits lie closest to one of the top pigmentation-associated SNPs in Africans (*8*), compared with 322 of 20,044 nonhits (two-sided Fisher's odds ratio 3.19; $P = 5.14 \times 10^{-3}$). Similar enrichments were observed for genes in the GWAS catalog (two-sided Fisher's odds ratio 11.3; $P = 6.13 \times 10^{-6}$) or the UKBB (two-sided Fisher's odds ratio 5.6; $P = 2.75 \times 10^{-5}$). Although some of the screen hits associated with GWAS peaks have known roles in pigmentation, others are newly identified. Of the screen hits in vicinity of the lead GWAS signals in the UKBB, three (*AP1G1*, *SLC12A9*, and *SLAIN1*) represent previously unknown associations with melanogenesis (Fig. S6B).

We further reasoned that if the expression levels of our screen hits causally affect pigmentation, then genetic variants that are quantitatively associated with increased expression (eQTLs) should also be associated with darker skin color in GWAS, and conversely, variants associated with decreased expression should be associated with lighter skin color. To this end, we identified the most significant and closest eQTL (with P value < 0.01) for each screen-hit gene by using a published melanocyte eQTL dataset (obtained mostly from European-ancestry skin samples) (*40*). We then correlated the eQTL effect of the alternate allele with the same allele's effect on skin color in GWAS from white British individuals in the UKBB (also requiring GWAS P value < 0.01). These filtering steps left only seven screen hits with both eQTL and GWAS effect sizes, but notably, the direction of the eQTL and GWAS effects agreed for all seven of these genes (binomial P value = 0.01563). Specifically, the expression-increasing alleles for *BACE2* and *GOLGA8M* are associated with darker skin color (positive on y axis means darker skin color) (Fig. 3G). *GOLGA8M* sits between the *OCA2-HERC2* locus and *APBA2* gene. A previous GWAS study (*9*) uncovered the association of noncoding variants in the intronic region of the *APBA2* with human skin color. Although the authors suggested *OCA2*—located ~1 Mb away—as a candidate target gene regulated by these variants, the association of *GOLGA8M* with melanogenesis in our screen along with the identification of the concordant eQTL and GWAS signals at the locus suggests that *GOLGA8M* should also be considered as a potential target of the skin color–associated noncoding variants in the *APBA2* introns. Conversely, expression-decreasing alleles for *OCA2*, *BNC2*, *RPRD2*, *DCT*, and *SLC24A4* are associated with lighter skin color. These results indicate that variable expression of select screen hits may contribute to the skin color variation in humans.

Select pigmentation screen hits display signatures of adaptive evolution in human populations

Skin color is thought to be under strong natural selection (*3*). To identify genes among our screen hits that might have undergone a recent adaptation for skin pigmentation variation among human populations, we used a tree-based statistic called population branch statistic (PBS) (*41*). In a three-population tree topology, PBS measures the change in allele frequency in the history of a target population since its divergence from the other two populations, with larger branch-specific PBS indicating population-specific, adaptively evolved SNPs. We computed genome-wide PBS per SNP using the African, European, and East Asian populations from the 1000 Genomes Reference Panel and created Manhattan plots of PBSs in the African and European target populations of this three-population tree (fig. S6, C and D).

Given that SNPs in the gene-regulatory regions are a prime target for selection (*42*, *43*), we included ± 100 Kb regions flanking the gene bodies of the screen hits in our analysis. For these loci (fig. S6, C and D, orange), we computed PBS statistics for the European, African, and East Asian populations of the 1000 Genomes Reference Panel (fig. S6, C and D, and tables S7 and S8). As shown in the Manhattan plot (fig. S6C) for the African population, several SNPs within these genic loci have PBS scores that are larger than the top 0.01% quantile of genome-wide PBS scores (orange dots above the dashed red line), which include *OCA2*, *VPS39*, *CDKN2A*, and *BACE2* (fig. S6C and table S7). In the more relaxed setting, several melanin-promoting genic loci (i.e., *COMMD3*, *SLC33A1*, *MTMR9*, and *TMED2*) SNPs are larger than the top 0.1% quantile of genome-wide PBS scores (fig. S6C, orange dots above the blue dotted line, and table S7). Similarly, European PBS scores, which were also computed in the African–European–East Asian trio, showed *SLC45A2*, *SLC24A5*, *OCA2*, *BNC2*, *LRMDA* (*44*), and *GOLGA8M* loci SNPs with PBS scores larger than the top 0.01% quantile of genome-wide threshold (fig. S6D and table S8). To our knowledge, this is the first time that *LRMDA* (*c10orf11*/*OCA7*), a locus previously associated with eyebrow color in Europeans, has been implicated in adaptive evolution in a human population (*44*). At a relaxed threshold of 0.1% quantile (fig. S6D, blue dotted line, and table S8), we found additional SNPs within melanin-promoting loci with high PBS values, including *ACTR3*, *TMEM163*, *HDAC4*, *RAB21*, and *NCOR1* loci. Our analysis reaffirms adaptive selective pressure on known pigmentation-associated genes such as *SLC45A2* and *SLC24A5* (*45*–*47*) and identifies variants near select candidate genes that are enriched for signatures of local adaptation. These newly identified variants will require further functional genomic analyses to pinpoint their cis-regulatory function and to confirm the target genes upon which they act.

If positive selection signatures observed for screen hits are because of selection on skin pigmentation, then alleles with increased frequency in a given population should be associated with pigmentation in a direction concordant with the overall change in pigmentation in that population relative to others. To test this hypothesis, we focused on SNPs with increased frequency in Europeans, owing to the availability of highly powered, publicly available summary statistics of skin color GWAS in white British individuals from the UKBB. In this GWAS, negative effect sizes for a given allele indicate a larger fraction of white British individuals self-reporting with lighter skin color categories, with the opposite for positive effect sizes. For SNPs within known pigmentation-associated screen hits, there was a significant, negative correlation between European PBS-score significance (the –log10 P value of the PBS score) and GWAS effect size (Spearman $\rho = -0.42$, $P = 3.23 \times 10^{-8}$) (fig. S7B). Alternatively, when we stratified variants associated with the loci on the basis of the significance of the PBS scores, it was apparent that alleles with the lower P value (<0.01) were preferentially associated with lighter self-reported skin color categories (as indicated by the negative GWAS effect size) compared with alleles with less significant (P value > 0.01) PBS scores (Wilcoxon rank-sum test $P = 8.01 \times 10^{-5}$) (fig. S7A). This indicates that alleles with increased frequency in Europeans are preferentially associated with lighter self-reported skin color categories. We observed analogous, although substantially weaker, effects when considering SNPs in screen hits with no previously known role in pigmentation both in correlational analysis (Spearman $\rho = -0.13$, $P = 0.00016$) (fig. S7C) and stratified analysis (Wilcoxon rank-sum test $P = 5.4 \times 10^{-3}$) (fig. S7A). This is to be expected, given that genes with strongest effect sizes on pigmentation in human populations have likely already been discovered. Nonetheless, our results demonstrate that both known and, to a lesser degree, newly identified loci harbor SNPs with some evidence for evolving under positive selection

for skin pigmentation changes, which warrants their deeper exploration in future studies.

Secondary validations confirm involvement of screen hits in different stages of melanosome biogenesis

Altogether, our results thus far uncover 135 new candidate melanin-promoting genes associated with diverse biological processes, demonstrate increased expression in dark-skin melanocytes for the majority of the screen hits, and suggest that some loci identified in our study may be involved in skin color variation and associated with evolutionary adaptations in human populations.

To further validate select hits representing a range of biological functions and screen-effect sizes, we introduced sgRNAs against *AP1G1*, *CCDC22*, *COMMD3*, *KHDRBS1*, *KLF6*, *SLC12A9*, *SLC33A1*, *TYR*, *KIAA1033* (*WASHC4*), and *WDR81* into the Cas9-MNT-1 cell line (Fig. 4, A and B, and fig. S8A). We conducted multiple gene-deactivation (knockout, KO) experiments using three distinct sgRNAs against each of the aforementioned genes, and the results confirmed their regulatory roles in human melanogenesis, as deactivating each gene significantly reduced pigmentation, albeit to varying degrees (Fig. 4, A and B). As we expected, the reduced pigmentation phenotype was accompanied by a diminished SSC (fig. S8B). Our validation experiments were done on bulk cell populations, which likely contained a mixture of heterozygous, homozygous, and unedited cells. Thus, melanin measurements underestimate the loss of gene pigmentation phenotype expected from a complete (homozygous) loss of gene function.

To gain insights into how select hits may affect melanosome biogenesis, we performed TEM imaging on *KLF6*-, *COMMD3*-, and *WDR81*-KO cells and quantified melanosomes at various stages of maturation in comparison to wild-type (control-edited) and *TYR*-KO cells (Fig. 4, C and D, and fig. S8C). We found that the loss of *KLF6* was associated with a significantly reduced proportion of stage IV melanosomes (one-sided two-sample test of proportions, $P = 2.62 \times 10^{-33}$) (Fig. 4D and fig. S8C), which explains the reduced pigmentation of the knockout cells (Fig. 4, A and B) and suggests that this transcription factor regulates expression of genes required for the later stages of melanosome maturation. Deletion of *COMMD3* led to a significant increase in stage I and II non-melanized melanosomes (one-sided two-sample test of proportions, $P = 9.43 \times 10^{-35}$) in which fibrillar structure was visible, but transition to stage III or IV appeared to be defective (Fig. 4D and fig. S8C), which was reminiscent of the *TYR*-KO phenotype (figs. S1I and S8C). We found that *WDR81*-KO cells had a significantly higher proportion of stage I melanosomes compared with controls (one-sided two-sample test of proportions, $P = 4.14 \times 10^{-31}$), which was evidenced by the presence of multiple vacuoles or vesicles (Fig. 4D and fig. S8C). Because stage I melanosomes are derived from vacuolar domains of the early endosomal compartments (*5*, *17*, *48*), *WDR81* KO likely affects the early endosomal compartments. In agreement, a recent study showed that loss of *WDR81* caused an increase in endosomal phosphatidylinositol 3-phosphate (PtdIns3P), leading to the enlargement of early endosomes (*49*). Thus, our screen hits are involved in the regulation of melanosome biogenesis and maturation at different stages, which suggests diverse biological mechanisms.

KLF6 regulates melanosome maturation in vivo

To gain deeper insights into the mechanisms by which these novel genes regulate pigmentation, we further focused on two hits that were involved in distinct molecular processes: transcription factor KLF6 and endosomal recycling protein COMMD3. First, we conditionally deleted one or both copies of the *Klf6* gene in the melanocytic lineage by crossing $Klf6^{fl/fl}$ (*50*) mice with *Tyr::Cre* mice that express Cre recombinase under melanocyte-specific *Tyr* gene promoter (*51*). Given that the *Tyr::Cre* transgene was located on the X chromosome (*51*), which was subject to random X inactivation in females, we focused our analyses only on male progenies. All animals with homozygous loss of *Klf6* (*TyrCre::*$Klf6^{fl/fl}$) displayed severe loss of melanin in hair coat color and complete loss of melanin in toe and tail, both of which are devoid of any hair and are equivalent to interfollicular epidermis in humans (Fig. 4E, fig. S9A, and table S9). By comparison, heterozygous melanocyte-specific loss of *Klf6* (*TyrCre::*$Klf6^{fl/+}$) resulted in partial loss of melanin in tail and toe, diffuse dilution of coat color, and variegated loss of melanin visible as white coat patches in all animals (Fig. 4E, fig. S9A, and table S9). These results indicate a strong and dosage-dependent effect of KLF6 on pigmentation with complete penetrance (table S9). To assess whether this pigmentation phenotype results from defective melanosome maturation or the loss of melanocytic lineage, we performed skin histology and electron microscopy studies (Fig. 4, F and G, and fig. S9B). The average number of melanocytes (per unit area) in *TyrCre::*$Klf6^{fl/fl}$ animals were similar to that of $Klf6^{fl/fl}$ animals, as ascertained by counting Melan-A–positive melanocytes [53.05 ± 4.9 (SEM) melanocytes per square milimeter in *TyrCre::*$Klf6^{fl/fl}$ animals versus 53.45 ± 5 (SEM) melanocytes per square milimeter in $Klf6^{fl/fl}$ animals; $P = 0.96$)] (Fig. 4F and table S10). These results confirmed that loss of *Klf6* does not affect development and survival of melanocytes (Fig. 4F and table S10). TEM analyses showed the presence of amelanotic melanosomes within *TyrCre::*$Klf6^{fl/fl}$ melanocytes, confirming that KLF6 regulates later stages of melanosome maturation, which is in agreement with our in vitro *KLF6*-KO TEM analysis (Fig. 4G).

Given that KLF6 is a transcription factor, we proceeded to examine effects of its loss on gene expression using human MNT-1 cells. To this end, we endogenously tagged one or both alleles of *KLF6* at the C-terminus with the $FKBP12^{F36V}$ and V5 tags, which allow for rapid degradation of KLF6 in response to treatment with degradation tag (dTAG) molecules and protein detection with immunoblotting, respectively (Fig. 4H and fig. S9, C to F) (*52*). Because different dTAG degrader molecules may have variable protein degradation responses (*52*), we tested two commonly used dTAG molecules—dTAG-13 and $dTAG^{v}$-1—and found $dTAG^{v}$-1 more effective in KLF6 degradation in MNT-1 cells (fig. S9F). Therefore, we used $dTAG^{v}$-1 for all subsequent KLF6 depletion experiments. Next, we depleted KLF6 in both homozygous and heterozygous MNT-1 cells and examined the effects of KLF6 loss on gene expression after 24 hours of $dTAG^{v}$-1 treatment. Combined RNA-seq analyses of homozygous and heterozygous cell lines treated with either $dTAG^{v}$-1 and dimethylsulfoxide (DMSO, vehicle control) revealed that more than 900 genes (410 down-regulated and 576 up-regulated) were differentially expressed in response to KLF6 depletion (Fig. 4I). Among 169 melanin-promoting genes uncovered through our CRISPR screen, the expression of 12 genes was significantly affected by the loss of KLF6 (Fig. 4I). Notably, 10 of these candidate genes (*TYR*, *AMBRA1*, *CHD8*, *HDAC4*, *ASCC3*, *SAFB*, *CANX*, *SMG7*, *RPRD2*, and *SCAF4*), including that of key melanogenic enzyme tyrosinase, were down-regulated in response to KLF6 depletion. This is in agreement with both their positive regulation by KLF6 and the promelanocytic role of KLF6 uncovered in our studies (Fig. 4I). Taken together, our results uncover a role for KLF6 in melanosome maturation and pigmentation and pinpoint candidate transcriptional targets that may mediate these functions.

Endosomal trafficking protein COMMD3 modulates melanosomal pH

We next focused on another hit from our screen: COMMD3, which belongs to the COMMD (copper metabolism MURR1 or COMM domain) family of proteins, comprising of 10 members (*33*, *34*). COMMD proteins homo- or heterodimerize and associate with CCDC22 and CCDC93 proteins to form the CCC complex, which is involved in endosomal receptor trafficking (*33*, *34*). *CCDC22*, *CCDC93*, and multiple *COMMD* genes (*COMMD2*, *COMMD3*, *COMMD4*, *COMMD5*, *COMMD8*, and *COMMD10*) of the CCC complex were identified as hits in

our screen (Fig. 2E). Notably, COMMD1, a CCC complex component, has been implicated in the recycling of copper-transporting adenosine triphosphatase (ATPase) 1 (ATP7A) (*33*, *34*). ATP7A regulates pigmentation by transporting copper to melanosomes, because copper binding to the TYR apoenzyme is essential for its holoenzyme activity (*53*). Contrary to our expectations, however, we found that COMMD3 KO does not affect the localization of ATP7A to melanosomes (fig. S10, A and B). We also did not detect any measurable effects of *COMMD3*

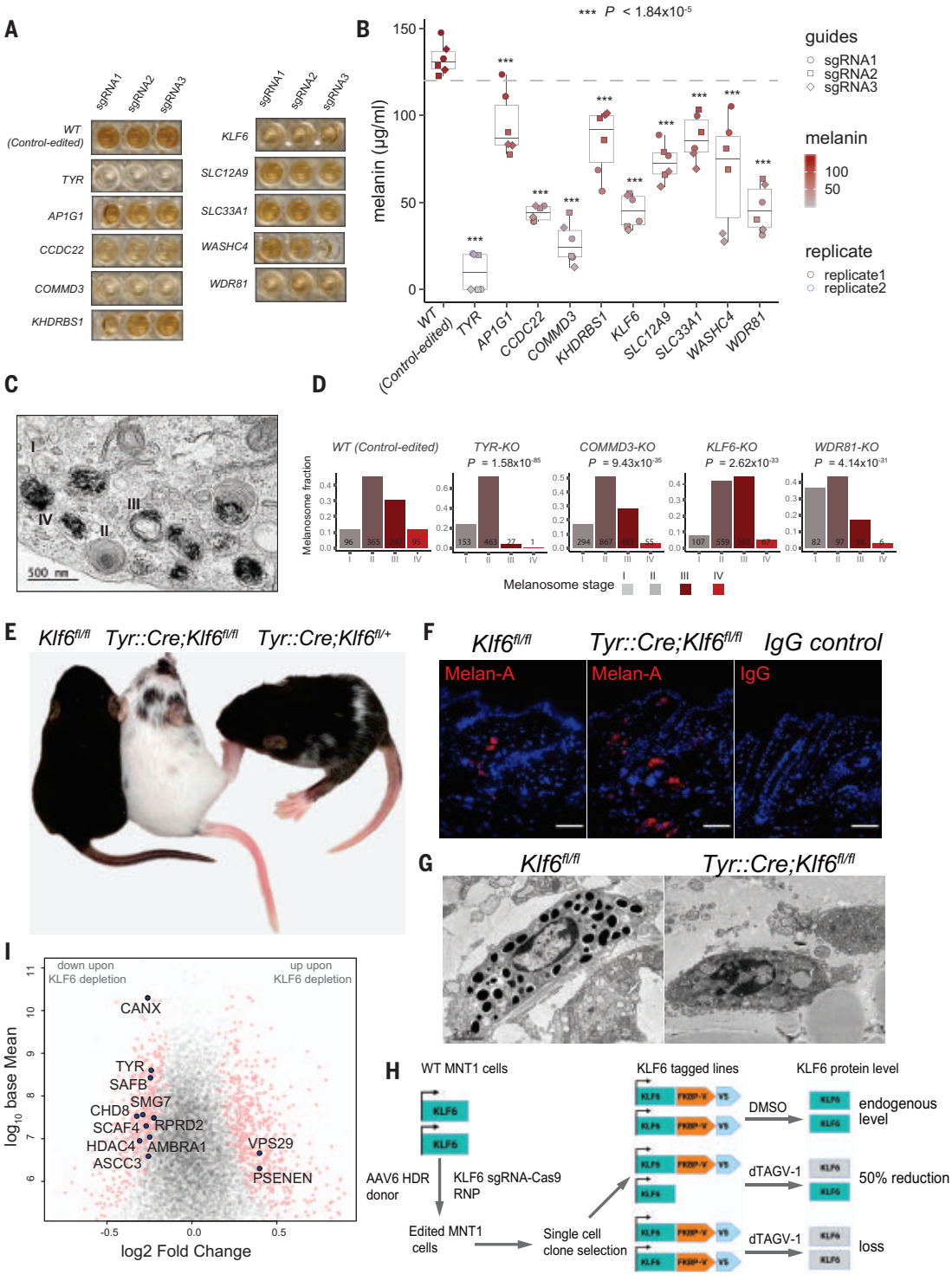

Fig. 4. Newly identified pigmentation genes affect different aspects of melanosome biogenesis and maturation. (**A**) CRISPR-Cas9–based validation of select previously unidentified pigmentation screen hits along with negative (safe-targeting sgRNAs; wild type) and positive (*TYR*) controls. Cas9-MNT-1 cell lysates show gross changes in melanin levels upon deactivation of indicated genes using three different sgRNAs. (**B**) Boxplots show median melanin measurements for select gene knockouts and controls. *P* values relative to control-edited cells ranged from smallest 2.46×10^{-20} (for *TYR*-KO cells) to largest 1.84×10^{-5} (for *AP1G1*-KO cells). $***P < 1.84 \times 10^{-5}$. (**C**) Representative TEM image showing melanosomes at stages I to IV of maturation. (**D**) Quantification of melanosomes at different stages of maturation among different indicated gene deactivations. Total counts are shown on each bar. *P* values from χ-squared test are shown. (**E**) KLF6 regulates melanosome maturation, and its loss leads to severe pigmentation defects in vivo. P15 mice pups with homozygous deletion of *Klf6* (*TyrCre::Klf6*$^{fl/fl}$) display loss of melanin in hair coat color, toes, and tail. Mice with heterozygous deletion of *Klf6* (*TyrCre::Klf6*$^{fl/+}$) display diffuse dilution of toe, tail, and hair coat color, and variegated white patches compared with those of control animals with no *Tyr::Cre* expression (*Klf6*$^{fl/fl}$). (**F**) Immunohistochemistry of mouse skin shows presence of Melan-A–positive melanocytes in *Klf6* null (*TyrCre::Klf6*$^{fl/fl}$) and control (*Klf6*$^{fl/fl}$) animals. (**G**) TEM images of mouse skin showing black melanosomes within the melanocytes of control (*Klf6*$^{fl/fl}$) animals compared with the presence of immature melanosomes in *Klf6* null (*TyrCre::Klf6*$^{fl/fl}$) mouse skin. (**H**) Schematic diagram of KLF6 endogenous tagging at C-terminus with FKBP12^{F36V} and V5 epitope. (**I**) RNA-seq volcano plot showing differentially expressed genes (highlighted in pink circles) in response to 24-hour dTAG^{V}-1 treatment. Labeled genes (blue solid circles) are melanin-promoting genes discovered in CRISPR screen. Scale bars in (F), 25 μm; (C), 500 nm; and (G), 2 μm.

KO on TYR levels (fig. S10, C and D). Nonetheless, COMMD3 was enriched within the melanosomal fraction, as determined with melanosome immunoprecipitation (melano-IP) (*32*), which suggests that it may regulate pigmentation by functioning in melanosomes or by promoting receptor trafficking to melanosomes (Fig. 5A).

An important regulator of TYR activity and pigmentation is melanosomal pH (*5*). Stage I and II melanosomes are characterized by an acidic environment, but stage III and IV melanosomes require neutral pH for optimal TYR enzymatic activity (*5*). To investigate the pH of melanosomes, we used lysoTracker Red DND-99, a fluorescent acidotropic pH indicator probe that stains all endosome-derived acidic organelles such as melanosomes and

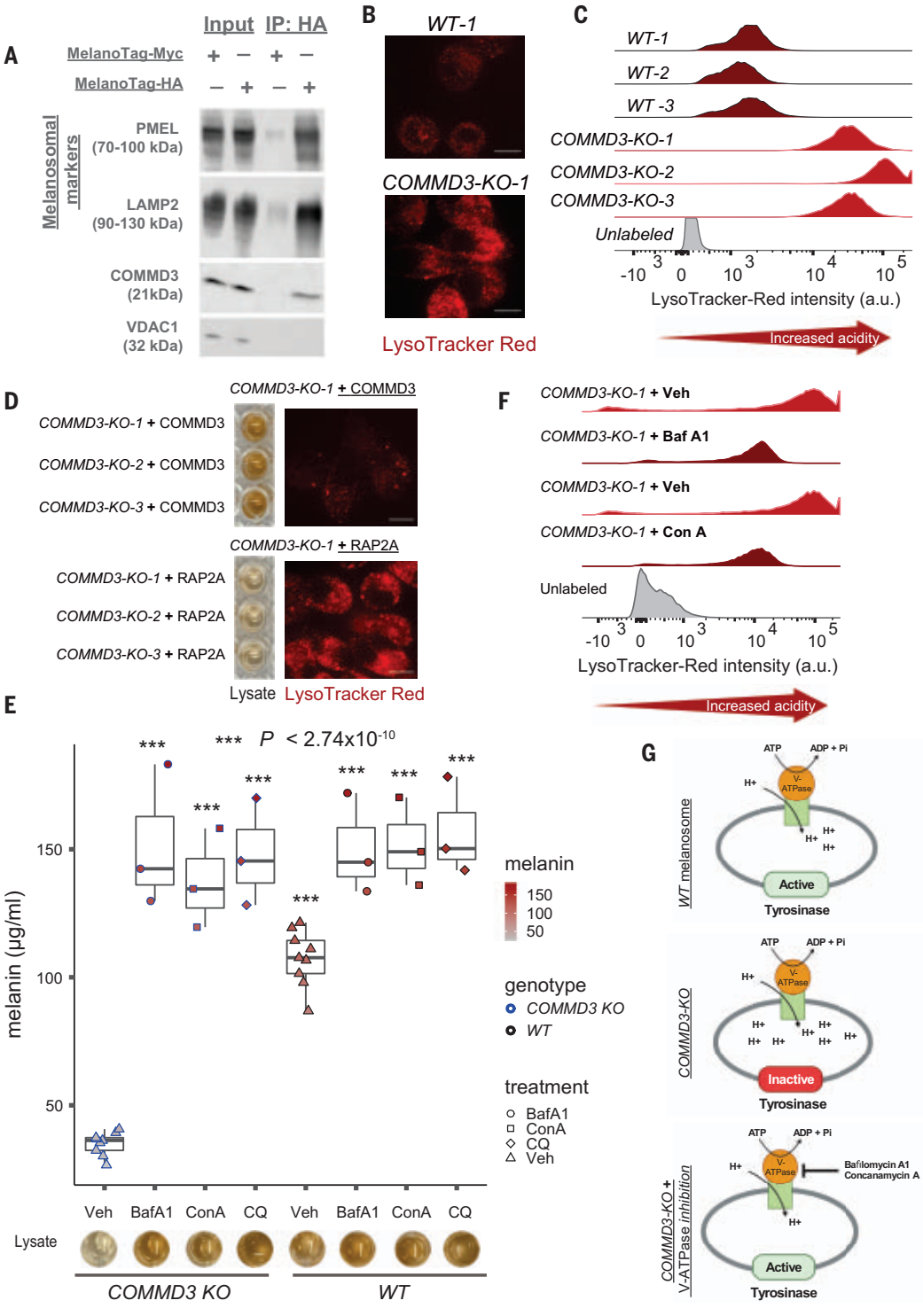

Fig. 5. COMMD3 is enriched in melanosomes and regulates melanosomal pH. (**A**) COMMD3 is enriched in purified melanosomes. Immunoblots showing whole-cell lysates (input), control (MNT-1 cells expressing a Myc-MelanoTag), and purified melanosome (MNT-1 cells expressing HA-MelanoTag) immunoprecipitates (IP). Melanosomal markers PMEL and LAMP2 are enriched in purified melanosomes in comparison with mitochondrial marker VDAC1. (**B**) *COMMD3*-KO cells display high acidity (low pH) of endosomal organelles (e.g., melanosomes) as confirmed with live cell imaging using LysoTracker Red dye (n = 3 clones). (**C**) Flow cytometry histograms showing increased LysoTracker Red fluorescence intensity in *COMMD3*-KO clones compared with wild-type (control-edited) clonal cells (n = 3). (**D**) COMMD3, but not RAP2A (*32*) (an unrelated and constitutively expressed protein), overexpression in *COMMD3*-KO cells rescues both melanin production and reduced pH (n = 3). (**E**) *COMMD3*-KO phenotype is rescued by neutralizing melanosomal pH. V-ATPase proton pump inhibitors bafilomycin A1 (BafA1, 0.1 μM), concanamycin A (ConA, 0.1 μM), and chloroquine (CQ, 50 μM) raise the pH of melanosomes in comparison with vehicle (Veh, DMSO and H2O) controls and restore melanin production as shown with melanin quantification and cell lysates (n = 3). Significance tested by ANOVA and two-sided Welch t-test. ***, $P < 2.74 \times 10^{-10}$ (for all groups, relative to vehicle group). (**F**) Flow cytometry histograms showing decreased fluorescence intensity of LysoTracker Red in *COMMD3*-KO cells treated with BafA1 (0.1 μM) and ConA (0.1 μM) compared with vehicle control (Veh) treated cells (n = 3). (**G**) Schematic diagram of putative COMMD3 function in melanosomes. *COMMD3*-KO cells fail to neutralize maturing stage III and IV melanosomes, affecting TYR enzymatic activity. Neutralizing (i.e., raising the pH) melanosomes by blocking V-ATPase proton pump restores TYR activity and melanogenesis. Scale bars in (B) and (D), 25 μm.

lysosomes. Notably, *COMMD3* KO resulted in significantly higher acidity (low pH) of endosomal compartments including melanosomes, which was confirmed by live imaging and flow cytometry with LysoTracker Red dye (Fig. 5, B and C). Notably, costaining with TYR and lysotracker Red dye confirmed that TYR-positive melanosomes of *COMMD3*-KO cells were indeed highly acidic compared with wild-type (control-edited) cells (fig. S10, E and F). Reintroduction of COMMD3—but not of the unrelated and constitutively expressed protein RAP2A (*32*)—to *COMMD3*-KO cells restored both pH and melanosomal melanin production, which indicated specificity of the observed effects (Fig. 5D and fig. S10, G to I). We further tested whether increasing (i.e., neutralizing) melanosomal pH with alternative approaches can rescue the *COMMD3*-KO phenotype and restore melanin production. To this end, we treated *COMMD3*-KO cells with bafilomycin A1 (BafA1) and concanamycin A (ConA), which bind at distinct sites of the vacuolar-type H^+-ATPase (V-ATPase) proton pump and selectively inhibit V-ATPase responsible for maintaining the acidity of endosomal compartments, including melanosomes (*54*). Both BafA1 (0.1 μm) and ConA (0.1 μm) raised the pH of endosomal compartments and completely restored melanin production in *COMMD3*-KO cells to a level similar to that of control cells (Fig. 5, E and F). In addition, treatment of *COMMD3*-KO cells with 50 μm chloroquine (CQ), which acts as a weak base and neutralizes luminal pH by accumulating within the endosomal organelles (*55*), also restored melanin production (Fig. 5E) (*55*). Thus, by restoring neutral melanosomal pH in a V-ATPase–dependent (BafA1 and ConA) and -independent (CQ) manner, we were able to completely restore melanosome maturation and melanin production in *COMMD3*-KO cells. These results strongly suggest that *COMMD3*-KO melanosomes contain all the required components for melanin production except for neutral melanosomal pH, which is essential for optimal TYR enzyme activity (Fig. 5G) (*5*). Thus, a plausible mechanism for COMMD3's role in pigmentation is the regulation of melanosomal localization of one or more transporters responsible for modulating luminal pH.

Discussion

We have demonstrated that changes in melanosomal composition can be robustly quantified by measuring the side-scattering property of pigment cells. By exploiting this relationship, we directly surveyed genes involved in melanosomal biogenesis and maturation without being confounded by the indirect factors influencing pigmentation through effects on melanocyte development, survival, migration, and other processes. The majority of previously unidentified melanogenesis genes uncovered in our study are more highly expressed in primary melanocytes of darkly pigmented individuals, which correlates well with their melanin-promoting function. Although it should be noted that our screen hits do not represent an exhaustive list of pigmentation genes, they nonetheless include 135 newly identified candidate regulators of melanogenesis involved in diverse molecular functions such as transcriptional and posttranscriptional gene regulation, vesicle organization, and intracellular transport, the latter including several molecular complexes involved in endosomal recycling. Although the key role of early endosomes in melanogenesis is well established, our work implicates new cargo recycling pathways in melanosome function. We showed that COMMD3, a component of the endosomal trafficking CCC complex, is enriched in melanosomes and regulates their luminal pH. Moreover, our work uncovered a new role for transcription factor KLF6 in regulating melanosome maturation and skin pigmentation in vivo. Prior studies have reported that loss of KLF6 in collagen-rich environments leads to increased melanoma proliferation, which is consistent with the role of KLF6 as a tumor suppressor in multiple cancers (*56*–*61*). In light of our findings, it would be informative to examine the role of KLF6 inactivation in melanoma initiation and how the extracellular matrix could modulate this process. Furthermore, these and other hits from our screen merit further exploration in the context of other diseases, because aberrant melanin production is associated not only with skin pigmentation disorders but also with Parkinson's disease and auditory disorders, which have been linked to loss of neuromelanin in substantia nigra and cochlear melanin in the inner ear, respectively (*62*, *63*). Furthermore, select loci identified in our screen show association with skin color variation and evidence of recent adaptations in human populations. Therefore, in addition to the aforementioned insights into melanosome biology and disease, results presented here will provide a rich resource for further studies of the genetic architecture of skin color diversity in humans.

Methods summary

To establish whether melanosome maturation can be monitored by measuring changes in SSC, we used two models of human melanogenesis: human pluripotent stem cell (PSC)–derived melanocytes and MNT-1 melanoma cells. We measured SSC and melanin content of human PSC–derived melanoblasts as they matured into melanocytes and conducted CRISPR deletion of *TYR* and rescue experiments in MNT-1 cells. Both orthogonal set-ups of experiments showed a strong positive correlation between melanin content and SSC. To perform the genome-wide CRISPR screen, we engineered a clonal MNT-1 cell line to express SpCas9 nuclease in a doxycycline-regulatable manner (Cas9-MNT-1 cell line). We infected the Cas9-MNT-1 cell line with a genome-wide lentiviral sgRNA library (with 10 targeting guides per gene) (*20*), so that each cell expressed a single sgRNA. In addition, the library also included negative control sgRNAs such as nontargeting guides (i.e., no binding sites in the genome) and safe-targeting control guides that targeted genomic loci with no annotated function (*20*).

REFERENCES AND NOTES

1. W. J. Pavan, R. A. Sturm, The Genetics of Human Skin and Hair Pigmentation. *Annu. Rev. Genomics Hum. Genet.* **20**, 41–72 (2019). doi: 10.1146/annurev-genom-083118-015230; pmid: 31100995
2. E. E. Quillen *et al*., Shades of complexity: New perspectives on the evolution and genetic architecture of human skin. *Am. J. Phys. Anthropol.* **168** (suppl. 67), 4–26 (2019). doi: 10.1002/ajpa.23737; pmid: 30408154
3. J. Rocha, The Evolutionary History of Human Skin Pigmentation. *J. Mol. Evol.* **88**, 77–87 (2020). doi: 10.1007/s00239-019-09902-7; pmid: 31363820
4. G. Raposo, M. S. Marks, Melanosomes—Dark organelles enlighten endosomal membrane transport. *Nat. Rev. Mol. Cell Biol.* **8**, 786–797 (2007). doi: 10.1038/nrm2258; pmid: 17878918
5. L. Le, J. Sirés-Campos, G. Raposo, C. Delevoye, M. S. Marks, Melanosome Biogenesis in the Pigmentation of Mammalian Skin. *Integr. Comp. Biol.* **61**, 1517–1545 (2021). doi: 10.1093/icb/icab078; pmid: 34021746
6. L. L. Baxter, D. E. Watkins-Chow, W. J. Pavan, S. K. Loftus, A curated gene list for expanding the horizons of pigmentation biology. *Pigment Cell Melanoma Res.* **32**, 348–358 (2019). doi: 10.1111/pcmr.12743; pmid: 30339321
7. A. R. Martin *et al*., An Unexpectedly Complex Architecture for Skin Pigmentation in Africans. *Cell* **171**, 1340–1353.e14 (2017). doi: 10.1016/j.cell.2017.11.015; pmid: 29195075
8. N. G. Crawford *et al*., Loci associated with skin pigmentation identified in African populations. *Science* **358**, eaan8433 (2017). doi: 10.1126/science.aan8433; pmid: 29025994
9. S. Beleza *et al*., Genetic architecture of skin and eye color in an African-European admixed population. *PLOS Genet.* **9**, e1003372 (2013). doi: 10.1371/journal.pgen.1003372 pmid: 23555287
10. E. Pairo-Castineira *et al*., Expanded Analysis of Pigmentation Genetics in UK Biobank. bioRxiv 2022.2001.2030.478418 [Preprint] (2022); https://doi.org/10.1101/2022.01.30.478418
11. H. Shi, G. Kichaev, B. Pasaniuc, Contrasting the Genetic Architecture of 30 Complex Traits from Summary Association Data. Contrasting the Genetic Architecture of 30 Complex Traits from Summary Association Data. *Am. J. Hum. Genet.* **99**, 139–153 (2016). doi: 10.1016/j.ajhg.2016.05.013; pmid: 27346688
12. P. Meredith, T. Sarna, The physical and chemical properties of eumelanin. *Pigment Cell Res.* **19**, 572–594 (2006). doi: 10.1111/j.1600-0749.2006.00345.x; pmid: 17083485
13. G. C. Salzman *et al*., Cell classification by laser light scattering: Identification and separation of unstained leukocytes. *Acta Cytol.* **19**, 374–377 (1975). pmid: 808927
14. Y. Mica, G. Lee, S. M. Chambers, M. J. Tomishima, L. Studer, Modeling neural crest induction, melanocyte specification, and disease-related pigmentation defects in hESCs and patient-specific iPSCs. *Cell Rep.* **3**, 1140–1152 (2013). doi: 10.1016/j.celrep.2013.03.025; pmid: 23583175
15. K. Hoek *et al*., Expression profiling reveals novel pathways in the transformation of melanocytes to melanomas. *Cancer Res.* **64**, 5270–5282 (2004). doi: 10.1158/0008-5472.CAN-04-0731; pmid: 15289333
16. A. Chi *et al*., Proteomic and bioinformatic characterization of the biogenesis and function of melanosomes. *J. Proteome Res.* **5**, 3135–3144 (2006). doi: 10.1021/pr060363j; pmid: 17081065
17. I. Hurbain *et al*., Electron tomography of early melanosomes: Implications for melanogenesis and the generation of fibrillar amyloid sheets. *Proc. Natl. Acad. Sci. U.S.A.* **105**, 19726–19731 (2008). doi: 10.1073/pnas.0803488105; pmid: 19033461

18. T. Kushimoto *et al*., A model for melanosome biogenesis based on the purification and analysis of early melanosomes. *Proc. Natl. Acad. Sci. U.S.A.* **98**, 10698–10703 (2001). doi: 10.1073/pnas.191184798; pmid: 11526213
19. A. K. Ganesan *et al*., Genome-wide siRNA-based functional genomics of pigmentation identifies novel genes and pathways that impact melanogenesis in human cells. *PLOS Genet.* **4**, e1000298 (2008). doi: 10.1371/journal.pgen.1000298; pmid: 19057677
20. D. W. Morgens *et al*., Genome-scale measurement of off-target activity using Cas9 toxicity in high-throughput screens. *Nat. Commun.* **8**, 15178 (2017). doi: 10.1038/ncomms15178; pmid: 28474669
21. D. W. Morgens, R. M. Deans, A. Li, M. C. Bassik, Systematic comparison of CRISPR/Cas9 and RNAi screens for essential genes. *Nat. Biotechnol.* **34**, 634–636 (2016). doi: 10.1038/nbt.3567; pmid: 27159373
22. H. M. Shapiro, *Practical Flow Cytometry* (Wiley-Liss, 2003).
23. T. Hart *et al*., High-Resolution CRISPR Screens Reveal Fitness Genes and Genotype-Specific Cancer Liabilities. *Cell* **163**, 1515–1526 (2015). doi: 10.1016/j.cell.2015.11.015; pmid: 26627737
24. R. J. Ihry *et al*., Genome-Scale CRISPR Screens Identify Human Pluripotency-Specific Genes. *Cell Rep.* **27**, 616–630.e6 (2019). doi: 10.1016/j.celrep.2019.03.043; pmid: 30970262
25. K. Tzelepis *et al*., A CRISPR Dropout Screen Identifies Genetic Vulnerabilities and Therapeutic Targets in Acute Myeloid Leukemia. *Cell Rep.* **17**, 1193–1205 (2016). doi: 10.1016/j.celrep.2016.09.079; pmid: 27760321
26. G. G. McGill *et al*., Bcl2 regulation by the melanocyte master regulator Mitf modulates lineage survival and melanoma cell viability. *Cell* **109**, 707–718 (2002). doi: 10.1016/S0092-8674(02)00762-6; pmid: 12086670
27. M. L. Harris *et al*., A dual role for SOX10 in the maintenance of the postnatal melanocyte lineage and the differentiation of melanocyte stem cell progenitors. *PLOS Genet.* **9**, e1003644 (2013). doi: 10.1371/journal.pgen.1003644; pmid: 23935512
28. L. Hou, H. Arnheiter, W. J. Pavan, Interspecies difference in the regulation of melanocyte development by SOX10 and MITF. *Proc. Natl. Acad. Sci. U.S.A.* **103**, 9081–9085 (2006). doi: 10.1073/pnas.0603114103; pmid: 16757562
29. G. Yang *et al*., Inhibition of PAX3 by TGF-beta modulates melanocyte viability. *Mol. Cell* **32**, 554–563 (2008). doi: 10.1016/j.molcel.2008.11.002; pmid: 19026785
30. P. Sulem *et al*., Two newly identified genetic determinants of pigmentation in Europeans. *Nat. Genet.* **40**, 835–837 (2008). doi: 10.1038/ng.160; pmid: 18488028
31. A. L. Ambrosio, J. A. Boyle, A. E. Aradi, K. A. Christian, S. M. Di Pietro, TPC2 controls pigmentation by regulating melanosome pH and size. *Proc. Natl. Acad. Sci. U.S.A.* **113**, 5622–5627 (2016). doi: 10.1073/pnas.1600108113; pmid: 27140606
32. C. H. Adelmann *et al*., MFSD12 mediates the import of cysteine into melanosomes and lysosomes. *Nature* **588**, 699–704 (2020). doi: 10.1038/s41586-020-2937-x; pmid: 33208952
33. C. A. Phillips-Krawczak *et al*., COMMD1 is linked to the WASH complex and regulates endosomal trafficking of the copper transporter ATP7A. *Mol. Biol. Cell* **26**, 91–103 (2015). doi: 10.1091/mbc.e14-06-1073; pmid: 25355947
34. P. J. Cullen, F. Steinberg, To degrade or not to degrade: Mechanisms and significance of endocytic recycling. *Nat. Rev. Mol. Cell Biol.* **19**, 679–696 (2018). doi: 10.1038/s41580-018-0053-7; pmid: 30194414
35. L. Ripoll, X. Heiligenstein, G. Raposo, C. Delevoye, Illuminating the dark side of recycling endosomes. *Cell Cycle* **15**, 1309–1310 (2016). doi: 10.1080/15384101.2016.1160682; pmid: 27184333
36. H. K. Long, S. L. Prescott, J. Wysocka, Ever-Changing Landscapes: Transcriptional Enhancers in Development and Evolution. *Cell* **167**, 1170–1187 (2016). doi: 10.1016/j.cell.2016.09.018; pmid: 27863239
37. P. J. Wittkopp, G. Kalay, Cis-regulatory elements: Molecular mechanisms and evolutionary processes underlying divergence. *Nat. Rev. Genet.* **13**, 59–69 (2011). doi: 10.1038/nrg3095; pmid: 22143240
38. H. K. Finucane *et al*., Partitioning heritability by functional annotation using genome-wide association summary statistics. *Nat. Genet.* **47**, 1228–1235 (2015). doi: 10.1038/ng.3404; pmid: 26414678
39. J. MacArthur *et al*., The new NHGRI-EBI Catalog of published genome-wide association studies (GWAS Catalog). *Nucleic Acids Res.* **45**, D896–D901 (2017). doi: 10.1093/nar/gkw1133; pmid: 27899670
40. T. Zhang *et al*., Cell-type-specific eQTL of primary melanocytes facilitates identification of melanoma susceptibility genes. *Genome Res.* **28**, 1621–1635 (2018). doi: 10.1101/gr.233304.117; pmid: 30333196
41. X. Yi *et al*., Sequencing of 50 human exomes reveals adaptation to high altitude. *Science* **329**, 75–78 (2010). doi: 10.1126/science.1190371; pmid: 20595611
42. B. Vernot *et al*., Personal and population genomics of human regulatory variation. *Genome Res.* **22**, 1689–1697 (2012). doi: 10.1101/gr.134890.111; pmid: 22955981
43. D. G. Torgerson *et al*., Evolutionary processes acting on candidate cis-regulatory regions in humans inferred from patterns of polymorphism and divergence. *PLOS Genet.* **5**, e1000592 (2009). doi: 10.1371/journal.pgen.1000592; pmid: 19662163
44. F. Peng *et al*., Genome-Wide Association Studies Identify Multiple Genetic Loci Influencing Eyebrow Color Variation in Europeans. *J. Invest. Dermatol.* **139**, 1601–1605 (2019). doi: 10.1016/j.jid.2018.12.029; pmid: 30703357
45. R. L. Lamason *et al*., SLC24A5, a putative cation exchanger, affects pigmentation in zebrafish and humans. *Science* **310**, 1782–1786 (2005). doi: 10.1126/science.1116238; pmid: 16357253
46. R. A. Sturm, D. L. Duffy, Human pigmentation genes under environmental selection. *Genome Biol.* **13**, 248 (2012). doi: 10.1186/gb-2012-13-9-248; pmid: 23110848
47. P. C. Sabeti *et al*., Genome-wide detection and characterization of positive selection in human populations. *Nature* **449**, 913–918 (2007). doi: 10.1038/nature06250; pmid: 17943131
48. G. Raposo, D. Tenza, D. M. Murphy, J. F. Berson, M. S. Marks, Distinct protein sorting and localization to premelanosomes, melanosomes, and lysosomes in pigmented melanocytic cells. *J. Cell Biol.* **152**, 809–824 (2001). doi: 10.1083/jcb.152.4.809; pmid: 11266471
49. K. Liu *et al*., Negative regulation of phosphatidylinositol 3-phosphate levels in early-to-late endosome conversion. *J. Cell Biol.* **212**, 181–198 (2016). doi: 10.1083/jcb.201506081; pmid: 26783301
50. S. K. Mallipattu *et al*., Krüppel-like factor 6 regulates mitochondrial function in the kidney. *J. Clin. Invest.* **125**, 1347–1361 (2015). doi: 10.1172/JCI77084; pmid: 25689250
51. V. Delmas, S. Martinozzi, Y. Bourgeois, M. Holzenberger, L. Larue, Cre-mediated recombination in the skin melanocyte lineage. *Genesis* **36**, 73–80 (2003). doi: 10.1002/gene.10197; pmid: 12820167
52. B. Nabet *et al*., Rapid and direct control of target protein levels with VHL-recruiting dTAG molecules. *Nat. Commun.* **11**, 4687 (2020). doi: 10.1038/s41467-020-18377-w; pmid: 32948771
53. S. R. Setty *et al*., Cell-specific ATP7A transport sustains copper-dependent tyrosinase activity in melanosomes. *Nature* **454**, 1142–1146 (2008). doi: 10.1038/nature07163; pmid: 18650808
54. B. J. Bowman, M. E. McCall, R. Baertsch, E. J. Bowman, A model for the proteolipid ring and bafilomycin/concanamycin-binding site in the vacuolar ATPase of Neurospora crassa. *J. Biol. Chem.* **281**, 31885–31893 (2006). doi: 10.1016/S0021-9258(19)84103-0; pmid: 16912037
55. P. W. Halcrow, J. D. Geiger, X. Chen, Overcoming Chemoresistance: Altering pH of Cellular Compartments by Chloroquine and Hydroxychloroquine. *Front. Cell Dev. Biol.* **9**, 627639 (2021). doi: 10.3389/fcell.2021.627639; pmid: 33634129
56. S. J. Huh *et al*., KLF6 Gene and early melanoma development in a collagen I-rich extracellular environment. *J. Natl. Cancer Inst.* **102**, 1131–1147 (2010). doi: 10.1093/jnci/djq218; pmid: 20660366
57. D. Cai, J. Zhao, Q. Sun, Krüppel-like factor 6 in the progression and prognosis of malignant melanoma. *J. Int. Med. Res.* **42**, 184–190 (2014). doi: 10.1177/0300060513499092; pmid: 24366496
58. G. Ito *et al*., Krüppel-like factor 6 is frequently down-regulated and induces apoptosis in non-small cell lung cancer cells. *Cancer Res.* **64**, 3838–3843 (2004). doi: 10.1158/0008-5472.CAN-04-0185; pmid: 15172991
59. G. Narla *et al*., KLF6, a candidate tumor suppressor gene mutated in prostate cancer. *Science* **294**, 2563–2566 (2001). doi: 10.1126/science.1066326; pmid: 11752579
60. G. Narla *et al*., In vivo regulation of p21 by the Krüppel-like factor 6 tumor-suppressor gene in mouse liver and human hepatocellular carcinoma. *Oncogene* **26**, 4428–4434 (2007). doi: 10.1038/sj.onc.1210223; pmid: 17297474
61. B. Zhang, D. D. Guo, J. Y. Zheng, Y. A. Wu, Expression of KLF6-SV2 in colorectal cancer and its impact on proliferation and apoptosis. *Eur. J. Cancer Prev.* **27**, 20–26 (2018). doi: 10.1097/CEJ.0000000000000410; pmid: 29084019
62. K. Double, W. Maruyama, M. Naoi, M. Gerlach, P. Riederer, in *Melanins and Melanosomes*, J. Borovansky, P. A. Riley, Eds. (Wiley-Blackwell, 2011), pp. 225–246.
63. Y. Yamaguchi, V. J. Hearing, Melanocytes and their diseases. *Cold Spring Harb. Perspect. Med.* **4**, a017046 (2014). doi: 10.1101/cshperspect.a017046; pmid: 24789876
64. V. K. Bajpai *et al*., A genome-wide genetic screen uncovers novel determinants of human pigmentation, Zenodo (2023); https://doi.org/10.5281/zenodo.7991815.

ACKNOWLEDGMENTS

We sincerely thank M. S. Marks (University of Pennsylvania) for providing MNT-1 cells, L. Studer (Memorial Sloan Kettering Cancer Center) for the H9 SOX10::GFP reporter cell line, and Y. Gilad (University of Chicago) for H20961 iPSC. We also thank J. C. He (Icahn School of Medicine at Mount Sinai) and S. Mallipattu (Stony Brook University) for providing *Klf6*-floxed mice. We thank S. Walsh (Indiana University Purdue University Indianapolis) for her advice on pigmentation GWAS analysis and M. Abu-Remaileh (Stanford University) for advice on melano-IP. We thank K. Brown (National Institute of Health) and W. Pavan (National Institute of Health) for sharing detailed information on the eQTL data. We thank J. Perrino (Stanford Cell Science Imaging Facility) for help with transmission electron microscopy and N. Arora for help with FACS sorting. **Funding:** This work was supported in part by the Howard Hughes Medical Institute, NIH R35 GM131757, and Ludwig Center for Cancer Stem Cell Research and Medicine and Stinehart-Reed award (J.W.); and Department of Defense grant CA160997 and Oklahoma Center for Adult Stem Cell Research grant 231016 (V.K.B.) **Author contributions:** V.K.B. conceived of and designed the study, performed experiments, analyzed data including bioinformatic analyses of CRISPR screen, and wrote the manuscript with input from all co-authors; V.K.B. performed FACS experiments with help from M.A. and T.C.K.; T.C.K. did blinded melanosome counting of TEM images; J.T. and M.B. provided advice and technical support with CRISPR screening; J.M. and S.N. performed evolutionary adaptation and heritability analyses, respectively; J.K.P. provided advice on evolutionary selection and heritability analyses; T.S. performed RNA-seq analyses and provided advice on data analyses and experimental design; J.W. conceptualized and supervised the project and cowrote the manuscript with V.K.B. **Competing interests:** J.W. is a paid member of Camp4 and Paratus Sciences SAB. The authors declare no other competing interests. **Data and materials availability:** All data needed to evaluate the conclusions and reproduce and extend the work of this study are present in the paper, supplementary materials, and/or in genomic datasets available in the Gene Expression Omnibus (GSE227015) and Zenodo repository (*64*). Plasmids generated in this study were submitted to Addgene (195506, 195507, 195508, 195509, and 195510). **License information:** Copyright © 2023 the authors, some rights reserved; exclusive licensee American Association for the Advancement of Science. No claim to original US government works. https://www.science.org/about/science-licenses-journal-article-reuse. This article is subject to HHMI's Open Access to Publications policy. HHMI lab heads have previously granted a nonexclusive CC BY 4.0 license to the public and a sublicensable license to HHMI in their research articles. Pursuant to those licenses, the author-accepted manuscript (AAM) of this article can be made freely available under a CC BY 4.0 license immediately upon publication.

SUPPLEMENTARY MATERIALS

science.org/doi/10.1126/science.ade6289
Materials and Methods
Figs. S1 to S10
Tables S1 to 10
References (*65*–*79*)
MDAR Reproducibility Checklist

Submitted 29 August 2022; accepted 28 June 2023
10.1126/science.ade6289

AAAS.ORG/COMMUNITY

AAAS' Member Community is a one-stop destination for scientists and STEM enthusiasts alike. It's "Where Science Gets Social": a community where facts matter, ideas are big and there's always a reason to come hang out, share, discuss and explore.

Member COMMUNITY
AAAS

AMERICAN ASSOCIATION FOR THE ADVANCEMENT OF SCIENCE

RESEARCH ARTICLE SUMMARY

EVOLUTIONARY BIOLOGY

DNA methylation networks underlying mammalian traits

Amin Haghani *et al.*

INTRODUCTION: Comparative epigenomics is an emerging field that combines epigenetic signatures with phylogenetic relationships to elucidate species characteristics such as maximum life span. For this study, we generated cytosine DNA methylation (DNAm) profiles (n = 15,456) from 348 mammalian species using a methylation array platform that targets highly conserved cytosines.

RATIONALE: Nature has evolved mammalian species of greatly differing life spans. To resolve the relationship of DNAm with maximum life span and phylogeny, we performed a large-scale cross-species unsupervised analysis. Comparative studies in many species enables the identification of epigenetic correlates of maximum life span and other traits.

RESULTS: We first tested whether DNAm levels in highly conserved cytosines captured phylogenetic relationships among species. We constructed phyloepigenetic trees that paralleled the traditional phylogeny. To avoid potential confounding by different tissue types, we generated tissue-specific phyloepigenetic trees. The high phyloepigenetic-phylogenetic congruence is due to differences in methylation levels and is not confounded by sequence conservation.

We then interrogated the extent to which DNA methylation associates with specific biological traits. We used an unsupervised weighted correlation network analysis (WGCNA) to identify clusters of highly correlated CpGs (comethylation modules). WGCNA identified 55 distinct comethylation modules, of which 30 were significantly associated with traits including maximum life span, adult weight, age, sex, human mortality risk, or perturbations that modulate murine life span.

Both the epigenome-wide association analysis (EWAS) and eigengene-based analysis identified methylation signatures of maximum life span, and most of these were independent of aging, presumably set at birth, and could be stable predictors of life span at any point in life. Several CpGs that are more highly methylated in long-lived species are located near *HOXL* subclass homeoboxes and other genes that play a role in morphogenesis and development. Some of these life span–related CpGs are located next to genes that are also implicated in our analysis of upstream regulators (e.g., *ASCL1* and *SMAD6*). CpGs with methylation levels that are inversely related to life span are enriched in transcriptional start site (TSS1) and promoter flanking (PromF4, PromF5) associated chromatin states. Genes located in chromatin state TSS1 are constitutively active and enriched for nucleic acid metabolic processes. This suggests that long-living species evolved mechanisms that maintain low methylation levels in these chromatin states that would favor higher expression levels of genes essential for an organism's survival.

The upstream regulator analysis of the EWAS of life span identified the pluripotency transcription factors *OCT4*, *SOX2*, and *NANOG*. Other factors, such as *POLII*, *CTCF*, *RAD21*, *YY1*, and *TAF1*, showed the strongest enrichment for negatively life span–related CpGs.

CONCLUSION: The phyloepigenetic trees indicate that divergence of DNA methylation profiles closely parallels that of genetics through evolution. Our results demonstrate that DNA methylation is subjected to evolutionary pressures and selection. The publicly available data from our Mammalian Methylation Consortium are a rich source of information for different fields such as evolutionary biology, developmental biology, and aging. ■

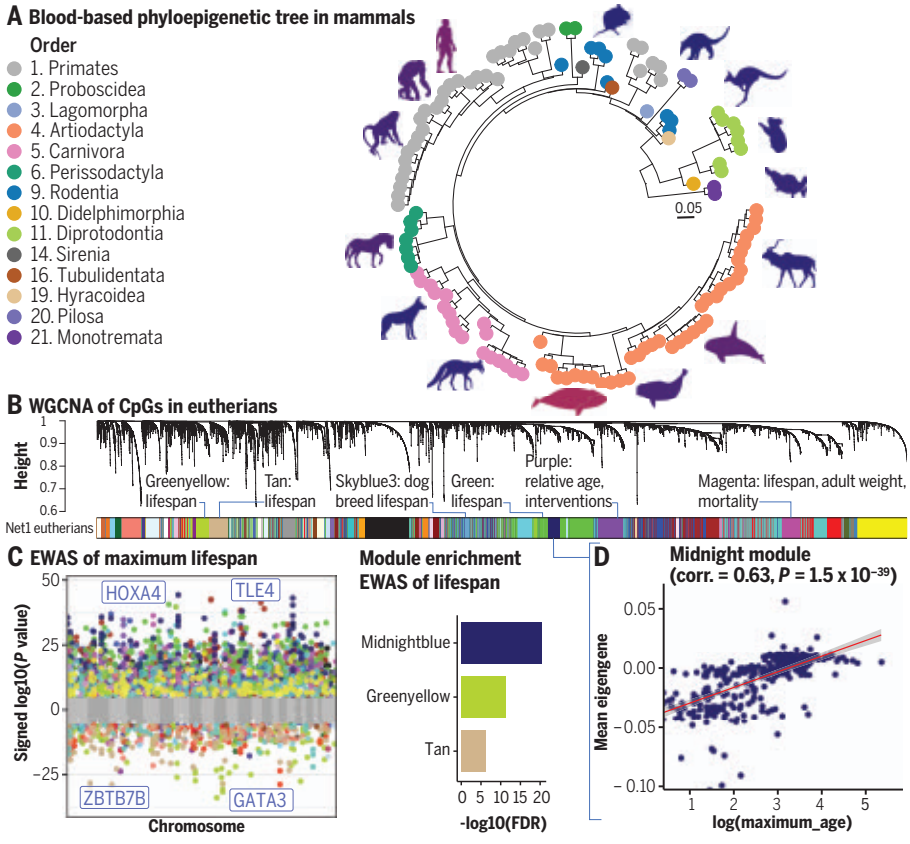

DNAm network relates to mammalian phylogeny and traits. (**A**) Phyloepigenetic tree from the DNAm data generated from blood samples. (**B**) Unsupervised WGCNA networks identified 55 comethylation modules. (**C**) EWAS of log-transformed maximum life span. Each dot corresponds to the methylation levels of a highly conserved CpG. Shown is the log (base 10)–transformed P value (y axis) versus the human genome coordinate Hg19 (x axis). (**D**) Comethylation module correlated with maximum life span of mammals. Eigengene (first principal component of scaled CpGs in the midnightblue module) versus log (base e) transformed maximum life span. Each dot corresponds to a different species.

The complete list of authors and their affiliations is available in the full article online.
Corresponding author. Email: shorvath@mednet.ucla.edu (S.H.); ahaghani@altoslabs.com (A.H.)
Cite this article as A. Haghani *et al.*, *Science* 381, eabq5693 (2023). DOI: 10.1126/science.abq5693

READ THE FULL ARTICLE AT
https://doi.org/10.1126/science.abq5693

RESEARCH ARTICLE

EVOLUTIONARY BIOLOGY

DNA methylation networks underlying mammalian traits

Amin Haghani[1,2]*†, Caesar Z. Li[3,4]†, Todd R. Robeck[5], Joshua Zhang[1], Ake T. Lu[1,2], Julia Ablaeva[6], Victoria A. Acosta-Rodríguez[7], Danielle M. Adams[8], Abdulaziz N. Alagaili[9], Javier Almunia[10], Ajoy Aloysius[11], Nabil M.S. Amor[12], Reza Ardehali[13], Adriana Arneson[14,15], C. Scott Baker[16], Gareth Banks[17], Katherine Belov[18], Nigel C. Bennett[19], Peter Black[20], Daniel T. Blumstein[21,22], Eleanor K. Bors[16], Charles E. Breeze[23], Robert T. Brooke[24], Janine L. Brown[25], Gerald Carter[26], Alex Caulton[27,28], Julie M. Cavin[29], Lisa Chakrabarti[30], Ioulia Chatzistamou[31], Andreas S. Chavez[26,32], Hao Chen[33], Kaiyang Cheng[34], Priscila Chiavellini[35], Oi-Wa Choi[36,37], Shannon Clarke[27], Joseph A. Cook[38], Lisa N. Cooper[39], Marie-Laurence Cossette[40], Joanna Day[41], Joseph DeYoung[36,37], Stacy Dirocco[42], Christopher Dold[5], Jonathan L. Dunnum[38], Erin E. Ehmke[43], Candice K. Emmons[44], Stephan Emmrich[6], Ebru Erbay[45,46,47], Claire Erlacher-Reid[42], Chris G. Faulkes[48,49], Zhe Fei[3,50], Steven H. Ferguson[51,52], Carrie J. Finno[53], Jennifer E. Flower[54], Jean-Michel Gaillard[55], Eva Garde[56], Livia Gerber[57,58], Vadim N. Gladyshev[59], Rodolfo G. Goya[35], Matthew J Grant[60], Carla B. Green[7], M. Bradley Hanson[44], Daniel W. Hart[19], Martin Haulena[61], Kelsey Herrick[62], Andrew N. Hogan[63], Carolyn J. Hogg[18], Timothy A. Hore[64], Taosheng Huang[65], Juan Carlos Izpisua Belmonte[2], Anna J. Jasinska[36,66,67], Gareth Jones[68], Eve Jourdain[69], Olga Kashpur[70], Harold Katcher[71], Etsuko Katsumata[72], Vimala Kaza[73], Hippokratis Kiaris[74], Michael S. Kobor[75], Pawel Kordowitzki[76], William R. Koski[77], Michael Krützen[78], Soo Bin Kwon[15,14], Brenda Larison[21,79], Sang-Goo Lee[59], Marianne Lehmann[35], Jean-François Lemaître[55], Andrew J. Levine[80], Xinmin Li[81], Cun Li[82,83], Andrea R. Lim[1], David T. S. Lin[84], Dana M. Lindemann[42], Schuyler W. Liphardt[85], Thomas J. Little[86], Nicholas Macoretta[6], Dewey Maddox[87], Craig O. Matkin[88], Julie A. Mattison[89], Matthew McClure[90], June Mergl[91], Jennifer J. Meudt[92], Gisele A. Montano[5], Khyobeni Mozhui[93], Jason Munshi-South[94], William J. Murphy[95,96], Asieh Naderi[74], Martina Nagy[97], Pritika Narayan[60], Peter W. Nathanielsz[82,83], Ngoc B. Nguyen[13], Christof Niehrs[98,99], Batsaikhan Nyamsuren[100], Justine K. O'Brien[41], Perrie O'Tierney Ginn[70], Duncan T Odom[101,102], Alexander G. Ophir[103], Steve Osborn[104], Elaine A. Ostrander[63], Kim M. Parsons[44], Kimberly C. Paul[80], Amy B. Pedersen[86], Matteo Pellegrini[105], Katharina J. Peters[78,106], Jessica L. Petersen[107], Darren W. Pietersen[108], Gabriela M. Pinho[21], Jocelyn Plassais[63], Jesse R. Poganik[59], Natalia A. Prado[109,110], Pradeep Reddy[111,2], Benjamin Rey[55], Beate R. Ritz[112,113,80], Jooke Robbins[114], Magdalena Rodriguez[115], Jennifer Russell[104], Elena Rydkina[6], Lindsay L. Sailer[103], Adam B. Salmon[116], Akshay Sanghavi[71], Kyle M. Schachtschneider[117,118,119], Dennis Schmitt[120], Todd Schmitt[62], Lars Schomacher[98], Lawrence B. Schook[117,121], Karen E. Sears[21], Ashley W. Seifert[11], Aaron B.A. Shafer[122], Anastasia V. Shindyapina[59], Melanie Simmons[43], Kavita Singh[123], Ishani Sinha[21], Jesse Slone[65], Russel G. Snell[60], Elham Soltanmohammadi[74], Matthew L. Spangler[107], Maria Spriggs[20], Lydia Staggs[42], Nancy Stedman[20], Karen J. Steinman[124], Donald T Stewart[125], Victoria J. Sugrue[64], Balazs Szladovits[126], Joseph S. Takahashi[7,127], Masaki Takasugi[6], Emma C. Teeling[128], Michael J. Thompson[105], Bill Van Bonn[129], Sonja C. Vernes[130,131], Diego Villar[132], Harry V. Vinters[133], Ha Vu[14,15], Mary C. Wallingford[70], Nan Wang[36,37], Gerald S. Wilkinson[8], Robert W. Williams[134], Qi Yan[3,2], Mingjia Yao[3], Brent G. Young[52], Bohan Zhang[59], Zhihui Zhang[6], Yang Zhao[6], Peng Zhao[13,135], Wanding Zhou[136,137], Joseph A. Zoller[3], Jason Ernst[14,15], Andrei Seluanov[138], Vera Gorbunova[138], X. William Yang[36,37], Ken Raj[139], Steve Horvath[1,2,139]*

Using DNA methylation profiles (n = 15,456) from 348 mammalian species, we constructed phyloepigenetic trees that bear marked similarities to traditional phylogenetic ones. Using unsupervised clustering across all samples, we identified 55 distinct cytosine modules, of which 30 are related to traits such as maximum life span, adult weight, age, sex, and human mortality risk. Maximum life span is associated with methylation levels in *HOXL* subclass homeobox genes and developmental processes and is potentially regulated by pluripotency transcription factors. The methylation state of some modules responds to perturbations such as caloric restriction, ablation of growth hormone receptors, consumption of high-fat diets, and expression of Yamanaka factors. This study reveals an intertwined evolution of the genome and epigenome that mediates the biological characteristics and traits of different mammalian species.

Comparative epigenomics is a burgeoning field that integrates epigenetic signatures with phylogenetic relationships to decipher gene-to-trait functions (*1*–*3*). Prior research has investigated the capacity of DNA methylation (DNAm) patterns in regulatory sequences to reflect evolutionary relationships among species (*3*, *4*). A recent study compared methylation data across multiple animal species at orthologous gene promoters using a sequencing-based assay that did not specifically target conserved CpGs (*4*). Previous investigations faced limitations regarding the measurement platform, particularly the low sequencing depth at conserved CpGs and the sample size per species.

Our study overcomes these constraints in several ways. First, we used a measurement platform ensuring high effective sequencing depth at conserved CpGs, allowing for a more precise analysis of DNAm patterns in highly conserved DNA regions. Second, we increased the sample size per species, aiming for many samples per species. We profiled 348 species from 25 of the 26 mammalian taxonomic orders. This comprehensive dataset enables examination of phylogenetic relationships, comethylation relationships between cytosines, and their associations with maximum life span and other species characteristics.

We profiled 15,456 samples (Fig. 1A and table S1) using a methylation array platform that provides effective sequencing depth at highly conserved CpGs across mammalian species (*5*). This dataset is the product of the multinational Mammalian Methylation Consortium. In previous studies, we applied supervised machine learning methods to generate DNAm-based predictors of age called epigenetic clocks for numerous species (*6*-*31*).

Here, we performed a large-scale cross-species unsupervised analysis of the entire dataset to reveal the relationship of DNAm with mammalian phylogeny. We show that we could construct phyloepigenetic trees that parallel traditional phylogenetic ones. We then proceed to interrogate the extent to which DNAm underpins specific biological traits by using unsupervised weighted correlation network analysis (WGCNA) to minimize the influence of bias on our observations. This approach identifies modules (clusters) of comethylated CpGs comethylation that are associated with species characteristics, including taxonomy, tissue type, sex, life span, and aging.

Results

Evolution and DNAm

We generated a dataset consisting of DNAm profiles of 15,456 DNA samples derived from 70 tissue types from 348 mammalian species using the mammalian methylation array (*5*). We evaluated whether methylation levels of cytosines (CpGs) in DNA sequences that are conserved across species would allow us to construct what could be called a phyloepigenetic tree. To avoid potential confounding by different tissue types, we generated tissue-specific phyloepigenetic trees (Fig. 1B and figs. S2 and S3). We defined the "congruence" between traditional phylogenetic trees and phyloepigenetic trees as the Pearson correlation coefficient between distances (branch length) based on phyloepigenetic trees and evolutionary

distances in traditional phylogenetic trees. We observed high congruence (0.93) (Fig. 1C and fig. S2) for the blood-based phyloepigenetic tree (124 species) and lower congruence values for nonblood tissues (congruence = 0.58 for liver and 0.72 for skin; fig. S2). The lower congruence in liver (158 species) and skin (133 species) may have been due to potential variability in sampling between species. The varying congruence across tissue types shows that the CpG probes do not serve as genotyping proxies. The tissue dependence of congruence indicates that phyloepigenetic trees are derived based on differences in methylation levels and not sequence conservation. This point was also corroborated by three sensitivity analyses, which confirmed that the high congruence was indeed due to differences in methylation levels

[1]Department of Human Genetics, David Geffen School of Medicine, University of California Los Angeles, Los Angeles, CA, USA. [2]Altos Labs, San Diego, CA, USA. [3]Department of Biostatistics, Fielding School of Public Health, University of California Los Angeles, Los Angeles, CA, USA. [4]Janssen Research & Development, Spring House, PA, USA. [5]Zoological Operations, SeaWorld Parks and Entertainment, Orlando, FL, USA. [6]Department of Biology, University of Rochester, Rochester, NY, USA. [7]Department of Neuroscience, Peter O'Donnell Jr. Brain Institute, University of Texas Southwestern Medical Center, Dallas, TX, USA. [8]Department of Biology, University of Maryland, College Park, MD, USA. [9]Department of Zoology, College of Science, King Saud University, Riyadh, Saudi Arabia. [10]Loro Parque Fundacion, Avenida Loro Parque, Puerto de la Cruz, Tenerife, Spain. [11]Department of Biology, University of Kentucky, Lexington, KY, USA. [12]Laboratory of Biodiversity, Parasitology, and Ecology, University of Tunis El Manar, Tunis, Tunisia. [13]Division of Cardiology, Department of Internal Medicine, David Geffen School of Medicine, University of California, Los Angeles, Los Angeles, CA, USA. [14]Bioinformatics Interdepartmental Program, University of California, Los Angeles, CA, USA. [15]Department of Biological Chemistry, University of California, Los Angeles, Los Angeles, CA, USA. [16]Marine Mammal Institute, Oregon State University, Newport, OR, USA. [17]Mammalian Genetics Unit, MRC Harwell Institute, Harwell Science and Innovation Campus, Oxfordshire, UK. [18]School of Life and Environmental Sciences, The University of Sydney, Sydney, New South Wales, Australia. [19]Department of Zoology and Entomology, University of Pretoria, Hatfield, South Africa. [20]Busch Gardens Tampa, Tampa, FL, USA. [21]Department of Ecology and Evolutionary Biology, University of California Los Angeles, Los Angeles, CA, USA. [22]The Rocky Mountain Biological Laboratory, Crested Butte, CO, USA. [23]Altius Institute for Biomedical Sciences, Seattle, WA, USA. [24]Epigenetic Clock Development Foundation, Los Angeles, CA, USA. [25]Center for Species Survival, Smithsonian National Zoo and Conservation Biology, Front Royal, VA, USA. [26]Department of Evolution, Ecology and Organismal Biology, The Ohio State University, Columbus, OH, USA. [27]AgResearch, Invermay Agricultural Centre, Mosgiel, Otago, New Zealand. [28]Department of Biochemistry, University of Otago, Dunedin, Otago, New Zealand. [29]Gulf World Marine Park - Dolphin Company, Panama City Beach, FL, USA. [30]School of Veterinary Medicine and Science, University of Nottingham, Nottingham, UK. [31]Department of Pathology, Microbiology & Immunology, School of Medicine, University of South Carolina, Columbia, SC, USA. [32]Translational Data Analytics Institute, The Ohio State University, Columbus, OH, USA. [33]Department of Pharmacology, Addiction Science and Toxicology, The University of Tennessee Health Science Center, Memphis, TN, USA. [34]Medical Informatics, David Geffen School of Medicine, University of California, Los Angeles, Los Angeles, CA, USA. [35]Biochemistry Research Institute of La Plata, Histology and Pathology, School of Medicine, University of La Plata, La Plata, Argentina. [36]Center for Neurobehavioral Genetics, Semel Institute for Neuroscience and Human Behavior, University of California, Los Angeles, Los Angeles, CA, USA. [37]Department of Psychiatry and Biobehavioral Sciences, David Geffen School of Medicine, University of California Los Angeles, Los Angeles, CA, USA. [38]University of New Mexico, Department of Biology and Museum of Southwestern Biology, Albuquerque, NM, USA. [39]Department of Anatomy and Neurobiology, Northeast Ohio Medical University, Rootstown, OH, USA. [40]Department of Environmental & Life Sciences, Trent University, Peterborough, Ontario, Canada. [41]Taronga Institute of Science and Learning, Taronga Conservation Society Australia, Mosman, New South Wales, Australia. [42]SeaWorld Orlando, Orlando, FL, USA. [43]Duke Lemur Center, Durham, NC, USA. [44]Conservation Biology Division, Northwest Fisheries Science Center, National Marine Fisheries Service, National Oceanic and Atmospheric Administration, Seattle, WA, USA. [45]Altos Labs, Bay Area Institute of Science, Redwood City, CA, USA. [46]Department of Cardiology, Smidt Heart Institute, Cedars-Sinai Medical Center, Los Angeles, CA, USA. [47]David Geffen School of Medicine, University of California, Los Angeles, CA, USA. [48]School of Biological and Chemical Sciences, Queen Mary University of London, London, UK. [49]School of Biological and Behavioural Sciences, Queen Mary University of London, London, UK. [50]Department of Statistics, University of California, Riverside, CA, USA. [51]Department of Biological Sciences, University of Manitoba, Winnipeg, Manitoba, Canada. [52]Fisheries and Oceans Canada, Winnipeg, Manitoba, Canada. [53]Department of Population Health and Reproduction, University of California, Davis School of Veterinary Medicine, Davis, CA, USA. [54]Mystic Aquarium, Mystic, CT, USA. [55]University of Lyon, CNRS, Laboratoire de Biométrie et Biologie Evolutive, Villeurbanne, France. [56]Greenland Institute of Natural Resources, Nuuk, Greenland. [57]School of Biological, Earth and Environmental Sciences, University of New South Wales, Sydney, New South Wales, Australia. [58]Australian National Wildlife Collection, CSIRO, Canberra, Australia. [59]Division of Genetics, Department of Medicine, Brigham and Women's Hospital, Harvard Medical School, Boston, MA, USA. [60]Applied Translational Genetics Group, School of Biological Sciences, Centre for Brain Research, The University of Auckland, Auckland, New Zealand. [61]Vancouver Aquarium, Vancouver, British Columbia, Canada. [62]SeaWorld San Diego, San Diego, CA, USA. [63]Cancer Genetics and Comparative Genomics Branch, National Human Genome Research Institute, National Institutes of Health, Bethesda, MD, USA. [64]Department of Anatomy, University of Otago, Dunedin, New Zealand. [65]Division of Human Genetics, Department of Pediatrics, University at Buffalo, Buffalo, NY, USA. [66]Division of Infectious Diseases, Department of Medicine, School of Medicine, University of Pittsburgh, Pittsburgh, PA, USA. [67]Department of Molecular Genetics, Institute of Bioorganic Chemistry, Polish Academy of Sciences, Poznan, Poland. [68]School of Biological Sciences, University of Bristol, Bristol, UK. [69]Norwegian Orca Survey, Andenes, Norway. [70]Mother Infant Research Institute, Tufts Medical Center, Boston, MA, USA. [71]Yuvan Research, Mountain View, CA, USA. [72]Kamogawa Sea World, Kamogawa, Chiba, Japan. [73]Peromyscus Genetic Stock Center, University of South Carolina, Columbia, SC, USA. [74]Department of Drug Discovery and Biomedical Sciences, College of Pharmacy, University of South Carolina, Columbia, SC, USA. [75]Edwin S. H. Leong Healthy Aging Program, Centre for Molecular Medicine and Therapeutics, University of British Columbia, Vancouver, British Columbia, Canada. [76]Institute of Veterinary Medicine, Nicolaus Copernicus University, Torun, Poland. [77]LGL Limited, King City, Ontario, Canada. [78]Evolutionary Genetics Group, Department of Anthropology, University of Zurich, Zurich, Switzerland. [79]Center for Tropical Research, Institute of the Environment and Sustainability, University of California, Los Angeles, Los Angeles, CA, USA. [80]Department of Neurology, David Geffen School of Medicine, University of California, Los Angeles, Los Angeles, CA, USA. [81]Technology Center for Genomics and Bioinformatics, Department of Pathology and Laboratory Medicine, University of California, Los Angeles, Los Angeles, CA, USA. [82]Texas Pregnancy and Life-course Health Center, Southwest National Primate Research Center, San Antonio, TX, USA. [83]Department of Animal Science, College of Agriculture and Natural Resources, Laramie, WY, USA. [84]Centre for Molecular Medicine and Therapeutics, BC Children's Hospital Research Institute, University of British Columbia, Vancouver, British Columbia, Canada. [85]Biology Department, University of New Mexico, Albuquerque, NM, USA. [86]Institute of Ecology and Evolution, School of Biological Sciences, University of Edinburgh, Edinburgh, UK. [87]White Oak Conservation Center, Yulee, FL, USA. [88]North Gulf Oceanic Society, Homer, AK, USA. [89]Translational Gerontology Branch, National Institute on Aging Intramural Research Program, National Institutes of Health, Baltimore, MD, USA. [90]ABS Global, DeForest, WI, USA. [91]Marineland of Canada, Niagara Falls, Ontario, Canada. [92]Biomedical and Genomic Research Group, Department of Animal and Dairy Sciences, University of Wisconsin Madison, Madison, WI, USA. [93]Department of Preventive Medicine, University of Tennessee Health Science Center, College of Medicine, Memphis, TN, USA. [94]Louis Calder Center - Biological Field Station, Department of Biological Sciences, Fordham University, Armonk, NY, USA. [95]Veterinary Integrative Biosciences, Texas A&M University, College Station, TX, USA. [96]Interdisciplinary Program in Genetics and Genomics, Texas A&M University, College Station, TX, USA. [97]Museum fur Naturkunde, Leibniz-Institute for Evolution and Biodiversity Science, Berlin, Germany. [98]Institute of Molecular Biology (IMB), Mainz, Germany. [99]Division of Molecular Embryology, DKFZ-ZMBH Alliance, Heidelberg, Germany. [100]Mammalogical Society of Mongolia, Ulaanbaatar, Mongolia. [101]Cancer Research UK Cambridge Institute, University of Cambridge, Cambridge, UK. [102]Deutsches Krebsforschungszentrum, Division of Regulatory Genomics and Cancer Evolution, Heidelberg, Germany. [103]Department of Psychology, Cornell University, Ithaca, NY, USA. [104]SeaWorld San Antonio, San Antonio, TX, USA. [105]Department Molecular Cell and Developmental Biology, University of California, Los Angeles, Los Angeles, CA, USA. [106]School of Earth, Atmospheric and Life Sciences, University of Wollongong, Wollongong, New South Wales, Australia. [107]Department of Animal Science, University of Nebraska, Lincoln, NE, USA. [108]Mammal Research Institute, Department of Zoology and Entomology, University of Pretoria, Hatfield, South Africa. [109]Department of Biology, College of Arts and Science, Adelphi University, Garden City, NY, USA. [110]Center for Species Survival, Smithsonian Conservation Biology Institute, Front Royal, VA, USA. [111]Salk Institute for Biological Studies, La Jolla, CA, USA. [112]Department of Epidemiology, UCLA Fielding School of Public Health, Los Angeles, CA, USA. [113]Department of Environmental Health Sciences, UCLA Fielding School of Public Health, Los Angeles, CA, USA. [114]Center for Coastal Studies, Provincetown, MA, USA. [115]Miami Seaquarium, Miami, FL, USA. [116]The Sam and Ann Barshop Institute for Longevity and Aging Studies and Department of Molecular Medicine, UT Health San Antonio, and the Geriatric Research Education and Clinical Center, South Texas Veterans Healthcare System, San Antonio, TX, USA. [117]Department of Radiology, University of Illinois at Chicago, Chicago, IL, USA. [118]Department of Biochemistry and Molecular Genetics, University of Illinois at Chicago, Chicago, IL, USA. [119]National Center for Supercomputing Applications, University of Illinois at Urbana-Champaign, Urbana, IL, USA. [120]College of Agriculture, Missouri State University, Springfield, MO, USA. [121]Department of Animal Sciences, University of Illinois at Urbana-Champaign, Urbana, IL, USA. [122]Department of Forensic Science, Environmental & Life Sciences, Trent University, Peterborough, Ontario, Canada. [123]Shobhaben Pratapbhai Patel School of Pharmacy & Technology Management, SVKM'S NMIMS University, Mumbai, India. [124]Species Preservation Laboratory, SeaWorld San Diego, San Diego, CA, USA. [125]Biology Department, Acadia University, Wolfville, Nova Scotia, Canada. [126]Department of Pathobiology and Population Sciences, Royal Veterinary College, Hatfield, UK. [127]Howard Hughes Medical Institute, Department of Neuroscience, University of Texas Southwestern Medical Center, Dallas, TX, USA. [128]School of Biology and Environmental Science, University College Dublin, Belfield, Dublin, Ireland. [129]Animal Care and Science Division, John G. Shedd Aquarium, Chicago, IL, USA. [130]School of Biology, The University of St. Andrews, Fife, UK [131]Neurogenetics of Vocal Communication Group, Max Planck Institute for Psycholinguistics, Nijmegen, Netherlands. [132]Blizard Institute, Faculty of Medicine and Dentistry, Queen Mary University of London, London, UK. [133]Department of Pathology and Laboratory Medicine, David Geffen School of Medicine, University of California Los Angeles, Los Angeles, CA, USA. [134]Department of Genetics, Genomics and Informatics, University of Tennessee Health Science Center, College of Medicine, Memphis, TN, USA. [135]Eli and Edythe Broad Center of Regenerative Medicine and Stem Cell Research, University of California, Los Angeles, Los Angeles, CA, USA. [136]Center for Computational and Genomic Medicine, Children's Hospital of Philadelphia, Philadelphia, PA, USA. [137]Department of Pathology and Laboratory Medicine, University of Pennsylvania, Philadelphia, PA, USA. [138]Departments of Biology and Medicine, University of Rochester, Rochester, NY, USA. [139]Altos Labs, Cambridge, UK.
***Corresponding author. Email: shorvath@mednet.ucla.edu (S.H.); ahaghani@altoslabs.com (A.H.)**
†These authors contributed equally to this work.

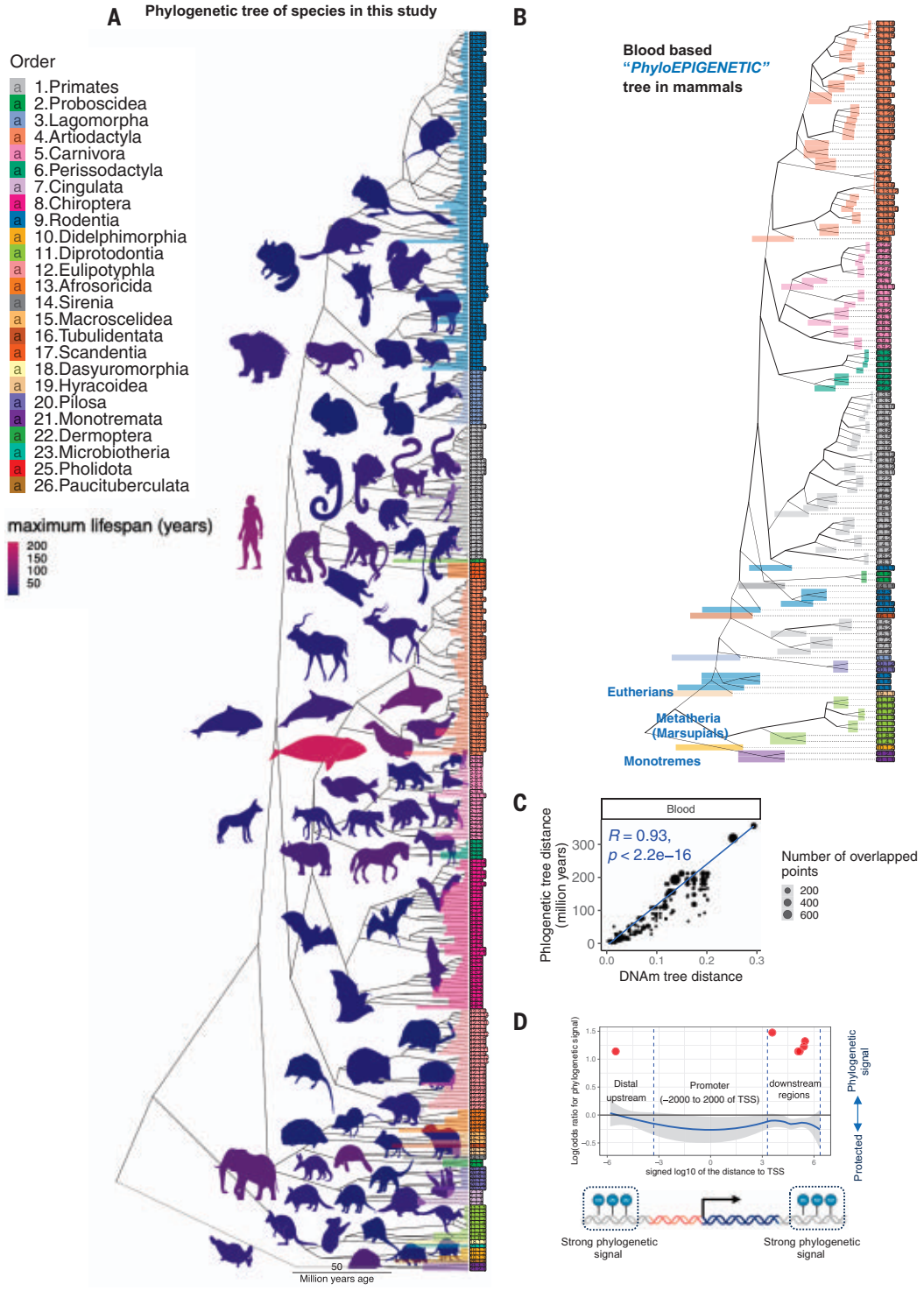

Fig. 1. Phyloepigenetic trees parallel the mammalian evolutionary tree. (**A**) The traditional phylogenetic tree from the TimeTree database (*44*) based on 321 (of 348) species in our study. A full description of the species in our study is reported in table S1. (**B**) Blood-based phyloepigenetic tree created from hierarchical clustering of DNAm data in this study (for additional analysis, see fig. S3, A and B). We formed the mean value per cytosine across samples for each species. The clustering used 1 minus the Pearson correlation (1-cor) as a pairwise dissimilarity measure and the average linkage method as intergroup dissimilarity. Phyloepigenetic trees for skin and liver can be found in fig. S2. Additional analyses, e.g., involving different choices of CpGs or intergroup dissimilarity measures, are reported in the supplementary materials (fig. S2). The colored bars reflect the branch height. (**C**) Scatter plot of the distances in blood phyloepigenetic (1-cor) versus the traditional evolutionary tree. (**D**) Scatter plots displaying the log-odds ratios of regions exhibiting phylogenetic signals relative to the TSS are presented. The phylogenetic signal is determined using Blomberg's K statistic (*32*). In this analysis, CpGs were grouped into categories using sliding windows relative to the TSS. To assess enrichment, the Fisher's exact overlap test was used, focusing on the top 500 CpGs displaying phylogenetic signals within each region. The red dots highlight the regions with the Fisher's exact *P* value < 0.05. The results indicate notable enrichment (OR > 3) in certain intergenic and genic regions but not in promoters. For additional analysis, see fig. S4.

(see the supplementary text). In particular, the phyloepigenetic trees based on the 180 CpGs with the most significant detection *P* values across all 348 species still are congruent with traditional trees (fig. S2, F and G).

To identify CpGs that exhibit a pronounced phylogenetic signal in relation to methylation and phylogenetic trees, we used Blomberg's K statistic (*32*). Among the top 500 CpGs showing significant phylogenetic signals (nominal Blomberg $P < 0.001$, selected by variance *z* score), we observed an enrichment in upstream intergenic regions [odds ratio (OR) = 1.4, Fisher's exact $P < 0.05$; fig. S4B]. To further investigate regions with the strongest phylogenetic signal, we divided the data into groups relative to the transcriptional start sites (TSSs). This analysis also confirmed that intergenic regions exhibit significant phylogenetic signals (OR > 3, Fisher's exact $P < 0.05$), whereas the promoter regions did not show such signals (Fig. 1D).

DNAm networks relate to individual and species traits

We used signed WGCNA, an unsupervised analysis (*33*), to cluster CpGs with similar methylation dynamics across samples into comethylation modules. We then summarized their methylation profiles as "module eigengenes." The respective eigengenes of these modules were used to identify their potential correlations with various traits within and across mammalian species.

Our data analysis proceeded in two sequential phases. First, we developed several comethylation networks using data from 11,099 DNA samples from 174 species (discovery dataset finalized March 2021). A eutherian network [network 1 (Net1)] was formed from 14,705 conserved CpGs using this dataset (Fig. 2A). Later, we generated a second dataset of 4357 samples from 30 tissues of 240 mammalian species (174 new species and 66 that are represented in the discovery set), which were not used to define modules and were used as an independent validation set. All eutherian modules were present in the independent validation dataset according to module preservation statistics (corKME) (*34*), validating the presence of these modules (corKME > 0.43, $P < 10^{-22}$; median corKME = 0.84) (fig. S5). These modules were designated with colors according to WGCNA convention (Fig. 2A). The smallest module (lavenderblush3) consisted of 33 CpGs and the largest (turquoise) had 1864 CpGs.

To characterize the 55 modules with respect to species characteristics (e.g., maximum life span and average adult weight), module eigengenes were calculated in all samples (discovery and validation set combined, 331 eutherian species). Because information on taxonomic order, tissues, maximum life span, age, sex and adult weight of each species was available, we were able to assess whether any of the module eigengenes correlated with these traits. Of the 55 modules, 30 were found to be correlated with at least one trait (Fig. 2B, fig. S7, and table S3). Specifically, 15 modules were related to taxonomic orders such as primates, rodents, or carnivores (Fig. 2B and fig. S11). Ten modules related to tissue type (fig. S11), two to sex (fig. S11), one to age, seven to maximum life span, and four to average adult species weight. Some modules were related to multiple characteristics. In the following sections, we mainly focus on the modules that relate to mammalian maximum life span, adult weight, and age. Other modules related to taxonomic order, tissue type, and sex are described in the supplementary materials (fig. S11). We performed two analyses to ascertain whether these eutherian modules are also applicable to marsupials and monotremes. Using the discovery dataset, we first trained a network (Net2) in both eutherians and marsupials based on only 7956 probes that are mappable to both. The color bands under the hierarchical tree reveal that all the Net1 modules were also preserved in Net2 (Fig. 2A). Second, we selected CpGs in Net1 modules that were also mapped to marsupials or monotremes and confirmed that their eigengene relationships to primary traits were retained in these mammalian clades (table S3). For example, the magenta module, which is related to blood in eutherians, was also found to be so in monotremes (table S3), which confirms that the Net1 modules can indeed be applied to other mammalian clades by selecting probes that are also mapped to those clades.

A functional enrichment study, accounting for the mammalian array background, revealed that the genes neighboring to module CpGs are implicated in many biological processes including development, immune function, metabolism, reproduction, stem cell biology, stress responses, aging, and various signaling pathways (Fig. 2C and fig. S9).

Relationship with protein-protein interactions

We investigated whether the proteins encoded by cognate genes (closest to respective CpGs) within modules are known to mutually interact or predicted to do so by STRING protein-protein interaction networks, which integrate known and predicted protein associations from >14,000 organisms (*35*). A permutation test analysis evaluating the global cluster coefficient (*36*) of each module showed that 14 modules are significantly enriched ($P < 0.001$) for genes encoding mutually interacting proteins (Fig. 2D). Overall, these results suggest that comethylation relationships can be reflected at the protein level for a subset of modules.

Modules related to maximum life span

To adjust for potential confounders, we used four regression modeling approaches to identify modules that are associated with the log-transformed maximum life span (dependent variable): (i) a univariate regression model with a covariate that was the module eigengene (averaged per species); (ii) a phylogenetic regression model with a covariate that was again the module eigengene (averaged per species); (iii) a multivariate linear regression model that included the module eigengene, sex, tissue, and relative age as covariates; and (iv) model approach (i) applied to specific tissue types.

The marginal analysis identified four modules: magenta, black, midnightblue, and tan, that related significantly to maximum life span (the absolute value of the Pearson correlation exceeded $r = 0.6$, Student's *t* test $P < 1 \times 10^{-33}$). The CpGs underlying the implicated modules exhibit the sample patterns, as can be seen from corresponding heatmaps (fig. S14C). Phylogenetic regression also identified associations of the same modules (table S3). Our fourth modeling approach, i.e., the tissue-stratified marginal analysis, indicates that the relationship of modules to maximum life span is often tissue specific. For example, the magenta and midnightblue modules relate to maximum life span in lung and liver (fig. S14A). By contrast, the black module relates to maximum life span only in skin, and the tan module exhibited a weak relationship to life span in the tissue-specific analysis.

For ease of comprehension, modules were labeled with the trait and direction of relationship by superscript plus and minus signs; for example, magenta is the Lifespan^{+}Weight^{+}Blood^{+} module). The two modules (magenta with 480 CpGs, and midnightblue with 249 CpGs) that correlated with life span in lung and liver also correlated significantly with average adult weight across all eutherian species ($r = 0.47$ to 0.55, $P < 1 \times 10^{-18}$; Fig. 3). The magenta module (Lifespan^{+}Weight^{+}Blood^{+}) is enriched with developmental genes such as *HOXA5*, *VEGFA*, *SOX2*, and *WNT11* (table S4). The midnightblue (Lifespan^{+}Weight^{+}) module implicates genes involved in transfer RNA metabolism ($P = 2 \times 10^{-6}$, e.g., *URM1*), lipopolysaccharides ($P = 5 \times 10^{-6}$, e.g., *CERCAM*), development ($P = 10^{-4}$, e.g., the *HOXL* gene family), and fatty acids ($P = 2 \times 10^{-3}$, e.g., *ACADVL*). The magenta module also relates to life span and average weight of dog breeds ($r = -0.30$, $P = 0.003$; Fig. 3C). Furthermore, it is related to the hazard of human death [hazard ratio (HR) = 0.91, MetaP = 0.0016; Fig. 3D) in epidemiological cohort studies.

After adjustment for phylogeny, the cyan module relates to mammalian life span phylogenetic contrast ($r = 0.42$, $P = 4 \times 10^{-14}$; fig. S13I). The Lifespan^{+}Liver^{-} (cyan) module consists of genes that play a role in adaptive immunity ($P = 2 \times 10^{-6}$), histone and protein demethylation ($P = 0.0001$), and metabolism ($P = 0.0004$) (table S4).

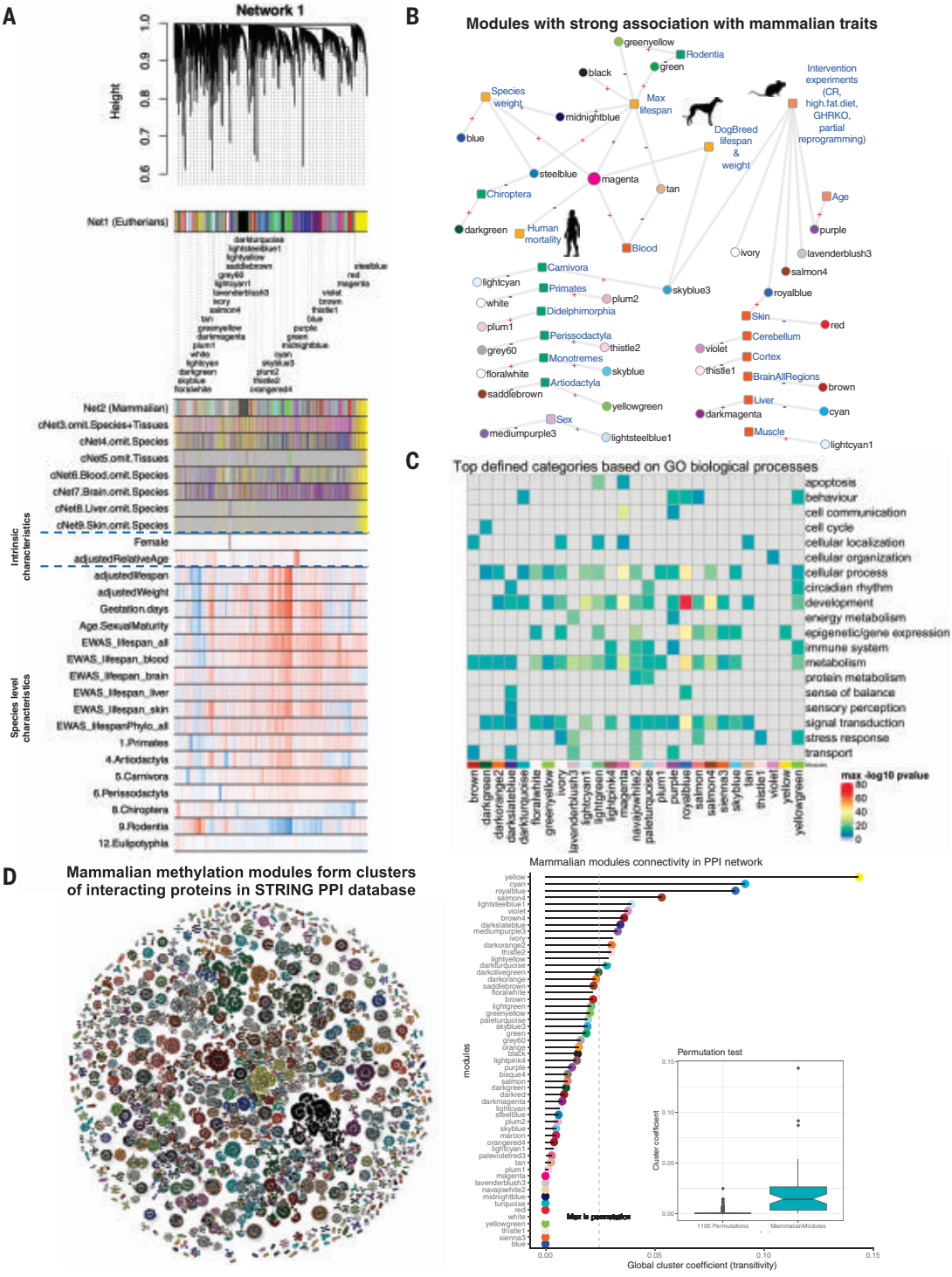

Fig. 2. DNAm network relates to species and individual characteristics in mammalian species. (**A**) the WGCNA network of 14,705 conserved CpGs in eutherian species (Net1). The identified modules related to species or individual sample characteristics. Net1 modules were compared with eight additional networks (fig. S5). The modules with strong associations with species and sample characteristics are labeled below the dendrogram. Gray color indicates CpGs that are outside of modules. (**B**) Summary of the modules showing strong associations with species and individual sample characteristics. The plus and minus labels are the direction of association with each trait. (**C**) Top defined functional biological processes related to Net1 modules (for details, see fig. S9 and table S4). (**D**) Mammalian comethylation modules form clusters of proteins in the STRING protein-protein interaction (PPI) network. For the sake of visualization, the analysis was limited to the top 50 CpGs with the highest module membership value per module. Colors indicate mammalian Net1. The lollipop plot shows the global cluster coefficient (*36*) of the proteins within a module (up to 500 top CpGs) in a PPI network. Our permutation analysis matched the distribution of the original module sizes. We evaluated 1100 random permutations, i.e., 20 for each of the 55 modules. The boxplot reports the global clustering coefficient per module (*y* axis) versus permutation status: module resulting from a random selection of proteins (left) versus original module resulting from WGCNA (right). The modules with cluster coefficients larger than the maximum permutation cluster coefficient were considered as significant at $P = 0.001$. The dashed vertical line corresponds to the maximum global clustering coefficient observed in the 1100 random permutations.

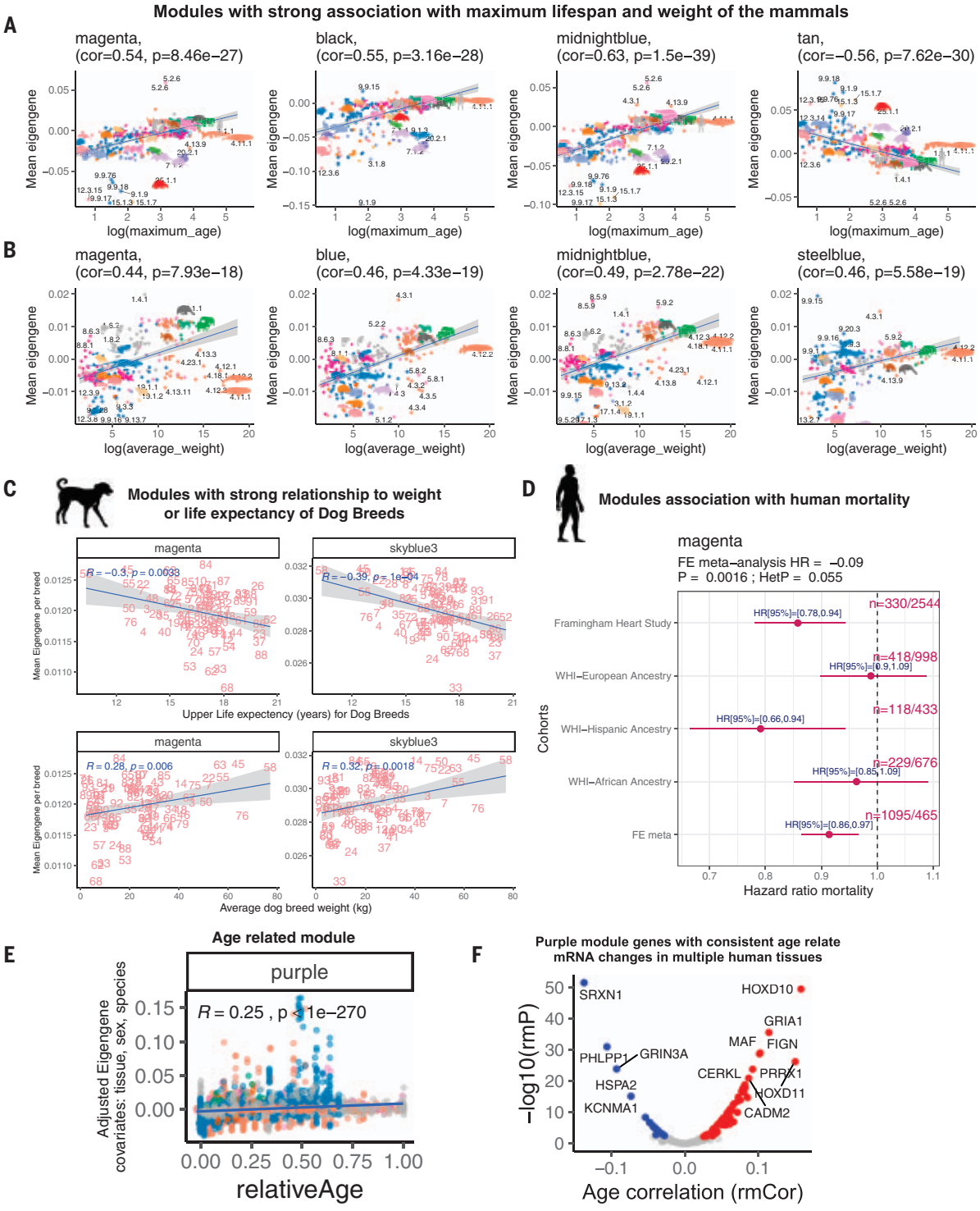

Fig. 3. Comethylation modules related to mammalian maximum life span, weight, human mortality, and age. (**A** and **B**) Modules associated with log maximum life span ($P < 10^{-20}$) (A) or log average species weight ($P < 10^{-17}$) (B) in marginal association (correlation test with the mean module eigengene of the species). The module eigengene is defined as the first principal component of the scaled CpGs underlying a module. The species are randomly labeled by their animal number (table S1). (**C**) The top modules associated with median life expectancy, upper limit life expectancy, or average adult weight of 93 dog breeds, model (marginal correlation test of the mean module eigengene with target variables; for detailed breed characteristics, see table S8). *R*, Pearson correlation* coefficient; *P*, correlation test *P* value. (**D**) Forest plots of the top modules associated with mortality risk in the Framingham Heart Study Offspring Cohort (FHS), and Women's Health Initiative (WHI) study totaling 4651 individuals (1095, 24% death). *n* denotes the number of deaths per total number of individuals in each study. We report the meta-analysis *P* value in the title of the forest plot. (**E**) Module that correlates significantly ($P < 1 \times 10^{-300}$) with relative age (defined as ratio of age/maximum life span) across mammalian species using a multivariate regression model. Covariates were tissue, sex, and species differences. Each dot corresponds to a eutherian tissue sample ($n = 14{,}542$). Dots are colored by taxonomic order as in Fig. 1. (**F**) Volcano plot of the rmCorr of all purple module genes in GTEx data (for additional analysis, see fig. S11).

The multivariate model analysis included sex, tissue type, and relative age as covariates to reveal additional modules that relate to life span in different tissues. The regression analysis found two modules with opposing correlations with maximum life span: the green module (life span $r = 0.42$, average weight $r = 0.38$, $P < 10^{-300}$) and the greenyellow module (life span $r = -0.44$, average weight $r = -0.35$, $P < 10^{-300}$; fig. S13J). The CpGs of the Lifespan^{-}Weight^{-}Rodentia^{-} (greenyellow) are located near genes that play a role in development ($P = 5 \times 10^{-13}$; table S4) and in RNA metabolism ($P = 6 \times 10^{-12}$).

Age-related consensus module in mammals

The purple module (denoted subsequently as RelativeAge^{+} module) exhibited the strongest positive correlation with relative age (relative age $r = 0.35$, $P < 10^{-300}$; Fig. 3E and fig. S13).

To remove the confounding effects of species and/or tissue type, we also constructed seven consensus networks (denoted cNet3,..., cNet9; for a description, see the supplementary materials). The RelativeAge^{+} module was preserved in three different consensus networks (cNet3, cNet4, and cNet6; Fig. 2A), suggesting conservation in different species and tissues (scatter plot in fig. S11H). The purple RelativeAge^{+} module is positively enriched for CpGs in regulatory regions (e.g., promoters and 5′ untranslated regions) and depleted in intron regions (fig. S15). Functional enrichment of this module highlighted embryonic stem cell regulation, axonal fasciculation, angiogenesis, and diabetes-related pathways (table S3). The CpGs in this module are adjacent to Polycomb repressor complex 2 (PRC2, EED) targets, which are marked by H3K27me3 (table S3).

Ingenuity pathway analysis implicated POU5F1 (alias OCT4), SHH, ASCL1, SOX2, and NEUROG2 proteins as putative upstream regulators of the RelativeAge^{+} module. We used Genotype-Tissue Expression project (GTEx) data to determine whether the mRNA levels of any of these upstream regulators are altered with age in several human tissues. *OCT4* [repeated-measures correlation (rmCorr) = 0.07, $P = 2 \times 10^{-14}$], which is among the four known Yamanaka factors for cellular dedifferentiation, showed a positive increase with age in several, but not all, human tissues (fig. S11F). Nine other genes (e.g., *HOXD10*, rmCorr = 0.16, $P = 4 \times 10^{-50}$; *SRXN1*, rmCorr = −0.14, $P = 4 \times 10^{-52}$) from the RelativeAge^{+} module also had a nominally significant rmCorr ($P < 0.005$) in GTEx data (Fig. 3F and fig. S11G), although opposite aging patterns could be found in select tissues. These observations highlight the relevance of genes in the RelativeAge^{+} module to stem cell biology and aging in human tissues.

Interventional studies in mice

We related our methylation modules to interventions that are known to modulate the life span of mice (Fig. 4, A to C). This included growth hormone receptor knockout (i.e., dwarf mice) (*37*) and caloric restriction (*38*), which extended life, and a high-fat diet, which elicited the opposite effect (*12*). Six modules, including the purple module (RelativeAge^{+}) showed a significant decrease ($P < 0.05$) of the module eigengene in dwarf mice and after caloric restriction and, conversely, a modest increase after a high-fat diet. Although the magenta, black, midnightblue, tan, and greenyellow modules have connections to the maximum life span in mammals, they did not present a clear relationship with interventions that modify murine life span (growth hormone receptor knockout, caloric restriction, and high-fat diet). This suggests a mutual exclusivity between the modules related to the maximum mammalian life span and those affected by interventions modulating the murine life span.

Transient expression of Yamanaka factors

We investigated whether a transient expression of the Yamanaka factors in the 4-factor (4F) mouse affects the module eigengenes. The experimental design is shown in Fig. 4D, with additional details reported in the original article (*39*). Four of six of the above-mentioned murine intervention modules showed a nominally significant dose-dependent rejuvenation in murine skin ($P < 0.06$), and two modules showed the same in kidney (dose refers to the duration of 4F treatment: 0, 1, 7, and 10 months of intermittent expression of 4F factors) (Fig. 4E). The purple, ivory, and lavenderblush3 modules were particularly sensitive to the 4F treatment (Pearson's $r \ll -0.64$ in skin). In addition, the purple RelativeAge^{+} module's response to the 4F treatment is consistent with bioinformatic findings that OCT4 is an upstream regulator of this module. Among the life span modules, only the black module demonstrates an increase ($P = 0.007$) in skin of 4F treated mice, but this was not observed in the kidney.

Epigenome-wide association analysis of maximum life span

We performed epigenome-wide association studies (EWASs) to identify individual CpGs with methylation levels that correlate with maximum life span. To reduce bias resulting from different levels of sequence conservation, our EWASs of maximum life span focused on 333 eutherian species, excluding marsupial and monotreme species. We restricted the analysis to 28,318 high-quality probes that are conserved between humans and mice.

When relating individual CpGs to log-transformed maximum life span, we used several modeling approaches (for details, see the supplementary text). Briefly, our first approach, generic modeling, applied regression analysis ignoring tissue type and age. In our second approach, we repeated the regression analysis after focusing on a given tissue type. Third, we focused on specific nonoverlapping age groups: young animals (defined as age <1.5 times the age at sexual maturity), middle-aged, and old (defined as age >3.5 times the age at sexual maturity; fig S19). Some of these regression models were further adjusted for average species weight (denoted LifespanAdjWeight).

For brevity, we will focus on linear regression models because phylogenetic regression models led to qualitatively similar conclusions (tables S13 and S14). The most significant life span–related CpGs are located in the distal intergenic region neighboring *TLE4* (Pearson's $r = 0.68$, $P = 5.8 \times 10^{-46}$; Fig. 5A and table S11) and two CpGs near the promoter region of *HOXA4* ($r = 0.66$, $P = 7.5 \times 10^{-45}$; Fig. 5A, midnightblue module) and are negatively correlated with a CpG in an intron of *GATA3* ($r = -0.65$, $P = 8.8 \times 10^{-42}$; Fig. 5A). Many of these significant CpGs remained so after phylogenetic adjustment, such as the CpGs neighboring *TLE4* and *HOXA4* ($P = 4.2 \times 10^{-5}$ and $P = 4.8 \times 10^{-3}$, respectively; fig. S17 and tables S11 and S12). The top 1000 life span–related CpGs (comprising 500 positively and 500 negatively life span–related CpGs) significantly overlapped (Fisher's exact $P = 5.5 \times 10^{-134}$) with those found in our weight-adjusted analysis (LifespanAdjWeight).

In general, methylation of life span–related CpGs does not change with age in mammalian tissues (Fig. 5B and fig. S20). The same can be seen from EWASs of life span restricted to animals of a given age group (e.g., only very young animals; fig. S20D). The EWASs of life span in all animals (irrespective of age) is highly correlated ($r > 0.7$), with the analogous EWASs restricted to animals that are young, middle-aged, or old.

EWASs of life span showed good consistency with the eigengene-based analysis in the mammalian comethylation network. As expected, the following previously discussed life span–related modules were enriched with CpGs implicated by our EWAS of life span: midnightblue (hypergeometric test $P = 2.2 \times 10^{-47}$; 67/249 overlapped CpGs), greenyellow (hypergeometric $P = 2.1 \times 10^{-36}$; 70/398 overlapped CpGs), tan (hypergeometric $P = 6.7 \times 10^{-23}$; 52/365 overlapped CpGs), and green (hypergeometric $P = 5.0 \times 10^{-18}$; 104/1542 overlapped CpGs).

In total, 1006 genes had a differential methylation association with life span (union of cognate genes resulting from the marginal model analysis for life span and LifespanAdjWeight). The gene expression levels of 16 of these genes exhibited a highly significant repeated-measures correlation with chronological age (rmCorr P value $< 10^{-50}$) in different human tissues (Fig. 5C). The cognate genes next to the top 500 positively life span–related CpGs play a

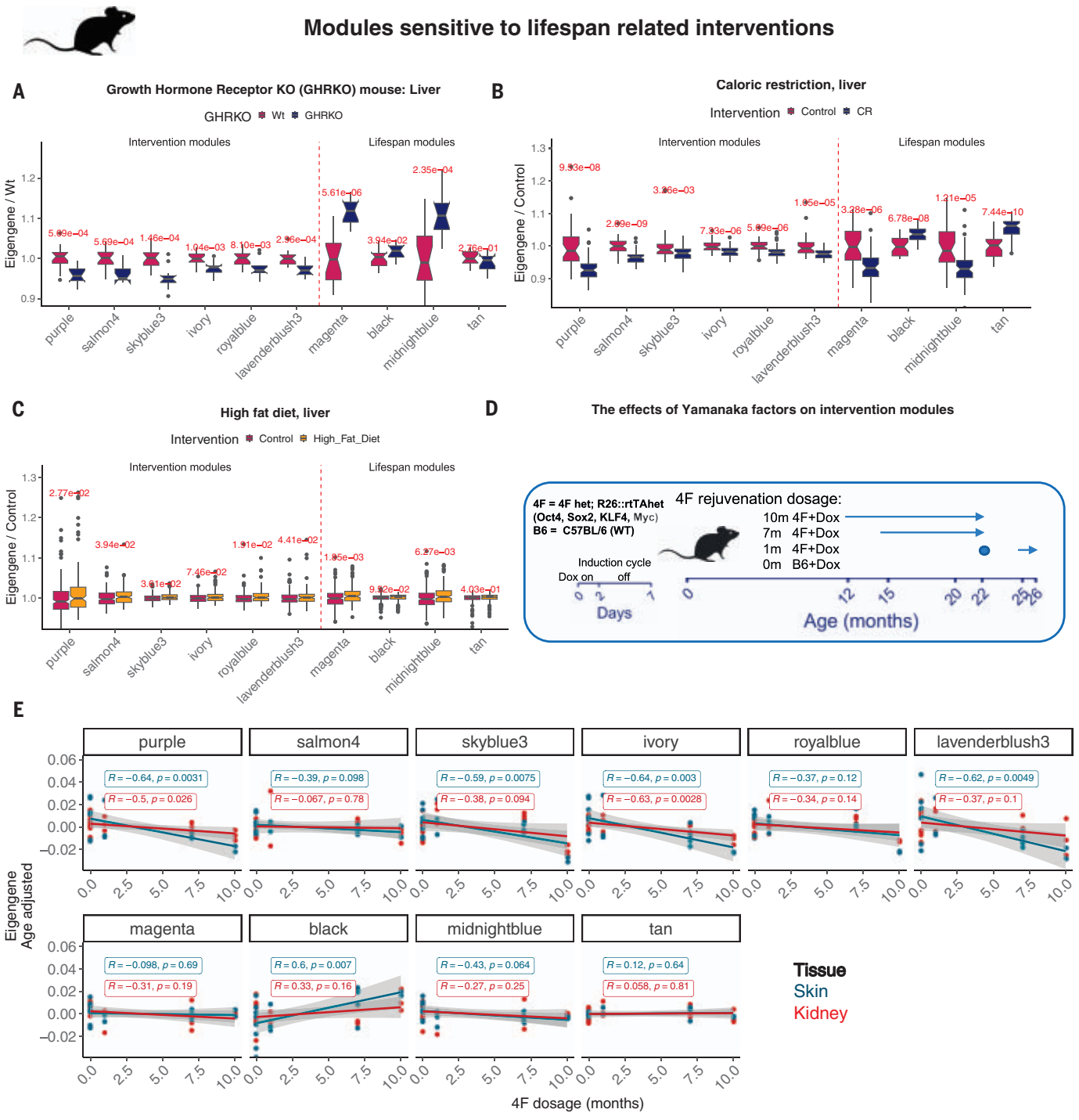

Fig. 4. The effects of different pro-aging and anti-aging interventions on selected DNAm modules. Six DNAm modules respond to life span–related intervention experiments and are associated with the life expectancy of the mouse models. By contrast, the mammalian maximum life span modules do not correspond directly to the benefits or stress triggered by the intervention in the murine samples. (**A**) Changes in the intervention modules in the liver parallel smaller size and longer life expectancy of growth hormone receptor mouse models (GHRKO). Sample size: GHRKO, n = 11 (n = 5 female, n = 6 male); wild type, n = 18 (n = 9 male, n = 9 female). Age range was 6 to 8 months. (**B**) Caloric restriction (CR) DNAm module signature predicts longer life span in this treated group (age = 18 months; sex = male; CR, n = 59; control, n = 36). (**C**) High-fat diet accelerates aging in five modules including the purple (RelativeAge^{+}) module. High-fat diet, n = 133 (n = 125 females, n = 8 males); control (ad libitum feeding), n = 212 (n = 10 male, n = 202 female). Age range was 3 to 32 months. (**D** and **E**) Examining the effects of in vivo partial reprogramming on intervention modules. (D) Schematic view of the partial programming experiment in 4F mice (*39*). A systemic Yamanaka factors expression (Oct4, Sox2, Klf4, and Myc) was periodically induced by adding doxycycline to the drinking water for 2 days per week. Partial programming was done at three different durations. Sample size: control (C57BL/6+dox), n = 7; 1 month (1m) 4F, n = 3; 7 months (7m) 4F, n = 5; 10 months (10m) 4F. All tissues except skin, n = 3; skin, n = 2. (E) scatter plots of the linear changes of the intervention modules in the skin and kidney of mice treated with different durations (dosages) of Yamanaka factors. Intervention modules indicate a dose-dependent rejuvenation of skin and kidney by this partial programming regimen.

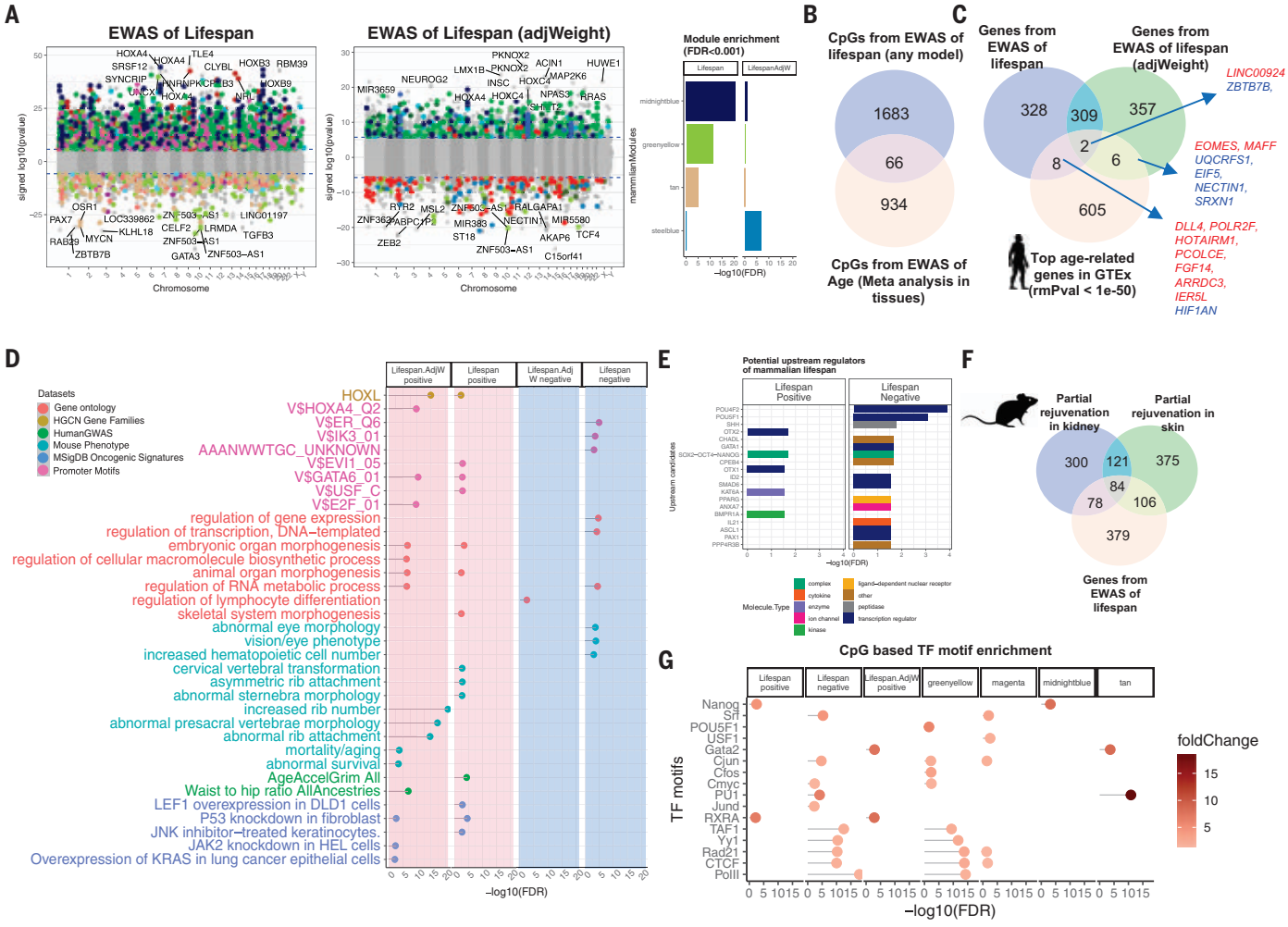

Fig. 5. EWAS of mammalian log-transformed maximum life span. (**A**) CpG-specific association with maximum life span across $n = 333$ eutherian species. For EWAS, the mean methylation values of each CpG (per species) were regressed on log maximum life span. The right portion of the panel reports EWAS results after adjustment for average adult weight. Genome annotation indicates human hg19. Blue dotted line indicates Bonferroni-corrected two-sided P value < 1.8×10^{-6}. The point colors indicate the corresponding modules. The bar plot indicates the top enriched (hypergeometric test, eutherian probes as background) modules for the top 1000 (500 negative CpGs, nominal $P < 1.1 \times 10^{-11}$, FDR = 1×10^{-10}; 500 negative and positive CpGs, nominal $P < 1.5 \times 10^{-21}$, FDR = 7.5×10^{-20}) significant CpGs for different EWASs. (**B**) Venn diagram of the overlaps between top hits from EWAS of maximum life span and meta-analysis of age [meta-analysis results are from (*7*); for additional analysis, see fig. S20]. (**C**) Venn diagram of the overlaps between the genes adjacent to the EWAS results and top age-related mRNA changes in human tissues ($P < 1 \times 10^{-50}$). (**D**) Gene set enrichment analysis of the genes proximal to CpGs associated with mammalian maximum life span. We only report enrichment terms that are significant after adjustment for multiple comparisons (hypergeometric FDR < 0.01) and contain at least five significant genes. The top three significant terms per column (EWAS) and enrichment database are shown. (**E**) Ingenuity potential upstream regulator analysis (*40*) of the differentially methylated genes related to mammalian maximum life span. Only significant (FDR < 0.05) regulators are represented in the bar plot. (**F**) Venn diagram of three gene lists. Gene list 1 is the top 646 genes adjacent to 1000 life span–related CpGs (500 positive and 500 negative). Gene lists 2 and 3 are based on CpGs that are differentially methylated (nominal Wald test $P < 0.005$, up to 500 positive and 500 negatively related CpGs) after OSKM overexpression in murine kidney (583 genes) and skin (686 genes) (*39*). We observed significant overlap between the gene lists (nominal Fisher's exact $P = 9.9 \times 10^{-30}$ for skin and life span; $P = 4.5 \times 10^{-25}$ for kidney and life span). (**G**) Transcriptional factor motif enrichment analysis of life span modules and life span–related CpGs. The enrichment results for LifespanAdjWeight. negative were not significant. The overlap is assessed by a hypergeometric test for the CpGs within the motifs based on the human hg19 genome.

critical role in animal organ morphogenesis [marginal model life span GREAT enrichment false discovery rate (FDR) = 3×10^{-4} and LifespanAdjWeight FDR = 3.3×10^{-7}; Fig. 5D] and in increased rib number in mice (FDR = 1×10^{-21}; Fig. 5D), and implicates the *HOXL* subclass homeobox genes (FDR = 0.004 and LifespanAdjWeight FDR = 1.3×10^{-15}) in abnormal survival in mice (FDR < 4×10^{-4}).

Upstream regulators of maximum life span

We used ingenuity pathway analysis (*40*) to identify potential upstream regulators of the genes cognate to the top 500 positively and top 500 negatively life span–related CpGs. The top-ranked candidate regulators of both gene lists included SOX2-OCT4-NANOG pluripotency factors (FDR = 5.7×10^{-4} life span negative, FDR = 5.7×10^{-4} life span positive), which play critical roles in cellular reprogramming. We performed a control analysis that ruled out potential confounding by sequence conservation (fig. S25). Upstream regulators also included several candidates related to development: sonic hedgehog (SHH), life span–negative FDR = 1.3×10^{-4}; POU4F2, life span–negative FDR = 3.3×10^{-7} and ASCL1, life span–negative FDR = 1.6×10^{-3} (Fig. 5E). These

findings suggest that expression of life span–related genes might be regulated to some extent by pluripotency factors. This prompted us to investigate whether expression of any of the life span–related genes identified above are altered by transient expression of pluripotency inducing factors (Yamanaka factors OSKM) in a mouse model (*39*). Indeed, this analysis revealed that transient expression of OSKM altered the expression of 190 of 647 life span–related genes in skin and 162 life span–related genes in the kidney (nominal Fisher's exact $P = 9.9 \times 10^{-30}$ for skin and life span; $P = 4.5 \times 10^{-25}$ for kidney and life span; Fig. 5F and fig. S32). Genomic positions that are known to be bound by pluripotency factors in at least one human or murine cell type according to chromatin immunoprecipitation sequencing (ChIP-seq) data from the Encyclopedia of DNA Elements (ENCODE) consortium are located near CpGs that are associated with maximum species life spans: NANOG-binding sites are enriched for CpGs that are positively correlated with life span (FDR = 0.002) and to CpGs underlying the midnightblue module (FDR = 0.0006), which has high methylation levels in long-lived species (Fig. 5G). OCT4 (POU5F1) (FDR = 0.02), and cMYC (FDR = 0.003) binding sites are enriched with CpGs in the greenyellow module, which has low methylation levels in long-lived species (Fig. 5G). The ChIP-seq binding location analysis also implicates other noteworthy factors such as POLII, CTCF, RAD21, YY1, and TAF1, which show the strongest enrichment for negatively life span–related CpGs (Fig. 5G).

Given the role of CTCF in regulating the three-dimensional organization of the genome, we conducted an enrichment analysis of topologically associating domain (TAD) boundaries and loop boundaries identified in both human and mouse cell lines (fig. S26). We found that both TAD and loop boundaries demonstrated significant enrichment of negatively life span–related CpGs (FDR = 3×10^{-4}) for TAD boundaries and (FDR = 6.7×10^{-4}) for loop boundaries in various cell lines such as olfactory receptor cells and the human fibroblasts IMR90 and HFFc6 (fig. S26).

CpGs linked to life span in various taxonomic orders and tissues

To pinpoint CpGs associated with log maximum life span independently of phylogenetic order or tissue type, we conducted a meta-analysis of EWAS findings from 25 distinct strata comprising phylogenetic order and tissue type. Using a nonparametric meta-analysis approach (rankPvalue), we assessed the EWAS of life span (meta.lifespan) in these strata to identify CpGs unconfounded by tissue type or phylogenetic order (table S24). Our meta.lifespan results demonstrated significant overlap with the previously mentioned EWASs of life span in all eutherian species (hypergeometric $P = 1 \times 10^{-175}$; Fig. 6A). By contrast, none of the meta.lifespan CpGs overlapped with EWASs of age, which further supports the idea that methylation of life span–related CpGs does not change with age in mammalian tissues. The top four CpGs from the meta.lifespan analysis are depicted in Fig. 6B, showing significant positive correlations for CpGs near LOXL1 and ZSCAN29 (exons) and negative correlations for those near RAB29 (exon) and GATA3 (downstream), with log maximum life span across various taxonomic orders and tissue types. Similar to our above-mentioned results, CpGs implicated by our meta.lifespan analysis (FDR < 0.05) overlap significantly (FDR < 0.01) with genes involved in organ morphogenesis, RNA biosynthesis, increased rib number in mice, Wnt signaling (Fig. 6C), and genes altered by transient expression of pluripotency-inducing factors in mouse models (nominal Fisher's exact $P < 10^{-5}$ for skin and meta.lifespan; $P < 10^{-11}$ for kidney and meta.lifespan; Fig. 6D).

Chromatin state analysis

Our large-scale mammalian DNAm data confirm that CpGs located in promoter regions (−2000 to 2000 bp of TSS regions) have low methylation levels (mean = 15%; Fig. 7A). By contrast, those in gene bodies and distal regions are highly methylated (mean = ~70%; Fig. 7A). CpGs having a high or low mean methylation level tend to have positive or negative correlation test Z statistics for life span, respectively (Fig. 7, A and B). We find that CpGs with low methylation levels in long-lived species are located close to the TSS of genes and near binding sites of PRC1 ($P = 6.4 \times 10^{-11}$; Fig. 7C) and PRC2 ($P = 2 \times 10^{-6}$). To test the hypothesis that long-lived species exhibit high or low methylation levels in chromosomal regions that are expected to have high or low methylation patterns, respectively, we used chromatin states that were identified and annotated based on >1000 epigenetic datasets encompassing a diverse range of human cell and tissue types (*41*).

The negatively life span–related CpGs are enriched with a constitutive TSS chromatin state (TSS1, $P = 2.5 \times 10^{-12}$) and promoter flanking states (PromF4, $P = 5.6 \times 10^{-10}$; PromF5, $P = 2.0 \times 10^{-9}$; PromF2, $P = 3.0 \times 10^{-4}$; Fig. 7C).

The CpGs with high methylation levels in blood samples of long-lived species are enriched in gene body–associated states (notably transcribed and exon state TxEx1, $P = 7.5 \times 10^{-8}$ and highly transcribed state TxEx4 $P = 1.7 \times 10^{-6}$; Fig. 7D). A detailed description of the chromatin state enrichment for EWASs of maximum life span is provided in the supplementary text and tables S21 and S22.

A biclustering analysis between chromatin annotations and comethylation modules based on fold enrichments (Fig. 8 and tables S21 and S22) revealed that the 55 mammalian comethylation modules fall into three large groupings (referred to as meta-modules). The bar plot to the left of Fig. 8 shows different mean methylation levels of the CpGs underlying the three meta-modules: mean methylation = 0.23, 0.66, and 0.77 for meta-modules 1, 2, and 3, respectively.

Meta-module 1 contains several chromatin states that are associated with Polycomb repression, including strong polycomb-repressed state ReprPC1 and bivalent promoters (BivProm1-2). Further, meta-module 1 contains chromatin states related to TSSs (TSS1 and TSS2) and several flanking promoters (PromF2, PromF3, PromF4, and PromF5). TSS1, PromF4, and PromF5 (associated with negatively life span–related CpGs) were previously associated among universal chromatin states with the strongest enrichments for CpG islands (71 to 101 fold) (*41*). The color band under Fig. 8 reveals that six modules underlying meta-module 1 are sensitive to murine life span interventions. Meta-module 1 is enriched with CpGs that have low methylation levels in long-lived species (overlap with EWASs of life span, tan and greenyellow modules; Fig. 8).

Meta-module 2 can be considered as a partially methylated module (mean methylation 0.66) and is enriched with several enhancer states, late replicating domains [partially methylated domains, commonPMD (*42*)], and solo CpGs [WCGW (*42*)]. Meta-module 2 also contains the module most related with life span (midnightblue) and the human mortality risk module (magenta). These two modules overlap with the CpGs that are positively related to life span. Three out of four average weight-related modules are also located in meta-module 2.

Discussion

In this study, we present an analysis of a cross-species DNAm dataset obtained from a mammalian array platform. This platform specifically focuses on highly conserved regions of DNA, making it a valuable resource for studying methylation patterns across mammalian species (*5*). The successful construction of mammalian phyloepigenetic trees suggests that the divergence of DNAm profiles is closely aligned with genetic changes throughout evolution. Sensitivity assessments reveal that the observed phyloepigenetic associations are not caused by technical issues associated with our measurement platform. Instead, the phyloepigenetic signal may stem from sources such as upstream regulators, transcription factors, or DNA sequence variations in distant regions.

The conserved CpGs exhibiting the strongest phylogenetic signals are situated in intergenic regions, whereas promoter regions do not display such signals. Previous studies reported a rapid evolutionary rate of enhancers as a shared feature among mammalian genomes,

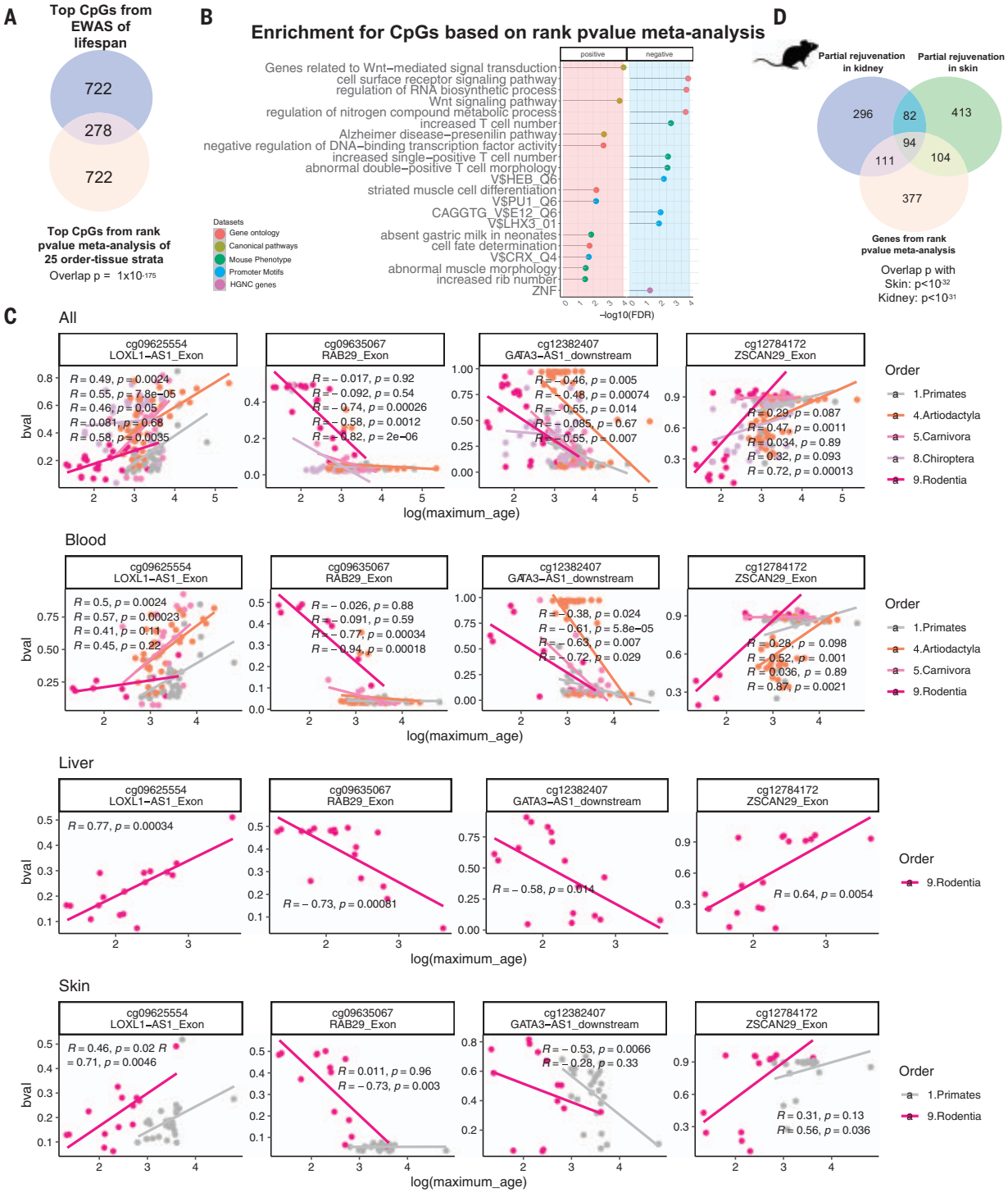

Fig. 6. CpGs linked to life span in various taxonomic orders and tissues. Using the nonparametric rankPvalue method (*33*), we combined 25 EWAS of life span results from various taxonomic order or tissue type strata, calculating the significance of a CpG's consistently high (or low) rank based on the 25 EWASs of log maximum life span (meta.lifespan and underlying EWAS results can be found in table S24 and data S19). (**A**) The overlap of top 1000 (500 per direction) meta.lifespan CpGs with EWAS of life span in all eutherians (nominal Fisher's exact $P = 1 \times 10^{-175}$). (**B**) Scatter plots illustrating the top meta.lifespan CpGs categorized into different tissue-phylogenetic order strata. Each panel displays only the strata that exhibit significant relationships. Each dot represents a species colored by taxonomic order. Each row corresponds to a different selection of tissue type. "bval" denotes the beta value, measuring DNAm at a CpG site, with 0 indicating no methylation and 1 indicating full methylation. (**C**) Gene set enrichment analysis of the genes proximal to CpGs associated with mammalian maximum life span. We only report enrichment terms that are significant after adjustment for multiple comparisons (hypergeometric FDR < 0.01) and contain at least five significant genes. The top three significant terms per column (EWAS) and enrichment database are shown. (**D**) Venn diagram of three gene lists. Gene list 1 (the bottom circle) is the top 407 genes adjacent to 1000 meta.lifespan CpGs (500 positive and 500 negative). Gene lists 2 and 3 (the top circles) are based on CpGs that are differentially methylated (nominal Wald test $P < 0.005$, up to 500 positive and 500 negatively related CpGs) after OSKM overexpression in murine kidney (583 genes) and skin (686 genes) (*39*).

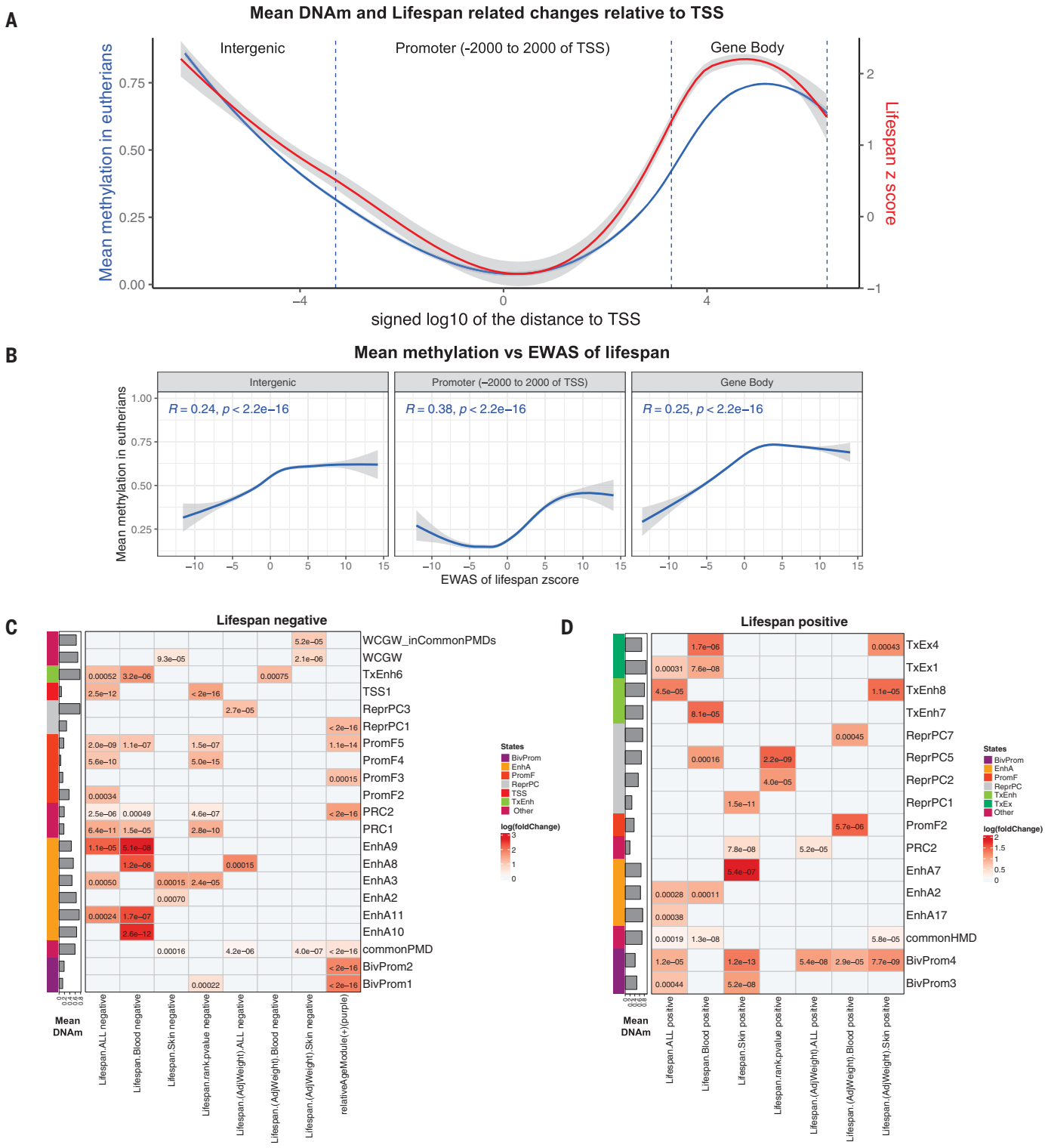

Fig. 7. Chromatin state analysis and distance to the TSS for the life span–related CpGs. (**A**) Illustrated plot presenting mean methylation across species (displayed on the left *y* axis) and EWAS of maximum life span Z statistics (shown on the right *y* axis), all plotted against the distances to the closest TSS (represented on the *x* axis). (**B**) Mean methylation across species (*y* axis) plotted against EWAS Z statistics for log maximum life span in different genomic regions (intergenic, promoter, and gene body). Additional EWAS results after adjustment for phylogenetic relationships can be found in figs. S17 to S20, and corresponding enrichment results can be found in figs. S22 to S24. Pearson correlation coefficients and *P* values are reported in different panels. (**C** and **D**) Chromatin annotation enrichment analysis of the top 500 negatively life span–related CpGs (C) and the top 500 positively life span–related CpGs (D). The columns in each panel correspond to EWAS results for log-transformed maximum life span across (i) all tissues combined (Lifespan.All), (ii) blood

samples only (Lifespan.Blood), and (iii) skin samples only (Lifespan.Skin), (iv) meta analysis of lifespan in different tissues (meta.lifespan), and the corresponding results after adjustment for average adult weight (LifespanAdjWeight). The last column reports enrichment with respect to the RelativeAge^{+} module (purple). We used the same significance thresholds as in Fig. 5. Cell shading corresponds to fold enrichment between comethylation modules and each chromatin state. Numeric values correspond to the *P* value of such enrichments based on the hypergeometric test, and only cell values with significant $P < 0.001$ (equivalent to FDR < 0.02) are shown. The chromatin states are learned based on epigenetic datasets profiling chromatin mark signals in different human cell and tissue types, resulting in a genome annotation shared across cell types (*41*). The common partially methylated domains (commonPMD), solo CpGs (WCGW), and highly methylated domain (HMD) annotations are from (*42*). PRC1 and PRC2 binding sites are obtained from the ChIP-seq datasets of PCR1 and PCR2 from ENCODE (*45*).

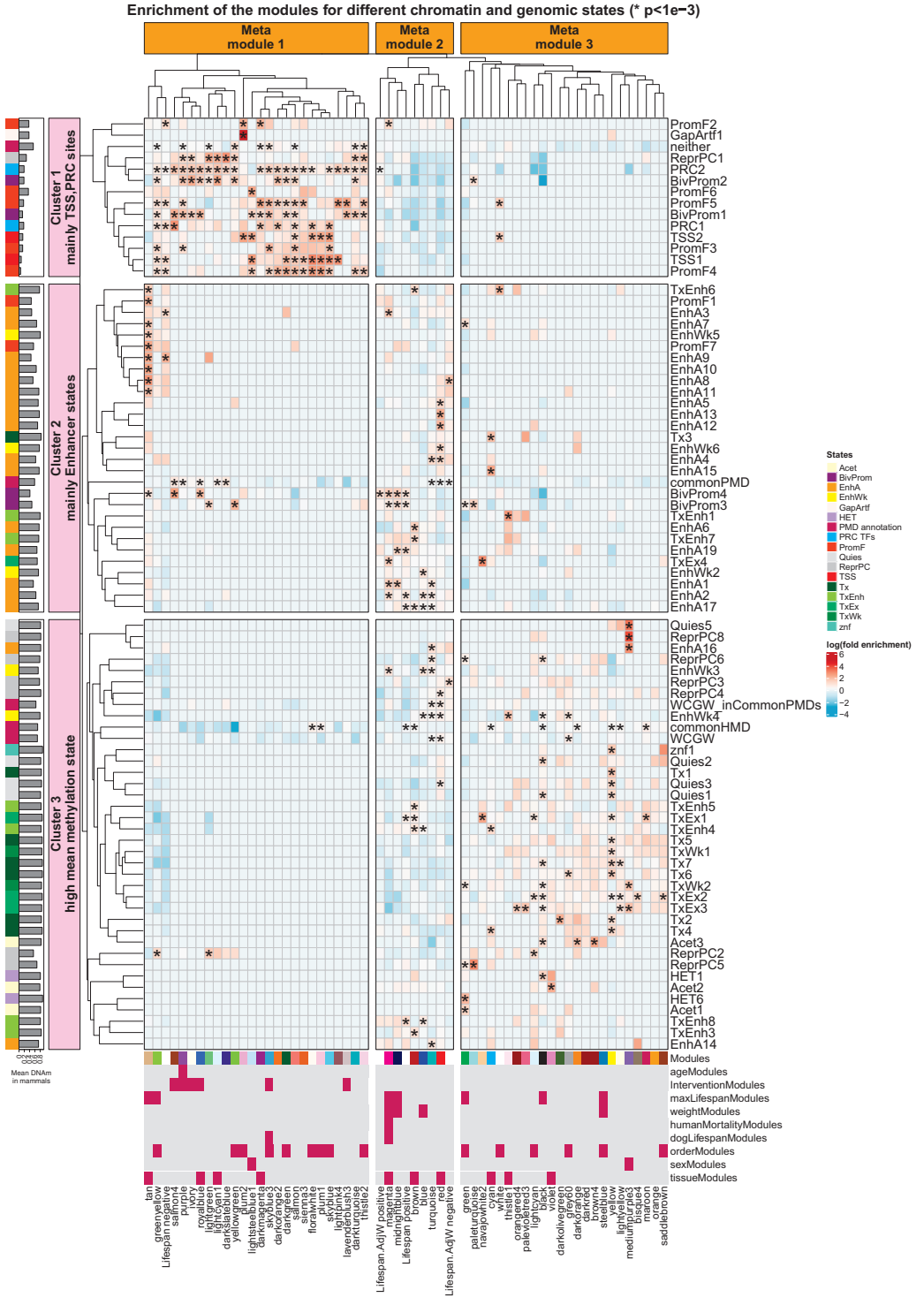

Fig. 8. Mammalian methylation meta-modules based on chromatin states and external genome annotations. The heatmap shows the enrichments between (*1*) mammalian comethylation modules and significant life span–related EWAS CpG groups (*x* axis) and (*2*) chromatin states or other genomic annotation (*y* axis). Cell shading corresponds to log-transformed fold enrichment values (observed CpG count divided by expected count). Hypergeometric tests were used to evaluate the enrichment significance in each cell. *Nominal $P < 0.001$ (FDR < 0.10). Only chromatin states and external genome annotations with at least one significant enrichment (FDR < 0.10) are shown. The chromatin states are based on a human-based universal chromatin annotation of human cell and tissue types (*41*). Other genomic annotations include the commonPMD, solo CpGs (WCGW), HMD annotations, and neither (CpGs outside these annotations) which are from (*42*). In addition, PRC1 and PRC2 binding sites are defined from the ChIP-seq data of PRC1 and PRC2 from ENCODE (*45*). The row and column hierarchical clustering trees (average linkage) are based on a dissimilarity measure (1 minus the pairwise Pearson correlation between log-transformed fold enrichment values). The left barplot indicates the mean methylation levels of the CpGs in each state for all eutherian samples in our data. We used the 14,705 eutherian CpGs as the background for enrichment of the comethylation modules. By contrast, 28,318 CpGs (high-quality probes in humans and mice) were used as a background for enrichment of significant life span–related EWAS CpG groups with chromatin states and genome annotations. Each EWAS CpG group includes up to 500 most significant CpGs per direction (positively or negatively related with life span), as detailed in the caption of Fig. 5.

but promoters demonstrate either full or partial conservation across species (*2*).

We found that 30 of the resulting 55 modules identified from an unsupervised machine learning method were readily associated with species traits (taxonomic order, maximum life span, and average adult weight) or individual traits (chronological age, tissue, and sex). We expect that many of the remaining 25 modules will be associated with biological characteristics about which we currently have no information. As a case in point, although the yellow module was not associated with any of our primary tested traits, it did show association with response to a murine circadian rhythm disruption study (light pollution during the night; fig. S7B). The upstream regulator analysis of the EWAS of life span identified the pluripotency transcription factors OCT4, SOX2, and NANOG. We showed that the transient overexpression of OSKM in murine tissues affects the methylation levels of CpGs near genes implicated by our EWAS of maximum life span (Fig. 5E). We speculate that the enhanced activity of the pluripotency network in long-lived species results in more efficient tissue repair and maintenance, ensuring a longer life span.

Both the EWAS and eigengene-based analyses identified methylation signatures of maximum life span presumably established at birth. Most of these were independent of aging and interventions that affect murine mortality risk. Several CpGs that are more highly methylated in long-lived species are located near *HOXL* subclass homeoboxes and other genes that play a role in morphogenesis and development. Some of these life span–related CpGs are located next to genes that are also implicated in our analysis of upstream regulators (e.g., *ASCL1* and *SMAD6*).

CpGs with methylation levels that are inversely related to life span are enriched in TSS1- and promoter flanking (PromF4 and PromF5)–associated chromatin states. Genes located in chromatin state TSS1 are constitutively active and enriched for nucleic acid metabolic processes (*41*). This could imply that long-lived species either evolved selective mechanisms to maintain low methylation levels near TSSs or may have adaptations that promote the high expression of essential genes. This high expression may indirectly prompt more active DNA demethylation mechanisms.

Methods summary

The Mammalian Methylation Consortium generated cytosine methylation data from n = 15,456 DNA samples derived from 70 tissue types of 348 mammalian species (331 eutherians, 15 marsupials, two monotremes) using a custom-designed mammalian methylation array that targets CpGs at conserved loci in mammals (*5*). DNAm data were used for phyloepigenetic tree development using 1-cor dissimilarity applied to mean methylation values per species. The choice of the correlation-based dissimilarity matrix is justified in the supplementary materials and methods.

For unsupervised analysis, we formed WGCNA networks based on two sets of CpG probes in our data. The first network was generated from 14,705 conserved CpGs in 10,927 samples of 167 eutherian species. The preservation of this network was evaluated in an independent dataset comprising 3692 samples from 29 tissues of 228 mammalian species (164 new species; 64 overlapped with the training set). The second network was a subset of 7956 conserved CpGs in 11,105 samples from 167 eutherian and nine marsupial species. In addition, we developed seven consensus comethylation networks to remove the confounding effects of species and tissue type. Consensus WGCNA can be interpreted as a meta-analysis across networks in different species and tissue types (*33*, *43*).

For the eutherian network (Net1), module eigengenes (MEs) were defined as singular vectors (corresponding to the highest singular value) from the singular value decomposition of the scaled CpGs that underlie the respective module. The eigengenes in the eutherian network (Net1) explained a range of 24 to 63% (average 43%) of the variance in the methylation data in the training set, replication set, and all data in each module (table S3). For a given module, we defined the measure of module membership (kME) as the Pearson correlation between the module eigengene and the CpGs. The association of module eigengenes was examined for different traits using individual regression models.

EWAS of life span was done in 28,318 CpGs that apply to mice and humans according to calibration and titration data (correlation with calibration exceeds 0.8) and mappability information as described in (*5*). Because the distribution of maximum life span and other life history traits were highly skewed, we imposed a log transformation on these phenotypes before conducting EWAS. Our tissue type–specific EWAS was conducted in tissues with enough species ($N > 25$) available. For our various EWAS of log-transformed maximum life span, we adopted a nominal significance threshold of 1.8×10^{-6} (0.01/28,318) based on the conservative Bonferroni adjustment. We report an FDR in our enrichment studies to adjust for multiple comparisons.

REFERENCES AND NOTES

1. S. Xiao *et al*., Comparative epigenomic annotation of regulatory DNA. *Cell* **149**, 1381–1392 (2012). doi: 10.1016/j.cell.2012.04.029; pmid: 22682255
2. D. Villar *et al*., Enhancer evolution across 20 mammalian species. *Cell* **160**, 554–566 (2015). doi: 10.1016/j.cell.2015.01.006; pmid: 25635462
3. J. Qu *et al*., Evolutionary expansion of DNA hypomethylation in the mammalian germline genome. *Genome Res.* **28**, 145–158 (2018). doi: 10.1101/gr.225896.117; pmid: 29259021
4. J. Klughammer *et al*., Comparative analysis of genome-scale, base-resolution DNA methylation profiles across 580 animal species. *Nat. Commun.* **14**, 232 (2023). doi: 10.1038/s41467-022-34828-y; pmid: 36646694
5. A. Arneson *et al*., A mammalian methylation array for profiling methylation levels at conserved sequences. *Nat. Commun.* **13**, 783 (2022). doi: 10.1038/s41467-022-28355-z; pmid: 35145108
6. K. M. Parsons *et al*., DNA methylation-based biomarkers for ageing long-lived cetaceans. *Mol. Ecol. Resour.* **23**, 1241–1256 (2023). doi: 10.1111/1755-0998.13791; pmid: 36994812
7. A. T. Lu *et al*., Universal DNA methylation age across mammalian tissues. bioRxiv 426733 [Preprint] (2021). doi: 10.1101/2021.01.18.426733
8. P. Kordowitzki *et al*., Epigenetic clock and methylation study of oocytes from a bovine model of reproductive aging. *Aging Cell* **20**, e13349 (2021). doi: 10.1111/acel.13349; pmid: 33797841
9. N. A. Prado *et al*., Epigenetic clock and methylation studies in elephants. *Aging Cell* **20**, e13414 (2021). doi: 10.1111/acel.13414; pmid: 34118182
10. T. R. Robeck *et al*., Multi-species and multi-tissue methylation clocks for age estimation in toothed whales and dolphins. *Commun. Biol.* **4**, 642 (2021). doi: 10.1038/s42003-021-02179-x; pmid: 34059764
11. B. Larison *et al*., Epigenetic models developed for plains zebras predict age in domestic horses and endangered equids. *Commun. Biol.* **4**, 1412 (2021). doi: 10.1038/s42003-021-02935-z; pmid: 34921240
12. K. Mozhui *et al*., Genetic loci and metabolic states associated with murine epigenetic aging. *eLife* **11**, e75244 (2022). doi: 10.7554/eLife.75244; pmid: 35389339
13. V. J. Sugrue *et al*., Castration delays epigenetic aging and feminizes DNA methylation at androgen-regulated loci. *eLife* **10**, e64932 (2021). doi: 10.7554/eLife.64932; pmid: 34227937
14. T. R. Robeck *et al*., Multi-tissue methylation clocks for age and sex estimation in the common bottlenose dolphin. *Front. Mar. Sci.* **8**, 713373 (2021). doi: 10.3389/fmars.2021.713373
15. S. Horvath *et al*., Methylation studies in *Peromyscus*: Aging, altitude adaptation, and monogamy. *Geroscience* **44**, 447–461 (2022). doi: 10.1007/s11357-021-00472-5; pmid: 34698996
16. S. Horvath *et al*., Epigenetic clock and methylation studies in marsupials: Opossums, Tasmanian devils, kangaroos, and wallabies. *Geroscience* **44**, 1825–1845 (2022). doi: 10.1007/s11357-022-00569-5; pmid: 35449380
17. S. Horvath *et al*., Epigenetic clock and methylation studies in the rhesus macaque. *Geroscience* **43**, 2441–2453 (2021). doi: 10.1007/s11357-021-00429-8; pmid: 34487267
18. S. Horvath *et al*., DNA methylation age analysis of rapamycin in common marmosets. *Geroscience* **43**, 2413–2425 (2021). doi: 10.1007/s11357-021-00438-7; pmid: 34482522
19. A. J. Jasinska *et al*., Epigenetic clock and methylation studies in vervet monkeys. *Geroscience* **44**, 699–717 (2021). doi: 10.1007/s11357-021-00466-3; pmid: 34591235
20. K. Raj *et al*., Epigenetic clock and methylation studies in cats. *Geroscience* **43**, 2363–2378 (2021). doi: 10.1007/s11357-021-00445-8; pmid: 34463900
21. K. M. Schachtschneider *et al*., Epigenetic clock and DNA methylation analysis of porcine models of aging and obesity. *Geroscience* **43**, 2467–2483 (2021). doi: 10.1007/s11357-021-00439-6; pmid: 34523051
22. M. L. Cossette *et al*., Epigenetics and island-mainland divergence in an insectivorous small mammal. *Mol. Ecol.* **32**, 152–166 (2023). doi: 10.1111/mec.16735; pmid: 36226847
23. J. F. Lemaître *et al*., DNA methylation as a tool to explore ageing in wild roe deer populations. *Mol. Ecol. Resour.* **22**, 1002–1015 (2022). doi: 10.1111/1755-0998.13533; pmid: 34665921
24. S. Horvath *et al*., DNA methylation clocks tick in naked mole rats but queens age more slowly than nonbreeders. *Nat. Aging* **2**, 46–59 (2022). doi: 10.1038/s43587-021-00152-1; pmid: 35368774
25. S. Horvath *et al*., Pan-primate studies of age and sex. *Geroscience* (2023). doi: 10.1007/s11357-023-00878-3; pmid: 493860
26. G. S. Wilkinson *et al*., DNA methylation predicts age and provides insight into exceptional longevity of bats. *Nat. Commun.* **12**, 1615 (2021). doi: 10.1038/s41467-021-21900-2; pmid: 33712580

27. S. Horvath *et al*., DNA methylation aging and transcriptomic studies in horses. *Nat. Commun.* **13**, 40 (2022). doi: 10.1038/s41467-021-27754-y; pmid: 35013267
28. G. M. Pinho *et al*., Hibernation slows epigenetic ageing in yellow-bellied marmots. *Nat. Ecol. Evol.* **6**, 418–426 (2022). doi: 10.1038/s41559-022-01679-1; pmid: 35256811
29. S. Horvath *et al*., DNA methylation clocks for dogs and humans. *Proc. Natl. Acad. Sci. U.S.A.* **119**, e2120887119 (2022). doi: 10.1073/pnas.2120887119; pmid: 35580182
30. K. J. Peters *et al*., An epigenetic DNA methylation clock for age estimates in Indo-Pacific bottlenose dolphins (*Tursiops aduncus*). *Evol. Appl.* **16**, 126–133 (2022). pmid: 36699128
31. P. Chiavellini *et al*., Hippocampal DNA methylation, epigenetic age and spatial memory performance in young and old rats. *J. Gerontol. A Biol. Sci. Med. Sci.* **77**, 2387–2394 (2022). doi: 10.1093/gerona/glac153; pmid: 35917578
32. S. P. Blomberg, T. GarlandJr.., A. R. Ives, Testing for phylogenetic signal in comparative data: Behavioral traits are more labile. *Evolution* **57**, 717–745 (2003). pmid: 12778543
33. P. Langfelder, S. Horvath, WGCNA: An R package for weighted correlation network analysis. *BMC Bioinformatics* **9**, 559 (2008). doi: 10.1186/1471-2105-9-559; pmid: 19114008
34. P. Langfelder, R. Luo, M. C. Oldham, S. Horvath, Is my network module preserved and reproducible? *PLOS Comput. Biol.* **7**, e1001057 (2011). doi: 10.1371/journal.pcbi.1001057; pmid: 21283776
35. D. Szklarczyk *et al*., Correction to 'The STRING database in 2021: Customizable protein-protein networks, and functional characterization of user-uploaded gene/measurement sets'. *Nucleic Acids Res.* **49**, 10800 (2021). doi: 10.1093/nar/gkab835; pmid: 34530444
36. A. Barrat, M. Barthélemy, R. Pastor-Satorras, A. Vespignani, The architecture of complex weighted networks. *Proc. Natl. Acad. Sci. U. S. A.* **101**, 3747–3752 (2004). doi: 10.1073/pnas.0400087101; pmid: 15007165
37. H. Pilcher, Money for old mice. *Nature* 10.1038/news030915-13 (2003). doi: 10.1038/news030915-13
38. V. Acosta-Rodríguez *et al*., Circadian alignment of early onset caloric restriction promotes longevity in male C57BL/6J mice. *Science* **376**, 1192–1202 (2022). doi: 10.1126/science.abk0297; pmid: 35511946
39. K. C. Browder *et al*., In vivo partial reprogramming alters age-associated molecular changes during physiological aging in mice. *Nat. Aging* **2**, 243–253 (2022). doi: 10.1038/s43587-022-00183-2; pmid: 37118377
40. A. Krämer, J. Green, J. PollardJr.., S. Tugendreich, Causal analysis approaches in Ingenuity Pathway Analysis. *Bioinformatics* **30**, 523–530 (2014). doi: 10.1093/bioinformatics/btt703; pmid: 24336805
41. H. Vu, J. Ernst, Universal annotation of the human genome through integration of over a thousand epigenomic datasets. *Genome Biol.* **23**, 9 (2022). doi: 10.1186/s13059-021-02572-z; pmid: 34991667
42. W. Zhou *et al*., DNA methylation loss in late-replicating domains is linked to mitotic cell division. *Nat. Genet.* **50**, 591–602 (2018). doi: 10.1038/s41588-018-0073-4; pmid: 29610480
43. P. Langfelder, S. Horvath, "Tutorials for the WGCNA package" (2014); https://horvath.genetics.ucla.edu/html/CoexpressionNetwork/Rpackages/WGCNA/Tutorials.
44. S. Kumar, G. Stecher, M. Suleski, S. B. Hedges, TimeTree: A resource for timelines, timetrees, and divergence times. *Mol. Biol. Evol.* **34**, 1812–1819 (2017). doi: 10.1093/molbev/msx116; pmid: 28387841
45. ENCODE Project Consortium, An integrated encyclopedia of DNA elements in the human genome. *Nature* **489**, 57–74 (2012). doi: 10.1038/nature11247; pmid: 22955616
46. A. Haghani, A. T. Lu, S. B. Kwon, A. Arneson, J. Ernst, S. Horvath, Data for: DNA methylation networks underlying mammalian traits, Zenodo (2023). doi: 10.5281/zenodo.8180547

ACKNOWLEDGMENTS

This is Duke Lemur Center publication #1563. **Funding:** The majority of the funding was contributed by the Paul G. Allen Frontiers Group (S.H.) and Open Philanthropy (S.H.). Additional financial support for specific aspects of data generation was obtained from the following sources: National Geographic Society grant 8941-11 (B.L.), British Heart Foundation (FS/18/39/33684 to D.V.), Wellcome (WT202878/Z/16/Z to D.T.O.), European Research Council (788937 to D.T.O.), Cancer Research UK (20412 to D.T.O.), Max Planck Research Group Award from the Max Planck Gesellschaft (S.C.V.), UKRI Future Leaders Fellowship (MR/T021985/1 to S.C.V.), DST-NRF SARChI chair of Mammalian Behavioral Ecology and Physiology (GUN 64756 to N.C.B.), Science Foundation Ireland Future Frontiers 19/FFP/6790 (ECT), National Institute on Aging Intramural Research Program, NIH (J.A.M.), U01 AG060908 (S.H.), AG055841 (K.M.), and AG043930/AG/NIA (R.W.W.), National Institute of Health AG065403 (V.N.G.), AG047200 (V.N.G.), AG067782 (V.N.G.), and AG076607 (V.N.G.), AG047200 (V.G.), AG045795 (T.G.), AG072736 (T.G.), NIA 1R21AG078784 (K.E.S), OOD 1R21OD022988 (K.E.S), National Science Foundation IOS 2017803 (K.E.S), DEB 1854469 (K.E.S), AG047200 (A. S.), Milky Way Research Foundation (V.G.), A.H. Schultz Foundation, Department of Evolutionary Anthropology, University of Zurich (M.K.), Leverhulme Trust RPG-2019-404 and Royal Society of Edinburgh Research Reboot Grant 1107 (A. Pederson), UCLA Jonsson Comprehensive Cancer Center and Eli and Edythe Broad Center of Regenerative Medicine and Stem Cell Research Ablon Scholars Program (J.E.), funds provided by the College of Computer, Mathematical and Natural Sciences at the University of Maryland, College Park (G.S.W.), Taronga Conservation Society Australia (J.K.O.), S.C.V. was supported by a Max Planck Research Group Award from the Max Planck Gesellschaft and a UKRI Future Leaders Fellowship (MR/T021985/1). N.C.B. was funded by a DST-NRF SARChI chair of Mammalian Behavioral Ecology and Physiology (GUN 64756). A.N.A was funded by DSFP, King Saud University, Riyadh, Saudi Arabia. K.J.P. was supported by a postdoctoral grant from the University of Zurich. Collection of plains zebra samples was supported by the National Geographic Society to B.L. (8941-11). **Author contributions:** Conceptualization: S.H., A.H.; Formal analysis: A.H., C.Z.L., A.T.L., Q.Y., J.Z.H.; Investigation: all authors; Visualization: A.H., C.Z.L.; Funding acquisition: S.H., B.L., D.V., D.T.O., S.C.V., N.C.B., ECT, J.A.M.; Project administration: S.H.; Supervision: S.H.; Writing – original draft: A.H., C.Z.L.; Writing – review and editing: A.H., S.H., K.R., J.E., and remaining authors. **Competing interests:** S.H., A.A., and J.E. are inventors on patent/patent application number WO2020150705 held/submitted by the University of California, Los Angeles that covers the mammalian methylation array technology. S.H. and R.T.B. are founders of the nonprofit Epigenetic Clock Development Foundation, which has licensed several patents from UC Regents and distributes the mammalian methylation array. **Data and materials availability:** All data from the Mammalian Methylation Consortium are posted on the Gene Expression Omnibus website (complete dataset: GSE223748). Subsets of the data sets can also be downloaded from accession numbers, GSE174758, GSE184211, GSE184213, GSE184215, GSE184216, GSE184218, GSE184220, GSE184221, GSE184224, GSE190660, GSE190661, GSE190662, GSE190663, GSE190664, GSE174544, GSE190665, GSE174767, GSE184222, GSE184223, GSE174777, GSE174778, GSE173330, GSE164127, GSE147002, GSE147003, GSE147004). The mammalian array platform is distributed by the nonprofit Epigenetic Clock Development Foundation (https://clockfoundation.org/). The mammalian data can also be downloaded from the Clock Foundation web page: https://clockfoundation.org/MammalianMethylationConsortium. The manifest file of the mammalian array, genome annotations of the CpGs, and codes can be found on Zenodo (*46*). **License information:** Copyright © 2023 the authors, some rights reserved; exclusive licensee American Association for the Advancement of Science. No claim to original US government works. https://www.science.org/about/science-licenses-journal-article-reuse

SUPPLEMENTARY MATERIALS

science.org/doi/10.1126/science.abq5693
Materials and Methods
Supplementary Text
Figs. S1 to S32
Tables S1 to S24
References (*47*–*95*)
MDAR Reproducibility Checklist
Data S1 to S19

Submitted 19 April 2022; resubmitted 13 June 2022
Accepted 21 June 2023
10.1126/science.abq5693

Pushing the Boundaries of Knowledge

As AAAS's first multidisciplinary, open access journal, *Science Advances* publishes research that reflects the selectivity of high impact, innovative research you expect from the *Science* family of journals, published in an open access format to serve a vast and growing global audience. Check out the latest findings or learn how to submit your research: **ScienceAdvances.org**

Science Advances
AAAS

GOLD OPEN ACCESS, DIGITAL, AND FREE TO ALL READERS

RESEARCH ARTICLES

NANOPHOTONICS

Wafer-scale δ waveguides for integrated two-dimensional photonics

Myungjae Lee[1,2]†, Hanyu Hong[3]†, Jaehyung Yu[3], Fauzia Mujid[3], Andrew Ye[4], Ce Liang[4], Jiwoong Park[1,3,4]*

The efficient, large-scale generation and control of photonic modes guided by van der Waals materials remains as a challenge despite their potential for on-chip photonic circuitry. We report three-atom-thick waveguides—δ waveguides—based on wafer-scale molybdenum disulfide (MoS_2) monolayers that can guide visible and near-infrared light over millimeter-scale distances with low loss and an efficient in-coupling. The extreme thinness provides a light-trapping mechanism analogous to a δ-potential well in quantum mechanics and enables the guided waves that are essentially a plane wave freely propagating along the in-plane, but confined along the out-of-plane, direction of the waveguide. We further demonstrate key functionalities essential for two-dimensional photonics, including refraction, focusing, grating, interconnection, and intensity modulation, by integrating thin-film optical components with δ waveguides using microfabricated dielectric, metal, or patterned MoS_2.

Thin-film waveguides that can confine, direct, and modulate light waves on-chip are key ingredients in modern photonic technologies (*1*–*6*). However, because the optical fields are located inside of the waveguides, the integration of multiple photonic components made of distinct materials requires careful tuning of each component's dimensions (characteristic size d), which are customized for individual operation wavelengths (λ) and the specific optical properties of the materials used (refractive index n) to keep the ratio nd/λ similar (typically of the order of unity) throughout the device (*1*–*11*). One fundamental challenge in integrated photonics is to develop an architecture that enables efficient waveguiding and interconnection free of such spectral and materials constraints—a challenging goal for waveguides with fixed dimensions.

δ Waveguides: Principle and operation

A conceptual approach is a δ waveguide, whose ultrasmall thickness t satisfying $nt/\lambda \ll 1$ enables broadband, single-mode operation, where the out-of-plane confinement of a guided mode and its in-plane propagation can be independently controlled. This type of waveguide has a unique analytic solution when $n > n_o$ (where n_o is the refractive index of the surrounding medium). The transverse electric (TE) field profile along the confining z direction [$E_y(z)$] (Fig. 1A) is an optical analog of a quantum mechanical eigenfunction for a one-dimensional (1D) δ-potential trap. In particular, the imaginary wave vector along the z direction $|k_z|$ is much smaller than $k_\parallel = (k_x^2 + k_y^2)^{1/2}$ regardless of n or λ (see supplementary text, section S1, for details). Because most of the optical fields are located outside of the waveguide owing to the thinness, this results in an effective mode index $n_{eff} \approx n_o$ and a phase velocity $v \approx v_o = c/n_o$ (where c is the speed of light). The guided mode is therefore described by $\omega = v \times k_\parallel$, which is the dispersion relation of a plane wave confined in 2D space.

van der Waals (vdW) materials, such as graphene and monolayer transition metal dichalcogenides (TMDs), provide an ultrathin platform that is ideal for a δ waveguide. For example, long-range propagation of guided waves was predicted in TMDs when the TMD is surrounded by identical optical environments (above and below) (*12*). However, efficient large-scale generation and control of photonic modes guided by vdW materials remains a challenge; although vdW materials have been used as waveguides in recent studies of surface polaritons (*13*–*20*) or exciton-polariton waves (*21*–*25*), their mechanisms of waveguiding are limited by unsuitable geometry for integration and short propagation lengths. Realizing the full potential of δ waveguides would require the careful implementation of several capabilities, including a large-scale, high-quality vdW film in optically homogeneous medium, systematic coupling and detection mechanisms with minimal interference to the guided wave propagation, and a means to manipulate the guided wave using integrated components.

[1]James Franck Institute, University of Chicago, Chicago, IL 60637, USA. [2]Department of Materials Science and Engineering, Seoul National University, Seoul 08826, South Korea. [3]Department of Chemistry, University of Chicago, Chicago, IL 60637, USA. [4]Pritzker School of Molecular Engineering, University of Chicago, Chicago, IL 60637, USA.
*Corresponding author. Email: jwpark@uchicago.edu
†These authors contributed equally to this work.

Fabrication and experimental results

Our results followed from two key experimental advances (Fig. 1, B and C): (i) the optical suspension of a wafer-scale MoS_2 waveguide (length $L > 1$ mm) in a homogeneous dielectric environment and (ii) the edge-on excitation and far-field detection of guided waves by free-space beams that ensure the minimal interference. To produce the δ waveguide, a monolayer MoS_2 film [$t \sim 0.6$ nm; bandgap $E_g \sim 1.9$ eV (*26*)] was used as the waveguide material and surrounded by an optically homogeneous polymer packaging (Fig. 1C). A continuous, wafer-scale monolayer film was grown on a growth substrate (e.g., fused silica) using metal-organic chemical vapor deposition (MOCVD) (materials and methods) (*27*). The monolayer MoS_2 film is delaminated from the growth substrate and then embedded inside silicone elastomer [polydimethylsiloxane (PDMS)] to provide a stable, homogeneous optical environment n_o (n_{PDMS}) over centimeter scales (Fig. 1D).

For an efficient excitation, we use electrodynamic simulations to design an optimal geometry for the incident laser beam. Figure 1E shows a calculated distribution of electric field intensity $|E(x, z)|^2$ (materials and methods) when a light wave propagates (from left to right) along a monolayer MoS_2 (mode width is approximately a few micrometers) and out-couples into free space at its end (Fig. 1E, dashed arrow). This explains how a guided wave in the δ waveguide couples with a free beam for its excitation and launching. In our experiments, a color-controlled (from 500 to 900 nm), slightly converging laser beam [numerical aperture (NA) ~ 0.1; focused beam width ~ 6 μm] is introduced at the edge of the MoS_2, with the beam center trajectory parallel to the MoS_2 surface (tilting angle θ ~ 0). For detection, the end-face microscopy measures the cross-sectional intensity profile at the end of the MoS_2 waveguide (Fig. 1B, dashed box), and the dark-field microscopy measures the optical fields distribution on MoS_2 film by collecting elastically scattered light from the waveguide surface (materials and methods).

Figure 1F (left) displays representative beam profiles measured in end-face imaging with (main panel) and without (inset) a monolayer MoS_2 waveguide ($L \sim 4$ mm) placed in the beam path ($\lambda = 720$ nm). The comparison reveals an intense out-coupled light field at the waveguide plane (arrow) that is observed only when the MoS_2 is present. The transverse line profile (right) confirms that the light field at the end of the MoS_2 is much stronger than the field outside the waveguide (red line) or that of the laser beam without the waveguide (gray). The intense light field is vertically confined (width ~ 3 μm) and detected only with TE polarized excitation. From the two profiles, we measure that 15% of the total incident beam energy out-couples from the waveguide. After considering

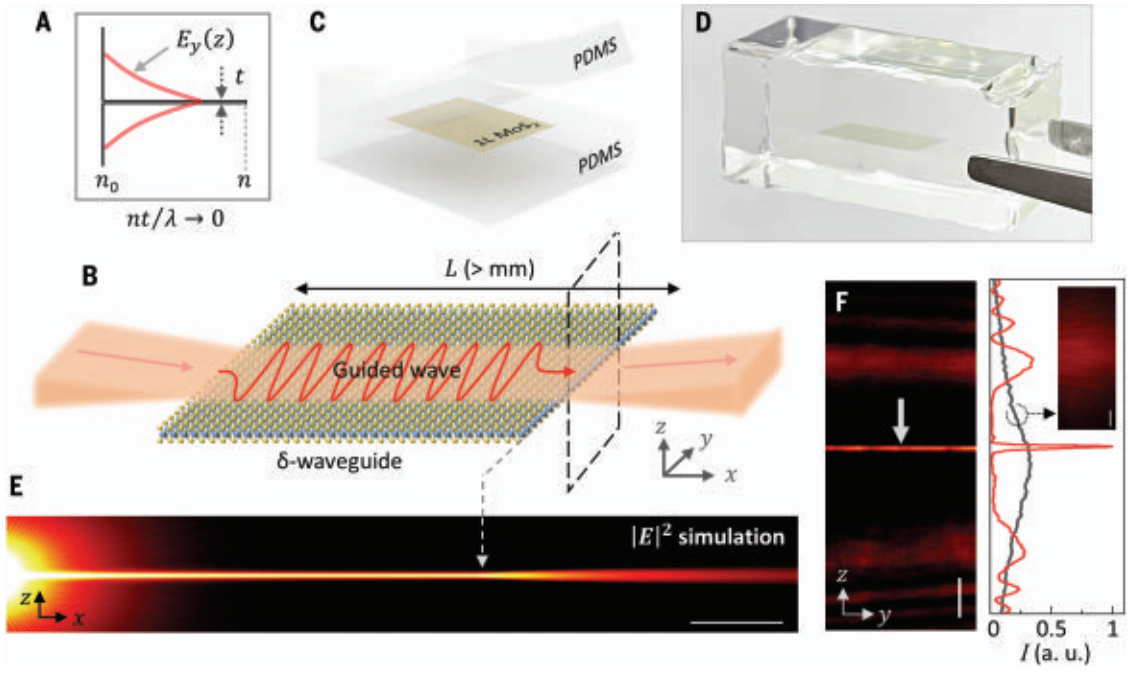

Fig. 1. Large-scale δ waveguides realized by monolayer MoS_2. (**A**) Schematic of a transverse profile of a light field trapped by an ultrathin waveguide. (**B**) Experimental schematic for the excitation and detection of a guided wave. A slightly converging laser beam is injected to the edge of the film with a beam trajectory nearly parallel to the film. These guided waves are observed through film-surface and end-face imaging microscopy. (**C**) Schematic of an optically suspended ultrathin film surrounded by optically homogeneous polymer packaging. (**D**) Photograph of a large-scale δ waveguide obtained by the optical suspension of a monolayer MoS_2 film. The size of the MoS_2 waveguide is ~0.5 × 2 cm^2. (**E**) Simulated electric field intensity when a light wave propagates along a waveguide and out-couples into free space at the end face of MoS_2 (arrow), calculated for a monolayer MoS_2. Scale bar, 20 μm. (**F**) Experimentally measured end-face image of δ waveguide with focus at the dashed box shown in (B) upon edge-on incidence of an excitation laser beam with a tailored wavefront (left), and corresponding line profiles measured with (red curve) and without (black curve) the waveguide (right). The inset shows the end-face imaging without the waveguide. Scale bars, 100 μm. a.u., arbitrary units.

the measured propagation power loss of ~3 dB (fig. S1), we estimate that the in-coupling efficiency is ~30%. Figure 2A further shows a top-view image measured from the MoS_2 plane under similar conditions (λ = 720 nm; TE polarization). The image clearly shows strong signals from the MoS_2 surface along the laser path (i.e., the x axis) having a lateral width similar to the beam diameter (~100 μm).

Figure 2B presents an array of top-view images [$I_{DF}(x, y)$; like Fig. 2A] collected for λ = 500 ~ 900 nm (Δλ = 20 nm) from a centimeter-long monolayer (1L) MoS_2 waveguide. For longer λ > 700 nm, the line remains intense over the entire image (length > 6 mm), whereas for shorter λ, it only maintains signal for a couple of millimeters or less. These dark-field signals are detected only with a TE-mode laser and completely disappear for transverse magnetic (TM) polarization (fig. S2), consistent with the prediction based on excitonic responses of MoS_2 film (*12*). For N dependence (where N is the layer number), similar dark-field images are shown for a trilayered (3L) MoS_2 waveguide (Fig. 2C), which is fabricated by stacking two additional MoS_2 monolayers on top of a monolayer MoS_2 waveguide (*28*). At all λ, the signal decays faster in the 3L waveguide. Similarly, fast decays are observed from a bilayer (2L) MoS_2 waveguide (fig. S3). Figure 2D shows the rate of dark-field signal decay [β = 2 × Im (k_x)] in monolayer MoS_2 waveguide (empty circles) as a function of λ, measured from the slopes of $I_{DF}(\propto e^{-\beta x})$ in log scale (fig. S4A). The β(λ) plot closely matches the expected loss (green curve) calculated on the basis of the absorption spectrum of a monolayer MoS_2 (fig. S4, B and C). For photon energies below E_g, where the MoS_2 absorption is small, the propagation loss is small (β ~ 0.5 dB/mm). A similar analysis conducted for different N at λ = 550 nm suggests that the decay rate substantially increases for thicker waveguides (Fig. 2E).

The guided wave is stable only under a highly symmetric optical environment (Δn ~ 0), which can be quantitatively described using a direct analogy with a quantum mechanical eigenfunction in a δ-potential well, as illustrated in Fig. 2F. When the vacuum level of a δ-potential trap is asymmetric (ΔV), the confinement becomes weaker on the side with the lower barrier height, and there no longer exists a trapped eigenstate when $\Delta V > 2m\alpha^2/\hbar^2$ (where α is the δ-potential strength, m is the mass of the trapped particle, and $\hbar$ is the reduced Planck constant). We experimentally test this prediction by introducing a liquid environment with tunable refractive index; a monolayer MoS_2 film grown on a fused silica substrate (n_{FS}) is placed inside an optical cube filled with a water-glycerol solution (n_{mix}; see Fig. 2G). We vary $\Delta n = n_{mix} - n_{FS}$ by changing the solution composition and measure the guided mode intensity from monolayer MoS_2 (λ = 750 nm). The results shown in Fig. 2H are fully consistent with our analytic predictions (fig. S4D). For $\Delta n/n_o \leq 0.1\%$, the strong signals are visible over the entire field of view (>3 mm). At higher $\Delta n/n_o \geq 0.2\%$, the signals are substantially weaker, disappearing completely at 0.9% (see supplementary text, section S3, for more quantitative analysis). Further analysis using a highly collimated laser confirms that $n_{eff} \sim n_o$ and $k_z/k_{\parallel} < 10^{-3}$ and thus that the guided waves are in a form of 2D light waves having negligible out-of-plane dispersion (fig. S5).

These results on the polarization-, wavelength-, layer number N-, and Δn-dependent properties confirm that a MoS_2 monolayer can be used to generate a large-scale δ waveguide with propagation loss as low as ~0.5 dB/mm for a broad range of λ and a high (~30%) coupling efficiency. The propagation loss and coupling efficiency could be further improved by material improvement [e.g., optical quality of PDMS and fused silica or reduction of midgap loss in MoS_2 (*29*)] and mode optimization of the excitation laser.

A platform for 2D photonics

The guided mode in a δ waveguide is essentially an evanescent wave whose optical fields are found mostly outside the waveguide (>98%; fig. S6). Engineering optical properties of the surrounding will directly tune the mode index ($n_{eff} \approx n_o$) and would change the propagation properties of the guided modes. In addition, the monolayer MoS_2 waveguide can be grown, delaminated, and transferred in large multi-inch scale, with both bottom and top surfaces

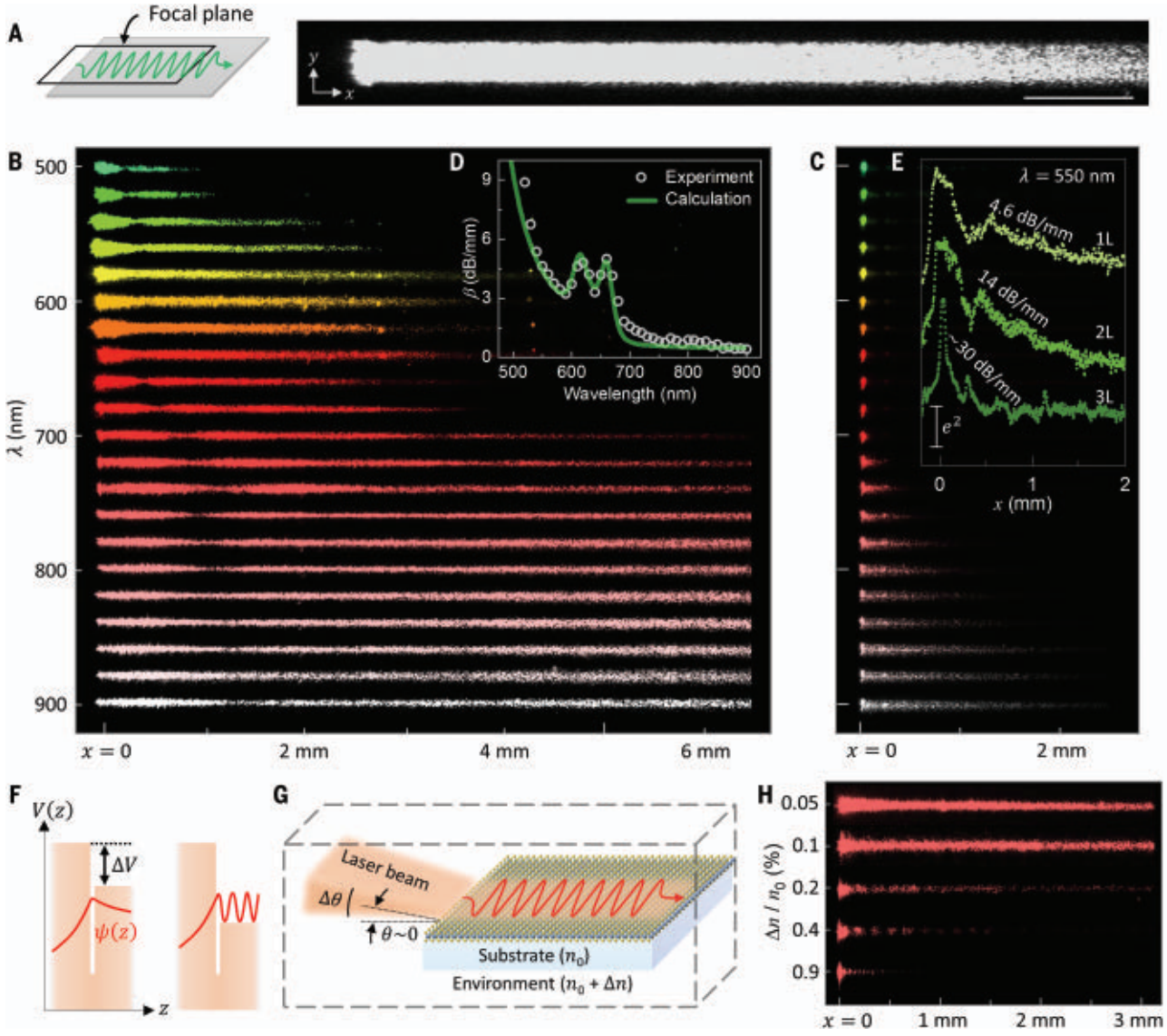

Fig. 2. Light modes guided by δ waveguides. (**A**) Film-surface microscopy image on a MoS_2 film, visualized by collecting dark-field signals at λ = 720 nm. Scale bar, 0.2 mm. (**B** and **C**) False-color dark-field images measured from monolayer (B) and 3L (C) MoS_2 waveguides excited at different λ (from 500 to 900 nm). (**D**) Rate of dark-field signal decays as a function of light wavelength (white dots), analyzed from intensity profiles shown in (B), by taking an average slope. The green curve plots the propagation loss of guided waves calculated independently by using the experimental values of sheet susceptibility of MoS_2. (**E**) Intensity profiles of dark-field images as a function of propagation distance *x*, measured on waveguides with different MoS_2 layer numbers at a single wavelength (550 nm). (**F**) Schematic illustrations of the δ-potential well with asymmetric vacuum levels $V(z)$ and its quantum mechanical eigenstate $\psi(z)$. The oscillation is exaggerated for clarity. (**G**) Schematic of coupling of free-space laser beam into δ waveguide in asymmetric dielectric environment. (**H**) Top-view dark-field signals (λ = 750 nm) measured from monolayer MoS_2 for several $\Delta n/n_0$.

independently available for thin-film microfabrication, integration, and optical access. We can use these properties to demonstrate two approaches of optical functionalization on a δ waveguide—integration of thin-film elements (Fig. 3) and direct microfabrication and optical excitation of MoS_2 (Fig. 4).

Figure 3A displays a scanning electron microscope image demonstrating our capability of integrating thin-film optical components on a δ waveguide. A transparent dielectric film (1.8-μm-thick SU-8) is fabricated through a standard lithography process on a monolayer MoS_2 waveguide into convex and concave geometries designed for wavefront shaping of guided waves (inset; see materials and methods for detailed fabrication). Similarly, an ultrathin metal (5-nm-thick Au) is used to form slits, the most basic element for diffractive optics, as well as gratings (fig. S7). Figure 3B schematically illustrates the key ideas about how they work: Transparent dielectric SU-8 films with thickness $t > w$ (where w is the mode width) can alter the effective refractive index (top) and therefore control the wavefront of guided modes; metallic films, which have a large extinction coefficient, can carry only TM modes (not allowing TE modes to propagate; fig. S8), thereby blocking the TE-guided modes in the δ waveguide (bottom). Our simulations confirm that the effective mode index (n_{eff}) changes from n_0 to n_d across the dielectric interface with negligible back scattering as a result of the similar mode widths ($\Delta w/w$ = 0.02; Fig. 3C, top). The simulation also shows that 5-nm-thick Au (yellow dashed line in the bottom of Fig. 3C)

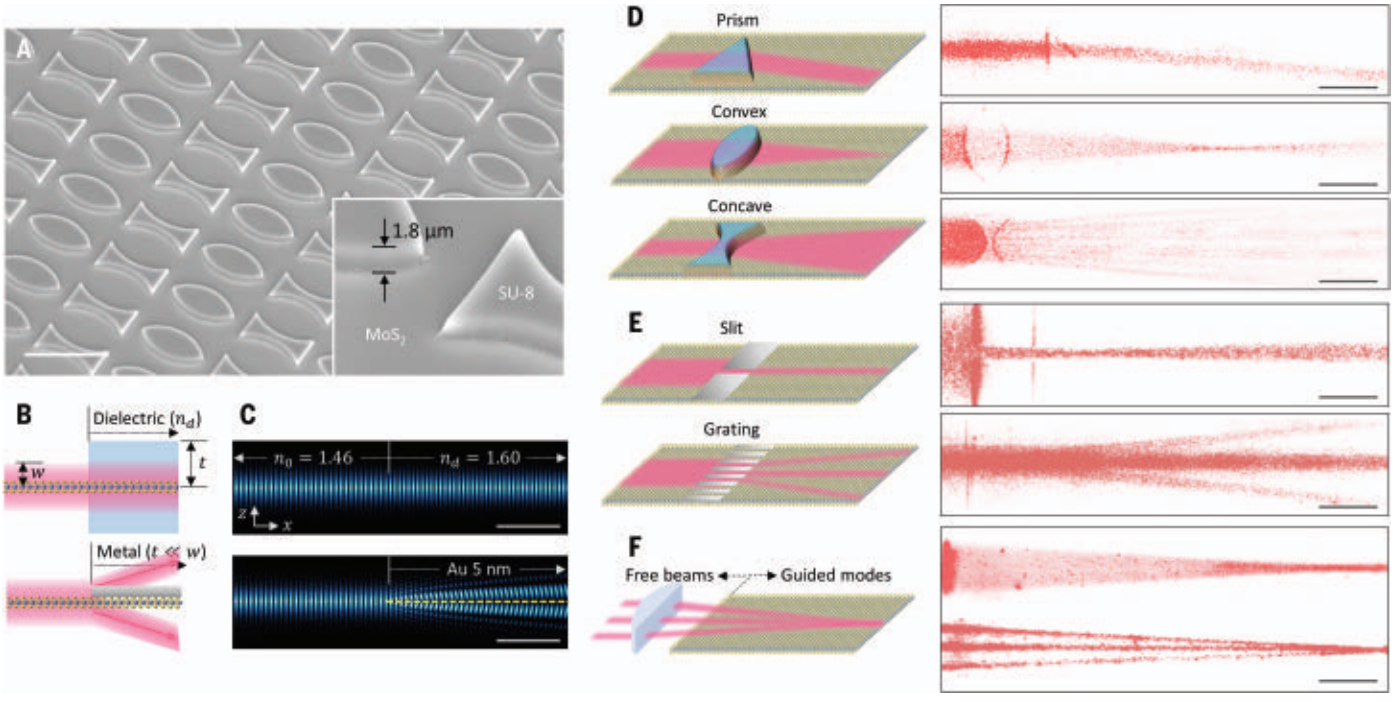

Fig. 3. Microfabricated thin-film components on δ waveguides. (**A**) Scanning electron microscope images of convex- and concave-shaped optical elements made of 1.8-μm-thick SU-8 film integrated on a monolayer MoS_2 film. Inset shows a magnified image. Scale bar, 20 μm. (**B**) Schematic illustration of effective index modulation of guided modes by using a thin film (top) and scattering of guided mode using a metallic film (bottom). (**C**) Simulated electric field intensity when a guided mode propagates and encounters an interface between different refractive indices of surrounding environment (top) and an interface between δ waveguides with a 5-nm-thick Au film and without the Au film (bottom). Scale bars, 2 μm. (**D**) Schematics on how guided waves interact with dielectric thin-film components microfabricated into prism, convex, and concave shapes (left) and corresponding experimental dark-field images measured in the top-view configuration (right) (λ = 720 nm). Scale bars, 0.2 mm. (**E**) Schematics of using metallic films as a slit or a grating (left) and corresponding experimental images (right). Scale bars, 0.5 mm. (**F**) Schematic of delivering a designed wavefront of 2D free beams into the guided waves (left) and corresponding experimental images (right). Scale bar, 1 mm.

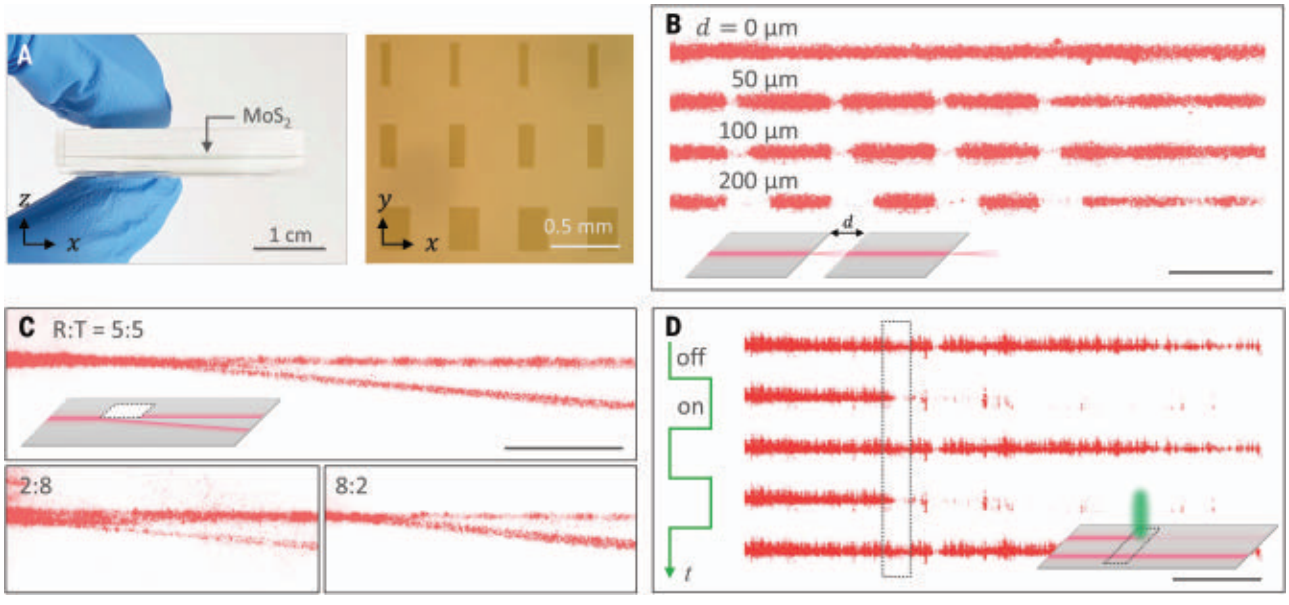

Fig. 4. Patterned and photo-modulated δ waveguides. (**A**) Cross-sectional photograph of a δ waveguide inside optically homogeneous polymer packaging (left) and an optical micrograph of patterned waveguides (right), generated by removing MoS_2 with a pulsed laser. (**B**) Dark-field images that demonstrate the transport of guided waves across interconnected waveguides (λ = 750 nm), where multiple waveguides are separated by a distance *d* (disconnected area in schematic). Scale bar, 0.5 mm. (**C**) Splitting and deflecting of guided waves (λ = 750 nm), where a square area of MoS_2 is removed (dotted area in schematic). Scale bar, 1 mm. (**D**) Modulation of guided waves (λ = 680 nm), actively switchable by using a pump beam (λ = 532 nm, intensity ~ 2 kW/cm^2) that is directed at a local area of MoS_2 (dotted box in schematic). Scale bar, 0.5 mm.

on monolayer MoS_2 fully scatters the incoming waves and completely blocks the propagation of guided waves.

Figure 3, D and E, displays experimental images showing how guided waves interact with different optical elements (right; λ = 720 nm) and corresponding schematics (left). The measured beam trajectories shown in Fig. 3D demonstrate that the refractive components change the propagation direction (by prism; top) and shape the wavefront of incident waves from planar to either convergent (by convex; middle) or divergent (by concave; bottom) forms. Placing optical elements only on top of a waveguide induces asymmetry, weakening the confinement and increasing the loss. Using symmetric refractive elements by transferring identical components on either side of MoS_2 improves the transmission by up to 85% (fig. S9). The top-view images in Fig. 3E show that the ultrathin metals clearly stop the propagation of guided waves, which allows their combinations to work for diffractive optics: (i) The slit geometry (top), made by two metal sheets with a gap space (3 μm), cuts the incident beam width to leave a narrow line matching with the gap size, and (ii) the diffraction grating (bottom), an arrangement of multiple slits of the same gap space with periodicity of 5 μm (Λ), generates the first-order diffracted beams deflecting at 5.6 degrees, which agrees with the phase-matching condition ($\lambda/n_0\Lambda$).

These results indicate that our approach for guided-wave optics on δ waveguides is conceptually similar to free-beam optics on an optics table. Because the guided wave is a 2D light wave with $k \approx k_{\parallel}$, the dispersion relation of the wave is practically identical to those in free space. This makes δ waveguides a unique platform that can take advantage of the near-zero structural dispersion along the trapping dimension. Figure 3F demonstrates this structural dispersion–free property, where a cylindrical convex lens is placed before the waveguide to focus one (upper image) or more (lower image) incoming laser beams in the *x*-*y* plane. The dark-field images show that the δ waveguide takes different incoming waves and makes sharp focuses within the waveguide regardless of the beam diameter and the number of incident beams. Our analysis further confirms that the wavefront designed for the 2D free beams is accurately transmitted into the guided waves, with the focal positions closely aligning with the predicted location based on the displacement of the cylindrical lens (fig. S10A). This demonstrates that δ waveguides allow impedance matching with free-space optics, and thus the 2D waveform remains during the transformation between free beams and guided modes.

In addition to guided wave optics based on thin-film integration, the MoS_2 monolayer can be patterned (Fig. 4A) or optically excited, which enables local control of the trapping potential. We demonstrate three basic functionalities for 2D photonics: interconnection, beam splitting, and modulation. Figure 4B shows how a guided wave propagates across the interconnection geometry where a δ waveguide is disconnected into several segments separated by regions void of MoS_2 with a varying gap distance d (materials and methods). The dark-field intensity suggests an excellent interconnection efficiency (~0.1-dB loss per 10-μm gap distance; fig. S10B), which is consistent with observations taken in the end-face microscopy (fig. S11) and agrees with the 2D nature of the guided wave and its free beam–like propagation. Figure 4C shows an example of how to split and divert a guided wave. For this, a square area of monolayer MoS_2 in the middle of the waveguide is removed by etching the material away using a pulsed laser (dotted line). When a guided wave is directed at a corner of the square, it divides into two—one continuing along the original direction and the second one along a different path. The deflection angle (up to ~10°) and splitting ratio (8:2, 5:5, or 2:8 shown in Fig. 4C) can be controlled by the position and relative angle of the missing MoS_2 square. This splitting behavior only occurs when a combination of a corner and tilted edges is placed in the guided beam path. It is not seen in other simpler configurations or when a corner is introduced to a decoupled beam (fig. S12). Fig. 4D presents an active switching of the guided wave transport. A pump beam (532 nm; intensity $I_P \sim 2$ kW/cm^2) is introduced normal to the MoS_2 waveguide that intersects with the guided wave (dotted area; see materials and methods). The 2D wave strongly attenuates when the pump beam is on and fully recovers its original intensity when the pump beam is off. This shows that the transport of a guided wave can be modulated using a pump beam absorbed by MoS_2. The efficiency of the photo-modulation increases monotonically with I_P, reaching 50% at 0.5 kW/cm^2, which suggests that the photo-modulation occurs in the linear absorption regime for MoS_2 (fig. S13). Although many of these observations can be explained by polariton-exciton interactions (*30*), more theoretical and experimental studies will be needed to fully understand these phenomena.

Conclusions

Our approach of producing δ waveguides can be extended to other atomically thin materials and heterostructures for the development of ultrathin integrated photonic circuits as well as to explore the specific properties of light waves guided by 2D materials. For example, light waves with widely different wavelengths (far-infrared to ultraviolet) can be guided by a single δ waveguide, enabling multioctave-spanning photonic architectures. The broadband, high-power, and dispersion-free operation of our δ waveguides could be used for 2D nonlinear photonics capable of on-chip manipulation of pulsed signals and highly efficient second-harmonic generator when combined with nonlinear properties of vdW materials. The extensive library of light-matter interactions in atomically thin materials could allow for the integration of advanced photonic devices with a δ waveguide, where multiple components with advanced plasmonic and excitonic properties can be deposited and patterned at large scale using conventional thin-film processes.

REFERENCES AND NOTES

1. L. Feng *et al*., *Science* **333**, 729–733 (2011).
2. A. Politi, M. J. Cryan, J. G. Rarity, S. Yu, J. L. O'Brien, *Science* **320**, 646–649 (2008).
3. Q. Xu, B. Schmidt, S. Pradhan, M. Lipson, *Nature* **435**, 325–327 (2005).
4. H. Rong *et al*., *Nature* **433**, 725–728 (2005).
5. H. Hodaei, M. A. Miri, M. Heinrich, D. N. Christodoulides, M. Khajavikhan, *Science* **346**, 975–978 (2014).
6. M. Lee, S. Callard, C. Seassal, H. Jeon, *Nat. Photonics* **13**, 445–448 (2019).
7. A. W. Elshaari, W. Pernice, K. Srinivasan, O. Benson, V. Zwiller, *Nat. Photonics* **14**, 285–298 (2020).
8. G. Crosnier *et al*., *Nat. Photonics* **11**, 297–300 (2017).
9. T. Harter *et al*., *Nat. Photonics* **12**, 625–633 (2018).
10. J. Wang, F. Sciarrino, A. Laing, M. G. Thompson, *Nat. Photonics* **14**, 273–284 (2020).
11. K. Y. Yang *et al*., *Nat. Photonics* **12**, 297–302 (2018).
12. J. B. Khurgin, *Optica* **2**, 740–742 (2015).
13. J. Chen *et al*., *Nature* **487**, 77–81 (2012).
14. G. X. Ni *et al*., *Nature* **557**, 530–533 (2018).
15. D. N. Basov, M. M. Fogler, F. J. García de Abajo, *Science* **354**, aag1992 (2016).
16. T. Low *et al*., *Nat. Mater.* **16**, 182–194 (2017).
17. E. Yoxall *et al*., *Nat. Photonics* **9**, 674–678 (2015).
18. Q. Zhang *et al*., *Nature* **597**, 187–195 (2021).
19. L. Xiong *et al*., *Sci. Adv.* **7**, eabe8087 (2021).
20. Y. Zhou *et al*., *Nat. Nanotechnol.* **12**, 856–860 (2017).
21. F. Hu *et al*., *Nat. Photonics* **11**, 356–360 (2017).
22. F. Hu *et al*., *Phys. Rev. B* **100**, 121301 (2019).
23. X. Zhang *et al*., *Nat. Nanotechnol.* **14**, 844–850 (2019).
24. F. Barachati *et al*., *Nat. Nanotechnol.* **13**, 906–909 (2018).
25. M. Mrejen, L. Yadgarov, A. Levanon, H. Suchowski, *Sci. Adv.* **5**, eaat9618 (2019).
26. Y. Li *et al*., *Phys. Rev. B* **90**, 205422 (2014).
27. K. Kang *et al*., *Nature* **520**, 656–660 (2015).
28. K. Kang *et al*., *Nature* **550**, 229–233 (2017).
29. A. M. van der Zande *et al*., *Nat. Mater.* **12**, 554–561 (2013).
30. P. Cristofolini *et al*., *Phys. Rev. Lett.* **110**, 186403 (2013).
31. M. Lee *et al*., Data and codes for: "Wafer-scale δ-waveguides for integrated two-dimensional photonics," Zenodo (2023); https://doi.org/10.5281/zenodo.8080270.

ACKNOWLEDGMENTS

We thank B. Cheng, P. Poddar, and T. Zhong for their helpful discussions. **Funding:** Primary funding for this work comes from the Air Force Office of Scientific Research (FA9550-21-1-0323 and FA9550-16-1-0347) and the MURI project (FA9550-18-1-0480). Additional funding was provided by the University of Chicago MRSEC (NSF DMR-2011854) and the Cornell Center for Materials Research (NSF DMR-1719875). F.M. acknowledges support by the NSF Graduate Research Fellowship Program under grant no. DGE-1746045. A.Y. is supported by the Department of Defense through the National Defense Science and Engineering Graduate (NDSEG) Fellowship Program. This work made use of the characterization facilities of the University of Chicago MRSEC (NSF DMR-2011854) and the fabrication facilities of the Pritzker Nanofabrication Facility at the University of Chicago, which receives support from SHyNE Resource (NSF ECCS-420 1542205), a node of NSF's NNCI network. **Author contributions:** M.L., H.H., and J.P. conceived the experiments. M.L. and H.H. fabricated the devices, conducted optical measurements, and performed electrodynamics simulations. J.Y. performed the laser patterning. F.M. and C.L. synthesized monolayer MoS_2 films. M.L., H.H., and A.Y. developed the polymer and liquid encapsulation processes for index matching. H.H. developed the thin-film element integration

process. M.L., H.H., and J.P. wrote the manuscript. All authors discussed and commented on the manuscript. **Competing interests:** The authors declare no competing interests. **Data and materials availability:** All data are reported in the main text and supplementary materials. Raw data and relevant codes can be found at Zenodo (*31*). **License information:** Copyright © 2023 the authors, some rights reserved; exclusive licensee American Association for the Advancement of Science. No claim to original US government works. https://www.science.org/about/science-licenses-journal-article-reuse

SUPPLEMENTARY MATERIALS

science.org/doi/10.1126/science.adi2322
Materials and Methods
Supplementary Text
Figs. S1 to S15
Table S1
References (*32*–*34*)

Submitted 12 April 2023; accepted 30 June 2023
10.1126/science.adi2322

MOLECULAR BIOLOGY

RHINO directs MMEJ to repair DNA breaks in mitosis

Alessandra Brambati[1]*†, Olivia Sacco[1]†, Sarina Porcella[1]†, Joshua Heyza[2,3], Mike Kareh[1], Jens C. Schmidt[2,3], Agnel Sfeir[1]*

Nonhomologous end-joining (NHEJ) and homologous recombination (HR) are the primary pathways for repairing DNA double-strand breaks (DSBs) during interphase, whereas microhomology-mediated end-joining (MMEJ) has been regarded as a backup mechanism. Through CRISPR-Cas9–based synthetic lethal screens in cancer cells, we identified subunits of the 9-1-1 complex (RAD9A-RAD1-HUS1) and its interacting partner, RHINO, as crucial MMEJ factors. We uncovered an unexpected function for RHINO in restricting MMEJ to mitosis. RHINO accumulates in M phase, undergoes Polo-like kinase 1 (PLK1) phosphorylation, and interacts with polymerase θ (Polθ), enabling its recruitment to DSBs for subsequent repair. Additionally, we provide evidence that MMEJ activity in mitosis repairs persistent DSBs that originate in S phase. Our findings offer insights into the synthetic lethal relationship between the genes *POLQ* and *BRCA1* and *BRAC2* and the synergistic effect of Polθ and poly(ADP-ribose) polymerase (PARP) inhibitors.

Microhomology-mediated end-joining (MMEJ) is an intrinsically mutagenic repair pathway. Nevertheless, it mitigates the harmful effects of double-strand breaks (DSBs) by preventing the accumulation of large-scale DNA rearrangements. Repair by MMEJ is necessary for the survival of cells with compromised homologous recombination (HR) and nonhomologous end-joining (NHEJ) (*1*–*3*). Targeting this pathway has emerged as a promising therapeutic approach for cancer patients with defective HR, including those carrying mutations in the *BRCA1* and *BRCA2* genes (*4*–*6*). MMEJ is characterized by the presence of 2 to 6 base pairs of microhomology, as well as insertions and deletions (indels) that scar the repair sites (*7*). These indels are introduced by DNA polymerase θ (Polθ), which is encoded by the *POLQ* gene. Polθ is a low-fidelity polymerase with a helicase-like activity and plays a central role in MMEJ (*8*, *9*).

The mutational signature associated with MMEJ has been found across different species, and the pathway is conserved from bacteria to humans (*10*). However, its mechanistic basis remains poorly defined. In mammalian cells, studies have demonstrated that after DSB formation, short-range DNA end resection by MRE11 and CtIP exposes flanking microhomologies that promote the annealing of opposite ends of the break (*11*–*13*). When internal homologies are base paired, the resulting single-stranded DNA (ssDNA) flaps are cleaved by APEX2 and FEN1 (*14*–*16*). Annealed intermediates are extended by Polθ (*17*–*19*) and sealed by XRCC1 and LIG3 to complete the end joining (*20*). Polθ also acts on transient "snap-back" substrates that are formed when the overhang of resected DSBs folds back and anneals to itself. Ultimately, Polθ-mediated insertions contribute to the mutagenicity of MMEJ (*19*). Although up-regulated in many cancer types, Polθ is generally low in abundance and must be actively recruited to DSB sites (*21*). Yet the mechanism by which the low-fidelity polymerase is recruited to break sites and the upstream factors that drive MMEJ remain unknown.

MMEJ was initially identified as an inefficient DNA end-joining activity in Ku-deficient *Saccharomyces cerevisiae* (*22*) and has been primarily regarded as a backup pathway that acts when preferred modes of DSB repair are absent (*1*–*3*). However, recent reports suggest that under certain conditions, MMEJ prevails. For instance, MMEJ is the primary repair mechanism for CRISPR-Cas9–induced DSBs in early zebrafish embryos (*23*). In human and mouse cells, MMEJ acts with NHEJ to promote the random integration of foreign DNA into the genome and repair CRISPR-Cas9–induced breaks at particular loci (*24*–*26*). Furthermore, recent evidence suggests that MMEJ plays a role in DSBs during mitosis, where HR and NHEJ are attenuated (*27*–*30*).

Because of the synthetic lethal relationship between MMEJ and HR, Polθ inhibitors are presently under investigation in phase 1 and 2 trials in the clinic as monotherapy and in combination with poly(ADP-ribose) polymerase (PARP) inhibitors (PARPi). Preclinical studies demonstrated that Polθ inhibitors target BRCA-deficient tumors, are synergistic with PARPi, and eliminate a subset of PARPi-resistant tumors (*4*, *6*, *31*). Elucidating the underlying mechanism of MMEJ and its temporal and spatial regulation is critical to understanding when and how cells opt for the mutagenic MMEJ and potentially explain the synthetic lethal interaction between MMEJ and HR.

Results

CRISPR-Cas9 synthetic lethal screen uncovers the full spectrum of MMEJ factors

To identify the full spectrum of MMEJ factors, we conducted a genome-wide CRISPR-based synthetic lethal screen in cells lacking HR and NHEJ [*BRCA2*$^{-/-}$*LIG4*$^{-/-}$*TP53*$^{-/-}$ cells or triple-knockout (TKO) cells]. We hypothesized that because cells that lack these canonical DSB repair pathways are highly dependent on MMEJ for survival, this approach would reveal the full spectrum of potential MMEJ factors (Fig. 1, A to C, and fig. S1, A to D). The synthetic lethal screen identified a set of genes that were preferentially depleted in TKO cells, including hits previously reported to be essential for the survival of *BRCA2*-null cells—such as *FEN1*; *RNaseH2A*, *RNaseH2B*, and *RNaseH2C* (*32*); *CIP2A* (*33*); and *ALC1* (*34*)—as well as known MMEJ factors, including *POLQ*, *HMCES* (*35*), and *APEX2* (*14*–*16*, *36*) (fig. S1, E to G). Notably, we identified members of the 9-1-1 complex (RAD9A-RAD1-HUS1) and its interacting partner RHINO (encoded by *RHNO1*) as essential in TKO cells (Fig. 1, D and E). To confirm the synthetic lethality, we individually targeted subunits of the complex using independent single guide RNAs (sgRNAs). We found that whereas depletion of 9-1-1 and RHINO had little impact on control cells, their loss compromised the survival of cells that lack HR and NHEJ (Fig. 1F and fig. S1, H to J).

RAD9-RAD1-HUS1 (9-1-1) and RHINO are critical MMEJ factors

To directly test whether the 9-1-1 complex and RHINO are required for MMEJ, we investigated the repair of dysfunctional telomeres. The six-subunit shelterin complex protects telomeres from being recognized as DSBs. When shelterin is absent, telomeres become deprotected, and the DNA damage response is activated at chromosome ends (*37*). In cells where telomeres are unprotected and the NHEJ

[1]Molecular Biology Program, Sloan Kettering Institute, Memorial Sloan Kettering Cancer Center, New York, NY, USA. [2]Institute for Quantitative Health Sciences and Engineering, Michigan State University, East Lansing, MI, USA. [3]Department of Obstetrics, Gynecology, and Reproductive Biology, Michigan State University, East Lansing, MI, USA.
***Corresponding author. Email: sfeira@mskcc.org (A.S.); brambata@mskcc.org (A.B.)**
†These authors contributed equally to this work.

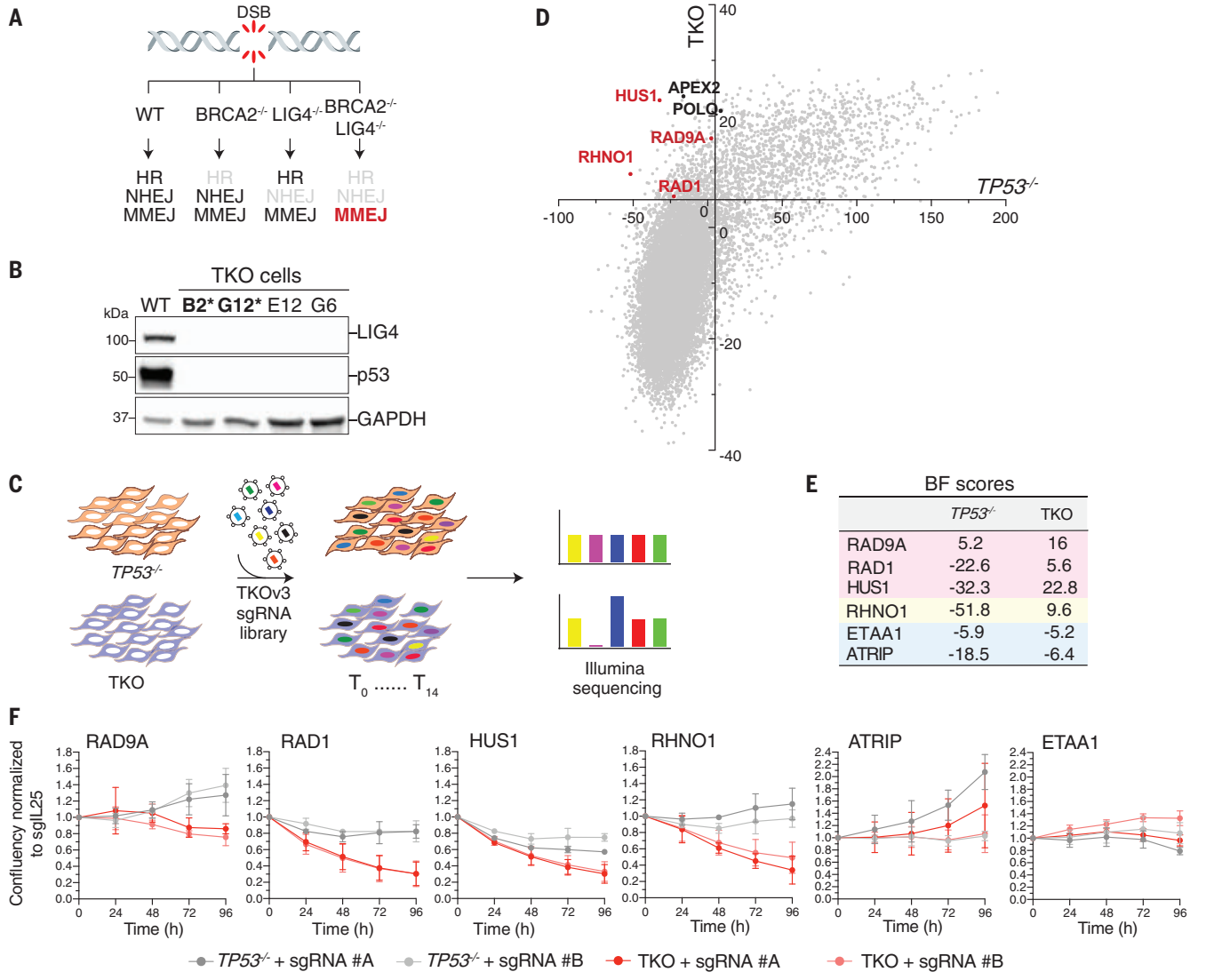

Fig. 1. A genome-wide CRISPR-Cas9 screen uncovers an essential function for 9-1-1 and RHNO1 in cells that lack BRCA2 and LIG4. (**A**) Schematic of the three major DSB repair pathways in mammalian cells. WT, wild type. (**B**) Western blot analysis of LIG4 and p53 in clonally derived *BRCA2*$^{-/-}$*LIG4*$^{-/-}$*TP53*$^{-/-}$ DLD1 cells (TKO). The asterisk indicates clones used in the screen. GAPDH, glyceraldehyde phosphate dehydrogenase. (**C**) Schematic of the dropout CRISPR-Cas9 screen to identify synthetic lethal interactions. (**D**) Genome-wide CRISPR-Cas9 screen result in TKO cells. Genes with a Bayes factor (BF) score >5 (intersection of *x* and *y* axes) were considered essential. (**E**) BF scores for the indicated genes. (**F**) Growth curve of TKO and *TP53*$^{-/-}$ cells treated with the indicated sgRNAs. Data are mean ± SD of three independent experiments normalized to time point zero (1 day after seeding) and a control sgRNA (sgIL25).

factors Ku70 and Ku80 are absent, MMEJ is the primary repair pathway leading to chromosome end-to-end fusions (*37*) (Fig. 2A). We targeted subunits of the 9-1-1 complex and RHINO in *TRF1/2*$^{\Delta/\Delta}$*Ku80*$^{-/-}$ cells (fig. S2, A and B) and noted a significant reduction in the frequency of MMEJ-dependent telomere fusions (Fig. 2, B and C). Depletion of the 9-1-1 subunits and RHINO in NHEJ-proficient settings had no impact on telomere fusions, suggesting that the activity of 9-1-1 and RHINO is specific to MMEJ (Fig. 2D). Despite the reduced MMEJ activity, the absence of 9-1-1 and RHINO did not prevent the accumulation of 53BP1 at shelterin-free telomeres (fig. S2, C and D). This implies that the canonical role of the 9-1-1 complex in activating DNA damage signaling through ATR kinase (*38*) does not completely account for its function in MMEJ. In an orthogonal approach, we measured MMEJ activities at a break induced by the endonuclease I-SceI using the traffic light reporter (TLR) system (*39*) (fig. S2E). Findings based on the fluorescent DSB reporter corroborated the results derived from the telomere fusion assay and are consistent with Repair-seq (*40*), which demonstrated a correlation between *POLQ* and the 9-1-1 complex as well as the Rad17-RFC clamp loader (Fig. 2, B and D, and figs. S1G and S2, E to I).

A noncanonical function for 9-1-1 and RHINO in MMEJ

9-1-1 is a heterotrimeric complex loaded onto 5′ ends of resected DNA and ssDNA gaps in response to replication stress (*38*). Its interaction with RHINO induces DNA damage signaling by ATR (*41*, *42*). ATR is also activated by ETAA1 and its interacting partner ATRIP (*43*, *44*). Notably, in the synthetic lethal screen, *ATRIP* and *ETAA1* did not emerge as potential hits (Fig. 1E), and CRISPR-Cas9–mediated deletion of these genes did not result in growth defects in TKO cells (Fig. 1F and fig. S1, K to N). Moreover, whereas the loss of ATRIP had a minor impact on telomere fusions, ETAA1 depletion did not impair MMEJ (fig. S3, A to E). By contrast, depletion of 9-1-1, RHINO, and Polθ significantly reduced telomere fusion events (Fig. 2, B and C, and fig. S3, A to E). These findings suggest that the established role of 9-1-1 and RHINO in ATR signaling does not entirely explain their function in MMEJ.

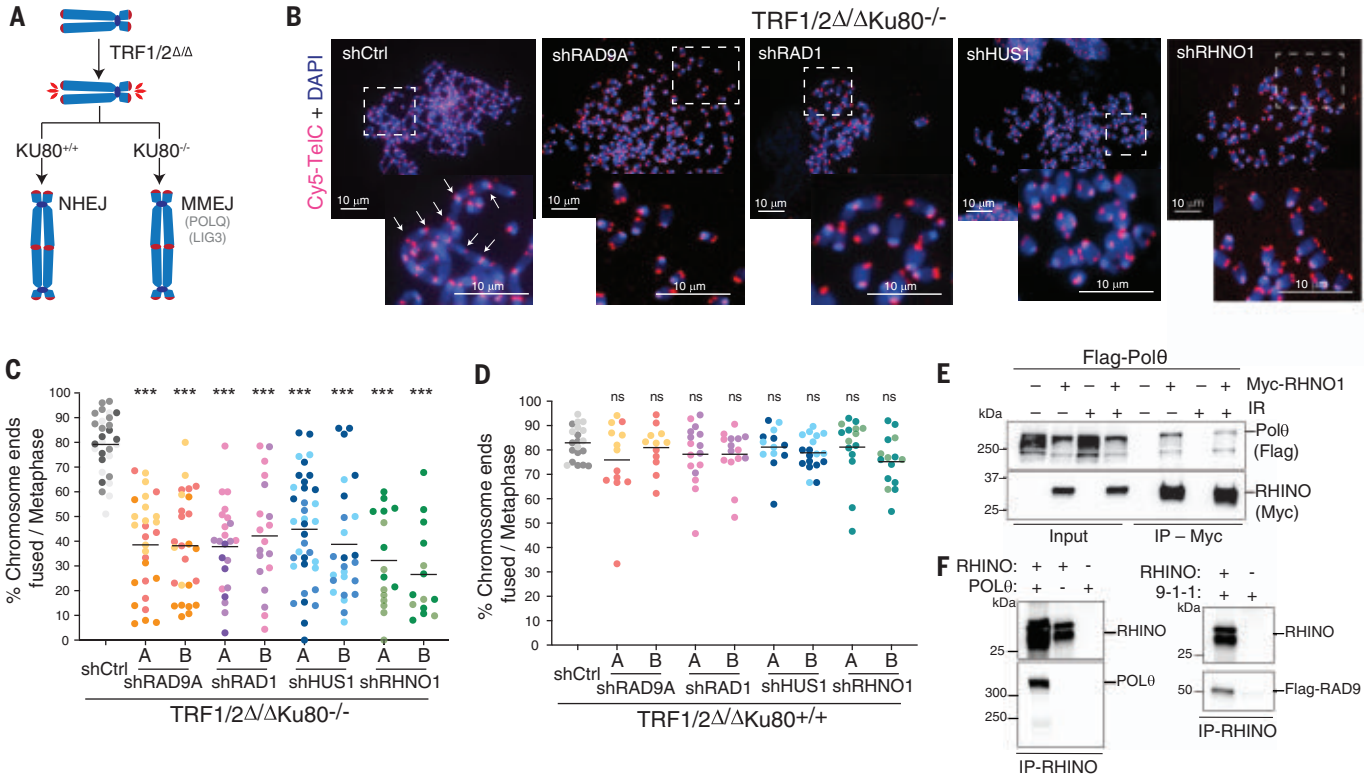

Fig. 2. A noncanonical function for 9-1-1–RHINO in MMEJ. (**A**) Schematic of the shelterin-free assay (*37*) to monitor MMEJ frequency at deprotected telomeres. (**B**) Representative images of metaphase spreads from *TRF1/2*$^{\Delta/\Delta}$*Ku80*$^{-/-}$ cells depleted for the subunits of the 9-1-1 complex and *RHNO1* with two independent short hairpin RNAs (shRNAs). Telomeres are marked by fluorescence in situ hybridization (FISH) using a Cy5-[CCCTAA]3 peptide nucleic acid (PNA) probe (red), and chromosomes are counterstained with 4′,6-diamidino-2-phenylindole (DAPI) (blue). White arrows indicate examples of telomeric fusions in the control (shCtrl) sample. The dashed rectangles highlight the magnification in (C). (**C**) Quantification of telomeric fusions mediated by MMEJ as shown in (B). The colors used indicate independent experiments. The black line represents the mean. (**D**) Quantification of telomere fusions by NHEJ in TRF1/2$^{\Delta/\Delta}$Ku80$^{+/+}$ cells. Data in (C) and (D) are the mean of at least two independent experiments. Significance was determined by one-way analysis of variance (ANOVA) (***$p < 0.001$; ns, not significant). (**E**) Co-IP experiment depicting the Polθ and RHINO interaction in whole-cell extracts from HEK293T cells cotransfected with plasmids expressing Flag-Polθ and RHINO-MYC. Co-IPs were performed in cells treated with ionizing radiation [+IR, 20 gray (Gy)] and control cells. (**F**) Co-IP experiments showing the interactions of Polθ-RHINO and 9-1-1–RHINO with purified proteins. Polθ was purified from HEK293T cells, RHINO from *Escherichia coli*, and 9-1-1 from *S. cerevisiae*.

The 9-1-1 subunits assemble into a ring-shaped complex that structurally resembles proliferating cell nuclear antigen (PCNA), which recruits DNA polymerases to the replisome (*45*). We speculated that 9-1-1 and RHINO might facilitate MMEJ by interacting with and recruiting Polθ to break sites. We performed coimmunoprecipitation (co-IP) experiments in human embryonic kidney 293T (HEK293T) cells coexpressing 9-1-1 proteins, RHINO, and Polθ. Although we could not detect an interaction between Polθ and any of the subunits of the 9-1-1 complex (fig. S3F), we observed an interaction between Polθ and RHINO, independent of DNA damage (Fig. 2E). In addition, using purified proteins, we found that RHINO bound full-length Polθ in vitro (Fig. 2F and fig. S3G).

RHINO is predominantly expressed in mitosis, and its phosphorylation by PLK1 stimulates the interaction with Polθ

To gain better insight into the function of RHINO, we sought to determine its genetic interactors. We carried out synthetic lethal screens in three clonally derived *RHNO1*$^{-/-}$ cell lines and the parental *RHNO1*$^{+/+}$ cells (Fig. 3A and fig. S4, A to G). Pathway analysis of top genes essential in *RHNO1*$^{-/-}$ cells revealed enrichment in several pathways related to mitosis (Fig. 3B), including cyclin-dependent kinase *CDK1*, members of the ESCRT complex, spindle checkpoint proteins, and the kinetochore factor *ZWILCH* (Fig. 3A and figs. S4, F and G, and S5, A and B). Independently, we analyzed the genetic dependencies in DepMap (*46*) and found that *RHNO1* correlated with *CIP2A*, *MDC1*, and *TOPBP1*, which form a complex that tethers mitotic DSBs together (*33*, *47*, *48*). DepMap analysis also uncovered a correlation between the essentiality scores of *POLQ*, *CIP2A*, and *RHNO1* (Fig. 3C).

The results from the synthetic lethal screen and DepMap analysis underscored a previously unrecognized role for RHINO in repairing DNA damage in mitosis. This observation was substantiated by the accumulation of large RHINO foci in cells arrested in M phase (Fig. 3, D and E, and fig. S5, C and D). Furthermore, Western blot analysis of samples collected at different cell cycle stages revealed that RHINO accumulated in mitosis and was rapidly degraded upon mitotic exit (Fig. 3F and fig. S6, A to D). By contrast, subunits of the 9-1-1 complex were expressed throughout all cell cycle stages (fig. S6, C to E). As anticipated by the strict expression of RHINO, Polθ interacted with Flag-RHINO, specifically in mitosis (Fig. 3G). Coincident with its stabilization, RHINO was phosphorylated in mitosis (fig. S6F).

RHINO contains two recognition sequences for the anaphase-promoting complex (APC/C), namely the Ken-box and D-box domains (*49*) (Fig. 3H). Expression of RHINO-ΔDK, which carries deletions in both degrons, resulted in RHINO stabilization beyond mitosis (Fig. 3I). Furthermore, the overexpression of the APC/C adaptor protein Cdh1, but not Cdc20, led to RHINO depletion, suggesting that its degradation is a late event in mitosis (fig. S6G) (*49*). Although RHINO-ΔDK remained stable during

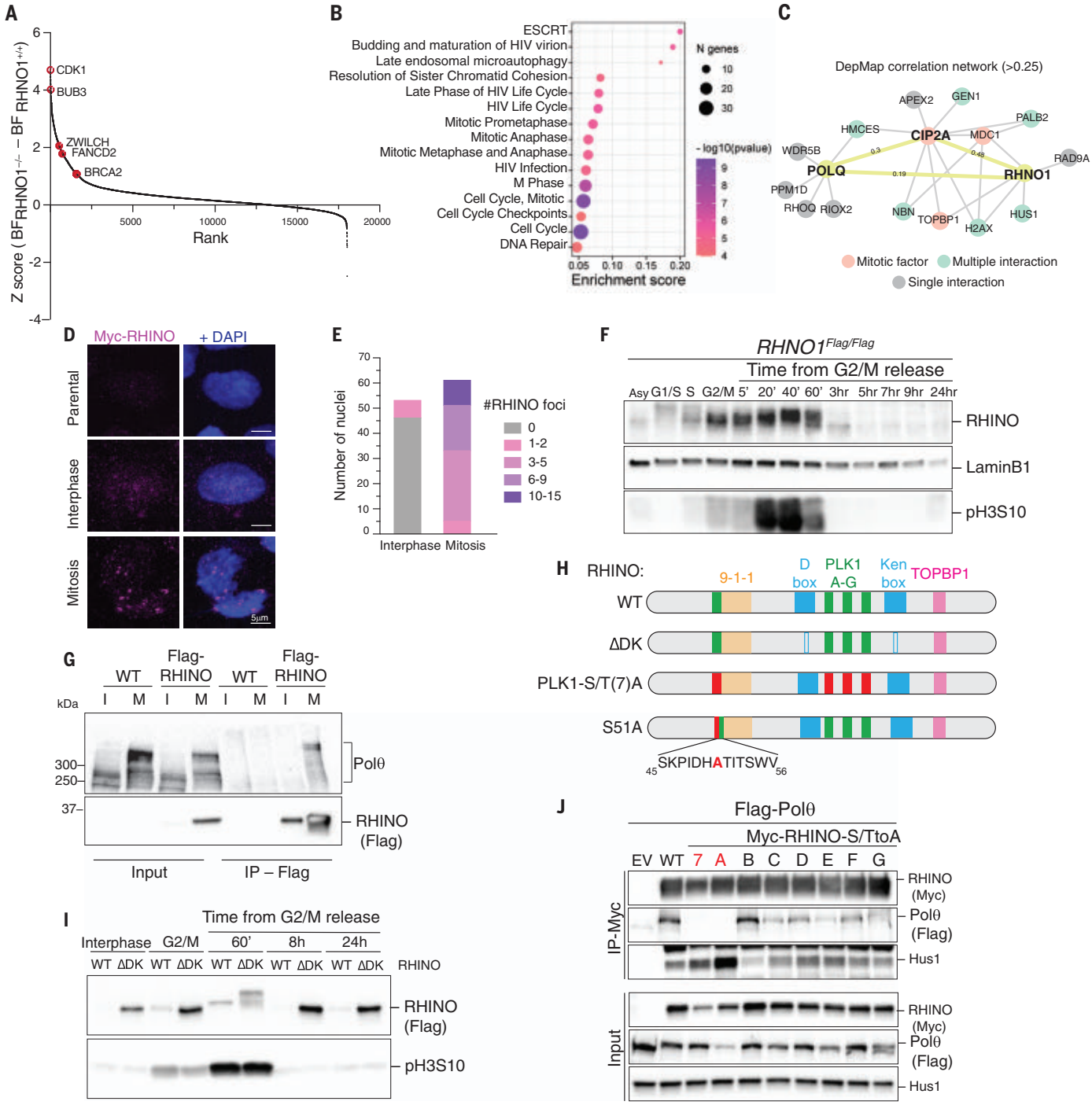

Fig. 3. RHINO is predominantly expressed in mitosis. (**A**) Results from the CRISPR-Cas9 dropout screen in *RHNO1*$^{-/-}$ and isogenic *RHNO1*$^{+/+}$ cells. Ranked *z*-scores of the difference in BF scores. (**B**) Reactome pathway overrepresentation analysis of synthetic lethal genes with *RHNO1*$^{-/-}$. The fold enrichment of each pathway is plotted on the *x* axis. The number of genes associated with each pathway is indicated by the size of the circle, and the color shade indicates the *p* value. (**C**) Network analysis for *POLQ* and *RHNO1* based on Pearson's correlation of dependency scores derived from DepMap. (**D**) Representative immunofluorescence images of RHINO in interphase and mitotic cells. (**E**) Quantification of RHINO foci from (D). (**F**) Western blot analysis of endogenous RHINO at different stages of the cell cycle. Extracts from *RHNO1*$^{Flag/Flag}$ cells at the indicated time points. pH3S10 antibody was used as a mitotic marker, and Lamin B1 was used as a loading control. (**G**) Control cells and cells expressing RHINO-MYC-Flag were synchronized in mitosis and subjected to anti-Flag immunoprecipitation followed by Western blot for endogenous Polθ. I, interphase; M, mitosis. (**H**) Schematic of RHINO protein highlighting the binding domains for 9-1-1 and TOPBP1, D and Ken boxes (ΔDK), and the PLK1 phosphorylation sites [PLK1(S/T)7A and S51A]. RHINO PLK1(S/T)A harbors alanine mutations in all seven predicted PLK1 sites. RHINO S51A harbors a single mutation of serine-51 (conserved among primates and rodents) to alanine. (**I**) Western blot analysis of RHINO and RHINOΔDK during the cell cycle. (**J**) Co-IP experiments in HEK293T cells cotransfected with plasmids expressing FLAG-Polθ and RHINO-MYC mutants. RHINO mutants with a single serine or threonine mutation to alanine are labeled A through G. EV, empty vector.

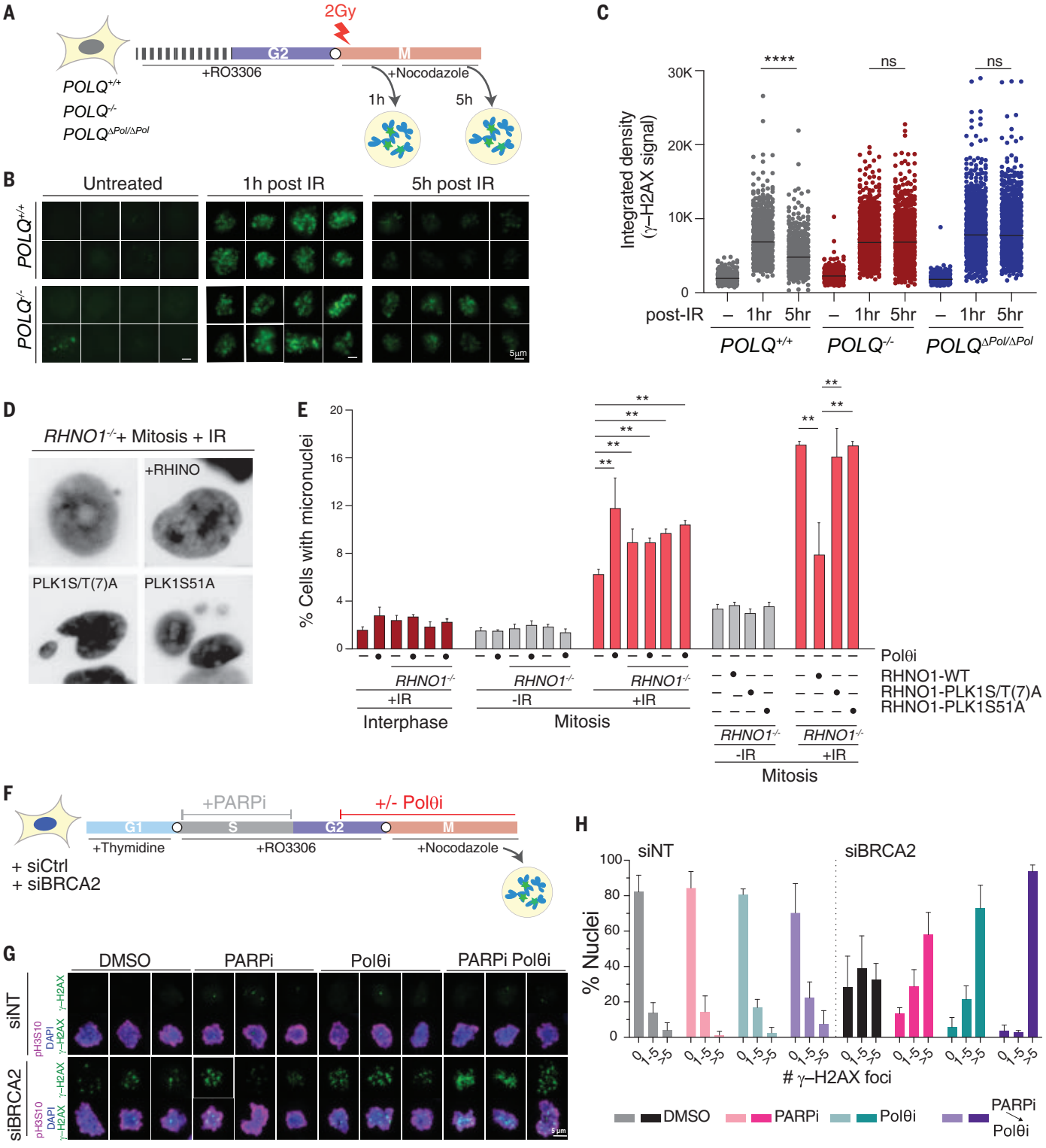

Fig. 4. MMEJ is the predominant DSB repair pathway during mitosis. (**A**) Schematic of the experimental design to detect MMEJ in mitosis that was used to obtain the results shown in (B) and (C). (**B**) Representative images of γ-H2AX in cells treated as described in (A). (**C**) Quantification of γ-H2AX intensity in mitotic cells with the indicated genotype. Black horizontal lines indicate means (n > 450 cells; paired t test; ****p < 0.0001; ns, not significant). (**D**) Representative images of micronuclei in cells with the indicated treatment and genotype. (**E**) Quantification of micronuclei formation after irradiation during interphase and mitosis as shown in (D). Bars represent the mean ± SD of three independent experiments (n > 250 cells; paired t test; **p < 0.01). (**F**) Schematic of the experimental pipeline for (G) and (H). (**G**) Representative immunofluorescence images of mitotic cells treated as described in (F) and stained with anti–γ-H2AX. pH3S10 is used to mark mitotic chromosomes. DNA is stained with DAPI. DMSO, dimethyl sulfoxide. (**H**) Quantification of γ-H2AX foci in mitotic cells with the indicated treatment. Bars represent the mean ± SD of three independent experiments (n > 50 cells).

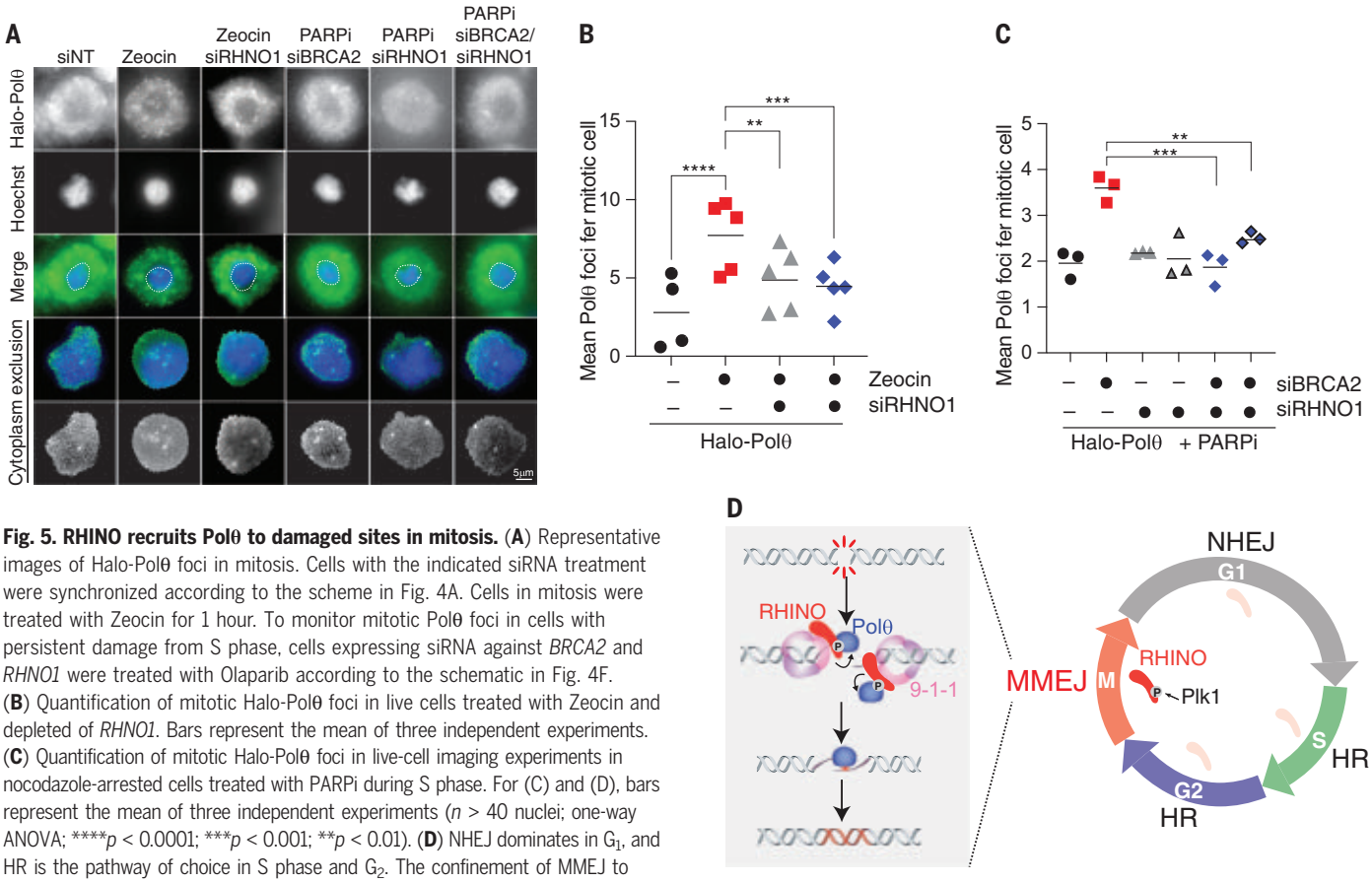

Fig. 5. RHINO recruits Polθ to damaged sites in mitosis. (**A**) Representative images of Halo-Polθ foci in mitosis. Cells with the indicated siRNA treatment were synchronized according to the scheme in Fig. 4A. Cells in mitosis were treated with Zeocin for 1 hour. To monitor mitotic Polθ foci in cells with persistent damage from S phase, cells expressing siRNA against *BRCA2* and *RHNO1* were treated with Olaparib according to the schematic in Fig. 4F. (**B**) Quantification of mitotic Halo-Polθ foci in live cells treated with Zeocin and depleted of *RHNO1*. Bars represent the mean of three independent experiments. (**C**) Quantification of mitotic Halo-Polθ foci in live-cell imaging experiments in nocodazole-arrested cells treated with PARPi during S phase. For (C) and (D), bars represent the mean of three independent experiments ($n > 40$ nuclei; one-way ANOVA; ****$p < 0.0001$; ***$p < 0.001$; **$p < 0.01$). (**D**) NHEJ dominates in G_1, and HR is the pathway of choice in S phase and G_2. The confinement of MMEJ to mitosis occurs because of the accumulation of RHINO during M phase, PLK1 phosphorylation, and the recruitment of Polθ to DNA breaks.

interphase, it only interacted with Polθ in mitosis (fig. S6H). Based on this observation, we explored whether the interaction between RHINO and Polθ could be stimulated by phosphorylation. We found that inhibiting the major mitotic kinase CDK1, and to a lesser extent Polo family kinase PLK1, hindered RHINO phosphorylation (fig. S6, I to K). RHINO contains seven Ser-Pro and/or Thr-Pro motifs that are susceptible to CDK1 targeting and seven Ser and/or Thr residues embedded within the consensus motif of PLK1. Using Phospho-Tag gels, we determined that RHINO phosphorylation was altered in the context of RHINO-PLK1S/T(7)A and abrogated in the RHINO-CDK1S/T(7)A allele (fig. S6, J and K). These findings are consistent with CDK1 phosphorylation being a priming event for subsequent PLK1 phosphorylation of RHINO. Such sequential modification is commonly observed in PLK1 targets, including BUB1, BUBR1, and CLASP2 (*50*–*52*). Notably, co-IP analysis showed that RHINO-PLK1S/T(7)A failed to bind Polθ (Fig. 3J and fig. S6L). Furthermore, by individually mutating seven PLK1 sites, we identified a single phosphorylation residue on RHINO (S51) that, when mutated to alanine, exhibited a reduced interaction with Polθ (Fig. 3J and fig. S6L).

MMEJ is a dominant DSB repair pathway in mitosis

Unresolved damage during S phase and G_2 of the cell cycle can be carried over to mitosis. However, it is well established that NHEJ and HR are repressed during M phase (*53*, *54*). Recently, a tethering complex comprising MDC1-CIP2A-TOPBP1 was reported to hold broken mitotic DNA ends together until cells progress into the next G_1 (*33*, *47*, *48*). Multiple studies implicated Polθ activity in repairing DNA damage in mitosis (*27*–*30*). An investigation using *Xenopus* egg extract showed that entry into mitosis before the completion of DNA replication leads to complex rearrangements driven by Polθ (*29*). In addition, Polθ was linked to the formation of sister chromatid exchanges (SCEs) as under-replicated DNA is transferred into mitosis (*30*). Last, it was shown that MMEJ activity is delayed until mitosis in cells that lack BRCA2, where Rad52 blocked Polθ activity in G_2 (*27*). We conducted individual and combined depletion of RHINO and CIP2A in *BRCA2*$^{-/-}$ cells and observed an additive effect on growth, suggesting that RHINO-mediated MMEJ is independent of mitotic tethering of DNA breaks (fig. S7, A and B). Consistent with the involvement of Polθ in mitotic repair, *POLQ*$^{-/-}$ cells were more sensitive to DNA damage when treated with ionizing radiation in mitosis relative to interphase (fig. S7, C and D).

Given the critical function of RHINO in MMEJ, its enrichment in mitosis, and its interaction with Polθ, we hypothesized that RHINO could promote mitotic MMEJ by facilitating Polθ recruitment to condensed chromosomes. To assay MMEJ activity in mitosis, we synchronized *POLQ*$^{-/-}$ and *POLQ*$^{+/+}$ cells at the G_2-M boundary using a CDK1 inhibitor. We then released cells into M phase in the presence of nocodazole, which prevented mitotic exit. We irradiated cells 30 min after release from CDK1 inhibition and monitored the dissolution of phosphorylated γ-H2AX (Fig. 4A). Wild-type cells accumulated maximal γ-H2AX 1 hour after irradiation, which significantly decreased after 5 hours (Fig. 4, B and C, and fig. S7E). As a control, we showed a similar resolution of γ-H2AX foci in *LIG4*$^{-/-}$ cells relative to wild-type cells, confirming the lack of NHEJ activity in mitosis (fig. S7F). By contrast, *POLQ*$^{-/-}$ cells and ones carrying inactivating mutations in the polymerase domain of Polθ (*POLQ*$^{\Delta Pol/\Delta Pol}$) failed to resolve γ-H2AX foci (Fig. 4, B and C, and fig. S7F). Furthermore, treatment of cells with Polθ inhibitor (Polθi-RP6685) (*31*) during mitosis, but not interphase, led to the persistence of γ-H2AX foci after

irradiation (fig. S7, G and H). Similarly, the absence of RHINO prevented the resolution of γ-H2AX after radiation treatment (fig. S7I). Last, we corroborated the essentiality of MMEJ activity in mitotic DSB repair by using the inducible restriction enzyme AsiSI (*55*) and observed a defect in γ-H2AX resolution in cells treated with Polθ inhibitor (fig. S7, J to L).

Unrepaired mitotic DSBs are especially toxic because they can result in lagging chromosome fragments that accumulate in micronuclei and trigger chromothripsis (*56*). We tested whether MMEJ activity prevents micronuclei formation after irradiation of cells in mitosis. Polθ inhibition and RHINO deletion significantly increased micronuclei formation (Fig. 4, D and E). Blocking Polθ in *RHNO1*$^{-/-}$ cells had no additive effect on the accumulation of micronuclei, suggesting that the two factors are epistatic (Fig. 4E). Furthermore, we expressed RHINO-WT, RHINO-PLK1-S/T(7)A, and RHINO-S51A alleles in *RHNO1*$^{-/-}$ cells and found that both mutants failed to rescue micronuclei formation after mitotic irradiation (Fig. 4, D and E). Similarly, *RHNO*$^{-/-}$ cells and ones complemented with the RHINO-S51A allele failed to resolve mitotic γ-H2AX accumulation (fig. S7I). In conclusion, our findings implicate the RHINO-Polθ interaction in stimulating MMEJ during mitosis.

Mitotic MMEJ resolves DNA breaks that originate in S phase in BRCA2 *mutant cells*

We next tested whether the activity of RHINO and Polθ in mitosis was necessary to repair DNA lesions that arise in S phase and G_2 but persist into M phase (Fig. 4F). We used small interfering RNA (siRNA) against *BRCA2* (fig. S8A) to block repair by HR and induced DNA damage in S phase by incubating cells with PARPi (Olaparib) (*57*). As cells progressed beyond S phase, we withdrew PARPi from the culture medium. Toward the end of G_2, we added Polθi, which was continuously present as cells entered mitosis. To prevent mitotic exit, cells were treated with nocodazole before fixing them for subsequent analysis for γ-H2AX (Fig. 4, F to H, and fig. S8B). We observed a baseline increase in γ-H2AX foci in mitotic cells treated with si*BRCA2* compared with those treated with control siRNA. As expected, the levels of γ-H2AX were more elevated in cells treated with either Olaparib in S phase or Polθ inhibitor in G_2 and M phase. Cells treated with PARP inhibitor in S phase and Polθ inhibitor in G_2-M displayed a synergistic increase in γ-H2AX accumulation (Fig. 4, F to H). Furthermore, this synergy was observed when the polymerase was inhibited in mitosis but not during S phase (fig. S8, C to E). To further substantiate the role of mitotic MMEJ in repairing unresolved S phase damage, we treated *RHNO1*$^{-/-}$ cells with siRNA against *BRCA2* and observed a similar synergistic effect with PARPi treatment (fig. S8F).

RHINO recruits Polθ to DSB sites in mitosis

Having established a role for MMEJ in repairing breaks in mitosis, we next investigated whether RHINO recruits Polθ to damage sites to facilitate mitotic repair. We used a two-step CRISPR-Cas9 targeting strategy to establish cells where *POLQ* was endogenously tagged with Halo at the N terminus (fig. S9, A to C). We treated *POLQ*$^{Halo/Halo}$ cells with a Halo-tag ligand (JFX650) and traced Polθ single particles using live-cell imaging in interphase and mitosis (fig. S9D and movies S1 and S2). To test whether RHINO acts upstream of Polθ, we arrested *POLQ*$^{Halo/Halo}$ cells treated with si*RHNO1* at the G_2-M boundary by CDK1 inhibition and released them into mitosis. Treatment of mitotic cells with Zeocin resulted in large and static Polθ foci. Polθ foci were significantly reduced upon *RHNO1* depletion but not affected by MDC1 loss and ATR inhibition (Fig. 5, A and B, and figs. S9, E to I, and S10, A to E). Last, we investigated the static Polθ foci in the context of unresolved S phase damage that persisted into mitosis. We treated *BRCA2*-depleted *POLQ*$^{Halo/Halo}$ cells with PARPi in S phase and showed that Polθ dynamics and colocalization with replication protein A (RPA) were largely unchanged when monitored in S phase (fig. S11A). However, this same treatment led to the accumulation of static Polθ foci in mitosis (Fig. 5, A to C, and figs. S9E and S11, B and C). These findings provide further evidence for the role of RHINO in recruiting Polθ to break sites during mitosis.

Discussion

NHEJ predominates in G_1, whereas HR is preferred for repairing DSBs in S phase and G_2 (*58*–*60*). In this work, we demonstrate that in mitosis, where both HR and NHEJ are repressed (*53*, *54*), MMEJ is the sole DSB repair pathway. MMEJ activity in M phase is driven by the accumulation of RHINO to promote Polθ recruitment to damage sites (Fig. 5D). The decoupling of DNA repair pathways during different stages of the cell cycle has implications for maintaining genome stability. Mitotic MMEJ may have evolved as a fail-safe mechanism that operates on highly condensed chromosomes and ensures that cells do not commit to cellular division with unrepaired lesions that trigger genome instability. Conversely, suppression of MMEJ in G_1 and S-G_2 could protect genomes from the intrinsic mutagenic potential of this pathway.

RHINO was previously identified as a 9-1-1–interacting protein that is required for activating ATR signaling (*41*, *42*) but now emerges as a critical factor that promotes MMEJ during mitosis. We show that RHINO, but not 9-1-1 complex members, is greatly stabilized in mitosis and degraded by the APC/C complex upon mitotic exit (Fig. 3, H and I). Based on our data, we propose that PLK1-dependent phosphorylation of RHINO facilitates its interaction with Polθ to stimulate MMEJ. A recent study has also identified PLK1 phosphorylation sites on Polθ that are critical for mitotic MMEJ (*61*). Furthermore, it has been established that the CDK1-PLK1 signaling axis attenuates NHEJ and HR by phosphorylating and inhibiting 53BP1 and BRCA2, respectively (*62*–*64*). These studies highlight the multifaceted role of PLK1 in controlling repair pathway choice in mitosis.

RHINO is highly unstructured and interacts with RAD1 and TOPBP1 through distinct domains (*41*, *42*). Unrepaired S phase damage may be marked by 9-1-1 through mitosis, where RHINO accumulates. Tethering RHINO to the 9-1-1 complex in M phase would subsequently lead to Polθ recruitment to break sites, thereby enabling MMEJ. RHINO-TOPBP1 interaction in mitosis could stabilize RHINO at break sites and form a complex that recruits Polθ. Further structural studies could provide a deeper insight into 9-1-1–RHINO–Polθ–TOPBP1 complex formation and probe the impact of PLK1 phosphorylation.

Our study does not rule out a role for Polθ in filling ssDNA gaps after replication, nor do we exclude the possibility of RHINO-independent MMEJ activity during S phase (*65*–*68*). However, our findings provide evidence suggesting that robust MMEJ activity in mitosis accounts for the synthetic lethal interaction between Polθ and BRCA2. Uncoupling DNA repair activities during different cell cycle stages provides a rationale for the reported synergy of Polθ inhibitors with PARPi and potentially other antineoplastic therapies that induce DNA damage during S phase (*4*, *6*).

REFERENCES AND NOTES

1. P. A. Mateos-Gomez *et al.*, *Nature* **518**, 254–257 (2015).
2. R. Ceccaldi *et al.*, *Nature* **518**, 258–262 (2015).
3. D. W. Wyatt *et al.*, *Mol. Cell* **63**, 662–673 (2016).
4. D. Zatreanu *et al.*, *Nat. Commun.* **12**, 3636 (2021).
5. A. Schrempf, J. Slyskova, J. I. Loizou, *Trends Cancer* **7**, 98–111 (2021).
6. J. Zhou *et al.*, *Nat. Cancer* **2**, 598–610 (2021).
7. A. Sfeir, L. S. Symington, *Trends Biochem. Sci.* **40**, 701–714 (2015).
8. S. J. Black *et al.*, *Nat. Commun.* **10**, 4423 (2019).
9. P. A. Mateos-Gomez *et al.*, *Nat. Struct. Mol. Biol.* **24**, 1116–1123 (2017).
10. D. A. Ramsden, J. Carvajal-Garcia, G. P. Gupta, *Nat. Rev. Mol. Cell Biol.* **23**, 125–140 (2022).
11. L. N. Truong *et al.*, *Proc. Natl. Acad. Sci. U.S.A.* **110**, 7720–7725 (2013).
12. A. Xie, A. Kwok, R. Scully, *Nat. Struct. Mol. Biol.* **16**, 814–818 (2009).
13. M. Lee-Theilen, A. J. Matthews, D. Kelly, S. Zheng, J. Chaudhuri, *Nat. Struct. Mol. Biol.* **18**, 75–79 (2011).
14. H. Fleury *et al.*, *Mol. Cell* **83**, 1429–1445.e8 (2023).
15. S. Sharma *et al.*, *Cell Death Dis.* **6**, e1697 (2015).
16. K. E. Mengwasser *et al.*, *Mol. Cell* **73**, 885–899.e6 (2019).
17. S. H. Chan, A. M. Yu, M. McVey, *PLOS Genet.* **6**, e1001005 (2010).
18. M. E. Arana, M. Seki, R. D. Wood, I. B. Rogozin, T. A. Kunkel, *Nucleic Acids Res.* **36**, 3847–3856 (2008).
19. T. Kent, P. A. Mateos-Gomez, A. Sfeir, R. T. Pomerantz, *eLife* **5**, e13740 (2016).
20. M. Audebert, B. Salles, P. Calsou, *J. Biol. Chem.* **279**, 55117–55126 (2004).

21. M. Seki, F. Marini, R. D. Wood, *Nucleic Acids Res.* **31**, 6117–6126 (2003).
22. S. J. Boulton, S. P. Jackson, *EMBO J.* **15**, 5093–5103 (1996).
23. S. B. Thyme, A. F. Schier, *Cell Rep.* **15**, 1611–1613 (2016).
24. J. Schimmel, H. Kool, R. van Schendel, M. Tijsterman, *EMBO J.* **36**, 3634–3649 (2017).
25. S. Saito, R. Maeda, N. Adachi, *Nat. Commun.* **8**, 16112 (2017).
26. B. Corneo *et al.*, *Nature* **449**, 483–486 (2007).
27. M. Llorens-Agost *et al.*, *Nat. Cell Biol.* **23**, 1095–1104 (2021).
28. H. Wang *et al.*, *Nucleic Acids Res.* **46**, 10724–10739 (2018).
29. L. Deng *et al.*, *Mol. Cell* **73**, 915–929.e6 (2019).
30. A. M. Heijink *et al.*, *Nat. Commun.* **13**, 6722 (2022).
31. M. Bubenik *et al.*, *J. Med. Chem.* **65**, 13198–13215 (2022).
32. M. Zimmermann *et al.*, *Nature* **559**, 285–289 (2018).
33. S. Adam *et al.*, *Nat. Cancer* **2**, 1357–1371 (2021).
34. P. Verma *et al.*, *Nat. Cell Biol.* **23**, 160–171 (2021).
35. V. Shukla *et al.*, *Mol. Cell* **77**, 1154 (2020).
36. A. Álvarez-Quilón *et al.*, *Mol. Cell* **78**, 1152–1165.e8 (2020).
37. A. Sfeir, T. de Lange, *Science* **336**, 593–597 (2012).
38. J. A. Melo, J. Cohen, D. P. Toczyski, *Genes Dev.* **15**, 2809–2821 (2001).
39. M. T. Certo *et al.*, *Nat. Methods* **8**, 671–676 (2011).
40. J. A. Hussmann *et al.*, *Cell* **184**, 5653–5669.e25 (2021).
41. C. Cotta-Ramusino *et al.*, *Science* **332**, 1313–1317 (2011).
42. L. A. Lindsey-Boltz, M. G. Kemp, C. Capp, A. Sancar, *Cell Cycle* **14**, 99–108 (2015).
43. T. E. Bass *et al.*, *Nat. Cell Biol.* **18**, 1185–1195 (2016).
44. D. A. Mordes, G. G. Glick, R. Zhao, D. Cortez, *Genes Dev.* **22**, 1478–1489 (2008).
45. C. S. Eichinger, S. Jentsch, *Trends Biochem. Sci.* **36**, 563–568 (2011).
46. Broad Institute, DepMap Portal (2021); https://depmap.org/portal/.
47. P. A. Leimbacher *et al.*, *Mol. Cell* **74**, 571–583.e8 (2019).
48. M. De Marco Zompit *et al.*, *Nat. Commun.* **13**, 4143 (2022).
49. M. Sullivan, D. O. Morgan, *Nat. Rev. Mol. Cell Biol.* **8**, 894–903 (2007).
50. P. Singh *et al.*, *Mol. Cell* **81**, 67–87.e9 (2021).
51. A. E. Elia *et al.*, *Cell* **115**, 83–95 (2003).
52. A. R. Maia *et al.*, *J. Cell Biol.* **199**, 285–301 (2012).
53. A. N. Blackford, M. Stucki, *Trends Biochem. Sci.* **45**, 321–331 (2020).
54. R. E. Zirkle, W. Bloom, *Science* **117**, 487–493 (1953).
55. J. S. Iacovoni *et al.*, *EMBO J.* **29**, 1446–1457 (2010).
56. C. Z. Zhang *et al.*, *Nature* **522**, 179–184 (2015).
57. J. Murai *et al.*, *Cancer Res.* **72**, 5588–5599 (2012).
58. A. Beucher *et al.*, *EMBO J.* **28**, 3413–3427 (2009).
59. K. Karanam, R. Kafri, A. Loewer, G. Lahav, *Mol. Cell* **47**, 320–329 (2012).
60. K. Nakamura *et al.*, *Nat. Cell Biol.* **21**, 311–318 (2019).
61. C. Gelot *et al.*, bioRxiv 2023.03.17.533134 [Preprint] (2023); https://doi.org/10.1101/2023.03.17.533134
62. F. Esashi *et al.*, *Nature* **434**, 598–604 (2005).
63. D. H. Lee *et al.*, *Mol. Cell* **54**, 512–525 (2014).
64. A. Orthwein *et al.*, *Science* **344**, 189–193 (2014).
65. S. F. Roerink, R. van Schendel, M. Tijsterman, *Genome Res.* **24**, 954–962 (2014).
66. O. Belan *et al.*, *Mol. Cell* **82**, 4664–4680.e9 (2022).
67. A. Schrempf *et al.*, *Cell Rep.* **41**, 111716 (2022).
68. A. Mann *et al.*, *Mol. Cell* **82**, 4218–4231.e8 (2022).

ACKNOWLEDGMENTS

We thank D. Durocher, R. Weiss, and R. Greenberg for providing critical reagents for this study. We thank D. Remus for providing 9-1-1 proteins and assisting with in vitro assays. S. Morris and M.-C. Mathieu from Repare Therapeutics generously provided reagents. We thank E. Lazzerini-Denchi and members of the Sfeir lab for commenting on the manuscript. We thank S. Deng, T. Lieber, Y. Fu, M. Selvaraj, and H. Shah for their experimental assistance. **Funding:** This work was supported by the following grants: National Institutes of Health (NIH) grant R01CA229161 (A.S.), NIH grant DP2CA195767-01 (A.S.), a Pershing Square-Sohn Cancer Foundation grant (A.S.), a V-foundation grant (A.S.), a New York Stem Cell Foundation training grant (A.B.), NIH grant F32GM139292 (J.H.), and NIH grant DP2GM142307 (J.C.S.).
Author contributions: Conceptualization: A.B., A.S.; Methodology: A.B., O.S., S.P., J.H., M.K., A.S.; Investigation: A.B., O.S., S.P., J.H., M.K., A.S.; Funding acquisition: J.C.S., A.S.; Project administration: A.S.; Supervision: A.S.; Writing – original draft: A.B., A.S.; Writing – review and editing: A.B., O.S., S.P., J.H., M.K., J.C.S., A.S. **Competing interests:** A.S. is a cofounder, consultant, and shareholder of Repare Therapeutics. All other authors have no competing interests. **Data and materials availability:** All data are available in the main text and supplementary materials. All material will be shared upon request.

License information: Copyright © 2023 the authors, some rights reserved; exclusive licensee American Association for the Advancement of Science. No claim to original US government works. https://www.science.org/about/science-licenses-journal-article-reuse

SUPPLEMENTARY MATERIALS

science.org/doi/10.1126/science.adh3694
Materials and Methods
Figs. S1 to S11
Tables S1 and S2
References (*69*–*75*)
MDAR Reproducibility Checklist
Movies S1 and S2

Submitted 27 February 2023; accepted 30 June 2023
10.1126/science.adh3694

PLASTIC UPCYCLING

Hydroformylation of pyrolysis oils to aldehydes and alcohols from polyolefin waste

Houqian Li[1], Jiayang Wu[1], Zhen Jiang[1], Jiaze Ma[1], Victor M. Zavala[1,2], Clark R. Landis[3], Manos Mavrikakis[1], George W. Huber[1]*

Waste plastics are an abundant feedstock for the production of renewable chemicals. Pyrolysis of waste plastics produces pyrolysis oils with high concentrations of olefins (>50 weight %). The traditional petrochemical industry uses several energy-intensive steps to produce olefins from fossil feedstocks such as naphtha, natural gas, and crude oil. In this work, we demonstrate that pyrolysis oil can be used to produce aldehydes through hydroformylation, taking advantage of the olefin functionality. These aldehydes can then be reduced to mono- and dialcohols, oxidized to mono- and dicarboxylic acids, or aminated to mono- and diamines by using homogeneous and heterogeneous catalysis. This route produces high-value oxygenated chemicals from low-value postconsumer recycled polyethylene. We project that the chemicals produced by this route could lower greenhouse gas emissions ~60% compared with their production through petroleum feedstocks.

Olefins are a central building block of modern chemicals and polymers (*1*). Polyolefins, polyesters, surfactants, alcohols, amines, and carboxylic acids all are manufactured from olefins (*2*). Natural petroleum products, such as crude oil, natural gas, and naphtha, have low concentrations (*3* wt %) of olefins (Fig. 1). A variety of energy-intensive chemical steps, such as steam cracking, are used to produce olefins from petroleum. More sustainable means for olefin production and use are desirable, for example, recovering olefins from waste plastics followed by upgrading the olefins. Here, we demonstrate how waste plastics can be converted into olefins by thermal depolymerization reactions such as pyrolysis. These olefins can then undergo hydroformylation and further hydrogenation to produce mono- and dialcohols. Specifically, we showcase a route to produce functional chemicals from postconsumer recycled (PCR) waste plastics collected from an operational material recovery facility using a combination of thermal depolymerization to produce an olefin-rich pyrolysis oil; homogeneous hydroformylation catalysis to transform a complex mixture of mono-olefins and diolefins in the pyrolysis oil into aldehydes; and heterogeneous catalysis to reduce, oxidize, or aminate the aldehydes. We also demonstrate a separation scheme to produce high-purity diolefins and mono-olefins that would be acceptable for polymer-grade applications.

Pyrolysis of polyolefins produces high concentrations (~50 wt %) of olefins (Fig. 1). Four different plastics were pyrolyzed in a fluidized bed reactor at a temperature of 500°C and a residence time of 20 s, which included PCR high-density polyethylene (HDPE), virgin HDPE, virgin polypropylene (PP), and virgin low-density polyethylene (LDPE), and generated pyrolysis oil with varied compositions (fig. S2A). The liquid product yields (pyrolysis oil) were >60 wt % for all of these plastics, with the remainder of the products being gas and char (details in table S1). For simplicity in our analytical work, the pyrolysis oil was distilled to light and heavy cut (details in supplementary materials). More than a thousand compounds (>1000 blobs in gas chromatogram) were identified in the whole pyrolysis oils depicted in Fig. 2A and fig. S5A. The zoomed-in chromatogram region in this figure shows a more detailed distribution of product classes. The light cut was analyzed by detailed hydrocarbon analysis, the heavy cut was analyzed by nitric oxide ionization spectroscopy evaluation, and both cuts were analyzed by gas chromatography measurements (details in

[1]Department of Chemical and Biological Engineering, University of Wisconsin–Madison, Madison, WI 53706, USA. [2]Mathematics and Computer Science Division, Argonne National Laboratory, Lemont, IL 60439, USA. [3]Department of Chemistry, University of Wisconsin–Madison, Madison, WI 53706, USA.
***Corresponding author. Email: gwhuber@wisc.edu**

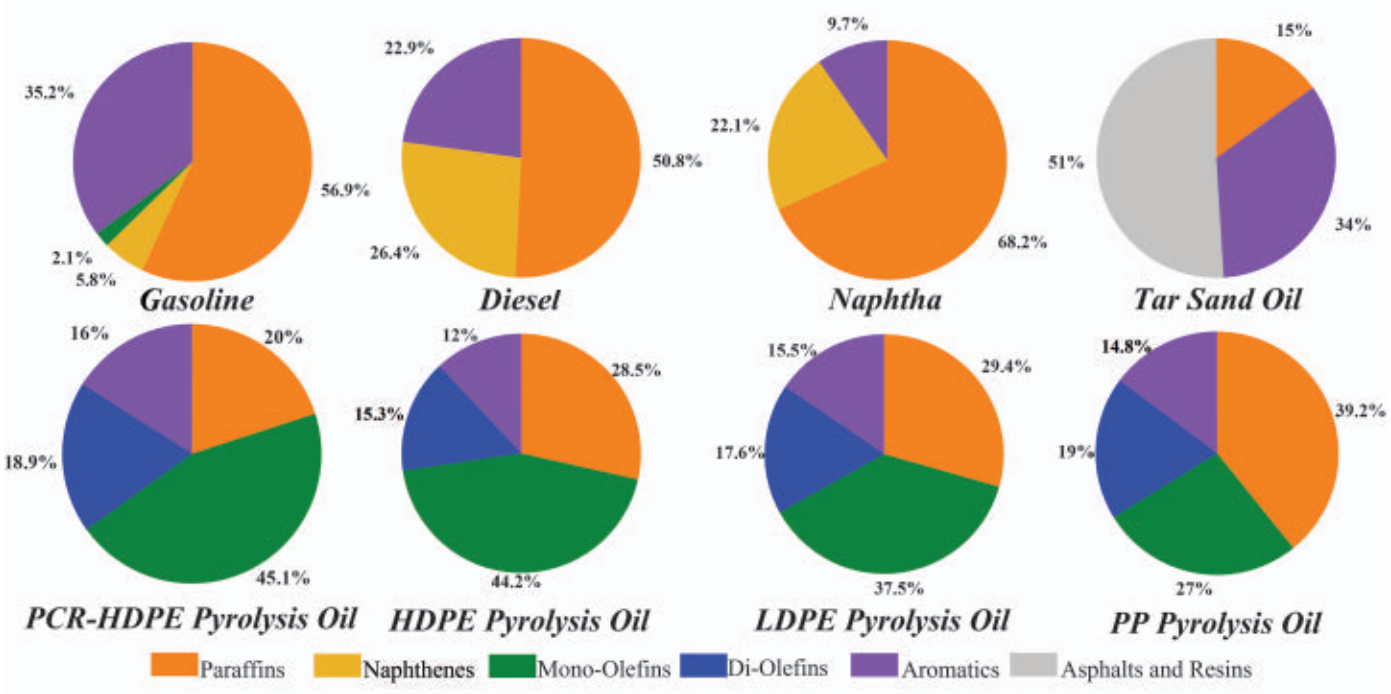

Fig. 1. Chemical composition of petroleum products and plastic oils derived from pyrolysis of PCR HDPE, HDPE, LDPE, and PP conducted in this work. Compositions of gasoline, diesel, naphtha, and tar sand oil are obtained elsewhere (*48*, *49*). See supplementary materials for detailed pyrolysis experiments.

supplementary materials), which confirmed that the pyrolysis oil is composed of mono-olefins (34 to 50 wt %), paraffins (20 to 39 wt %), monoaromatics (11 to 23 wt %), diolefins (6 to 13 wt %), and dicycloaromatics (<5 wt %) that ranged from C5 to C40 (fig. S3). These results agree with the literature reported values with 40 to 70 wt % of mono-olefins, 8 to 40 wt % paraffins, 4 to 13 wt % of monoaromatics, and 5 to 20 wt % of diolefins (*3*–*6*). The structure of these products changes depending on the type of polyolefin that is used. For example, HDPE products are highly linear, whereas LDPE products are more branched. Thermal depolymerization, by pyrolysis or liquefaction, of waste plastics is currently receiving tremendous industrial interest with >10 companies having made recent announcements on building commercial facilities (*7*–*11*). For example, Dow Inc. recently announced the construction of the world's largest plastic depolymerization plant [120 kilo–metric tons (kton)/year] in Europe (*12*). These companies primarily use pyrolysis oils as feedstocks to replace naphtha in petroleum refineries or steam cracking (*13*). These approaches typically require hydrotreating of the pyrolysis oil and do not take advantage of the olefin functionality. It has been estimated that the overall yield of polyolefins from this route is <30 wt % of the virgin plastic (*10*, *13*).

Hydroformylation of pyrolysis oil followed by hydrogenation

A commercial $Co_2(CO)_8$ catalyst was modified with or without phosphine ligands [2-bis (diphenylphosphino) ethane monoxide and tri-*n*-butylphosphine] for the hydroformylation of hexenes and hexadienes to establish appropriate reaction conditions. Low aldehyde yields (<40%) were obtained when ligands were used (table S2). Near-complete conversion of hexene was obtained with unmodified $Co_2(CO)_8$, which is consistent with Zhang and co-workers' recent report (*14*). Hydroformylation of 1-hexene, *cis*-2-hexene, and 1,5-hexadiene produced the respective aldehydes in near-quantitative yields under these same conditions, as shown in table S2. A high heptanal selectivity (>80%) was observed for the hydroformylation of both 1-hexene and *cis*-2-hexene (fig. S4), which suggests that the internal olefins can also be converted into terminal aldehydes under this reaction condition. As shown in Fig. 2B, hydroformylation of pyrolysis oils under the same reaction condition produced up to 60 wt % yield of the aldehydes from the pyrolysis oil without a solvent (Fig. 3). Recent studies have demonstrated that heterogeneous catalysts can also be used for hydroformylation (*15*–*18*). Hydroformylation of the light cut (table S3) of the pyrolysis oil was performed separately from that of the heavy cut (table S4), and the products were characterized by two-dimensional (2D) gas chromatography (GC × GC), 1D/2D nuclear magnetic resonance (NMR), and CHN(O)S elemental analysis.

The formation of aldehydes from pyrolysis oil (light cut) was evidenced by the appearance of features in the region characteristic of alcohols and aldehydes in GC × GC chromatogram as exhibited in the inset of Fig. 2B. Compared with Fig. 2A, changes in the positions of the features in the second dimension (^{2}D) retention time are observed in Fig. 2B, which indicates that the hydroformylation changed the polarity of the pyrolysis oil. Minor changes in the positions of the features in first dimension (^{1}D) retention time suggest that the carbon number changed slightly after the hydroformylation process. More than 90% of the olefins in the pyrolysis oil were converted into aldehydes, as can be calculated by subtracting the volume of the features in Fig. 2A from that in Fig. 2B (table S2; see supplementary materials). A similar performance was observed in the hydroformylation of the pyrolysis oil heavy cut (table S2 and fig. S5). The formation of aldehydes was further supported by ^{13}C-NMR analysis as depicted in Fig. 2E (full spectrum in fig. S6). Simultaneous decrease in peaks in the C=C region [105 to 150 parts per million (ppm)] and appearance of the peaks in the 200- to 210-ppm region indicates the formation of C=O groups after hydroformylation. The ^{1}H-^{13}C heteronuclear single quantum coherence (HSQC) spectrum of the upgraded oil after hydroformylation confirms the formation of the aldehydes (fig. S7). Peaks in the 55- to 70-ppm region of Fig. 2E indicate alcohol formation. The oxygen content in the hydroformylation products was further confirmed by CHN(O)S elemental analysis as 14 and 5 wt % oxygen in the light and heavy cut of the oil, respectively. Pyrolysis oils generated from waste plastics can contain a number of other elements in both organic and inorganic forms, including N, O, Cl, Fe, Si, K, Ca, S, Zn, Cu, Ti,

and Al (*10*). Catalytic hydroformylation is tolerant of several of these contaminants, which include carbonyls, ethers, alcohols, carboxamides, amines, silanes, siloxanes, halide salts, and iron impurities (*19*–*23*). Vinyl/allyl halides and conjugated diolefins (*24*) are expected to be catalyst poisons during hydroformylation and can be removed by pretreating waste plastics before pyrolysis or adjusting parameters in the plastic pyrolysis.

Catalytic hydrogenation of the hydroformylated pyrolysis oils by using varied metal catalysts, after removal of the Co catalyst (table S5), yields alcohols. The shifting of the GC × GC features to longer ^{1}D retention time (Fig. 2C) implies that the aldehydes in the "hydroformylated pyrolysis oil" light cut were converted to alcohols because the alcohols have

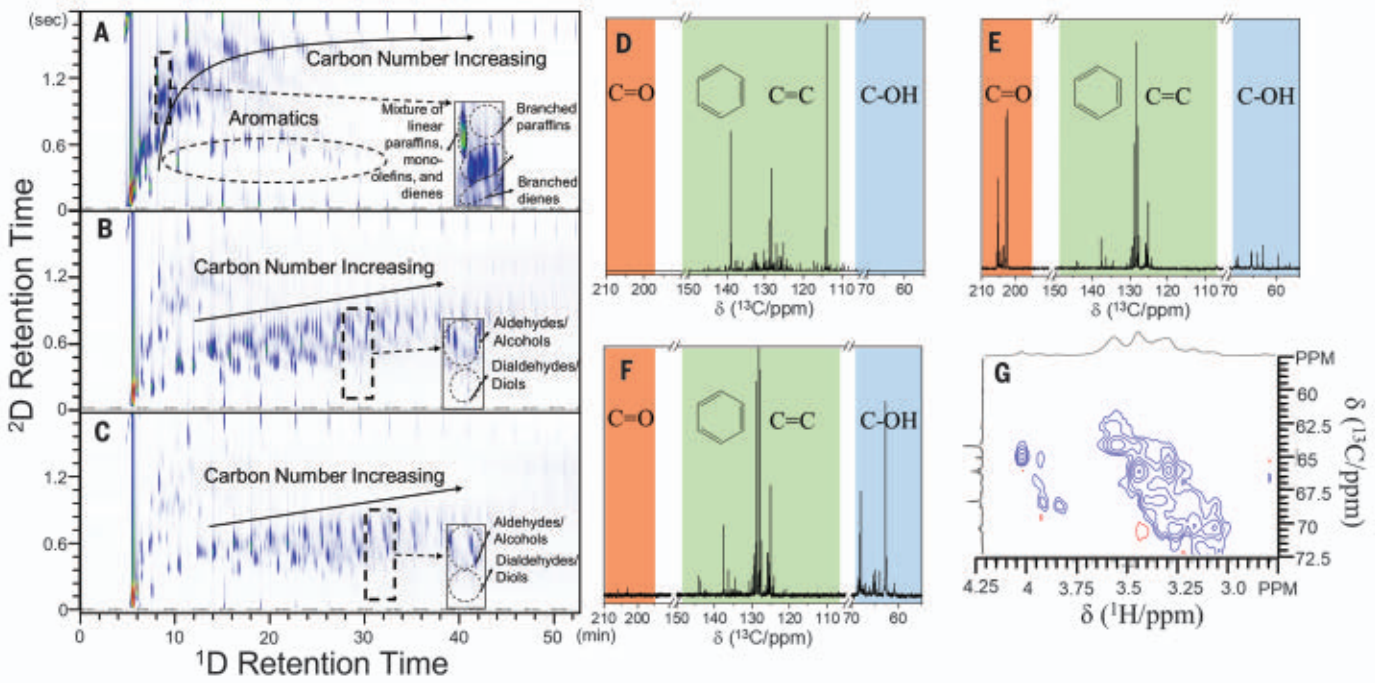

Fig. 2. Hydroformylation of pyrolysis oil (light cut) catalyzed by $Co_2(CO)_8$ and hydrogenation of the "hydroformylated oil" catalyzed by 20% Ni/SiO_2. (**A**) GC × GC analysis of HDPE pyrolysis oil light cut. (**B**) GC × GC analysis of the oil after hydroformylation catalyzed by $Co_2(CO)_8$ in a 350-ml stainless steel batch reactor for 3 hours. Conditions: 120°C, 70 bar synthesis gas (CO/H_2 = 1), 900 rpm, 10 wt % $Co_2(CO)_8$ in oil. (**C**) GC × GC analysis of the hydroformylated oil after hydrogenation catalyzed by 20%Ni/SiO_2 in a continuous flow reactor for 5 hours. Conditions: 100°C, 78 bar H_2, weight hourly space velocity 1 hour^{-1}. Insets in (A) to (C) represent magnified boxed region. The species concentration increases from blue to green. (**D**) ^{13}C NMR spectra of HDPE pyrolysis oil light cut. (**E**) ^{13}C NMR spectra of hydroformylated oil. (**F**) ^{13}C NMR spectra of hydroformylated oil after hydrogenation. (**G**) ^{1}H-^{13}C HSQC NMR spectrum of hydroformylated oil after hydrogenation. Blue and red represent primary and secondary carbons, respectively.

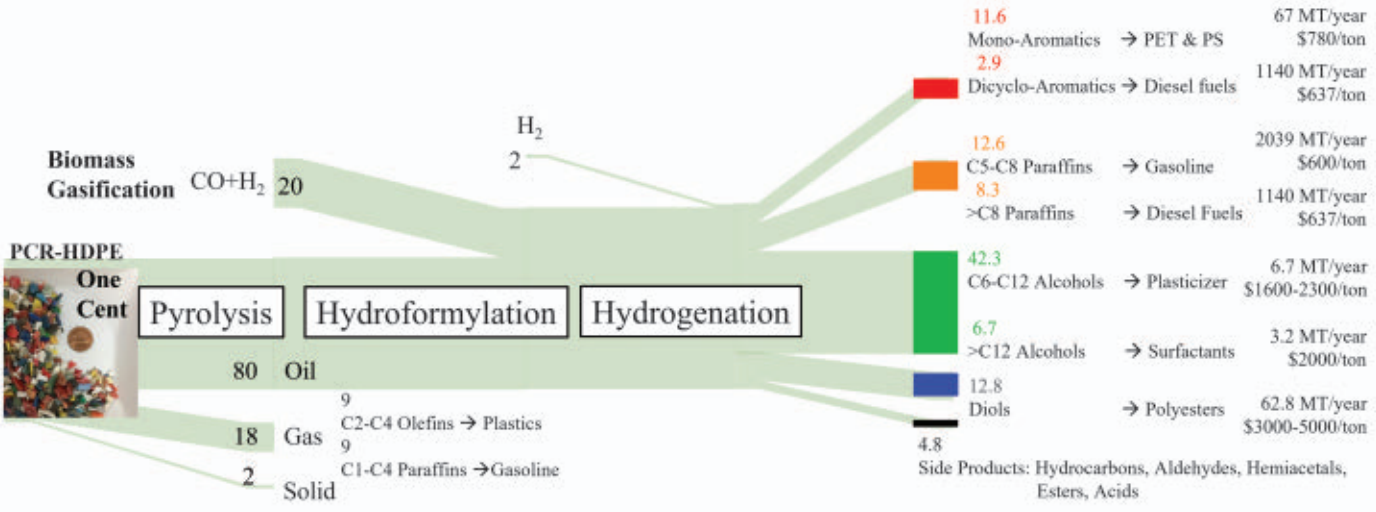
Biomass Gasification
CO+H2
20
H2
2
PCR-HDPE
Pyrolysis
Hydroformylation
Hydrogenation
80 Oil
18 Gas
2 Solid
9 C2-C4 Olefins → Plastics
9 C1-C4 Paraffins → Gasoline
11.6 Mono-Aromatics → PET & PS 67 MT/year $780/ton
2.9 Dicyclo-Aromatics → Diesel fuels 1140 MT/year $637/ton
12.6 C5-C8 Paraffins → Gasoline 2039 MT/year $600/ton
8.3 >C8 Paraffins → Diesel Fuels 1140 MT/year $637/ton
42.3 C6-C12 Alcohols → Plasticizer 6.7 MT/year $1600-2300/ton
6.7 >C12 Alcohols → Surfactants 3.2 MT/year $2000/ton
12.8 Diols → Polyesters 62.8 MT/year $3000-5000/ton
4.8
Side Products: Hydrocarbons, Aldehydes, Hemiacetals, Esters, Acids

Fig. 3. Input–output analysis, global production, and market price for the production of aromatics, paraffins, monoalcohols, and dialcohols from waste plastics. Mass balance in the pyrolysis, hydroformylation, and hydrogenation steps are in the range of 100 ± 15%. MT, million metric tons.

large ^{1}D retention time compared with the same carbon number aldehydes (fig. S8). Standard ^{1}H NMR and quantitative ^{13}C NMR were used to estimate the aldehyde conversion in the "hydroformylated pyrolysis oil" (figs. S6 and S7). The hydrogenation of the "hydroformylated pyrolysis oil" was also conducted in a fixed bed reactor with 20% Ni/SiO_2, with >90% of the aldehydes being reduced to the alcohols for both the light and heavy cut as shown in table S5 and in Fig. 2F. The peaks in the C=O region disappeared, and peaks in the C-OH region appeared. Most of the alcohols are primary alcohols as evidenced by the ^{1}H-^{13}C HSQC spectrum (light cut in Fig. 2G, heavy cut in fig. S7).

Input–output analysis

The overall mass balances of products from PCR colored HDPE are plotted as a Sankey diagram in Fig. 3. Pyrolysis of PCR HDPE generates pyrolysis oil, which undergoes hydroformylation and hydrogenation that produces primarily paraffins, aromatics, monoalcohols, and dialcohols in the range of C5 to C20. For example, pyrolysis of 100 kg of HDPE would generate 80 kg of plastic oil that contained 51 kg of olefins. The olefins then undergo hydroformylation to form aldehydes, which are subsequently hydrogenated into alcohols that generate 49 kg of monoalcohols and 13 kg of diols in the final product (assuming a 100-kg HDPE feed input). The synthesis gas ($CO + H_2$) and hydrogen required for this conversion could be produced from biomass, which further lowers the process carbon and energy input (*25*). The monoaromatics, C5 to C8 paraffins, and >C8 hydrocarbons (paraffins and multicyclic aromatics) can be used for polyethylene terephthalate (PET) and polystyrene (PS) manufacture, gasoline, and diesel, respectively, at $600 to $800 per ton (*26*). The C6 to C12 alcohols (0.42 tons per ton of HDPE) can be sold as plasticizers, which sell for $1600 to $2300 per ton (*27*). The >C12 alcohols (0.07 tons per ton of HDPE) can be used as surfactants and sold for >$2000 per ton (*27*). The diols (0.13 tons per ton of HDPE) are the most valuable product and sell for $3000 to $5000 per ton and can be used to produce polyesters and polyurethanes (*27*).

Theoretical simulations

The ratio of diols to monoalcohols produced by the hydroformylation/hydrogenation process is determined by the diene:mono-olefin ratio in the pyrolysis oil. The hydroformylated products could alternatively be oxidized to carboxylic acids, aminated to amines, or condensed into larger aldehydes. In all cases, the difunctional compound is more valuable than the monofunctional compound; hence, it would be desirable to tune the pyrolysis to produce more dienes. Previous work modeling pyrolysis has been focused on the development of kinetic models with limited attention to molecular scale bond-breaking or –making events (*8*, *28*). Accordingly, we performed an ab initio investigation of the thermal depolymerization chemistry that leads to the formation of mono-

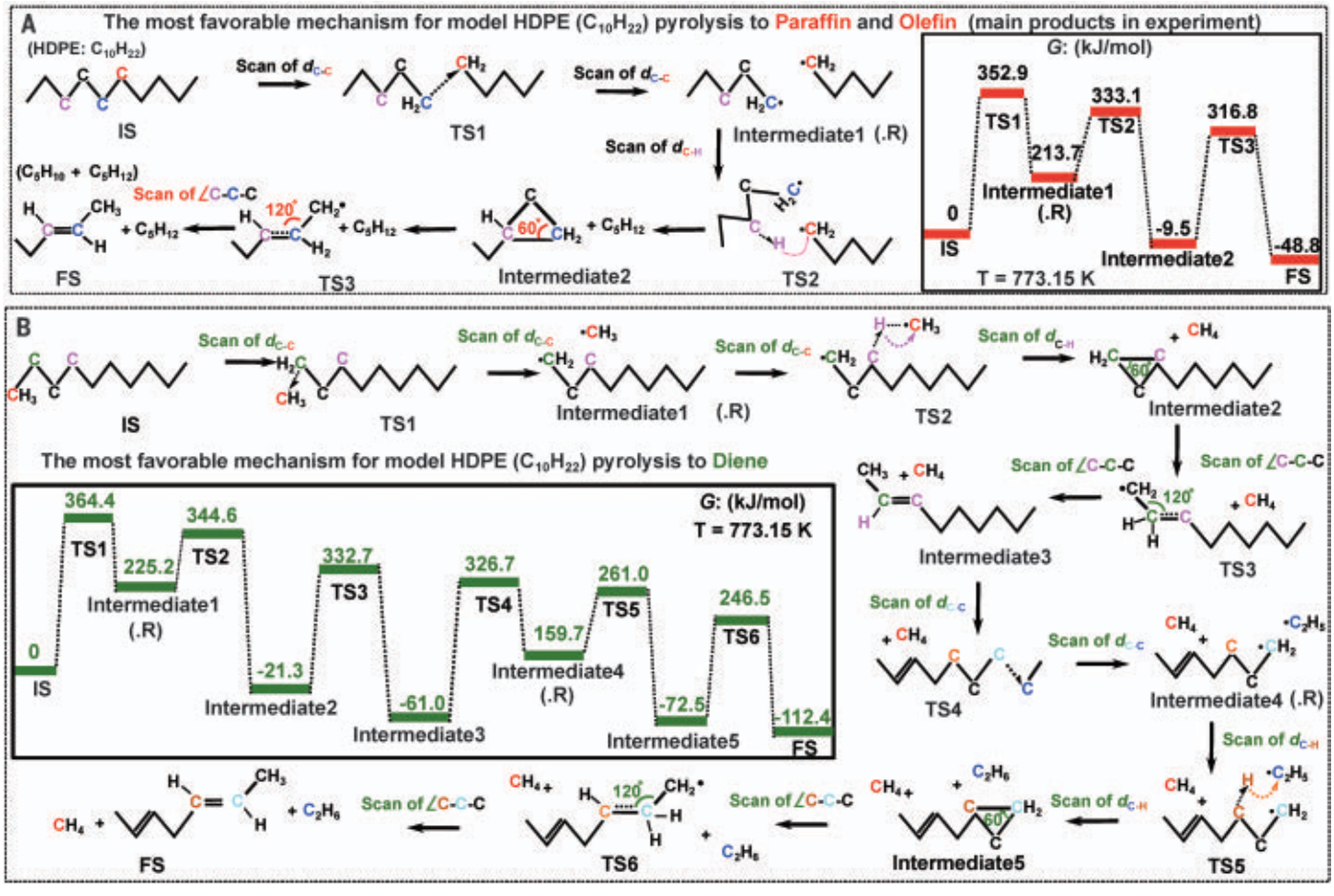

Fig. 4. Mechanistic simulations. (**A** and **B**) The thermodynamically and kinetically most favorable mechanisms for the formation of paraffin and mono-olefin (A) and diolefin (B). Linear decane ($C_{10}H_{22}$) was used as a surrogate molecule for HDPE and its pyrolysis to pentane (C_5H_{12}), pentene (C_5H_{10}), and heptadiene (C_7H_{12}) because of their largest concentrations in each product category according to our experimental results in fig. S3. For comparison, the less favorable mechanisms for the formation of paraffin, mono-olefin, and diolefin are shown in figs. S10, S11, and S14. The simulation temperature (773.15 K = 500°C) is the temperature at which the pyrolysis experiments were performed. FS, final state; IS, initial state.

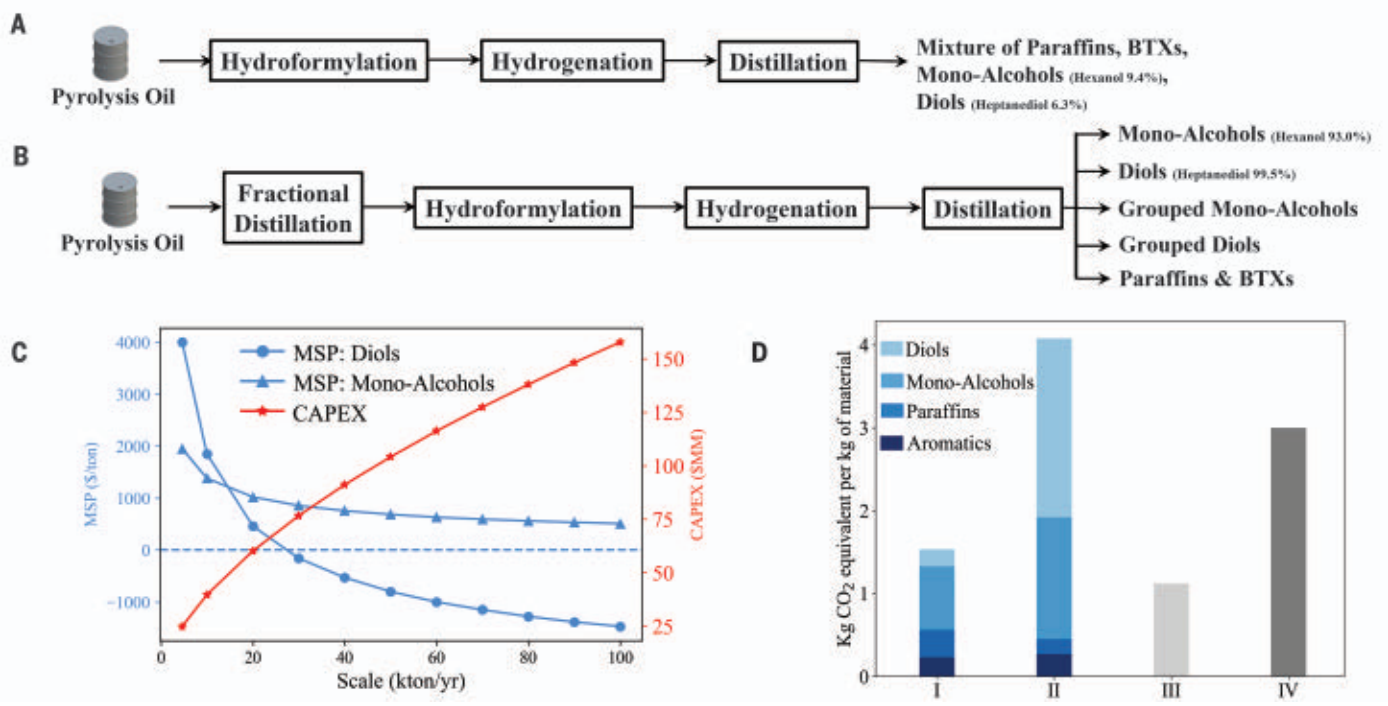

Fig. 5. Technoeconomics. (**A**) Process without pretreatment of pyrolysis oil before hydroformylation. (**B**) Process includes the pyrolysis oil pretreatment into different cuts, followed by hydroformylation, hydrogenation, and separation of each cut. (**C**) Capital expenditure (CAPEX) and MSP of products. (**D**) GHGs from (I) the proposed technology for converting 1 kg of plastic into chemicals, (II) conventional technologies for producing the same amount of chemicals, (III) converting 1 kg of plastic to olefins through pyrolysis and steam cracking, and (IV) incinerating 1 kg of plastic. Details of GHGs are provided in the supplementary materials.

olefins, paraffins, and dienes in the pyrolysis oils using the second Møller–Plesset perturbation theory (*29*) and 6-31++G** basis sets (*30*, *31*) in the *Gaussian 09* package (computational details in supplementary materials). The minimum energy path for the thermal decomposition of HDPE (modeled by decane) is initiated by backbone C-C bond breaking with a transition state (TS) energy of G^* = 352.9 kJ/mol, which leads to the formation of two radicals ($\bullet C_5H_{11}$) (intermediate 1) (Fig. 4A). That step is followed by a H abstraction step that proceeds from a middle $-CH_2-$ site of one radical (identified as the most feasible site for H transfer; details in fig. S11) to the other radical (terminal $.CH_2-$ site) characterized by an activation Gibbs free energy barrier of ΔG^* = 119.4 kJ/mol. This step leads to the formation of pentane (C_5H_{12}) and a metastable C_5H_{10} structure that contains a triangular C-ring (intermediate 2). Lastly, 326.3 kJ/mol is required to open the triangular C-ring, which leads to the final pyrolysis products of pentane and internal pentene (C_5H_{12} and C_5H_{10}, respectively). The overall reaction is exergonic by −48.8 kJ/mol. Three additional reaction paths initiated by H transfer along the HDPE backbone (without radical formation) were also studied, but they are all less favorable than the free-radical path (Fig. 4) already discussed because of the much higher TS energies (G^* = 468.1, 474.5, or 690.6 kJ/mol) (fig. S10). Then, we turned our attention to the diene formation mechanism. First, we determined that the internal conjugated C_7H_{12} is the most stable of the nine linear isomers considered (fig. S12). The most exergonic path (P1, among three possible paths shown in fig. S13) is provided in Fig. 4B with the associated TS energetics. From decane to heptadiene, two consecutive backbone C-C bond-breaking steps and H transfers were needed with mono-olefin as intermediate and paraffins (CH_4 and C_2H_6) as byproducts without hydrogen evolution. This is in good agreement with our experimental findings of <1 wt % yield of H_2 product in both HDPE and LDPE pyrolysis oil (table S7). Along this path, the highest TS energy (G^* = 364.4 kJ/mol) is higher than that (G^* = 352.9 kJ/mol) for the formation of pentane (C_5H_{12}) and internal pentene (C_5H_{10}) discussed above. This TS energy difference leads to a reaction rate for diene production that is lower than the production rate of paraffin plus olefin by a little less than one order of magnitude at 500°C, an estimate that is in near-quantitative agreement with our experimental product distribution (fig. S3). The other two pathways studied for diene (C_7H_{12}) formation (P2 and P3; see details in fig. S13) were both found to be thermodynamically unfavorable compared with P1. We envision that using suitable catalysts to facilitate the radical formation and H abstraction can further enhance selectivity of the pyrolysis process toward production of olefins and diolefins.

Technoeconomic modeling and life cycle assessment

We then developed a process model for producing monoalcohols and diols from the pyrolysis oils with hydroformylation technology (fig. S15 and tables S8 to S10) and used this to estimate the economics and environmental impacts. We considered two different approaches to separate our products as shown in Fig. 5, A and B. Distillation of the hydrogenated products (as shown in Fig. 5A) produces mixtures of monoalcohols, diols, benzene, toluene, and xylenes (BTX), and paraffins. High-purity diols are not attainable if this separation scheme uses only distillation after hydroformylation (details in supplementary materials). However, high-purity diols with <500 ppm of monoalcohols can be produced by fractional distillation of the pyrolysis oil into different fractions, followed by hydroformylation and hydrogenation of each cut, as shown in Fig. 5B. Further separation leads to high-purity monoalcohols (e.g., hexanol 91%) or diols (e.g., heptanediol 99.5%) as an individual component (Fig. 5B and tables S9 and S10). Thus, we show how polymer-grade diols can be produced with a proper separation scheme. The economic potential of the proposed technology is largely influenced by the selling prices of monoalcohol and diol because these products account for >80% of revenue. Accordingly, a sensitivity analysis was conducted to determine the minimum selling

prices (MSPs) of monoalcohols and diols under various processing capacities. The MSPs for alcohols equal current market prices ($4000 per and $1950/ton for diols and monoalcohols, respectively) when the plant capacity is set at 4600 tons of plastic per year (Fig. 5C). Because of economies of scale, increasing the plant capacity from 4600 to 16,000 tons per year results in a twofold increase in capital costs, whereas the MSPs for monoalcohol and diol decrease by >50% (compared with market prices). When the production scale reaches 24,000 tons per year, the MSP of diol goes to zero. This suggests that the proposed technology could be economically viable even without revenue from diol at this production level. When setting the production scale to 100,000 tons per year, which is similar to the production scale of a typical chemical plant, the MSPs of two critical products, alcohols and dialcohols, are $508 per ton and −$1470 per ton, respectively. The negative MSP of dialcohols implies that the revenue from other products can not only cover the cost but also generate a profitable stream. Moreover, at this level of production, the annual net profit can amount to as much as $100 million, with a relatively short payback period of 3 years.

The greenhouse gas emissions (GHGs) from recycling 1 kg of plastic waste by using this technology are 1.6 kg CO_2 equiv (tables S11 to S13 and fig. S17), which is ~50% lower than that of incinerating 1 kg of plastic waste (Fig. 5D, I versus IV). Other plastic upcycling strategies, such as producing olefins from plastic pyrolysis oil by using steam cracking, emit ~1.2 kg CO_2 equiv (*13*) per kilogram of plastic processed (fig. S17). The carbon footprint of the proposed technology in this work is comparable with that of the plastic-to-olefin route. GHGs of each grouped species in the final product were calculated by multiplying the total GHGs of this technology by the weight percentage of the specific grouped species. As shown in Fig. 5D, I and II, the diol production route is associated with 0.20 kg CO_2 equiv per 0.14 kg dialcohol produced from 1 kg plastic (or 1.4 kg CO_2 equiv per kilogram of diols). Producing the same diol conventionally from petroleum has >10 times higher emissions [15.1 kg of CO_2 equiv per kilogram of diols (*32*)]. Compared with producing the same amount of chemicals via the traditional route from fossil feedstocks, the proposed technology results in 60% lower GHGs (Fig. 5D, I versus II).

The approach outlined here demonstrates a platform technology for upcycling of waste plastic oils by hydroformylation chemistry. ExxonMobil has filed a patent application for the production of monoalcohols from plastic pyrolysis oils by using hydroformylation and noncatalytic reduction of aldehydes to alcohols with sodium borohydride (*33*). However, a detailed characterization of the reaction chemistry, the product analysis, the economics of the technology, and the environmental impacts are not reported in the patent application. Additionally, the ExxonMobil route did not produce dialcohols. In this study, we elucidated the mechanisms for thermal depolymerization of polyolefin, which provides insights in tuning plastic oil distribution. The aldehydes produced from hydroformylation can be used to produce a range of chemicals that include alcohols, carboxylic acids, and amines. The separation process produces high-purity diols and monoalcohols that are suitable for polymer applications. The olefins in the pyrolysis oil can also undergo hydroaminoalkylation, which generates amines in a single step (*34*–*36*). The branching in the products can be controlled by tuning the plastic feedstocks. For example, HDPE produces straight-chain products, whereas PP and LDPE create different types of branching in the products (details in figs. S20 and S21 and table S14). Many approaches have been developed to recycle or upcycle waste plastics into varied products, which include hydrogenolysis (*37*, *38*) and catalytic deconstruction (paraffins, olefins, and aromatics) (*39*–*41*), dissolution-based approaches (plastic resins with virgin properties) (*42*), functionalization (plastics with new properties) (*43*), and oxidation (oxygenates) (*44*, *45*). Compared with these routes, the key benefits of the approach reported are production of high-value (>$1600 per ton) monoaldehydes, dialdehydes, monoalcohols, and dialcohols (*46*, *47*), which can be done by using existing hydroformylation infrastructure.

REFERENCES AND NOTES

1. I. Amghizar, L. A. Vandewalle, K. M. Van Geem, G. B. Marin, *Engineering* **3**, 171–178 (2017).
2. Nexant, Independent Market Report on the Global and Indonesian Petrochemicals Industry (2011); https://www.scribd.com/document/217378314/201105151926340-Nexant-Industry-Report-2011 [accessed 2 October 2022].
3. M. Kusenberg *et al*., *Fuel Process. Technol.* **227**, 107090 (2022).
4. A. Gala, M. Guerrero, B. Guirao, M. E. Domine, J. M. Serra, *Energy Fuels* **34**, 5969–5982 (2020).
5. Y. Zhang *et al*., *ACS Sustain. Chem. Eng.* **10**, 91–103 (2022).
6. D. Zhao, X. Wang, J. B. Miller, G. W. Huber, *ChemSusChem* **13**, 1764–1774 (2020).
7. H. Li *et al*., *Green Chem.* **24**, 8899–9002 (2022).
8. O. Dogu *et al*., *Prog. Energy Combust. Sci.* **84**, 100901 (2021).
9. A. Eschenbacher *et al*., *Appl. Catal. B* **309**, 121251 (2022).
10. M. Kusenberg *et al*., *Waste Manag.* **141**, 104–114 (2022).
11. A. Milbrandt, K. Coney, A. Badgett, G. T. Beckham, *Resour. Conserv. Recycling* **183**, 106363 (2022).
12. "Dow and Mura Technology plan to locate Europe's largest advanced recycling facility at Dow's site in Böhlen, Germany," *Cision PR Newswire*, 14 September 2022; https://www.prnewswire.com/news-releases/dow-and-mura-technology-plan-to-locate-europes-largest-advanced-recycling-facility-at-dows-site-in-bohlen-germany-301624125.html [accessed 15 October 2022].
13. J. Ma *et al*., *Green Chem.* **25**, 1032–1044 (2023).
14. B. Zhang, C. Kubis, R. Franke, *Science* **377**, 1223–1227 (2022).
15. I. Ro *et al*., *Nature* **609**, 287–292 (2022).
16. S. Lee, A. Patra, P. Christopher, D. G. Vlachos, S. Caratzoulas, *ACS Catal.* **11**, 9506–9518 (2021).
17. I. Ro, M. Xu, G. W. Graham, X. Pan, P. Christopher, *ACS Catal.* **9**, 10899–10912 (2019).
18. B. Liu *et al*., *Chem* **8**, 2630–2658 (2022).
19. A. C. Brezny, C. R. Landis, *Acc. Chem. Res.* **51**, 2344–2354 (2018).
20. D. S. Laitar, J. W. Kramer, B. T. Whiting, E. B. Lobkovsky, G. W. Coates, *Chem. Commun.* (38): 5704–5706 (2009).
21. M. Mulzer, G. W. Coates, *Org. Lett.* **13**, 1426–1428 (2011).
22. J. Yang, F. G. Delolo, A. Spannenberg, R. Jackstell, M. Beller, *Angew. Chem. Int. Ed.* **61**, e202112597 (2022).
23. F. E. Paulik, *Catal. Rev. Sci. Eng.* **6**, 49–84 (1972).
24. M. F. Mirbach, *Trans. Met. Chem.* **9**, 465–468 (1984).
25. G. W. Huber, S. Iborra, A. Corma, *Chem. Rev.* **106**, 4044–4098 (2006).
26. EIA, Petroleum & Other Liquids Spot Prices; https://www.eia.gov/dnav/pet/pet_pri_spt_s1_d.htm [accessed 2 October 2022].
27. *Plasticizer Alcohols (C4-C13) Chemical Economics Handbook* (S&P Global, 2021); https://ihsmarkit.com/products/plasticizer-alcohols-chemical-economics-handbook.html.
28. I. Mastalski *et al*., *Chem. Mater.* **35**, 3628–3639 (2023).
29. M. J. Frisch, M. Head-Gordon, J. A. Pople, *Chem. Phys. Lett.* **166**, 275–280 (1990).
30. R. Ditchfield, W. J. Hehre, J. A. Pople, *J. Chem. Phys.* **54**, 724–728 (1971).
31. G. A. Petersson *et al*., *J. Chem. Phys.* **89**, 2193–2218 (1988).
32. A. Ciroth, *Int. J. Life Cycle Assess.* **12**, 209–210 (2007).
33. C. L. Hans, K. T. Goris, D. Bien, A. E. Carpenter, C. M. Diaz, Methods for producing higher alcohols from waste plastic pyrolysis oil and the higher alcohols obtained therefrom, Patent WO2022084238A1 (2022); https://patentimages.storage.googleapis.com/a5/54/1f/25178be8451df5/WO2022084238A1.pdf.
34. R. C. DiPucchio, S.-C. Rosca, L. L. Schafer, *J. Am. Chem. Soc.* **144**, 11459–11481 (2022).
35. S. S. Scott, S.-C. Roşca, D. J. Gilmour, P. Brant, L. L. Schafer, *ACS Macro Lett.* **10**, 1266–1272 (2021).
36. P. M. Edwards, L. L. Schafer, *Org. Lett.* **19**, 5720–5723 (2017).
37. A. Tennakoon *et al*., *Nat. Catal.* **3**, 893–901 (2020).
38. G. Zichittella *et al*., *JACS Au* **2**, 2259–2268 (2022).
39. R. J. Conk *et al*., *Science* **377**, 1561–1566 (2022).
40. N. M. Wang *et al*., *J. Am. Chem. Soc.* **144**, 18526–18531 (2022).
41. S. Dong *et al*., *Appl. Catal. B* **324**, 122219 (2023).
42. T. W. Walker *et al*., *Sci. Adv.* **6**, eaba7599 (2020).
43. T. J. Fazekas *et al*., *Science* **375**, 545–550 (2022).
44. K. P. Sullivan *et al*., *Science* **378**, 207–211 (2022).
45. U. Kanbur *et al*., *Chem* **7**, 1347–1362 (2021).
46. J. Klier, J. Bohling, M. Keefe, *AIChE J.* **62**, 2238–2247 (2016).
47. L. Zheng *et al*., *ACS Sustain. Chem. Eng.* **10**, 5781–5791 (2022).
48. J. Risher, (US Department of Health and Human Services, 1995); https://stacks.cdc.gov/view/cdc/6251.
49. J. G. Speight, in *Subsea and Deepwater Oil and Gas Science and Technology* (Gulf, 2015), pp. 1–43.

ACKNOWLEDGMENTS

The authors acknowledge K. L. Vorst and G. W. Curtzweiler for providing the postconsumer colored HDPE material, mostly from personal care packaging, used for this study. The authors acknowledge H. Radhakrishnan for performing the CHN(O)S elemental analysis. H.L. thanks Y. Jiang, M. S. Kim, and J. C. Chan for helpful discussion. The authors also acknowledge J. Dumesic for providing helpful comments on the manuscript. **Funding:** This material is based on work supported by the US Department of Energy (DOE), Office of Energy Efficiency and Renewable Energy, Bioenergy Technologies Office under Award Number DEEE0009285. Z.J. and M.M. used resources at the National Energy Research Scientific Computing Center, a DOE Office of Science User Facility that is supported by the DOE, Office of Science, under contract no. DE-AC02-05CH11231 using NERSC award BES-ERCAP0022773. Part of the computational work was carried out by using supercomputing resources at the Center for Nanoscale Materials (CNM), a DOE Office of Science User Facility located at Argonne National Laboratory that is supported by DOE contract DE-AC02-06CH11357, and at the UW-Madison Center for High Throughput Computing (CHTC). CHTC is supported by UW-Madison, the Advanced Computing Initiative, the Wisconsin Alumni Research Foundation, the Wisconsin Institutes for Discovery, and the National Science Foundation. **Author contributions:** H.L. and G.W.H. designed the experiments, wrote the manuscript, and reviewed and edited the manuscript. J.W. performed pyrolysis experiments, assisted with the modeling, and reviewed and edited the manuscript. Z.J. and M.M. designed pyrolysis modeling, analyzed data, wrote modeling section, and reviewed and edited the manuscript. C.R.L. provided experimental guidance, and reviewed and edited the manuscript. H.L. and J.M. performed the technoeconomic analysis and life cycle assessment. V.M.Z. and G.W.H. provided guidance for technoeconomic analysis and life cycle assessment, and reviewed and edited the manuscript. **Competing interests:** H.L., J.W., C.R.L., and G.W.H. are inventors on US patent

application P230014US01 "Method for making aldehydes, alcohols, amides, and carboxylic acids from plastic pyrolysis oil" (UW-Madison, WARF, filed 1 November 2022). G.W.H. has an ownership interest in Anellotech, which is commercializing the PlasTCat technology. **Data and materials availability:** All data are available in the main text or the supplementary materials. **License information:** Copyright © 2023 the authors, some rights reserved; exclusive licensee American Association for the Advancement of Science. No claim to original US government works. https://www.sciencemag.org/about/science-licenses-journal-article-reuse

SUPPLEMENTARY MATERIALS
science.org/doi/10.1126/science.adh1853
Materials and Methods
Figs. S1 to S21
Tables S1 to S14
References (*50*–*71*)

Submitted 15 February 2023; resubmitted 12 May 2023
Accepted 15 June 2023
10.1126/science.adh1853

PLASTIC UPCYCLING

Chemical upcycling of polyethylene, polypropylene, and mixtures to high-value surfactants

Zhen Xu[1]†, Nuwayo Eric Munyaneza[1]†, Qikun Zhang[2], Mengqi Sun[1], Carlos Posada[1], Paul Venturo[1], Nicholas A. Rorrer[3,4], Joel Miscall[3,4], Bobby G. Sumpter[5]*, Guoliang Liu[1,6]*

Conversion of plastic wastes to fatty acids is an attractive means to supplement the sourcing of these high-value, high-volume chemicals. We report a method for transforming polyethylene (PE) and polypropylene (PP) at ~80% conversion to fatty acids with number-average molar masses of up to ~700 and 670 daltons, respectively. The process is applicable to municipal PE and PP wastes and their mixtures. Temperature-gradient thermolysis is the key to controllably degrading PE and PP into waxes and inhibiting the production of small molecules. The waxes are upcycled to fatty acids by oxidation over manganese stearate and subsequent processing. PP β-scission produces more olefin wax and yields higher acid-number fatty acids than does PE β-scission. We further convert the fatty acids to high-value, large–market-volume surfactants. Industrial-scale technoeconomic analysis suggests economic viability without the need for subsidies.

As the two most widely used commodity plastics, polyethylene (PE) (Table 1) and polypropylene (PP) contribute nearly 60% of the world's plastic production (~400 million tonnes), primarily for short-term applications (*1*). The manufacturing of PE and PP is associated with the highest energy consumption among all plastics (*1*, *2*) and contributes substantially to annual greenhouse gas emissions (*2*). Short-term use plastics quickly turn into waste and cause substantial pollution (*3*). To recycle PE and PP, the waste collection and sorting processes must be economically efficient to lower the cost (*4*), and the recycled products should ideally be high value and high volume to have a major impact on waste accumulation. Although PE and PP can be separated from heavier-than-water polymers such as polyvinyl chloride (PVC) and polyethylene terephthalate (PET) through a sink-float method that uses water as the medium (Fig. 1A), further separation of PE and PP is much more challenging because of their similar structures and densities. The two polymers are furthermore incompatible and cannot be blended unless expensive and sophisticated compatibilizers are used (*5*). Finding a generic and profitable method to recycle or upcycle both PE and PP while increasing their final product value over that of virgin plastics is thus imperative (*3*, *6*–*8*).

Chemical upcycling increases product value and is envisioned as a solution that converts postconsumer wastes into high-value chemicals, e.g., the conversion of polystyrene (PS) into aryl carbonyls and aryl alkyls (*9*–*11*). Chemical upcycling of PP and PE, however, is difficult because of the high ceiling temperatures involved (*12*). Moreover, the lack of heteroatom-associated weak links within the polymer chains (e.g., esters in PET) provides no selective chain-scission sites. Product control is thus exceptionally challenging. Recently, chemical reactions that use iridium- (*13*) and platinum-based catalysts (*14*) and ionic liquids (*15*) generated fuels and improved selectivity toward aryl moieties in the upcycling of PE. On a laboratory scale, PE can also be converted to propylene by dehydrogenation and tandem isomerizing ethenolysis (*16*, *17*). Considering the technoeconomic potential for increased product value and generalizability to both PE and PP, the conversion of polyolefins to high-value fatty acids or ionic surfactants is appealing because PE and PP are aliphatic by nature. In addition, surfactant products have huge market demands (i.e., comparable to plastics) and high economic values (i.e., higher than fuels, waxes, and regular aromatic compounds) (table S1). Moreover, surfactant products such as soaps are made from fatty acids of varying chain lengths and are often blended with ketones and aldehydes to soften the product and modulate fragrance release (*18*), diminishing the need to remove ketone and aldehyde by-products in the upcycling process of PE and PP. Biodegradation converts PE to fatty acids by means of microbial strains, but the fermentation period is too long (>10 days) to be practically deployable in the chemical industry (*19*). Chemically, the Novoloop method and hydrothermal reactions with strong oxidants quickly degrade PE but require harsh reaction conditions, such as strong nitric acid and high pressure (*20*, *21*). Most recently, metallization of PE over Zr and alkyl aluminum has afforded products with controllable average carbon-chain lengths, and the catalysts must operate under O_2-, CO_2-, and H_2O-free conditions (*22*). Therefore, time- and material-efficient methods that use noncorrosive chemicals, atmospheric pressure, and air-tolerant reaction conditions are highly sought to efficiently transform both PE and PP into large–market-volume fatty acids, preferably without the need for additional sorting and separation but with high selectivity and conversion.

Here we report a gradient-temperature thermolysis method that can selectively break PE, PP, and their mixtures into waxes under atmospheric pressure (Fig. 1, A and B). The key is that the temperature gradient prevents violent pyrolysis reactions, quenches vaporized waxes, and inhibits complete degradation to small molecules (Fig. 1C and figs. S1 and S2; see discussion in supplementary materials). PE- and PP-derived waxes are subsequently transformed into fatty acids with high acid numbers (ANs) and number-average molar masses of up to ~700 and 670 Da, respectively (Fig. 1D and tables S2 to S4). Through subsequent saponification, we obtain an ionic surfactant product that contains salts of fatty acids. Simply mixing with additives (e.g., fragrances) can produce commercial products, such as soap bars and liquid detergents (examples in Fig. 1A), which have higher market values than typical chemical products such as fuels and alkylaromatics (*11*, *14*).

Polyethylene conversion to fatty acids

Initially, pulverized lab-grade PE (~500 mg; M_w, 97 kDa; polydispersity Đ = 2) was loaded into a custom-designed quartz reactor (Fig. 1A and fig. S1) and purged with gases of controlled compositions (N_2, 10 vol % O_2 in N_2, or

[1]Department of Chemistry, Virginia Tech, Blacksburg, VA 24061, USA. [2]Department of Chemistry, Chemical Engineering and Materials Science, Ministry of Education Key Laboratory of Molecular and Nano Probes, Shandong Normal University, Shandong 250014, PR China. [3]Renewable Resources and Enabling Sciences Center, National Renewable Energy Laboratory, Golden, CO 80401, USA. [4]BOTTLE Consortium, Golden, CO 80401, USA. [5]Center for Nanophase Materials Sciences, Oak Ridge National Laboratory, Oak Ridge, TN 37831, USA. [6]Department of Chemical Engineering, Department of Materials Science and Engineering, Macromolecules Innovation Institute, Virginia Tech, Blacksburg, VA 24061, USA.
***Corresponding author. Email: gliu1@vt.edu (G.L.); sumpterbg@ornl.gov (B.G.S.)**
†These authors contributed equally to this work.

air). The degradation was initiated by heating the bottom of the reactor to ~360°C stepwise with a step size of ~100°C per 5 min. Polymer smokes (fig. S2) appeared, indicating the vaporization of fragmented polyolefins or waxes. The waxes were condensed in the cold part of the reactor, preventing further fragmentation to shorter hydrocarbons. The wax yields from PE degradation in N_2 (PE-N_2-wax), 10 vol % O_2 (PE-O-wax), or air (PE-air-wax) were 86, 79, and 55 wt % (Fig. 2A and table S2, experiments 1 to 3, 7 to 9, and 13), respectively. In a control experiment under N_2 without a temperature gradient, the products were mostly short-chain hydrocarbons of C8 and below (Fig. 1C).

Gas chromatography–mass spectrometry (GC-MS) was used to characterize the wax composition (Fig. 2B), showing mainly solid waxes with minor fractions of light hydrocarbons (~10 wt % of C8 and below, fig. S3). Each primary peak could be resolved into a doublet of alkene and alkane with the same carbon number (figs. S4 and S5), similarly to degradation in flow reactors (*23*). In the presence of O_2, PE-O-wax and PE-air-wax exhibited GC-MS peaks and molecular ion signals similar to those of PE-N_2-wax. PE-O-wax and PE-air-wax showed stronger intensities at shorter elution times than PE-N_2-wax (Fig. 2B), indicating more short hydrocarbons and lower average molecular weights as a result of accelerated degradation by oxygen radicals (*24*). The PE-air-wax yield was too low (~55%), albeit higher than those in the literature (*25*, *26*), to be practically useful for generating hydrocarbons suitable for downstream production of surfactants (Fig. 2A); therefore, no further characterization of PE-air-wax was conducted. High-temperature gel permeation chromatography (HT-GPC) confirmed the degradation of polymers (fig. S6). Because HT-GPC cannot resolve the exact molecular weights in this range, and because GC cannot detect low-volatility heavy hydrocarbons (>C40) (*27*), atmospheric pressure chemical ionization mass spectrometry (APCI-MS) was used to analyze the full composition. The spectra of PE-N_2-wax and PE-O-wax showed waxes of mass/charge ratio (m/z) centered at ~630 and 540 (fig. S6 and table S3), corresponding to a carbon number of ~45 and 42, respectively. Despite m/z ranges of 300 to 1000 for PE-N_2-wax and 200 to 900 for PE-O-wax (fig. S6C), the polydispersities were relatively small (<1.1, table S3). The PE-N_2-wax and PE-O-wax were further characterized by nuclear magnetic resonance (NMR) spectroscopy through heteronuclear multiple bond correlation (HMBC) and heteronuclear single quantum correlation (HSQC) experiments (Fig. 2C and figs. S7 and S8) to investigate the waxes' structures. NMR confirmed the presence of unsaturated carbon in both PE-N_2-wax and PE-O-wax, showing primarily 2-propenyl at the chain end (^{1}H NMR δ 5.0 and 5.8, ^{13}C NMR δ 114 and 138) and minor internal alkenes (^{13}C NMR δ 123 to 131). The presence of O_2 partially oxidized PE-O-wax and produced ketones, aldehydes, and esters (fig. S8).

Upcycling of the waxes was conducted over Mn compounds for 10 hours in an airflow at

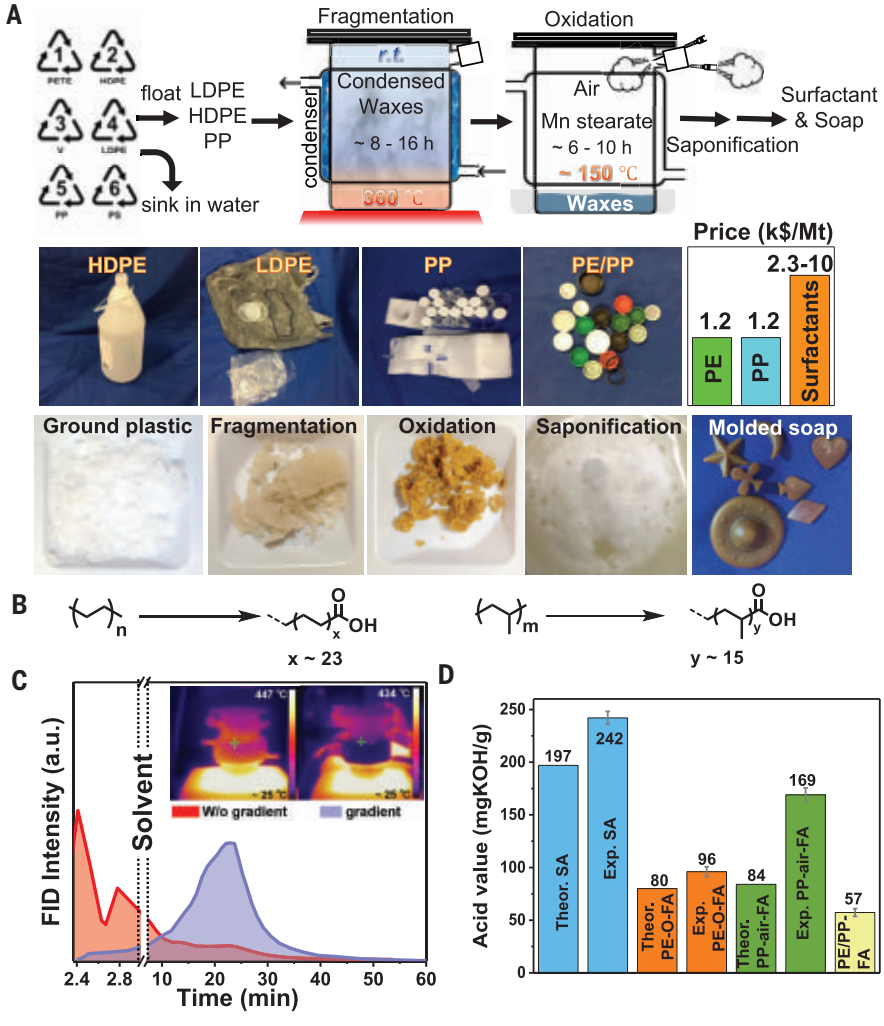

Fig. 1. Upcycling of PE and PP to fatty acids in a temperature-gradient reactor. (**A**) Schematic process flow of separation and upcycling of commercial polyolefins, including high-density PE (HDPE), low-density PE (LDPE), and PP to soap products performed using a custom-designed gradient thermal reactor. The temperature-gradient reactor has a hot and cold zone, preventing complete thermolysis of PE and PP to small molecules, and is key to controlling the chain length of fragmented products. Photographs show representative PE and PP wastes used in this study (HDPE container, grocery bags, sandwich bags, bottle caps, PP centrifuge tubes, and PP foam), as well as the products of intermediate waxes, fatty acids, surfactant solution, and soap molded into various shapes. The market price per metric ton of common surfactant products is almost double that of virgin plastics (table S1). (**B**) Reaction schemes of upcycling PE and PP to fatty acids. (**C**) Representative product distributions after PE degradation in the reactor with and without temperature gradient. The distribution and intensity were measured with GC. Signals from 3 to 7 min overlapped with the toluene solvent and thus were not shown for clarity. (Inset) Infrared thermal image of the reactor with and without temperature gradient. (**D**) AN of resulting fatty acids compared with that of stearic acid (SA, C18) and theoretical values of fatty acids with average carbon numbers of C47 for PE and C45 for PP. The error bars are the standard deviation of at least three replicates.

150°C. Although inorganic MnO_2 and $KMnO_4$ have shown effectiveness in paraffin oxidation (*28*), they were ineffective in oxidizing PE-derived wax, probably because of low miscibility, showing no appreciable carbonyl signals after 24 hours (fig. S9). By contrast, Mn stearate catalyzed the oxidization of PE-derived wax much faster owing to the better dispersion of the catalyst in the organic media (*29*, *30*). The oxidation rates of PE-N_2-wax or PE-O-wax were similar over Mn stearate (5 wt % loading) under a constant air flow, as shown by the similar slopes of carbonyl index (CI) changes as a function of time. PE-O-wax showed a higher final CI because of the higher initial value than did PE-N_2-wax. We conclude on the basis of HMBC analysis that the oxidation of PE-O-wax over Mn stearate intensified the carbonyl concentration in the first 6 hours (figs. S9 and S10, ^{13}C NMR δ 160 to 206), producing primarily aldehydes and minor esters, ketones, and carboxylic acids. The oxidation likely occurred by means of a radical addition mechanism (*31*, *32*), possibly through epoxy intermediate rearrangement to aldehydes and ketones (*33*). The presence of aldehyde was confirmed by NMR-HMBC, whereas epoxy signals were too weak to be confirmed. The dominance of aldehyde intermediates agreed well with the simulation results. Because aldehydes were susceptible to further oxidation, they were converted to acids (Fig. 2D, ^{13}C NMR δ 180) in the latter 2 hours of oxidation and subsequent saponification in 0.1 M aqueous KOH. The saponification hydrolyzed minor fatty esters and increased the amount of fatty acids; it also helped remove undesired short-chain acids (e.g., acetic acids). Hydroxyl signals were too weak to confirm the presence of alcohols in the product. The saponified solution was neutralized with HCl, crashing out fatty acid (PE-O-FA). After washing and drying under a vacuum, PE-O-FA was characterized by HMBC, showing primarily carboxylic acids and minor ketones. Aldehydes were no longer detectable (fig. S11). The carboxyl in the fatty acid correlated with two types of protons (Fig. 2D, ^{1}H NMR δ 2.0 and 1.5), potentially indicating a carboxyethyl end group. The AN of the PE-O-FA was determined by titration, giving an ordinary AN of 96 mg KOH/g (Fig. 1D and table S4) that slightly exceeded the theoretical value of ~80 mg KOH/g for a 700 g/mol monocarboxylic acid (C47).

Table 1. Abbreviations.

Full name	Abbreviation
Chemicals	
Polyethylene	PE
Polypropylene	PP
Polyvinyl chloride	PVC, or V
Polyethylene terephthalate	PET
High-density PE	HDPE
Low-density PE	LDPE
Stearic acid	SA
Wax yielded from PE degradation in N_2	PE-N_2-wax
Wax yielded from PE degradation in 10 vol % O_2	PE-O-wax
Wax yielded from PE degradation in air	PE-air-wax
PE-O-wax derived fatty acid	PE-O-FA
Wax yielded from PP degradation in N_2	PP-N_2-wax
Wax yielded from PP degradation in 10 vol % O_2	PP-O-wax
Wax yielded from PP degradation in air	PP-air-wax
PP-air-wax derived fatty acid	PP-air-FA
Instrumentation and methods	
Gas chromatography	GC
Gas chromatography-mass spectrometry	GC-MS
High-temperature gel permeation chromatography	HT-GPC
Atmospheric pressure chemical ionization mass spectrometry	APCI-MS
Nuclear magnetic resonance spectroscopy	NMR
Heteronuclear multiple bond correlation	HMBC
Heteronuclear single quantum correlation	HSQC
Proton NMR	^{1}H NMR
Quantitative NMR	q-NMR
Flame ionization detector	FID
Mass selective detector	MSD
Density functional–based tight-binding	DFTB
ab initio molecular dynamics	AIMD
Fourier transform infrared spectroscopy	FTIR
Thermogravimetric analysis	TGA
Parameters	
Number-average molar mass	M_n
Weight-average molar mass	M_w
Polydispersity	Đ
Carbonyl index	CI
Acid number	AN
Activation energy	E_a
Pre-exponential factor	A
Selectivity of thermolysis (T) or upcycling (U)	s_T or s_U
Yield of thermolysis (T) or upcycling (U)	α_T or α_U
Concentration of alkenyl groups	$c_{c=c}$
Concentration of total waxes	c_{wax}
Concentration (mmol/g) of acid group in fatty acids	c_{acid}
Concentrations (mmol/g) of alkenyl groups in fatty acids	$c_{c=c,FA}$

Extension to polypropylene and mixtures

After successfully converting PE to fatty acids, the process was applied to pulverized lab-grade PP (500 mg; M_w, 158 kDa; Đ=4) under reaction conditions similar to those used for PE (N_2, 10 vol % O_2 in N_2, and air). Degradation products in N_2 (PP-N_2-wax), 10 vol % O_2 (PP-O-wax), and air (PP-air-wax) showed total wax yields of 90, 85, and 87 wt %, respectively (Fig. 3A and table S2, experiments 4 to 6, 10 to 12, and 14), with a small amount of coke and gaseous products (fig. S12). The *m*/*z* ranges were 170 to 950 (centered at 560) for PP-N_2-wax and 150 to 700 (centered at 450) for PP-air-wax (fig. S6C), and the molecular weight polydispersities were relatively small (table S3). Unlike that for PE, the PP wax yield remained high in the air, eliminating the need for controlled gases in the process and making the method more economically attractive. Therefore, the degradation of PP in 10 vol % O_2 was not investigated further. GC-MS analysis of PP-N_2-wax showed broad

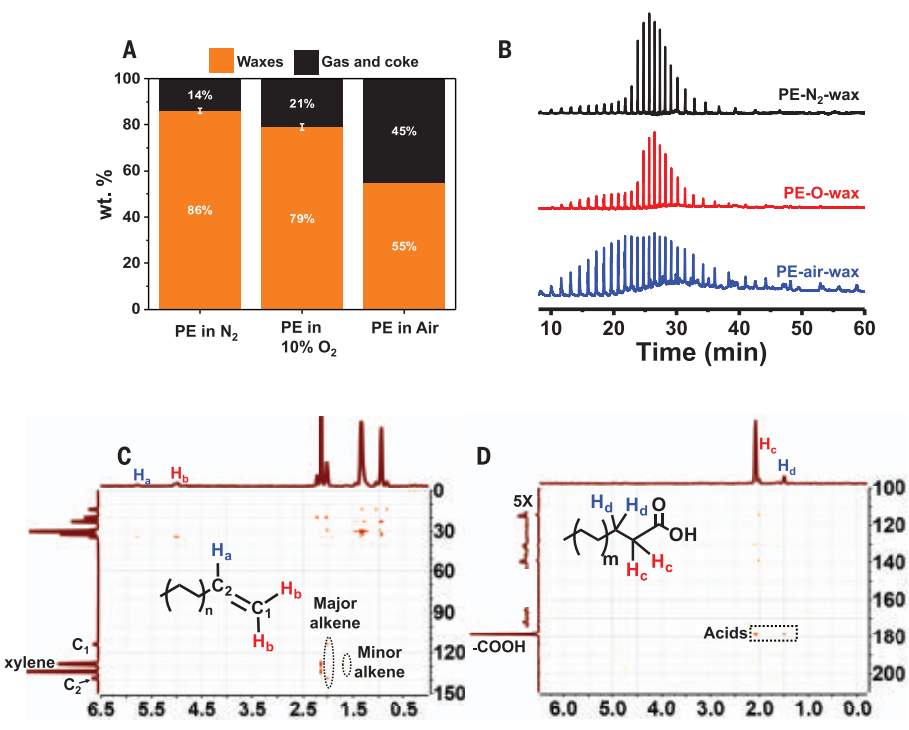

Fig. 2. Degradation of PE into intermediate waxes and upcycling into fatty acids. (**A**) Yields and (**B**) GC-MS chromatograms of intermediate waxes after degrading lab-grade PE in N_2, 10 vol % of O_2 balanced with N_2, or air. (**C**) NMR-HMBC spectra of PE-N_2-wax in deuterated *p*-xylene. The circles highlight the C-H correlations of the major and minor alkene products. (**D**) NMR-HMBC spectrum of the fatty acid derived from PE-O-wax. The black box highlights the two carboxyl carbon correlations with protons. [Insets in (C) and (D)] Chemical structures of the major alkene and fatty acid products.

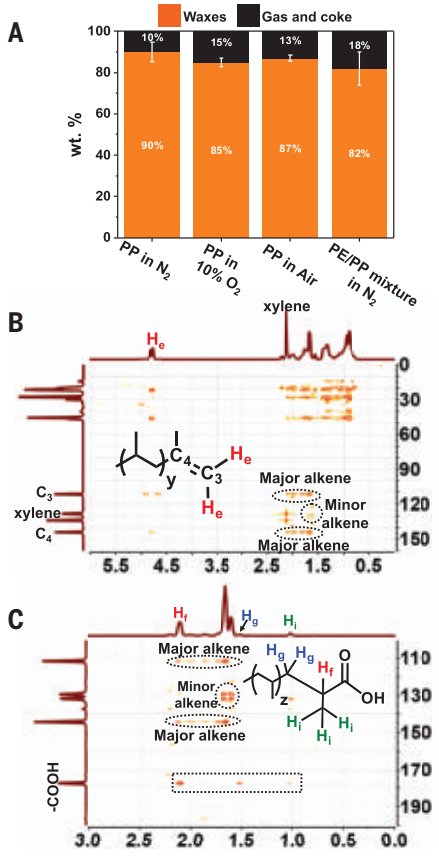

Fig. 3. Degradation of PP and PE/PP mixture into intermediate waxes and upcycling into fatty acids. (**A**) The intermediate wax yield of lab-grade PP upon degradation in N_2, N_2/O_2 mixture (10 vol % O_2), or air, along with the wax yield from a PE/PP waste mixture (including 25 wt % HDPE, 25 wt % PP, 25 wt % LDPE, and 25 wt % PE/PP unsorted) upon degradation in N_2. The ANs are shown in table S4. The low wax yield from the PE/PP waste mixture was due to solid contaminants such as paper labels, paints, and dyes. (**B**) NMR-HMBC spectra of PP-N_2-wax in deuterated *p*-xylene. (Inset) Chemical structure of the major alkene product. The circles highlight the C-H correlations of the major and minor alkene products, respectively. (**C**) NMR-HMBC spectra of PP-air-FA. (Inset) Chemical structure of the major fatty acid product. The black box highlights the three carboxyl carbon correlations with protons.

multimodal distributions of primarily alkene products in GC-MS (fig. S13). The carbon numbers of alkenes were mostly multiples of 3 (or 3n in the range of C9 to C36), and those of the rest of alkanes, alkenes, and dienes were mainly 3n+1. This distribution suggested that the primary degradation mechanism could be chain scission on the PP backbone because each PP repeating unit has three carbons (which is in agreement with our simulations below). With air present, the chromatogram of PP-air-wax became crowded and hard to analyze (fig. S6A). PP-N_2-wax and PP-air-wax were characterized by APCI-MS (fig. S6, B and C), and the latter showed a slightly higher proportion of short hydrocarbons because of air-induced oxidation, which is similar to the finding in a previous report. (*34*) As with the PE degradation product, PP-N_2-wax and PP-air-wax were primarily composed of terminal alkenes with minor internal alkenes (Fig. 3B and figs. S14 and S15). The primary form of the terminal alkene was possibly 2-methyl-2-propenyl, as suggested by the correlations in the HMBC and HSQC. Additionally, some minor forms of alkenes were detected in the ^{13}C NMR spectra and could be ascribed to internal alkenyl structures (fig. S14A). PP-air-wax contained ketones, aldehydes, and esters because of partial oxidation (fig. S15), but the alkenyl region resembled that of the PP-N_2-wax.

As with the PE-derived waxes, upcycling of PP-N_2-wax and PP-air-wax was conducted in air at 150°C over Mn stearate. PP-air-wax oxition was faster than that for PP-N_2-wax; the former showed a CI of ~0.9 after 4 hours (fig. S9C). Moreover, a possible epoxy structure was detected in oxidized PP-air-wax (fig. S16), indicating that poxy could be a potential oxidation intermediate between alkenyl and aldehydes. The fatty acids (PP-air-FA) that resulted from hydrolysis were characterized by NMR-HMBC and showed no detectable aldehyde but stronger ketone carbonyl signals than those of PE-O-FA. The acid carbonyl showed three correlations with protons (Fig. 3C and fig. S17), possibly indicating a 2-carboxylpropyl terminal structure. PP-air-FA exhibited an AN of 169 mg KOH/g, substantially higher than the theoretical value of 84 mg KOH/g for a monocarboxylic acid at 670 g/mol (C46) (table S4, entry 6), suggesting the presence of polyacids.

After both PE and PP were successfully converted to wax and fatty acids at high conversions, municipal PE/PP wastes (obtained in Blacksburg, VA) were sorted (if labeled), pulverized, and mixed to mimic a waste stream [high-density PE (HDPE, 25 wt %), PP (25 wt %), low-density PE (LDPE, 25 wt %), and PE/PP unsorted (25 wt %)]. Three batches of the PE/PP waste mixtures (500 mg per batch) were degraded into wax, resulting in an average yield of 82% in N_2. The lower wax yield of PE/PP mixtures from municipal waste streams was ascribed to the additives, paint, dye, and labels. The wax was further upcycled to fatty acids, giving an average AN of 57.3 mg KOH/g (Fig. 1D and table

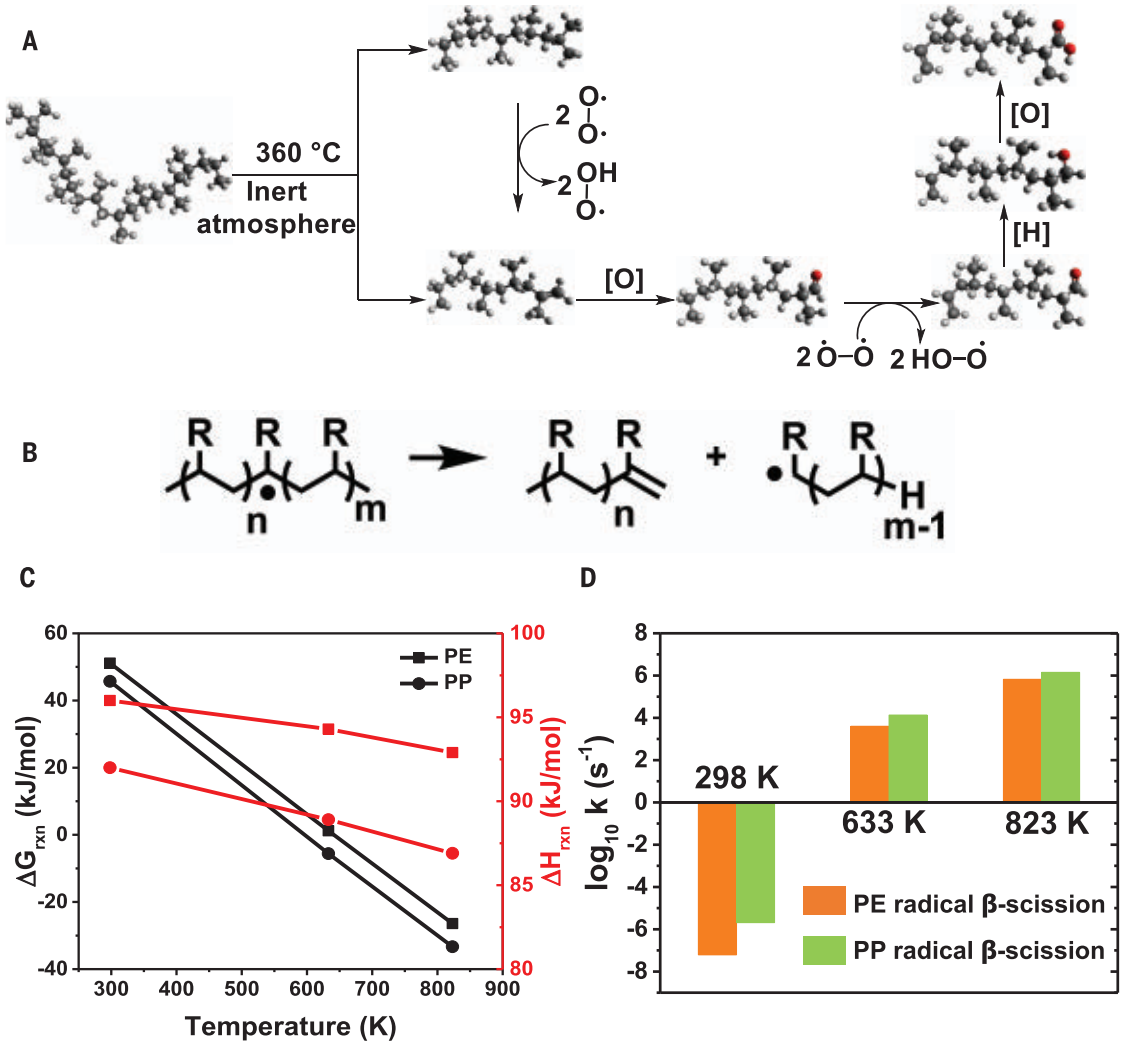

Fig. 4. Plausible reaction pathway, thermodynamics, and kinetics of β-chain scission in PE and PP. (**A**) The thermolysis of a model polymer chain into an alkane and alkene fragment and subsequent oxidation to a fatty acid, as captured by the simulations. (**B**) β-Scission of a radical in PE or PP, R=H or CH_3. (**C**) Thermodynamic parameters and (**D**) kinetic constants of PE β-scission and PP β-scission at 298, 633, and 823 K, as calculated according to the Benson group-additivity method (*39*, *40*).

S4, entry 8). The AN can be improved by tuning the oxygen level during degradation, the airflow during oxidation, and the upcycling temperature. Ketones and aldehydes could potentially be present in the product and can adjust the product viscosity, function as soap softeners (*35*), and modulate fragrance release (*18*).

Theoretical simulations

Density functional–based tight-binding (DFTB) simulations were used to gain a molecular understanding of the temperature-gradient degradation of PE and PP and to evaluate the subsequent oxidative upcycling reactions. DFTB and the extended tight-binding methods enable simulations of relatively large systems and reasonable timescales with good accuracy but are considerably faster than typical ab initio density functional theory (DFT) methods (*36*). Multiple (>10) molecular-dynamics trajectories were used to evaluate the PP and PE chain behavior. The model polymer chains undergo significant coiling and dynamical oscillations during the ab initio molecular dynamics (AIMD) simulations. The mechanisms of alkene formation from PE and PP are primarily radical β-scission and secondarily disproportionation (Fig. 4A and fig. S18), similar to the findings of previous reports (*3*, *7*, *38*). We focus the discussion on PP because it produces more olefin wax during degradation than does PE. The results show that chain scission occurs somewhat randomly along the backbone of the PP chain and that multiple bonds are broken to form alkene and alkane fragments (Fig. 4A and fig. S19). We note that the simulated fragment-size distributions agree with experimental observation and that there are more alkenes formed for PP than for PE. For example, in the experimental PE degradation, the initial C=C concentration in PE-N_2-wax was ~1.15 mmol/g on the basis of quantitative NMR (q-NMR, fig. S20 and table S5). By contrast, the C=C concentration in PP-N_2-wax was ~3.15 mmol/g, showing good qualitative agreement with the simulation results.

The degradation fragments from the simulations were then annealed by geometry optimization and modeled for reactivity toward oxygen at reduced temperatures. During the oxidation step, hydrogen extraction from a methyl or methylene group in the fragment was predicted to form a hydroperoxyl radical, which is prone to react with a readily formed aldehyde from alkenyl oxidation at the fragment end (Fig. 4A). This sequence initially produces an alcohol-like intermediate (H is transferred to carbonyl O on the aldehyde) that ultimately forms a carboxylic acid, by using a modified Baeyer-Villiger reaction. After the aldehyde accepts a H from the HOO•, the O-O• binds to the intermediate C-OH to form a carboxylic acid. The aldehyde intermediate was confirmed by the NMR-HMBC experiments on partially oxidized wax (fig. S16). The primary

intermediates found in this work also agree with the results of a previous study of paraffin oxidation over stearate (*29*), but we cannot rule out other potential oxidation pathways at this time.

Applying the qualitative insights from the DFTB simulations, we then used the Benson group-additivity method (*39*, *40*) to evaluate the standard Gibbs free energy (ΔG^{o}) (Fig. 4B and table S6) of PE β-scission (ΔG^{o}_{PE} = 51.1 kJ/mol) and PP β-scission (ΔG^{o}_{PP} = 45.7 kJ/mol). Thermodynamically, alkene formation from PP and PE is disfavored at 298 K (Fig. 4C and table S7). At elevated temperatures (633 K and 823 K), PE β-scission and PP β-scission become increasingly thermodynamically favorable. Under our experimental conditions (633 K), the reaction enthalpies and ΔG^{o} of PE and PP degradation are reduced ($\Delta H_{PP,633K}$ = 88.9 kJ/mol and $\Delta G_{PP,633K}$ = −5.60 kJ/mol; $\Delta H_{PE,633K}$ = 94.3 kJ/mol and $\Delta G_{PE,633K}$ = 1.20 kJ/mol). However, the process is still slightly disfavored for PE. Upon increasing the temperature to 823 K, both PE and PP have favored β-scission pathways ($\Delta H_{PP,823K}$ = 86.9 kJ/mol and $\Delta G_{PP,823K}$ = −33.1 kJ/mol; $\Delta H_{PE,823K}$ = 92.9 kJ/mol and $\Delta G_{PE,823K}$ = −26.5 kJ/mol). The kinetic parameters and constants of β-scission were also predicted by using the group-additivity method on the basis of model reactions (fig. S21A) (*41*). PP β-scission showed lower activation energies and higher kinetic constants than did PE at all temperatures (Fig. 4D and table S8). In general, alkene formation from PP β-scission is more favored and faster than that from PE (this agrees well with our experiments and simulations above). Our observation of PE– and PP–β-scission dependence on temperature also agrees well with the literature, in which the alkene yield from PE thermolysis increased from ~30% at ~600 K to ~70% at above 800 K, whereas that from PP thermolysis stayed high (>70%) regardless of the temperature (fig. S22) (*23*, *37*, *42*–*48*).

Technoeconomic analysis (TEA) of the process was assessed on the basis of a 10,000-ton/year capacity (tables S9 to S14). The total capital investment was estimated at USD 2.70 million with an annual net profit of USD 1.03 million, resulting in an internal rate of return of 39.1%, a payback period of 2.63 years, and an average return of investment of 33.0%, without any government subsidies or tax returns (table S15).

Outlook

The fatty acids produced in this study have a wide range of applications, either for being kept in the plastic loop or for downstream uses. The downstream surfactant products have at least twice the market value of virgin plastics, representing an economically competitive process for plastic-waste utilization. In addition, surfactants have a market volume matching that of end-of-life plastic wastes, thus representing a volume-impactful method for plastic-waste removal. Controlled thermolysis in a temperature-gradient reactor is the key to controlling the high yield of the wax products relative to small gaseous molecules. Unlike existing processes (*22*), our process tolerates oxygen and requires no expensive catalysts or stringent reaction conditions. The resulting products show good ANs for PE- (96 mg KOH/g) and PP-derived fatty acids (169 mg KOH/g), which can be further optimized by inhibiting side reactions (figs. S23 and S24). We anticipate the process to be amenable to a diverse range of other plastic wastes for producing high-value, large–market-volume products (e.g., fatty alcohols and sulfates) (*49*–*51*).

REFERENCES AND NOTES

1. R. Geyer, J. R. Jambeck, K. L. Law, *Sci. Adv.* **3**, e1700782 (2017).
2. S. R. Nicholson, N. A. Rorrer, A. C. Carpenter, G. T. Beckham, *Joule* **5**, 673–686 (2021).
3. J. Hopewell, R. Dvorak, E. Kosior, *Philos. Trans. R. Soc. Lond. Ser. B* **364**, 2115–2126 (2009).
4. Y. Zhang, G. Wang, Q. Zhang, Y. Ji, H. Xu, *Environ. Impact Assess. Rev.* **93**, 106728 (2022).
5. B. A. Abel, R. L. Snyder, G. W. Coates, *Science* **373**, 783–789 (2021).
6. L. T. J. Korley, T. H. Epps III, B. A. Helms, A. J. Ryan, *Science* **373**, 66–69 (2021).
7. C. Jehanno *et al*., *Nature* **603**, 803–814 (2022).
8. H. Chen, K. Wan, Y. Zhang, Y. Wang, *ChemSusChem* **14**, 4123–4136 (2021).
9. Z. Huang *et al*., *J. Am. Chem. Soc.* **144**, 6532–6542 (2022).
10. R. Cao *et al*., *Nat. Commun.* **13**, 4809–4819 (2022).
11. Z. Xu *et al*., *Proc. Natl. Acad. Sci. U.S.A.* **119**, e2203346119 (2022).
12. R. Conley, Ed., *Thermal Stability of Polymers* (Marcel Dekker, 1970).
13. X. Jia, C. Qin, T. Friedberger, Z. Guan, Z. Huang, *Sci. Adv.* **2**, e1501591 (2016).
14. F. Zhang *et al*., *Science* **370**, 437–441 (2020).
15. W. Zhang *et al*., *Science* **379**, 807–811 (2023).
16. R. J. Conk *et al*., *Science* **377**, 1561–1566 (2022).
17. N. M. Wang *et al*., *J. Am. Chem. Soc.* **144**, 18526–18531 2022).
18. A. Trachsel, C. Chapuis, A. Herrmann, *Flavour Fragrance J.* **28**, 280–293 (2013).
19. S. Kumar Sen, S. Raut, *J. Environ. Chem. Eng.* **3**, 462–473 (2015).
20. L. R. Melby, *Macromolecules* **11**, 50–56 (2002).
21. J. Y. Yao *et al*., Methods for the Decomposition of Contaminated Plastic Waste. US Patent US 11,220,586 B2 (2012).
22. U. Kanbur *et al*., *Chem* **7**, 1347–1362 (2021).
23. U. R. Gracida-Alvarez, M. K. Mitchell, J. C. Sacramento-Rivero, D. R. Shonnard, *Ind. Eng. Chem. Res.* **57**, 1912–1923 (2018).
24. A. Holmström, E. Sörvik, *J. Appl. Polym. Sci.* **18**, 3153–3178 (1974).
25. S. M. Al-Salem, A. Dutta, *Ind. Eng. Chem. Res.* **60**, 8301–8309 (2021).
26. G. Celik *et al*., *ACS Cent. Sci.* **5**, 1795–1803 (2019).
27. V. Vrkoslav, R. Miková, J. Cvačka, *J. Mass Spectrom.* **44**, 101–110 (2009).
28. J. W. Frankenfeld, Ed., *Study of Methods for Chemical Synthesis of Edible Fatty Acids and Lipids* (NASA, 1968).
29. P. George, E. K. Rideal, A. Robertson, *Proc. R. Soc. Lond. Ser. A* **185**, 288–309 (1946).
30. P. K. Roy, P. Surekha, R. Raman, C. Rajagopal, *Polym. Degrad. Stabil.* **94**, 1033–1039 (2009).
31. F. Xiao, X. Sun, Z. Li, X. Li, *ACS Omega* **5**, 12777–12788 (2020).
32. M. S. Stark, *J. Am. Chem. Soc.* **122**, 4162–4170 (2000).
33. A. K. Pandey, R. K. Varshnaya, P. Banerjee, *Eur. J. Org. Chem.* **2017**, 1647–1656 (2017).
34. K. P. Sullivan *et al*., *Science* **378**, 207–211 (2022).
35. A. Meziani, D. Touraud, A. Zradba, M. Clausse, W. Kunz, *J. Mol. Liq.* **84**, 301–311 (2000).
36. B. Hourahine *et al*., *J. Chem. Phys.* **152**, 124101 (2020).
37. H. Bockhorn, A. Hornung, U. Hornung, D. Schawaller, *J. Anal. Appl. Pyrolysis* **48**, 93–109 (1999).
38. T. Kuroki, T. Sawaguchi, S. Niikuni, T. Ikemura, *Macromolecules* **15**, 1460–1464 (1982).
39. S. W. Benson, J. H. Buss, *J. Chem. Phys.* **29**, 546–572 (1958).
40. R. L. Brown, S. E. Stein, in *NIST Chemistry WebBook*, NIST Standard Reference Database Number 69, P. J. Linstrom, W. G. Mallard, Eds. (National Institute of Standards and Technology, 2023); https://webbook.nist.gov/chemistry/.
41. M. K. Sabbe, M. F. Reyniers, V. Van Speybroeck, M. Waroquier, G. B. Marin, *ChemPhysChem* **9**, 124–140 (2008).
42. A. Marcilla, M. I. Beltrán, R. Navarro, *J. Anal. Appl. Pyrolysis* **86**, 14–21 (2009).
43. D. Zhao, X. Wang, J. B. Miller, G. W. Huber, *ChemSusChem* **13**, 1764–1774 (2020).
44. J. K. Y. Kiang, P. C. Uden, J. C. W. Chien, *Polym. Degrad. Stabil.* **2**, 113–127 (1980).
45. M. T. S. P. De Amorim, C. Comel, P. Vermande, *J. Anal. Appl. Pyrolysis* **4**, 73–81 (1982).
46. J. Michal, J. Mitera, S. Tardon, *Fire Mater.* **1**, 160–168 (1976).
47. G. Elordi, M. Olazar, G. Lopez, M. Artetxe, J. Bilbao, *Ind. Eng. Chem. Res.* **50**, 6650–6659 (2011).
48. P. Das, P. Tiwari, *Resour. Conserv. Recycling* **128**, 69–77 (2018).
49. H. Sabine, Oxidation of paraffinic hydrocarbons. US Patent US2391236A (1945).
50. D. V. Favis, Selective ozone oxidation of hydrocarbons. US Patent US2955123 (1956).
51. W. H. de Groot, *Sulphonation Technology in the Detergent Industry* (Springer, 1991).
52. Z. Xu *et al*., Chemical upcycling of polyethylene, polypropylene, and mixtures to high-value surfactants, Dryad (2023); https://doi.org/10.5061/dryad.c866t1gc5.

ACKNOWLEDGMENTS

The authors acknowledge the Chemistry Chromatography Center at Virginia Tech, especially M. Ashraf-Khorassani, for providing GC and GC-MS support. The authors also acknowledge the Mass Spectrometry Incubator at Virginia Tech, especially R. Helm and K. Ray for their support on APCI-MS. The molecular simulations were performed at the Center for Nanophase Materials Sciences, a US Department of Energy (DOE) Office of Science User Facility operated at Oak Ridge National Laboratory. **Funding:** G.L. acknowledges support from the Department of Chemistry and the Dean's Discovery Fund at Virginia Tech. This material is partially based on the work supported by NSF Award DMR-1752611 through the CAREER award. Mechanistic studies of the deconstruction processes were partially supported by the US DOE Office of Science, Materials Sciences and Engineering Division. The simulations used resources of the Compute and Data Environment for Science (CADES) at the Oak Ridge National Laboratory, which is supported by the Office of Science of the US DOE under contract no. DE-AC05-00OR22725. Funding for N.A.R. and J.M. was provided in part by the US DOE Office of Energy Efficiency and Renewable Energy, Advanced Manufacturing Office (AMO) and Bioenergy Technologies Office (BETO). This work was performed as part of the BOTTLE Consortium and was supported by AMO and BETO under contract no. DE-AC36-08GO28308 with the National Renewable Energy Laboratory, operated by Alliance for Sustainable Energy. **Author contributions:** G.L. conceived and supervised the project. G.L. and Z.X. designed the project. Z.X. and N.E.M. conducted degradation-upcycling reactions and GC, GC-MS, and FTIR measurements. Z.X. and P.V. performed NMR experiments. B.G.S. conducted DFT simulations. Q.Z. performed TEA and heat and mass transfer analyses. N.E.M. and C.P. performed rheological experiments. N.R. and J.M. conducted HT-GPC measurements. Z.X. determined the standard Gibbs free energies for the degradation reactions. M.S. performed titrations to determine the ANs. N.E.M. evaluated the effect of temperature gradient on the degradation reactions. G.L., B.G.S., Z.X., and N.E.M. analyzed the data, interpreted the results, and wrote the manuscript. All authors proofread the manuscript. **Competing interests:** G.L., Z.X., and N.E.M. are inventors on Provisional Patent Application no. 63/462,863 pertaining to this work. **Data and materials availability:** Data pertaining to this work are available in the supplementary materials and Dryad (*52*). **License information:** Copyright © 2023 the authors, some rights reserved; exclusive licensee American Association for the Advancement of Science. No claim to original US government works. https://www.science.org/about/science-licenses-journal-article-reuse

SUPPLEMENTARY MATERIALS

science.org/doi/10.1126/science.adh0993
Figs. S1 to S31
Tables S1 to S18
References (*53*–*103*)

Submitted 9 February 2023; accepted 16 June 2023
10.1126/science.adh0993

PLANT WATER USE

Global water use efficiency saturation due to increased vapor pressure deficit

Fei Li[1,2]*, Jingfeng Xiao[3]*, Jiquan Chen[2], Ashley Ballantyne[4,5], Ke Jin[1], Bing Li[1], Michael Abraha[2], Ranjeet John[6]

The ratio of carbon assimilation to water evapotranspiration (ET) of an ecosystem, referred to as ecosystem water use efficiency (WUE_{eco}), is widely expected to increase because of the rising atmospheric carbon dioxide concentration (C_a). However, little is known about the interactive effects of rising C_a and climate change on WUE_{eco}. On the basis of upscaled estimates from machine learning methods and global FLUXNET observations, we show that global WUE_{eco} has not risen since 2001 because of the asymmetric effects of an increased vapor pressure deficit (VPD), which depressed photosynthesis and enhanced ET. An undiminished ET trend indicates that rising temperature and VPD may play a more important role in regulating ET than declining stomatal conductance. Projected increases in VPD are predicted to affect the future coupling of the terrestrial carbon and water cycles.

The rapid rise of atmospheric CO_2 concentration (C_a) has led to substantial changes in global terrestrial carbon (C) and water cycles, including an increase in the net assimilation of C through photosynthesis (A) and/or a decrease in transpiration (T) through declining stomatal conductance (g_s) (*1*–*3*). Although the theoretical importance of rising C_a in regulating plant water use efficiency (WUE, which is equal to A/T), a metric reflecting the trade-off between C gain and water loss, has been recognized since the 1970s (*4*), its underlying mechanisms remain debatable (*5*, *6*). Studies based on free-air CO_2-enrichment experiments have found increases in A and decreases in g_s across C3 and C4 plants, resulting in enhanced plant WUE (*6*–*8*). Mathias and Thomas (*9*) showed an ~40% increase in the intrinsic WUE of trees due to rising C_a based on a global database of tree-ring isotopic discrimination. At the ecosystem level, numerous studies have reported a substantial increase in ecosystem WUE (WUE_{eco}) over various biomes and scales (*10*, *11*), with a 48 ± 22% increase at the global scale (*12*). Previous studies have focused on quantifying the magnitude of increased WUE_{eco} (*11*–*13*). To date, few studies have reported on WUE_{eco} trends in response to the environmental forcings at the global scale.

[1]Grassland Research Institute, Chinese Academy of Agricultural Sciences, Hohhot 010010, China. [2]Center for Global Change and Earth Observations, Michigan State University, East Lansing, MI 48823, USA. [3]Earth Systems Research Center, Institute for the Study of Earth, Oceans, and Space, University of New Hampshire, Durham, NH 03824, USA. [4]Department of Ecosystem and Conservation Science, University of Montana, Missoula, MT 59801, USA. [5]Laboratoire des Sciences du Climat et de l'Environnement, CEA-CNRS-UVSQ, 91190 Gif-sur-Yvette, France. [6]Department of Biology and Department of Sustainability, University of South Dakota, Vermillion, SD 57069, USA.
*Corresponding author. Email: lifei01@caas.cn; j.xiao@unh.edu

Increased WUE_{eco} is believed to result from the CO_2 fertilization effect that enhances gross primary productivity (GPP) through photosynthesis and reduces water loss through evapotranspiration (ET) because of declining g_s (*6*, *13*). The determinants of WUE_{eco} (WUE_{eco} = GPP/ET) are highly dependent on vegetation types and are influenced by environmental changes (*9*, *14*). Increasingly, vapor pressure deficit (VPD) is recognized as the most important atmospheric forcing after C_a because it imposes water stress on photosynthesis (*9*, *11*, *15*). Recently, a meta-analysis of eddy covariance (EC) observations and simulations of satellite-driven models indicated a weakening response in plant growth since 2000 due to rising VPD and/or nutrient limitation (*15*–*17*). At the same time, climate warming and increasing leaf area index (LAI) may intensify the ET response, which in turn will down-regulate the WUE_{eco} increase (*18*). Additional constraints on WUE_{eco} might stem from the stoichiometric availability of nitrogen (N) and phosphorus (P), which could slow plant growth due to the progressive nutrient limitation of CO_2 fertilization (*17*, *19*, *20*). Unfortunately, it remains unknown how these multifaceted factors affect global WUE_{eco} (*16*).

Here, we found that global WUE_{eco} has saturated since 2001 due to increased VPD. To examine the trends in WUE_{eco} of global terrestrial ecosystems, estimates of GPP, ET, and WUE_{eco} were achieved using 24 machine learning (ML) approaches (supplementary text S1 and figs. S1 to S8) by fusing the FLUXNET in situ observations of CO_2 and water vapor fluxes, satellite-derived observations, and climate reanalysis data (table S1). The range and median values for all models are presented to show the uncertainties in the analysis. We examined how climate change and elevated C_a interactively affect the underlying processes of GPP and ET, as well as global WUE_{eco}.

Results and discussion

Changes in WUE_{eco}

Average global terrestrial WUE_{eco} over the study period (1982–2016) was 1.96 g C kg^{-1} H_2O (table S2), which is determined by a total CO_2 uptake of 1155.57 g C m^{-2} $year^{-1}$ through photosynthesis and water loss of 541.04 kg H_2O m^{-2} $year^{-1}$ through ET. In response to the 18% rise in C_a (i.e., from 341 to 403 ppm) between 1982 and 2016, the overall global WUE_{eco} increased significantly (trending slope = 0.0005 g C kg^{-1} H_2O $year^{-1}$, P = 0.03), as did GPP and ET, which increased at rates of 1.42 ± 0.48 g C m^{-2} $year^{-2}$ and 0.7 ± 0.15 kg H_2O m^{-2} $year^{-2}$, respectively. The significant increase in WUE_{eco} was mainly due to a significant trend during 1982–2000 (0.0022 g C kg^{-1} H_2O $year^{-1}$, P < 0.001); thereafter, WUE_{eco} exhibited no significant trending (0.0005 g C kg^{-1} H_2O $year^{-1}$, P = 0.38). The Michaelis-Menten model indicates that the global WUE_{eco} saturated during 2001–2016 and stabilized at ~1.96 g C kg^{-1} H_2O (Fig. 1A).

The apparent saturation in global WUE_{eco} during 2001–2016 was most likely due to the adverse forcing of continued VPD rise, as evidenced by a significant correlation between [C_a/VPD] and WUE_{eco} (r = 0.65, P < 0.001, fig. S9A), but with little evidence of saturation due to vegetation regrowth or land cover change (supplementary text S2 and figs. S10 to S12). WUE_{eco} is physically regulated by VPD, which suppresses ecosystem CO_2 fertilization through g_s controlling the inward diffusion of CO_2 (*1*), i.e., $A = g_s \cdot (c_a - c_i)$, where $(c_a - c_i)$ represents the difference between the ambient and leaf intercellular mole fractions of CO_2 and the outward diffusion of H_2O, i.e., $T = 1.6 \cdot g_s \cdot (e_i - e_a)$, where $(e_i - e_a)$ represents the difference between leaf intercellular and ambient water vapor pressure and is commonly substituted by atmospheric VPD (*11*). The strong influence of [C_a/VPD] on WUE_{eco} was consistent in both the Northern Hemisphere (r = 0.44, P = 0.008; fig. S9B) and the Southern Hemisphere (r = 0.66, P < 0.001; fig. S9C). Concurrently, the increasing rate of GPP slowed by a factor of 2.14 (2.96 ± 0.55 g C m^{-2} $year^{-2}$ during 1982–2000 compared with 1.38 ± 1.15 g C m^{-2} $year^{-2}$ during 2001–2016), whereas the rate of ET increase declined by a factor of 1.65 (1.19 ± 0.15 kg H_2O m^{-2} $year^{-2}$ during 1982–2000 compared with 0.72 ± 0.28 kg H_2O m^{-2} $year^{-2}$ during 2001–2016) (Fig. 1B). Our finding of the saturation of WUE_{eco} increase at the global scale was corroborated by ecosystem scale FLUXNET observations: 71% of the EC sites demonstrated a WUE_{eco} increase with a higher median trend during 1997–2000, whereas only 51% of the EC sites showed WUE_{eco} increases with a lower median trend after 2000 (Fig. 1C).

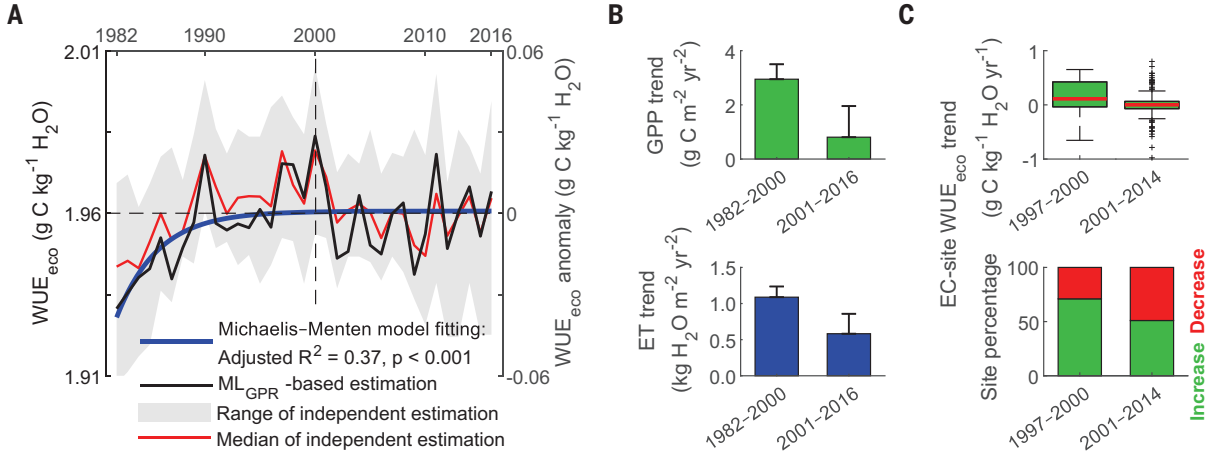

Fig. 1. Changes in WUE_{eco} and its determinants (GPP and ET) over vegetated lands during 1982–2000 and 2001–2016. (**A**) Changes in WUE_{eco} from an ensemble of 24 ML algorithms and Michaelis-Menten model fitting to the optimal estimation using ML Gaussian process regression (i.e., the ML_{GPR}) model. (**B**) Annual rates of change (trend) in gridded estimates of GPP and ET from 24 ML algorithms. (**C**) Box statistics describing changes in the rate of WUE_{eco} and corresponding percentages of increase and decrease among EC sites obtained from the global FLUXNET network.

Significant increases in WUE_{eco} across global biomes during 1982–2000 were primarily due to increases in the Northern Hemisphere (Fig. 2A and table S2). From 1982 through 2000, the Northern Hemisphere showed a stronger increase in GPP than did the Southern Hemisphere (Fig. 2B). By contrast, ET in the Northern Hemisphere showed a smaller increase than that of the Southern Hemisphere. During 2001–2016, although GPP in the Northern Hemisphere increased, the continuously strong ET responses, which were strikingly above 53°N (Fig. 2C), down-regulated WUE_{eco}, resulting in an insignificant WUE_{eco} trend in the Northern Hemisphere (supplementary text S3 and figs. S13 and S14) and apparent saturation over global terrestrial ecosystems. Significant decreasing trends for GPP and ET were observed in Africa and parts of South America. Among the five major biomes, divergent changes in WUE_{eco} were observed, with a noticeable decline in shrublands, grasslands, and croplands during 2001–2016, whereas forests and savannas showed insignificant trends over the study period 1982–2016 (fig. S15).

Climate change impacts on ecosystem CO_2 uptake

Our GPP estimates based on an ensemble of 24 ML algorithms show that ecosystem photosynthesis also slowed down after the year 2000 (Fig. 3A). Our analysis based on six independent GPP products (table S3) revealed a similar pattern (Fig. 3A). Stepwise regression analysis indicated that 72% of the variance in GPP was attributed to climate change and rising C_a, with effective coefficients of 0.66, 1.07, and −1.02 for air temperature (T_a), C_a, and VPD, respectively (Table 1). This implies that the enhancement effect of CO_2 fertilization and the net negative effect of climate change jointly influence ecosystem CO_2 uptake over global terrestrial ecosystems. Given the complex direct and indirect interactions among the effective variables (e.g., T_a and VPD), partial least-squares structural equation modeling analysis achieved consistent results, with path coefficients of 0.5, 0.82, and −0.81 for T_a, C_a, and VPD, respectively, providing additional evidence for the stronger VPD constraint than T_a enhancement of global GPP (fig. S16).

To futher examine the underlying interactive effects of these three factors (i.e., the physical effects of [C_a/VPD] to WUE_{eco} and the positive factor of T_a), we combined these factors with the form of [$T_a \times C_a$/VPD], which explained 74% of the variance in GPP, as evidenced by the well-matched changing trajectories between GPP and [$T_a \times C_a$/VPD] (Fig. 3A). This implies that the combined effects of [$T_a \times C_a$/VPD] dominate photosynthesis. After removing the positive effect of C_a, [T_a/VPD] increased before 2000 but declined throughout the remaining period, concurrent with the slowdown in GPP and LAI increases (fig. S17) (*21*, *22*) that appears to have down-regulated WUE_{eco}.

The negative effects of increasing VPD almost completely offset the positive effects of CO_2 fertilization on WUE_{eco} of global terrestrial ecosystems (Fig. 3B), which is more pronounced in the Southern Hemisphere (−0.95 VPD versus 0.74 C_a) than in the Northern Hemisphere (−0.61 VPD versus 0.77 C_a) (Table 1). Furthermore, rising T_a imposed a 0.73 positive effect on ecosystem CO_2 uptake in the Northern Hemisphere but not in the Southern Hemisphere. The combination of these influences resulted in more robust increases in GPP in the Northern Hemisphere than in the Southern Hemisphere (*23*). Consequently, global WUE_{eco} trends were dominated by changes in the Northern Hemisphere throughout the study period. Extensive decreases in [T_a/VPD] were observed over the land areas below 53°N from the period 1982–2000 to the period 2001–2016 (Fig. 3C). This led to consistent decreases in GPP, thus slowing the rate of WUE_{eco} increase. By contrast, areas north of 53°N showed increased [T_a/VPD], which has enhanced GPP, but has also enhanced ET to a much greater extent, resulting in a declining WUE_{eco} (fig. S14). This finding is inconsistent with the view that WUE_{eco} in high latitudes responds positively to rising T_a (*24*). The stronger response of ET to rising T_a than GPP may be an important factor in the down-regulation of WUE_{eco}.

The combined effect of [$T_a \times C_a$/VPD] was consistent among the five major biomes, showing the strongest effect on shrublands (78%) and the weakest effect on savannas (35%) (Table 1). For forests, grasslands, and croplands, the effect varied from 45 to 76% due to the positive effects of increasing T_a and the negative effects of increasing VPD on GPP. Precipitation had a positive effect on GPP on the global scale, particularly in savannas and grasslands, and the overall impact was greater in the Southern Hemisphere than in the Northern Hemisphere. This finding corresponds well with the extensive droughts that have occurred in the Southern Hemisphere in recent decades (*25*). Enhanced CO_2 uptake was previously assumed to be associated with increasing photosynthetically active radiation (PAR) at the ecosystem to biome scale (*16*, *26*). However, our study did not detect a strong PAR

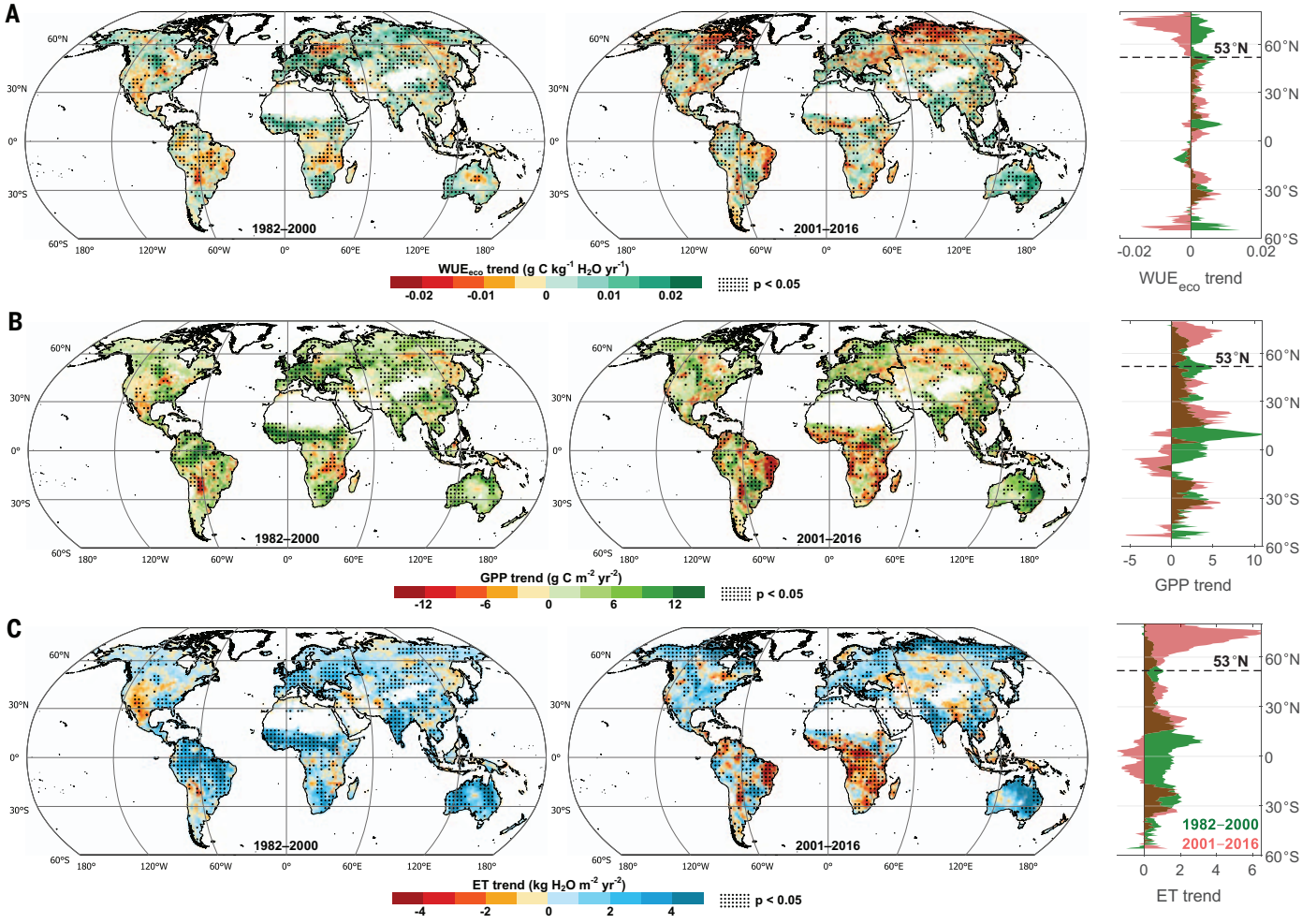

Fig. 2. Global patterns in trends of WUE_{eco} and its determinants, GPP and ET, over 1982–2000 and 2001–2016. (**A**) WUE_{eco}. (**B**) GPP. (**C**) ET. The changing trends are calculated on a per-pixel basis (0.5 × 0.5°) over time and dotted if statistically significant ($P < 0.05$). Trends aggregated by latitude are illustrated in the far right panels, where recent trends during 2001–2016 (red) are compared with past trends during 1982–2000 (green).

effect at the global scale. Instead, increasing PAR exhibited a negative impact on GPP of shrublands in the Southern Hemisphere, likely because excessive increases in PAR can elevate VPD and thus reinforce water stress on vegetation (*15, 25*). Plants must open their stomata to allow CO_2 molecules to diffuse into the chloroplast stroma for ongoing photosynthesis. Once the moist interior of the leaf is exposed to the drier air, vapor pressure inside the stomata will decrease, resulting in the counteraction of CO_2 fertilization (*9*). This indicates that although CO_2 fertilization imposes a substantial effect on global biome WUE_{eco}, this enhancement is down-regulated by the ET response (*27*).

Climate change impacts on ecosystem ET

There has been an intense debate over whether CO_2 fertilization reduces g_s, and thereby decreases ET and enhances WUE_{eco} (*6, 28*). However, consistent with 26 global ET products derived from different mechanistic models and ML algorithms (table S3), our estimates based on 24 ML models indicate that global ET over vegetated lands has increased significantly (Fig. 4A), with a stronger increase during 1982–2000 and a weaker increase during 2001–2016. On the basis of an ET decomposition model developed from the Penman-Monteith equation (*18*), ET showed a significant positive correlation with transpiration (fig. S18), indicating that the increasing trends in ET were significantly associated with a rise in transpiration, including sparsely vegetated areas north of 53°N (fig. S19). This increasing rate in ET also corresponded to the increasing rate in GPP across EC sites ($r = 0.62$, $P < 0.001$; Fig. 4B). This suggests that the saturation in global WUE_{eco} during 2001–2016 was synchronously attributable to reduced GPP and increased ET, largely driven by increases in transpiration. Consistent with the currently prevailing view that CO_2 fertilization reduces plant g_s (*7, 8*), significant decreases in canopy g_s over the global biomes from 1982 to 2016 were observed in this study (fig. S20) and were inferred to reduce ecosystem ET (*6, 11*). However, this school of thought fails in considering the strong response of ET due to climate warming (e.g., north of 53°N). Other similar studies did not detect widespread g_s reductions (*9, 10*). In this case, ecosystem ET was expected to increase according to the approximately linear relationship of ET with g_s and VPD (see supplementary equation 5). Thus, we challenge the view that g_s-induced ET decline favors soil water conservation and enhances plant water-deficit resistance in arid ecosystems (*29, 30*). Instead, we propose that the negative effects of the continuous increase in VPD associated with global warming counteract the effects of CO_2 fertilization, thereby impairing plant growth, as evidenced by satellite-derived observations of vegetation browning (*21, 22*).

Oligotrophication

There is controversy over whether elevated C_a depresses WUE_{eco} by inducing stoichiometric limitation of CO_2 uptake by N and P (i.e., oligotrophication) and/or their disequilibrium

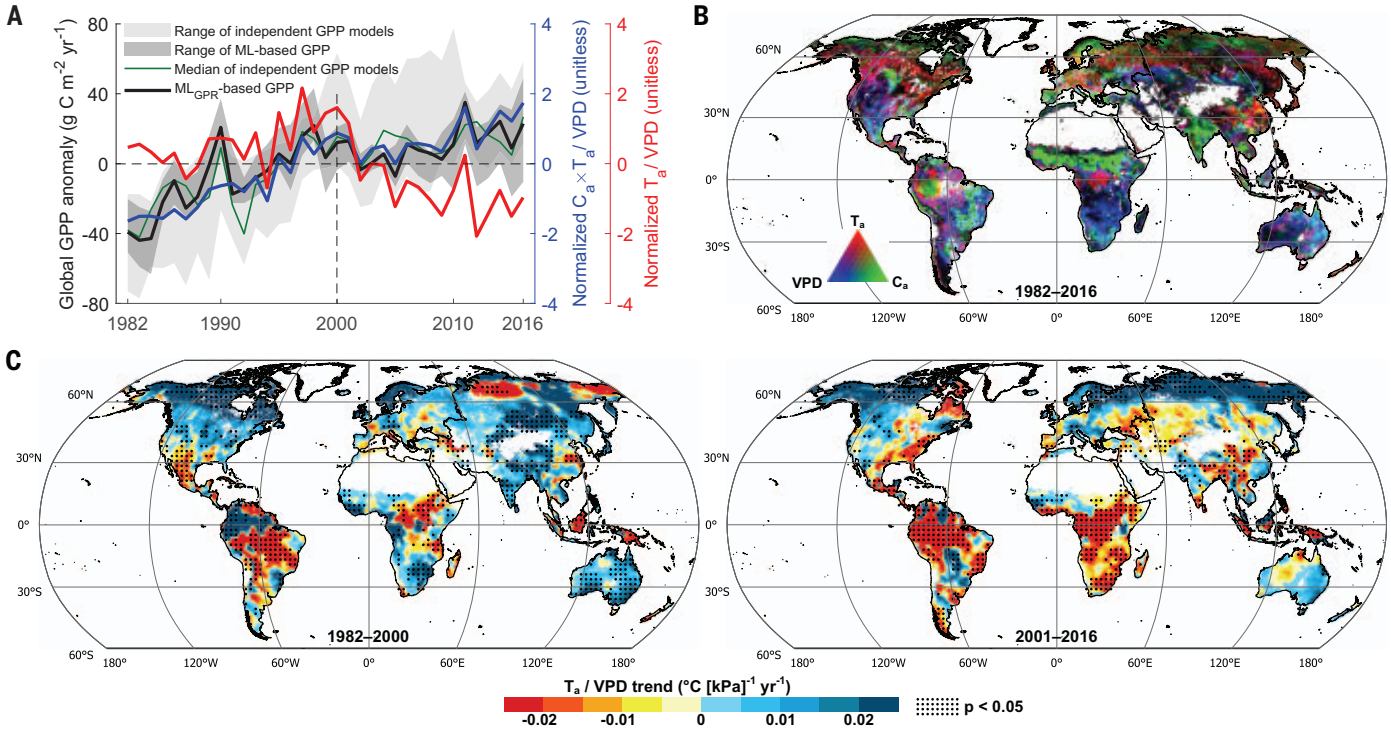

Fig. 3. Changes in GPP resulting from the combined effects of T_a, C_a, and VPD. (**A**) Changes in global GPP estimates based on an ensemble of 24 ML algorithms of this study and independent GPP products against driving factors of [$T_a \times CO_2$/VPD] and [T_a/VPD]. (**B**) Spatial patterns of composited RGB image of T_a, CO_2, and VPD covariance with GPP over global vegetated lands. (**C**) Changes in the spatial patterns of trends in [T_a/VPD] during the periods 1982–2000 and 2001–2016; trends are dotted if statistically significant ($P < 0.05$).

Table 1. Changes in GPP due to the effects of LAI and environmental variables, independently and interactively, over the globe, the Northern Hemisphere (NH), the Southern Hemisphere (SH), and the five major vegetation types in the period 1982–2016. The relationships between environmental variables and GPP were calculated using stepwise regression analysis, where the environmental variables were normalized by subtracting the mean of each term and dividing by the standard deviation for cross-comparison of the effective coefficients. A higher absolute coefficient value indicates a stronger effect on promoting or diminishing GPP changes. The relationships of GPP with LAI and combined environmental variables, i.e., [$T_a \times C_a$/VPD], were quantified with a statistical measure of R^2. For the excluded variables through stepwise regression analysis, correlation analysis was individually implemented to indicate a significantly positive or negative effect on GPP changes in cases with a significance level of 0.05.

Driving factors		GPP changes							
		Globe	NH	SH	Forests	Shrublands	Savannas	Grasslands	Croplands
Effects of LAI	R^2	0.80	0.84	0.61	0.61	0.19	0.62	0.85	0.87
Effects of environmental variables	C_a	1.07	0.77	0.74	0.93	0.99		+	0.80
	T_a	0.66	0.73		0.68	+		0.71	0.57
	PAR			–		−0.34		−0.33	
	P_r	+		+			0.40	+	
	VPD	−1.02	−0.61	−0.95	−0.79	−0.34	–		−0.55
	Adjusted R^2	0.72	0.81	0.59	0.66	0.84	0.14	0.49	0.77
Effects of [$T_a \times C_a$/VPD]	R^2	0.74	0.82	0.51	0.45	0.78	0.35	0.62	0.76

with widespread changes in N deposition input to ecosystems (*19*, *20*). With the effective coefficient of CO_2 fertilization separated from the linear regression analysis (Fig. 3B), we examined the effects of CO_2 fertilization in relation to leaf N and P limitations. First, we examined changes in foliar N and P concentrations using observations of various tree species collected from 410 sites during 1990–2016, and found that 20.7 and 22.7% of the sites showed a significant decline in leaf N and P, respectively (*17*). However, we did not identify any significant relationships between changes in leaf N and P concentrations and the effects of CO_2 fertilization (Fig. 5A). Second, we examined disequilibrium quantified by the ratios of foliar N resorption efficiency (N_{RE}) and P resorption efficiency (P_{RE}) (i.e., N_{RE}/P_{RE}

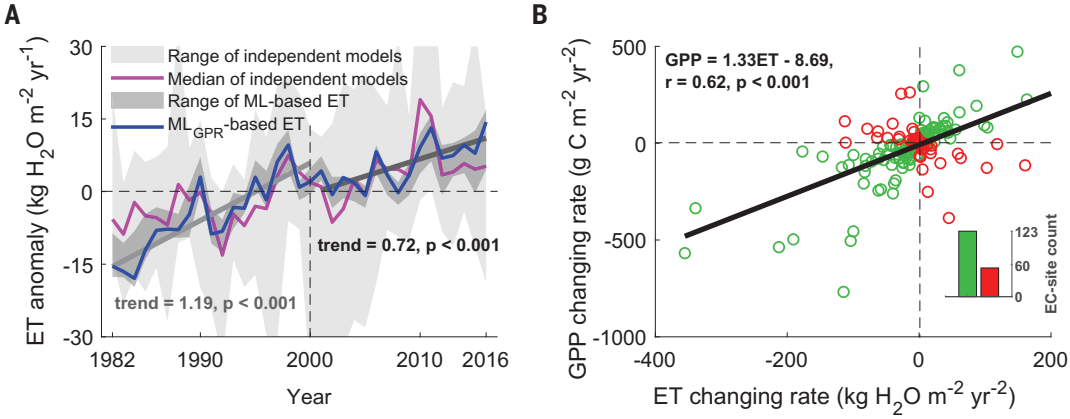
A
Range of independent models
Median of independent models
Range of ML-based ET
ML$_{GPR}$-based ET
trend = 0.72, p < 0.001
trend = 1.19, p < 0.001
ET anomaly (kg H$_2$O m^{-2} yr^{-1})
Year
B
GPP = 1.33ET - 8.69,
r = 0.62, p < 0.001
GPP changing rate (g C m^{-2} yr^{-2})
ET changing rate (kg H$_2$O m^{-2} yr^{-2})
EC-site count

Fig. 4. Changes in ET over global vegetated lands during 1982–2016. (**A**) Comparisons between the ML-based ET estimates and 26 ET products used in previous studies. (**B**) Relationship between changing rates in ET and GPP derived from global FLUXNET observations collected in the period 1997–2014, where green circles represent ET and GPP showing consistent directions and red circles represent those showing inconsistent directions.

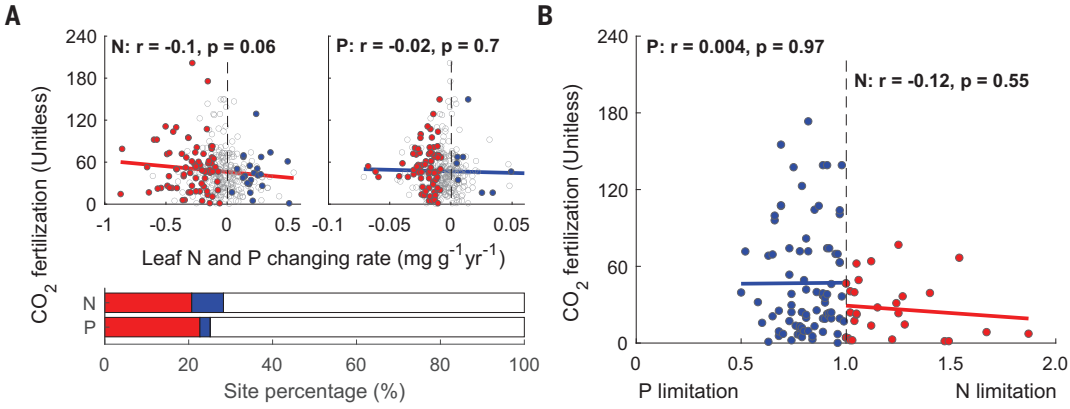
A
N: r = -0.1, p = 0.06
P: r = -0.02, p = 0.7
Leaf N and P changing rate (mg g^{-1}yr^{-1})
CO$_2$ fertilization (Unitless)
Site percentage (%)
B
P: r = 0.004, p = 0.97
N: r = -0.12, p = 0.55
P limitation
N limitation

Fig. 5. Responses of CO_2 fertilization to nutrient limitations by N and P. (**A**) Relationship between changing rate in leaf N and P concentrations and C_a coefficients separated from the linear regression analysis, where the percentage of sites with significant changes ($P < 0.05$) in leaf N and P concentrations are stacked as red (decrease) and blue (increase) bars. (**B**) Relationship between N_{RE}/P_{RE} ratios and C_a coefficients.

ratios) (*31*). We did not find significant decreases in the effects of CO_2 fertilization linked to the N_{RE}/P_{RE} ratios deviating from the equilibrium state (i.e., $N_{RE}/P_{RE} = 1$) (Fig. 5B). To examine the potential influence of scale mismatches between upscaled GPP estimates and site-level N and P data, we conducted the same analysis with finer-resolution flux estimates to analyze the effect of nutrient limitations and found similar results (supplementary text S4 and fig. S21). Previous studies suggested that in response to increasing nutrient limitations, plants intensify transpiration to facilitate the uptake of stoichiometric elements from the soil (*32*). Although our results indicate an increase in transpiration, especially at high latitudes, this is probably the result of increasing atmospheric demand rather than nutrient demand. Many studies have suggested that global ecosystems have been widely fertilized by atmospheric N and P deposition and anthropogenic nutrient enrichment (*33*, *34*), but their effectiveness at enhancing ecosystem CO_2 uptake is generally believed to be lower than the negative impacts (*35*). Nevertheless, with so little known about the amount of N and P equilibrium across global ecosystems, it is not affirmative yet to conclude that oligotrophication may be altering coupled C and water cycles.

Conclusions

Focusing on the widespread assertions that plant-to-ecosystem WUE has increased because of the rising C_a, we examined the combined effects of rising C_a, T_a, and VPD on WUE_{eco} over global biomes. We observed an overall significant increase in WUE_{eco} throughout 1982–2016, with a substantial contribution from the period 1982–2000; thereafter, increasing WUE_{eco} has evidently stalled, indicating saturation. The T_a rise–induced increases in VPD diminished WUE_{eco} by suppressing ecosystem gross photosynthesis. At the same time, the apparent saturation in WUE_{eco} was also influenced by increased ET, thus challenging the currently prevailing view that g_s decline reduces transpiration and thus increases WUE_{eco}. Existing climate data and climate projections indicate a likely sustained WUE_{eco} "saturation" into the future because of a durable VPD increase (supplementary text S5 and fig. S22). With other biogeochemical elemental constraints starting to emerge, it remains to be seen whether WUE_{eco} deviates from this course. Furthermore, the saturation of WUE_{eco} does not appear to be the result of changes in vegetation regrowth and land cover, nor in nutrient constraints on photosynthesis due to N and P changes or their disequilibrium. This study emphasizes that human reliance on nature-based climate sinks to achieve C neutrality may be undermined by the adverse effects of climate warming.

REFERENCES AND NOTES

1. M. A. Adams, T. N. Buckley, T. L. Turnbull, *Nat. Clim. Chang.* **10**, 466–471 (2020).
2. M. K. Cao, F. I. Woodward, *Nature* **393**, 249–252 (1998).
3. A. P. Ballantyne, C. B. Alden, J. B. Miller, P. P. Tans, J. W. C. White, *Nature* **488**, 70–72 (2012).
4. J. L. Hatfield, C. Dold, *Front. Plant Sci.* **10**, 103 (2019).
5. P. E. López-Calcagno *et al.*, *Nat. Plants* **6**, 1054–1063 (2020).
6. C. J. Bernacchi, B. A. Kimball, D. R. Quarles, S. P. Long, D. R. Ort, *Plant Physiol.* **143**, 134–144 (2007).
7. S. J. E. Wand, G. F. Midgley, M. H. Jones, P. S. Curtis, *Glob. Chang. Biol.* **5**, 723–741 (1999).
8. E. A. Ainsworth, A. Rogers, *Plant Cell Environ.* **30**, 258–270 (2007).
9. J. M. Mathias, R. B. Thomas, *Proc. Natl. Acad. Sci. U. S. A.* **118**, e2014286118 (2021).
10. R. Guerrieri *et al.*, *Proc. Natl. Acad. Sci. U. S. A.* **116**, 16909–16914 (2019).
11. T. F. Keenan *et al.*, *Nature* **499**, 324–327 (2013).
12. S. C. Dekker, M. Groenendijk, B. B. B. Booth, C. Huntingford, P. M. Cox, *Earth Syst. Dyn.* **7**, 525–533 (2016).

13. M. Saurer *et al*., *Glob. Chang. Biol.* **20**, 3700–3712 (2014).
14. S. S. Cooley, J. B. Fisher, G. R. Goldsmith, *Nat. Plants* **8**, 341–345 (2022).
15. W. Yuan *et al*., *Sci. Adv.* **5**, eaax1396 (2019).
16. D. Baldocchi, J. Penuelas, *Glob. Chang. Biol.* **25**, 1191–1197 (2019).
17. S. Wang *et al*., *Science* **370**, 1295–1300 (2020).
18. Y. Q. Zhang *et al*., *Remote Sens. Environ.* **222**, 165–182 (2019).
19. C. Terrer *et al*., *Nat. Clim. Chang.* **9**, 684–689 (2019).
20. J. M. Craine *et al*., *Nat. Ecol. Evol.* **2**, 1735–1744 (2018).
21. R. de Jong, J. Verbesselt, M. E. Schaepman, S. de Bruin, *Glob. Chang. Biol.* **18**, 642–655 (2012).
22. N. Q. Pan *et al*., *Remote Sens. Environ.* **214**, 59–72 (2018).
23. P. Ciais *et al*., *Nature* **568**, 221–225 (2019).
24. M. Huang *et al*., *Glob. Chang. Biol.* **21**, 2366–2378 (2015).
25. M. Zhao, S. W. Running, *Science* **329**, 940–943 (2010).
26. J. K. Green *et al*., *Glob. Chang. Biol.* **28**, 2940–2955 (2022).
27. S. Zhou *et al*., *Global Biogeochem. Cycles* **31**, 1639–1655 (2017).
28. B. E. Medlyn *et al*., *New Phytol.* **149**, 247–264 (2001).
29. X. Lian *et al*., *Nat. Rev. Earth Environ.* **2**, 232–250 (2021).
30. G. W. Wall *et al*., *Agron. J.* **98**, 354–381 (2006).
31. E. Z. Du *et al*., *Nat. Geosci.* **13**, 221–226 (2020).
32. T. S. El-Madany *et al*., *J. Geophys. Res. Biogeosci.* **126**, e2020JG006005 (2021).
33. E. Tipping *et al*., *Environ. Sci. Process. Impacts* **16**, 1608–1617 (2014).
34. D. Ackerman, D. B. Millet, X. Chen, *Global Biogeochem. Cycles* **33**, 100–107 (2019).
35. N. Gruber, J. N. Galloway, *Nature* **451**, 293–296 (2008).

ACKNOWLEDGMENTS

We thank the reviewers for valuable comments, global FLUXNET communities for making the EC measurements of C and water fluxes available, and Y. Zhang for providing programming code to estimate transpiration. **Funding:** This project was supported by the Natural Science Foundation of Inner Mongolia Autonomous Region (grant 2021SHZR1945) and the Agricultural Science and Technology Innovation Program of CAAS (grant CAAS-ASTIP-2020-IGR-04). J.X. was supported by the University of New Hampshire and the Iola Hubbard Climate Change Endowment. J.C. was supported by the Fulbright Global Scholar program. **Author contributions:** F.L. designed the study, conducted model simulations, and analyzed results. J.X. contributed to the improvement of study design and text drafting. J.C., A.B., K.J., M.A., and R.J. provided critical insights on results interpretation and text editing. B.L. contributed to the collection of public GPP and ET data products and saturation analysis. **Competing interests:** The authors declare no competing financial interests. **Data and materials availability:** All datasets of the ML and FLUXNET based Carbon and Water Fluxes (MF-CW), including monthly ET, GPP, and yearly WUE_{eco}, are available at the Global Ecology Group Data Repository at https://globalecology.unh.edu/data/MF-CW.html. **License information:** Copyright © 2023 the authors, some rights reserved; exclusive licensee American Association for the Advancement of Science. No claim to original US government works. https://www.science.org/about/science-licenses-journal-article-reuse

SUPPLEMENTARY MATERIALS

science.org/doi/10.1126/science.adf5041
Materials and Methods
Supplementary Text S1 to S5
Figs. S1 to S22
Tables S1 to S3
References (*36*–*83*)

Submitted 26 October 2022; accepted 6 July 2023
10.1126/science.adf5041

2D MATERIALS

Programming twist angle and strain profiles in 2D materials

Maëlle Kapfer[1]†, Bjarke S. Jessen[1]†, Megan E. Eisele[1], Matthew Fu[1], Dorte R. Danielsen[2,3], Thomas P. Darlington[4], Samuel L. Moore[1], Nathan R. Finney[4], Ariane Marchese[4], Valerie Hsieh[1], Paulina Majchrzak[5], Zhihao Jiang[5], Deepnarayan Biswas[5]‡, Pavel Dudin[6], José Avila[6], Kenji Watanabe[7], Takashi Taniguchi[7], Søren Ulstrup[5], Peter Bøggild[2,3], P. J. Schuck[4], Dmitri N. Basov[1], James Hone[4], Cory R. Dean[1]*

Moiré superlattices in twisted two-dimensional materials have generated tremendous excitement as a platform for achieving quantum properties on demand. However, the moiré pattern is highly sensitive to the interlayer atomic registry, and current assembly techniques suffer from imprecise control of the average twist angle, spatial inhomogeneity in the local twist angle, and distortions caused by random strain. We manipulated the moiré patterns in hetero- and homobilayers through in-plane bending of monolayer ribbons, using the tip of an atomic force microscope. This technique achieves continuous variation of twist angles with improved twist-angle homogeneity and reduced random strain, resulting in moiré patterns with tunable wavelength and ultralow disorder. Our results may enable detailed studies of ultralow-disorder moiré systems and the realization of precise strain-engineered devices.

The interference pattern between twisted or lattice-mismatched layers of two-dimensional (2D) materials leads to a periodic electrostatic scattering potential superimposed over the atomic lattice (*1*, *2*). Additionally, periodic structural distortions from in-plane lattice relaxation and out-of-plane deformations can occur as a result of the interference pattern (*3*–*5*). This so-called moiré pattern can cause the appearance of flat bands in the electronic energy spectrum, which are found to host a variety of interaction-driven many-body states such as correlated insulators, superconductivity, and magnetic order as well as nontrivial topology (*6*, *7*). The ability to laminate 2D materials with different atomic composition and lattice constants, and at arbitrary twist angles, allows for wide tunability of the moiré wavelength, amplitude, and symmetry (*8*), with further modification possible through in situ rotation (*9*–*11*), pressure (*5*, *12*), and strain (*13*–*16*). Moiré patterning in 2D materials therefore provides a promising and flexible platform to realize correlated physics and topology in quantum materials by design (*8*).

Small variations in the moiré pattern, however, can lead to dramatically different behaviors, making it difficult to uncover the exact relationship between structural details of the superlattice and resulting electronic properties. For example, the flat band–hosting superconductivity in twisted-bilayer graphene emerges for twist angles between the layers within only ±0.1° of 1.1° (*17*, *18*), corresponding to a difference in moiré wavelength of just ±1 nm. This places stringent demands on the fabrication process (*19*). Moreover, experimental studies have found that spatially varying twist angle and distortion of the moiré unit cell caused by random strain fluctuations are ubiquitous when using current assembly techniques (*20*–*23*). Such nonuniformity compromises the ability to deterministically engineer specific band structures through well-defined moiré patterns or even correlate experimental measurement with predictive theoretical modeling (*24*–*28*). The inability to control this "moiré disorder" and the lack of any systematic understanding of its influence represents a critical roadblock toward continued progress in this field (*29*).

In this work, we demonstrate a technique that addresses these issues by using global strain fields to manipulate local moiré structures. We used an atomic force microscope to bend ribbon-shaped monolayers of 2D materials in-plane resulting in a continuously varying twist angle along the length of the ribbon. We confirmed through real-space imaging using piezoresponse force microscopy (PFM) and lateral force microscopy (LFM), as well as optical mapping by means of Raman spectroscopy and nanophotoluminescence (nanoPL), that the resulting twist-angle and strain gradients vary smoothly and with a predictable spatial dependence. The ability to vary the relative twist angle by several degrees allows us to span wide-ranging moiré length scales in a

[1]Department of Physics, Columbia University, New York, NY, USA. [2]Center for Nanostructured Graphene, Technical University of Denmark, DK-2800, Denmark. [3]DTU Physics, Technical University of Denmark, DK-2800, Denmark. [4]Department of Mechanical Engineering, Columbia University, New York, NY, USA. [5]Department of Physics and Astronomy, Aarhus University, 8000 Aarhus C, Denmark. [6]Synchrotron SOLEIL, Université Paris-Saclay, F-91192 Gif sur Yvette, France. [7]National Institute for Materials Science, 1-1 Namiki, Tsukuba, 305-0044, Japan.
***Corresponding author. Email: cd2478@columbia.edu**
†These authors contributed equally to this work.
‡Present address: Diamond Light Source, Division of Science, Didcot, UK.

single device. Most unexpectedly, we found substantially reduced moiré disorder in the bent ribbon geometry.

Bending 2D material ribbons

A schematic of the bending process is shown in Fig. 1A, illustrated for the case of a bent monolayer graphene (bMLG) ribbon on an hexagonal boron nitride (hBN) substrate. The heterostructure was first assembled by using the dry transfer technique in which we used the hBN to sequentially pick up a straight graphene ribbon, followed by a few-layer graphite manipulator shaped into a gear-like geometry (*30*). Using an atomic force microscope tip to slide the manipulator over the end of the ribbon allows us to apply an in-plane load (*9*). In response, the ribbon bends at the load end, with the far end effectively clamped owing to interfacial friction. Using the atomic force microscope tip, we thus directly control the displacement of the ribbon through a loop of topographic imaging and nanomanipulation.

We characterize the deformed ribbon using an (x, y) coordinate system, where x follows the neutral axis before bending, and y is the distance from the neutral axis perpendicular to x (Fig. 1B). We also introduce W and L as the width and bending length, respectively; $d(x)$ as the deflection; and $\Delta\theta(x)$ as the local twist angle relative to the orientation of the unbent ribbon. The local twist angle relates to the slope of the deflection curve through

$$\Delta\theta(x) = \tan^{-1}[d(x)'] \qquad (1)$$

An atomic force microscopy (AFM) image of a bMLG on hBN is shown in Fig. 1C, with the bMLG highlighted in blue, showing the initially unbent (Fig. 1C, top) and final bent (Fig. 1C, bottom) geometries. The bending process is both reversible and robust because we can bend and unbend the ribbon up to several degrees without evidence of plastic deformation (fig. S5). Upon releasing the load, static friction is sufficient to secure the deflection profile of the bent beam, and conventional dry transfer techniques can be used to add additional layers to the heterostructure without negatively affecting the geometry. We have applied the bending geometry to varying combinations of graphene, hBN, and transition-metal dichalcogenides and observed similar results in all cases.

Owing to the closely matched lattice constants of graphene and hBN, a large-wavelength moiré superlattice λ emerges in the small twist angle regime, varying with the twist angle, θ, according to

$$\lambda = \frac{(1+\delta)a}{2(1+\delta)[1-\cos(\theta)]+\delta^2} \qquad (2)$$

where a is the graphene lattice constant, θ is the twist angle, and δ is the lattice mismatch (0.017 for graphene on hBN) (*2*). Thus, measuring the moiré wavelength provides a way to directly determine the local twist angle (*31*, *32*). Shown in Fig. 1D are real-space and Fourier-space images acquired with PFM from two different locations on the bMLG shown in Fig. 1C. From the positions of the peaks in the fast Fourier transform (FFT), we extracted the average moiré wavelength and used Eq. 2 to determine the average twist angle within the scan window. Repeating this measurement along multiple points on the bMLG, we spatially mapped the twist angle along the ribbon. The measured change in twist angle, $\Delta\theta$, is shown in Fig. 1E as a function of x for three different ribbons widths of 0.8, 1.3, and 5 μm.

In terms of modeling the deflection curves of the bent ribbon, $d(x)$, we observed key differences compared with a classical cantilever: (i) upon bending, only part of the ribbon, closest to the loading point, is deflected; (ii) the length, L, over which bending occurs is larger for wider ribbons; and (iii) upon releasing the load at the end of the ribbon, the ribbon retains its bent shape. We found that all deflection curves for bent graphene ribbons, regardless of width or orientation to the underlying substrate, follow

$$d(x) = \frac{d_0}{L^3}(L-x)^3 \qquad (3)$$

where d_0 is the deflection at the load point, and L is the length over which bending occurs (fig. S4). We found an approximately linear relation between W and L, which we surmise reflects the role of friction in the system (fig. S4). On the basis of this understanding, we explored the limits of the bending approach. In Fig. 1F, we show the measured maximum twist angle variation as a function of the ribbon width for different graphene ribbons on hBN. We observed that beyond a critical displacement, some bMLGs buckle (*33*), suddenly transitioning into two mostly straight sections separated by a highly strained fold (fig. S5). By balancing the van der Waals energy between the ribbon and the substrate with the elastic energy from strain, we calculated a critical strain of ~2.5%, after which buckling

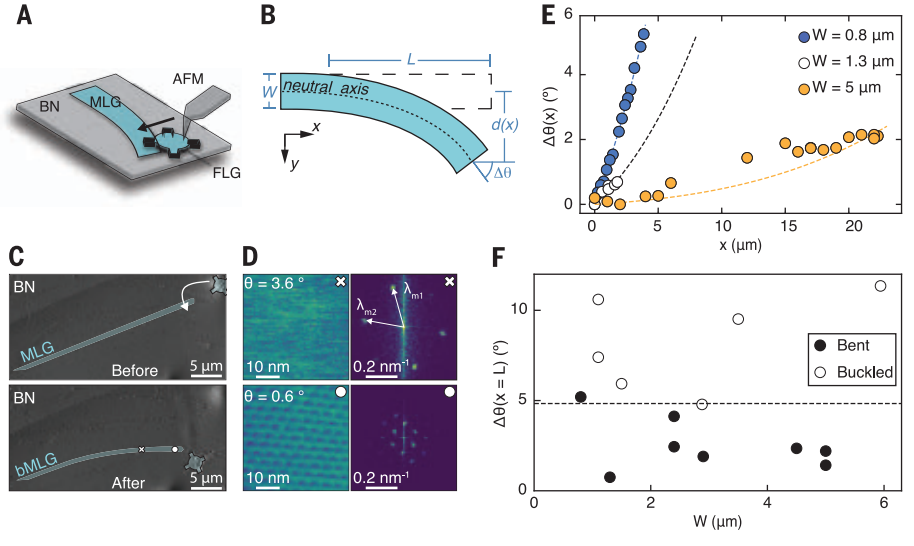

Fig. 1. Mechanical bending of 2D materials and twist-angle control. (**A**) Schematic of bending of a 2D material ribbon by using a nanomanipulator and the tip of an atomic force microscope. (**B**) Schematic of a 2D-material ribbon as a beam of width W and bending length L. A coordinate system, (x, y), marks the initial position of the ribbon. Deflections from the unbent neutral axis are denoted by $d(x)$, resulting in a twist angle $\Delta\theta(x)$ from the initial position. (**C**) AFM images of a bent monolayer graphene on hBN (top) before and (bottom) after bending. (**D**) (Left) PFM scans taken at the marked spots indicated in (C) and (right) their corresponding FFTs. (**E**) Twist angle calculated from the measured moiré wavelength, as a function of position along the ribbon. Data for three different ribbon widths are shown. The dashed lines indicate the expected twist angle evolution based on the displacement at the load point and ribbon width (*30*). (**F**) Maximum twist-angle variation as a function of width measured in graphene ribbons on hBN. The solid circles are ribbons that show a continuous twist-angle variation, whereas the open circles are ribbons that buckled owing to high strain. The twist angle of buckled ribbons are estimated from their width and load point deflection. The dashed line indicates the calculated strain of 2.5%, above which buckling is more favorable than in-plane strain (*30*).

becomes energetically favorable, shown as the dashed line in Fig. 1F (*30*). This sets an upper limit on Δθ of ~5° for bMLG, which is consistent with the approximate trend seen in Fig. 1F.

Mapping strain

The strain caused by bending varies both in the longitudinal (x) and transverse (y) directions and is given by $\varepsilon(x, y) = -y/\rho(x)$, where $\rho(x) = \{1 + [d(x)]^2\}^{3/2}/d(x)$ is the local radius of curvature. The calculated spatial strain maps for two ribbons are shown in Fig. 2A, one 1 μm wide and one 5 μm wide, each bent by a maximum twist-angle variation of 1°. The strain evolves linearly in both the transverse and longitudinal directions, with the maximum strain found at the load end of the ribbon. In the transverse direction, the ribbon is under compressive strain on the inside radius and tensile strain on the outside, with an unstrained neutral axis separating the two. The maximum transverse strain gradient, $\sim\varepsilon_{max}/(W/2)$, reaches as high as 0.47% per micrometer for the 1-μm-wide ribbon but only 0.09% per μm for the 5-μm-wide ribbon. Similarly, the maximum longitudinal strain gradient, $\sim\varepsilon_{max}/L$, reaches 0.03% per micrometer and 0.006% per micrometer for the narrow and wide ribbon, respectively. This indicates that the bending geometry allows us to effectively program the twist-angle and strain gradients individually through choice of ribbon

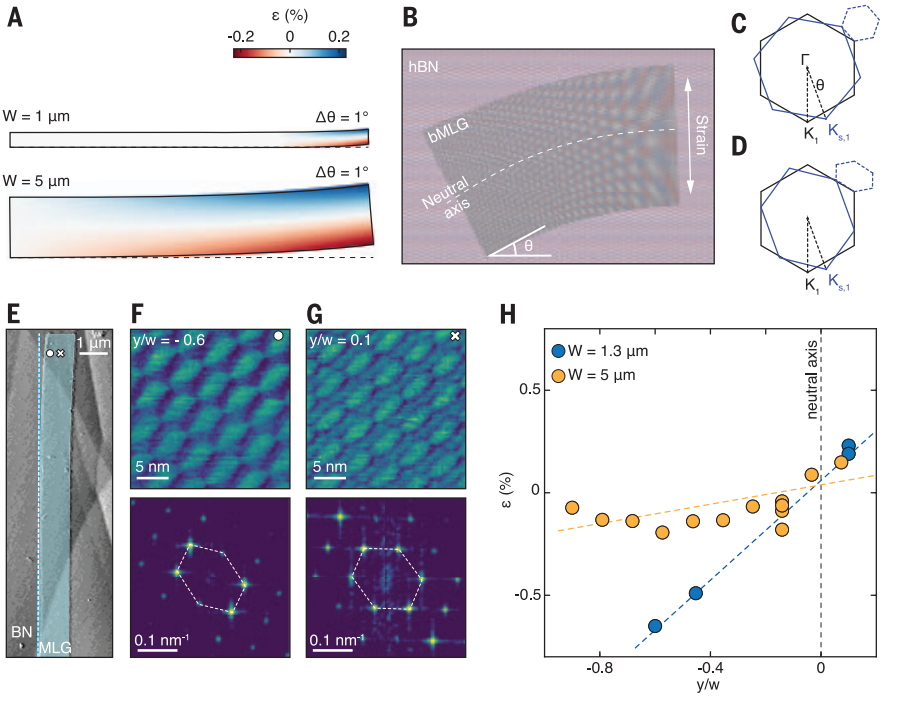

Fig. 2. Tunable strain gradients. (**A**) Calculated strain gradient in a (top) 1-μm-wide and (bottom) 4-μm-wide bMLG, each bent to a maximum twist-angle variation of 1°, with the dashed lines indicating their initial positions. The deflection has been exaggerated by a factor of 5 for illustrative purposes. (**B**) Sketch of a distorted moiré superlattice, highlighting the effect of strain in the low-angle limit. For moderate twist angles (left side; θ = 27°), the strain has only a minute effect on the fidelity of the moiré superlattice, whereas for low twist angles (right side; θ = 2°), the lattice is heavily distorted for both compressive and tensile strain. (**C** and **D**) BZs of two twisted graphene layers at no strain and tensile strain, respectively, highlighting the sensitivity of the superlattice BZ toward strain. (**E**) AFM image of a thin bMLG on hBN. The dashed line indicates the position before bending. (**F** and **G**) (Top) PFM scans taken across the bMLG in (E), with positions of the PFM scans marked on the AFM image of the sample. (Bottom) The corresponding FFTs, highlighting the increasingly distorted moiré pattern away from the neutral axis of the sample. (**H**) Summary of the strain gradient across a thin (blue) and wide (yellow) bMLG as a function of the normalized y position. The dashed lines indicate the strain gradient predicted with a mechanical model for the corresponding geometry and deflection.

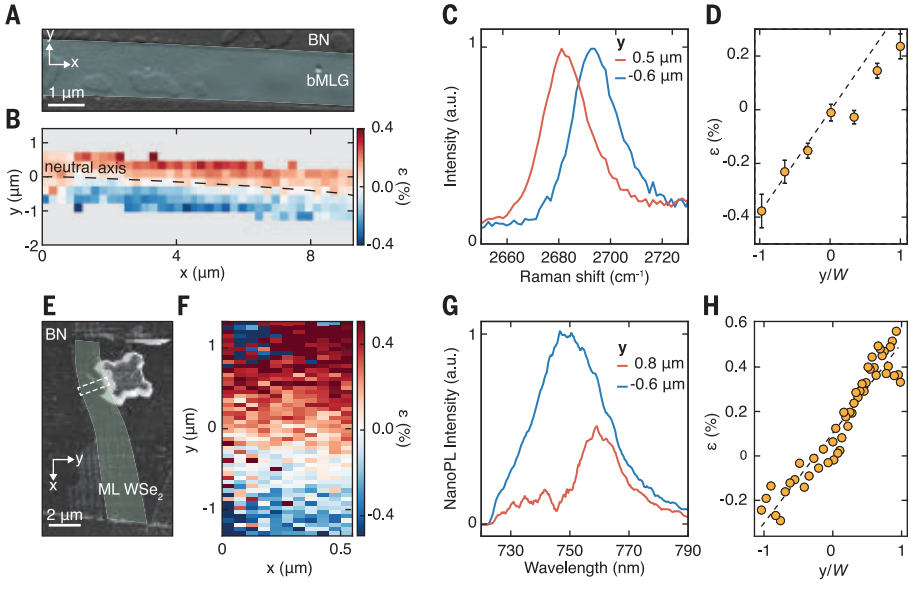

Fig. 3. Characterization of strain without moiré magnification. (**A** and **B**) (Top) An AFM image of a 1.6-μm-wide bMLG. (Bottom) The corresponding strain map extracted from Raman spectroscopy. Red indicates tensile strain, and blue indicates compressive strain, with a white neutral axis identified in the middle of the bMLG. (**C**) Raman spectra at fixed twist angle but varying strain for the bMLG shown in (A). (**D**) Extracted strain of the sample in (A), with the dashed line indicating the beam bending model for a 1.6-μm-wide beam deflected by d_0 = 300 nm, yielding a strain gradient of 0.64% per micrometer. (**E**) An AFM image of a 2.4-μm-wide ribbon of monolayer WSe_2 on hBN. (**F**) A strain map of the sample, from the dashed area in (E). The strain is extracted from nano-PL mapping, where the peak position is related to changes in band alignment caused by strain. (**G**) Representative spectra of areas of compressive (blue) and tensile (red) strain in the WSe_2. (**H**) Extracted strain versus distance from the neutral axis of the sample in (E), with the dashed line indicating a linear fit, yielding a strain gradient of 0.33% per micrometer.

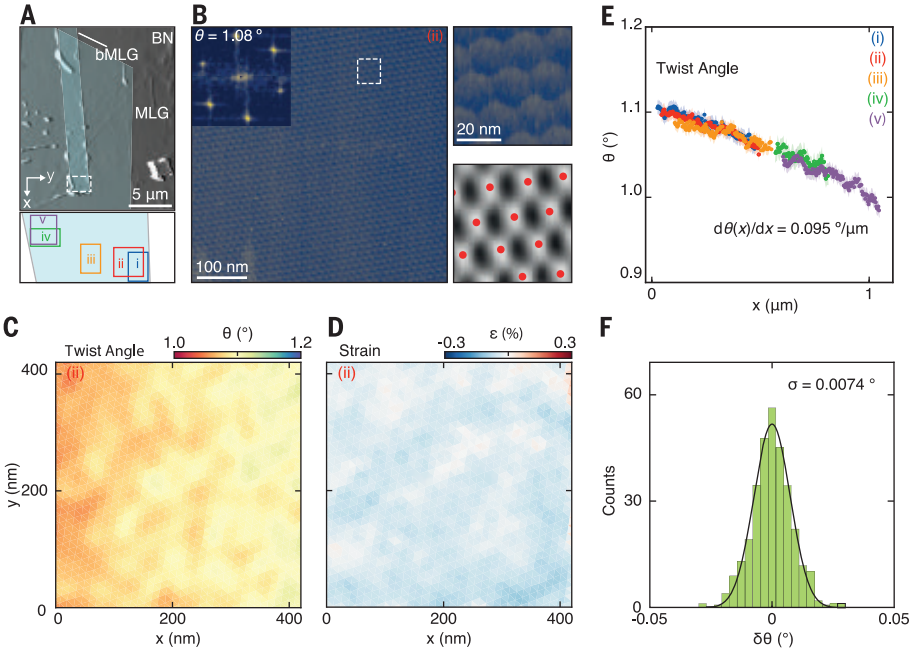

Fig. 4. Ultralow-disorder twisted-bilayer graphene. (**A**) Optical microscope image of a bMLG sample. The dashed square indicates the position of detailed LFM scans, which is further highlighted at bottom. (**B**) Large-area LFM scan of the bBLG sample, with (inset) the corresponding FFT. A global twist angle of 1.08° is extracted from the FFT peak positions. A series of such scans along the *x* direction of the ribbon reveals a uniform global twist-angle gradient of 0.095° per micrometer (fig. S10). (Top right) A 53- by 53-nm zoom-in of the LFM scan. (Bottom right) A nonlocal means denoised result of the zoom-in, where the red dots indicate the center of the moiré sites used for local twist-angle and strain extraction. (**C**) Map of the local twist angle calculated from the moiré sites positions of LFM scan area (ii). A twist-angle gradient is visible along the *x* direction of the map, with an average twist angle of 1.08°. (**D**) Map of the local strain of LFM scan area (ii). The average strain of the map is at a low value of around 0.05%. (**E**) Local twist-angle evolution as a function of the *x* position for LFM scan areas (i) to (v), revealing a local twist-angle gradient of 0.095° per micrometer, identical to the extracted global twist-angle gradient. (**F**) With an established twist-angle gradient, we extracted the residual local twist angle for all five scans in (A), yielding an intrinsic twist-angle disorder of 0.0074°.

width and maximum displacement. We confirmed this independent tuning through the use of (nano) angle-resolved photoemission spectroscopy, in which we spatially mapped out the band structure of a 4-μm-wide bMLG bent 4°. As expected from a low-strain ribbon, we observed a significant Brillouin zone (BZ) rotation but otherwise minimal impact on the band structure (fig. S9).

Analysis of the moiré pattern allows us to map the local strain field, in addition to twist angle, because the moiré pattern magnifies any distortion in the constituent lattices (*34*). This is visualized in Fig. 2B, where we show a schematic of a bent bMLG on hBN. The impact of the strain is apparent from the heavily distorted moiré lattice (*35*–*37*), which is especially visible for the large moiré periods in the low-twist-angle regime. The effect is maximal at the top and bottom edges of the bMLG and gradually decreases toward the unstrained neutral axis, near the middle. The resulting BZs of the twisted layer in the unstrained and tensile regions are shown in Fig. 2, C and D, respectively.

Examples of distorted moiré patterns acquired by means of PFM from a 1.3-μm-wide bMLG on hBN are shown in Fig. 2, E to G. The dashed line in Fig. 2E indicates the initial position of the bMLG (highlighted in blue) before bending. High-resolution moiré patterns and corresponding FFTs are shown in Fig. 2, F and G, top and bottom, respectively, acquired from two locations (indicated in Fig. 2, F and G, with white symbols) of the bBLG shown in Fig. 2E. The scan windows correspond to two different *y* positions (different strain points) but fixed *x* positions (same twist angle). Following (*38*) and (*39*), the average of the reciprocal lattice vectors measured from the FFT gives the local twist angle, whereas the ratio of the reciprocal vectors gives a measure of the local strain. The pattern in Fig. 2F, acquired close to the neutral axis, gives $\theta \sim 1.37°$ and $\varepsilon \sim 0.2\%$, whereas that in Fig. 2G, taken in the compressive part of the bMLG, gives $\theta \sim 1.34°$ and $\varepsilon \sim -0.65\%$.

A plot of the strain versus normalized *y* position y/w is shown in Fig. 2H, where *y* is the distance from the neutral axis, and $w = W/2$, the half-width of the bMLG (Fig. 2H, blue circles). The strain gradient is approximately linear, with a slope that matches the value of ~1% per micrometer calculated from the displacement curve (Fig. 2H, dashed blue line) with no free parameters. For comparison, strain versus y/w from a wider 5-μm ribbon is also shown (Fig. 2H, yellow circles). Again we found good agreement between the strain field measured from the distortions in the moiré pattern and the strain calculated from the displacement curve (Fig. 2H, dashed yellow line). Moreover, as expected, the wider ribbon gives a substantially reduced strain gradient, confirming the ability to use the bMLG width to tune the strain gradient independently of the twist angle.

So far, we have focused on bMLGs with a visible moiré pattern. However, for large twist angles (>5°), the resulting moiré wavelength is below our resolution limit. For those systems, the strain can instead be probed from optical measurements. Shown in Fig. 3A is a bMLG on hBN where no moiré was detected in the PFM scans, which indicates a twist angle larger than 10° (*31*). The corresponding strain map extracted from Raman spectroscopy is seen in Fig. 3B. The strain is calculated from the position of the 2D peak, where we expect a shift of ~27 cm^{-1} per percent of strain (*40*). Spectra taken along various positions to the neutral axis are shown in Fig. 3C, with the red and blue curves corresponding to tensile and compressive strain, respectively. Using multiple peak positions at a constant *x* position, we extracted the strain evolution along *y* (Fig. 3D), with the dashed line showing the strain gradient expected for a 1.6-μm-wide ribbon deflected by $d_0 = 300$ nm.

Shown in Fig. 3E is a bent monolayer tungsten diselenide (WSe_2) ribbon on hBN, demonstrating the capability to apply this technique to 2D materials other than graphene. Because of the substantial lattice mismatch between these two materials, no moiré superlattice was observed. We instead used nanoPL to determine the strain in the WSe_2. When subject to strain, the direct band gap of WSe_2 is expected to shift by –50 meV per percent (*41*). Figure 3F is a spatial map of the strain distribution in the WSe_2 ribbon calculated from the shift of the peak wavelength (Fig. 3G). Similar to bMLG, we observed a strain gradient evolving from tensile (Fig. 3H, blue) to compressive (Fig. 3H, red) strain and with a linear slope that matches theory (Fig. 2H).

Ultralow disorder in bBLG

Last, we exploited the bent geometry to fabricate twisted-bilayer graphene with continuously varying twist angles through the magic angle. An optical image of the bBLG is shown in Fig. 4A (details of the device fabrication are provided in fig. S2). We performed LFM scans along the ribbon and report the results for five different scan areas, all near the region where the magic angle is reached. The scan locations, shown schematically at the bottom of Fig. 4A, span in total 1 μm in the x direction and 2.5 μm in the y direction. We show one of these scans with the corresponding FFT in the Fig. 4B inset; the remaining can be found in figs. S10 and S11. The real-space image shows a notably uniform moiré pattern, with little evidence of varying twist angle or notable distortion. We observed similar high-quality moiré patterns in each of the scan regions. We extracted the moiré wavelength from the FFTs and used Eq. 2 to calculate the twist angle. Repeating this for different positions along the ribbon, we found that the twist angle between the layers varies from $\theta = 2.5°$ in the unbent region to $\theta = 1°$ at the end of the bBLG (fig S10), with an approximately linear gradient of 0.095° per micrometer.

Although we can extract an average twist angle over a single LFM scan from its FFT, the high quality of our scans opened the possibility to analyze the real-space moiré pattern and extract the local twist angle and strain by locating the center of each moiré site (Fig. 4B, bottom right). The spatial distributions of twist angles and strain, extracted from Fig. 4B, are shown in Fig. 4, C and D, respectively. Whereas the overall twist-angle variation remains small (±0.05°), we observed a gradient of the twist angle along the x axis (bending axis) and minimal evolution along the y axis. For the strain, we observed highly uniform values of around −0.05% over the whole area, which is in line with the visually uniform pattern seen in Fig. 4B.

To characterize the apparent twist-angle gradient, we averaged twist-angle values along the y axis, and we report this average as a function of the position along the x axis, or bending axis. We repeated this averaging for all five scans, and we report the twist-angle evolution in Fig. 4E. We observed a uniform gradient of the twist angle of 0.095° per micrometer, which is identical to the global twist-angle gradient found with FFT peak positions. The identical local and global twist-angle gradients confirmed that the twist-angle evolution along the bBLG is smooth and continuous over the whole bMLG. Having established the bend-induced twist-angle gradient as the primary source of angle variation in our samples, we set out to estimate the intrinsic twist-angle disorder as a deviation from the global twist-angle gradient. The resulting distribution of the gradient-corrected twist angles is presented in Fig. 4F. We found an intrinsic disorder value of 0.0074°, which is around three times lower than results obtained with conventional twisted-bilayer graphene samples prepared by using a tear and stack method (*20*, *38*).

Discussion and outlook

The ability to precisely tune the twist angle and strain within a 2D heterostructure, in the absence of uncontrolled distortions, paves the way for moiré band structure engineering in the disorder-free limit, including the exciting possibility that moiré patterning can be used as a generalized quantum simulation platform to study strongly correlated physics and topology in quantum materials (*8*). The dramatically reduced moiré disorder observed in our bent geometry is not yet understood. We conjecture that this may relate to the lattice relaxation dynamics in the presence of an externally applied strain field, but further theoretical and experimental work will be required to fully understand both the origin of this behavior and how this interplay may be exploited to realize new control opportunities. Last, the reversible in-plane bending geometry that we demonstrate, realized through local mechanical actuation, provides an alternative approach toward generalized strain engineering (*42*, *43*) beyond moiré patterning.

REFERENCES AND NOTES

1. G. Li *et al*., *Nat. Phys.* **6**, 109–113 (2010).
2. M. Yankowitz *et al*., *Nat. Phys.* **8**, 382–386 (2012).
3. C. R. Woods *et al*., *Nat. Phys.* **10**, 451–456 (2014).
4. H. Li *et al*., *Nat. Phys.* **17**, 1114–1119 (2021).
5. M. Yankowitz *et al*., *Nature* **557**, 404–408 (2018).
6. L. Balents, C. R. Dean, D. K. Efetov, A. F. Young, *Nat. Phys.* **16**, 725–733 (2020).
7. K. F. Mak, J. Shan, *Nat. Nanotechnol.* **17**, 686–695 (2022).
8. D. M. Kennes *et al*., *Nat. Phys.* **17**, 155–163 (2021).
9. R. Ribeiro-Palau *et al*., *Science* **361**, 690–693 (2018).
10. C. Hu *et al*., *Sci. Rep.* **12**, 204 (2022).
11. A. Inbar *et al*., *Nature* **614**, 682–687 (2023).
12. M. Yankowitz *et al*., *Science* **363**, 1059–1064 (2019).
13. J.-B. Qiao, L.-J. Yin, L. He, *Phys. Rev. B* **98**, 235402 (2018).
14. Z. Bi, N. F. Q. Yuan, L. Fu, *Phys. Rev. B* **100**, 035448 (2019).
15. X. Gao *et al*., *Sci. Rep.* **11**, 21402 (2021).
16. F. Mesple *et al*., *Phys. Rev. Lett.* **127**, 126405 (2021).
17. R. Bistritzer, A. H. MacDonald, *Proc. Natl. Acad. Sci. U.S.A.* **108**, 12233–12237 (2011).
18. Y. Cao *et al*., *Science* **372**, 264–271 (2021).
19. K. Kim *et al*., *Nano Lett.* **16**, 1989–1995 (2016).
20. A. Uri *et al*., *Nature* **581**, 47–52 (2020).
21. S. Grover *et al*., *Nat. Phys.* **18**, 885–892 (2022).
22. Y. Choi *et al*., *Nature* **589**, 536–541 (2021).
23. S. Turkel *et al*., *Science* **376**, 193–199 (2022).
24. G. Wagner, Y. H. Kwan, N. Bultinck, S. H. Simon, S. A. Parameswaran, *Phys. Rev. Lett.* **128**, 156401 (2022).
25. P. A. Pantaleón, T. Low, F. Guinea, *Phys. Rev. B* **103**, 205403 (2021).
26. T. A. de Jong *et al*., *Nat. Commun.* **13**, 70 (2022).
27. N. Nakatsuji, M. Koshino, *Phys. Rev. B* **105**, 245408 (2022).
28. Y. H. Kwan *et al*., *Phys. Rev. X* **11**, 041063 (2021).
29. C. N. Lau, M. W. Bockrath, K. F. Mak, F. Zhang, *Nature* **602**, 41–50 (2022).
30. Materials and methods are available as supplementary materials.
31. L. J. McGilly *et al*., *Nat. Nanotechnol.* **15**, 580–584 (2020).
32. X. Zheng *et al*., *Nat. Commun.* **7**, 13204 (2016).
33. J. van der Lit, P. H. Jacobse, D. Vanmaekelbergh, I. Swart, *New J. Phys.* **17**, 053013 (2015).
34. D. A. Cosma, J. R. Wallbank, V. Cheianov, V. I. Fal'ko, *Faraday Discuss.* **173**, 137–143 (2014).
35. D. L. Miller *et al*., *Phys. Rev. B Condens. Matter Mater. Phys.* **81**, 125427 (2010).
36. D. Halbertal *et al*., *Nat. Commun.* **12**, 242 (2021).
37. Y. Hou *et al*., *Opt. Lasers Eng.* **152**, 106946 (2022).
38. A. Kerelsky *et al*., *Nature* **572**, 95–100 (2019).
39. D. Halbertal, S. Shabani, A. N. Passupathy, D. N. Basov, *ACS Nano* **16**, 1471–1476 (2022).
40. Z. H. Ni *et al*., *ACS Nano* **2**, 2301–2305 (2008).
41. S. B. Desai *et al*., *Nano Lett.* **14**, 4592–4597 (2014).
42. B. Amorim *et al*., *Phys. Rep.* **617**, 1–54 (2016).
43. R. Roldán, A. Castellanos-Gomez, E. Cappelluti, F. Guinea, *J. Phys. Condens. Matter* **27**, 313201 (2015).
44. M. Kapfer *et al*., Programmable twist angle and strain profiles in 2D materials, *Dryad* (2023); https://doi.org/10.5061/dryad.fn2z34v0k.
45. M. Kapfer *et al*., Zenodo (2023); https://doi.org/10.5281/zenodo.7803742.

ACKNOWLEDGMENTS

The authors acknowledge J. Li at Oxford Instrument Asylum Research for experimental assistance with the LFM imaging, and acknowledge D. Halbertal and S. Turkel for helpful discussions. **Funding:** Fabrication and characterization of the bent-ribbon structures was primarily supported as part of Programmable Quantum Materials, an Energy Frontier Research Center funded by the US Department of Energy (DOE), Office of Science, Basic Energy Sciences (BES), under award DE-SC0019443. Synthesis of TMD crystals and fabrication of TMD structures was accomplished by using facilities at the Columbia MRSEC on Precision-Assembled Quantum Materials (PAQM)–DMR-2011738. C.R.D. and J.H. acknowledge additional support from the Gordon and Betty Moore Foundation's EPiQS Initiative, grant GBMF10277. D.N.B. is a Moore Investigator in Quantum Materials EPIQS. P.B. and D.R.D. acknowledge support from Danish National Research Foundation (DNRF) Center for Nanostructured Graphene (DNRF103) and EU Graphene Flagship Core 3 (881603). The nanoARPES experiments were carried out at the ANTARES beamline of Synchrotron SOLEIL under proposal 20210204, and supported by Independent Research Fund Denmark under the Sapere Aude program (grant 9064-00057B), VILLUM FONDEN under the Young Investigator Program (grant 15375), and the Centre of Excellence for Dirac Materials (grant 11744). **Author contributions:** M.K., B.S.J., M.E.E., and C.R.D. wrote the manuscript, with input from all authors. M.K., B.S.J., and N.R.F. prepared the graphene devices and performed AFM, PFM, and LFM measurements, and M.K. and B.S.J. analyzed the data. T.P.D. performed Raman measurements, and T.P.D., B.S.J., and M.K. analyzed the data. M.E.E. prepared the TMD device. M.F. and S.L.M. performed nanoPL measurements and together with M.E.E. analyzed the data. D.R.D. calculated the critical buckling strain. B.S.J., M.K., M.F., D.R.D., and A.K.M. did the beam bending calculations. B.S.J. and M.K. prepared samples for nanoARPES; P.M., Z.J., S.U., B.S.J., M.K., D.B., J.A., and P.D. performed the measurements; and P.M., Z.J., and S.U. analyzed the data. V.H. assisted with LFM measurements. K.W. and T.T. grew and provided the hBN crystals. **Competing Interests:** The authors declare no competing interests. **Data and materials availability:** All data used to generate figures are available at (*44*), and code is available at (*45*).

License information: Copyright © 2023 the authors, some rights reserved; exclusive licensee American Association for the Advancement of Science. No claim to original US government works. https://www.science.org/about/science-licenses-journal-article-reuse

SUPPLEMENTARY MATERIALS

science.org/doi/10.1126/science.ade9995
Materials and Methods
Supplementary Text
Figs. S1 to S15
References (*46*–*61*)

Submitted 21 September 2022; accepted 21 June 2023
10.1126/science.ade9995

CANCER DETECTION

Engineered bacteria detect tumor DNA

Robert M. Cooper[1]†, Josephine A. Wright[2]†, Jia Q. Ng[3], Jarrad M. Goyne[2], Nobumi Suzuki[2,3], Young K. Lee[3], Mari Ichinose[2,3], Georgette Radford[3], Feargal J. Ryan[2,4], Shalni Kumar[5], Elaine M. Thomas[3], Laura Vrbanac[3], Rob Knight[6,7,8,9], Susan L. Woods[2,3]*, Daniel L. Worthley[2,10]*, Jeff Hasty[1,5,6,9]*

Synthetic biology has developed sophisticated cellular biosensors to detect and respond to human disease. However, biosensors have not yet been engineered to detect specific extracellular DNA sequences and mutations. Here, we engineered naturally competent *Acinetobacter baylyi* to detect donor DNA from the genomes of colorectal cancer (CRC) cells, organoids, and tumors. We characterized the functionality of the biosensors in vitro with coculture assays and then validated them in vivo with sensor bacteria delivered to mice harboring colorectal tumors. We observed horizontal gene transfer from the tumor to the sensor bacteria in our mouse model of CRC. This cellular assay for targeted, CRISPR-discriminated horizontal gene transfer (CATCH) enables the biodetection of specific cell-free DNA.

Bacterial engineering has allowed the development of living cell diagnostics and therapeutics (*1*–*3*), including microbes that respond to gut inflammation (*4*), intestinal bleeding (*5*), pathogens (*6*), and hypoxic tumors (*7*). Bacteria can access the entire gastrointestinal tract to produce outputs measured in stool (*4*) or urine (*7*). Cellular memory, such as bistable switches (*4*, *8*, *9*) or genomic rearrangements (*10*), enables bacteria to store information over time. Some bacteria are naturally competent for transformation and can sample extracellular DNA directly from their environment (*11*). Natural competence is one mechanism of horizontal gene transfer (HGT), the exchange of genetic material between organisms outside vertical, "parent to offspring" transmission (*12*). HGT is common between microbes (*12*). It may also occur from microbes into animals and plants (*13*) and, in the opposite direction, from eukaryotes to prokaryotes (*14*). The forward engineering of bacteria to detect and respond to mammalian DNA through HGT, however, has not been explored.

Acinetobacter baylyi is a highly competent and well-studied bacterium (*15*, *16*) that is largely nonpathogenic in healthy humans (*17*), can colonize the murine gastrointestinal tract (*18*), and acquires unpurified, environmental DNA from lysed cells (*19*). Our cellular assay for targeted, CRISPR-discriminated horizontal gene transfer (CATCH) strategy delivers bacterial biosensors to sample and genomically integrate target DNA (Fig. 1). To demonstrate this concept, we used the biosensor to detect engineered tumor cells. We then developed genetic circuits to detect natural, nonengineered tumor DNA sequences, discriminating oncogenic mutations at the single-base level. Because the target sequence and output gene are modular, our approach can be generalized to detect arbitrary DNA sequences and respond in a programmable manner.

[1]Synthetic Biology Institute, University of California, San Diego, La Jolla, CA 92093, USA. [2]Precision Cancer Medicine Theme, South Australia Health and Medical Research Institute, Adelaide, SA 5000, Australia. [3]Adelaide Medical School, University of Adelaide, Adelaide, SA 5000, Australia. [4]Flinders Health and Medical Research Institute, Flinders University, Bedford Park, SA 5042, Australia. [5]Department of Bioengineering, University of California, San Diego, La Jolla, CA 92093, USA. [6]Molecular Biology Section, Division of Biological Sciences, University of California, San Diego, La Jolla, CA 92093, USA. [7]Department of Pediatrics, University of California, San Diego, La Jolla, CA 92093, USA. [8]Department of Computer Science and Engineering, University of California, San Diego, La Jolla, CA 92093, USA. [9]Center for Microbiome Innovation, University of California, San Diego, La Jolla, CA 92093, USA. [10]Colonoscopy Clinic, Brisbane, QLD 4000, Australia.
***Corresponding author. Email: susan.woods@adelaide.edu.au (S.L.W.); dan@colonoscopyclinic.com.au (D.L.W.); hasty@ucsd.edu (J.H.)**
†These authors contributed equally to this work.

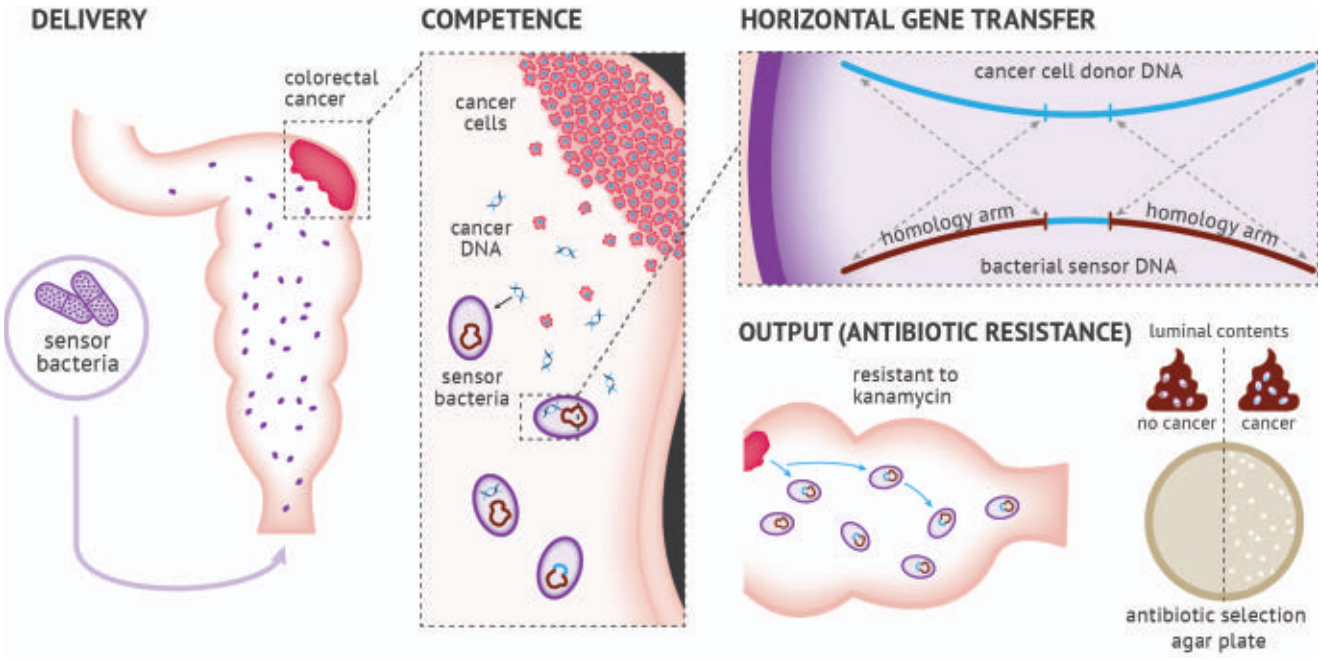

Fig. 1. Engineered bacteria to detect tumor DNA. Engineered *A. baylyi* bacteria are delivered rectally in an orthotopic mouse model of CRC. The naturally competent *A. baylyi* take up tumor DNA shed into the colorectal lumen. The tumor donor DNA is engineered with a *kanR* cassette flanked by *KRAS* homology arms. The sensor bacteria are engineered with matching *KRAS* homology arms that promote homologous recombination. Sensor bacteria that undergo HGT from tumor DNA acquire kanamycin resistance and are quantified from luminal contents by serial dilution on antibiotic selection plates.

Results

Engineering cancer cell lines, organoids, and sensor bacteria

To test the hypothesis that bacteria could detect specific mammalian DNA, we generated transgenic donor human cancer cells with a kanamycin resistance gene (*kanR*) inside *KRAS* homology arms (Figs. 1 and 2, A to C, and figs. S1 and S2). *KRAS* is an important oncogene in human cancer, and a driver mutation in *KRAS* often accompanies the progression of simple into advanced colorectal adenomas (*20*). Our technology is currently confined to the detection of specific sequences and thus for cancer detection is limited to hotspot mutations, such as *KRASG12D*.

We stably transduced this donor cassette into three conventional human colorectal cancer (CRC) cell lines with differing background genetic alterations [RKO is microsatellite instability high (MSI-H), *BRAFV600E*; LS174T is MSI-H, *KRASG12D*; SW620 is microsatellite stable (MSS), *KRASG12V*] and two human CRC organoid lines (RAH057T is MSS, *KRASG12D*; RAH038T is MSI-H, *BRAFV600E*) using a lentiviral vector. To construct the sensor bacteria, we inserted a complementary landing pad with *KRAS* homology arms into *A. baylyi*. We tested both a "large insert" design, where 2 kb of donor cassette must transfer (Fig. 2, A and B; fig. S2A; and data file S1), and a "small insert" design, where only 8 base pairs (bp) must transfer to repair two stop codons (Fig. 2C, fig. S2B, and supplementary materials and methods) (*21*). The initial biosensor output was growth on kanamycin plates (Fig. 2 and fig S2).

Detection of cell-free DNA from cancer cell lines

We tested these designs using various donor DNA sources, both in liquid culture and on solid agar (Fig. 2A). The "large insert" biosensors detected donor DNA from purified plasmids and genomic DNA both in liquid (Fig. 2D) and on agar (Fig. 2E). On agar, they also detected raw, unpurified lysate, albeit at just above the limit of detection (Fig. 2E). As expected (*22*), the "small insert" design improved detection efficiency ~10-fold, reliably detecting even raw lysate (Fig. 2, F and G, and movie S1). Across conditions, detection on solid agar was more efficient than in liquid culture. Notably, these experiments confirmed that the biosensors did not require DNA purification (*19*).

Mutations in codon 12 of *KRAS* occur in 27% of CRC tumors (*23*), accounting for 72% of all CRC *KRAS* mutations (*24*), and are common in solid tumors generally (*25*). To test whether sensor bacteria could discriminate between wild-type and mutant *KRAS* (*KRASG12D*), we used *A. baylyi*'s endogenous type I-F CRISPR-Cas system (*26*). We stably transduced a donor RKO cell line with the *kanR-GFP* (green fluorescent protein) donor cassette flanked by wild-type *KRAS*, and a second line with *KRASG12D* flanking sequences. Next, we designed three CRISPR spacers targeting the wild-type *KRAS* sequence at the location of the *KRASG12D* mutation, using the *A. baylyi* protospacer-adjacent motif (PAM) (Fig. 2H). We inserted these as single-spacer arrays into a neutral locus in the "large insert" *A. baylyi* sensor genome.

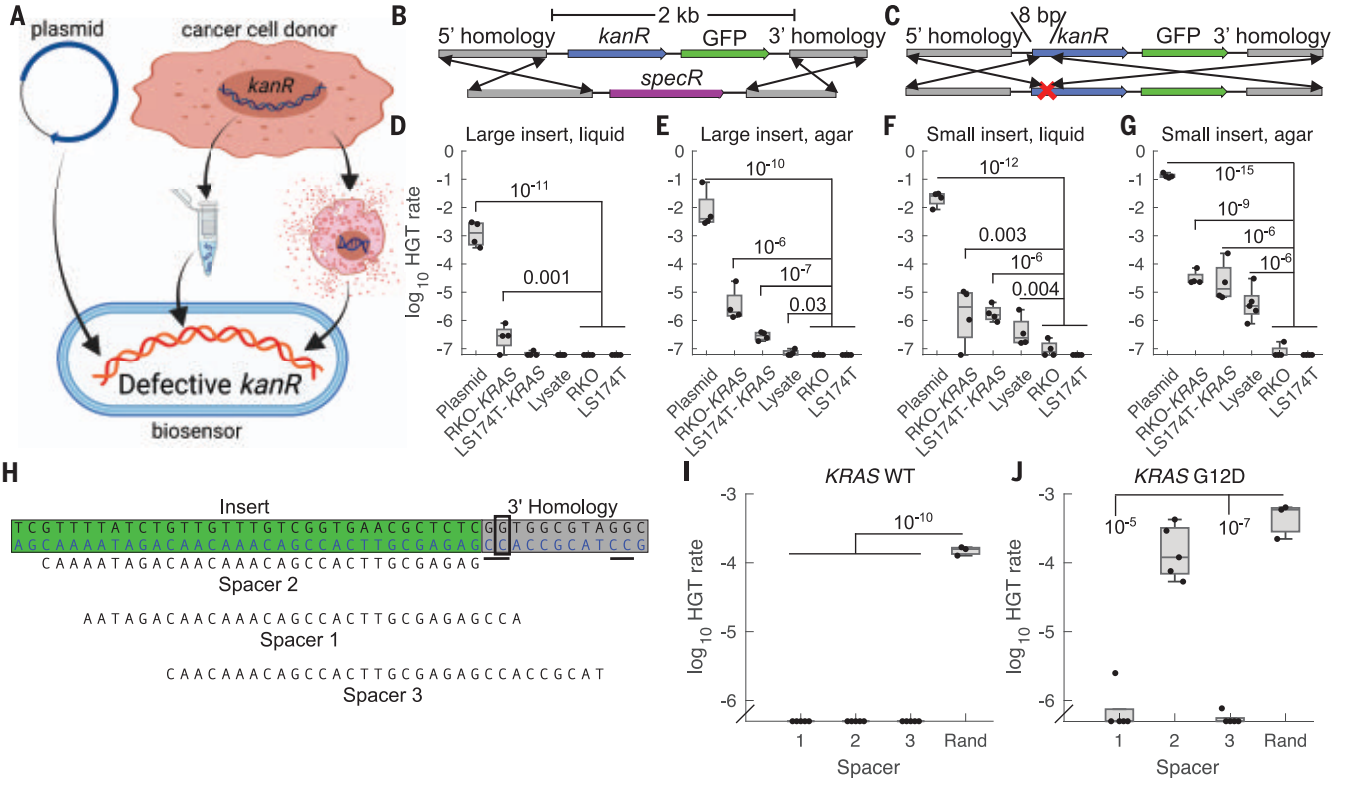

Fig. 2. Sensing *KRASG12D* DNA in vitro. (**A**) Donor DNA was derived from plasmid, purified cancer cell genomic DNA, or raw lysate (top) that recombined into biosensor *A. baylyi* cells (bottom). Horizontal gene transfer included either a large, 2-kb insert (**B**) or a small, 8-bp insert to repair two stop codons (**C**), in both cases conferring kanamycin resistance. (**D** to **G**) *A. baylyi* biosensors were incubated with plasmid DNA, purified RKO-*KRAS* or LS174T-*KRAS* genomic DNA, or raw RKO-*KRAS* lysate, all containing the donor cassette, or purified RKO or LS174T genomic DNA as controls. Biosensor cells included either "large insert" [(B), (D), and (E)] or "small insert" [(C), (F), and (G)] designs, and transformations were performed in liquid culture [(D) and (F)] or on solid agar surfaces [(E) and (G)]. Two sample *t* tests compared data to RKO and LS174T genomic DNA controls under the same conditions. (**H**) CRISPR spacers targeting the *KRAS* G12D mutation (boxed), using the underlined PAMs. (**I** and **J**) Fraction of total biosensor cells expressing the indicated CRISPR spacers that were transformed by plasmid donor DNA with wild type (I) or mutant G12D (J) *KRAS*. Statistics were obtained by using two sample, one-sided *t* tests, with *P* values displayed on the figures. Data points below detection are shown along the *x* axis, at the limit of detection.

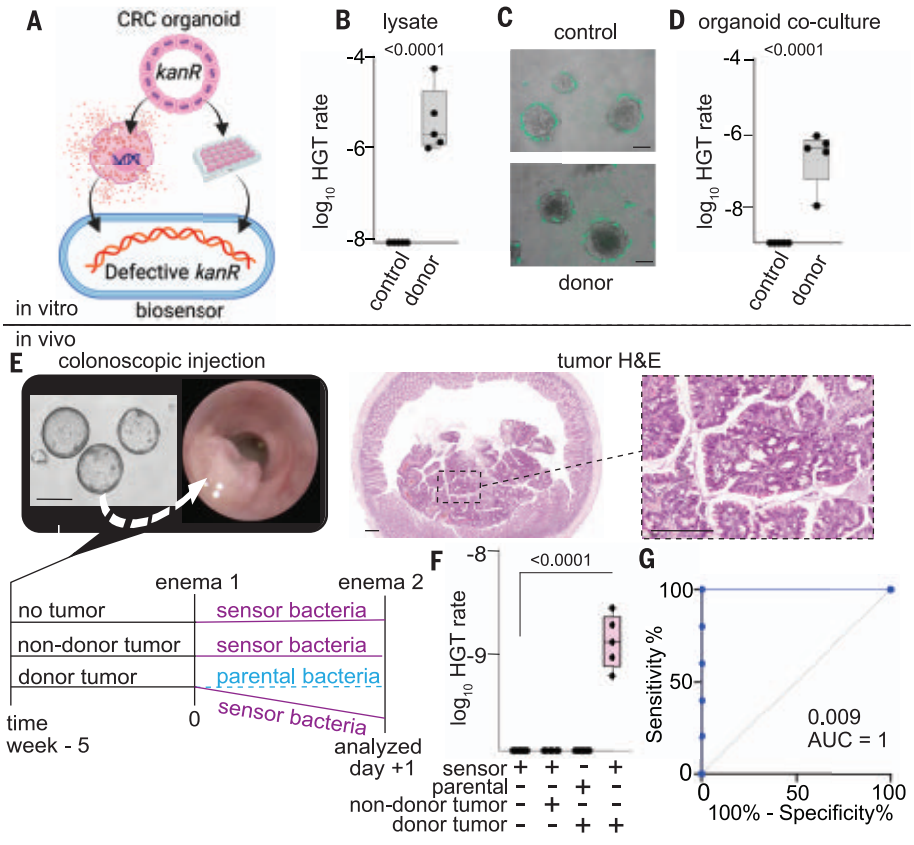

Fig. 3. Detection of donor DNA from BTRZI-*KRAS-kanR* organoids in both an in vitro and an in vivo model of colorectal cancer. (**A**) Schema depicting in vitro coculture of *A. baylyi* sensor bacteria with BTRZI-*KRAS-kanR* (CRC donor) organoid lysates or viable organoids to assess HGT repair of kanamycin resistance gene (*kanR*). (**B**) Recombination with DNA from crude lysates enables growth of *A. baylyi* sensor on kanamycin. (**C**) Representative images of GFP-tagged *A. baylyi* biosensor surrounding parental BTRZI (control) and BTRZI-*KRAS-kanR* donor organoids at 24 hours. Scale bar, 100 μm. (**D**) Coculture of established CRC BTRZI-*KRAS-kanR* donor organoids with *A. baylyi* sensor enables growth of *A. baylyi* sensor on kanamycin. In (B) and (D), n = 5 independent experiments each with 5 technical replicates; one sample t test on transformed data was used for statistical analysis with P values as indicated. (**E**) Schema depicting in vivo HGT experiments: generation of BTRZI-*KRAS-kanR* (CRC donor) tumors in mice through colonoscopic injection, with tumor pathology validated by hematoxylin and eosin (H&E) histology, administration of biosensors, and analysis of luminal contents. Scale bars, 200 μm. (**F**) Rectal delivery of *A. baylyi* biosensor to mice bearing CRC donor tumors results in kanamycin-resistant *A. baylyi* biosensor in luminal contents through HGT with transformation efficiency of 1.5×10^{-9} (limit of detection 1.25×10^{-10}). HGT rate calculated from colony-forming units (CFU) on kanamycin–chloramphenicol–vancomycin (transformants) and chloramphenicol–vancomycin (total *A. baylyi*) selection plates, n = 3 to 5 mice per group. One-way analysis of variance with Tukey's post-hoc on $\log_{10}$-transformed data was used for statistical analysis. (**G**) ROC (receiver operating characteristic) curve analysis of HGT CFU following enema; area under the curve = 1, P = 0.009.

The sensor bacteria should reject wild-type *KRAS* through CRISPR-mediated DNA degradation but allow integration of the *KRASG12D* sequence. Two of the three spacers blocked transformation by both wild-type and mutant DNA (Fig. 2, I and J). However, spacer 2, for which the *KRASG12D* mutation eliminated the PAM site, selectively permitted only *KRASG12D* donor DNA (Fig. 2, I and J). The other common mutations in codon 12 of *KRAS* all eliminate this PAM as well (*23*). Thus, sensor *A. baylyi* can be engineered to detect a mutational hotspot in the *KRAS* gene with single-base specificity.

Detection of cell-free DNA from tumorigenic organoid lines

Next, we evaluated our sensor and donor constructs in organoid culture (Fig. 3A). We previously used CRISPR-Cas9 genome engineering to generate compound $Braf^{V600E}$; $Tgfbr2^{\Delta/\Delta}$; $Rnf43^{\Delta/\Delta}$; $Znrf3^{\Delta/\Delta}$; $p16Ink4a^{\Delta/\Delta}$ (BTRZI) mouse organoids that recapitulate serrated CRC when injected into the mouse colon (*27*). We transduced BTRZI organoids with the donor DNA construct to generate donor CRC organoids and incubated their lysate with the more efficient "small insert" *A. baylyi* biosensors. Using quantitative polymerase chain reaction (qPCR), we confirmed that the BTRZI organoids that we generated contained only two copies of the target donor DNA (fig. S3). As with the CRC cell lines, the sensor *A. baylyi* incorporated DNA from donor organoid lysate, but not from control lysates from the parental organoids (Fig. 3B and figs. S4 and S5A). Next, we cocultured GFP-expressing sensor *A. baylyi* with parental or donor organoids for 24 hours on Matrigel. The GFP-expressing sensor bacteria enveloped the organoids (Fig. 3C). After coculture with donor, but not parental, organoids, the *A. baylyi* sensor bacteria acquired donor DNA through HGT (Fig. 3D and fig. S5, B and C). Finally, we estimated the detection limit of our biosensor for target DNA in stool. To achieve this, we added increasing amounts of donor plasmid to a defined mixture of biosensor and stool (5×10^7 biosensor mixed with 0.017 g per 100 μl of stool slurry). The detection limit was 3 pg of plasmid or 2.7×10^5 copies of target DNA, for a given incubation volume and time (fig. S6).

Detection of cell-free tumor DNA in an orthotopic mouse model of colorectal cancer

Given that cancer-to-bacterial HGT occurred in vitro and in the presence of stool, we sought to test the CATCH system in vivo. We first confirmed that our BTRZI, orthotopic CRC model released tumoral DNA into the colorectal lumen. Engineered CRC organoids were injected orthotopically, by mouse colonoscopy, into the mouse colon to form colonic tumors, as previously described (*27*). Using digital droplet PCR, we measured *Braf* mutant tumor DNA in stools collected from tumor-bearing and control mice. The BTRZI model reliably released tumor DNA into the colorectal lumen (fig. S7).

We next conducted an orthotopic CRC experiment (Fig. 3E). Immunodeficient NSG mice were injected with donor or nondonor organoids, or neither. At week 5, once the tumors had grown into the lumen, sensor (or parental) *A. baylyi* bacteria were delivered twice through rectal enema. The mice were subsequently euthanized and the colorectum harvested with the luminal effluent plated for analysis. Serial dilutions were then plated on agar with different antibiotic combinations (Fig. 3F).

HGT from tumors to biosensors was only detected in donor tumor-bearing mice that were administered sensor bacteria. There was no HGT detected in any control group (Fig. 3F). The resistant colonies were confirmed to be the engineered biosensor strain by antibiotic resistance, green fluorescence, 16*S* sequencing, and HGT-mediated *kanR*

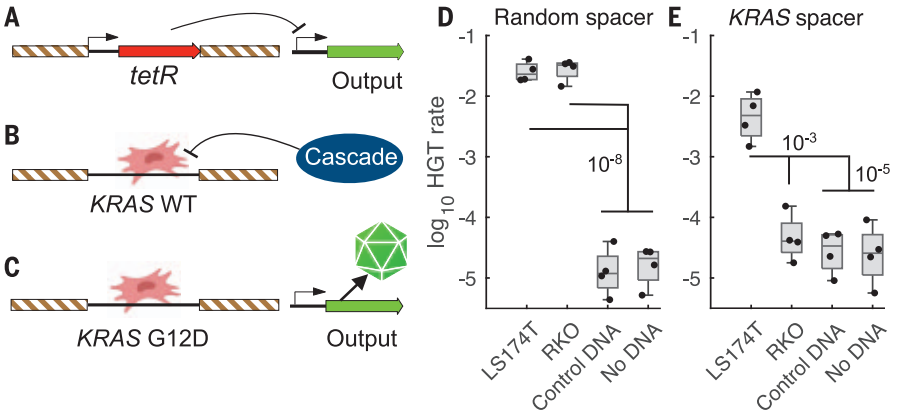

Fig. 4. Detection of nonengineered DNA. (**A**) *tetR* located between the homology arms on the *A. baylyi* genome represses expression of the output gene. (**B**) Target DNA with wild-type *KRAS* sequence is recognized and degraded by the type I-F CRISPR-Cas effector complex, Cascade. (**C**) Target DNA with the *KRASG12D* mutation avoids degradation, replaces *tetR* in the biosensor genome, and relieves repression of the output gene. (**D** and **E**) Fraction of biosensors with either a random CRISPR spacer (D) or a spacer targeting wild-type *KRAS* (E) that detected donor DNA. Statistics were obtained in two sample *t* tests and are displayed on the figure.

repair of individual colonies (fig. S8). Thus, CATCH discriminated mice with and without CRC in our experimental model (Fig. 3G).

Detection of nonengineered DNA

Finally, we designed living biosensors to detect and analyze nonengineered cancer DNA. The *tetR* repressor gene was inserted between the *KRAS* homology arms in the biosensor, and in a second locus, we placed an output gene under control of the P_LtetO-1 promoter (*28*) (Fig. 4A). Here, the output gene was kanamycin resistance for ease of measurement, but the output gene is arbitrary and exchangeable.

In this design, expression of the output gene is constitutively repressed (Fig. 4A). Upon recombination with the *KRAS* target DNA, the repressor *tetR* is deleted from the genome. If the incoming *KRAS* sequence is wild type at the G12 locus, Cascade, the type I-F CRISPR-Cas effector complex, detects and degrades it (Fig. 4B). However, if the G12 locus is mutated, the PAM site and therefore CRISPR-Cas targeting are eliminated, and expression from the output gene turns on (Fig. 4C).

We tested this natural DNA sensor design in vitro using PCR products from LS174T and RKO genomes as donor DNA. Natural DNA biosensors with a random CRISPR spacer detected DNA sequences from both cell lines (Fig. 4D), and biosensors with the *KRAS* spacer accurately detected only DNA sequence from LS174T cells, which contain the *KRASG12D* mutation (Fig. 4E), demonstrating biosensor detection and discrimination of natural target DNA.

Discussion

The sensor bacteria described here demonstrate that a living biosensor can detect specific mammalian DNA shed from CRC in vivo in the gut, with no sample preparation or processing. Engineered donor cassettes are not required for CATCH biosensors to detect, discriminate, and report on target sequences, although the final natural DNA biosensors will need an improved signal-to-background ratio to reliably detect sequences within whole genomic DNA. The homology arms and CRISPR spacers are modular, so this strategy could be readily adapted to detect and analyze arbitrary target sequences of interest.

Our technology is not yet ready for clinical application. This approach requires further development to ensure that future versions, at least those designed for gastrointestinal use, may be delivered orally and achieve sufficient luminal density to allow reliable detection by noninvasive sampling such as in stool or blood. As the technology advances toward clinical care, we will also need to more critically evaluate the performance of CATCH compared to other relevant disease-specific tests such as, in this case, colonoscopy and in vitro nucleic acid assays (*29*, *30*). Further bioengineering is required to limit the risk of biosensors escaping circuit-mediated cell death and to improve the efficiency of natural DNA detection. As our technology progresses, careful analysis is essential to ensure patient safety, to minimize the risk of spreading antibiotic resistance, and to satisfy biocontainment concerns. These necessary next steps are being actively pursued and are important as CATCH is applied to additional preclinical models and before it is trialed in humans.

In vitro DNA analysis helps detect and manage important human diseases, including cancer and infection (*31*). However, in vitro sensing requires potentially invasive removal of samples, and many DNA diagnostics do not achieve clinically relevant sequence resolution, with more advanced techniques remaining too expensive for routine use in all settings (*32*). Direct sampling of the gut in vivo may offer important advantages. The gastrointestinal tract contains marked deoxyribonuclease (DNase) activity (*33*), which limits the lifetime of free DNA in both rodents and humans (*18*, *34*, *35*) and may thus reduce the information content of downstream fecal samples. Bacterial biosensors located in situ could capture and preserve DNA shortly after its release before degradation by local DNases. Perhaps the most exciting aspect of CATCH, however, is that unlike in vitro diagnostics, once target DNA is captured, it could be coupled to direct and genotype-complementary delivery of nanobodies, peptides, or other small molecules for the treatment of cancer or infection (*36*, *37*). CATCH allows for the cellular detection of cell-free DNA and thus may prove useful in future synthetic biology applications, wherever, and whenever, DNA detection and analysis are important.

REFERENCES AND NOTES

1. S. Slomovic, K. Pardee, J. J. Collins, *Proc. Natl. Acad. Sci. U.S.A.* **112**, 14429–14435 (2015).
2. F. Sedlmayer, D. Aubel, M. Fussenegger, *Nat. Biomed. Eng.* **2**, 399–415 (2018).
3. W. A. Lim, C. H. June, *Cell* **168**, 724–740 (2017).
4. D. T. Riglar *et al.*, *Nat. Biotechnol.* **35**, 653–658 (2017).
5. M. Mimee *et al.*, *Science* **360**, 915–918 (2018).
6. N. Mao, A. Cubillos-Ruiz, D. E. Cameron, J. J. Collins, *Sci. Transl. Med.* **10**, eaao2586 (2018).
7. T. Danino *et al.*, *Sci. Transl. Med.* **7**, 289ra84 (2015).
8. J. W. Kotula *et al.*, *Proc. Natl. Acad. Sci. U.S.A.* **111**, 4838–4843 (2014).
9. T. S. Gardner, C. R. Cantor, J. J. Collins, *Nature* **403**, 339–342 (2000).
10. A. Courbet, D. Endy, E. Renard, F. Molina, J. Bonnet, *Sci. Transl. Med.* **7**, 289ra83 (2015).
11. J. C. Mell, R. J. Redfield, *J. Bacteriol.* **196**, 1471–1483 (2014).
12. S. M. Soucy, J. Huang, J. P. Gogarten, *Nat. Rev. Genet.* **16**, 472–482 (2015).
13. K. M. Robinson, K. B. Sieber, J. C. Dunning Hotopp, *PLOS Genet.* **9**, e1003877 (2013).
14. J. C. Dunning Hotopp, *Trends Genet.* **27**, 157–163 (2011).
15. D. M. Young, D. Parke, L. N. Ornston, *Annu. Rev. Microbiol.* **59**, 519–551 (2005).
16. R. Palmen, B. Vosman, P. Buijsman, C. K. D. Breek, K. J. Hellingwerf, *J. Gen. Microbiol.* **139**, 295–305 (1993).
17. T.-L. Chen *et al.*, *J. Clin. Microbiol.* **46**, 2938–2944 (2008).
18. L. Nordgård *et al.*, *Environ. Biosafety Res.* **6**, 149–160 (2007).
19. R. M. Cooper, L. Tsimring, J. Hasty, *eLife* **6**, e25950 (2017).
20. B. Vogelstein *et al.*, *N. Engl. J. Med.* **319**, 525–532 (1988).
21. See supplementary materials.
22. D. J. Simpson, L. F. Dawson, J. C. Fry, H. J. Rogers, M. J. Day, *Environ. Biosafety Res.* **6**, 55–69 (2007).
23. F. André *et al.*, *Cancer Discov.* **7**, 818–831 (2017).
24. W. Li *et al.*, *Int. J. Clin. Exp. Pathol.* **12**, 957–967 (2019).
25. P. Priestley *et al.*, *Nature* **575**, 210–216 (2019).
26. R. M. Cooper, J. Hasty, *ACS Synth. Biol.* **9**, 1129–1137 (2020).
27. T. R. M. Lannagan *et al.*, *Gut* **68**, 684–692 (2019).
28. R. Lutz, H. Bujard, *Nucleic Acids Res.* **25**, 1203–1210 (1997).
29. C. Myhrvold *et al.*, *Science* **360**, 444–448 (2018).
30. J. S. Chen *et al.*, *Science* **360**, 436–439 (2018).
31. Y. Zhong, F. Xu, J. Wu, J. Schubert, M. M. Li, *Ann. Lab. Med.* **41**, 25–43 (2021).
32. M. Iwamoto *et al.*, *MMWR Morb. Mortal. Wkly. Rep.* **64**, 252–257 (2015).

33. O. Shimada *et al*., *J. Histochem. Cytochem.* **46**, 833–840 (1998).
34. A. Wilcks, A. H. A. M. van Hoek, R. G. Joosten, B. B. L. Jacobsen, H. J. M. Aarts, *Food Chem. Toxicol.* **42**, 493–502 (2004).
35. T. Netherwood *et al*., *Nat. Biotechnol.* **22**, 204–209 (2004).
36. M. O. Din *et al*., *Nature* **536**, 81–85 (2016).
37. G. D. Sepich-Poore *et al*., *Science* **371**, eabc4552 (2021).

ACKNOWLEDGMENTS

We thank P. Winning (Winning Media) for design assistance with Fig. 1. Figures 2A and 3A were created with BioRender.com. We thank B. Leggett and V. Whitehall (Queensland Institute of Medical Research) for the original gift of the parental RKO, SW620, and LS174T human CRC cell lines used in this study. **Funding:** This work was supported by NIH grant R01CA241728 (J.H.) and NHMRC ideas grant 2020555 (D.W.). **Author contributions:** R.C., D.W., and J.H. conceived of the study and study plan. R.C., J.W., J.N., J.G., N.S., Y.L., M.I., G.R., F.R., S.K., E.T., L.V., S.W., D.W., and J.H. contributed to data acquisition and or interpretation. R.C., J.W., R.K., S.W., D.W., and J.H. wrote and revised the final manuscript. **Competing interests:** J.H. is a cofounder and board member of, and J.H., D.W., and S.W. have equity in, GenCirq Inc., which focuses on cancer therapeutics. D.W., J.H., R.C., S.W., and J.W. are inventors on a provisional patent application, "Detecting disease-associated target nucleic acids in a mammal and treatment thereof," filed by the University of California San Diego with the US Patent and Trademark Office (application no. 63/528,234). All other authors declare that they have no competing interests. **Data and materials availability:** All data are available in the manuscript or the supplementary materials. Living biosensor for arbitrary DNA is available from J.H. under a material transfer agreement with UCSD. Correspondence and requests for materials should be addressed to J.H. (hasty@ucsd.edu), D.W. (dan@colonoscopyclinic.com.au), or S.W. (susan.woods@adelaide.edu.au). **License information:** Copyright © 2023 the authors, some rights reserved; exclusive licensee American Association for the Advancement of Science. No claim to original US government works. https://www.sciencemag.org/about/science-licenses-journal-article-reuse

SUPPLEMENTARY MATERIALS

science.org/doi/10.1126/science.adf3974
Materials and Methods
Figs. S1 to S8
References (*38*–*41*)
MDAR Reproducibility Checklist
Movie S1
Data File S1

Submitted 20 October 2022; resubmitted 6 April 2023
Accepted 21 June 2023
10.1126/science.adf3974

BIOMATERIALS

Bioadhesive polymer semiconductors and transistors for intimate biointerfaces

Nan Li[1,2], Yang Li[1], Zhe Cheng[2], Youdi Liu[1], Yahao Dai[1], Seounghun Kang[1], Songsong Li[1], Naisong Shan[1], Shinya Wai[1], Aidan Ziaja[1], Yunfei Wang[3], Joseph Strzalka[4], Wei Liu[1], Cheng Zhang[1], Xiaodan Gu[3], Jeffrey A. Hubbell[1,5,6], Bozhi Tian[2], Sihong Wang[1,7]*

The use of bioelectronic devices relies on direct contact with soft biotissues. For transistor-type bioelectronic devices, the semiconductors that need to have direct interfacing with biotissues for effective signal transduction do not adhere well with wet tissues, thereby limiting the stability and conformability at the interface. We report a bioadhesive polymer semiconductor through a double-network structure formed by a bioadhesive brush polymer and a redox-active semiconducting polymer. The resulting semiconducting film can form rapid and strong adhesion with wet tissue surfaces together with high charge-carrier mobility of ~1 square centimeter per volt per second, high stretchability, and good biocompatibility. Further fabrication of a fully bioadhesive transistor sensor enabled us to produce high-quality and stable electrophysiological recordings on an isolated rat heart and in vivo rat muscles.

Integrating biocompatible electronic devices with living biological tissues is emerging as a promising avenue for achieving the real-time measurement of biological signals with high spatiotemporal resolutions for biological studies and health monitoring (*1*–*3*). An overarching goal for the development of bioelectronic devices is to achieve conformable and stable interfacing between the sensing surface and the tissue (*4*–*6*). This requires soft and stretchable properties on devices for adapting to curvilinear tissue surfaces, combined with stable bonding between the electrical sensing surface and the tissue. Progress has been made in the development of stretchable bioelectronic materials and devices (*7*–*12*). However, for interface bonding (*13*) that necessitates the adhesion property of electronic materials to wet tissue surfaces, successes have been limited to conductors (*14*–*17*), which can only be used for passive sensing that has moderate sensitivity.

To realize higher sensitivity, transistor-based active sensing devices are the more advanced option that can provide built-in amplification (*18*, *19*). For biointerfaced sensing, organic electrochemical transistors (OECTs) (*20*–*23*) based on semiconducting polymers (Fig. 1A) are one of the more promising options with several advantages, including high amplification, low operation voltage, intrinsic compatibility with ion-based biological events, and the possibility of achieving tissue-like stretchability. The sensing function of an OECT is achieved by directly attaching its semiconducting channel to the tissue surface (Fig. 1A), so that a biopotential or targeted biochemical signal can electrostatically modulate the bulk conductivity of the channel (*24*–*27*). Because such biosignal transduction is essentially determined by the microscopic distance between the semiconducting channel and a tissue surface (*4*), neither the conventional periphery fixation through suturing or stapling (Fig. 1B) nor applying a separate adhesive (Fig. 1C) can give the most conformable and stable contact between the semiconducting polymers and tissue surfaces. Instead, the more desired interfacing is to have direct adherence of the semiconducting channel to the tissue surface.

We report the design of a bioadhesive polymer semiconductor (BASC) film that can form robust and rapid adhesion (Fig. 1D) with biotissues under gentle pressure while providing high charge-carrier mobility. This is achieved through a double-network structure formed by a semiconducting polymer and a separate tissue-adhesive polymer. Although there have been reports of tissue-adhesive polymers and hydrogels (*28*–*31*), none of these are suitable for the creation of bioadhesive semiconductor films. First, because semiconducting polymers typically have long side chains, it is a challenge to ensure the accessibility of the bioadhesive groups on the film surface. Second, the bioadhesive polymer needs to have coprocessibility with semiconducting polymers that are typically soluble in organic solvents. To achieve good electrical performance, the obtained morphology needs to both keep continuous charge-transport pathways and have only a moderate level of aqueous swellability.

Design of the bioadhesive semiconductor

We designed a brush-architectured bioadhesive polymer (BAP) (Fig. 1E) for forming a double-network film with a semiconducting polymer. This bioadhesive polymer has a polyethylene backbone with long linear side chains terminated with two types of functional units in a controlled ratio: carboxylic acid (COOH) and *N*-hydroxysuccinimide (NHS) ester. The COOH group provides water absorption for temporarily drying the tissue surface and forms electrostatic interactions with tissue surfaces. The NHS ester group, as the primary contributor to bio-adhesion, covalently bonds with the primary amine groups on the tissue surface (*28*, *29*). To allow the effective exposure of these groups on the film surface when blending with

[1]Pritzker School of Molecular Engineering, The University of Chicago, Chicago, IL 60637, USA. [2]Department of Chemistry, The University of Chicago, Chicago, IL 60637, USA. [3]School of Polymer Science and Engineering, University of Southern Mississippi, Hattiesburg, MS 39406, USA. [4]X-Ray Science Division, Argonne National Laboratory, Lemont, IL 60439, USA. [5]Committee on Immunology, The University of Chicago, Chicago, IL 60637, USA. [6]Committee on Cancer Biology, The University of Chicago, Chicago, IL 60637, USA. [7]Nanoscience and Technology Division and Center for Molecular Engineering, Argonne National Laboratory, Lemont, IL 60439, USA.
***Corresponding author. Email: sihongwang@uchicago.edu**

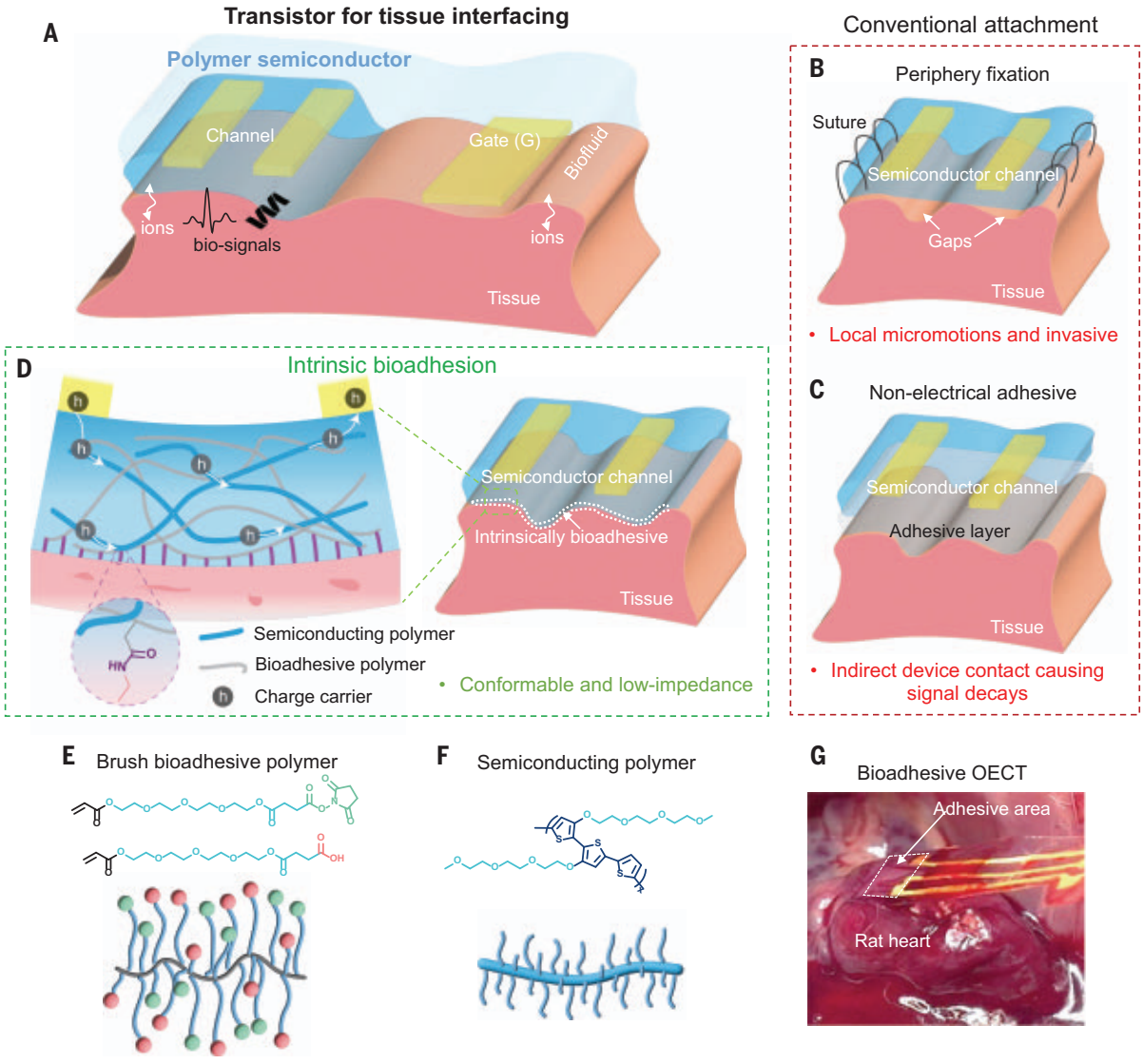

Fig. 1. Bioadhesive polymer semiconductors for electrochemical transistor–based tissue interfacing. (**A**) Use of electrochemical transistors at tissue interfaces for biosensing with built-in amplification, for which biosignals couple into the polymer semiconductor channels through direct tissue contact. (**B** and **C**) Conventional device attachment methods on tissue surfaces, such as peripheral suturing and applying a nonelectrical adhesive layer, and their corresponding limitations. (**D**) Direct adhesive attachment achieved by a BASC channel and a wet tissue surface. The double-network design of the BASC contains a semiconducting polymer and an adhesive polymer that achieves covalent bonding with tissue surfaces. (**E**) Chemical structures of the adhesive monomers with even longer linear side chains terminated with NHS ester and COOH groups, and the schematic of formed BAP. (**F**) Chemical structure and a schematic of the utilized polymer semiconductor p(g2T-T) with long linear side chains. (**G**) Photograph showing a fully bioadhesive OECT with BASC channel adhered to a rat heart for ECG recording, which can stand for mechanical agitations.

a semiconducting polymer, a key innovation in our design is the extension of the side-chain length by inserting tetra(ethylene glycol) (TEG) structure (Fig. 1E). This structure was selected for its moderate level of polarity for providing a suitable level of swelling, which can help to drain the fluid on the tissue surface and facilitate ion transport and, by contrast, will not cause exaggerated swelling and volume expansion.

The semiconductor phase is served by a type of redox-active polymer semiconductor, poly (3,3′-bis(2-(2-(2-methoxyethoxy)ethoxy)ethoxy)-2,2′:5′,2″-terthiophene) [p(g2T-T); Fig. 1F], which has shown high performance in OECT devices for biosensing functions (*32*, *33*). For the preparation of the double-network film, we blended p(g2T-T) with two types of acrylate monomers (COOH-terminated and NHS ester–terminated, respectively) in a controlled ratio (table S2) in chloroform. We then spin-coated the blended solution on a substrate to form thin films and further polymerized and cross-linked the bioadhesive monomers in the films under ultraviolet (UV) light (fig. S1). Such an in situ polymerization process not only solves the cosolubility issue, but also controls the phase separation scale for achieving better percolation connectivity of the p(g2T-T) phase (fig. S2). The obtained bioadhesive semiconductor further enables us to fabricate a fully bioadhesive and stretchable OECT sensor and realize tissue-interfaced sensing (e.g., electrophysiological recording on a wet heart; Fig. 1G) with stable bonding and built-in signal amplification.

Water absorption, morphology, and adhesion properties

According to our hypothesis, when the BASC is in contact with the tissue surface, the brush-type BAP phase starts to absorb and remove water on the tissue surface. To validate this,

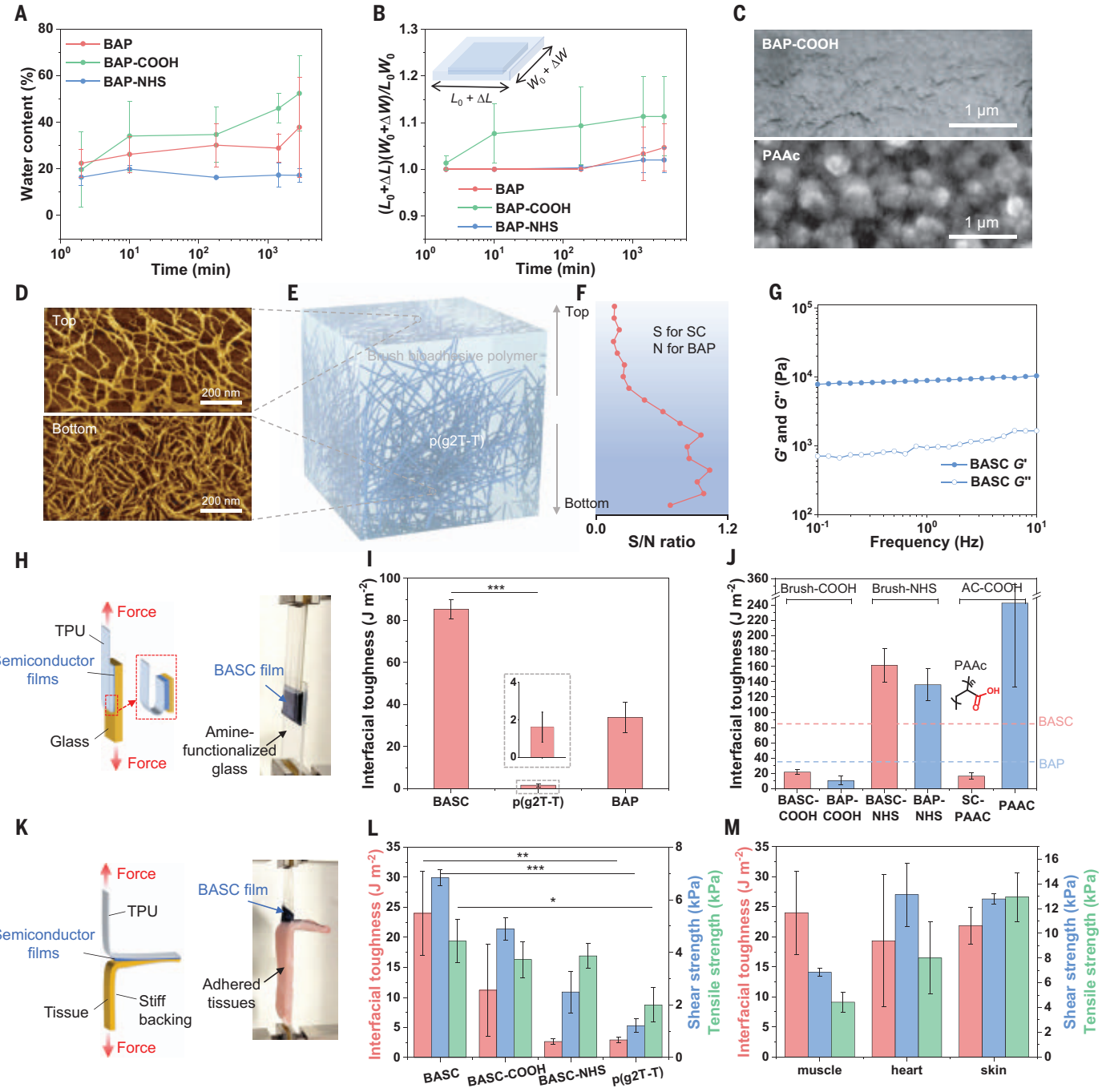

Fig. 2. Adhesive-relevant properties of the BASC films. (**A** and **B**) Water content measured through gravimetric analysis (A) and dimensional swelling (B) of the BAPs with three types of side-chain designs when soaked in PBS solution over time. (**C**) SEM images showing the microscale features of a BAP-COOH film and a PAAc film in the dry state. (**D**) AFM phase images showing the top and bottom surfaces of a BASC film. (**E**) Three-dimensional (3D) schematic morphology of a BASC film. (**F**) XPS-measured ratios between the S element and the N element from the top to the bottom surface of a BASC film. (**G**) Rheological measurement of the BASC polymer in the dry state. (**H**) 180° peel test (ASTM D3330) for interfacial toughness measurement on rigid substrates. (**I**) Interfacial toughness of the adhesion between a BASC film and an amine-functionalized, dry glass substrate, in comparison to a neat p(g2T-T) film and a BAP film. (**J**) On amine-functionalized glass substrates, interfacial toughness achieved by BASC films and BAP (including PAAc) films with different types of side chains. The two dashed lines mark the levels of interfacial toughness for the BASC and BAP films from (I). (**K**) 180° peel test (ASTM F2256) for interfacial toughness measurement on biotissues. (**L**) Interfacial toughness, shear strength, and tensile strength of the adhesion between wet pig-muscle tissues and a BASC film, a BASC-COOH film, a BASC-NHS film, and a neat p(g2T-T) film, respectively. (**M**) Interfacial toughness, shear strength, and tensile strength achieved by BASC films on various wet tissue surfaces. Values in (I), (J), (L), and (M) represent the mean and the standard deviation (n = 3 independent measurements). Statistical significance and P values are determined by two-sided Student's t test: *P < 0.05, **P < 0.01.

we first investigated the water absorption and swelling behavior of a neat-brush BAP. After soaking in phosphate-buffered saline (PBS) solution, the mass of BAP increased by ~20% after 2 min from rapid water absorption, which was followed by slow absorption over the next 24 hours (Fig. 2A). This was also reflected by the volumetric swelling, which had a lateral expansion ratio of ~1.05 (Fig. 2B). Comparatively, the 1:1 blending of the more hydrophilic COOH group and less hydrophilic NHS ester group renders the BAP with a moderate level of water absorption and swelling, which stands between the levels of the two brush polymers with only COOH- or NHS ester–terminated side chains (BAP-COOH and BAP-NHS, respectively) (fig. S3). The water-absorption behaviors of these three brush-architectured polymers are all much milder than that of poly(acrylic acid) (PAAc) (fig. S4), which could come from the different film morphologies and porosities (Fig. 2C and fig. S5) of the two different polymer architectures (i.e., brush versus nonbrush) (*34*, *35*). Overall, the moderate level of water absorption for BAP is beneficial for the stability of electrical performance from BASC films.

When the BAP is blended with p(g2T-T) to form BASC films through spin-coating processes, the p(g2T-T) phase self-assembles into interconnected nanofibril structures (Fig. 2E), as evidenced by atomic force microscopy (AFM) images (Fig. 2D and fig. S6) for the top and bottom surfaces of a film with the blending ratio of 1:40 (in mass) for p(g2T-T)-to-BAP. In the thickness direction, depth-profiling x-ray photoelectron spectroscopy (XPS) showed an increasing fraction of p(g2T-T) from the top to the bottom surface (Fig. 2F). This high ratio of BAP was chosen to ensure sufficient surface density of NHS ester groups for high adhesive property, which we validate further in the next paragraph. Such a dominant amount of BAP in the BASC film also renders the BASC film with similar mechanical properties to BAP, as featured by a low modulus and viscoelasticity (Fig. 2G and figs. S7 and S8). These tissue-like mechanical properties are crucial for achieving conformal physical contact with tissue surfaces and further forming adhesion (*36*).

We next studied the adhesion behavior of BASC films through 180° peel, lap-shear, and tensile tests on various synthetic materials and biotissues, by first holding these films [supported on thermoplastic polyurethane (TPU) substrates] to the different surfaces with gentle pressure (around 5 kPa) for 1 min (fig. S9). On amine-treated glass surfaces, which can form covalent interaction with NHS ester, BASC films displayed much stronger and tougher adhesion than neat p(g2T-T) films with an over 40-fold increase in the interfacial toughness, which achieves even higher level than the BAP film (Fig. 2, H and I, and fig. S10). Tests of BASC films with other blending ratios manifested the general trend of higher adhesion from higher ratios of BAP in the film (fig. S11). On several other synthetic surfaces (i.e., gold, TPU, and PDMS), BASC films also formed much stronger adhesion than neat p(g2T-T) films (fig. S12).

With the side-chain design of the BAP playing the key role in the adhesion property of BASC films, we further compare the BAP (1:1 ratio of COOH and NHS ester) with three polymers with the same backbone but different side chains: BAP-COOH, BAP-NHS, and regular PAAc. We also made comparisons between the three blended semiconducting films (namely BASC-COOH, BASC-NHS, and SC-PAAc) from each of these polymers with p(g2T-T) in the ratio of 1:40. Through testing on amine-functionalized glass surfaces, several observations can be made. First, among the three types of brush BAPs and the resulting BASCs, the higher amount of NHS ester gives higher adhesion, which proves that the adhesion is mainly provided by the NHS group. Second, the three BASCs built with the three brush BAPs all provide comparable or higher adhesion properties with their corresponding BAPs. By contrast, the blending of PAAc with p(g2T-T) results in a decrease of adhesion by about 90% (Fig. 2J). This validates our design

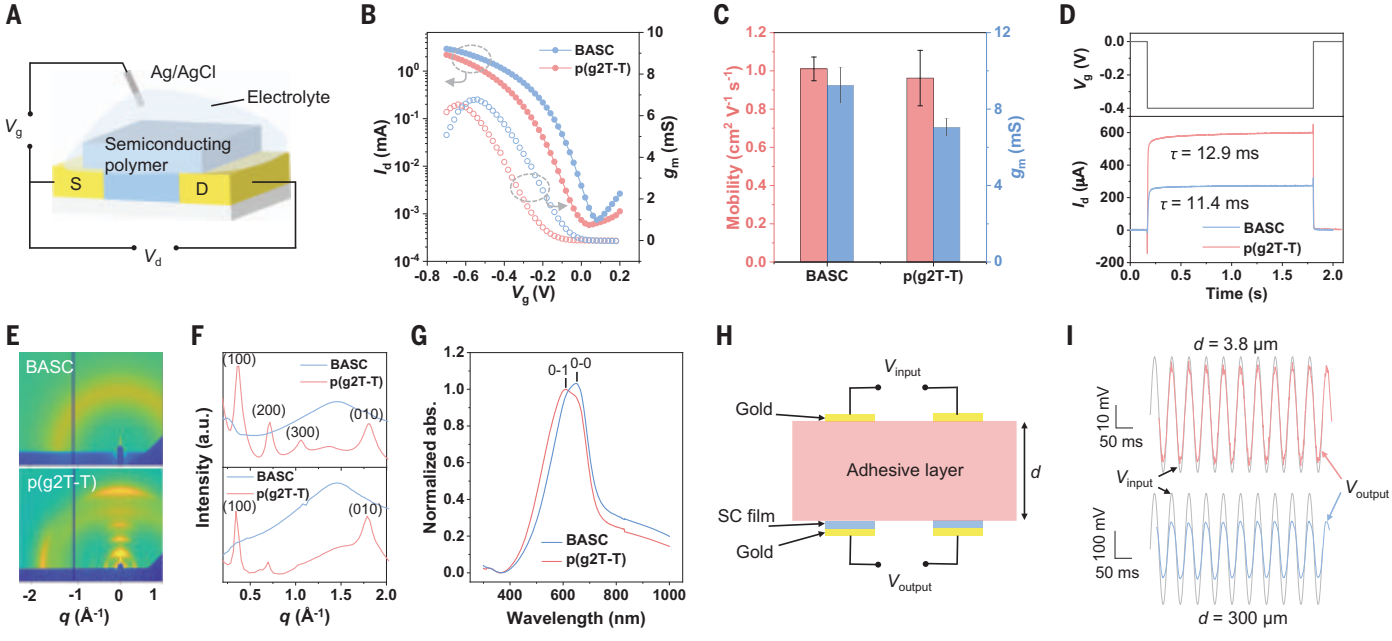

Fig. 3. Electrical and structural characterizations of the BASC film. (**A**) Setup for the OECT-based characterizations. (**B**) Transfer curves from a BASC film and a p(g2T-T) film serving as the OECT channel. V_g, gate voltage; I_d, drain current; V_d, drain voltage; g_m, transconductance. (**C**) Charge-carrier mobility and g_m for the BASC and p(g2T-T) films. Values represent the mean and the standard deviation (n = 5 independent measurements). (**D**) Response-speed measurement with applied gate-voltage pulse and drain-current response. (**E**) 2D GIXD patterns of the BASC and p(g2T-T) films. (**F**) 1D linecuts in the out-of-plane direction (top) and in-plane direction (bottom) of a BASC and a p(g2T-T) film. a.u., arbitrary units. (**G**) Normalized UV-vis absorption of a BASC and a p(g2T-T) film. (**H**) Schematic diagram showing the setup for characterizing the influence of the device-tissue distance caused by the use of a separate bioadhesive layer. (**I**) AC signal input (gray) and acquired signals between the p(g2T-T) electrodes that are covered with a layer of BAP with two different thicknesses. The thin adhesive layer (thickness, d = 3.8 μm) decreases the signal amplitude by 15% whereas the thick adhesive layer (d = 300 μm) decreases the amplitude by 50%.

hypothesis for BAP that states that long side chains are needed for overcoming the shielding effect from the long side chains of p(g2T-T) on the adhesive groups.

We then characterized the adhesion performance of BASC films on wet tissue surfaces (figs. S13 and S14). As shown for pig muscle surfaces, BASC films achieve an interfacial toughness of ~24 J m^{-2}, a shear strength of ~7 kPa, and a tensile strength of ~4.4 kPa, which are values that are ~10 times greater than those of neat p(g2T-T) films for interfacial toughness (Fig. 3, K and L). These adhesion properties are achieved with an equal ratio of brush COOH and NHS-ester side chains and are greater than those with COOH- or NHS ester–only side chains (i.e., BASC-COOH and BASC-NHS) (Fig. 2L and fig. S15) or other unbalanced mixing ratios of the two groups (figs. S16 and S17). Such a trend of the side-chain influence is different from the adhesion behaviors on dry amine-glass surfaces,

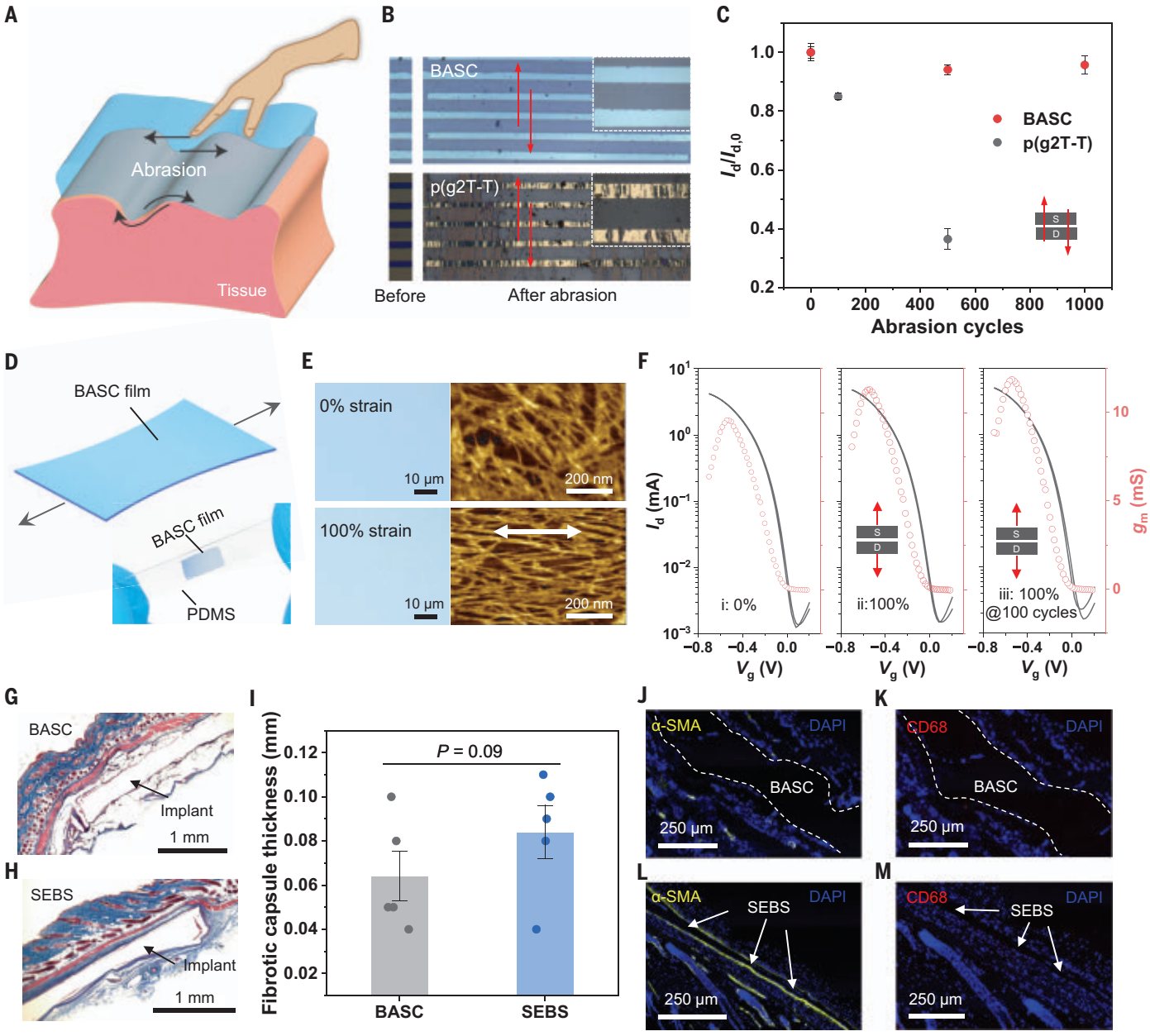

Fig. 4. Abrasion resistance, stretchability, and biocompatibility of BASC films. (**A**) Schematic diagram illustrating physical abrasions that can happen on the surfaces of implantable devices. (**B**) Photographs showing a BASC film and a p(g2T-T) film before and after abrasion by a PTFE-covered glass plate under 1 kPa for 500 cycles. The arrows indicate the direction of the abrasion. (**C**) Changes of OECT on current from the two films after the abrasion cycles along the charge-transport direction. Values represent the mean and the standard deviation (n = 4 or 5 independent measurements). (**D**) Schematic that illustrates a BASC film under stretching. The bottom photograph shows a stretched BASC film on a PDMS substrate at 100% strain. (**E**) Optical microscopy and AFM images showing a BASC film stretched to 100% strain without forming cracks. (**F**) Transfer curves of BASC films in the pristine state and stretched to 100% strain for 1 and 100 cycles, which were measured with V_d = −0.6 V. (**G** and **H**) Masson's trichrome staining of surrounded tissues of a subcutaneously implanted BASC film (G) and a SEBS film (control) (H) after one month in mice. (**I**) Calculated fibrotic-capsule thickness. (**J** to **M**) Immunofluorescence staining of α-SMA for fibroblasts (yellow) [(J) and (L)] and CD68 for macrophages (red) [(K) and (M)]. Statistical significance and P values are determined by two-sided Student's t test: ns, not significant; $^{**}P < 0.01$.

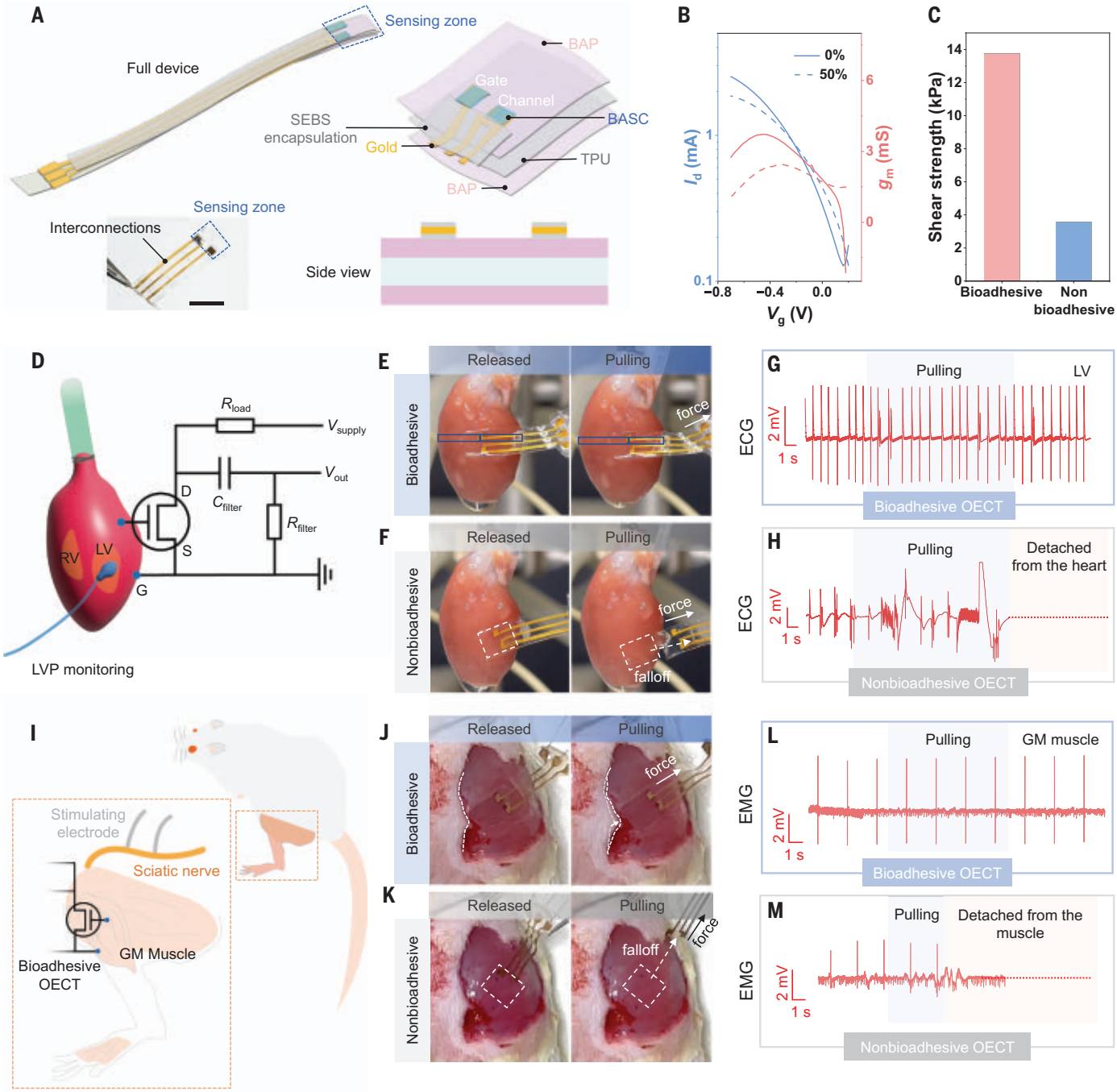

Fig. 5. Fully bioadhesive OECT sensor and the use for ex vivo and in vivo electrophysiological recording. (**A**) Device structure and picture. Scale bar, 5 mm. (**B**) Transfer curves for a fully bioadhesive OECT under 0 and 50% strains. (**C**) Shear strength of the adhesion between a fully bioadhesive OECT on the pig muscle tissue, in comparison to an OECT with nonbioadhesive surface. (**D**) Schematic that shows the use of the OECT sensor for ECG recording on a heart surface and the circuit diagram. LVP, left ventricular pressure; *G*, gate electrode; *D*, drain electrode; *S*, source electrode; *R*, resistor; *C*, capacitor. (**E**) Photographs that show a fully bioadhesive OECT attached to an isolated rat-heart surface maintaining stable contact during mechanical agitation. (**F**) Comparison with a nonbioadhesive OECT, for which capillary-based attachment cannot maintain conformable and stable contact. (**G**) ECG signals recorded by the fully bioadhesive OECT on the LV. (**H**) ECG recording by the nonbioadhesive OECT, which ceased after the device detached from the heart. (**I**) Schematic that shows the use of the OECT sensor for EMG recording on the GM muscles upon stimulation of the sciatic nerve. (**J**) Photographs that show a fully bioadhesive OECT attached to the GM muscle maintaining stable contact during mechanical agitation. (**K**) Comparison with a nonbioadhesive OECT, for which capillary-based attachment cannot maintain conformable and stable contact. (**L**) EMG signals recorded by the fully bioadhesive OECT on the GM muscle. (**M**) EMG signals recorded by the nonbioadhesive OECT on the GM muscle, which ceased after the device detached from the muscles.

which demonstrates the importance of hydrophilic COOH groups for absorbing water in establishing adhesion on wet tissue surfaces. The BASC film can also be applied to various wet tissues—including the heart, skin, and spleen—with high interfacial toughness, high shear strength, and high tensile strength (Fig. 2M and fig. S15).

Electrical performance in OECT devices

Designed as a semiconductor, the electrical performance of BASC films was characterized in OECT devices (Fig. 3A). The OECT's transfer curve with an on/off ratio of 10^4 indicates ideal semiconducting performance from the BASC film (Fig. 3B and fig. S18), which is on par with that of p(g2T-T). As calculated from the transconductance (g_m), the obtained charge-carrier mobility of the BASC film approaches 1 $cm^2 V^{-1} s^{-1}$, which is comparable to that of the neat p(g2T-T) film (Fig. 3C and figs. S19 and S20). This is given by the percolated charge-transport pathway formed by the p(g2T-T) phase in the BASC film. On the device level, the maximum transconductance (i.e., the key figure-of-merit for OECT performance) of the BASC film displays a slight increase compared with the p(g2T-T) film (Fig. 3C), which should result from the much greater thickness (1.9 μm) of the BASC film compared with that (35 nm) of the neat p(g2T-T) film. In the meantime, the measurement of the OECT response speed of these semiconducting films shows that the higher thickness of the BASC film does not lead to a slower response to the gating compared with the neat p(g2T-T) film (Fig. 3D), as ions can transport very efficiently in the blended BAP.

We carried out grazing-incidence x-ray diffraction (GIXD) and UV-visible (UV-vis) spectroscopy (Fig. 3G and fig. S21) to study interchain packing morphology of the p(g2T-T) phase in the film. The GIXD results (Fig. 3, E and F) show that blending with the brush-architected BAP almost completely suppresses the long-range crystallization, which could decrease the modulus of the p(g2T-T) phase. However, the UV-vis absorption spectroscopies show that the p(g2T-T) phase in the BASC film has a higher level of short-range aggregation than the neat film, which is represented by the ratios between 0-0 and 0-1 optical transition peaks (Fig. 3G). At the molecular level, this explains the well-maintained mobility from the BASC film.

For the direct interfacing of a semiconducting polymer with a biotissue surface for sensing biophysical or biochemical signals, the other two important interface factors that influence the recorded signal amplitudes are interfacial impedance and the separation distance between the recording and tissue surfaces. For the interfacial impedance, electrochemical impedance spectroscopy (EIS) measurements do show that our double-network BASC design gives lower impedance than applying a separate adhesive at the interface (figs. S22 to S24). Our BASC design helps to keep the closest distance between the semiconducting film and the tissue surface during recording. To semiquantitatively assess the effect of using separate adhesion layers in increasing the distance between the device and tissue surfaces (*37*–*40*), we coated our BAP polymer in two different thicknesses (3.8 and 300 μm) onto a pair of p(g2T-T)–based recording electrodes (Fig. 3H). This layout emulates the channel and the gate in OECT devices. To show the recording capability, we applied alternating current (AC) signals through another pair of gold electrodes that are attached to the top surface of the BAP coating layer, which was fully soaked with PBS solution. Increasing the thickness of the BAP layers from 3.8 to 300 μm led to substantial decreases in the potential sensed between the two p(g2T-T) electrodes (Fig. 3I), which shows major signal decay caused by the use of a separate adhesive layer.

Abrasion resistance, stretchability, and biocompatibility

When a polymer semiconductor is interfaced with biotissues, several other properties, including abrasion resistance, stretchability, and biocompatibility, are important to the robustness and long-term stability of the interface and the function. During insertion and/or attachment of a device into or onto biotissues, physical abrasion can occur on the device surface (Fig. 4A). With conjugated polymers typically having relatively low stretchability and toughness, the films are generally susceptible to abrasions (*41*). Our BASC film shows abrasion resistance, which should come from the ultrasoft and viscoelastic properties (fig. S26) of the film. To characterize this, we used a piece of polytetrafluoroethylene (PTFE)–covered glass to slide back and forth on a BASC film under a pressure of 1 kPa. After 1000 cycles of such surface sliding, the BASC film remained mostly intact in appearance under an optical microscope and electrical performance in an OECT device (Fig. 4, B and C). By comparison, a neat p(g2T-T) film was damaged by the surface abrasion processes. To better mimic the abrasion during device implantation processes, we also carried out the comparison using pig skin, which gives a similar trend (fig. S25). The brief tissue contact during typical abrasion processes would not be sufficient for BASC films to generate adhesion with the tissue surfaces and further create higher frictional force.

As both p(g2T-T) and the BAP gel are highly stretchable (*10*), the resulting BASC films also have high stretchability (Fig. 4D), which benefits conformability to curvilinear tissue surfaces and robustness under tissue deformations. From the optical microscopy and AFM images, the BASC film can be stretched to 100% strain without forming any cracks (Fig. 4E). Instead, we observed strain-induced alignment of the p(g2T-T) nanofibers. When tested in OECT devices, the BASC film displayed highly stable electrical performance during stretching to 100% strain, even after 100 repeated cycles (Fig. 4F and fig. S27).

When a device is interfaced with tissue, the foreign-body response (FBR) is one of the main factors that limit the longevity (*42*, *43*), which is influenced by the modulus and the surface chemistry of an implant. We studied this behavior of our BASC films by laminating them on both sides of SEBS [polystyrene-*block*-poly(ethylene-*ran*-butylene)-*block*-polystyrene] substrates and implanting them subcutaneously in mice. After one month of implantation, the fibrotic capsules that formed around the BASC samples are thinner than those formed around SEBS control samples, which is shown by Masson's trichrome staining results (Fig. 4, G to I). Additionally, immunofluorescence imaging of FBR-related biomarkers (i.e., α-SMA and CD68) shows lower amounts of fibroblasts and macrophages deposited on the BASC surface than those on the SEBS samples (Fig. 4, J to M). These results collectively show that BASC films have better biocompatibility than SEBS, which further elevates the promise for directly interfacing with biotissues through implantable devices. In addition, in vitro cell culture (fig. S28) confirms minimal cytotoxicity of the films.

Fully bioadhesive OECT sensor for ex vivo and in vivo electrophysiological recording

We designed and fabricated an OECT-based sensor (Fig. 5A and fig. S29) using BASC films as both the semiconducting channel and the redox-active gate. The surrounding area is occupied by the substrate, which is covered by our BAP film. With the use of microcrack-based stretchable gold (figs. S30 and S31) as the electrodes (*44*, *45*) and thin SEBS layers (~570 nm thick) as the encapsulation for the interconnects and the bottom side of the electrodes, the OECT sensor is also stretchable. An as-fabricated fully bioadhesive OECT displays ideal transfer behavior at 0% strain and when stretched to 50% strain (Fig. 5B and fig. S32) and forms strong adhesion when attached to the surface of a wet pig muscle (Fig. 5C).

We further demonstrated the benefit of the bioadhesive property of the OECT sensor on an epicardial electrocardiogram (ECG) recording from an isolated rat heart (Fig. 5D). The bioadhesive OECT can be conveniently adhered to the wet heart surface by gently pressing for 20 s. During the recording process, the bioadhesive and stretchable properties working in conjunction helped the OECT to well accommodate the heart beating, thereby maintaining spatially stable and conformable contact on the heart (Fig. 5E, fig. S34, and movie S1). Even under external mechanical perturbation (e.g., pulling), stable attachment was still maintained.

The ECG recording from both the left ventricle (LV) and right ventricle (RV) surfaces also remained stable (Fig. 5G and fig. S34). By comparison, for a nonbioadhesive OECT (figs. S35 and S36), which can only stay on the heart surface by means of capillary force from the fluid, gradual drifting and complete detachment can happen as a result of either heart beating or external perturbation (e.g., pulling) (Fig. 5F, fig. S34, and movie S2). This substantially affects the quality and stability of ECG recording (Fig. 5H).

We also demonstrated the in vivo use of the bioadhesive OECT on an under-skin electromyogram (EMG) recording from the gastrocnemius medialis (GM) muscle of a live rat, for which the OECT can also form stable adhesion by gentle pressing (Fig. 5I and fig. S37). During electrical stimulation of the sciatic nerve for triggering leg movements, EMG signals corresponding to each stimulation can be stably recorded without being affected by mechanical perturbation (e.g., pulling) (Fig. 5, J and L, and movie S3), which is in stark contrast with the nonbioadhesive OECT (Fig. 5, K and M, and movie S4). Furthermore, we also validated the benefits of such direct tissue adhesion as compared with suturing (fig. S38) or a separate adhesive layer (fig. S39) in low invasiveness and/or higher signal amplitude and stability. Such benefits couple with the built-in amplification ability of OECT-based active sensor [illustrated by the comparison with a poly(3,4-ethylenedioxythiophene) polystyrene sulfonate (PEDOT:PSS)–based passive recording device; fig. S40].

REFERENCES AND NOTES

1. S.-H. Sunwoo, K.-H. Ha, S. Lee, N. Lu, D.-H. Kim, *Annu. Rev. Chem. Biomol. Eng.* **12**, 359–391 (2021).
2. H. Yuk, B. Lu, X. Zhao, *Chem. Soc. Rev.* **48**, 1642–1667 (2019).
3. I. You *et al.*, *Science* **370**, 961–965 (2020).
4. J. Rivnay, H. Wang, L. Fenno, K. Deisseroth, G. G. Malliaras, *Sci. Adv.* **3**, e1601649 (2017).
5. S. Liu, Y. Rao, H. Jang, P. Tan, N. Lu, *Matter* **5**, 1104–1136 (2022).
6. H. Yuk, J. Wu, X. Zhao, *Nat. Rev. Mater.* **7**, 935–952 (2022).
7. J. Xu *et al.*, *Science* **355**, 59–64 (2017).
8. S. Wang *et al.*, *Nature* **555**, 83–88 (2018).
9. Y. Jiang *et al.*, *Science* **375**, 1411–1417 (2022).
10. Y. Dai *et al.*, *Adv. Mater.* **34**, e2201178 (2022).
11. Z. Yan *et al.*, *Science* **375**, 852–859 (2022).
12. K. Sim *et al.*, *Nat. Electron.* **3**, 775–784 (2020).
13. Q. Yang *et al.*, *Nat. Mater.* **20**, 1559–1570 (2021).
14. X. Wang *et al.*, *Matter* **5**, 1204–1223 (2022).
15. I. K. Han *et al.*, *Adv. Mater.* **35**, 2203431 (2022).
16. J. Deng *et al.*, *Nat. Mater.* **20**, 229–236 (2021).
17. S. Li, Y. Cong, J. Fu, *J. Mater. Chem. B Mater. Biol. Med.* **9**, 4423–4443 (2021).
18. F. Torricelli *et al.*, *Nat. Rev. Methods Primers* **1**, 66 (2021).
19. A. Marks, S. Griggs, N. Gasparini, M. Moser, *Adv. Mater. Interfaces* **9**, 2102039 (2022).
20. J. Rivnay *et al.*, *Nat. Rev. Mater.* **3**, 17086 (2018).
21. B. D. Paulsen, K. Tybrandt, E. Stavrinidou, J. Rivnay, *Nat. Mater.* **19**, 13–26 (2020).
22. J. Chen *et al.*, *Nat. Mater.* **21**, 564–571 (2022).
23. Y. Jimbo *et al.*, *Proc. Natl. Acad. Sci. U.S.A.* **118**, e2022300118 (2021).
24. G. D. Spyropoulos, J. N. Gelinas, D. Khodagholy, *Sci. Adv.* **5**, eaau7378 (2019).
25. C. Cea *et al.*, *Nat. Mater.* **19**, 679–686 (2020).
26. S. L. Bidinger *et al.*, *Sci. Adv.* **8**, eadd4111 (2022).
27. K. Guo *et al.*, *Nat. Biomed. Eng.* **5**, 666–677 (2021).
28. J. Li *et al.*, *Science* **357**, 378–381 (2017).
29. H. Yuk *et al.*, *Nature* **575**, 169–174 (2019).
30. B. Xue *et al.*, *Nat. Commun.* **12**, 7156 (2021).
31. Z. Ma *et al.*, *Science* **377**, 751–755 (2022).
32. C. B. Nielsen *et al.*, *J. Am. Chem. Soc.* **138**, 10252–10259 (2016).
33. S. Inal, G. G. Malliaras, J. Rivnay, *Nat. Commun.* **8**, 1767 (2017).
34. M. Zhang, A. H. E. Müller, *J. Polym. Sci. A Polym. Chem.* **43**, 3461–3481 (2005).
35. E. Dashtimoghadam *et al.*, *Nat. Commun.* **12**, 3961 (2021).
36. C. M. Tringides *et al.*, *Nat. Nanotechnol.* **16**, 1019–1029 (2021).
37. A. H. Marblestone *et al.*, *Front. Comput. Neurosci.* **7**, 137 (2013).
38. J. Du *et al.*, *J. Neurophysiol.* **101**, 1671–1678 (2009).
39. O. Herreras, *Front. Neural Circuits* **10**, 101 (2016).
40. N. Pérez-Prieto, M. Delgado-Restituto, *Front. Neurosci.* **15**, 681085 (2021).
41. A. X. Chen, A. T. Kleinschmidt, K. Choudhary, D. J. Lipomi, *Chem. Mater.* **32**, 7582–7601 (2020).
42. S. Capuani, G. Malgir, C. Y. X. Chua, A. Grattoni, *Bioeng. Transl. Med.* **7**, e10300 (2022).
43. R. Biran, D. C. Martin, P. A. Tresco, *Exp. Neurol.* **195**, 115–126 (2005).
44. N. Matsuhisa, X. Chen, Z. Bao, T. Someya, *Chem. Soc. Rev.* **48**, 2946–2966 (2019).
45. Y. Lee *et al.*, *Sci. Adv.* **7**, eabg9180 (2021).

ACKNOWLEDGMENTS

We thank the University of Chicago Animal Resources Center (RRID:SCR_021806), especially A. Solanki for his assistance with animal surgery and housing. All the animal experiments performed in this research were approved by the Institutional Animal Care and Use Committee of the University of Chicago under the protocols of ACUP 72378 and ACUP 72450. **Funding:** This work was supported by the National Science Foundation (NSF) (award no. 2105367), the US National Institutes of Health Director's New Innovator Award (1DP2EB034563), and the US Office of Naval Research (N00014-21-1-2266) and N00014-21-1-2581). This work was partially supported by the University of Chicago Materials Research Science and Engineering Center (which is funded by the NSF under award no. DMR-2011854) and the start-up fund from the University of Chicago. This work used the Soft Matter Characterization Facility (SMCF) at the University of Chicago. This research used resources of the Advanced Photon Source, a US Department of Energy (DOE) Office of Science user facility operated for the DOE Office of Science by Argonne National Laboratory under contract no. DE-AC02-06CH11357. Y.W. and X.G. thank the financial aid from NSF grant DMR-2047689. **Author contributions:** S.Wang conceived of and supervised this research. N.L. and S.Wang designed the experiments. N.L. and N.S. synthesized and characterized the monomers and polymers. N.L. and Y.Li performed the mechanical tests. N.L., Y.Li, Y.Liu, Y.D., S.L., and A.Z. fabricated the transistor devices and performed the measurements. N.L., Y.D., and J.S. performed the GIXD characterization. Z.C., N.L., and B.T. performed the ex vivo ECG and in vivo EMG measurements. S.K., N.L., S.Wai, and J.A.H. performed the biocompatibility study. Y.W. and X.G. conducted the film-on-water test. W.L. and C.Z. participated in the discussions. N.L. and S.Wang cowrote the paper. All authors reviewed and commented on the manuscript. **Competing interests:** S.Wang and N.L. are inventors on patent application no. UCHI 23-T-101 submitted by the University of Chicago. **Data and materials availability:** All data are available in the manuscript or the supplementary materials. **License information:** Copyright © 2023 the authors, some rights reserved; exclusive licensee American Association for the Advancement of Science. No claim to original US government works. https://www.science.org/about/science-licenses-journal-article-reuse

SUPPLEMENTARY MATERIALS

science.org/doi/10.1126/science.adg8758
Materials and Methods
Figs. S1 to S40
Tables S1 to S4
References (*46*–*72*)
MDAR Reproducibility Checklist
Movies S1 to S4

Submitted 26 January 2023; accepted 14 June 2023
10.1126/science.adg8758

HUMAN EVOLUTION

Extreme glacial cooling likely led to hominin depopulation of Europe in the Early Pleistocene

Vasiliki Margari[1], David A. Hodell[2], Simon A. Parfitt[3,4], Nick M. Ashton[5], Joan O. Grimalt[6], Hyuna Kim[7,8], Kyung-Sook Yun[7,9], Philip L. Gibbard[10], Chris B. Stringer[4], Axel Timmermann[7,9]*, Polychronis C. Tzedakis[1]*

The oldest known hominin remains in Europe [~1.5 to ~1.1 million years ago (Ma)] have been recovered from Iberia, where paleoenvironmental reconstructions have indicated warm and wet interglacials and mild glacials, supporting the view that once established, hominin populations persisted continuously. We report analyses of marine and terrestrial proxies from a deep-sea core on the Portugese margin that show the presence of pronounced millennial-scale climate variability during a glacial period ~1.154 to ~1.123 Ma, culminating in a terminal stadial cooling comparable to the most extreme events of the last 400,000 years. Climate envelope–model simulations reveal a drastic decrease in early hominin habitat suitability around the Mediterranean during the terminal stadial. We suggest that these extreme conditions led to the depopulation of Europe, perhaps lasting for several successive glacial-interglacial cycles.

The earliest published fossil hominin (*Homo* sp.) evidence in Europe is a mandible and a hand phalanx found with stone tools at the site of Sima del Elefante, Sierra de Atapuerca, northern Spain (*1*, *2*), as well as a deciduous molar and stone tools from the sites of Barranco León and Fuente Nueva *3*, Guadix-Baza Basin, southeastern Spain (*3*, *4*). Analysis of traits of the Sima del Elefante hominin suggests a possible Eurasian (rather

[1]Environmental Change Research Centre, Department of Geography, University College London, London WC1E 6BT, UK. [2]Department of Earth Sciences, University of Cambridge, Cambridge CB2 3EQ, UK. [3]Institute of Archaeology, University College London, London WC1H 0PY, UK. [4]Centre for Human Evolution Research, The Natural History Museum, London SW7 5BD, UK. [5]Department of Britain, Europe and Prehistory, British Museum, London N1 5QJ, UK. [6]Department of Environmental Chemistry, Institute of Environmental Assessment and Water Research (IDAEA), Spanish Council for Scientific Research (CSIC), 08034 Barcelona, Spain. [7]Institute for Basic Science, Center for Climate Physics, Busan 46241, South Korea. [8]Department of Climate System, Pusan National University, Busan 46241, South Korea. [9]Pusan National University, Busan 46241, South Korea. [10]Scott Polar Research Institute, University of Cambridge, Cambridge CB2 1ER, UK.
***Corresponding author. Email: p.c.tzedakis@ucl.ac.uk (P.C.T.); axel@ibsclimate.org (A.T.)**

than African) evolutionary origin (*5*) for the population that it represents. Given that hominins were present at Dmanisi, Georgia, ~1.8 million years ago (Ma) (*6*), dispersal into Europe could have taken place at any time after that, but sites in Italy and Spain yielding stone tools and human remains over a broad time window of ~1.6 to ~1.1 Ma indicate a delay of ~200 thousand years (kyr) (Fig. 1 and table S1) (*7*). This dispersal lag may be attributed to a period of cooler interglacials ~1.8 to ~1.6 Ma, which in turn may be related to the 1.2-million-year (Myr) amplitude modulation of the obliquity cycle (*8*).

Considerable disagreement remains on whether early hominin occupation was permanent (*9*–*11*) or restricted to interglacials, implying that southern Europe was repeatedly colonized from Southwest Asia (*12*–*14*). Although various factors (geographical, biological, technocultural, and demographic) influence hominin occupation patterns, environmental conditions ultimately act as a limiting factor. Therefore, reconstructions of the climatic background to hominin occupation can constrain the likelihood of different scenarios.

Before 1.2 Ma, glacial-interglacial cycles occurred with a period of ~41 kyr, with maximum ice volumes ranging between one-half and one-third of the Last Glacial Maximum value (*15*, *16*). The less-extensive ice sheets and shorter glacial periods of the Early Pleistocene have been linked to smaller decreases in temperature compared with those of the Middle and Late Pleistocene. Nonetheless, North Atlantic records point to the occurrence of iceberg discharges from marine-terminating ice sheets and disruptions of the Atlantic meridional overturning circulation (AMOC) during the interval ~1.43 to ~1.25 Ma (*17*–*20*), but their downstream impacts on European climate remain largely unknown. A lengthening and intensification of glacial-interglacial cycles took place over the so-called Early-Middle Pleistocene Transition [~1.25 to ~0.70 Ma (*21*)], after which ice volume varied with a dominant ~80- to ~120-kyr periodicity.

Paleoenvironmental reconstructions based on animal and plant remains from the Atapuerca and Guadix-Baza occupation levels indicate a diverse mosaic of Mediterranean and temperate woodlands, open shrublands, and extensive wetlands, with mean annual temperatures similar to those of the present, but higher mean annual precipitation (*10*, *22*–*25*). The presence of thermophilous species within a mosaic of woodland and open habitats throughout the Sima del Elefante sequence has been used to infer relative ecological stability during both interglacials and glacials and to argue for the continuity of occupation (*10*), but stratigraphical hiatuses and preservation biases may have led to intermittent representation, complicating such interpretations. Early Pleistocene pollen sequences are available from northeastern Spain (*26*) but are fragmentary and lack precise chronologies. In the Guadix-Baza Basin, the Palominas pollen record contains a succession of ~10 forest and open-vegetation phases, representing interglacial and glacial periods, respectively (*27*). In the absence of independent chronological controls, biostratigraphical correlations point to the record extending from ~1.6 to ~1.2 Ma (*27*). Pollen-based climate reconstructions suggest that mean annual precipitation levels during glacials were similar to modern levels and higher during interglacials; temperature reconstructions for both glacials and interglacials indicate values similar to those of the present (*27*). The implication is that these conditions would have allowed hominin populations to persist through glacials and expand during interglacials (*11*).

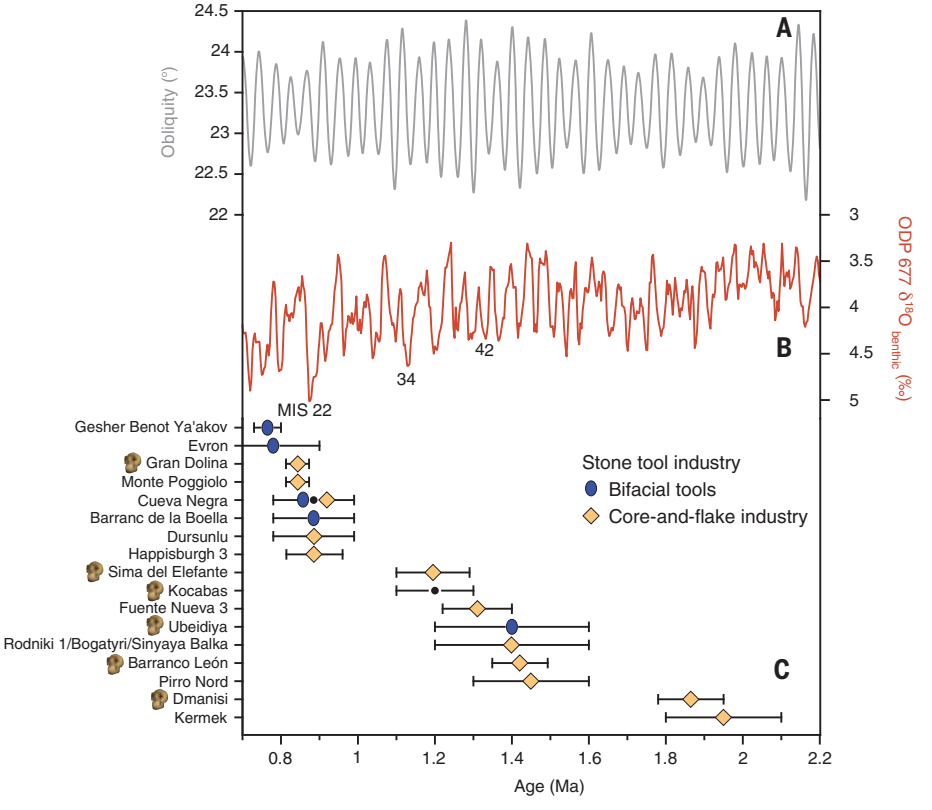

Fig. 1. Age estimates of European and Southwest Asian early hominin sites and paleoclimate context. (**A**) Obliquity variations (*60*). (**B**) Benthic oxygen isotope record from eastern equatorial Pacific Site ODP677 (*15*). (**C**) Age estimates of European and Southwest Asian early hominin sites (table S1). Stone-tool industries are shown; sites with hominin remains are indicated by skulls. Site selection is based on presence of human remains, strong evidence of humanly manufactured lithic artifacts, and a secure chronological framework (*7*).

Assessing climate impacts on human populations

To address the pervasive issues with stratigraphical continuity and chronological control in terrestrial sedimentary sequences, we have undertaken an examination of the paleoenvironmental context during the interval of early human occupation at deep-sea Site U1385 on the southwestern Portuguese margin (*28*) (fig. S1), a prime location for joint marine-terrestrial analyses and correlations (*29*–*32*). Sites on the southwestern Portuguese margin are also well situated to record past changes in North Atlantic surface and deep-ocean circulation: During Marine Isotope Stage (MIS) 3 [59 to 24 thousand years ago (ka)], the oxygen isotopic composition of planktic foraminifera ($\delta^{18}O_{planktic}$) closely matched the Greenland temperature record, with abrupt transitions marking the onset and end of interstadials, whereas the oxygen isotopic composition of benthic foraminifera ($\delta^{18}O_{benthic}$) resembled the Antarctic temperature record, both in its shape and phasing relative to Greenland (*33*). This asynchronous phasing between $\delta^{18}O_{planktic}$ and $\delta^{18}O_{benthic}$ has been interpreted as a fingerprint of AMOC changes associated with interhemispheric heat transport and the bipolar seesaw (*31*). Here, we focus on reconstructing sea and land changes during two time windows of the interval of early hominin occupation, representing distinct climatic contexts: a 41-kyr cycle, MIS 43 to 42 (~1.380 to ~1.338 Ma), and one cycle from the Early-Middle Pleistocene Transition, MIS 35 to 34 (~1.192 to ~1.123 Ma). Analyses (*7*) were undertaken with respect to (i) $\delta^{18}O_{planktic}$ and $\delta^{18}O_{benthic}$, reflecting changes in surface-water conditions, and in

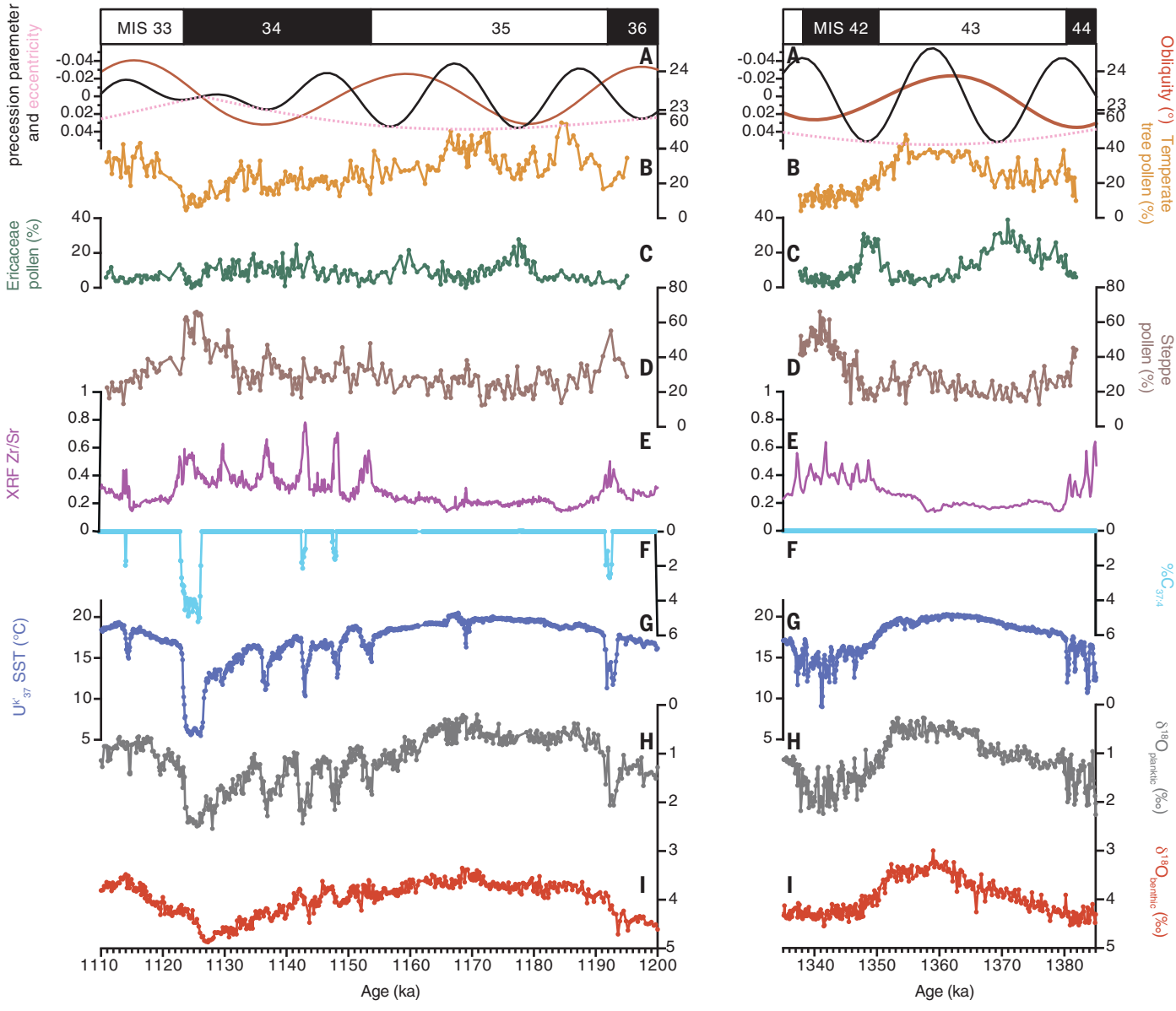

Fig. 2. U1385 paleoclimate records. The figure shows MIS 43 to 42 (right) and MIS 35 to 34 (left). (**A**) Obliquity, eccentricity, and precession parameter (*60*). (**B**) Temperate (Mediterranean+Eurosiberian) tree-pollen percentages. (**C**) Ericaceae (heathland)–pollen percentages. (**D**) Pollen percentages of steppe taxa (Poaceae, *Artemisia*, Amaranthaceae, and *Ephedra*). (**E**) XRF Zr/Sr ratio. (**F**) Abundance of tetra-unsaturated C37 alkenones ($\%C_{37:4}$). (**G**) Alkenone-based $U^{k'}_{37}$ SST. (**H**) Planktic $\delta^{18}O$ of *Globigerina bulloides*. (**I**) Benthic $\delta^{18}O$ of *Cibicidioides* spp. Marine Isotope Stages (MISs) are indicated.

global ice-volume and deep-water hydrography, respectively; (ii) the relative composition of C37 unsaturated alkenones, reflecting surface-water conditions; (iii) pollen content, providing an integrated picture of regional vegetation changes in southwestern Portugal; and (iv) x-ray fluorescence (XRF) sediment-composition changes, reflecting variations in the relative proportion of detrital (Zr) and biogenic (Sr) sediment supply.

To assess and further quantify the climate impact on human occupation, we developed a climate envelope model that is based on climate data from a 2-Myr transient coupled general circulation model simulation (*34*) and a new database of early hominin sites for Europe and Southwest Asia (table S1) (*7*). This model, which calculates hominin habitat suitability as a function of net primary productivity and minimum annual temperature, was then forced with the respective climate data obtained from a freshwater perturbation model experiment (*7*).

Paleoenvironmental reconstructions

Figure 2 (right) shows the results of our analyses for the interval MIS 43 to 42. The onset of warm conditions occurred at ~1.380 Ma, marked by a decrease in detrital sediment supply and a shift to higher alkenone-based sea surface temperature (SST) and temperate tree-pollen values, while sea level was gradually rising. A decrease in summer insolation at ~1.370 Ma led to an expansion of heathland pollen, reflecting moisture availability under reduced summer evaporation regimes in Portugal (*35*), but steppe-pollen values remained low. Peak interglacial conditions occurred at ~1.366 to ~1.353 Ma, when SSTs reached 20°C and values of deciduous oak and Mediterranean sclerophyll pollen exceeded 40%. Subsequently, benthic and planktic $\delta^{18}O$ values gradually increased, mirrored by a gradual decline in SST and temperate tree-pollen values. The MIS 42 glacial (~1.350 to ~1.338 Ma) contained a series of small, centennial-scale oscillations in $\delta^{18}O_{planktic}$ and SST and an increase in steppe-pollen percentages.

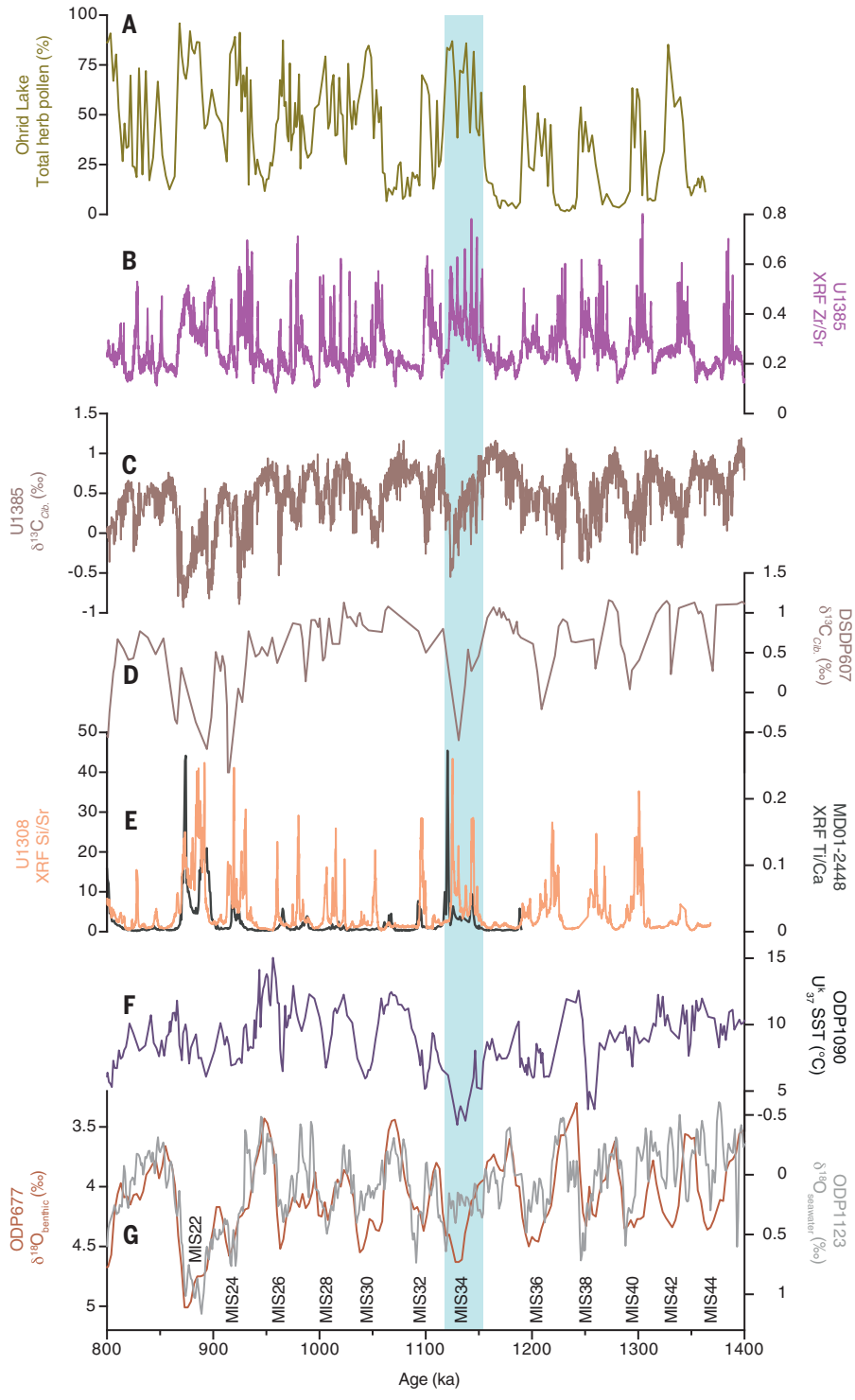

Fig. 3. Comparison of paleoclimate records over the interval 800 to 1400 ka. (**A**) Lake Ohrid (Albania and North Macedonia) total herb pollen percentages (*56*). (**B**) U1385 Zr/Sr record (*28*). (**C**) U1385 benthic $\delta^{13}C$ of *Cibicidioides* spp. (*28*). (**D**) DSDP607 benthic $\delta^{13}C$ of *Cibicidioides* spp. from the North Atlantic (*54*). (**E**) U1308 XRF Si/Sr ratio from the North Atlantic (*18*) and MD01-2448 XRF Ti/Ca ratio from the Bay of Biscay (*50*). (**F**) ODP1090 alkenone-based U^{K}_{37} SST from the South Atlantic (*55*). (**G**) ODP677 benthic foraminiferal $\delta^{18}O$ (orange) from the eastern equatorial Pacific (*15*) and ODP1123 deconvolved $\delta^{18}O$ composition of seawater (gray) from the southwest Pacific (*16*). Marine Isotope Stages (MISs) are indicated.

For the second time window, MIS 35 to 34 (Fig. 2, left), all proxies indicate the onset of MIS 35 at ~1.192 Ma, with interglacial conditions extending over two precessional cycles until ~1.154 Ma. The pollen record shows two temperate-tree maxima followed by expansions of heathland, suggesting continued moisture availability, but not an intervening increase in steppe-pollen frequencies. The long MIS 35 (~1.192 to ~1.154 Ma) interglacial was succeeded by a long MIS 34 glacial (~1.154 to ~1.123 Ma), together forming an unusually protracted climate cycle (*15*, *36*) characterized by weak eccentricity forcing (Fig. 2A, left). MIS 34 is marked by the occurrence of four stadials and interstadials from ~1.154 to ~1.127 Ma, similar to the Middle and Late Pleistocene millennial-scale climate variability, including abrupt interstadial onsets and asynchronous phasing of the planktic and benthic $\delta^{18}O$ curves, bearing the fingerprint of the bipolar seesaw (*31*, *33*). A large increase in the abundance of tetra-unsaturated C37 alkenones ($\%C_{37:4}$), indicating the advection of low-salinity polar water masses to the Portuguese margin (*37*, *38*), was accompanied by major decrease in SST, thermocline cooling (*39*), activation of the bipolar seesaw, and maximum expansion of steppe communities at ~1.127 Ma, ushering in a terminal stadial of extreme cold and arid conditions that persisted for 4 kyr before the transition into MIS 33.

Long interglacials and contrasting glacials

Reconstructions from large-mammal remains across the western Paleoarctic indicate alternating open savannah and forested savannah landscapes from ~1.8 to ~1.2 Ma, with increased habitat variability from ~1.2 to ~0.9 Ma; the large diversity of resources, especially along river systems and coastal plains, is considered to have supported hominin dispersal and occupation during both interglacials and glacials (*40*). Our results partly support this view. Both of the interglacial periods that we examined (Fig. 2) were characterized by the persistence of mild and relatively stable conditions with a mosaic of Mediterranean plant communities and open habitats, representing long windows of opportunity for hominin dispersal and occupation. The evidence from the two glacials, however, reveals distinct environmental conditions.

The MIS 42 glacial interval was short (~12 kyr) with subdued centennial-scale SST oscillations (16° to 12°C) and steppe vegetation communities with residual woodland [apart from a brief event with lower SST (9°C) and higher steppe values]. The absence of $C_{37:4}$ suggests minimal advection of cold and fresh polar water masses. The overall environmental conditions correspond to terrestrial reconstructions from Iberia (*27*), indicating relatively mild glacials before 1.2 Ma that would not present barriers to

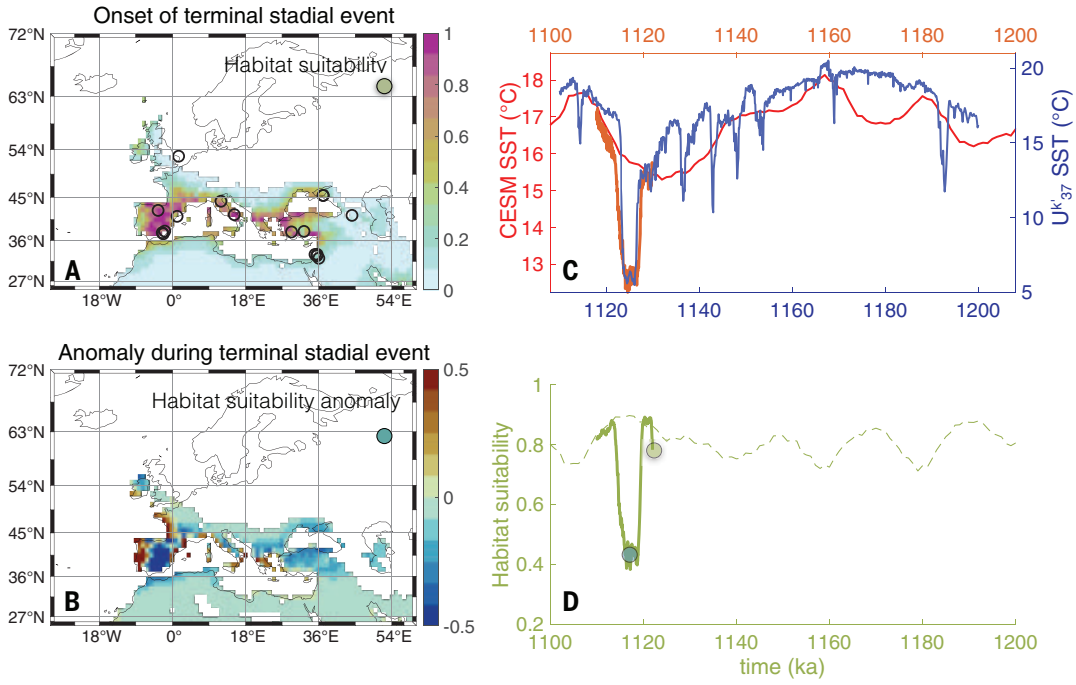

Fig. 4. MIS 34 terminal stadial event impact on early European human habitats. (**A**) Simulated habitat suitability (shaded) for the climate background conditions corresponding to the onset of MIS 34 terminal stadial event conditions (1122 ka CESM1.2 initial conditions), along with locations (circles) of hominin sites included in analysis discussed in text. Habitat suitability values smaller than 0.05 are not displayed. (**B**) Anomaly of habitat suitability during the peak of the MIS 34 terminal stadial event [corresponding to model year 1117 ka (D)]. (**C**) Western Iberian margin SST simulated by the "2Ma" transient CESM1.2 experiment (*34*) (thin red line) and by the freshwater perturbation experiment (thick orange line) (*7*), and alkenone SST from U1385. The offset between the two timescales arises from differences between the U1385 age model (blue) (*7*) and the CESM1.2 age model (red), whose CO_2 forcing before 784 ka is based on the model estimates of (*59*). (**D**) Simulated habitat suitability for "2Ma" (dashed line) and for CESM1.2 MIS34 terminal stadial event simulation (solid olive line) for the western Iberian Peninsula (averaged over 4°W to 0°E, 38°N to 43°N). The timescale in olive corresponds to the model age. The climate envelope model used in (A), (B), and (D) is calculated by using 17 early hominin sites (*7*) and 1000-year mean data of minimum annual temperature and calculated net primary productivity for these sites obtained from the "2Ma" simulation.

hominin dispersal and occupation. By contrast, MIS 34 was a long glacial (~31 kyr) with a series of pronounced and increasingly colder stadial-interstadial oscillations as low eccentricity allowed the continued growth of ice sheets under the influence of internal climate feedbacks (*41*). This culminated at ~1.127 Ma in a long terminal stadial sustained by meltwater from disintegrating ice sheets, leading to (i) AMOC weakening as suggested by negative $\delta^{13}C_{Cibicidioides}$ anomalies (Fig. 3C) and (ii) cold (SST 5.6°C) and arid (maximum steppe pollen 65%) conditions comparable to the most extreme events of the last 400 kyr (at ~345, ~265, and ~155 ka) recorded on the southwestern Portuguese margin (fig. S2).

The first major glaciation of the Early-Middle Pleistocene Transition is traditionally considered to have occurred during MIS 22, around 0.9 Ma (*21*). However, the Site ODP677 record from the eastern equatorial Pacific shows a shift toward larger $\delta^{18}O_{benthic}$ values in MIS 34 (*15*), implying increasing global ice volume, although this is not as clear in the deconvolved $\delta^{18}O$ of seawater in Site ODP1123 from the southwest Pacific (*16*) (Fig. 3G). In North America, ice from the Keewatin ice center became more extensive during the pre-Illinoian G glaciation, which includes MIS 34 (*42*, *43*). Compilation of sediment volumes and ice-rafted detritus records along the northeast Atlantic continental margin indicates large-scale ice sheet activity in the Kara–Barents-Sea–Svalbard region and more-restricted Fennoscandian and British-Irish ice sheets from ~2.7 to ~1.5 Ma; while an extensive Kara–Barents-Sea–Svalbard ice sheet persisted over the interval ~1.5 to ~0.8 Ma, glacial activity intensified around the North Sea, with ice sheets coalescing during peak glaciations (*44*). More specifically, there is evidence of Fennoscandian and British-Irish ice sheet expansion at ~1.2 to ~1.1 Ma, with the Fedje Till in the Norwegian Channel (*45*, *46*), influx of glaciofluvial deposits from Britain in the central North Sea (*47*), and glacial erratics in the Hattem Beds in the northern Netherlands and adjacent Germany during the Menapian Cold Stage, which has been broadly correlated with MIS 34 (*43*, *47*–*49*).

Considering the interval from 1.4 to 0.8 Ma (Fig. 3, B and E), MIS 34 stands out in the U1385 XRF record (*28*) as an extended period with pronounced Zr/Sr peaks, indicating increases in detrital sediment supply during cold stadials. This compares with results from Site U1308, located near the center of the so-called "ice-rafted detritus belt" of the North Atlantic, which shows high MIS 34 XRF Si/Sr values, reflecting increased delivery of detrital silicate minerals (*18*) of the same order as those from MIS 22. Lithological changes in core MD01-2448 in the Bay of Biscay also show a prominent peak in terrigenous fluxes in MIS 34, suggesting ice-rafted material (*50*), whereas the ice-rafted detritus record from Site ODP983 south of Iceland shows a series of peaks during MIS 34, but whose absolute values do not stand out relative to those of other glacials (*20*).

Previously published North Atlantic SST reconstructions do not show particularly extreme cooling during MIS 34 (fig. S3), but they are of low temporal resolution or do not capture the entire MIS 34 period. Rodrigues *et al.* (*51*) observed that the major cooling events at ~265 and ~155 ka on the southwestern Portuguese margin were amplified relative to those recorded in the central North Atlantic and suggested that the subpolar front may have been deflected southward in the eastern North Atlantic, with the Portugal Current transporting cold water to the vicinity of Site U1385. Climate models simulating the distribution of glacial meltwater in the North Atlantic show the most pronounced negative salinity anomalies on the eastern boundary and along the Iberian Peninsula (*52*), and this is supported by large negative oxygen isotope excursions in deglacial speleothem records from Iberia (*53*), representing meltwater source effects. It is possible that a similar advection of meltwater toward the Portuguese margin occurred during the terminal stadial of MIS 34, as indicated by our $\%C_{37:4}$ record (Fig. 2F, left), which may have contributed to a regional stratification–driven amplification of negative SST anomalies relative to the open North Atlantic. However, prominent MIS 34 changes are also observed beyond the Portuguese margin, suggesting wider-scale impacts, in contrast to the

eastern-amplification view: (i) Over the interval 1.4 to 0.8 Ma, the $\delta^{13}C_{Cibicidioides}$ record of Site DSDP607 (*54*) in the central North Atlantic shows the largest reductions in MIS 34 and then MIS 24 and 22, similar to the $\delta^{13}C_{Cibicidioides}$ record of U1385 (*28*), pointing to step changes in deep-ocean circulation (Fig. 3, C and D); (ii) South Atlantic Site ODP1090 has the lowest-recorded SST (2°C, Fig. 3F) of the past 3.5 Myr in MIS 34, together with a major increase in $\%C_{37:4}$, indicating a large expansion of polar waters into the sub-Antarctic region (*55*); and (iii) in southeastern Europe, a pollen sequence of the past 1.36 Myr from Lake Ohrid (*56*) reveals a step change in the intensity and duration of glacials at MIS 34 (Fig. 3A). Whereas earlier glacials were characterized by short expansions of herbs, MIS 34 had sustained high abundances of herbs reaching 85% of total pollen, indicating longer and colder-drier conditions across southern Europe. Taken together, the evidence from Europe and the Atlantic suggests an intensification of millennial-scale climate variability and glaciation during MIS 34, which we attribute to its long duration that allowed the expansion of ice sheets, and a subsequent large terminal meltwater release during the deglaciation.

Implications for early hominin occupation in Europe

The picture that emerges for the interval of hominin presence before 1.15 Ma is one of long, stable interglacial conditions and short glacials that would have allowed hominin establishment and occupation. However, the character of glacial periods changed at MIS 34. Its pervasive climatic instability would have placed hominin populations under considerable stress. The likely much-lower carrying capacity of the environment would have challenged small hunter-gatherer bands, compounded by the likelihood that early hominins lacked sufficient fat insulation and the means to make fire, effective clothing, or shelters (*57*, *58*), leading to much-lower population resilience. The terminal stadial event, with an abrupt drop in southwestern Portuguese margin SSTs of ~7°C, represents a drastic climate disruption, which likely affected climate and vegetation patterns across southern Europe with potential implications for early hominin occupation.

To further explore and quantify the possible impacts of this event on early hominin habitability, we conducted a realistic climate model simulation with the Community Earth System Model (CESM), version 1.2, under MIS 34 boundary conditions. Ice sheets were prescribed from a modeling study (*59*), which simulated geographically more-restricted European ice sheets compared with the glacial evidence discussed above. The numerical experiment (*7*) mimics a terminal stadial event by applying anomalous deglacial freshwater forcing to the northern North Atlantic, corresponding to a 23-m sea-level equivalent, which is at the low end of MIS 34 ice-volume estimates (*16*). In response to the freshwater perturbation, the AMOC weakens by about 95%, and SSTs over the west Iberian margin drop by ~3°C—a fraction of the amplitude of the reconstructed temperature anomaly (Fig. 4C). The simulation, therefore, represents a conservative estimate of the climatic changes that occurred during the terminal stadial event. To estimate the corresponding impact on early human occupation of Europe, we developed a climate envelope model (*7*) that links climatic data (minimum annual temperature and net primary productivity) from a transient Pleistocene simulation (*34*) with fossil and archeological evidence of human occupation in Europe and Southwest Asia covering the time period from 2.0 to 0.7 Ma (table S1) (*7*). The climate envelope model is then used to determine how the simulated terminal stadial climate evolution at every grid point impacted habitat suitability. The results (Fig. 4, B and D) show a massive drop in habitat suitability around the Mediterranean by more than 50% around 1.117 Ma on the model timescale (corresponding to 1.125 Ma on the U1385 timescale), which is absent in the transient Pleistocene simulation without the millennial-freshwater perturbation. Climate conditions move far away from the preferred climate niche of early European hominins (Fig. 4B and fig. S4). Lasting for about 4 kyr, this event triggered large-scale shifts in vegetation and ecosystems, as documented by the 45% increase of steppe pollen at Site U1385 and the simulated reduction of 50% in net primary production (fig. S5) over the Iberian Peninsula.

The climatic instability of MIS 34 and the severity of its terminal stadial emerging from this study imply that Iberia, and more generally southern Europe, was depopulated at least once in the Early Pleistocene. Dennell *et al.* (*13*, p. 1514) suggested that the question "When was Europe first colonized?" might be rephrased, "How often was Europe uninhabited after hominins first entered it?" We propose that the question may be further qualified by adding, "and for how long [was Europe uninhabited]?" Although the simulated habitat suitability rebounds following the terminal stadial perturbation (Fig. 4D), Fig. 1 and table S1 hint at a possible longer-lasting hiatus in European and Southwest Asian occupation. If Southwest Asia was depopulated during MIS 34, reoccupation of Europe may have been delayed until as late as MIS 25, or after the marked glaciation of MIS 22, during MIS 21. This hypothesis can be tested through newly discovered archaeological or hominin sites with robust chronological constraints. If there was the extirpation of hominins in Europe for such an extended period, it implies that repopulation was by *Homo antecessor*, which may have been a more resilient species with evolutionary or behavioral changes that allowed survival under the increasing intensity of glacial conditions.

REFERENCES AND NOTES

1. E. Carbonell *et al.*, *Nature* **452**, 465–469 (2008).
2. C. Lorenzo *et al.*, *J. Hum. Evol.* **78**, 114–121 (2015).
3. O. Oms *et al.*, *Proc. Natl. Acad. Sci. U.S.A.* **97**, 10666–10670 (2000).
4. I. Toro-Moyano *et al.*, *J. Hum. Evol.* **65**, 1–9 (2013).
5. J. M. Bermúdez de Castro *et al.*, *J. Hum. Evol.* **61**, 12–25 (2011).
6. D. Lordkipanidze *et al.*, *Nature* **449**, 305–310 (2007).
7. Materials and methods are available as supplementary materials.
8. T. Mitsui, P. C. Tzedakis, E. W. Wolff, *Clim. Past* **18**, 1983–1996 (2022).
9. J. Garcia, K. Martínez, E. Carbonell, *C. R. Palevol* **10**, 279–284 (2011).
10. J. Rodríguez *et al.*, *Quat. Sci. Rev.* **30**, 1396–1412 (2011).
11. Y. Altolaguirre *et al.*, *Rev. Palaeobot. Palynol.* **260**, 51–64 (2019).
12. R. Dennell, *J. Hum. Evol.* **45**, 421–440 (2003).
13. R. W. Dennell, M. Martinón-Torres, J. M. Bermúdez de Castro, *Quat. Sci. Rev.* **30**, 1511–1524 (2011).
14. K. MacDonald, M. Martinón-Torres, R. W. Dennell, J. M. Bermúdez de Castro, *Quat. Int.* **271**, 84–97 (2012).
15. N. J. Shackleton, A. Berger, W. R. Peltier, *Trans. R. Soc. Edinb. Earth Sci.* **81**, 251–261 (1990).
16. H. Elderfield *et al.*, *Science* **337**, 704–709 (2012).
17. M. E. Raymo, K. Ganley, S. Carter, D. W. Oppo, J. McManus, *Nature* **392**, 699–702 (1998).
18. D. A. Hodell, J. E. T. Channell, J. H. Curtis, O. E. Romero, U. Rohl, *Paleoceanography* **23**, PA4218 (2008).
19. B. Birner, D. A. Hodell, P. C. Tzedakis, L. C. Skinner, *Paleoceanography* **31**, 203–217 (2016).
20. S. Barker *et al.*, *Science* **376**, 961–967 (2022).
21. P. U. Clark *et al.*, *Quat. Sci. Rev.* **25**, 3150–3184 (2006).
22. H.-A. Blain *et al.*, *Quat. Sci. Rev.* **29**, 3034–3044 (2010).
23. C. Sánchez-Bandera *et al.*, *Quat. Sci. Rev.* **243**, 106466 (2020).
24. J. Saarinen *et al.*, *Quat. Sci. Rev.* **268**, 107132 (2021).
25. J. Ochando *et al.*, *Rev. Palaeobot. Palynol.* **304**, 104725 (2022).
26. P. González-Sampériz *et al.*, *Rev. Palaeobot. Palynol.* **162**, 427–457 (2010).
27. Y. Altolaguirre, A. A. Bruch, L. Gibert, *Quat. Sci. Rev.* **231**, 106199 (2020).
28. D. A. Hodell *et al.*, *Clim. Past* **19**, 607–636 (2023).
29. N. J. Shackleton, M. Chapman, M. F. Sánchez-Goñi, D. Pailler, Y. Lancelot, *Quat. Res.* **58**, 14–16 (2002).
30. P. C. Tzedakis, K. H. Roucoux, L. de Abreu, N. J. Shackleton, *Science* **306**, 2231–2235 (2004).
31. V. Margari *et al.*, *Nat. Geosci.* **3**, 127–131 (2010).
32. M. F. Sánchez Goñi *et al.*, *Front. Plant Sci.* **9**, 38 (2018).
33. N. J. Shackleton, M. A. Hall, E. Vincent, *Paleoceanography* **15**, 565–569 (2000).
34. A. Timmermann *et al.*, *Nature* **604**, 495–501 (2022).
35. V. Margari *et al.*, *Geology* **42**, 183–186 (2014).
36. E. L. McClymont, S. M. Sosdian, A. Rosell-Melé, Y. Rosenthal, *Earth Sci. Rev.* **123**, 173–193 (2013).
37. E. Bard, F. Rostek, J.-L. Turon, S. Gendreau, *Science* **289**, 1321–1324 (2000).
38. B. Martrat *et al.*, *Science* **317**, 502–507 (2007).
39. A. Bahr *et al.*, *Quat. Sci. Rev.* **179**, 48–58 (2018).
40. R.-D. Kahlke *et al.*, *Quat. Sci. Rev.* **30**, 1368–1395 (2011).
41. L. E. Lisiecki, *Nat. Geosci.* **3**, 349–352 (2010).
42. R. W. Barendregt, A. Duk-Rodkin, in *Developments in Quaternary Sciences*, vol. 15, *Quaternary Glaciations - Extent and Chronology - A Closer Look*, J. Ehlers, P. L. Gibbard, P. D. Hughes, Eds. (Elsevier, 2011), pp. 419–426.
43. J. Ehlers, P. L. Gibbard, *Quat. Int.* **164-165**, 6–20 (2007).

44. Ø. F. Lien, B. O. Hjelstuen, X. Zhang, H. P. Sejrup, *Quat. Sci. Rev.* **282**, 107433 (2022).
45. H. P. Sejrup *et al*., *Nor. Geol. Tidsskr.* **75**, 65–87 (1995).
46. D. Ottesen, C. L. Batchelor, J. A. Dowdeswell, H. Løseth, *Mar. Pet. Geol.* **98**, 836–859 (2018).
47. J. R. Lee, F. S. Busschers, H. P. Sejrup, *Quat. Sci. Rev.* **44**, 213–228 (2012).
48. W. H. Zagwijn, *Geol. Mijnbouw* **64**, 17–24 (1985).
49. C. Laban, J. J. M. van der Meer, in *Developments in Quaternary Sciences*, vol. 15, *Quaternary Glaciations - Extent and Chronology - A Closer Look*, J. Ehlers, P. L. Gibbard, P. D. Hughes, Eds. (Elsevier, 2011), pp. 247–260.
50. S. Toucanne *et al*., *Quat. Sci. Rev.* **28**, 1238–1256 (2009).
51. T. Rodrigues *et al*., *Quat. Sci. Rev.* **172**, 118–130 (2017).
52. R. Ivanovic *et al*., *Paleoceanogr. Paleoclimatol.* **33**, 807–824 (2018).
53. H. M. Stoll *et al*., *Nat. Commun.* **13**, 3819 (2022).
54. W. F. Ruddiman, M. E. Raymo, D. G. Martinson, B. M. Clement, J. Backman, *Paleoceanography* **4**, 353–412 (1989).
55. A. Martínez-Garcia, A. Rosell-Melé, E. L. McClymont, R. Gersonde, G. H. Haug, *Science* **328**, 1550–1553 (2010).
56. T. Donders *et al*., *Proc. Natl. Acad. Sci. U.S.A.* **118**, e2026111118 (2021).
57. W. Roebroeks, P. Villa, *Proc. Natl. Acad. Sci. U.S.A.* **108**, 5209–5214 (2011).
58. R. T. Hosfield, *Curr. Anthropol.* **57**, 653–682 (2016).
59. M. Willeit, A. Ganopolski, R. Calov, V. Brovkin, *Sci. Adv.* **5**, eaav7337 (2019).
60. J. Laskar *et al*., *Astron. Astrophys.* **428**, 261–285 (2004).
61. V. Margari, D. A. Hodell, J. O. Grimalt, P. C. Tzedakis, Benthic and planktic oxygen and carbon isotopes, alkenone, pollen, and XRF data at IODP 339-U1385 for MIS 34-35 and MIS 42-43 southern Portuguese Margin, PANGAEA (2023); https://doi.org/10.1594/PANGAEA.961070.
62. V. Margari *et al*., MIS34 transient climate model simulation data, Institute for Basic Science ICCP data server (2023); https://doi.org/10.22741/iccp.20230006.
63. V. Margari *et al*., Matlab code for MIS34 human habitat simulation, Institute for Basic Science ICCP data server (2023); https://doi.org/10.22741/iccp.20230007.

ACKNOWLEDGMENTS

We are grateful to M. Casado and Y. Gonzalez (IDAEA-CSIC) for their assistance in the analyses of the alkenones and J. Jadhav for preliminary analysis of Mediterranean climate variability in the CESM1.2 "2Ma" simulation. We thank H.-A. Blain for discussions and M. Irving for drafting fig. S1. The "2Ma" CESM1.2 simulations were conducted on the Institute for Basic Science (IBS) Center for Climate Physics (ICCP) supercomputer Aleph, a Cray XC50-LC system. **Funding:** We gratefully acknowledge financial support from The Leverhulme Trust grant RPG-2014-417 (P.C.T., V.M., and D.A.H.); the Catalan Government, Research Group 2021SGR00986 (J.O.G.); IBS, South Korea grant IBS-R028-D1 (A.T., K.-S.Y., and H.K.); the Human Origins Research Fund (C.B.S.); and the Calleva Foundation (C.B.S., S.A.P., and N.M.A.). **Author contributions:** P.C.T., V.M., and A.T. designed the study. V.M. and P.C.T. wrote the manuscript with contributions from A.T., S.A.P., N.M.A., C.B.S., P.L.G., and D.A.H. V.M., D.A.H., and J.O.G. undertook the pollen, foraminiferal isotope, and alkenone analyses, respectively. S.A.P., N.M.A., and C.B.S. developed the database for the early hominin sites for Europe and Southwest Asia. P.L.G. discussed the glacial geological record. A.T. developed and coded the two-dimensional climate envelope model and downscaled the CESM1.2 data. K.-S.Y. conducted the CESM1.2 "2Ma" simulation and the MIS 34 freshwater perturbation experiments. H.K. conducted a series of isotope-enabled CESM1.2 freshwater perturbation simulations to estimate the overall amplitude of the freshwater forcing for the MIS 34 terminal stadial event. All authors contributed to the ideas in this paper. **Competing interests:** The authors declare that they have no competing interests. **Data and materials availability:** The paleoenvironmental data (*61*) reported in this manuscript are available through PANGAEA. The CESM1.2 climate model data from the MIS 34 water-hosing experiment (*62*) and the MATLAB model code for the habitat suitability model (*63*) used to generate Fig. 4 and figs. S4 and S5 are available on the ICCP data server. The previously published data from the CESM1.2 "2Ma" simulation are available on the OpenDAP and LAS server: https://climatedata.ibs.re.kr/data/hominin-habitats/2ma-transient-climate-simulation-data. The maps in Fig. 4 were generated with M_Map: a mapping package for MATLAB, version 1.4m, available at https://www.eoas.ubc.ca/~rich/map.html. The CESM1.2 code is available at https://www2.cesm.ucar.edu/models/cesm1.2/.

License information: Copyright © 2023 the authors, some rights reserved; exclusive licensee American Association for the Advancement of Science. No claim to original US government works. https://www.science.org/about/sciencelicenses-journal-article-reuse

SUPPLEMENTARY MATERIALS

science.org/doi/10.1126/science.adf4445
Materials and Methods
Figs. S1 to S5
Table S1
References (*64*–*139*)
MDAR Reproducibility Checklist

Submitted 21 October 2022; accepted 22 June 2023
10.1126/science.adf4445

HUMAN EVOLUTION

Climate shifts orchestrated hominin interbreeding events across Eurasia

Jiaoyang Ruan[1,2]*, Axel Timmermann[1,2]*, Pasquale Raia[3], Kyung-Sook Yun[1,2], Elke Zeller[1,4], Alessandro Mondanaro[5], Mirko Di Febbraro[6], Danielle Lemmon[1,2], Silvia Castiglione[3], Marina Melchionna[3]

When, where, and how often hominin interbreeding happened is largely unknown. We study the potential for Neanderthal-Denisovan admixture using species distribution models that integrate extensive fossil, archaeological, and genetic data with transient coupled general circulation model simulations of global climate and biomes. Our Pleistocene hindcast of past hominins' habitat suitability reveals pronounced climate-driven zonal shifts in the main overlap region of Denisovans and Neanderthals in central Eurasia. These shifts, which influenced the timing and intensity of potential interbreeding events, can be attributed to the response of climate and vegetation to past variations in atmospheric carbon dioxide and Northern Hemisphere ice-sheet volume. Therefore, glacial-interglacial climate swings likely played an important role in favoring gene flow between archaic humans.

Genomic studies of living and fossil individuals revealed a complex history of interbreeding between *Homo sapiens*—our direct ancestors—and their ancient relatives (*1*–*7*). As a result, non-Africans today carry ~2% of *Homo neanderthalensis* (Neanderthal) DNA, whereas people from Southeast Asia and Oceania share as much as 2 to 5% of the Denisovan genome (fig. S1) (*7*, *8*).

Neanderthals and Denisovans (Fig. 1A) had inhabited and intermittently interbred in Eurasia long before *Homo sapiens* arrived on the continent some 100 thousand years ago (ka) (*1*–*3*). Direct evidence for their genetic admixture comes from the discovery of the first-generation (F1) daughter of a Neanderthal mother and a Denisovan father from the Altai mountains ~90 ka (*9*). Further analysis of her father's genome hinted at a deeper-rooted Neanderthal ancestry, which implies a complex history of bidirectional gene flow between the two hominin groups. Recent work (*10*) revealed interbreeding events that date back to ~200 ka. Apart from these genetically reconstructed encounters in Siberia (*9*–*11*), little is known about where and how frequently Neanderthals and Denisovans interbred throughout their shared history (~400 to 30 ka).

For over a century now, Neanderthal fossils and associated archaeological artifacts have been excavated in Europe, western Asia, and southern Siberia (Fig. 1A) (*12*, *13*), which provided fundamental information about their geographical range, climatic preference, behavior, diet, and genetic diversity. By contrast, the fossil remains attributed to Denisovans have been only recovered from the Altai mountains, the Tibetan Plateau, and the northern Annamite Range (*3*, *14*–*16*), with further potential fossil candidates proposed in East Asia (Fig. 1A) (*17*). Genetic analysis further reveals the existence of three deeply divergent Denisovan sublineages, two of which occur in East Asia, that contribute to the present-day human genome pool (*5*, *18*). This scattered evidence suggests that Denisovans likely occupied regions characterized by widely different climate and vegetation conditions (fig. S2). The warm and humid conditions of the Southeast Asia monsoon region may

[1]Center for Climate Physics, Institute for Basic Science, Busan, South Korea. [2]Center for Climate Physics, Pusan National University, Busan, South Korea. [3]DiSTAR, Monte Sant'Angelo, Napoli Università di Napoli Federico II, Naples, Italy. [4]Department of Climate System, Pusan National University, Busan, South Korea. [5]DST, Università degli Studi di Firenze, Florence, Italy. [6]Department of Biosciences and Territory, University of Molise, C. da Fonte Lappone, Pesche, Italy.
***Corresponding author. Email: jiaoyangruan@pusan.ac.kr (J.R.); axel@ibsclimate.org (A.T.)**

have further limited the preservation potential (*19*, *20*), which led to the current paucity of fossil remains there. Unfortunately, this scarcity of fossil remains has made it difficult to draw further conclusions regarding their spatiotemporal distribution and possible encounters with other archaic hominins.

Neanderthal and Denisovan habitats

To address these questions, we compiled Denisovan occurrences in space and time (n = 22) (data S1) and used a similar compilation prepared for Neanderthals (n = 773) drawn from our recent studies (*21*, *22*). In these compilations, the same site can have multiple hominin occurrence ages, which are treated as individual samples. By using these hominin presence data and paleoclimate and biome simulations, we built two species distribution models (SDMs)—i.e., a habitat suitability model (HSM) and an environmental niche factor analysis model with phylogenetic imputation (ENphylo), which is specifically designed to give reliable habitat suitability estimates under low number of occurrences (*23*, *24*). These models help determine how environmental preferences for the two hominin groups have changed in space and time (fig. S3). Climatic data for the past 400,000 years (CLIM400ka) were extracted from a transient Pleistocene climate simulation conducted with the Community Earth System Model, version 1.2 (*22*). CLIM400ka captures late Pleistocene orbital-scale climate variations in good agreement with various paleo temperature and hydroclimate reconstructions (figs. S4 and S5). Ecological variables used in the SDM, which include net primary productivity (NPP), leaf area index, and megabiome types, were derived from our CLIM400ka-forced version of the BIOME4 simulation (*23*, *25*).

Because Denisovans have no formal morphological definition, the identity of the remains that can be ascribed to this hominin lineage is disputed and mostly based on genetic evidence and scanty fossil remains. Therefore, we generated three different versions of Denisovan datasets (data S1) (*23*), with increasing confidence levels regarding the recognition of possible Denisovan presence. They include an extremely conservative, a conservative, and an extended, more liberal compilation (*23*). The main results of our analyses presented here (Figs. 1 to 4) are obtained for the conservative dataset, and sensitivity experiments with the other data are shown in the supplementary materials. By comparing the corresponding species distribution predictions generated with the three datasets, we gain very similar insights while addressing in part the effect of potential preservation biases (*19*, *20*), which are presumably very pronounced in the Asian monsoon region.

Both Neanderthals and Denisovans are simulated to have lived primarily in environments characterized by annual temperature, precipitation, and NPP of ~−10° to 20°C, ~500 to 1300 mm/year, and ~200 to 800 g of carbon per square meter per year, respectively (Fig. 1B). Yet, compared to Neanderthals, Denisovans were present in hot and humid climates, which points to a comparatively wider niche space. Whereas Neanderthals were more abundant in temperate forests, Denisovans were present in both boreal forest and tundra (Fig. 1C). Fisher's exact test applied to the megabiome preferences (Fig. 1C) of Neanderthals and Denisovans, as well as a Kolmogorov-Smirnov test applied to the three-dimensional climate niche space of both species (Fig. 1B), reveals statistically different distributions (P <

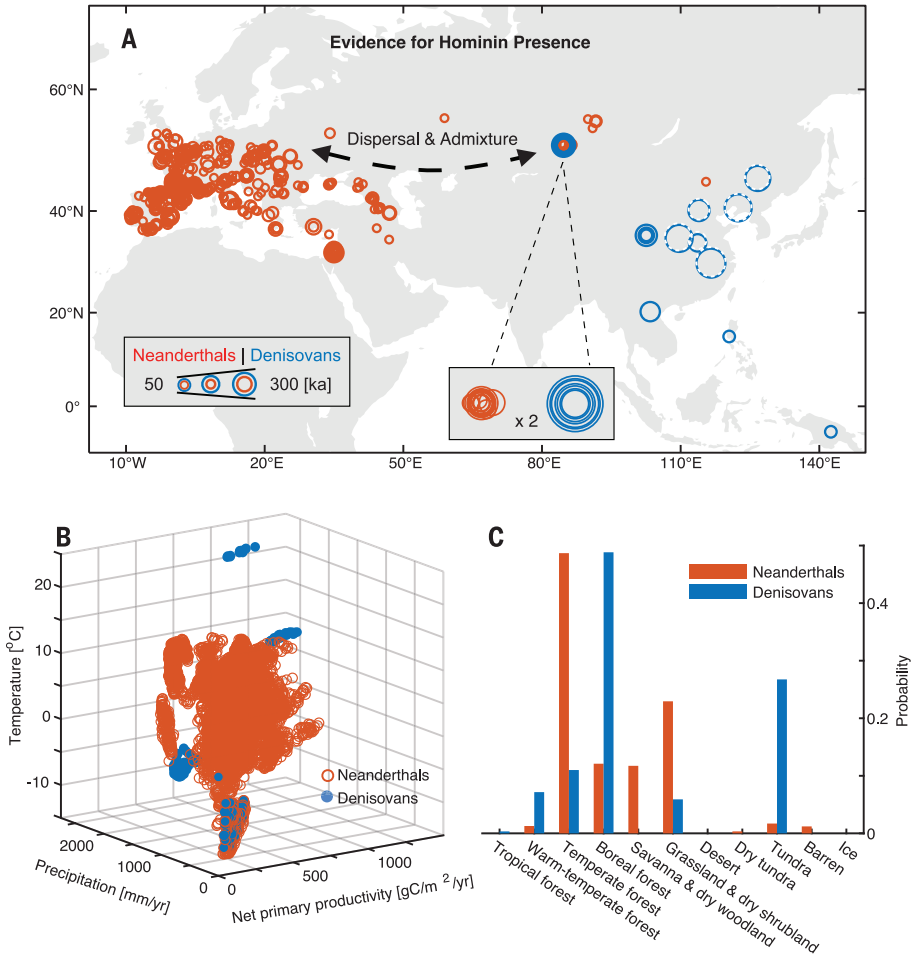

Fig. 1. Neanderthal and Denisovan locations and their corresponding climate and biome conditions. (**A**) Hominin fossil, archaeological, and genetic data compiled for HSMs; candidate Denisovans (dashed circle). (**B**) Annual mean temperature, precipitation, and NPP extracted for hominin locations and respective age distributions. (**C**) Age-weighted probability of hominin presence in 11 megabiomes.

0.001), which suggests that the two hominins interacted only where and when their environmental preferences overlapped (Fig. 1A and Fig. 2).

The 400 ka–averaged habitat maps from both SDMs (Fig. 2) document suitable environments for Neanderthals in Europe, consistent with fossil evidence (Fig. 1A), and some fragmented and low-probability regions occurring in western and far eastern Asia and in eastern Africa. Comparatively, Denisovan habitats were geographically more diverse and map to the present-day Eurasian Steppe extending from the Sarmatic Plain to the Mongolian Plateau, parts of Scandinavia, and some pockets in central-eastern Asia. Notably, ENphylo and some fossil input sensitivity experiments simulate suitable Denisovan habitats in central Europe and parts of northeastern Asia (Fig. 2 and fig. S7). Although Denisovan fossils have not been identified with certainty in these regions, the skulls found at Jinniushan, Harbin, and Hualongdong in northeastern China were proposed to be possible Denisovans (Fig. 1) (*17*, *26*). Uncertainties in Denisovan habitat suitability in Europe as simulated by the SDMs (Fig. 2) may be due to the different choice of climate and vegetation input variables (table S1) (*23*) or because the HSM may be less optimized to handle small sample sizes as compared to ENphylo. Overall, our multimodel simulations of elongated and relatively fragmented Denisovan habitats are qualitatively consistent with the complex admixture patterns of multiple Denisovan sublineages in present-day people (*5*, *18*).

The two hominin habitats show large spatiotemporal variations in response to orbital-scale climate and vegetation shifts (Fig. 3; figs. S7, S8, and S10 to S14; and movies S1 and S2). Empirical orthogonal function (EOF) analysis (*27*) of Eurasian Neanderthal habitats reveals that the first two leading EOF modes, which explain ~63% of the total variance, are dominated by climate variability associated with the eccentricity, CO_2 (80– to 120–thousand year periodicity) and precession forcings (19– to 23–thousand year periodicity) (fig. S12), respectively. In three selected regions of anthropological interest (i.e., the Altai, Sarmatic Plain, and Iberia), high habitat suitability consistently occurs during periods of elevated eccentricity and precession (Fig. 3, C to E). At the Altai, these periods coincide with warmer and wetter climates suggested by both our model simulation and regional proxy data (figs. S4, S5, and S13). Notably, the widespread lower habitability at two precession minima in the marine isotope stage (MIS) 5 corresponds well with the phylogenetically inferred Neanderthal turnover events in Europe at ~135 ka and ~105 ka (Fig. 3B) (*28*). Neanderthal habitats expand in central and northeastern Europe and southern Siberia (fig. S10A), with a ~69%

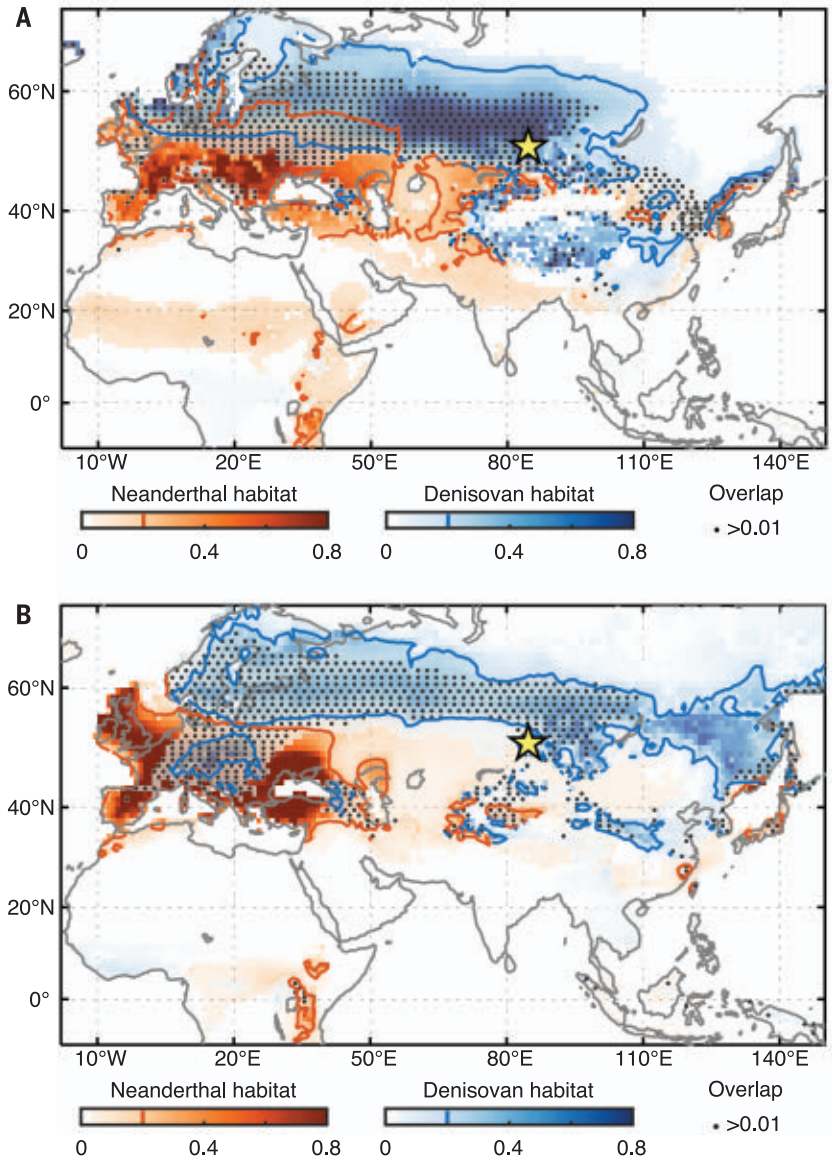

Fig. 2. Neanderthal-Denisovan habitat overlap. (**A** and **B**) Averaged 400- to 30-ka habitats (shading) and overlap (dots) from Mahalanobis HSM (A) and ENphylo- and ecological niche factor analysis (ENFA)–based SDMs (B). The yellow star indicates Denisova cave.

increase in habitable area (at suitability >0.2) during the past four interglacial periods relative to glacial periods. Conversely, glacial Neanderthal habitats are concentrated in southern Europe and north to the Black Sea (fig. S10B), as documented by the moderate habitability in northern Iberia throughout glacial cycles (Fig. 3E). These regions coincide with the previously reported glacial refugia of various fauna (*29*) and Neanderthals (*30*). The spatially diverse responses of glacial-interglacial habitats may have been one of the reasons for past hominin migrations inside Europe and a candidate hypothesis to explain Neanderthal haplogroup separations (*31*).

The principal components of the first two leading EOF modes of Eurasian Denisovan habitats, which explain ~60% of the total variance, show similar orbital-scale variability as for Neanderthals (fig. S14). There is a small expansion (~10%) in habitable areas (at suitability >0.2) during interglacial periods. Responding to glacial cooling, Denisovan habitats vanish in Scandinavia, mildly increase in its core areas from eastern Europe to Siberia, and show massive fragmentation in Asia (fig. S11). Unlike Neanderthals in the Altai and the Sarmatic Plain, optimal Denisovan habitats appear under low eccentricity yet high precession (boreal summer insolation minimum) conditions (Fig. 3, G and H), whereas opposing behaviors occur in the Northeast Tibetan Plateau (Fig. 3I). These spatiotemporal Denisovan habitat patterns were repeatedly observed in

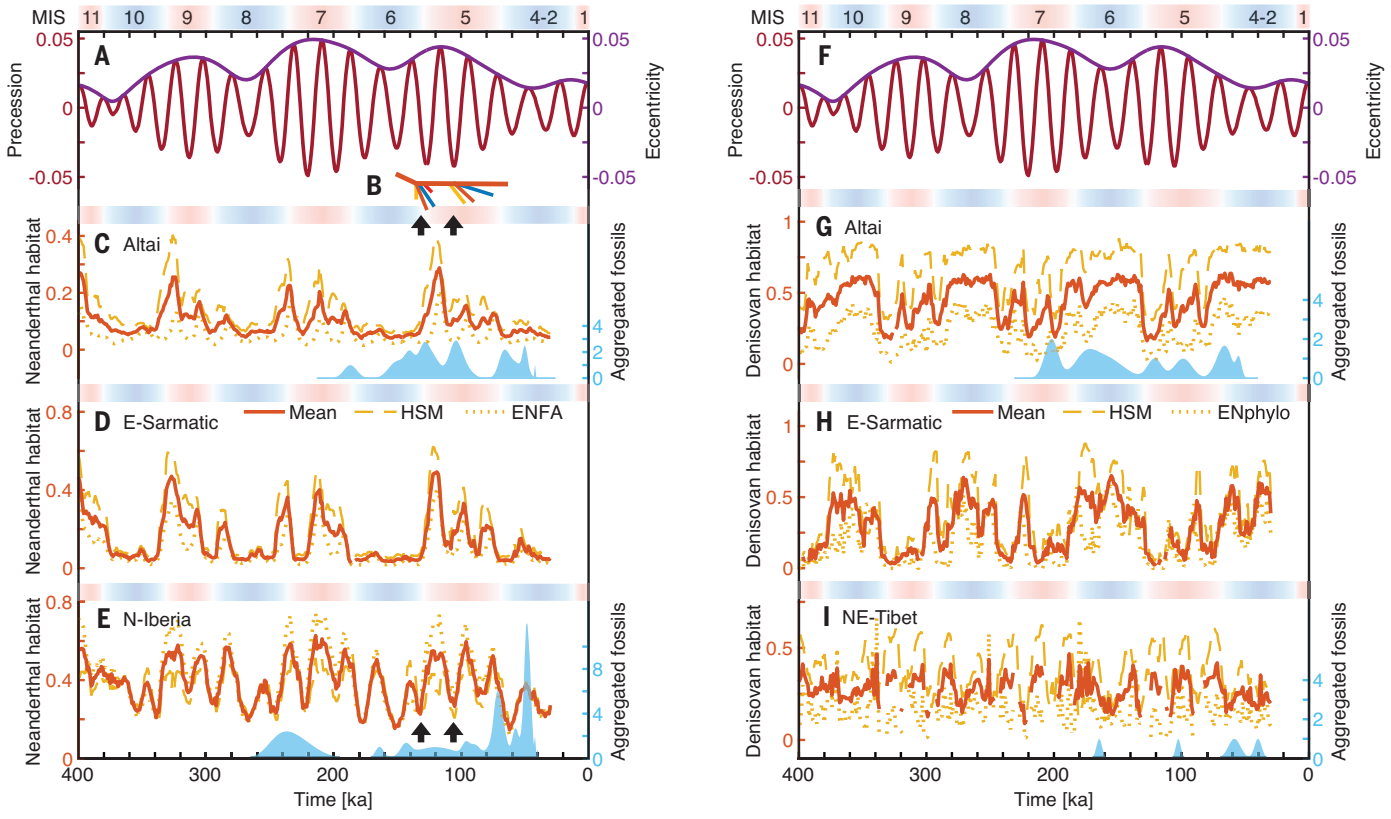

Fig. 3. Temporal evolution of Neanderthal-Denisovan habitat suitability. (**A** to **F**) Eccentricity and precession index. (B) Phylogenetically inferred Neanderthal population turnover events at ~135 ka and ~105 ka (*28*). (C to E) Neanderthal habitat suitability averaged over two SDMs compared with regionally aggregated (3° × 6°) fossil evidence at three selected locations. (**G** to **I**) Same as (C) to (E), but for Denisovans.

the Denisovan data sensitivity simulations with both extended and extremely conservative compilations (figs. S7 and S8).

Habitat overlap as a proxy for interbreeding

To determine where and when Neanderthals and Denisovans potentially interbred, we computed the covariance (or overlap) of their respective habitat suitability over time (*23*). The 400-ka habitat overlaps from both SDMs reveal contact hotspots in central Eurasia, the Caucasus, and the Tianshan and Changbai mountain ranges (Fig. 2, dotted areas). The first region, which encloses the Altai as its eastern end, is consistent with the presence of an F1 hybrid (*9*). A closer examination of this hybridization zone reveals temporal shifts in an east-west direction that occur in unison with the glacial-interglacial climate variability over the past 400 ka (Fig. 4 and fig. S15). For instance, Denisovans and Neanderthals exhibited high contact probability in the Siberian Altai, mostly during interglacial periods MIS 5, 7, and 9. There is also a close match between this zonal seesaw pattern of Denisovan and Neanderthal contact and the long-term change in atmospheric carbon dioxide concentration (Fig. 4A) (*32*). We find that the elevated CO_2 and mild interglacial climate promote the temperate forest to extend across central Eurasia (fig. S16A), which facilitates the northeastward dispersal of Neanderthals (fig. S10A) (*12*) and leads to a territorial encroachment with preexisting Altai Denisovans. By contrast, the lower CO_2 and corresponding harsher glacial climate jointly push the boreal forest range equatorward in central Eurasia (fig. S16B), which may facilitate the backflow of Denisovans into Europe (fig. S11B). This analysis suggests that greenhouse gases played a pivotal role in regulating past population dispersal and admixture across Eurasia, through their direct influences on surface temperature and overall moisture availability and because of the simulated CO_2 fertilization effect on vegetation (*33*). Nevertheless, the relative contribution to vegetation shifts on Milanković scales may vary regionally; a recent study pointed to a more complex interplay of climate, CO_2, and other environmental factors in determining vegetation covers such as in tropical Africa (*34*). To further document the role of extratropical temperatures in orchestrating the Neanderthal-Denisovan admixture dynamics, we conducted additional sensitivity experiments (*23*), in which we artificially scaled the amplitude of global temperature variations on Milanković timescales by 0, 70, and 130%. The results (fig. S17) show that CO_2-driven extratropical temperature fluctuations are necessary to obtain the 80– to 120–thousand year variability in hominin overlap. Calculations for a 70 and 130% temperature scaling further reveal similar EOF patterns in habitat overlap variability compared with the original simulation (fig. S12), which thereby demonstrates the robustness of our results regarding uncertainties in the simulated temperature evolution.

Paleogenomic implications

We further compared our simulation of hominin overlap with a recent synthesis study of fossil genomes from the Altai regions, which had identified at least six episodes of interbreeding between Denisovans and Neanderthals (*10*). To facilitate this comparison, we calculated the absolute times of these episodes by adding the fossil dates from original publications to the molecular clock–based relative mixture time estimates (data S2) and accounting for dating error propagation. The results show that among these six episodes (*10*), the five younger events cluster during the warm MIS 5, whereas the oldest event, although with considerable dating uncertainty, occurs in the cooler MIS 6 (Fig. 4C). Because some of these

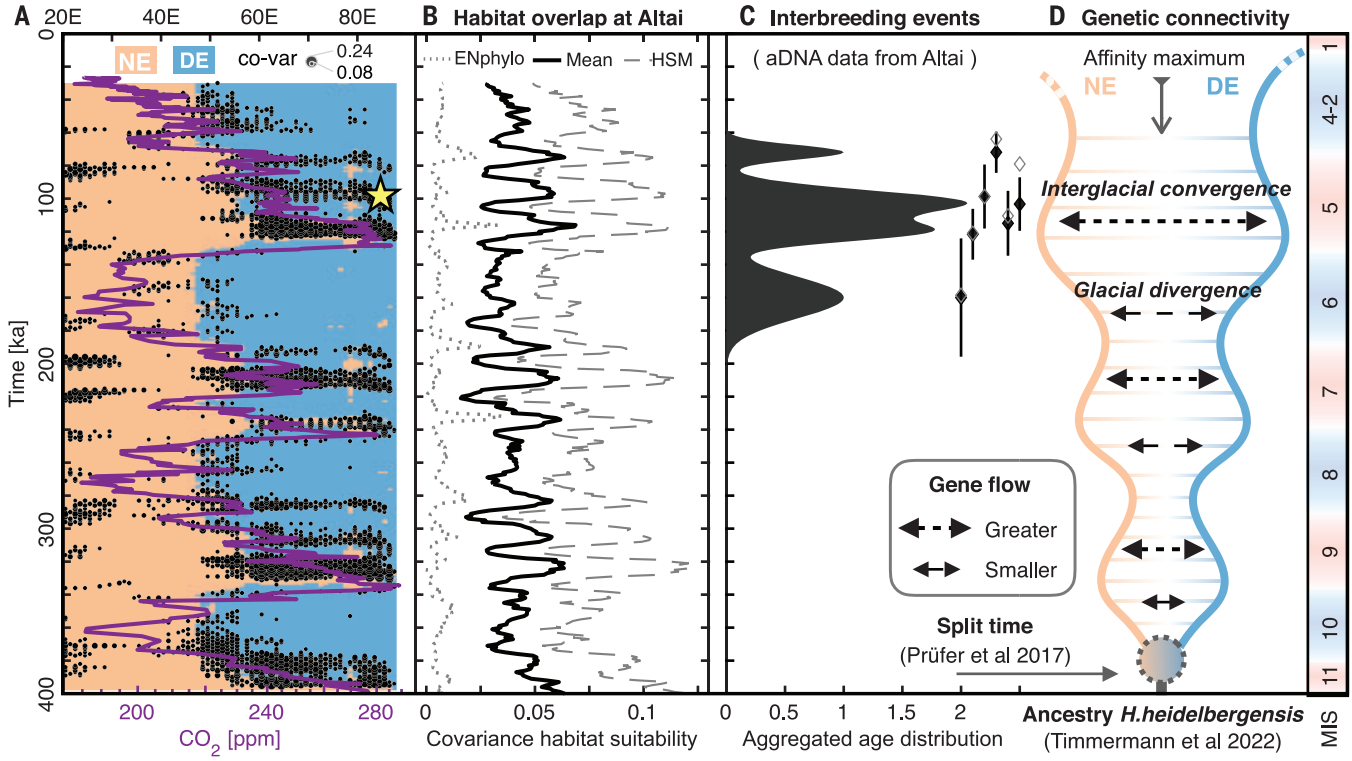

Fig. 4. Spatiotemporal habitat overlap and genetic Denisovan-Neanderthal connectivity. (**A**) Time-longitude diagram of HSM-simulated Neanderthal-Denisovan habitats (shading at suitability >0.2) and overlap (dots); atmospheric CO_2 content (magenta line). Inserted star indicates Denisova cave ~90-thousand-year-old F1 hybrid. co-var, covariability between Denisovan and Neanderthal habitats; DE, preferred Denisovan habitat; NE, preferred Neanderthal habitat; ppm, parts per million. (**B**) Altai habitat overlap probability averaged over 3° × 6° box encompassing Denisova cave. (**C**) Interbreeding chronology of two populations derived from the Altai fossil genomes with aggregated age probability distribution of six identified interbreeding events (shading). aDNA, ancient DNA. (**D**) Schematic of climate effects on genetic Neanderthal-Denisovan connectivity after hypothesized split from common ancestry ~400 ka (*1*, *22*).

events occurred thousands of years earlier than the fossil dates, they could have happened in places far away from the places where the specimens were found. Our simulation of Neanderthal-Denisovan overlap suggests that these MIS 5 interbreeding events took place in central-southern Siberia (Fig. 4, A and B), which is consistent with the finding of the F1 hybrid fossil (*9*). By contrast, the MIS 6 event likely happened in eastern Europe.

Whereas bidirectional gene flow between Denisovans and Neanderthals occurred in Siberia, the few European Neanderthal genomes have shown little evidence for admixtures with the Altai Denisovans (*10*). Nevertheless, large-sample genetic analyses have recently revealed Denisovan ancestry in modern European populations in France (*35*) and in Iceland (*36*), which suggests the possibility for more widespread and prevalent interbreeding than previously thought. These results are consistent with our model simulations, which indicate the presence of suitable Denisovan habitats in Europe under optimal orbital conditions (Figs. 2 and 4 and figs. S7, S8, and S14).

Although Denisovans and Neanderthals went through distinct population histories since their split from common ancestry (*2*, *3*), we argue that they were not subject to any reproductive isolation during past glacial cycles (*9*, *10*). In line with previous findings, our analyses support the notion of long-term connectivity between the two hominins and document an admixture hotspot region in central Eurasia (Fig. 2). Moreover, our study reveals that orbitally driven changes in regional climate and vegetation shifted this hybrid zone in an east-west direction with interglacial conditions favoring an eastward intensification and genetic convergence, whereas glacial conditions were associated with occasional interbreeding events in Europe. Our results further demonstrate that climate-driven variations in paired hominin habitats can explain the interbreeding dynamics of Neanderthals and Denisovans during the late Pleistocene and the corresponding flow of genes (Fig. 4). These climate-mediated events have played an essential role in shaping the genomic ancestry of modern humans, which leaves an important legacy even in our present-day population.

REFERENCES AND NOTES

1. K. Prüfer *et al.*, *Science* **358**, 655–658 (2017).
2. K. Prüfer *et al.*, *Nature* **505**, 43–49 (2014).
3. D. Reich *et al.*, *Nature* **468**, 1053–1060 (2010).
4. D. Reich *et al.*, *Am. J. Hum. Genet.* **89**, 516–528 (2011).
5. G. S. Jacobs *et al.*, *Cell* **177**, 1010–1021.e32 (2019).
6. R. E. Green *et al.*, *Science* **328**, 710–722 (2010).
7. M. Larena *et al.*, *Curr. Biol.* **31**, 4219–4230.e10 (2021).
8. S. Sankararaman, S. Mallick, N. Patterson, D. Reich, *Curr. Biol.* **26**, 1241–1247 (2016).
9. V. Slon *et al.*, *Nature* **561**, 113–116 (2018).
10. B. M. Peter, bioRxiv 2020.03.13.990523 [Preprint] (2020).
11. Z. Jacobs *et al.*, *Nature* **565**, 594–599 (2019).
12. K. A. Kolobova *et al.*, *Proc. Natl. Acad. Sci. U.S.A.* **117**, 2879–2885 (2020).
13. W. Roebroeks, M. Soressi, *Proc. Natl. Acad. Sci. U.S.A.* **113**, 6372–6379 (2016).
14. F. Chen *et al.*, *Nature* **569**, 409–412 (2019).
15. F. Demeter *et al.*, *Nat. Commun.* **13**, 2557 (2022).
16. D. Zhang *et al.*, *Science* **370**, 584–587 (2020).
17. A. Bergström, C. Stringer, M. Hajdinjak, E. M. L. Scerri, P. Skoglund, *Nature* **590**, 229–237 (2021).
18. S. R. Browning, B. L. Browning, Y. Zhou, S. Tucci, J. M. Akey, *Cell* **173**, 53–61.e9 (2018).
19. E. Cornelissen, in *Africa from MIS 6-2: Population Dynamics and Paleoenvironments*, S. C. Jones, B. A. Stewart, Eds. (Springer, 2016), pp. 301–319.
20. C. Padilla-Iglesias *et al.*, *Proc. Natl. Acad. Sci. U.S.A.* **119**, e2113936119 (2022).
21. P. Raia *et al.*, *One Earth* **3**, 480–490 (2020).
22. A. Timmermann *et al.*, *Nature* **604**, 495–501 (2022).
23. Materials and methods are available as supplementary materials.
24. A. Mondanaro *et al.*, *Methods Ecol. Evol.* **14**, 911–922 (2023).
25. E. Zeller *et al.*, *Science* **380**, 604–608 (2023).
26. A. Gibbons, *Science* **355**, 899 (2017).
27. A. Hannachi, I. T. Jolliffe, D. B. Stephenson, *Int. J. Climatol.* **27**, 1119–1152 (2007).
28. B. Vernot *et al.*, *Science* **372**, eabf1667 (2021).
29. G. Hewitt, *Nature* **405**, 907–913 (2000).
30. M. Melchionna *et al.*, *Palaeogeogr. Palaeoclimatol. Palaeoecol.* **496**, 146–154 (2018).
31. V. Fabre, S. Condemi, A. Degioanni, *PLOS ONE* **4**, e5151 (2009).

32. B. Bereiter *et al*., *Geophys. Res. Lett.* **42**, 542–549 (2015).
33. W. Chen *et al*., *Quat. Sci. Rev.* **218**, 293–305 (2019).
34. W. D. Gosling *et al*., *Science* **376**, 653–656 (2022).
35. A. Bergström *et al*., *Science* **367**, eaay5012 (2020).
36. L. Skov *et al*., *Nature* **582**, 78–83 (2020).
37. J. Ruan *et al*., Neanderthal and Denisovan Habitat Simulation, ICCP Dataserver (2023).
38. J. Ruan *et al*., Ruan et al 2023 Science, ICCP Dataserver (2023).

ACKNOWLEDGMENTS

Simulations were conducted on the ICCP-IBS supercomputer Aleph. **Funding:** This study received support from the Institute for Basic Science IBS-R028-D1 (J.R., A.T., K.-S.Y., E.Z., and D.L.).

Author contributions: Conceptualization: J.R., A.T., and P.R.; Methodology: J.R., A.T., E.Z., K.-S.Y., D.L., P.R., A.M., S.C., M.M., and M.D.F.; Supervision: A.T.; Writing – original draft: J.R.; Writing – review & editing: A.T., P.R., E.Z., K.-S.Y., and D.L. **Competing interests:** The authors declare that they have no competing interests. **Data and materials availability:** Denisovan presence data are provided in the supplementary materials. Simulated hominin habitat data (*37*) and source codes for reproducing the figures (*38*) are available on https://climatedata.ibs.re.kr/.

License information: Copyright © 2023 the authors, some rights reserved; exclusive licensee American Association for the Advancement of Science. No claim to original US government works. https://www.science.org/about/science-licenses-journal-article-reuse

SUPPLEMENTARY MATERIALS

science.org/doi/10.1126/science.add4459
Materials and Methods
Figs. S1 to S17
Table S1
References (*39*–*84*)
MDAR Reproducibility Checklist
Movies S1 and S2
Data S1 and S2

Submitted 29 August 2022; accepted 19 April 2023
10.1126/science.add4459

Science Careers helps you advance your career. Learn how!

- Register for a free online account on **ScienceCareers.org**.
- Search hundreds of job postings and find your perfect job.
- Sign up to receive e-mail alerts about job postings that match your criteria.
- Upload your resume into our database and connect with employers.
- Watch one of our many webinars on different career topics such as job searching, networking, and more.

Visit **ScienceCareers.org** today — all resources are free

ScienceCareers
FROM THE JOURNAL SCIENCE AAAS

SCIENCECAREERS.ORG

TENURE-TRACK ASSISTANT PROFESSOR POSITIONS IN MOLECULAR BIOLOGY

The Department of Biochemistry, Molecular Biology and Biophysics (BMBB) at the University of Minnesota invites applications for **two tenure-track Assistant Professor positions in the area of eukaryotic molecular biology**. New faculty will be supported by a highly competitive startup package and salary, state-of-the art research space and access to exceptional core facilities.

Ideal candidates will develop an innovative, federally funded research program in the area of eukaryotic molecular biology with relevance to molecular mechanisms of disease pathology. They will contribute to medical, graduate, and undergraduate educational programs, research mentorship, and academic and professional service. Criteria for selection will include past research accomplishments and productivity, significance and innovation of planned future research, and commitment to teaching and mentorship. Candidates must hold a PhD in life sciences.

The BMBB department has strengths in biochemistry, metabolism, proteomics, molecular genetics, signaling, biotechnology, synthetic and structural biology. BMBB supports robust graduate and postdoctoral programs as well as a large undergraduate major in biochemistry. The University of Minnesota provides a rich environment for collaborations and a wide array of facilities and resources to promote cross-disciplinary research. Research areas of emphasis for new faculty include, but are not limited to, mechanisms of gene expression, epigenetics and epitranscriptomics, and molecular mechanisms of disease.

The University of Minnesota provides equal access to and opportunity in its programs, facilities, and employment without regard to race, color, creed, religion, national origin, gender, age, marital status, disability, public assistance status, veteran status, sexual orientation, gender identity, or gender expression. To learn more about diversity at the U: **http://diversity.umn.edu**

How to apply:
To learn more about this opportunity and to apply, go to **https://hr.umn.edu/Jobs/Find-Job** and search for **Job # 356872**. Application materials include: CV, Cover Letter (maximum 1 page), Research Statement (maximum 3 pages), Teaching Statement (maximum 1 page), and Diversity Statement (maximum 1 page). A single PDF of those application materials should also be emailed to **mbsearch@umn.edu**. In addition, applicants should have three referees email letters of recommendation to **mbsearch@umn.edu**. Applications will be evaluated on a rolling basis until the positions are filled. It is anticipated that successful candidates will be on campus for the beginning of the 2024-2025 academic year.

For additional information, contact the faculty search committee at: **mbsearch@umn.edu.**

IT'S NOT
JUST A JOB.
IT'S A CALLING.
Find your next job at ScienceCareers.org
Whether you're looking to get ahead, get into, or just plain get advice about careers in science, there's no better or more trusted authority. Get the scoop, stay in the loop with *Science* Careers.
ScienceCareers
FROM THE JOURNAL SCIENCE AAAS

By **Matthew Jordan Dean**

Sustained by science

When the master's student in my lab was selected to give an oral presentation at a conference, I was thrilled. I had started my faculty position 2 years earlier, and this was the first time we could share our results in this type of venue. It was a milestone for our new lab, and deserved recognition for my student. But the moment was bittersweet. I could not attend. I would be in the hospital, undergoing a stem cell transplant to treat my metastatic brain cancer. Still, thinking of my student's progress and my lab's work offered a welcome bright spot. It was one of many times when my love of research and teaching—together with supportive colleagues and family—helped me through my diagnosis and treatment.

When I started my faculty job, things couldn't have been better. The position offered the right mix of teaching and research at an institution with many wonderful colleagues. My wife and I decided to buy a house and start a family. Even when COVID-19 hit and I had to shut down my lab after barely getting it off the ground, I was sure things would soon be back on track.

But a few months later, I developed shortness of breath that forced me to go to the hospital. A CT scan revealed a large mass in my chest. I had cancer. That night, I sat in the hospital bed and cried, wondering whether I would get to meet my unborn daughter.

Over the next few days, I went through a battery of scans and tests. I was diagnosed with lymphoma and immediately started chemotherapy. After a 3-week hospital stay—during which my wife couldn't visit because of COVID-19 restrictions—I spent the rest of the summer alternating between 1 week in the hospital for chemotherapy and 1 week at home to recover.

Through it all, work offered a welcome distraction. During the weeks between treatments, I went to campus as much as I could. My weakened immune system meant I couldn't go into the lab or animal facilities, but I found solace and intellectual stimulation in talking with my students and colleagues, reading and writing papers and grant proposals, recording lectures, and writing exam questions for the class I was co-teaching. My graduate students pushed our research forward and excellent colleagues were happy to answer their questions and teach them when I could not.

About 6 months after my diagnosis, I was in remission. I was there when my daughter was born. Things seemed back to normal. Work no longer needed to serve as a distraction, but I still held a special appreciation for it after seeing how quickly and easily I could lose it all.

"Work remained an escape, a way to keep my mind off my cancer."

But this new normal didn't last. About a year after my initial diagnosis, I started to have headaches that became too severe to ignore. An MRI scan showed the cancer was back and had spread to my brain. I had more chemo, followed by the stem cell transplant.

It was hard to stay optimistic in the face of brain metastasis. But work remained an escape, a way to keep my mind off my cancer. I couldn't attend my master's student's presentation, but I had frequent virtual meetings with my students and wrote and submitted grant proposals and papers from my hospital bed. I went into my office when I was able and found respite in sitting at my desk, reading, writing, and thinking about my research. Thankfully, the treatments seem to have worked and I've now gone almost 2 years without a reoccurrence.

When I was first diagnosed, I hoped things would eventually get back to normal. I have now accepted that things will never be normal. Every ache or pain makes me wonder whether the cancer is back. The brain metastasis resulted in epilepsy, and each seizure leaves me depressed for several days. However, I've also learned to appreciate the wins more than ever. I missed my daughter's first birthday and first steps while I was in the hospital, yet I have gotten to see her learn to walk and talk. In another year, she and I will get to watch my wife defend her Ph.D. As for my lab, I'm grateful for every day I get to work with my amazing students and colleagues. And I'm grateful I have work I love to help sustain me through the hard times. ■

Matthew Jordan Dean is a professor at the University of Illinois Urbana-Champaign. Send your career story to SciCareerEditor@aaas.org.

ILLUSTRATION: ROBERT NEUBECKER

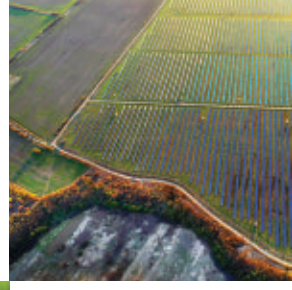

AAAS
IGNITING PROGRESS FOR
THE NEXT 175

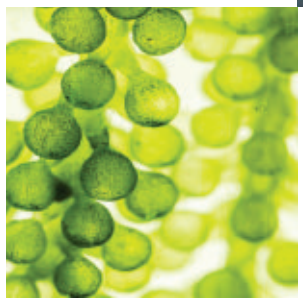

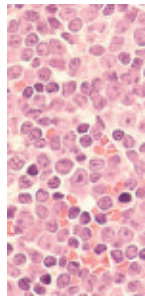

With Our Thanks

The American Association for the Advancement of Science gratefully thanks the individuals listed here whose leadership in giving fuels our work on behalf of science and society – including publishing the world's most advanced, innovative research and engaging in the issues that matter locally, nationally and around the world.

- Carolyn Ainslie
- Ersen Arseven
- David R. and Patricia D. Atkinson Foundation
- Neal Baer
- G. Leonard Baker, Jr. and Mary Ann Baker
- Reinier and Nancy Beeuwkes
- A. Christine Berger†
- Karen Sachs Besson Foundation
- Mani L. Bhaumik
- Kim Bleimann
- Fred A. and Diane F. Blum
- The Boger Family Foundation
- Ann and Doug Bostrom, *in memory of Sharon Dunwoody*
- The Brinson Foundation
- W. Ford Calhoun
- William H. Calvin and Katherine Graubard
- Marc A. and Linda M.A. Carrasco
- Janet Chen
- Steven Chu
- Roy Curtiss and Josephine Clark-Curtiss
- Troy E. and Leslie Daniels
- Gary and Denise David
- Louis S. Davis†
- Chris and Mary E. Diorio
- Albert T. Dosser
- Elizabeth E. Ehrenfeld
- Martin Elvis and Giuseppina Fabbiano
- Kaye Husbands Fealing and Burt Fealing
- Julie Fischer and Mark Lacy
- Bruce A. Fowler and Mary J. Sexton
- Claire M. Fraser
- Joseph W. Goodman
- Margaret A. Hamburg and Peter F. Brown
- Benjamin C. and Ruth† Hammett
- Daniel A. Hitchcock and Linda Arvin
- Michael W. Hunkapiller
- David W. Ignat
- Irwin and Joan Jacobs
- Arthur J. Kendall and Patricia A. Bulman
- Sadie E. Kendall
- Pauline P. Lee, *in memory of Bernard S. Lee*
- Alan and Agnes Leshner
- John J. McCarthy
- Bethany and Robert B. Millard
- Leo Model Foundation
- Gordon E.† and Betty I. Moore
- Thomas P. and Lydia Moran
- Sherie L. and Donald Morrison
- Kathryn Murdoch
- Gilbert S. Omenn and Martha A. Darling
- Sudip S. Parikh
- Babak Parviz
- Gregory A. Petsko and Laurie H. Glimcher
- Daniel Pinkel
- Julian† and Frieda† Reitman
- William and Eleanor Revelle
- Charles M. Rice III
- David A. and Janet H. Rice
- Juan and Beatriz† Roederer
- Rothrock Family Foundation
- Sapere Aude Fund
- Thomas D. Sharkey
- Leslie Sternlieb
- David M. Stonner
- Anne S. Tsui
- Jan T. and Marica Vilcek
- Christy R. Walton
- Michael S. Waterman
- Dyann F. and Peter K. Wirth
- Daniel L. Wulff
- Zakaria Family Foundation

These donors' pledges and contributions were received between January 1, 2022 and December 31, 2022.

† *Deceased*

To learn more about how a gift to AAAS can make a difference, visit us at aaas.org/support.

QUALITY CONTENT FOR THE GLOBAL SCIENTIFIC COMMUNITY

Multiple ways to stay informed on issues related to your research

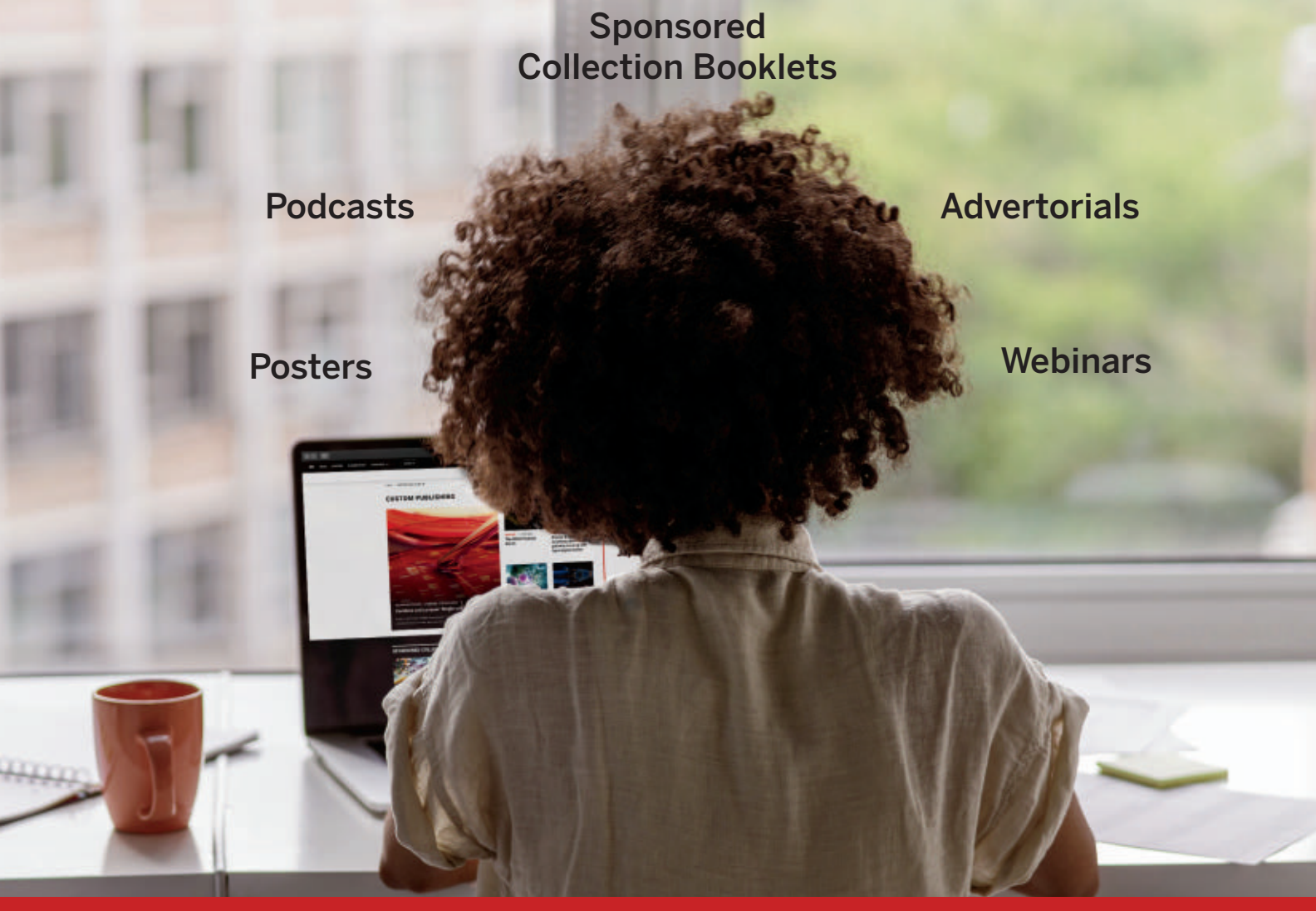

Science
AAAS

Scan the code and start exploring the latest advances in science and technology innovation!

Science.org/custom-publishing

Brought to you by the *Science*/AAAS Custom Publishing Office.

Posters **Podcasts** **Sponsored Collection Booklets** **Advertorials** **Webinars**